ULPGC Universidad de Las Palmas de Gran Canaria | Escuela de Doctorado

Programa de Doctorado en Calidad Ambiental y Recursos Naturales

Tesis Doctoral

ANÁLISIS MULTIESCALA DE MEZCLAS BINARIAS DE LÍQUIDOS IÓNICOS BASADOS EN EL CATIÓN IMIDAZOL Y DISOLVENTES EUTÉCTICOS PROFUNDOS DE ORIGEN NATURAL.

Ylenia F. Rodríguez Delgado

Las Palmas de Gran Canaria

2025

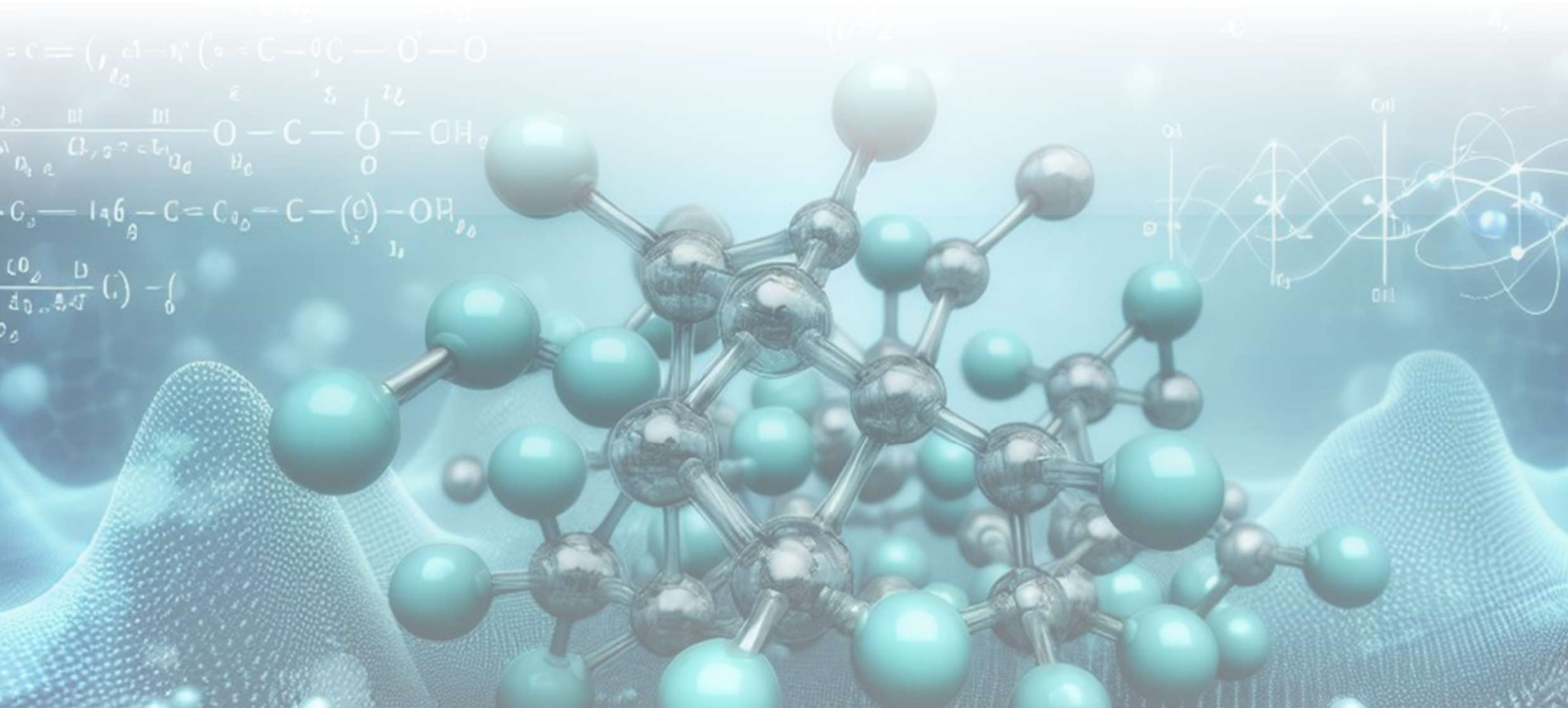

ANÁLISIS MULTIESCALA DE MEZCLAS BINARIAS DE LÍQUIDOS IÓNICOS BASADOS EN EL CATIÓN IMIDAZOL Y DISOLVENTES EUTÉCTICOS PROFUNDOS DE ORIGEN NATURAL.

Ylenia Fátima Rodríguez Delgado

ULPGC Universidad de Las Palmas de Gran Canaria | Escuela de Doctorado

DIRECTORES

Dr. José Luis Trenzado Diepa

Dr. Santiago Aparicio Martínez

Programa de Doctorado en Calidad Ambiental y Recursos

Naturales Las Palmas de Gran Canaria, abril 2025

UNIVERSIDAD DE LAS PALMAS DE GRAN CANARIA

UNIVERSIDAD DE LAS PALMAS DE GRAN CANARIA
ESCUELA DE DOCTORADO

Programa de doctorado Calidad Ambiental y Recursos Naturales

Título de la Tesis

Análisis multiescala de mezclas binarias de líquidos iónicos basados en el catión imidazol y disolventes eutécticos profundos de origen natural.

Tesis Doctoral presentada por Dª Ylenia Fátima Rodríguez Delgado

Dirigida por el Dr. D. José Luis Trenzado Diepa

Codirigida por el Dr. D. Santiago Aparicio Martínez

El Director, **El Codirector** **La Doctoranda,**

Las Palmas de Gran Canaria, a 13 de marzo de 2025

She believed
she could
so she did it.

Siempre acabamos llegando a donde nos esperan.

José Saramago (El viaje del elefante, 2008)

Agradecimientos

Me gustaría expresar mi más sincero agradecimiento:

A José Luis, primero amigo y luego director, por apoyarme, animarme y guiarme, en particular durante el desarrollo de esta tesis y en general durante todos estos años. Gracias por todo.

A Santiago Aparicio, por haber compartido su conocimiento y experiencia a lo largo de este camino académico. Su aportación y compromiso han sido pilares fundamentales en el desarrollo de este trabajo.

A Chuso, Héctor y Emilio, por su inestimable ayuda, su atención y su paciencia conmigo.

A mis amigos, los de siempre y los nuevos, por su interés, sus palabras de aliento y por celebrar conmigo cada pequeño avance.

A mi familia, por su amor, comprensión y apoyo incondicional, y por confiar en mí incluso cuando ni yo misma lo hacía.

Abstract

Los líquidos iónicos y los disolventes eutécticos profundos representan una clase emergente de solventes que han ganado considerable atención debido a sus propiedades únicas y su potencial en aplicaciones sostenibles. En este trabajo de investigación se estudian las propiedades de mezclas binarias de líquidos iónicos con catión común imidazol ([EMIM][BF_4] + [EMIM][$EtSO_4$], [EMIM][$EtSO_4$] + [EMIM][$MeSO_3$] y [EMIM][BF_4] + [EMIM][$MeSO_3$]) y disolventes eutécticos profundos formados por componentes de origen natural (HBD: ácido decanoico, ácido tetradecanoico, ácido octadecanoico, ácido (Z)-9-octadecenoico y ácido (Z,Z)-9,12-octadecadienoico; y HBA: mentol, timol, eucaliptol, D-carvone y geraniol).

En este trabajo se integran de manera sinérgica técnicas experimentales y computacionales con el objetivo de analizar en profundidad la complejidad de las interacciones que rigen las propiedades de estas mezclas. De manera experimental, estas mezclas se caracterizaron mediante el análisis de propiedades termofísicas como son la densidad y la viscosidad, en función de su composición y la temperatura. Además, se tuvieron en cuenta las desviaciones de la idealidad y las propiedades de mezcla. A través del uso de métodos computaciones de mecánica cuántica y dinámica molecular, se llevaron a cabo simulaciones moleculares que aportaron información sobre las interacciones intermoleculares, incluido el comportamiento de los enlaces de hidrógeno y los efectos estéricos, en análisis de la difusión de los aniones en las diferentes interfaces o inferir los diferentes mecanismos de agregación. Este estudio multiescala proporciona una caracterización global de estas mezclas, aportando información que contribuye en la optimización del diseño de estos disolventes emergentes.

Índice

Capítulo 1 - Introducción 17

1.1. Introducción 19

1.2. Objetivos 21

1.3. Justificación y estructura del trabajo 23

Capítulo 2 - Background 25

2.1. Líquidos iónicos 27

2.1.1. Clasificación 31

2.1.2. Propiedades 36

2.1.3. Aplicaciones 43

2.1.4. Sistemas considerados en la tesis 49

2.2. Disolventes Eutécticos Profundos 53

2.2.1. Classification 57

2.2.2. Propiedades 60

2.2.3. Aplicaciones 67

2.2.4. Sistemas considerados en la tesis 72

Capítulo 3 - Metodología 79

3.1. Experimental 81

3.1.1. Preparación de las muestras 81

3.1.2. Densidad 82

3.1.3. Viscosidad 85

3.1.4. Propiedades termofísicas analizadas 91

3.1.5. Correlaciones y modelos 94

3.2. Métodos computacionales 96

3.2.1. Mecánica cuántica (QM) 96

3.2.2. Mecánica molecular (MM). 106

Capítulo 4 - Consistencia de las publicaciones 117

4.1. Consistencia de las publicaciones 119

Capítulo 5 - Publicaciones 123

5.1. Publicaciones líquidos iónicos 125

5.1.1. Publicación 0 125

5.1.2. Publicación I 155

5.1.3. Publicación II 187

5.1.4. Publicación III 217

5.2. Publicaciones DES 271

5.2.1. Publicación IV 271
5.2.2. Publicación V 293
Capítulo 6 - Conclusiones y líneas futuras 341
6.1. Conclusiones 343
6.2. Líneas de investigación futuras 347
Capítulo 7 - Referencias 349
Anexo I - Geles DSILs 367
I. Estudio [EMIM][TSFI] + [EMIM][$MeSO_3$] 370
II. Estudio [EMIM][TSFI] + [EMIM][$EtSO_4$] 376

Lista de publicaciones

Publicación 0	J. L. Trenzado, Y. Rodríguez, A. Gutiérrez, A. Cincotti, S. Aparicio, Experimental and molecular modeling study on the binary mixtures of [EMIM][BF_4] and [EMIM][TFSI] ionic liquids, Journal of Molecular Liquids, 334 (2021) 116049.
Publicación I	Y. Rodríguez, S. Aparicio, J. L. Trenzado, Properties and intermolecular forces of ionic liquid mixtures: the archetypical case of [EMIM][BF_4] + [EMIM][$EtSO_4$], Industrial & Engineering Chemistry Research, 64 (2025) 1774−1791.
Publicación II	Y. Rodríguez, S. Aparicio, J. L. Trenzado, Unveiling the Intermolecular Forces and Unique Properties of [EMIM][$EtSO_4$] + [EMIM][$MeSO_3$], Journal of Molecular Liquids, 418 (2025) 126395.
Publicación III	Y. Rodríguez, S. Aparicio, J. L. Trenzado, Alkylimidazolium-based Ionic Liquid Mixtures: the case of [EMIM][BF_4] + [EMIM][$MeSO_3$], Journal of Molecular Liquids. *En revisión*.
Publicación IV	Y. Rodríguez, C. Benito, S. Aparicio, J. L. Trenzado, Unveiling the high-pressure behavior of Thymol + Carvone NADES: a combined experimental-computational approach, Journal of Supercritical Fluids, 215 (2025) 106408.
Publicación V	Y. Rodríguez, S. Aparicio, J. L. Trenzado, Harnessing nature's building blocks: Deep Eutectic Solvents derived from monoterpenoids and fatty acids, Journal of Chemical Physics. *En revisión.*

Lista de abreviaturas

ADF	Funciones De Distribución Angular
AIL	Líquidos Iónicos Apróticos
$[BF_4]^-$	Anión Tetrafluoroborato
C10AC	Ácido decanoico / Ácido Cáprico
C14AC	Ácido tetradecanoico / Ácido Mirístico
C18AC	Ácido octadecanoico / Ácido Esteárico
C18AC	Ácido (Z)-9-octadecenoico / Ácido Oléico
C18AC	Ácido (Z,Z)-9,12-octadecadienoico / Ácido Linoléico
CAR	D-Carvone
CAS	Chemical Abstracts Service
CDF	Función De Distribución Combinada
CIN	Eucaliptol
$[C_nMIM]^+$	Catión 1–Alquil$_n$–3–Metilimidazolio
CP	Puntos Críticos
CVB	Bifurcación Núcleo-Valencia
DDF	Funciones De Distribución Diédrica
DES	Disolventes Eutécticos Profundos
DFT	Teoría Del Funcional De La Densidad
DSILs	Líquidos Iónicos Doble Sal
ELF	Función De Localización De Electrones
$[EMIM]^+$	Catión 1-Etil-3-Metilimidazol
$[EMIM][BF_4]$	1-Etil-3-Metilimidazol Tetrafluoroborato
[EMIM][Cl]	Cloruro De 1-Etil-3-Metilimidazol
$[EMIM][ESO_4]$	1-Etil-3-Metilimidazol Etilsulfato
$[EMIM][MeSO_3]$	1-Etil-3-Metilimidazol Metanosulfonato
[EMIM][TSFI]	1-Etil-3-Metilimidazol Bis(Trifluorometilsulfonil)Imida
EOR	Recuperación Mejorada De Combustibles Fósiles
GER	Geraniol
GGA	Aproximaciones Generalizadas Del Gradiente
HBA	Compuesto Aceptor De Enlace De Hidrógeno
HBD	Compuesto Donador De Enlaces De Hidrógeno
HDES	DES Hidrófobos

IL	Líquido Iónico
LDA	Aproximación Local De La Densidad
MD	Dinámica Molecular
MEN	Mentol
MSD	Desplazamiento Cuadrático Medio
NADES	Disolventes Eutécticos Profundos De Origen Natural
NSAID	Fármacos Antiinflamatorios No Esteroideos
PBC	Condiciones De Límite Periódicas
PILs	Líquidos Iónicos Próticos
QAS	Sal De Amonio Cuaternario
QM	Mecánica Cuántica
QTAIM	Teoría Cuántica De Átomos En Moléculas
ρ	Densidad
RDF	Funciones De Distribución Radial
RDG	Gradiente De La Densidad Electrónica Reducido
RTIL	Líquidos Iónicos A Temperatura Ambiente
$[TSFI]^-$/$[Tf2N]^-$	Anión Bis(Trifluorometilsulfonil)Imida
SDF	Funciones De Distribución Espacial
THY	Timol
x	Fracción Molar
ν	Viscosidad Cinemática
VDF	Funciones De Distribución De La Velocidad
η	Viscosidad Dinámica
VFT	Vogel-Fulcher-Tammann
V^E	Volumen Molar De Exceso
VOC	Compuestos Orgánicos Volátiles

Capítulo 1
Introducción

1.1. Introducción

La Química Verde se define como el «*diseño de productos y procesos químicos para reducir o eliminar el uso y la generación de sustancias peligrosas*». Esta definición y el propio concepto de Química Verde se formularon por primera vez a principios de la década de 1990 (Anastas et al., 2010). Desde entonces, ha dado lugar a la creación de numerosos programas e iniciativas enfocadas al diseño de alternativas sostenibles. Una de las áreas más activas dentro del campo de la Química Verde es el desarrollo de disolventes sostenibles (Figura 1). Esto implica un desafío considerable, dado que el empleo de disolventes constituye, en la mayoría de los casos, la principal fuente de residuos en los procesos. El diseño de procesos libres de disolventes sería ideal; no obstante, resultan inevitables debido a su función esencial en las diferentes etapas como la disolución, la separación o la transferencia de calor; así como medio de reacción o subproducto. En este contexto, el diseño de disolventes sostenibles que permitan continuar avanzando tecnológicamente, pero que, de forma paralela e indispensable, sean respetuosos con el medioambiente, se ha convertido en un objetivo prioritario para la Química Verde (Espino et al., 2016).

Figura 1. Características de un disolvente verde. Adaptado de la referencia (Chen et al., 2021).

Hasta aproximadamente inicios del siglo XXI, la mayoría de los disolventes contemplados para su utilización en reacciones químicas eran disolventes moleculares (Earle et al., 2000). En primer lugar, eminentemente medios acuosos y a medida que se producía cierto avance industrial, comenzaron a estudiarse los compuestos orgánicos volátiles, más conocidos por sus siglas en inglés VOC (*Volatile Organic Compounds*), como nuevos disolventes que rompieron algunas de las barreras que presentaba el medio acuoso. En el siglo XIX, Friedrich Wöhler y Justus von Liebig contribuyeron en gran medida a la comprensión de la química orgánica y la clasificación de los VOC (Wöhler et al., 1838). Estos permitían aumentar la eficiencia de algunas reacciones y mejorar la industrialización de determinados productos, sin embargo, años más tarde comenzaron a manifestarse las consecuencias toxicológicas y medioambientales de la utilización de este tipo de disolventes, la mayoría de ellos regulados o incluso prohibidos hoy en día (Y. Chen

et al., 2021). La búsqueda de una alternativa a los VOC era continúa, hasta que hace varias décadas la comunidad científica centra su atención en los Líquidos Iónicos, ILs (por sus siglas en inglés *Ionic Liquids*). Este novedoso tipo de disolvente obtuvo gran relevancia en muy poco tiempo debido a sus ventajosas propiedades frente a los disolventes tradicionales. Su característica principal es que sus propiedades pueden ser diseñadas según los requisitos de su aplicación final mediante la correcta combinación de cationes y aniones. El abanico de posibilidades que brindan los líquidos iónicos los ha postulado como los disolventes preferidos para el estudio de múltiples aplicaciones. Sin embargo, aunque las ventajas que presentan son indiscutibles, existen algunos puntos que aún quedan por perfilar, como es su verdadera categorización como disolventes "verdes", debido a su baja biodegradabilidad, biocompatibilidad o sostenibilidad, en algunos casos (Paiva et al., 2014). Es por ello que, como alternativa a los ILs, surgen los Disolventes Eutécticos Profundos, más conocidos como DES (por sus siglas en inglés *Deep Eutectic Solvents*). Consisten en combinaciones de dos o más componentes cuya mezcla presenta un punto de fusión más bajo que el de cada uno de los componentes por separado. Estos mantienen la ventaja principal de poder ser diseñados de manera óptima según la combinación de sus componentes, pero solventan muchos de los problemas que plantean los líquidos iónicos relacionados con su toxicidad y su coste.

Ambos tipos de solventes han demostrado ser prometedores; no obstante, a pesar de las ventajas de los ILs y los DES, no significa que se puedan considerar disolventes perfectos. De hecho, presentan ciertos inconvenientes, como estabilidad baja o moderada, algunos de ellos alta higroscopicidad o elevada viscosidad (Figura 2). Esto no debe pasarse por alto, ya que pueden continuar siendo mejorados mediante un diseño adecuado (Chen et al., 2021).

Figura 2. Retos para mejorar el diseño de ILs y DES . Adaptado de la referencia (Chen et al., 2021).

A pesar de los progresos en la investigación de IL y DES, la comprensión total de sus propiedades fisicoquímicas y su comportamiento a distintas escalas sigue planteando desafíos. Debido al alto número de combinaciones posibles que pueden dar lugar a uno de estos disolventes, la determinación experimental de sus propiedades puede resultar una tarea larga y costosa. Es por lo que se vuelve imprescindible el desarrollo de enfoques teóricos predictivos que permitan seleccionar la combinación estructural adecuada para adaptar con precisión sus propiedades físicas (Izgorodina, 2011). Además, la complejidad intrínseca debido a la diversidad de interacciones intermoleculares que ocurren en estos sistemas dificulta las interpretaciones moleculares y da lugar a muchas especulaciones (Weingärtner, 2008). Estas interacciones, que incluyen fuerzas iónicas, puentes de hidrógeno y fuerzas de Van der Waals, influyen en las propiedades macroscópicas de las mezclas, tales como la viscosidad, la conductividad y la solubilidad. Las configuraciones estructurales y las dinámicas moleculares a nivel microscópico desempeñan un papel fundamental en la determinación de las propiedades de las mezclas.

Esta complejidad hace que la caracterización de estas mezclas líquidas puede enfocarse desde varios niveles: desde una perspectiva molecular hasta una escala macroscópica. Este enfoque integra métodos experimentales avanzados con técnicas de simulación computacional para proporcionar una visión comprensiva y detallada de los sistemas estudiados. La escala macroscópica se orienta hacia el análisis de datos empíricos de diversas propiedades físicas con el objetivo de calcular, entre otros, los valores de las magnitudes termodinámicas de exceso, lo cual brinda una visión general de las interacciones moleculares presentes en las mezclas líquidas. El análisis microscópico se aborda con la ayuda de la química computacional, una rama de la química en la que se incorporan a programas informáticos modelos químicos teóricos con el fin de calcular las estructuras y propiedades de modelos moleculares. Este análisis multiescala es una herramienta tremendamente útil para abordar la complejidad molecular que presentan las mezclas de estos líquidos, permitiendo la formulación de modelos teóricos que puedan predecir sus propiedades. Este enfoque acelera el descubrimiento de nuevos materiales, además de facilitar la optimización de los ya conocidos, lo que ofrece valiosas perspectivas sobre la química verde y los avances tecnológicos que permitan desarrollar soluciones sostenibles y energéticamente eficientes a problemas globales.

1.2. Objetivos

Aunque se han logrado avances significativos en el conocimiento de los ILs y los DES durante las últimas décadas, sigue siendo un desafío el entendimiento profundo de sus propiedades fisicoquímicas, el comportamiento de sus interacciones y sus mecanismos de acción a diferentes escalas. Por lo que la presente tesis plantea varios objetivos multinivel:

- El interés que han despertado estos líquidos ha provocado que la literatura disponible sobre los mismos haya crecido exponencialmente en las últimas décadas. Sin embargo, los artículos disponibles sobre las propiedades y el comportamiento de las mezclas

binarias de ILs y DES, continúan siendo relativamente escasos. Se plantea como uno de los objetivos contribuir a la bibliografía ya existente sobre estos líquidos y sus mezclas, aportando nuevos datos que sirvan de punto de partida para realizar futuras investigaciones.

- Se plantea como objetivo la determinación experimental de propiedades fundamentales en la caracterización física de los componentes puros y las mezclas binarias. Se propone determinar experimentalmente los valores de la densidad y la viscosidad cinemática, en todo el intervalo de composiciones a presión atmosférica normal, en un rango de temperaturas comprendido entre 283.15 K y 313.15 K (en saltos de 5.00 K). Además de determinar, por derivación analítica, otras propiedades termodinámicas, como son las funciones de exceso, la desviación de la viscosidad o el coeficiente de expansión térmica isobárico.

- También se ha establecido como objetivo analizar la influencia de la composición y de la temperatura en las propiedades mencionadas previamente, y en otras propiedades derivadas que están estrechamente relacionadas con la estructura de estos líquidos y sus interacciones intermoleculares. Así como, estudiar el ajuste a modelos conocidos como Redlich y Kister o Vogel-Fulcher-Tammann (VFT).

- Otro de los objetivos propuestos en este estudio consiste en modelar y predecir de manera precisa el comportamiento a escala nanoscópica de estos sistemas, mediante un análisis exhaustivo de las interacciones moleculares para lograr una comprensión precisa de la relación entre la estructura y las propiedades. Con este fin, se plantea emplear una combinación de métodos computacionales cuánticos y clásicos, como la teoría del funcional de la densidad, DFT (del inglés *Density Functional Theory*) o simulaciones en dinámica molecular, MD (del inglés *Molecular Dynamics*). A través de la comparación de los resultados obtenidos *in silico* con las mediciones experimentales (propiedades macroscópicas) llevadas a cabo, se podrá validar la información nanoscópica deducida a partir de los estudios teóricos, relacionando este comportamiento microscópico con sus propiedades fisicoquímicas macroscópicas.

A nivel general el objetivo de la tesis consiste en el análisis multiescala de mezclas binarias de ILs y DES, mediante la determinación experimental de sus propiedades físicas macroscópicas, y la realización de un análisis microscópico de sus estructuras y comportamientos a través de métodos computacionales. Mediante el empleo de estos métodos se logra predecir y comprender las propiedades estructurales y termodinámicas de estas mezclas con gran precisión y eficiencia. Esto permite lograr grandes avances en el conocimiento fundamental de estos sistemas, identificando con mayor facilidad mejoras y nuevas oportunidades para su aplicación en procesos industriales sostenibles y tecnológicamente relevantes

1.3. Justificación y estructura del trabajo

Hay una amplia cantidad de estudios sobre ILs y DES. Sin embargo, en cuanto a la naturaleza de los líquidos estudiados, la mayoría de ellos se centran en investigaciones sobre ILs puros o en combinación con otros disolventes. No hay gran cantidad de estudios que analicen el comportamiento de las mezclas binarias compuestas por dos tipos de ILs, mezclas que se conocen como DSILs (por sus siglas en ingles *Double Salt Ionic Liquids*). Por otro lado, los DES son un tipo de disolvente más reciente y menos explorado, especialmente los DES de origen natural, más conocidos como NADES (por sus siglas en inglés *Natural Deep Eutectic Solvents*) objeto de este trabajo. Como ya se ha mencionado anteriormente, debido a sus características, estos líquidos han suscitado gran interés en las últimas décadas debido al auge de la búsqueda de alternativas más sostenibles a los solventes tradicionales. En lo que respecta al campo de investigación, se han llevado a cabo numerosos estudios tanto experimentales (propiedades macroscópicas) como teóricos (propiedades microscópicas). Sin embargo, los estudios que combinan ambos enfoques aún son escasos. La complejidad de estos estudios a múltiples escalas, junto con los recursos necesarios para llevarlos a cabo, limita su aplicación principalmente a líquidos con composiciones de alto interés industrial.

Por lo tanto, el principal objetivo de este trabajo consiste en modelar y predecir con precisión el comportamiento de diversos tipos de sistemas, basados fundamentalmente en DSILs y NADES, combinando mediciones experimentales con un enfoque *in silico*. En primer lugar, se eligen una serie de combinaciones iniciales para ambos tipos de líquidos que implican varios cambios estructurales. Para los sistemas definidos, se llevan a cabo mediciones experimentales con las que se determinan las propiedades macroscópicas de estas mezclas. Además, se ejecutan simulaciones con el fin de obtener datos precisos sobre las propiedades energéticas y estructurales de las mismas Posteriormente, se llevan a cabo simulaciones de MD para obtener una visión más detallada del mecanismo de interacción entre las distintas moléculas de los sistemas analizados, así como de sus principales propiedades microscópicas. Finalmente, se comparan los resultados obtenidos *in silico* con las mediciones experimentales, lo cual permite tanto mejorar la metodología de diseño *in silico* como validar adecuadamente la información deducida a partir de los estudios experimentales.

Esta tesis doctoral se presenta como un compendio de publicaciones en diferentes revistas científicas, recogiendo 4 trabajos ya publicados y 2 pendientes de publicación, en revistas que se han mantenido durante los últimos años en el primer y segundo cuartil (Q1, Q2) del ranking del Journal Citation Reports (JCR). Además, de recoger la colección de artículos publicados, el presente documento consta de 7 capítulos y un anexo. En primer lugar, el presente capítulo da lugar a la introducción del tema y la motivación de la investigación, además de ofrecer una breve descripción de la organización y estructura del documento. En el segundo capítulo, se realiza una contextualización según la tipología de mezcla, detallando sus propiedades y aplicaciones, entre otros aspectos. A continuación, en el tercer capítulo, se detalla la metodología aplicada en el

estudio experimental, así como en los estudios *in silico*. En el capítulo cuarto, se realiza un análisis de la conexión de los artículos y se relacionan con las publicaciones individuales. Posteriormente, en el capítulo número cinco, se recopila la colección de artículos relacionados manteniendo su formato de revista, junto con los resultados experimentales obtenidos. En el sexto capítulo se presentan las conclusiones generales de la investigación realizada, así como las líneas de investigación futuras deducidas durante su desarrollo. El séptimo y último capítulo recoge las referencias bibliográficas citadas a lo largo del documento. Finalmente, se incluye un anexo en el que documenta una sección del trabajo experimental realizado, en el cual se obtuvieron resultados inesperados con respecto al comportamiento habitual de las mezclas líquidas. Estos hallazgos son significativos, ya que ponen de manifiesto un nuevo camino para futuras investigaciones.

Capítulo 2
Background

2.1. Líquidos iónicos

Teniendo en cuenta su evolución en el último siglo, los líquidos iónicos se presentan como uno de los campos de investigación más prometedores de la química actual. Una de las características principales de estos solventes es que su estructura está formada exclusivamente por iones, a diferencia de los disolventes convencionales, compuestos en su totalidad por moléculas (por ejemplo, agua o compuestos orgánicos volátiles). Además, para poder considerar un líquido iónico como tal, estos han de presentarse en estado líquido a temperaturas inferiores a 100 °C (Singh et al., 2020). La primera publicación sobre líquidos iónicos de la que se tiene constancia está registrada en 1914, cuando Paul Walden publicó por primera vez información relacionada con la síntesis del nitrato de etilamonio (Walden, 1914). Los ILs de primera generación, a pesar de poseer múltiples ventajas frente al comportamiento habitual de los disolventes convencionales, presentaban inestabilidad en presencia de aire y agua, lo que retrasó su progreso y desarrollo. En la década de 1990, Wilkes y Zaworoto dieron el primer paso hacia los líquidos iónicos de segunda generación, más fáciles de manejar que sus predecesores. En su trabajo, presentaron por primera vez el tetrafluoroborato de 1-etil-3-metil-imidazolio como sal líquida estable al aire y al agua (Wilkes et al., 1992). Recientemente, la tercera generación de ILs, identificada como «tarea específica» (en inglés *task-specific*), ha ganado terreno en términos de popularidad debido a la posibilidad de diseñar las propiedades de estos líquidos acorde a los requerimientos de una aplicación específica (

Figura *3*). En 1998, Michael Freemantle introdujo la idea del «disolvente de diseño» en algunos artículos publicados en *Chemical & Engineering News*. Este concepto se fundamentaba en la noción de que se dispone de un vasto abanico de combinaciones posibles entre cationes y aniones, lo que da lugar un enorme número de líquidos iónicos potenciales (Freemantle, 1998). Se ha estimado que existen aproximadamente 10^{18} posibles combinaciones de iones que pueden dar lugar a líquidos iónicos (por ahora, solo ha sido posible caracterizar alrededor de 1600). Este alto número de combinaciones permite desarrollar la idea de diseñar un líquido iónico con propiedades ideales para cualquier aplicación (Silva et al., 2020). La cantidad de artículos científicos sobre líquidos iónicos publicados ha experimentado un notable crecimiento, partiendo de un pequeño

número en 1996 y superando los 9000 en 2018 (Lei et al., 2017). Actualmente la base de datos SCOPUS cuenta con 6457 entradas que contienen documentos de investigación con el término «líquido iónico» indexado.

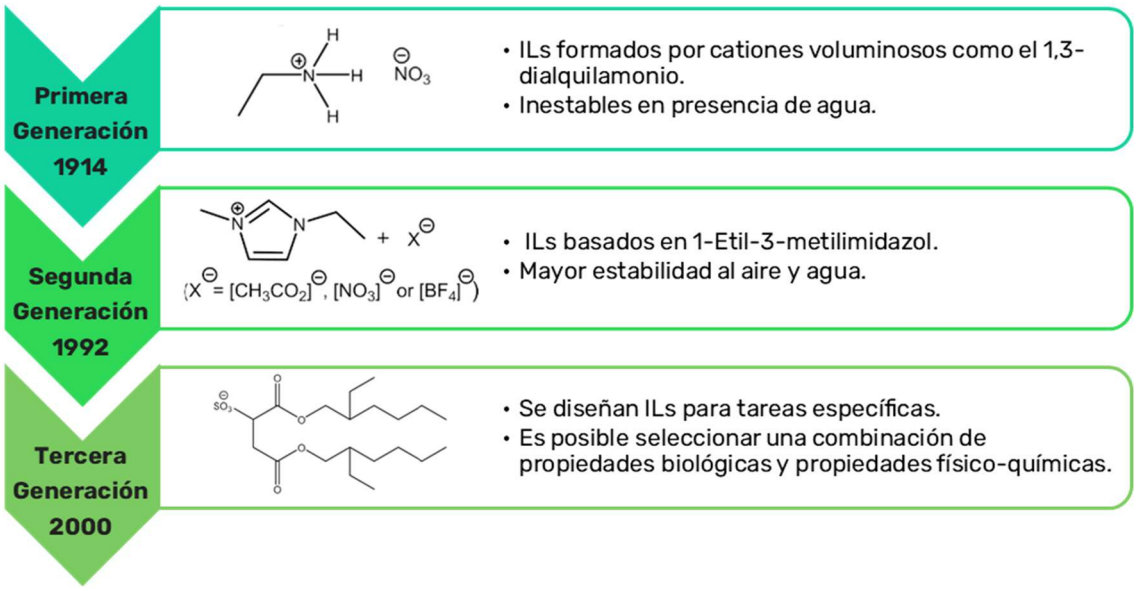

Figura 3. Esquema diferentes generaciones ILS. Adaptado de la referencia (Silva et al., 2020).

Sin embargo, independientemente de la combinación seleccionada, los líquidos iónicos presentan ciertas propiedades comunes como son presión de vapor extremadamente baja o casi nula volatilidad en condiciones ambiente, un amplio rango de trabajo en estado líquido, polaridad y conductividad ajustable, alto espectro de solubilidad según la combinación de sus iones, así como alta estabilidad térmica (Wang et al., 2017). Como ya se ha descrito, todas estas propiedades pueden modificarse o ajustarse con la selección adecuada del catión o anión que conforma la estructura del líquido iónico. Por ejemplo, Dong y sus colaboradores relacionan el aumento de la viscosidad con el incremento en la longitud de las cadenas alquílicas en el catión (Dong et al., 2017). Otra de las propiedades relacionadas con la selección del catión es la conductividad, se ha reportado la disminución de la conductividad con el aumento del volumen del catión (Ghandi, 2014). Por otra parte, las características físicas del anión también pueden afectar a propiedades como la densidad, la cual aumenta con la masa molecular del anión, o la estabilidad térmica, la cual aumenta con el tamaño del anión (Kong, 2009; Yadav et al., 2018). La relación entre las estructuras propias del catión y el anión seleccionado también impacta en las propiedades finales del líquido iónico. Por ejemplo, la asimetría entre los iones dificulta el proceso de cristalización lo que resulta en puntos

de fusión bajos; o una gran diferencia de tamaños entre los iones pueden influir en a viscosidad (Izgorodina, 2011; Philippi et al., 2021).

La mayoría de la literatura disponible hasta la actualidad se ha centrado en el análisis de los ILs puros, compuestos por un único tipo de catión y un único tipo de anión, en múltiples ocasiones en combinación con otro disolvente (Figura 4). Sin embargo, se puede conseguir una mayor variedad estructural a través de la combinación de más de un tipo de anión o catión, convirtiendo esta nueva combinación en una alternativa más para diseñar disolventes a medida.

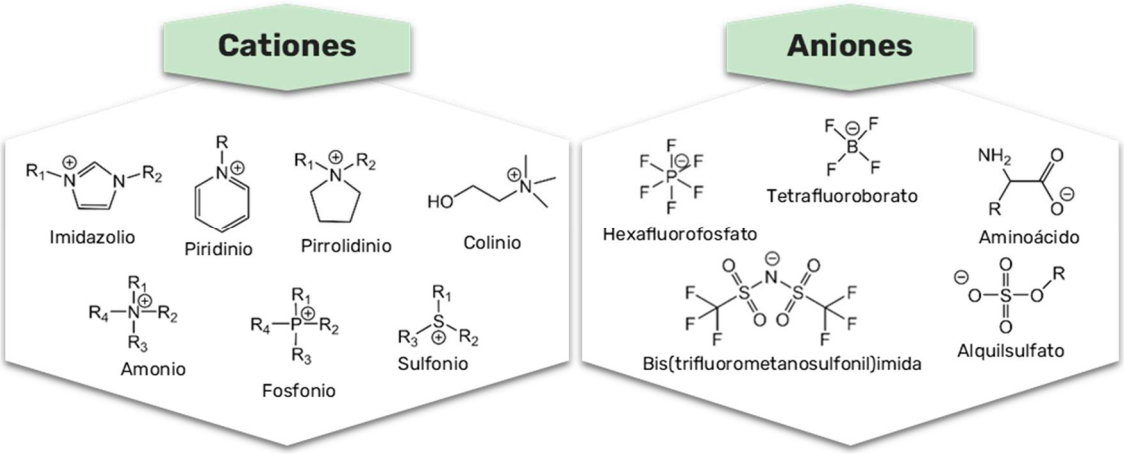

Figura 4. Ejemplos de cationes y aniones más comunes. Adaptado de la referencia (Silva et al., 2020).

Estos líquidos iónicos que contienen más de un catión o anión se denominan DSILs, estas mezclas suelen presentar propiedades interesantes y a menudo impredecibles (Chatel et al., 2014; Sappidi et al., 2021). Debido a la gran cantidad de posibles combinaciones, es fundamental comprender la organización molecular de los aniones y cationes e identificar correlaciones entre estructura y propiedades. Además, es necesario estudiar su relación con los solutos, su papel como soportes y otras aplicaciones, lo que requiere una estrecha integración de métodos experimentales, teóricos y computacionales. Un objetivo altamente deseable es el desarrollo de herramientas predictivas que faciliten el diseño de nuevos líquidos iónicos, ya que la posibilidad de combinar varios tipos de iones aumenta varios órdenes de magnitud las combinaciones potenciales. Sin embargo, la naturaleza compleja de las interacciones moleculares plantea un desafío importante para alcanzar este objetivo (Lei et al., 2017).

La verdadera ventaja de entender cómo la combinación catión-anión afecta a las propiedades de los líquidos iónicos, radica en la capacidad de ajustarse según el área de aplicación. Los ILs han demostrado ser de gran interés para una amplia gama de aplicaciones (Figura 5), tales como polímeros para membranas de separación de gases, agentes de separación para romper mezclas azeotrópicas, adsorbentes y separación de dióxido de carbono (Macfarlane et al., 2014; Ventura et al., 2017; Wang et al., 2013), electrolitos para baterías, electrolitos para supercondensadores electroquímicos (Sato et al., 2013), catalizadores y soportes de catalizadores (Zhang et al., 2011), lubricantes o aditivos (Xiao, 2017; Zhou et al., 2009; Zhou, 2017), aditivos antimicrobianos, y recientemente el desarrollo de productos farmacéuticos (Sappidi et al., 2021; Singh et al., 2020; Welton, 2018).

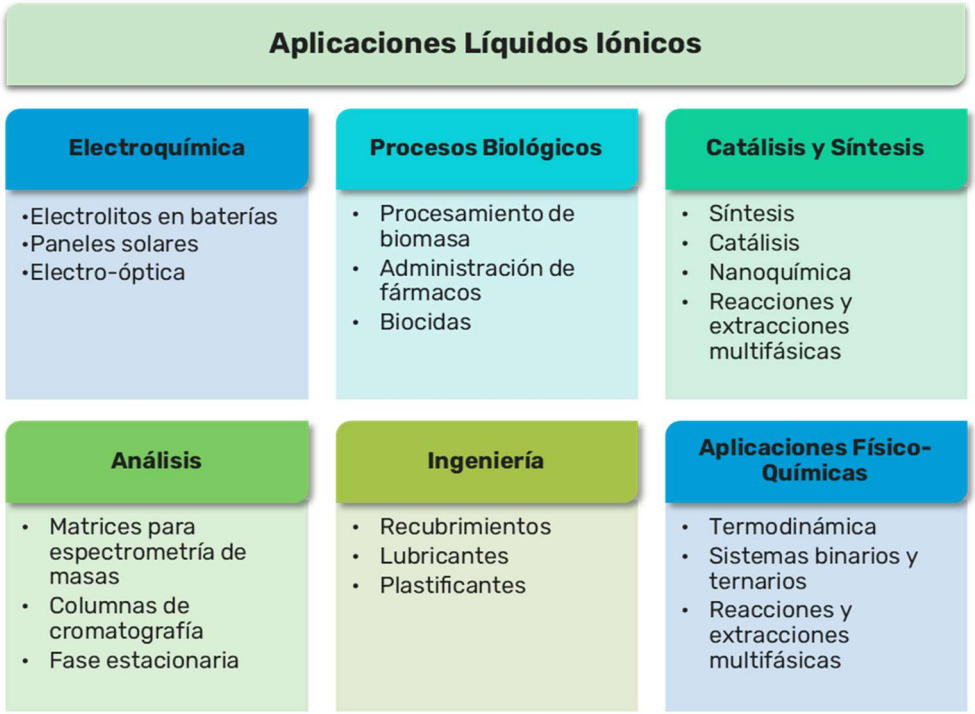

Figura 5. Algunas de las principales aplicaciones de los ILs. Adaptado de la referencia (Kar et al., 2019).

En el campo de la catálisis, los líquidos iónicos han surgido como una alternativa ecológica a los disolventes orgánicos (Zhang et al., 2011). Su baja volatilidad unida a su capacidad para disolver una amplia variedad de compuestos contribuye a mejorar la eficiencia y sostenibilidad de diversos procesos catalíticos. Además, estos han demostrado un gran potencial en aplicaciones electroquímicas, como electrolitos en baterías y supercondensadores, gracias a sus amplias ventanas electroquímicas y su baja

inflamabilidad (Zheng et al., 2022). Khupse y Kumar también llevaron a cabo un estudio sobre la utilización de líquidos iónicos en dispositivos electroquímicos, como supercondensadores, baterías de iones de litio o pilas de combustible de polímero electrolítico. Una de las principales ventajas encontradas fue su baja volatilidad, así como la prevención de la formación de electrolitos (W. Zhou et al., 2021). El concepto de IoNanofluidos, propuesto por Nieto de Castro y colaboradores, representa una nueva clase de líquidos en los que nanomateriales como partículas, tubos y varillas se dispersan en líquidos iónicos.

Los IoNanofluidos son una de las aplicaciones más recientes de los sistemas complejos de líquidos iónicos y nanomateriales, pudiendo ser utilizados en diversos campos como la transferencia de calor, la catálisis, lubricantes o materiales luminiscentes (Castro et al., 2013). Su aplicación en el campo farmacéutico también se ha extendido a numerosos procesos, desde la síntesis de fármacos hasta el desarrollo de nuevas formas de solubilización y dosificación de principios activos farmacéuticos (active pharmaceutical ingredients, API-ILs), investigándose también en otras etapas del desarrollo y administración de fármacos. La selección adecuada de las combinaciones anión/catión tiene un impacto significativo en el mecanismo de solubilización de los APIs poco solubles en agua (Pedro et al., 2020). Se debe considerar que también se han presentado ciertas críticas sobre la posible aplicación a gran escala de los ILs, basadas en la preocupación sobre propiedades fisicoquímicas inadecuadas (por ejemplo, alta viscosidad), toxicidad o escasa biodegradación. Sin embargo, muchos de estos posibles inconvenientes pueden evitarse mediante la selección adecuada de los iones que conforman los ILs entre la variedad de compuestos disponibles (Chen et al., 2021; Philippi et al., 2021).

2.1.1. Clasificación

Teniendo en cuenta el amplio abanico de líquidos iónicos que es posible encontrar, es complicado encontrar una única forma de clasificarlos. Las clasificaciones más comunes atienden a la naturaleza de sus iones, a su aplicación o a sus propiedades (Figura 6). En este trabajo se utiliza una de sus clasificaciones más populares, según si son donadores

de protones o próticos, PILs (del inglés *Protic Ionic Liquids*); o no donadores de protones o apróticos, AILs (del inglés *Aprotic Ionic Liquids*) (Aghaie et al., 2018).

Figura 6. Clasificación estructural de los ILS. Adaptado de la referencia (Singh et al., 2020).

2.1.1.1. Líquidos iónicos apróticos (AILs)

Estos líquidos iónicos no contienen protones transferibles entre el catión y el anión (Aghaie et al., 2018). Su estructura habitual está formada por cationes orgánicos que no pueden donar protones, como son los cationes imidazol. A estos líquidos iónicos se les atribuye el exponencial aumento de publicaciones a mediados de los 90. Además de cationes imidazol, otros frecuentemente utilizados en los AILs son cationes alquil piridinio o dialquil imidazolio (Austen et al., 2012). Estos suelen ser menos económicos que los líquidos iónicos próticos, tienen un perfil toxicológico más alto y peor biodegradabilidad. Por otra parte, su síntesis suele ser más compleja y consiste en dos etapas (Borja, 2015):

- **Formación del catión**: reacción de cuaternización de una amina o fosfina, principalmente con un haluro de alquilo o reacción de protonación con un ácido.

- **Reacción de intercambio aniónico**: tratamiento directo de las sales del haluro con ácidos de Lewis o reacciones de metátesis aniónica. La metátesis se refiere a un proceso en el cual se produce un intercambio de iones en una solución que contiene dos pares iónicos, lo que resulta en la formación del par de iones que es termodinámicamente más estable.

Una de las principales características que hacen a los AILs tan relevantes es su baja presión de vapor. Esta propiedad suele estar relacionada con su ionicidad (Austen et al., 2007). Aunque la baja volatilidad es una propiedad común de los AILs, existen algunos líquidos de este tipo en los que sí se ha reportado presiones de vapor relativamente altas, como es el caso de algunos tetrafluoroboratos de cationes apróticos. Las conductividades y viscosidades de los líquidos iónicos dependen de la temperatura como en el caso de los demás líquidos, pero en el caso de los AILs las energías de cohesión hace que el valor de estar propiedades sea demasiado alto, provocando que no favorezcan la utilización de estos en diversas aplicaciones (Austen et al., 2012).

2.1.1.2. Líquidos iónicos próticos (PILs) o sales de Brönsted

Estos líquidos iónicos poseen la capacidad de transferir un protón, es decir, pueden actuar tanto como donadores como aceptores de protones, lo que les confiere la capacidad de formar redes de enlaces de hidrógeno (Fumino et al., 2014). Esto hace que presenten características más interesantes que los AILs. Su síntesis es mucho más sencilla, ya que consiste en la transferencia de un protón desde un ácido de Brönsted hasta una base del mismo tipo (Greaves et al., 2008). Esto hace que su obtención sea más sencilla, más económica y más sostenible, ya que no implica la formación de subproductos. Los PILs suelen tener mayor conductividad y fluidez que los AILs, así como puntos de fusión más bajos (Ghandi, 2014).

Los PILs suelen tener mayor capacidad para formar una red de enlaces de hidrógeno, lo que limita su ionicidad en comparación con los AILs. Sin embargo, estas energías también pueden modificarse ajustando la transferencia de protones, obteniendo conductividades y volatilidades similares a los AILs (Austen et al., 2012). Otras de sus propiedades fisicoquímicas más características son baja presión de vapor, estabilidad electroquímica y no inflamabilidad, junto con la conducción de protones en condiciones anhidras.

También se ha demostrado que gracias a las polaridades que presentan los PILs y a su carácter hidrofílico, son mejores disolventes de sales metálicas que los AILs (Iida et al., 2011; Miran et al., 2011).

En lo que respecta a sus aplicaciones, son buenos candidatos para su uso en reacciones catalíticas que requieran aplicación de microondas, ya que son buenos absorbentes de estas (Ghandi, 2014), y otro tipo de reacciones como hidrolíticas o electroquímicas (Singh et al., 2020).

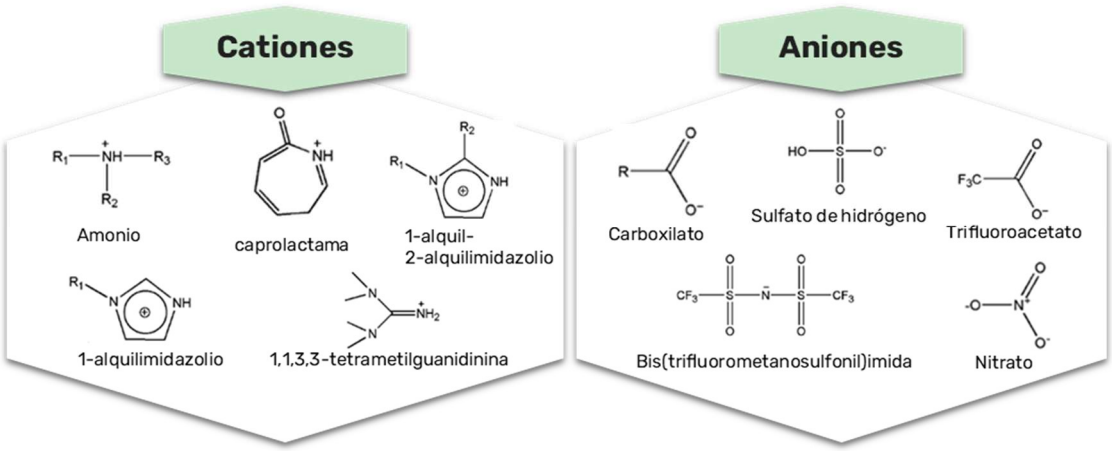

Figura 7. Cationes y aniones representativos en los PILs. Adaptado de la referencia (Greaves et al., 2008).

2.1.1.3. DSIL

Habitualmente la categorización que contempla la mayoría de la literatura existente se refiere a los «líquidos iónicos puros», es decir, ILs compuestos por la combinación de un único tipo de anión y un único tipo de catión. Además de como ILs puros, estos han sido estudiados en conjunto con múltiples alternativas de disolventes, como por ejemplo variando su contenido en agua (Gutiérrez et al., 2018), alcoholes (Hauk et al., 2023) y otros disolventes orgánicos (García-Miaja et al., 2009; González et al., 2018).

Sin embargo, existe una combinación no tan estudiada formada por la combinación de varios tipos de iones en la misma mezcla, conocida por sus siglas en inglés DSILs (*Double Salt Ionic Liquids*) (Chatel et al., 2014). Esta posibilidad puede conducir a una nueva estrategia de diseño de estos disolventes, ya que, el conjunto de posibles combinaciones se incrementa en varios órdenes de magnitud y las propiedades pueden afinarse más mediante la selección de los iones adecuados (García et al., 2015). Muchas propiedades de los DSILs dependen de la proporción de cada ion en la mezcla. Dado que las

estructuras y el comportamiento de los ILs están controlados por una serie de interacciones intermoleculares, entre las que se incluyen las fuerzas de Coulomb, las interacciones de dispersión, los enlaces de hidrógeno y las interacciones π (pi), la combinación de iones en un DSILs puede inducir una orientación preferente de las especies iónicas y sitios de interacción no covalentes, totalmente diferente a las que se encuentran en los ILs de un solo componente (Matthews et al., 2016; Niedermeyer et al., 2012). La ventaja de utilizar DSILs reside en poder seleccionar una combinación anión-catión más acertada con el objetivo de lograr unas propiedades más ajustadas a los requisitos de diseño. Por ejemplo, Pinto y su equipo observaron que la viscosidad de la mezcla $[C_2MIm][NTf_2]$ and $[C_4EIm][EtSO_4]$ varía de 32.6 to 255.2 mPas a medida que aumenta la fracción molar de $[C_4EIm][EtSO_4]$ (Pinto et al., 2014); o el caso de Lei y sus colaboradores, que observaron que la solubilidad del CO_2 en la mezcla $[C_8MIm]$ $[NTf_2]$ y $[C_nMIm][BF_4]$ (n = 2, 4) podía ser ajustada según la composición (Lei et al., 2012). Aunque las DSILs ofrecen ventajas significativas sobre los ILs clásicos, los estudios de los primeros son todavía escasos (Trenzado et al., 2021).

No obstante, aunque se han divulgado resultados relevantes y prometedores, todavía el número de trabajos publicados es escaso comparado con otras mezclas (Figura 8) Asimismo, el aumento de las posibles combinaciones hace necesario desarrollar una estrategia de análisis de las propiedades, dado que la determinación experimental de las propiedades de estas mezclas resulta inabarcable en un plazo de tiempo realista.

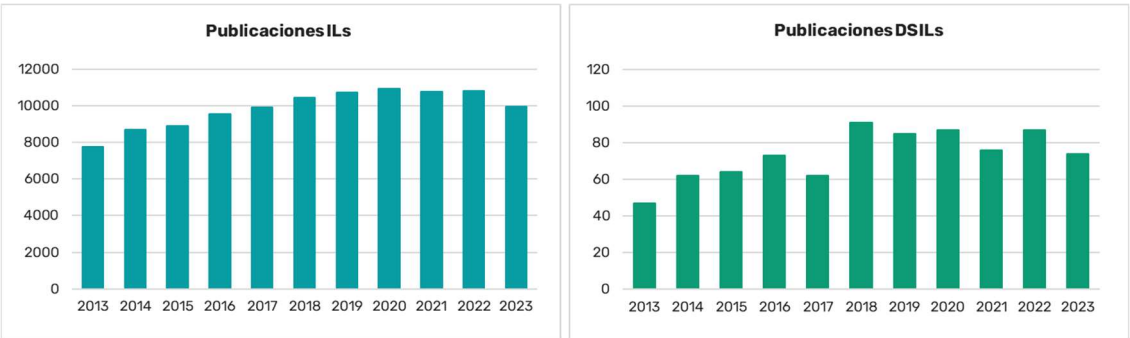

Figura 8. Evolución del número de publicaciones de ILs y DSILs en la última década (datos obtenidos de la ISI Web of Science, utilizando las palabras clave «Ionic Liquids» y «Double Salt Ionic Liquids», respectivamente).

2.1.2. Propiedades

Las propiedades de los líquidos iónicos están directa e intrínsecamente relacionadas con las características de los iones que los conforman. Por ejemplo, el tamaño del catión o la longitud de la cadena alquílica del mismo pueden influir en propiedades como la viscosidad o la temperatura de fusión. La humedad y la presencia de impurezas son otros factores que afectan su comportamiento. La amplia gama de combinaciones catión-anión hace que los líquidos iónicos puedan considerarse disolventes *tailor-made* (Zhao, 2006), es decir, que es posible diseñar sus propiedades finales mediante la selección de los iones, de tal forma que estas se ajusten lo máximo posible con las exigencias del proceso al que irá destinado.

Además de sus propiedades, hay otras variables que también influyen en la elección de un líquido iónico, como su coste y su toxicidad. El coste de los líquidos iónicos es aún demasiado elevado como para participar en los procesos industriales a gran escala y su implementación requeriría cambios en las instalaciones que implicarían costos adicionales. En cuanto a su toxicidad, debido a su baja volatilidad no parece que presenten ningún problema a la hora de trabajar con ellos, sin embargo, la toxicidad producto de la presencia de estos en medios acuáticos es un campo aún por estudiar.

A continuación, se realiza una revisión de las propiedades más analizadas de los líquidos iónicos.

2.1.2.1. Presión de vapor

Una de las propiedades más destacadas y relevantes de los líquidos iónicos es su reducida presión de vapor. Gran parte de la comunidad científica está de acuerdo en que su presión de vapor es tan baja que a temperatura ambiente se considera prácticamente indetectable, lo que permite clasificarlos como disolventes no volátiles (Weingärtner, 2008). Sin embargo, recientemente algunos autores han reportado que sí es posible medir la presión de vapor en algunos de estos líquidos (Yoshizawa et al., 2003). No obstante, existen pruebas contradictorias en la bibliografía sobre si la fase gaseosa de estos ILs está formada sólo por especies moleculares neutras o si coexisten agregados moleculares e iónicos. La tendencia general es que los AILs son muy poco volátiles,

mientras que los PILs tienen una volatilidad intermedia entre los AILs y los moleculares. En los AILs el emparejamiento de iones puede reducir el blindaje simétrico de la carga que es característico de una red cristalina iónica (energía de Madelung), es el componente que marca la diferencia entre la presión de vapor de un líquido molecular fuertemente polar y un PILs (mucho menos volátil). En un líquido iónico con baja presión de vapor, cada ion está rodeado por una pantalla uniforme de iones de carga opuesta, pero si la pantalla es demasiado simétrica, es probable que el punto de fusión sea demasiado elevado cumplir el criterio (Austen et al., 2012). En el caso de los líquidos iónicos apróticos, algunos de los cuales pueden destilarse al vacío sin descomponerse, la fase gaseosa consiste en pares de iones neutros (Greaves et al., 2008).

Las fuertes interacciones de Coulomb en estos líquidos anión-catión se reflejan en las presiones de vapor extremadamente bajas y las altas entalpías de vaporización (Fumino et al., 2014). El aumento de la longitud de las cadenas alquílicas de los iones también provoca un aumento de la presión de vapor (Marcus, 2016).

2.1.2.2. Densidad

Es una de las propiedades más medidas de los líquidos iónicos y de las esenciales a la hora de caracterizar nuevos compuestos, además de ser necesaria para determinar otras propiedades como la viscosidad dinámica. Por otro lado, esta propiedad también está directamente relacionada con la composición de la mezcla, una de sus aplicaciones más útiles es la determinación exacta de las fracciones molares de los componentes. La densidad es muy sensible a la temperatura o presencia de agua e impurezas en la mezcla. Habitualmente los ILs tienen una densidad mayor que la del agua, aunque generalmente la presencia de agua e impurezas tienda a disminuir sus valores. Esto se asocia con un debilitamiento producido en la red de puentes de hidrógeno y el aumento del volumen hueco en la estructura ante la presencia del contaminante.

Otros factores que influyen en la densidad es la relación entre los iones y su estructura. El volumen de los iones y su naturaleza determinan el tamaño del volumen libre en la mezcla y la forma en que se distribuye dentro del líquido, así que es posible predecir la densidad de una mezcla conociendo el tipo de anión y su volumen molecular (Silva et al., 2020). La simetría y la presencia de unidades cíclicas suelen aumentar la densidad,

ya que disminuyen los grados de libertad de las estructuras y por lo tanto su volumen libre entre ellas (Branco et al., 2011). En general podría afirmarse que la densidad de los líquidos iónicos disminuye cuando aumenta el volumen del catión. Sin embargo, con la longitud de la cadena del alquilo en el catión imidazolio suele disminuir sus valores (Kong, 2009) . En cuanto al anión, tanto el peso molecular del mismo como su especie afecta a la densidad. Para un catión dado, la densidad aumenta con el aumento de la masa molecular del anión y disminuye con la longitud de sus cadenas, excepto cuando en ellas aparecen átomos pesados como flúor (Wilkes et al., 1992; Zhao, 2006)

2.1.2.3. Viscosidad

La viscosidad es considerada una propiedad de transporte, ya que sucede cuando el sistema se encuentra fuera del equilibrio porque la materia o la energía presentan un transporte dentro del propio sistema o entre este y sus alrededores. Las fuerzas intermoleculares son responsables de la atracción entre moléculas. Al ejercer una determinada fuerza, estas presentan una resistencia a su movimiento respecto a las otras. La viscosidad es la magnitud que representa esta resistencia. En casos ideales, donde la viscosidad es cero, se interpreta que no existe resistencia a la fluidez de las moléculas, siendo el ejemplo más cercano el comportamiento de los gases. En el extremo opuesto se encuentran los sólidos, donde la rigidez de la estructura restringe totalmente el movimiento individual de las moléculas. En síntesis, la viscosidad de un fluido se puede definir como la oposición que presenta al fluir, lo cual refleja las fricciones internas propias del fluido. Así, el análisis de la viscosidad sobre líquidos proporciona datos sobre su respuesta ante una fuerza externa y las fuerzas intermoleculares. En general los líquidos iónicos presentan un comportamiento newtoniano y valores de viscosidad mayores que los disolventes convencionales.

Uno de los factores que más influyen en los valores de viscosidad es la temperatura, presentando un patrón más complejo en los ILs que en otros fluidos. Esta propiedad disminuye con el gradiente de temperatura, debido a la relación de esta variable con el movimiento de las moléculas. Un aumento en la temperatura conlleva a un incremento en la energía de las moléculas, lo que favorece su movimiento (Zhao, 2003). Un modelo extendido para determinar la evolución de la viscosidad es el modelo de Arrhenius,

cuando los resultados no se ajustan a este modelo se asocia a que la energía de activación no es constante en el intervalo de temperaturas (Petrowsky et al., 2013). La presencia de agua e impurezas también provoca grandes variaciones en la viscosidad de los líquidos iónicos: una concentración de 2 wt% de agua en el seno del líquido disminuye su viscosidad aproximadamente un 50%, mientras que impurezas de Cl^- entre 1,5 y 6 wt% la aumentan entre un 30 y un 600 % (Anthony et al., 2002). La disminución de la viscosidad con el incremento de la proporción de agua se asocia al debilitamiento y destrucción de los puentes de hidrógeno que participan en la estructura del líquido iónico (Zarrougui et al., 2015).

Así como en otras propiedades, la viscosidad se ve afectada por la naturaleza, tamaño y estructura de los iones. El tamaño de los iones no parece presentar una correlación directa con la viscosidad, parece estar más relacionado con su habilidad para formar puentes de hidrógeno y otras interacciones moleculares. Sin embargo, podría decirse que la estructura del anión suele tener un mayor efecto sobre la viscosidad que la del catión (Ghandi, 2014).

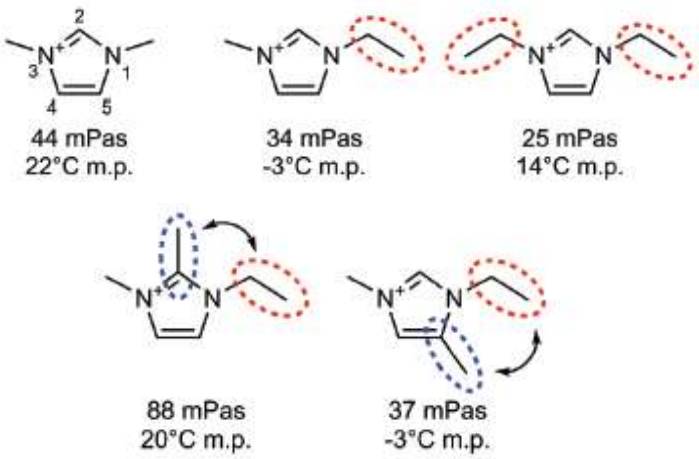

Figura 9. Variación de la viscosidad (20 °C) y el punto de fusión según la configuración de las cadenas alquílicas en el catión ($[NTf_2]^-$ como anión). Adaptado de la referencia (Philippi et al., 2021).

Para líquidos iónicos con el mismo anión se ha observado que cuanto mayor es el tamaño del catión y mayor es la longitud de la cadena de los sustituyentes en los anillos de imidazol, mayor es la viscosidad del fluido. Este incremento de la viscosidad se relaciona con que las fuerzas de interacción de Van der Waals en los agregados apolares son más fuertes al incrementar la cadena alquílica. Asimismo, el incremento del volumen de la

zona apolar aumenta los impedimentos para el movimiento. Por otro lado, el incremento de la viscosidad con la cadena alquílica también se explica parcialmente desde los dominios polares, donde se ha descrito un mayor número de puentes-H (Umapathi et al., 2014). Otro factor que contribuye es la simetría del catión: cuanto más asimétrico es el catión, menor viscosidad presenta el fluido (Salvador, 2008).

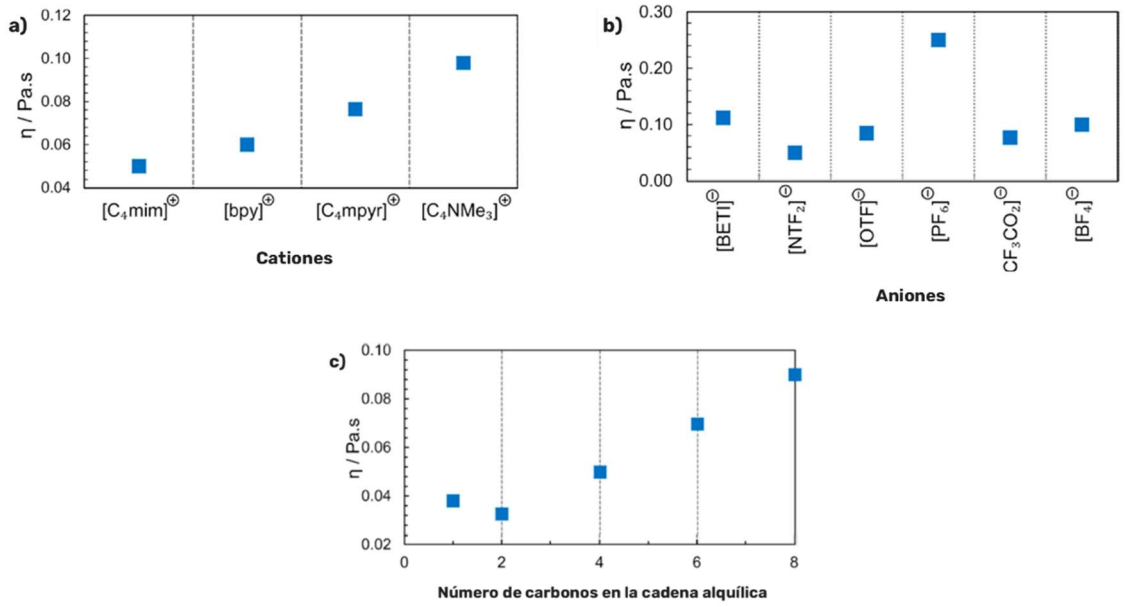

Figura 10.Evolución de la viscosidad en función de diferentes variables: a) En función del catión (Anión común $[NTf_2]^-$). b) En función del anión (Catión común $[C_4mim]^+$). c) En función del número de carbonos del catión (ILs $[C_nmim][NTf_2]$). Adaptado de la referencia (Silva et al., 2020).

2.1.2.4. Conductividad eléctrica

La conductividad se rige por la movilidad de los iones, que en líneas generales depende de la viscosidad y del número de portadores de carga. Al igual que la viscosidad, la conductividad es una propiedad de transporte, y ambas se encuentra íntimamente relacionadas. A su vez, estos parámetros se encuentran totalmente influenciados por características de los iones como su peso molecular, su tamaño o la densidad del líquido. Los líquidos iónicos con iones poco asociados, es decir, cargas deslocalizadas y menos interacciones, tendrán conductividades más altas, ya que esta situación favorece el movimiento de los iones (Greaves et al., 2008). La incorporación de agua en la mezcla afecta directamente a la conductividad eléctrica, ya que, al disminuir la viscosidad, permite una mayor movilidad de los iones y, por lo tanto, genera un aumento de la conductividad eléctrica. Al igual que en otras propiedades, la temperatura también influye en la conductividad eléctrica. A mayor temperatura, los iones aumentan su

capacidad de movilidad al tener más energía, lo que se traduce en una mayor conductividad.

Como se ha indicado, las características de los iones también influyen en esta propiedad. En general, las conductividades de ILs con catión imidazolio son mayores que las de los basados en cationes de piridinio y pirrolidinio (Marcus, 2016). La conductividad de los líquidos con cationes de alquilamonio y alquilimidazolio disminuye a medida que aumenta el tamaño del catión o la longitud de la cadena alquílica. Este cambio es más pronunciado con cadenas cortas (C1-C4). Por otro lado, la disminución en la masa molecular de los iones o la asimetría del catión, aumentan la conductividad (Ghandi, 2014).

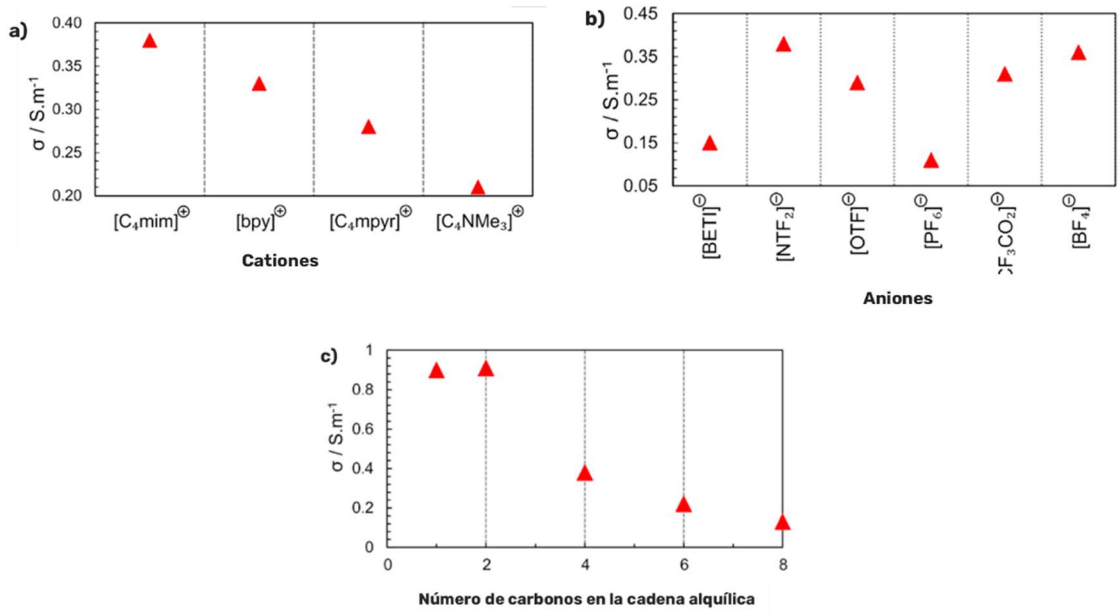

Figura 11.Evolución de la conductividad eléctrica en función de diferentes variables: a) En función del catión (Anión común $[NTf_2]^-$). b) En función del anión (Catión común $[C_4mim]^+$). c) En función del número de carbonos del catión (ILs $[C_nmim][NTf_2]$). Adaptado de la referencia (Silva et al., 2020).

2.1.2.5. Punto de fusión

Se define el punto de fusión como la temperatura más baja a la que la sustancia puede permanecer en estado líquido (Zainal-Abidin et al., 2021). De manera general un ILs lleva implícito en su definición aquel que se encuentra en estado líquido a temperatura ambiente o que presenta un punto de fusión por debajo de los 100 °C.

El principal motivo por el que los ILs existen en estado líquido a temperatura ambiente es debido a su estructura química. El anión y el catión desestabilizan la estructura cristalina de la fase sólida, esto se consigue combinando las interacciones entre los iones seleccionados y su simetría (Hayes et al., 2015). En líneas general podría resumirse que el principal factor que influye en esta temperatura es del tamaño de los iones, tanto los cationes como los aniones, ya que el incremento en el volumen de los mismos da lugar menor empaquetamiento y mayor deslocalización de las cargas. En la Tabla 1 se muestra líquidos iónicos con el catión común $[EMIM]^+$ y diferentes aniones, es posible observar la influencia del anión en la temperatura de fusión de los diferentes líquidos iónicos.

Tabla 1.Puntos de fusión para líquidos iónicos con catión común [EMIM][X] (Anthony, 2002).

Anión [X]	Punto de fusión (ºC)
Cl^-	87
Br^-	81
$[AlCl_4]^-$	7
$[AuCl_3]^-$	58
$[PF_6]^-$	62
$[AsF_6]^-$	53
$[NO_3]^-$	38
$[NO_2]^-$	55
$[CF_3SO_3]^-$	-9
$[CF_3CO_2]^-$	-14

La longitud de las cadenas también afecta a esta temperatura, cuando aumentan las interacciones entre las cadenas de alquilo, la temperatura de fusión sufre un aumento. Se ha observado que cationes aromáticos con radicales de cadena corta (C_n<3) presentan temperaturas de fusión más altas que los mismos cationes con longitudes de cadena entre 4 y 10 carbonos. Sin embargo, cuando la cadena es muy larga (C_n>12), la temperatura de fusión incrementa drásticamente (Anthony et al., 2002). La simetría del catión también influye en la temperatura de fusión. Cationes simétricos permiten un mejor empaquetamiento de los iones, lo que aumenta la temperatura de fusión. Los

iones de imidazol, muy asimétricos, distorsionan la distribución de fuerzas de Coulomb (Weingärtner, 2008). La clave para entender estos comportamientos reside en la proporción de enlaces de hidrógeno presenten en la mezcla. A medida que se incrementa la red de enlaces de hidrógeno, aumenta la temperatura de fusión de estos líquidos (Greaves et al., 2008).

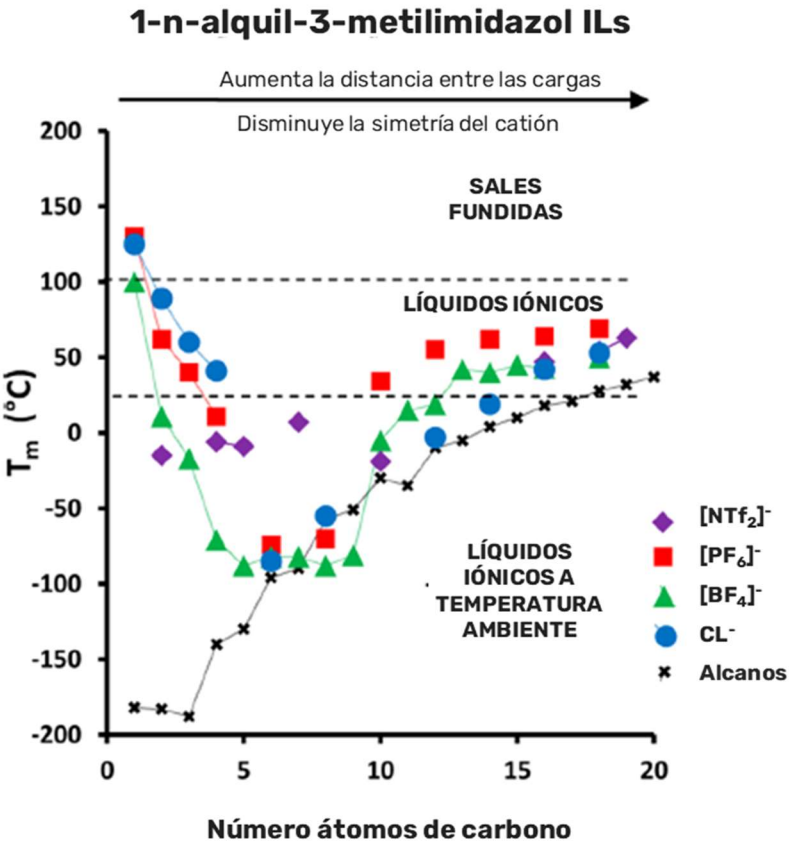

Figura 12. Punto de fusión en función de la longitud de la cadena alquílica del catión. Adaptado de la referencia (Hayes et al., 2015).

2.1.3. Aplicaciones

Como se ha mencionado en secciones previas, la versatilidad de los líquidos iónicos es abrumadora. Su potencial de uso ha comenzado a ser investigado y aprovechado hace relativamente poco tiempo, siendo utilizados tanto en aplicaciones de carácter académico como industrial. Se perfilan como opciones prometedoras para dar solución a algunos de los principales desafíos ecológicos que afectan a la sociedad en la actualidad, pero debido a la rápida expansión de los campos de aplicación de los líquidos iónicos, todavía hay muchos en los que siguen siendo objeto de estudio.

Figura 13. Principales desafíos a los que se enfrentan los ILs para su aplicación futura a escala industrial. Adaptado de la referencia (Kaur et al., 2022).

En la actualidad es complicado enumerar de manera exhaustiva todas las aplicaciones en las que estos pueden ser utilizados. A continuación se presentan algunas de las aplicaciones más relevantes y estudiadas de los líquidos iónicos, así como otras más recientes y en proceso de desarrollo.

2.1.3.1. Procesos de extracción y separación

La utilización de técnicas de extracción y separación es esencial en todos los procesos. Se pueden definir como la distribución de componentes entre distintos sistemas de disolventes con el fin de aislar el componente deseado. La sustitución de los disolventes orgánicos en procesos de extracción por ILs es un tema de investigación de gran relevancia. Estos presentan una selectividad inusual con una '«naturaleza dual», en la que separan compuestos como si fueran fases estacionarias polares y no polares. La utilización de ILs hace que los procesos de separación y extracción sean más rápidos, más eficientes y con menor volumen de disolventes, en comparación con disolventes orgánicos tradicionales.

Debido a sus implicaciones medioambientales, una de las aplicaciones más exploradas en la utilización de ILs es la separación de CO_2 (Aghaie et al., 2018). Una separación eficiente está influenciada por el método de separación, así como por la selección del ILs. Se ha observado que la naturaleza del anión tiene mayor impacto en la solubilidad del CO_2 que la del catión (Cadena et al., 2004). Sudhir y sus colaboradores (2004) evaluaron la solubilidad del CO_2 en diferentes ILs con catión común imidazol, obteniendo

que los aniones con grupos fluoro alquílicos favorecen la solubilidad del CO_2. También se ha analizado la selectividad frente a la presencia de otros gases. De acuerdo a los estudios llevados a cabo por el equipo de investigación de Zhang (Zhang et al., 2012), el CO_2 habitualmente presenta mayor selectividad que otros gases como CO, H_2 o O_2, en los líquidos iónicos tradicionales. Otros autores también apoyan que la solubilidad de este es mayor que la de N_2 o H_2, pero que el aumento de temperatura también aumenta la solubilidad de estos (Kumełan et al., 2011; Shiflett et al., 2010).

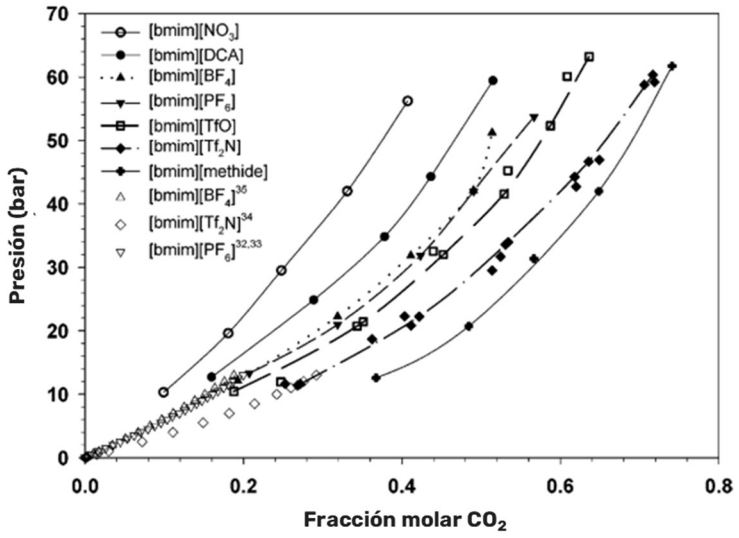

Figura 14. Solubilidad del CO_2 en líquidos iónicos basados en el catión [bmim] a 25 °C, en función del anión y la presión. Adaptado de la referencia (Sudhir, 2004).

Los líquidos iónicos también han sido estudiados en el ámbito de las tecnologías de tratamiento de agua gracias a su capacidad para extraer diversos componentes (Isosaari et al., 2019). Múltiples autores han analizado la extracción de componentes tanto orgánicos como metálicos de diversas fuentes de agua (Herce-Sesa et al., 2020; Li et al., 2007; Liu et al., 2009; Tian et al., 2020). Por ejemplo, Sas y sus colaboradores utilizaron varios ILs como agentes de extracción para la eliminación de compuestos fenólicos tóxicos de corrientes de aguas residuales (Sas et al., 2020). Almeida y su equipo de investigación prepararon materiales a base de sílice con el catión 1-metil-3-propilimidazolio combinado con seis aniones diferentes como adsorbentes para la eliminación eficaz de fármacos antiinflamatorios no esteroideos, NSAID (por sus siglas en inglés *Non-Steroidal Anti-Inflammatory Drugs*), como es el diclofenaco, de muestras acuosas (Almeida et al., 2020).

Otras aplicaciones de extracción y separación populares son la extracción de componentes de biomasa (Tan et al., 2020; Weldemhret et al., 2020) recuperación mejorada de combustibles fósiles, EOR (por sus siglas en inglés *Enhanced Oil Recovery*) (Bera et al., 2020; Nandwani et al., 2020), o separación de azeótropos (Arce et al., 2007; Zhang et al., 2008).

2.1.3.2. Medios en reacciones químicas

Los líquidos iónicos tienen la capacidad de ser utilizados como disolventes y catalizadores en procesos de síntesis química, ya que presentan muchas propiedades que los hacen candidatos atractivos para llevar a cabo diferentes tipos de reacciones: presión de vapor casi nula, estabilidad térmica, capacidad para disolver compuestos de diferentes naturalezas, etc. Aunque todavía su aprovechamiento a escala industrial está sujeto a algunas condiciones. Entre ellas que el rendimiento de las reacciones sea comparable al obtenido con disolventes convencionales y que el proceso permita reciclar el líquido iónico utilizado, ya que estos disolventes aún tienen un elevado coste (Salvador, 2008; Tan et al., 2011).

Muchos de los desarrollos realizados en el campo de la catálisis se enfrentan al desafío de separar los productos generados y poder reutilizar el catalizador. Los líquidos iónicos permiten reutilizar el catalizador sin que implique un descenso de la reactividad ni de la selectividad (Borja, 2015). Das y sus colaboradores reportaron ILs con ácido sulfónico para la síntesis eficiente de derivados acaloides indólicos cuya ventaja es que podrían reutilizarse hasta 10 ciclos sin pérdida sustancial de actividad catalítica (Das et al., 2010). Wang y su equipo describieron la reacción de Friedel-Crafts de PCl_3 y benceno en líquido iónico [trEHAm]Cl-$XAlCl_3$ para la síntesis limpia de diclorofenilfosfina (Wang et al., 2004). En comparación con los métodos clásicos, este protocolo permite un aislamiento del producto y un menor consumo de catalizador reutilizable, haciendo el proceso más ecológico. Brandt y su equipo aplicaron con éxito los líquidos iónicos [C_4C_1im][HSO_4] y [C_4C_1im][$MeSO_3$] para el tratamiento de biomasa lignocelulósica incluso en presencia de cantidades significativas de agua, eliminando así la necesidad de condiciones anhidras durante el pretratamiento (Brandt et al., 2013).

Los líquidos iónicos también han sido utilizados como disolventes y estabilizadores en la síntesis de nanopartículas, que debido a sus propiedades y a su tamaño han llamado la atención en campos como la medicina, la ingeniería o rehabilitación medioambiental (Kaur et al., 2022). Se han utilizado como solventes en la síntesis de nanopartículas GaN (Gaiser et al., 2020), AuPd inferiores a 3 nm (Zhang et al., 2021) o como agente estabilizador en nanopartículas de plata (AgNPs) (Patil et al., 2020). Otras reacciones en las que se exploran los líquidos iónicos como medios de reacción es la como la síntesis de ésteres de azúcar catalizada por lipasa (Yang et al., 2012) o la solubilidad de la celulosa (Ohno et al., 2019; Yang et al., 2018).

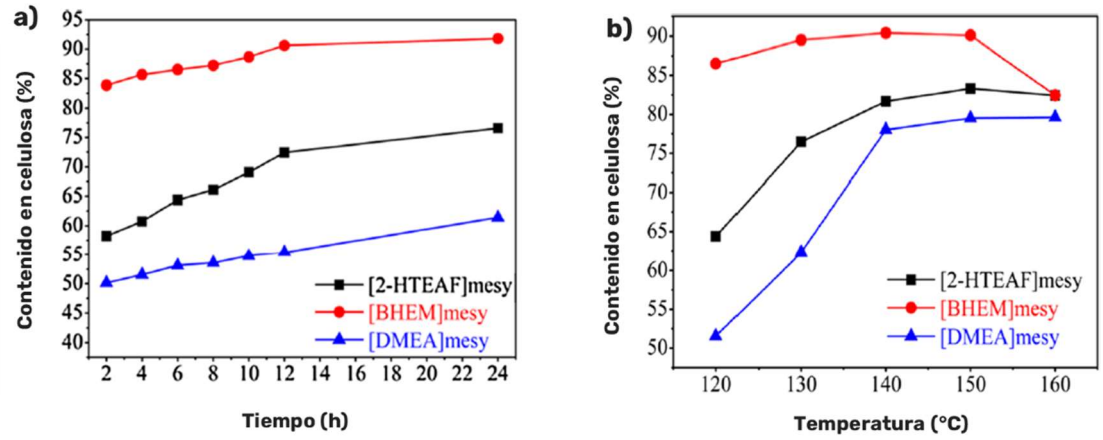

Figura 15. Disolución de celulosa procedente de cultivos de maíz en diferentes líquidos iónicos en función de a) tiempo de pretratamiento y b) temperatura. Adaptado de la referencia (Yang et al., 2018).

2.1.3.3. Aplicaciones electroquimicas

Existen numerosas aplicaciones en el campo de la electroquímica donde se han utilizado o se está investigando el uso de líquidos iónicos. Esto se debe a que propiedades fundamentales para estas aplicaciones como son viscosidad, ventana electroquímica o conductividad; presentan límites más amplios que los disolventes moleculares convencionales (Singh et al., 2020).

En los últimos años de la década de 1990, se publicó uno de los primeros informes sobre baterías recargables que utilizaban electrolitos de Li, donde se estudiaron sales fundidas de cloruro para lograr la deposición/disolución reversible de Li y Na (Gray et al., 1995). A partir de ese momento se desarrollaron gran cantidad de cationes y aniones innovadores para utilizar en las baterías de ion litio y en los supercondensadores

eléctricos de doble capa, EDLC (por sus siglas en inglés *Electronic Double-Layer Capacitor*)(Hagiwara et al., 2002; Xu et al., 1996), se realizaron numerosos estudios sobre la influencia del ion seleccionado en la ventana electroquímica (Sakaebe et al., 2003) y la reversibilidad de los electrolitos en los procesos de electrodeposición en presencia de líquidos iónicos (Gao et al., 2019).

El uso de líquidos iónicos como disolventes y electrolitos de soporte en el proceso de electrodeposición de metales, ha aumentado debido a su interés en el desarrollo de revestimientos protectores en las industrias automovilística y aeroespacial, por su naturaleza respetuosa con el medio ambiente. Por ejemplo, Rahali y sus colaboradores estudiaron la electrodeposición de plata en el electrodo de platino utilizando butil piridinio dicianamida ($Pyri_4$-DCA) debido a su alta conductividad iónica y baja viscosidad dinámica (Rahali et al., 2020). Otro de sus usos actuales en su aplicación en varios tipos de dispositivos sensores, como sensores de gas, químicos o biosensores. Chen y su equipo fabricaron una serie de ionogeles (material compuesto por un líquido iónico y celulosa) hidrófobos reticulados que contenían poli(fluoruro de vinilideno-hexafluoropropileno) (PVDF-HFP) y bis(trifluorometilsulfonil)imida de 1-alquil-3-metilimidazolio ($[C_nMIm][NTf_2]$), con el objetivo de aumentar la fiabilidad de sensores para monitorizar en tiempo real los movimientos humanos (Chen et al., 2020).

2.1.3.4. Principios activos farmacéuticos

Uno de los principales objetivos de la utilización de los líquidos iónicos en la industria farmacéutica es la mejora de la administración de diversos fármacos, facilitando su solubilidad y permeabilidad. Además, muchas industrias farmacéuticas se basan en el procesamiento de sólidos y utilizan disolventes orgánicos volátiles, que también se utilizan para disolver los fármacos, los cuales podrían ser sustituidos por líquidos iónicos (Kaur et al., 2022; Singh et al., 2020).

Zandu y colaboradores exploraron la actividad biológica de los ILs desarrollando la idea de Ingredientes Farmacéuticos Activos-Líquidos Iónicos (API-ILs) para el desarrollo de sistemas de administración más eficientes para fármacos orales, transdérmicos y tópicos (Zandu et al., 2020). Por ejemplo, Vaidya y Mitragotri fabricaron un parche polimérico biodegradable basado en quitosano y líquidos iónicos para la administración bucal eficaz

de insulina (Vaidya et al., 2020). En un estudio realizado por Júlio y colaboradores, se desarrollaron sistemas híbridos de líquido iónico y nanotransportador con el objetivo de mejorar la administración de fármacos poco solubles (Júlio et al., 2020). Enfocado al tratamiento quimoterapéutico, Chowdhury y su equipo analizaron la aplicación de ILs a base de colinio como co-solventes en formulaciones de paclitaxel (Chowdhury et al., 2018).

En lo que respecta a los procesos de síntesis, por su naturaleza cargada, los ILs pueden generar un calentamiento rápido por microondas, lo que conduce a reacciones más rápidas y eficientes. Por ejemplo, este enfoque se ha aplicado con éxito a la lactamización directa de lactonas, obteniendo altos rendimientos y reduciendo tiempos de reacción (Orrling et al., 2008). Las propiedades de los principios activos cristalinos dependen principalmente de su polimorfismo. Por lo tanto, el diseño del polimorfo correcto representa un requisito crítico en el desarrollo y la producción de fármacos. Muchos estudios han reportado cómo los líquidos iónicos pueden contribuir al diseño de nuevos cristales, así como a su correcta separación (An et al., 2016, 2013)

2.1.4. Sistemas considerados en la tesis

Los líquidos iónicos puros utilizados durante la investigación han sido 1-etil-3-metilimidazol tetrafluoroborato ([EMIM][BF_4]), 1-etil-3-metilimidazol bis(trifluorometilsulfonil)imida ([EMIM][TSFI]), 1-etil-3-metilimidazol metanosulfonato ([EMIM][$MeSO_3$]) y 1-etil-3-metilimidazol etilsulfato ([EMIM][$EtSO_4$]). A partir de estos se han generado 6 mezclas binarias con el catión común $[EMIM]^+$, detalladas en la Tabla 2. A continuación, se describen algunas de las aplicaciones y estudios de los líquidos puros utilizados, y en la Tabla 3 se expone una recopilación de sus propiedades más características.

Tabla 2. Relación de DSIL estudiados en el presente trabajo de investigación.

Mezcla	Sistema	Publicación
DSIL	[EMIM][BF_4] + [EMIM][TSFI]	0
	[EMIM][BF_4] + [EMIM][$EtSO_4$]	I
	[EMIM][$EtSO_4$] + [EMIM][$MeSO_3$]	II
	[EMIM][BF_4] + [EMIM][$MeSO_3$]	III
	[EMIM][TSFI] + [EMIM][$MeSO_3$]	Anexo I
	[EMIM][TSFI] + [EMIM][$EtSO_4$]	Anexo I

2.1.4.1. 1-etil-3-metilimidazol tetrafluoroborato ([EMIM][BF_4])

El 1-etil-3-metilim idazol tetrafluoroborato ([EMIM][BF_4]) es uno de los líquidos iónicos de la familia de imidazoles más estudiado. Catalogados como disolvente verde, presenta unas propiedades que lo hacen apropiado para participar en múltiples aplicaciones, por ejemplo la eliminación de CO_2 del gas natural y también en la desulfuración de combustibles líquidos (Narsimlu et al., 2019). Finotello y su equipo también estudian la selectividad y la solubilidad de la mezcla de [EMIM][BF_4] y [EMIM][TSFI] para los gases CO_2, CH_4 y N_2. El estudio concluye en que la solubilidad es óptima cuando la mezcla contiene >90% molar de [EMIM][BF_4] (Finotello et al., 2008). Otra de las propiedades analizadas para este líquido iónico es su capacidad calorífica, de cara a su utilización en medios industriales como agente de transferencia de calor. Gupta y colaboradores analizaron en el impacto en su capacidad calorífica en mezclas binarias (Gupta et al., 2016) y ternarias con otros componentes (Gupta et al., 2018).

2.1.4.2. 1-etil-3-metilimidazol bis(trifluorometilsulfonil)imida ([EMIM][TSFI])

En la literatura es posible encontrar referencias al 1-etil-3-metilimidazol bis(trifluorometilsulfonil)imida como [EMIM][TSFI] o [EMIM][NTf_2]. En 1996 Bonhôte y colaboradores publicaron por primera vez sobre la síntesis de este líquido iónico y sus propiedades, analizado, entre otras, su densidad, viscosidad, estabilidad térmica y el comportamiento de las mismas en función de la proporción en la mezcla con agua u otros disolventes orgánicos, concluyendo ya desde ese momento su prometedor comportamiento como disolvente para aplicaciones electroquímicas, fotovoltaicas y sintéticas (Bonhôte et al., 1996). Otro de los campos en los que ha tenido mayor impacto es en el almacenamiento y distribución de energía: baterías, células solares sensibilizadas, actuadores o supercondensadores (MacFarlane et al., 2014).

2.1.4.3. 1-etil-3-metilimidazol metanosulfonato ([EMIM][$MeSO_3$])

Desde 2010 se tiene en cuenta al 1-etil-3-metilimidazol metanosulfonato ([EMIM][$MeSO_3$]) como alternativa prometedora a los desecantes utilizados comúnmente en la industria como son el trietilenglicol y el bromuro de litio (Zheng et al., 2020). También se han investigado sus propiedades termofísicas de cara a su

aplicación industrial por su capacidad calorífica. Bioucas y su equipo analizaron el comportamiento de propiedades como conductividad térmica o viscosidad para la mezcla de este líquido iónico con agua en todo el intervalo de concentraciones, obteniendo que estas mezclas contribuyen al ahorro de energía en diferentes procesos industriales (Bioucas et al., 2018). En la misma línea, el equipo de Vataščin analizó la capacidad de refrigeración del [EMIM][$MeSO_3$] en mezclas terciarias con otros líquidos iónicos y agua. Obteniendo resultados positivos para concentraciones bajas de los otros dos componentes, en comparación con los valores de [EMIM][$MeSO_3$] puros (Vataščin et al., 2021).

2.1.4.4. 1-etil-3-metilimidazol etilsulfato ([EMIM][$EtSO_4$])

Este líquido iónico, también considerado como disolvente verde, se ha estudiado desde diferentes ámbitos debido a su carácter sostenible. Pereiro y colaboradores estudiaron su aplicación como disolvente para la separación de mezclas azeotrópicas, en concreto n-heptano + etanol. Obteniendo como resultado eficiencias particularmente altas del [EMIM][$EtSO_4$] y el [EMIM][$MeSO_3$] como solventes de extracción (Oliveira et al., 2016). Sen y su equipo se centran en la optimización de su síntesis a través de un microcapilar sencillo sin utilizar ningún disolvente. Le prestan especial atención por su potencial para eliminar compuestos de azufre durante la desulfuración de hidrocarburos o para ser utilizado en la producción de hidrógeno mediante ciclos termoquímicos (Sen et al., 2023). Otros equipos han analizado sus propiedades como disolvente de azúcares como el xilitol o el sorbitol, obteniendo que el [EMIM][$EtSO_4$] presenta mayores capacidades para disolver estos azúcares que otros líquidos iónicos semejantes (Carneiro et al., 2012).

Tabla 3. Descripción y propiedades de los ILs analizados en el presente trabajo de investigación.

Nombre	Tetrafluoroborato de 1-etil-3-metil-imidazolio	1-etil-3-metil-imidazolio bis(trifluorometilsulfonil)imida	Metanosulfonato de 1-etil-3-metil-imidazolio	Etilsulfato de 1-etil-3-metil-imidazolio
Abreviatura	[EMIM][BF_4] [C_2mim][BF_4]	[EMIM][TSFI] [C_2mim][TSFI]	[EMIM][$MeSO_3$] [C_2mim][$MeSO_3$]	[EMIM][$EtSO_4$] [C_2mim][$EtSO_4$]
Fórmula	$C_6H_{11}BF_4N_2$	$C_8H_{11}F_6N_3O_4S_2$	$C_7H_{14}N_2O_3S$	$C_8H_{16}N_2O_4S$
CAS	143314-16-3	174899-82-2	145022-45-3	342573-75-5
Pm (g/mol)	197,97	391,31	206,26	236,29
Tª Fusión (°C)	15 °C	-9 °C	33 °C	< -30 °C
Densidad (g/ml) (25°C)	1,28005	1,55006	1,24078	1,23682
Viscosidad (mm^2/s) (25°C)	27,09975	37,71447	132,62966	77,08337
Estructura	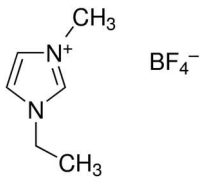	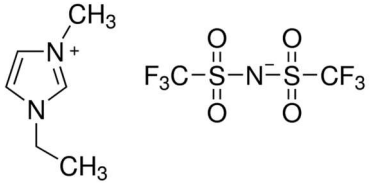	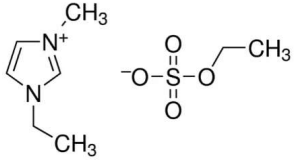	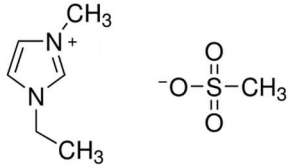

2.2. Disolventes Eutécticos Profundos

La Química Verde tiene como uno de sus principales propósitos la búsqueda de alternativas que puedan reemplazar diferentes compuestos perjudiciales para el medio ambiente, sin comprometer sus propiedades o su eficacia. Aunque los líquidos iónicos han sido durante décadas una gran alternativa a los disolventes tradicionales, las implicaciones medioambientales de los ILs siguen siendo un tema de intenso debate, principalmente debido a su escasa biodegradabilidad, biocompatibilidad y sostenibilidad (Paiva et al., 2014). Para superar los inconvenientes ecológicos de los ILs, los DES han surgido como una nueva y prometedora generación de disolventes alternativos

A pesar de las diferencias en las propiedades químicas entre los ILs y los DES, se ha observado que comparten propiedades físicas similares. Ambos son solventes que pueden ser diseñados con el objetivo de ajustar sus propiedades a la aplicación deseada, presentan bajas presiones de vapor a temperatura ambiente, son líquidos en un amplio rango de temperaturas y la mayoría no son inflamables. Una de las ventajas principales de los DES sobre los ILs es su mayor facilidad de preparación, sus componentes están disponibles fácilmente y se pueden obtener de fuentes naturales y/o biodegradables, y en general presentan un coste menor. No obstante, es importante destacar que los DES suelen ser menos inertes químicamente. El principal proceso de preparación de DES se realiza mediante la mezcla de dos componentes y el aporte de calor, lo que reduce significativamente los costos de producción en comparación con los ILs convencionales, permitiendo su aplicación en procesos a gran escala (Smith et al., 2014).

En 2003, Abbott et al. publican por primera vez sobre los disolventes eutécticos profundos, provocando un impacto significativo en el campo de los disolventes (Abbott et al., 2003). El término «eutéctico» proviene del griego εύτήξις y significa *fácil fusión*. Esencialmente, una mezcla eutéctica consiste en una combinación de elementos que, en proporciones específicas, presenta un punto de fusión más bajo que sus componentes por separado (Liu et al., 2018). Sin embargo, no todas las mezclas eutécticas pueden considerarse a priori como DES desde un punto de vista termodinámico. En sentido estricto, el uso del adjetivo «profundo» sólo debería emplearse para las mezclas que

poseen una temperatura de punto eutéctico significativamente inferior a la de una mezcla líquida ideal.

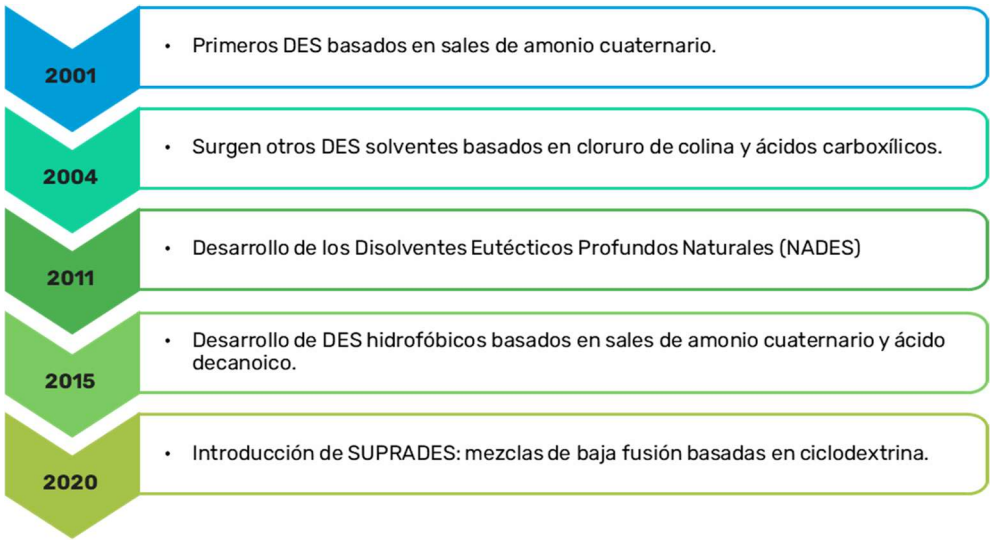

Figura 16. Resumen de hitos en la evolución del desarrollo de los DES. Adaptado de la referencia (Achkar et al., 2021).

Martins y colaboradores desarrollan una descripción exhaustiva de lo que se considera disolvente eutéctico profundo, basada fundamentalmente en la depresión de la temperatura de la mezcla. Esta disminución en la temperatura real frente a la ideal se atribuye a la formación de complejos enlaces de hidrógeno entre lo que se denomina donador de enlaces de hidrógeno, HBD (del inglés *Hydrogen Bond Donor*) y aceptor de enlace de hidrógeno, HBA (por sus siglas en inglés *Hydrogen Bond Acceptor*) en una proporción estequiométrica concreta (Martins et al., 2019). Ambos componentes se encuentran asociados entre sí a través de enlaces de hidrógeno, lo que conduce a la aparición de nuevas propiedades como la naturaleza dipolar, la no inflamabilidad y la estabilidad térmica, entre otras (Perna et al., 2020). Aunque las interacciones fundamentales entre HBA y HBD se basan en enlaces de hidrógeno, también se observan interacciones de Van der Waals y, ocasionalmente, fuerzas electrostáticas. En determinadas circunstancias, dependiendo de los elementos, también es factible la formación de enlaces de hidrógeno HBD-HBD, lo que da lugar a redes estructurales más complejas (Santana-Mayor et al., 2021).

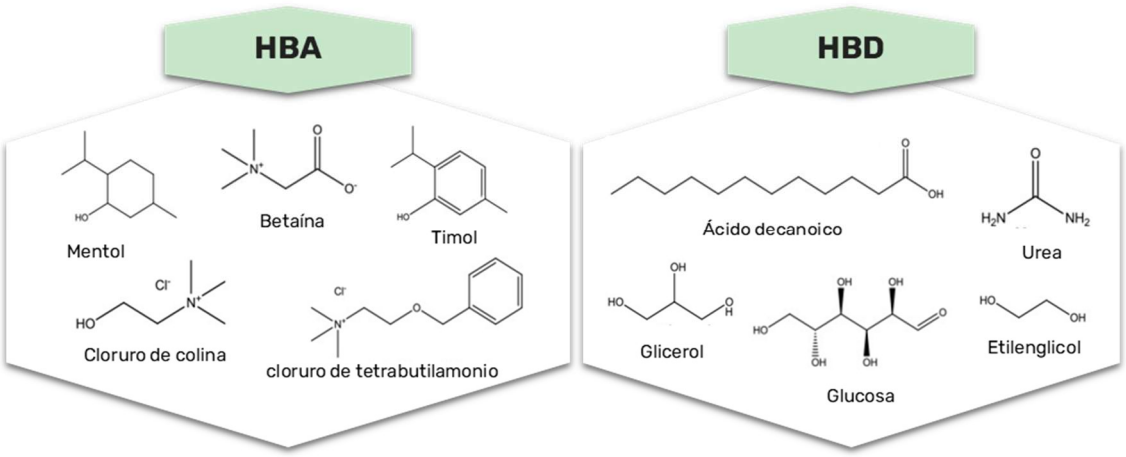

Figura 17. Ejemplos de HBA y HBD más comunes utilizados en DES. Adaptado de la referencia (Florindo et al., 2019)

Otro factor significativo a la hora de definir un DES, además de la disminución de su punto de fusión, es su composición. La diferencia principal entre un IL y un DES radica en que un IL está compuesto por sales iónicas líquidas a temperatura ambiente, mientras que un DES puede estar compuesto por sales iónicas, especies no iónicas, o combinaciones de ambas especies. Los DES pueden ser mezclas binarias o terciarias, sin embargo, la mayor parte de la literatura disponible abarca únicamente mezclas binarias. La clasificación de los DES acorde a su composición permite disponer de un marco en el que comprender sus diversas propiedades. Es posible describirlos a través de la formula general $Cat^{+}X^{-}zY$, y el sistema de clasificación más común los distingue según la naturaleza de sus componentes, y actualmente esta clasificación da lugar a 5 tipos. De maneral general los tipos I, II y III están formados por la combinación entre una sal de amonio cuaternario, QAS (del inglés *Quaternary Ammonium Salt*) como HBA y un haluro metálico, un haluro metálico hidratado o un componente molecular orgánico (como un ácido orgánico, un azúcar o un alcohol) respectivamente, como HBD. Los tipo IV están formados por complejos de metales de transición como HBA o HBD y son menos comunes. Por último, los DES del tipo V el HBA como el HBD carecen de componentes iónicos (Al-Bodour et al., 2023; Deepika et al., 2022; Rozas et al., 2023). La elevada viscosidad y la total miscibilidad con el agua de los cuatro primeros los hacen menos atractivos para varias aplicaciones industriales y farmacéuticas. Los DES de tipo I, II y la mayoría de los de tipo IV son típicamente iónicos, mientras que los de tipo III y V pueden ser iónicos o no iónicos en función de los componentes específicos utilizados.

Por otra parte, existe un subgrupo de DES dentro del tipo V basado en la fuente de los componentes. Este subgrupo está formado por compuestos de origen natural, por lo que se han denominado disolventes eutécticos profundos naturales, NADES (Liu et al., 2018). Las principales características de los NADES son su bajo coste de producción, su baja toxicidad y que son, en general, respetuosos con el medio ambiente. Esto los convierte en una opción atractiva para aplicaciones sostenibles como material alternativo para los ILs y los VOC (Benito et al., 2023). Además, una subclase prometedora de los DES convencionales para superar la inestabilidad al agua, etiquetados como DES hidrófobos, HDES (del inglés *Hydrophobic Deep Eutectic Solvent*). La hidrofobicidad está asociada a la afinidad de sus componentes por el agua. Hay dos tipos de HDES: el primer tipo consiste principalmente en sales de amonio cuaternario con cadenas largas de alquilo, y el segundo tipo es una mezcla de dos compuestos neutros, como ácidos carboxílicos o alcoholes con ácidos de cadena larga de alquilo. Los DES naturales e hidrófobos combinan la mayoría de las características relevantes, por lo que son actualmente la categoría más estudiada y ampliamente utilizada debido a sus diversas propiedades, capacidad de ajuste y potencial de sostenibilidad. El desarrollo de NADES que combinen monoterpenoides y ácidos grasos de cadena larga ha atraído el interés de la comunidad científica (Ribeiro et al., 2015). Los DES hidrófobos muestran una baja afinidad por el agua, lo que los hace adecuados para disolver compuestos poco solubles en agua. Esto es especialmente valioso para aplicaciones farmacéuticas y medioambientales. Por el contrario, los DES hidrófilos se mezclan fácilmente con el agua, lo que ofrece ventajas para aplicaciones que requieren solubilidad en agua, manteniendo al mismo tiempo sus propiedades únicas.

Los DES se han utilizado en una amplia gama de aplicaciones. Una de las primeras áreas de interés ha sido la de los procesos metalúrgicos, como la extracción/reciclado de metales en solución, el refinado y la electrodeposición (Hansen et al., 2021). Debido a sus propiedades ecológicas, los estudios se han orientado hacia la demostración de su eficacia en la eliminación de diversos contaminantes de las aguas residuales (Yuan et al., 2022), la eliminación de compuestos nitrogenados de los combustibles o la exploración de su potencial en el ámbito del procesamiento de la biomasa, en particular en el pretratamiento de la lignocelulosa y la conversión de azúcares (Gunny et al., 2015;

Maletta et al., 2023). Además, se ha propuesto el uso de DES en diferentes campos como las operaciones de extracción (Dai et al., 2013), los procesos de biocatálisis (Gotor-Fernández et al., 2019) o la industria farmacéutica (Díaz et al., 2012).

Figura 18. Algunas de las principales aplicaciones de los DES.

2.2.1. Clasificación

En líneas generales podría decirse que los DES son una clase emergente de disolventes sostenibles que se forman mediante la combinación de un donador y un aceptor de enlaces de hidrógeno. La selección adecuada de sus componentes permite diseñar un disolvente con características ajustadas a su aplicación final. En este epígrafe se aborda su categorización según sus componentes, proporcionando una base para entender sus diferentes tipos. Atendiendo a la naturaleza de los componentes, los DES pueden clasificarse en 5 tipos:

2.2.1.1. Tipo I: sal de amonio cuaternaria + haluro metálico anhidro

Están formados por la combinación entre un haluro metálico como donante de enlaces de hidrógeno y una sal de amonio cuaternario como aceptor de enlaces de hidrógeno. La gran mayoría de los DES preparados e investigados hasta la fecha pertenecen a este grupo. Estos DES son conocidos por su alto carácter iónico y su buena estabilidad térmica (Al-Bodour et al., 2023). Aunque generalmente son más caros y tóxicos, lo que provoca que recientemente no estén siendo tan utilizados como disolventes (Sitze et al., 2001).

2.2.1.2. Tipo II: sal de amonio cuaternaria + haluro metálico hidratado

En estos el HBA sigue siendo un QAS, pero el HBD es un haluro metálico hidratado. Este tipo suele presentar puntos de fusión más bajos que los DES de tipo I y son más económicos (Abbott et al., 2004).

2.2.1.3. Tipo III: sal de amonio cuaternaria + compuestos dadores de hidrógeno

Esta categoría combina un QAS como HBA con un HBD neutro, habitualmente un componente molecular orgánico como un ácido orgánico, un azúcar o un alcohol. Los DES de tipo III presentan una variedad más amplia de funcionalidades y mayor capacidad para ajustar sus propiedades finales, son más comunes en la literatura debido a su facilidad de preparación, uso como disolventes sostenibles, baja reactividad con el agua, presentan una alta biodegradabilidad y su coste es relativamente bajo (Gutiérrez, 2020).

2.2.1.4. Tipo IV: haluro metálico + ácido de Lewis o de Bröwsted

Aunque por lo general los cationes inorgánicos no forman mezclas eutécticas de bajo punto de fusión debido a su alta densidad de carga, estos DES incorporan complejos de metales de transición como HBA o HBD son menos comunes (Smith et al., 2014), pero ofrecen propiedades únicas, como una mayor actividad catalítica o la producción de complejos catiónicos metálicos, lo que garantiza una alta concentración de iones metálicos cerca de la superficie de los electrodos (Abbott et al., 2014).

2.2.1.5. Tipo V: compuestos no iónicos

Se trata de un tipo relativamente reciente de DES, en el que, tanto el HBA como el HBD carecen de componentes iónicos, lo que puede suponer ventajas como una menor viscosidad y una mayor estabilidad térmica. Esta categoría emergente en 2015 de la mano de Van Osch y sus colaboradores (Van Osch et al., 2015). Estos DES son objeto de una activa investigación y pueden considerarse como iónico o no iónicos, y con un alto grado de hidrofobicidad (Deepika et al., 2022; Rozas et al., 2023).

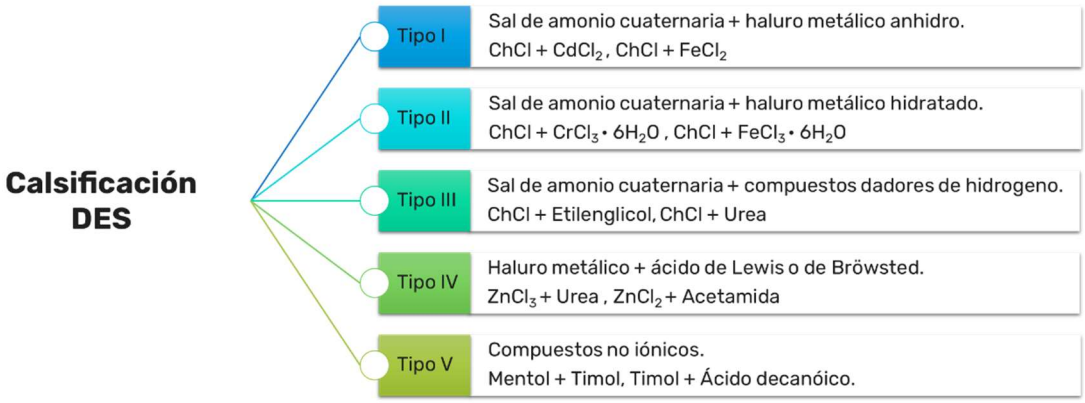

Figura 19. Clasificación de los DES. Adaptado de la referencia (Prabhune et al., 2023).

Los DES también puede categorizarse según su afinidad por el agua, su hidrofobicidad está directamente relacionada con la hidrofobicidad de sus componentes (Zainal-Abidin et al., 2021). La mayoría de los DES basados en los tipos I y II son de carácter hidrofílico. Estos DES tienen la ventaja de poder ajustar sus propiedades mediante el contenido de agua en su composición. Por ejemplo, es posible modificar la alta viscosidad manteniendo el resto de propiedades (Hayyan et al., 2012). Aunque también, el aporte de agua a la composición puede generar inestabilidad en la mezcla, lo que puede provocar la desintegración de la misma (Zainal-Abidin et al., 2021). Fue en 2015 cuando comienzan a reportarse estudios relacionados con la búsqueda de DES hidrofóbicos, que permanecieran estables en contacto con el agua (Florindo et al., 2019). Los HDES suelen pertenecer a los tipos III y IV, y estar constituidos por sales cuaternarias de amonio con compuestos de largas cadenas alquílicas, por ejemplo el primero reportado estaba constituido por ácido decanoico con sales de amonio de cadenas alquílicas largas (Van Osch et al., 2015). Otra posible combinación son mezclas formadas por compuestos naturales hidrófobos que actúan como HBA con algunos HBD hidrófobos, como ácidos carboxílicos o alcoholes con ácidos de cadena alquílica larga, o la combinación de dos compuestos de ácidos grasos, en los que ambos ácidos grasos pueden actuar como HDB y también como HBA, como la lidocaína con ácido decanoico (Zainal-Abidin et al., 2021).

En 2011, Choi y su equipo comienzan a trabajar con DES cuyos componentes son de origen natural, como por ejemplo azúcares, alcoholes, aminoácidos, ácidos orgánicos y derivados de la colina (Choi et al., 2011). A este subgrupo de solventes se les denomina NADES y podrían representar todos los principios de la Química Verde. Sus componentes se encuentran fácilmente disponibles, presentan una preparación sencilla, son

biodegradables y seguros, su reutilización es posible y presentan un bajo coste. (Fernández et al., 2018). Algunos autores proponen una clasificación de estos de acuerdo a sus componentes en cuatro grupos: derivados de ácidos orgánicos, derivados de cloruro de colina, mezclas de azúcares y otras combinaciones (Espino et al., 2016). A pesar de su escaso recorrido, la aplicación de los NADES como alternativa sostenible ya ha sido explorada en múltiples campos. Por ejemplo, como medio alternativo al agua en procesos biológicos (Dai et al., 2013), como medio de extracción en biorrefinería (Mišan et al., 2020) o en la industria alimentaria para garantizar la estabilidad de otros componentes (Dai et al., 2014).

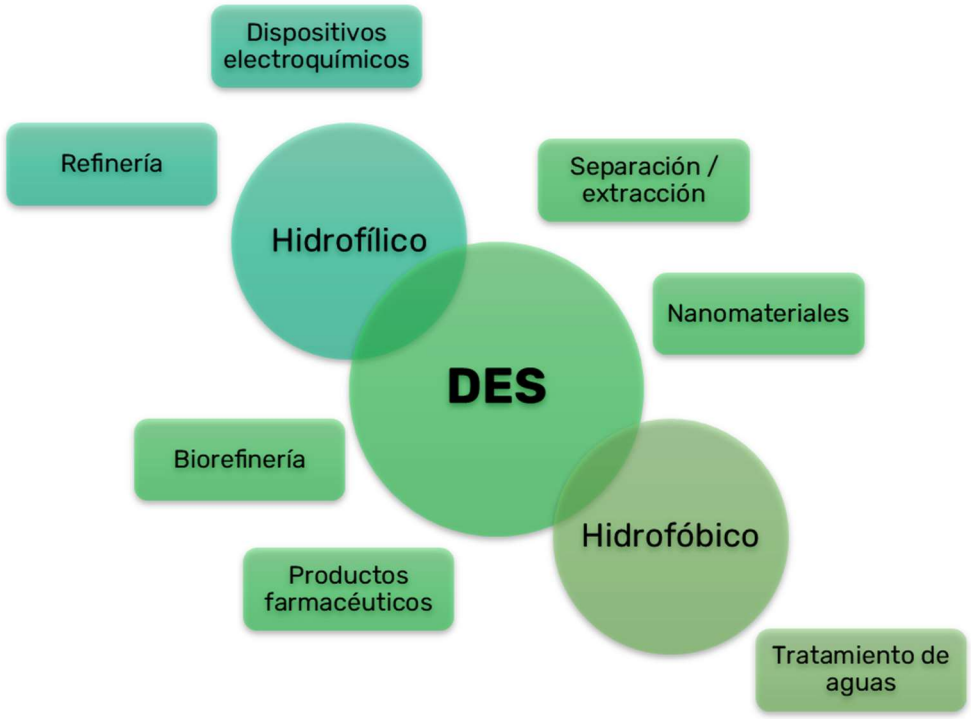

Figura 20. Aplicaciones potenciales de DES hidrofílicos e hidrofóbicos. Adaptado de la referencia (Florindo et al., 2019).

2.2.2. Propiedades

El análisis de las propiedades físicas de los DES es fundamental para determinar sus aplicaciones. Ya que sus propiedades pueden ajustarse con la selección adecuada de los componentes, resulta esencial comprender la relación existente entre las características macroscópicas de dichas mezclas y sus estructuras moleculares, dado que su conocimiento posibilita optimizar el diseño de estos solventes. En los siguientes

apartados se analizan las propiedades de mayor interés para una gran variedad de aplicaciones.

2.2.2.1. Temperatura de fusión

La temperatura de fusión es una de sus propiedades más relevantes, sin embargo, en el caso de los DES adquiere una importancia aún mayor (Fernández et al., 2018). En general las mezclas eutécticas se caracterizan por presentar puntos de fusión inferiores a sus componentes puros, pero en el caso de los DES es necesario definir claramente qué diferencia a estas mezclas eutécticas «profundas» de las convencionales.

En los últimos años, se ha observado un uso indiscriminado de la denominación de DES en mezclas que podrían no cumplir con los criterios establecidos. Es importante destacar la distinción entre un DES y una mezcla eutéctica para evitar confusiones (Florindo et al., 2019). Una mezcla eutéctica se define como «*una mezcla isotérmica reversible entre diferentes componentes que no reacciona durante el enfriamiento de un sistema líquido, lo que da lugar a una disminución del punto de congelación del sistema en comparación con la temperatura de fusión de los compuestos puros*» (Martins et al., 2019). La denominación de «profundas» surge principalmente de su marcada disminución del punto de congelación con respecto al comportamiento de la solución ideal.

El punto eutéctico representa la composición y la temperatura mínima de fusión a lo largo de las dos curvas de fusión que se cruzan, es un parámetro invariante isobárico del sistema. Martins y su equipo realizan una definición ampliamente aceptada que acota el significado del adjetivo profundo en estas mezclas. Para que un DES se pueda considerar como tal, su temperatura del punto eutéctico ha de ser inferior a la de la mezcla líquida ideal. Se observa en la figura 21 que la depresión de temperatura debe definirse como la diferencia (ΔT_2) entre el punto eutéctico ideal ($T_{E,ideal}$) y el punto eutéctico real (T_E) y no como la diferencia (ΔT_1) entre la combinación lineal de los puntos de fusión de los componentes puros y el punto eutéctico real (Martins et al., 2018).

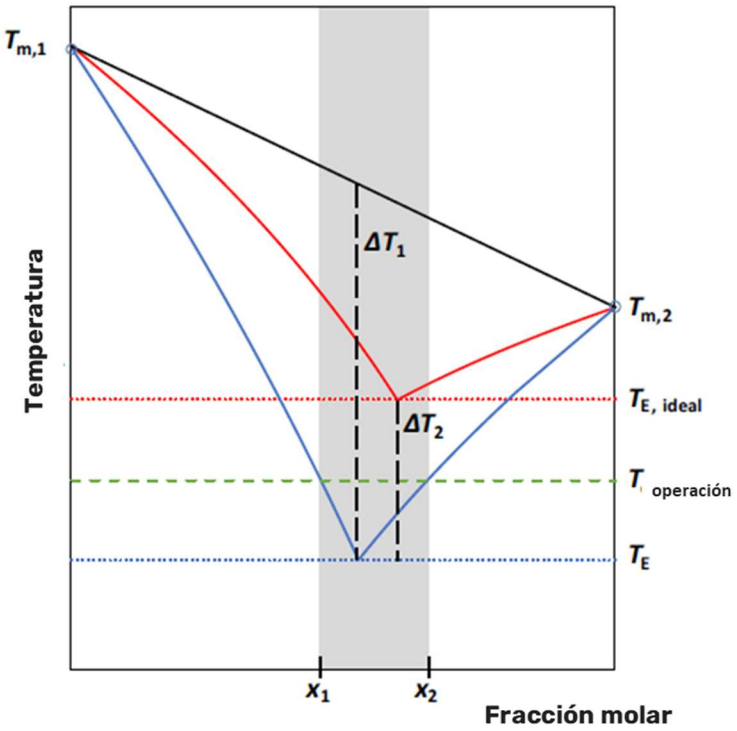

Figura 21. Representación esquemática de un diagrama de fase sólido-líquido en el que se representa la definición de mezcla eutéctica (línea roja) y mezcla eutéctica profunda (línea azul). Adaptada de la referencia (Martins et al., 2018).

Aunque no se ha encontrado una correlación clara entre los puntos de fusión de los componentes puros y la temperatura eutéctica, muchas publicaciones recientes señalan a los enlaces de hidrógeno como la fuerza molecular clave tras esta pronunciada depresión en el punto eutéctico: los enlaces de hidrógeno entre el HBA y el HBD dan lugar a una interacción más débil, lo que se traduce en temperaturas de fusión más bajas. Aunque también tienen cierta contribución los efectos estéricos y las fuerzas intermoleculares (Achkar et al., 2021; Hansen et al., 2021). El punto eutéctico varía en función de múltiples parámetros: la relación HBA:HBD, el contenido en agua, el tipo de HBD o la longitud de la cadena alquílica (Omar et al., 2022). Por ejemplo, para el caso de los DES hidrófobos, el aumento de la cadena alquílica en los ácidos grasos (HBD) aumenta el punto de fusión. Sin embargo, cuando este aumento se produce en las sales de amonio (HBA), este disminuye (Zainal-Abidin et al., 2021). Abbott observó que el incremento de la asimetría de los cationes, el aumento de su volumen o la disminución del peso molecular del HBD, podrían provocar una deslocalización de las cargas que influyera en las interacciones, disminuyendo la temperatura de fusión (Abbott et al.,

2003). La presencia de agua en el DES también disminuye de manera lineal el punto de fusión (Achkar et al., 2021).

Hasta la fecha, pocos estudios publican información específica sobre la composición eutéctica y los diagramas de fase binarios. Estos diagramas son de gran relevancia, ya que proporcionan información sobre el intervalo de temperatura y composición que cabe esperar de un líquido. La publicación de esta información contribuye a la optimización del diseño de sistemas DES para sus aplicaciones específicas (Zainal-Abidin et al., 2021).

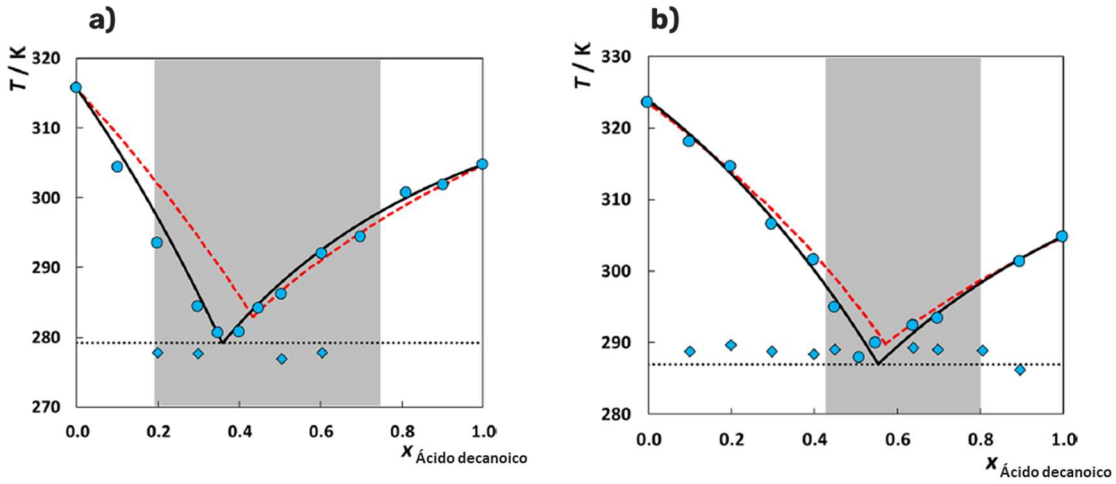

Figura 22. Diagramas de fase sólido-líquido de mezclas compuestas de ácido decanoico con a) mentol y b) timol. Los símbolos representan datos experimentales y las líneas representan los resultados del modelado: línea discontinua roja, Ideal; línea continua negra, modelo predictivo. La zona gris representa el rango de concentraciones en el que la mezcla es líquida a temperatura ambiente. Adaptado de la referencia (Martins et al., 2019).

2.2.2.2. Densidad

La densidad es una de las propiedades clave, ya que puede proporcionar información sobre el nivel de empaquetamiento molecular e interacción de las fuerzas intermoleculares. La mayoría de los DES presentan densidades mayores que la del agua, excepto algunos DES hidrofóbos (Omar et al., 2022). Como en la mayoría de solventes, el valor de la densidad muestra un comportamiento inversamente proporcional al aumento de la temperatura. Esto puede estar relacionado con el incremento del movimiento iónico y del volumen libre en el DES líquido (El Achkar et al., 2021). El volumen libre también se encuentra relacionado con la formación de enlaces de hidrógeno. La presencia de grupos hidroxilos en el HBD aumenta la formación de enlaces

de hidrógeno, lo que disminuye el volumen libre disponible y provoca un aumento de la densidad (Hansen et al., 2021).

Las características moleculares del HBD y la relación molar entre HBA y HBD también afecta a la densidad. En el caso de los DES formados por HBD con grupos hidroxilo, la densidad disminuye con la introducción de grupos aromáticos (García, Aparicio, et al., 2015). En concreto la densidad de los DES hidrófobos está correlacionada con la densidad de sus componentes (Cao et al., 2021). En general, en HDES con el mismo HBD, la densidad disminuye con el aumento de la longitud de la cadena alquílica de los HBA. No obstante, existe una excepción para los HDES preparados con timol y ácidos, en estos la densidad disminuye a medida que disminuye la cadena de los ácidos (Martins et al., 2018). La densidad de los DES puede modificarse a través del contenido de agua. La inclusión de agua en su composición debilita las interacciones de los enlaces de hidrógeno, Van der Waals y las fuerzas electrostáticas entre los componentes, así que la densidad disminuirá (Al-Bodour et al., 2023)

2.2.2.3. Viscosidad

Los altos valores de viscosidad que suelen presentar los DES constituyen uno de los principales obstáculos para su aplicación en la industria, aunque los DES hidrófobos parecen superar estos inconvenientes presentando valores de viscosidad más bajos que los DES tradicionales (Rozas, 2024).

La existencia de una extensa red de enlaces de hidrógeno, responsable de la conformación los DES, provoca en parte estos altos valores de viscosidad, ya que dificulta el libre movimiento de las moléculas en el pequeño volumen vacío dentro de los DES líquidos (Zainal-Abidin et al., 2021). La viscosidad de los DES se ven afectada sobre todo por la naturaleza química de los HBA, pero también influyen los HBD, su masa y volumen y la relación molar entre ellos (Zhang et al., 2012). De manera general es posible aceptar que los DES cuyos componentes puros presentan carácter neutral presentan valores de viscosidad mucho más bajos que aquellos compuestos por iones, esto puede estar relacionado con la mayor presencia de fuerzas de Coulomb en estos últimos (Cao et al., 2021).

El equipo de Van Osch determinó que los DES formados por ácidos grasos de cadena larga presentan valores de viscosidad más bajos. Además, observaron que para los HDES con HBA común, la viscosidad disminuye a medida que disminuye la longitud de cadena de los HBD (Van Osch et al., 2015). Sin embargo, Zainal-Abidin y colaboradores determinaron que el aumento de la cadena alquílica de las sales de amonio disminuye la viscosidad de los DES hidrófobos (Zainal-Abidin et al., 2021). Otro de los factores que influyen en la viscosidad, es la presencia de agua. La viscosidad disminuye a medida que aumenta el porcentaje de agua en la mezcla (El Achkar et al., 2021).

Asimismo, la temperatura tiene un gran impacto sobre esta propiedad, ya que la energía aportada al aumentar la temperatura es capaz de romper la red de enlaces de hidrógeno entre los HBA y los HBD, lo que provoca una menor viscosidad de los DES (Abbott et al., 2006). Diferentes grupos han tratado de caracterizar el comportamiento de la viscosidad de los DES, analizando los diferentes modelos teóricos que mejor describan su evolución. Aunque existen diversos modelos, los dos más comúnmente aplicados a los DES son el modelo de Arrhenius y el modelo Vogel-Fulcher- Tamman (Hansen et al., 2021).

2.2.2.4. Conductividad

La conductividad es la capacidad de un material para transmitir una corriente eléctrica y tiene relación inversa con la viscosidad. A temperatura ambiente los DES presentan bajas conductividades debido a los altos valores de viscosidad, lo que suele condicionar su uso en diferentes aplicaciones (Hansen et al., 2021). Una de las teorías que se ha desarrollado para explicar el movimiento de los iones en estos líquidos, es la teoría de los agujeros. Se basa en que, al fundirse, el volumen líquido y el volumen libre aumentan, aumentando así el número y el volumen de los espacios vacíos en la estructura del líquido (Smith et al., 2014). El tamaño promedio de los espacios vacíos es similar al tamaño del ion correspondiente, lo que facilita que un ion pequeño se mueva hacia un lugar vacante y, por lo tanto, la viscosidad del líquido es baja. No obstante, a temperaturas más bajas, el tamaño promedio de los agujeros es menor, lo cual, junto con un mayor tamaño de los iones, dificulta la movilidad de estos y explica las viscosidades más altas. Un fluido tendrá una distribución dada de tamaños de cavidad, y un ion sólo podrá moverse si hay un volumen de cavidad adyacente de dimensión

adecuada. Para lograr una movilidad óptima, los iones deben ser relativamente pequeños, pero el líquido debe contener cavidades grandes. Esto se puede lograr al producir un líquido con baja tensión superficial y, por ende, con huecos más amplios (Abbott, 2004; Abbott et al., 2006).

La conductividad de estas mezclas depende en gran medida de la temperatura, ya que al aumentar rompe su red de enlaces de hidrógeno, facilitando su movilidad iónica y aumentando su conductividad. Además, existen otros factores propios de las moléculas que lo conforman como es la longitud de la cadena alquílica del catión, la relación molar entre HBD:HBA y la fuerza de las interacciones entre estos (Omar et al., 2022).

2.2.2.5. Hidrofobicidad

La hidrofobicidad de los DES depende de la naturaleza química de la mezcla eutéctica de HBA y HBD, estos DES se reconocen por sus bajas densidades y su viscosidad moderada a temperatura ambiente. Las propiedades de los DES hidrofóbicos están influenciadas por el tamaño del anión y las longitudes de las cadenas alquílicas de los HBA: un mayor tamaño del anión, así como cadenas largas, conducen a una mayor viscosidad (Omar et al., 2022).

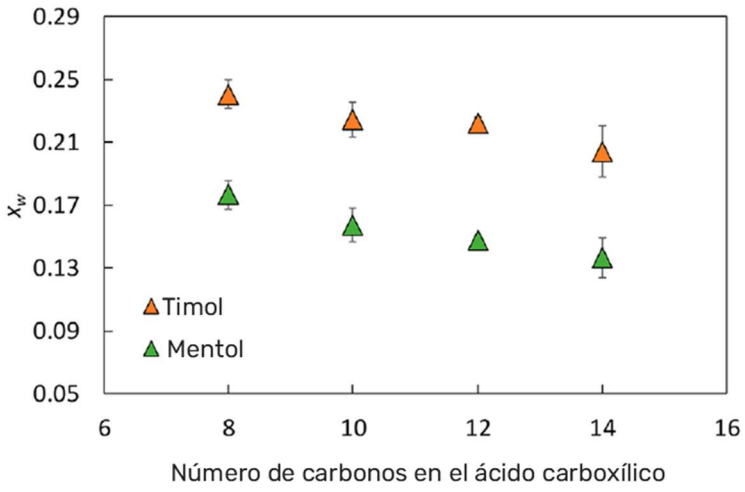

Figura 23. Solubilidad del agua en mezclas eutécticas de timol y mentol con ácidos carboxílicos en función de la longitud del ácido a 298.15 K. Adaptado de la referencia (Martins et al., 2018).

Otro de los factores que indica el grado de hidrofobicidad de estos solventes en el ángulo de contacto, cuanto mayor es, más hidrofóbicos son los DES (Li et al., 2020). La naturaleza hidrófoba de los DES facilita su uso en la extracción o eliminación de componentes en

entornos acuosos. Por lo tanto, resulta crucial investigar su estabilidad en agua para estos fines específicos, sobre todo en el caso de los HDES formados por un componente hidrófobo y otro hidrófilo. Los HDES ideales han de presentan poca contaminación cruzada con el agua (Cao et al., 2021).

2.2.3. Aplicaciones

Como se ha mencionado, uno de los principales focos de investigación de la Química Verde consiste en el diseño y la investigación de disolventes sostenibles. A pesar del protagonismo adquirido por los líquidos iónicos gracias a sus propiedades, los DES comienzan a postularse como sustitutos favoritos tanto de estos como de los disolventes tradicionales. En particular, los ya mencionados NADES representan plenamente los principios de la Química Verde. El proceso de fabricación consiste en una mezcla de dos compuestos, sin generarse residuos durante la producción y ni formación de subproductos no deseados. Así que es en realidad una mezcla de dos compuestos, por lo que el rendimiento del proceso puede considerarse del 100%, la economía atómica también del 100% y el total de residuos producidos es 0 (Paiva et al., 2018). Además de esto, presentan otras ventajas frente a los líquidos iónicos como es su bajo coste y su insignificante toxicidad (Florindo et al., 2017). Los DES ya han sido reconocidos como los disolventes de próxima generación y aplicados en numerosas áreas de relevancia como catálisis, extracción de contaminantes, industria farmacéutica o electroquímica (Al-Bodour et al., 2023). A continuación se mencionan algunas de estas aplicaciones, así como otras que se encuentran en proceso de desarrollo.

2.2.3.1. Eliminación de contaminantes del aire y el agua.

Dentro de los grandes problemas de contaminación mundial se encuentran la contaminación del agua y del aire. La contaminación de estos recursos puede poner en riesgo la salud humana.

En el caso del agua, los principales contaminantes son microcontaminantes antropogénicos en concentraciones traza que no pueden eliminarse con los tratamientos tradicionales. El papel del agua en la estructura de los DES continúa en vías de investigación, por ello se ha abordado el desarrollo de técnicas para soluciones hídricas

haciendo uso tanto de DES hidrófilos como hidrófobos (Florindo et al., 2019). Los DES hidrofílicos se han utilizado esencialmente como medios de preconcentración, permitiendo reducir los límites de detección de microcontaminantes, como los colorantes (Kaur et al., 2018). Los DES hidrófobos se han utilizado principalmente en la eliminación de microcontaminantes del agua, aplicándose sobre todo en tecnologías de extracción líquido-líquido para la eliminación de iones alcalinos y de metales de transición (Van Osch et al., 2015). Florindo y su equipo también han propuesto DES más respetuosos con el medio ambiente basados en compuestos naturales como el mentol y ácidos grasos (Florindo et al., 2018). Algunos de estos, se utilizaron para la eliminación de plaguicidas mostrando niveles del 80% de eficiencia de extracción (Florindo et al., 2017).

Aparte de afectar la salud de las personas, la contaminación del aire representa un importante desafío ambiental a nivel global. Un ejemplo de esto es el reconocimiento del CO_2 como responsable del incremento de la temperatura en la atmósfera, lo cual ha motivado un considerable número de estudios centrados en la aplicación de DES para la captura de CO_2. Li y sus colaboradores comenzaron analizando la solubilidad del CO_2 en estos solventes (Li et al., 2008). A partir de ahí, los trabajos publicados han abarcado desde la influencia de la estructura en la absorción de CO_2 (Altamash et al., 2020), sus propiedades interfaciales (García et al., 2015) o la utilización de compuestos naturales (Altamash et al., 2018). Los DES hidrófilos han demostrado ser un disolvente prometedor con una gran capacidad de disolución tanto de gases tóxicos, así como de CO_2 (Chen et al., 2020). Sin embargo, en estos el agua también puede ser absorbida, lo que puede disminuir la capacidad de disolución. Por ello, la búsqueda de disolventes de alta eficacia para capturar CO_2 se orientó hacia los disolventes hidrófobos. En estos la solubilidad del CO_2 aumenta con el aumento de la presión y la disminución de la temperatura. Por lo tanto, los métodos habituales para regenerar los HDES son reducir la presión o aumentar la temperatura. Esto permite reutilizarlos al menos durante cinco ciclos sin que se reduzca la eficiencia de disolución (Zubeir et al., 2018).

2.2.3.2. Tecnología de los alimentos.

La seguridad alimentaria se ha convertido en un tema de gran preocupación. Los diferentes procesos que se llevan a cabo en la cadena de suministro de alimentos, desde la obtención de las materias primas hasta el envasado y almacenamiento, pueden representar un riesgo de contaminación de los productos alimenticios. Por esta razón, resulta de vital importancia investigar y desarrollar tecnologías de detección de contaminantes en los alimentos.

En los primeros pasos de la cadena, los DES se han utilizado en la extracción de pesticidas en el agua, en vegetales y en animales. El equipo de Florindo demostró por primera vez en 2017 que los HDES formados por mentol y ácidos alifáticos podían ser utilizados como extractantes de pesticidas en agua (Florindo et al., 2018). Farajzadeh y sus colaboradores se han centrado en la investigación de los HDES en la extracción de pesticidas para obtener disolventes más ecológicos y eficientes. Por ejemplo, utilizando el cloruro de colina y el 4-clorofenol como agente de extracción, se han obtenido factores de enriquecimiento altos, así como mayor repetitividad en el método (Farajzadeh et al., 2016). En otro estudio utilizaron componentes naturales, como el mentol y el ácido dicloroacético, diseñando un DES con menor viscosidad, lo que facilitó la transferencia de masa y la eficiencia en la extracción (Farajzadeh et al., 2019). El equipo de Farajzadeh también ha avanzado en el desarrollo de técnicas que permiten maximizar los beneficios de los HDES, como una nueva separación de fases basada en la solidificación de una gota orgánica flotante aprovechando la temperatura de congelación adecuada de los HDES. El grupo de Farajzadeh propuso el uso de HDES basados en cloruro de colina y ácido decanoico en el método basada en la solidificación de una gota orgánica flotante para la extracción y preconcentración de diferentes clases de pesticidas en muestras de leche (Jouyban et al., 2020).

Entre otros usos, la industria alimentaria también investiga sobre la utilización de los DES para detectar otras sustancias en los alimentos. Estas sustancias pueden ser legales, como colorantes (Ahmadi et al., 2019; Faraji, 2019) o conservantes (Zhang et al., 2019); o ilegales, como pigmentos tóxicos (Liu et al., 2019), blanqueadores (Shi et al., 2020) o metales pesados (Sorouraddin et al., 2021). Además, también existen líneas de

investigación enfocadas en la detección de contaminantes en los envases de los alimentos. Como es el caso de la detección de ésteres de ftalato (Li et al., 2020), bisfenoles (Yang et al., 2020), que pueden llegar a actuar como disruptores endocrinos.

2.2.3.3. Purificación y producción de biodiesel.

El biodiésel se obtiene a través de una reacción de transesterificación de aceites vegetales utilizando metanol o etanol. Durante esta reacción, se produce glicerol como subproducto, este se separa del biodiésel mediante un proceso de decantación. Sin embargo, siempre permanece una cantidad significativa de glicerol en el seno del biodiésel, lo que requiere tratamientos adicionales para cumplir con las especificaciones de la Sociedad Estadounidense para Pruebas y Materiales, ASTM (por sus siglas en inglés *American Society for Testing and Materials*), antes de poder ser utilizado (Zhang et al., 2012). El uso de DES se ha incorporado en el proceso de fabricación de biodiésel con dos objetivos: el primero, actuar como catalizadores en la reacción de transesterificación; el segundo, como agente para la separación del glicerol remanente gracias a su alta polaridad (Troter et al., 2016).

Ya en el año 2007 Abbott y su equipo analizaron la capacidad de varias sales de amonio para formar mezclas eutécticas en presencia de glicerol. Estos DES eran miscibles con el agua e inmiscibles con el biodiésel. Inicialmente, se añadieron estas sales puras al biodiésel crudo para evaluar si se podía formar espontáneamente un DES con el glicerol residual, pero el sistema no funcionó. El mismo equipo, decidió modificar la relación molar entre el DES y el biodiésel con el objetivo de extraer el glicerol. Esta prueba sí obtuvo los resultados esperados, alcanzando con un ratio 1:1 de DES/biodiésel una extracción que alcanzó un ratio molar 1:2 sal de amonio/glicerol (Abbott et al., 2007). Esto mismo fue corroborado por Shahbaz y su equipo estudiando la capacidad de extraer el glicerol de biodiésel procedente de aceite de palma pero con diversos DES basados en cloruro de colina, obteniendo que la relación molar óptima para la extracción era de 1:1 entre el DES y el biodiésel (Shahbaz et al., 2010). Kleiner y colaboradores fueron más allá al desarrollar un método de transesterificación enzimática que permite obtener biodiesel de alta calidad a partir de aceite de colza refinado y aceites de cocina de baja

calidad, con porcentajes de ácidos grasos residuales dentro de los límites de la norma estándar, sin necesidad de utilizar pasos adicionales de purificación (Kleiner et al., 2016).

2.2.3.4. Nanotecnología

Los nanomateriales presentan propiedades únicas, como magnéticas, electroquímicas y fotónicas, por esta razón, han encontrado una amplia gama de aplicaciones en diversos campos, como la catálisis, la electrónica o los dispositivos ópticos (Azzouz et al., 2023). El control de la morfología de las nanopartículas es fundamental, ya que da lugar a materiales con propiedades y funciones fisicoquímicas diferentes. Por lo tanto, la fabricación a gran escala de nanopartículas con un tamaño y una funcionalidad bien definidos constituye un gran reto (Zhang et al., 2012). Se ha comprobado que los DES generan una mejora en el tamaño y la forma de los nanomateriales durante el proceso de síntesis (Abo-Hamad et al., 2015).

En 2008, Liao y colaboradores trabajaron en la síntesis controlada para nanopartículas de oro en la que se sustituyeron los tensoactivos tradicionales por DES formado por cloruro de colina y urea. La forma estrellada de las nanopartículas obtenidas presentaba una actividad superior para la reducción electrocatalítica de H_2O_2 (Liao et al., 2008). Otra posibilidad es el uso de NADES como agentes funcionalizadores de nanomateriales. En 2015, se utilizaron por primera vez como agentes funcionalizadores del grafeno, dando lugar a un nuevo material que puede utilizarse en aplicaciones relacionadas con la administración de fármacos o el tratamiento de aguas residuales (Hayyan et al., 2015). Długosz y su equipo estudiaron la formación de nanopartículas de sulfuro de selenio (SeS_2), un material bioactivo contra microorganismos, utilizando disolventes eutécticos profundos naturales. El análisis confirmó que la síntesis de SeS_2 transcurrió con éxito, obteniendo partículas estables y homogéneas, comprobando también que la actividad antibacteriana y antiviral aumentó (Długosz et al., 2022).

En lo que respecta a la tecnología de los sensores y los materiales conductores, los nanocristales de celulosa presentan propiedades interesantes en estos campos. Wang y sus colaboradores propusieron un método de extracción para producir nanocristales de celulosa utilizando DES, la cual aumentaba la estabilidad de la suspensión de nanocristales, permitiendo reciclar y reutilizar el disolvente durante al menos tres ciclos

(Wang et al., 2020). Además, Zhang y su equipo se centraron en la preparación de nanocristales de celulosa. Los autores descubrieron que el aumento del tiempo de tratamiento con DES de 0,5 horas a 2,5 horas aumentaba el rendimiento de los nanocristales de celulosa del 27% al 65,2% (Zhang et al., 2022).

2.2.4. Sistemas considerados en la tesis

A continuación, se detallan los componentes específicos utilizados en el presente trabajo de investigación, así como las combinaciones estudiadas Tabla 4. Todas las mezclas objeto de estudio pertenecen al subgrupo de los NADES con carácter hidrófobo. Se realiza una breve descripción de cada uno de los componentes y en las tablas 5 y 6 se muestra un resumen de sus propiedades más relevantes.

Tabla 4. Relación de NADES estudiados en el presente trabajo de investigación.

Mezcla	Sistema						Publicación
	HBD	HBA					
NADES	C10AC	MEN	THY	CIN	CAR	GER	IV
	C14AC	MEN	THY	CIN	CAR	GER	IV
	C18AC	MEN	THY	CIN	CAR	GER	IV
	CAR			THY			V

2.2.4.1. HBA - Aceptor de enlaces de hidrógeno.

Timol (THY)

Monoterpenoide de origen natural que se encuentra habitualmente entre los aceites esenciales del tomillo y el orégano. Debido a sus propiedades se ha utilizado en múltiples aplicaciones en el campo de la medicina, la industria alimentaria o la agricultura.

El timol presente una amplia actividad antimicrobiana, se ha utilizado directamente contra microorganismos patógenos (Pérez-Recalde et al., 2018), aunque más recientemente se está explorando su uso como aditivo en materiales biopoliméricos para el tratamiento de heridas (Walczak et al., 2020).

Mentol (MEN)

La Química Verde postula al mentol como un gran candidato para generar mezclas eutécticas sostenibles, por su carácter hidrófobo, su bajo coste y su disponibilidad en la

naturaleza. Puede extraerse de medios naturales abundantes y económicos, como la menta piperita, o a través de síntesis (Ribeiro et al., 2015).

Ha sido utilizado por ejemplo como vehículo para la administración de fármacos (Stott, 1998), como analgésico en sí mismo (Patel et al., 2007) o antitusivo (Kamatou et al., 2013). También se ha explorado su uso como agente extractante en el desarrollo de nuevos métodos de extracción de bisfenoles (Liu et al., 2020).

Eucaliptol o Cineol (CIN)

Terpeno también conocido como 1,8-cineol. Es un aceite esencial natural procedentes de varias especies naturales, incluido el aceite de hoja de eucalipto o lavanda.

Recientemente se ha estudiado su uso como medio de administración transdérmica de fármacos antiinflamatorios, como el ibuprofeno (Rahman et al., 2021). Sin embargo, comúnmente es utilizado en dolencias que tienen que ver con el aparato respiratorio, como bronquitis o sinusitis (Juergens et al., 2003).

D-Carvone (CAR)

También conocido con carvona, es un terpenoide de origen natural procedente de los aceites esenciales de semillas de mandarina, menta verde y hierba de jengibre.

En estudios con ratas, ha demostrado presentar un efecto supresor contra el aumento de peso (Alsanea et al., 2017). Sin embargo, Rozas y su equipo enfocan el estudio de las propiedades de la carvona como uno de los componentes de un NADES en aplicaciones para la captura de CO_2 (Rozas et al., 2021).

Geraniol (GER)

También se trata de un monoterpenoide volátil, pero a diferencia de los anteriores es acíclico. Aunque también se puede obtener de forma sintética, es más habitual a partir de plantas aromáticas como el geranio, la hierba limón y la valeriana

Presenta un efecto desinflamatorio en el hígado y su administración en ratas ha demostrado tener un efecto hepatoprotector y regenerador (Chen et al., 2016), además de reducir los niveles de grasa en el torrente sanguíneo (Jayachandran et al., 2015).

2.2.4.2. HBD - Donador de enlaces de hidrógeno.

Ácido decanoico (C10AC)

También conocido como ácido cáprico, es un ácido graso saturado que de manera natural se puede encontrar en el aceite de coco o en el aceite de palma, además de en la leche de algunos mamíferos.

Además de sus conocidos usos en la industria alimentaria o farmacéutica, recientemente se está estudiando su uso en el campo de la extracción de CO2 en combinación con otros componentes naturales para formar NADEs (Haider et al., 2020; Rozas, 2024).

Ácido mirístico (C14AC)

El ácido mirístico es un ácido graso saturado con 14 átomos de carbono que se obtiene del fraccionamiento de aceites de tipo láurico. Estos pueden ser de origen vegetal como el aceite de coco y de palma, o grasas animales como la mantequilla y la leche.

El ácido mirístico tiene un alto poder antimicrobiano. En estudios recientes se ha analizado su potencial en conjunto con otros componentes naturales, resultando no solo que conservan la actividad antimicrobiana frente a bacterias como el Escherichia coli, sino que presentan efectos sinérgicos con otros ácidos saturados como el ácido cáprico o esteárico (Silva et al., 2019).

Ácido esteárico (C18AC)

El ácido esteárico, también conocido como ácido octadecanóico, es un ácido graso saturado de origen natural que se obtiene mediante la saponificación de aceites y grasas vegetales, como caco o karité; y animales, como lácteos o pescados.

Además de su utilización como agente antimicrobiano, Silva y su equipo analizó la combinación entre el ácido esteárico y mentol en su aplicación en apósitos para heridas, con el objetivo de neutralizar cepas de Estafilococos (Silva et al., 2019). Otro uso reciente de este ácido es como aditivo en el recubrimiento de tejidos para convertir su superficie en hidrófoba (Xu et al., 2022).

Ácido linoléico (C18AC)

El ácido linoleico es un ácido graso esencial que se encuentra de forma natural en aceites de soja, girasol y nueces, entre otros. También se puede obtener sintéticamente mediante la hidrólisis de estos aceites vegetales.

Este ácido graso ha sido utilizado como alternativa potencial a los catalizadores tradicionales, de cara a simplificar las operaciones de filtración y pretratamiento en las reacciones de esterificación de del aceite de palma como materia prima para la producción de biodiésel (Hayyan et al., 2014). También se ha aplicado como agente extractante de ácidos esenciales existentes en microalgas (Moreno et al., 2022).

Ácido oleico (C18AC)

Es un ácido graso monoinsaturado de la familia de los ácidos grasos omega 9. Aunque es posible obtenerlo sintéticamente, lo más habitual es su obtención de manera natural a través de aceites vegetales, como el aceite de oliva o de girasol, y grasas de origen animal, como la de cerdo.

Entre las diferentes aplicaciones que se están estudiando con este ácido se encuentra la administración de fármacos quimioterápicos, gracias a su biocompatibilidad (Kim et al., 2021); o a su uso como extractante de pigmentos de ciertas microalgas sin necesidad de tratamientos previos (Pitacco et al., 2022).

Tabla 5. Descripción y propiedades de los HBA analizados en el presente trabajo de investigación.

NOMBRE	2-iso-propil-5-metilfenol	2-Isopropyl-5-methylcyclohexanol	3,7-Dimetil-2,6-octadien-1-ol	1,8-Cineole	(S)-5-Isopropenyl-2-methyl-2-cyclohexanona
Abreviatura	**Timol THY**	**Mentol MEN**	**Geraniol GER**	**Eucaliptol CIN**	**D-Carvone CAR**
Fórmula	$C_{10}H_{14}O$	$C_{10}H_{20}O$	$C_{10}H_{18}O$	$C_{10}H_{18}O$	$C_{10}H_{14}O$
CAS	89-83-8	89-78-1	106-24-1	470-82-6	2244-16-8
Pm (g/mol)	150,22	156,27	154,25	154,25	150,22
Tª Fusión (°C)	48 - 51 °C	34 - 36 °C	-15 °C	1 - 2 °C	< 15 °C
Densidad (g/ml)	0,965 (25°C)	0,89 (25°C)	0,879 (20 °C)	0,921 (25 °C)	0,96 (25 °C)
Viscosidad (mm^2/s)	-[a]	-[a]	5,0 (20 °C)	3,4 (20 °C)	2,4 (20 °C)

[a] *Sólido a temperatura ambiente*

Timol	**D-Carvone**	**Mentol**	**Geraniol**	**Eucaliptol**
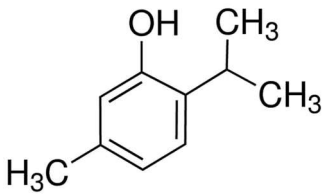	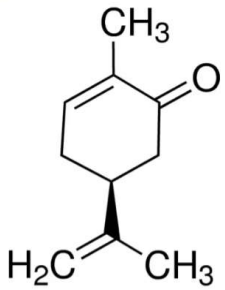	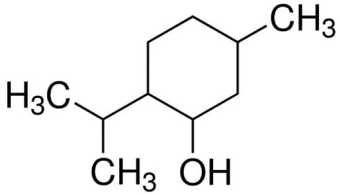	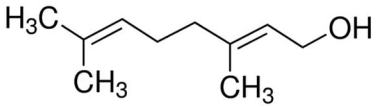	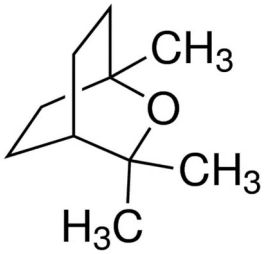

Tabla 6. Descripción y propiedades de los HBD analizados en el presente trabajo de investigación.

NOMBRE	Ácido decanoico	Ácido tetradecanóico	Ácido cis-12-octadecanóico	Ácido cis-9-octadecanóico	Ácido octadecanóico
Abreviatura	**Ácido cáprico C10AC**	**Ácido mirístico C14AC**	**Ácido linoléico C18AC**	**Ácido oléico C18AC**	**Ácido esteárico C18AC**
Fórmula	$C_{10}H_{20}O_2$	$C_{14}H_{28}O_2$	$C_{18}H_{32}O_2$	$C_{18}H_{34}O_2$	$C_{18}H_{36}O_2$
CAS	334-48-5	544-63-8	60-33-3	112-80-1	57-11-4
Pm (g/mol)	172,26	228,38	280,45	282,46	284,48
Tª Fusión (°C)	27 - 32 °C	52 - 54 °C	-5 °C	13 - 14 °C	67 - 72 °C
Densidad (g/ml)	0,893 (25 °C)	0,8622 (54 °C)	0,902 (25 °C)	0,89 (25 °C)	0,845 (25 °C)
Viscosidad (mm^2/s)	-[a]	-[a]	30,6 (30°C)	26,9 (30°C)	-[a]

[a] *Sólido a temperatura ambiente*

Ácido decanoico	**Ácido mirístico**	**Ácido esteárico**
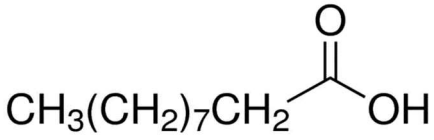	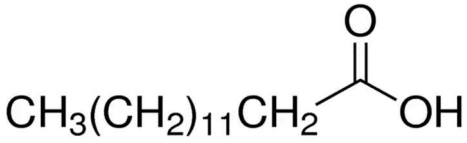	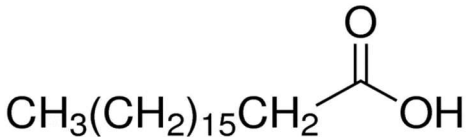

Ácido linoléico	**Ácido oléico**
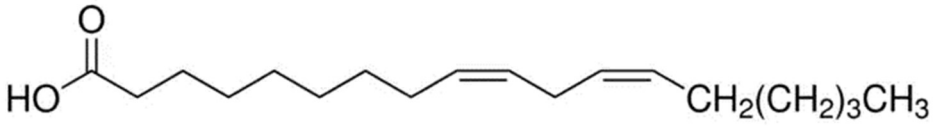	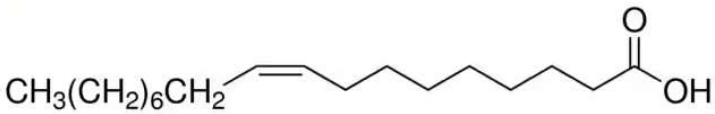

Capítulo 3
Metodología

3.1. Experimental

En el presente apartado se describen los métodos de preparación de las distintas mezclas binarias, DSILs y NADES. Además, se realiza la descripción de los fundamentos teóricos en los que se basan las medidas experimentales de densidad y viscosidad, así como los equipos utilizados y el procedimiento para llevar a cabo las medidas.

3.1.1. Preparación de las muestras

3.1.1.1. Líquidos iónicos

Se prepararon mezclas binarias de líquidos iónicos cuyas composiciones, calculadas en fracciones molares, fueron las siguientes: 0.05, de 0.10 a 0.90 en intervalos de 0.10, y 0.95. Además de estas once composiciones, también se incluyeron los componentes puros. Estas fracciones molares fueron suficientes para describir el comportamiento viscosimétrico y, en la mayoría de los casos, las propiedades derivadas de la densidad. En los casos en los que no fueron suficientes para tener una descripción adecuada, se prepararon nuevas mezclas para describir las regiones menos definidas y para las cuales se determinaba solo la densidad. El volumen preparado de las mezclas fue el suficiente para poder medir la densidad y la viscosidad cinemática.

Inicialmente los líquidos iónicos fueron sometidos a un proceso de desgasificación. En sus recipientes originales, se sumergieron varios centímetros en un baño de ultrasonidos de acero inoxidable (JP Selecta™) durante 10 min. Una vez desgasificados, los recipientes fueron sellados herméticamente con Parafilm y almacenados en un desecador con sílica-gel, en un lugar protegido de la luz.

Las muestras fueron preparadas en lotes con el objeto de minimizar la exposición a la atmósfera de los líquidos puros. En cada lote se abarcó el rango completo de fracciones molares de la mezcla binaria. Los componentes de cada una de las muestras se añadieron por pesada, haciendo uso de una balanza analítica Mettler (modelo AE240), este equipo presenta una precisión de 10^{-5} g. En primer lugar, se tara el frasco a utilizar vacío, limpio y seco. Posteriormente, se vertió y se pesó la cantidad calculada de cada uno de los líquidos iónicos puros, obteniendo las cantidades reales por diferencia. Los líquidos se añadieron en el frasco cuidadosamente para evitar turbulencias que pudieran introducir burbujas de aire en el seno de la mezcla. Una vez incorporados ambos líquidos iónicos puros, los frascos fueron cerrados con tapones herméticos.

El último paso consistió en homogeneizar las mezclas binarias. Se realizó una agitación suave de los frascos a temperatura ambiente, hasta que se comprobó que la mezcla resultante era totalmente homogénea. El proceso de agitación se realizó intentando reducir la posibilidad de incorporar aire a la mezcla.

3.1.1.2. Disolventes Eutécticos Profundos

En el caso de los NADES, los ratios molares seleccionados para la determinación de las propiedades de las mezclas, variaron acorde a su comportamiento a temperatura ambiente. Algunos de los ratios molares analizados se presentaban en estado sólido en todo el rango de temperaturas estudiado.

Algunos de los componentes presentan una temperatura de fusión alta, haciendo que se encuentren en estado sólido durante su manipulación en la preparación de las mezclas. A pesar de esto, el proceso de preparación de las mezclas se realizó de la misma forma que para las mezclas de líquidos iónicos. Sin embargo, la homogeneización de las mezclas sí se llevó a cabo de manera diferente. Los NADES fueron sometidos a al menos 8 horas agitación entre temperatura ambiente y 313,15 K. Los NADES de los cuales se obtuvieron mezclas homogéneas y estables a temperatura ambiente, fueron almacenados en tarros cerrados, en un lugar seco y protegido de la luz.

3.1.2. Densidad

En este epígrafe se describe de forma detallada el fundamento teórico relativo a la densidad, así como sus propiedades derivadas. Además, también se detalla el principio del funcionamiento de los equipos empleados en la determinación de la densidad de los líquidos iónicos puros y las diferentes mezclas binarias analizadas, tanto ILs como NADES.

3.1.2.1. Fundamento teórico

La densidad (ρ) es una propiedad física esencial en la caracterización de los sistemas líquidos. Su importancia radica en la cantidad de información que proporciona su valor, ya que está vinculado con la composición de las sustancias y es consecuencia, entre otras cosas, de las interacciones intermoleculares y el grado de empaquetamiento de las estructuras de las mezclas. Por esta razón, su determinación es fundamental tanto en el análisis experimental como el teórico, además de ser necesaria para el cálculo de otras magnitudes físicas, como la viscosidad dinámica (η). En la caracterización de nuevas sustancias, la comparación entre los valores de ρ obtenidos para un compuesto puro y sus mezclas puede aportar información acerca de cómo se relacionan los componentes de la mezcla y qué cambios se producen en la estructura.

3.1.2.2. Densímetro

Existen múltiples métodos y equipos enfocados a la medida de la densidad. En este caso, para todas las mezclas analizadas, se ha utilizado un densímetro digital basado en el principio de oscilación mecánica. En este, la masa del fluido genera una variación en la masa efectiva del oscilador, lo que conlleva a un ajuste en la frecuencia de oscilación del mismo. El equipo utilizado

para la medida de la densidad ha sido el densímetro Anton-Paar DMA 5000, denominado de tipo oscilador en U o tubo vibrante (Figura 24).

Figura 24. Imagen del densímetro utilizado.

El principio de operación del densímetro se fundamenta en la variación de la frecuencia del oscilador hueco en forma de «U» cuando dispone de un fluido en su interior. El tubo vibra perpendicularmente al plano horizontal y cuando dispone de fluido en su interior produce un cambio en la masa efectiva del mismo, lo que provoca a una variación en la frecuencia de oscilación. Por ello es imprescindible que el tubo se encuentre completamente lleno y que haya el menor número posible de burbujas en su seno. En la Figura 25 se representa de forma esquemática la forma del tubo vibrante en forma de U. La vibración puede definirse como una simple oscilación armónica, que permite definir la densidad a través de la expresión (1) (Fortin et al., 2013).

$$\mathrm{P} = K\tau^2 + L \tag{1}$$

$$\mathrm{K} = \frac{C}{4\pi^2 V_t} \tag{2}$$

$$\mathrm{L} = \frac{m_t}{V_t} \tag{3}$$

Donde:

- τ: período de oscilación.
- V_t: volumen del tubo U.
- m_t: masa del tubo U.
- C: constante, que depende del tamaño y la forma del tubo y es proporcional al módulo de Young del material.

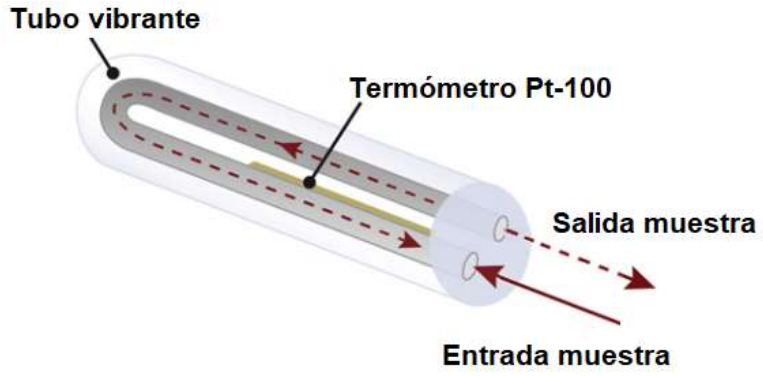

Figura 25. Esquema del oscilador en U que contiene el densímetro.

Se trata de una tecnología desarrollada y patentada por Anton-Paar que permite obtener medidas de densidad del orden de 10^6 g/cm^3 en menos de 1 minuto. En la Tabla 7 se presentan las especificaciones técnicas principales del equipo.

Con este equipo es posible programar rampas de temperatura para llevar a cabo mediciones de manera continua y automática en un rango de 0 °C a 90 °C con una precisión de 0,001 °C. El tubo vibrante se sitúa dentro de una pequeña cámara que, además de facilitar un rápido equilibro térmico, protege al tubo y lo aísla de vibraciones externas. Esta cámara está equipada con un visor que permite la observación de la muestra durante la inyección, para poder comprobar que el fluido llena por completo el tubo y que haya la menor cantidad de burbujas posible en su interior, dos condiciones indispensables para garantizar una medida precisa.

Tabla 7. Datos técnicos del equipo ANTON-PAAR DMA 5000

Rango de medida densidad	0 – 3 g/cm^3
Precisión	Densidad – ±0,000005 g/cm^3 Temperatura – 0,01 °C
Repetibilidad	Densidad – ±0,000001 g/cm^3 Temperatura – 0,001 °C
Rango de temperatura trabajo	0 °C a 90 °C
Volumen muestra necesario	1 ml
Tiempo de medida (tras alcanzar equilibrio térmico)	40 segundos
Material tubo vibrante	Vidrio borosilicato

3.1.2.3. Procedimiento de medida

Una vez configurado el densímetro con la rampa de temperatura de trabajo y antes de introducir la muestra, es fundamental asegurarse de que el oscilador esté limpio y seco. Para ello, con la ayuda de una jeringa, se limpia el oscilador con acetona seca, se extrae la acetona seca con la

propia jeringa y se acciona la bomba del densímetro, la cual bombea aire seco a través del oscilador.

Se sigue el mismo procedimiento para la determinación de los ILs puros, las mezclas binarias de ILs y los NADES en estado líquido a temperatura ambiente. Con una jeringa se extrae una alícuota de 1,5 ml de las mezclas binarias y se inyecta en el tubo vibrante. El volumen mínimo necesario para llenar el tubo es 1 ml, pero se toma 1,5 ml por seguridad. Como ya se ha indicado, es fundamental que no existan burbujas de aire en el seno de las mezclas líquidas, ya que la presencia de estas puede interferir en la medida las propiedades. Se inicia el programa de medidas y el densímetro de forma automática alcanza el equilibrio térmico a las temperaturas indicadas y registra el valor de la densidad. Para todos los sistemas estudiados se registró la densidad en el rango de temperaturas comprendido entre 283,15 K y 313,15 K en gaps de 5 K. Una vez obtenidos los valores de la densidad deseados, para realizar las medidas de la siguiente mezcla se inicia el proceso desde la limpieza de la celda.

3.1.3. Viscosidad

En esta sección se explica detalladamente el fundamento teórico relativo a la viscosidad y sus propiedades derivadas. Asimismo, se describe el principio de funcionamiento de los equipos utilizados en la determinación de la viscosidad cinemática (ν) de los líquidos iónicos puros y las diferentes mezclas de ILs y NADES analizadas.

3.1.3.1. Fundamento teórico

La cinética física es la disciplina científica que se dedica al estudio de las velocidades y mecanismos de los fenómenos de transporte. Estos fenómenos se producen cuando el sistema no se encuentra en un estado de equilibrio, debido al transporte de materia o energía dentro del sistema mismo o entre el sistema y su entorno. La viscosidad es la magnitud que representa la resistencia al movimiento que ejercen las moléculas respecto a las otras cuando se ejerce una fuerza sobre las mismas. La viscosidad se encuentra enmarcada dentro de las propiedades de transporte de materia. En el caso ideal de que el valor de la viscosidad fuera cero, no existiría resistencia entre las moléculas de la sustancia, siendo el comportamiento de los gases el más cercano a este supuesto. Por consiguiente, analizar la viscosidad en líquidos permite obtener información sobre las fuerzas intermoleculares presentes en ellos y su respuesta ante una fuerza externa. Estos aspectos resultan fundamentales para la caracterización de sustancias, como es el caso de los líquidos y las mezclas estudiadas en este trabajo. La viscosidad dinámica (η) se define como la fuerza por unidad de área necesaria para mantener una diferencia entre las velocidades de dos capas de fluido paralelas entre sí. Dicho de otro modo, podría decirse que es la resistencia interna de las moléculas de un fluido en movimiento.

3.1.3.2. Viscosímetro

Al igual que para las densidades, también existen diversos métodos o dispositivos para la determinación de viscosidades de líquidos newtonianos, que son aquellos donde la viscosidad no depende de la velocidad. En este trabajo, para medir la viscosidad dinámica de todos los sistemas, se han utilizado microviscosímetros capilares de tipo Ubbelohde. Estos microviscosímetros presentan un tercer tubo que permite desahogar el viscosímetro durante la medida (Figura 26), haciendo que el resultado sea independiente del volumen de líquido introducido, eliminando los efectos de carga.

La viscosidad dinámica (η) fue definida por Navier y Stokes en su teoría sobre los fluidos viscosos. Para los microviscosímetros capilares, la ecuación de Poiseuille (4) define la viscosidad dinámica de un fluido newtoniano como la relación entre la velocidad de flujo del fluido, que resulta de una diferencia de presión, y las características geométricas del tubo capilar.

$$\mathrm{H} = \frac{\pi R^4 \Delta p}{8VL} t \tag{4}$$

Donde:

- V: volumen de fluido que fluye a través del capilar.
- t: tiempo que tarda el volumen de fluido en trascurrir por el capilar.
- Δp: diferencia de presiones aplicada.
- R, L: respectivamente, radio y longitud del capilar.

Ya que el movimiento del fluido se debe a la caída vertical por efecto de la gravedad, puede decirse que $\Delta p = \rho g H$, donde *g* es la aceleración de la gravedad, *H* la altura de la caída y *ρ* la densidad del fluido.

A la hora de deducir la expresión de Poiseuille (4) una de las premisas consiste en considerar que el flujo es laminar y constante. Para respetar esta, los viscosímetros se diseñan teniendo en cuenta siempre operar en intervalos donde el número de Reynolds es inferior a 300. Ya que no es posible verificar la condición de flujo constante en la entrada y la salida del capilar, es necesario incluir un término en la expresión que corrija los resultados. La corrección de Hagenbach o corrección de energía cinética, corrección se consideran las más acertadas en este caso. Se fundamenta en que la presión aplicada no interviene solo en vencer las fuerzas de viscosidad dinámica, sino que también acelera el líquido a la entrada del depósito (Kaiser et al., 1989; Van Wazcr et al., 1963). El valor de esta corrección es proporcionado por el fabricante del viscosímetro y depende del tiempo de flujo del líquido a través del capilar. Con esta corrección se obtiene la expresión (5), la cual contiene un factor m que aumenta con el número de Reynolds y depende de la forma de los terminales del capilar (Cannon et al., 1960).

$$\mathrm{N} = \frac{\pi R^4 g H}{8VL} t - \frac{mV}{8\pi L t} \tag{5}$$

Esta expresión suele escribirse de forma simplificada como:

$$\mathrm{N} = K(t - \vartheta) \tag{6}$$

$$\mathrm{K} = \frac{\pi R^4 g H}{8 V L} \tag{7}$$

en la que:

- K*:* constante del viscosímetro utilizado.
- t*:* tiempo que tarda el fluido en atravesar las marcas de medición.
- ϑ: corrección de tiempo aplicada (corrección de tiempo de Hagenbach).

Para las medidas de viscosidad cinemática realizadas han sido necesarios varios microviscosímetros Ubbelohde, un baño térmico con termostato y enfriador para realizar medidas de las mezclas a diferentes temperaturas y un termopar de precisión que permitiera garantizar el equilibrio térmico. En los siguientes apartados se detallan cada uno de los elementos, sus características y su funcionamiento.

Microviscosímetro Ubbelohde

El viscosímetro utilizado para determinar la viscosidad cinemática es un microviscosímetro capilar Ubbelohde con detección optoelectrónica, de SI Analytics. Su configuración y volumen los hace los más apropiados para el trabajo experimental llevado a cabo.

El viscosímetro consta de tres tubos (Figura 26):

- Tubo A: se encuentra el capilar con la esfera de medición y las marcas de referencia.
- Tubo B: se utiliza para la aspiración.
- Tubo C: se utiliza para el llenado del microvisocsímetro.

El líquido asciende a través del capilar mediante aspiración, llenando la esfera y atravesando las marcas de medición. Cuando la unidad de control lo detecta, anula la aspiración y el líquido comienza a bajar por gravedad a través del capilar. La unidad de control cuantifica el tiempo que tarda el líquido en atravesar ambas marcas de medición.

Cada viscosímetro dispone de una constante *K* certificada, gracias a esta se puede realizar posteriormente el cálculo de la viscosidad. La elección del viscosímetro depende de la viscosidad del líquido a medir: cuando mayor es la *K*, mayor diámetro tendrá el capilar y por lo tanto menor resistencia al paso del líquido. Las características de los microviscosímetros utilizados en este trabajo se detallan en la Tabla 8.

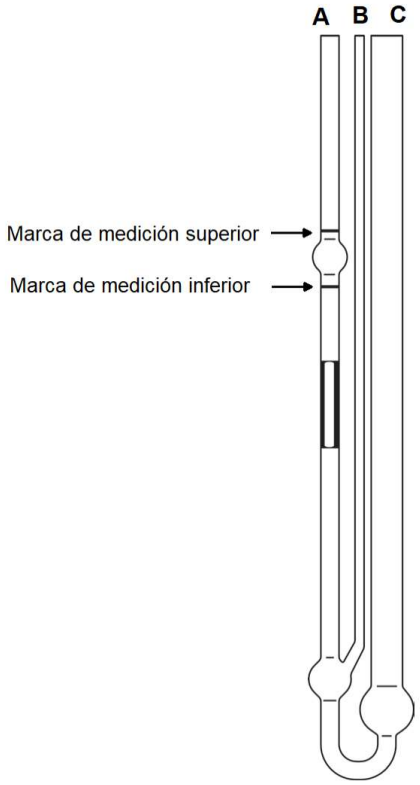

Figura 26. Esquema del microviscosímetro Ubbelohde.

Tabla 8. Características de los viscosímetros utilizados en el proyecto de investigación.

Nº Tipo	Nº Capilar	Ø Capilar (mm)	k	Rango medida (mm^2/s)
537 23	IIc	1.50	0.3142	10 - 100
537 23	IIc	1.50	0.3288	10 - 100
536 21	IIa	1.69	0.4882	50 - 500
537 30	III	2.01	0.9655	100 - 1000

Unidad de control automático AVS 350 y soporte AVS/S.

La viscosimetría capilar es uno de los métodos más precisos a la hora de determinar la viscosidad de fluidos newtonianos. El método consiste en medir el tiempo que requiere el líquido para recorrer un capilar con longitud y diámetro definidos. Este tiempo es posible medirlo de manera automática gracias al conjunto unidad de control automático AVS 350 y soporte AVS/S (Schott, ViscoSystem). La utilización de estos equipos garantiza la reducción de los errores propios de las medidas manuales, proporcionando una precisión de ±0,01 s.

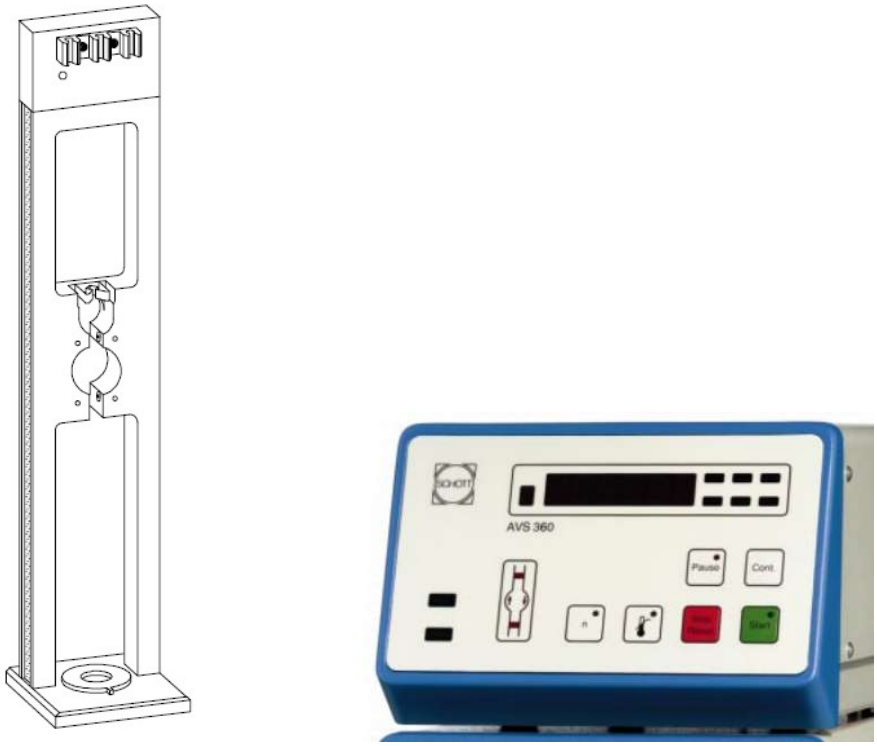

Figura 27. a) Soporte AVS/S. b) Unidad de control automático ViscoSystem AVS 350.

El soporte AVS/S (figura 27.a) se encuentra conectado a la unidad de control y se encarga de sujetar al viscosímetro en el interior del baño térmico de forma totalmente vertical y dispone de los sensores optoelectrónicos responsables de medir el tiempo de paso del líquido entre ambas marcas de medición (Figura 26. *Esquema del microviscosímetro Ubbelohde.*6).

La unidad de control automático ViscoSystem AVS 350 (figura 27.b) permite medir la viscosidad mediante un sistema de sensores optoelectrónicos, regidos por la transmisión de un haz de luz. Cuando se inicia el programa de medida, el equipo realiza una homogeneización de la temperatura del líquido con la del baño térmico, y bombea este a través del capilar durante 3 minutos. Una vez transcurrido este tiempo, se inician las medidas de forma automática.

Termostato CT-52 y enfriador CK 300

Se trata de un baño termostatizado que permite sumergir el soporte AVS/S para determinar la viscosidad de las mezclas binarias a diferentes temperaturas. Presenta un rango de trabajo entre 10 °C y 60 °C configurable a través del termostato CT-52 (Schott Instruments) (figura 28.a). Dispone de una bomba de circulación, una central de calefacción y un control electrónico que adapta automáticamente el suministro de calor necesario para mantener la temperatura de trabajo en el baño. El termostato presenta un visor que permite realizar un seguimiento del comportamiento de las muestras líquidas en el interior del microviscosímetro.

Para asegurar la estabilidad de la temperatura se dispone de un accesorio que permite regular mejor la temperatura del baño de agua, el enfriador CK 300 (Schott Instruments)(figura 28.b).

Este equipo disminuye el rango de temperaturas de trabajo hasta los +5 °C, lo que lo hace más apropiado para los ensayos a realizar.

a) 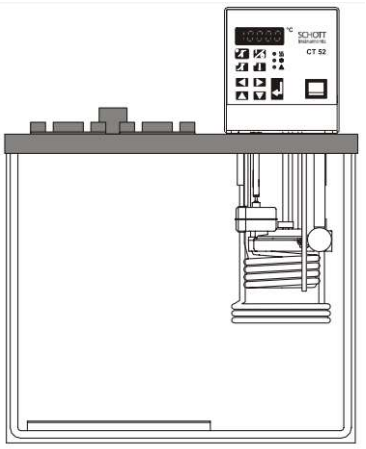

b)

Figura 28. a) Baño termostatizado CT-52. B) Enfriador CK 300.

Termómetro de precisión Anton-Paar CKT-100

La temperatura influye de manera directa en la viscosidad de los líquidos, así que disponer de un control de temperatura que la mantenga lo más estable posible es fundamental. Así que, aunque el termostato CT-52 disponga de un PID para ajustar la temperatura del baño de agua, se ha utilizado como apoyo un termómetro de precisión Anton-Paar CKT 100 (Anton-Paar) (figura 29). Este termómetro permite medir la temperatura con una precisión de 0,001 °C. Este termómetro presenta una sonda formada por un filamento sumergido en un material conductor dentro de un capilar de vidrio, la cual se encuentra sumergida continuamente en el baño de agua.

Figura 29. Termómetro de precisión Anton-Paar CKT 100.

3.1.3.3. Procedimiento de medida

La medida de la viscosidad es un procedimiento menos automatizado que la medida de la densidad. En primer lugar, se toma una alícuota de 4,5 ml de muestra con una pipeta, ya sea

líquidos iónicos puros, DSILs o NADES, y se introduce por el tubo C del microviscosímetro Ubbelohde, quedando almacenada en el bulbo. El viscosímetro se coloca cuidadosamente en el soporte de la unidad de control AVS/S, y se sitúan las mangueras de aspiración en los tubos B y C. Para regular la temperatura del baño térmico, se ajusta la consigna en el termostato y se controla la temperatura con la ayuda del termómetro Anton-Paar CKT-100.

Una vez el baño haya alcanzado el equilibrio térmico se sumerge el soporte AVS/S con el viscosímetro en él y se comienza a medir con la unidad de control AVS/S. Una vez hayan finalizado las medidas, se ajusta el termostato a la siguiente temperatura y se espera de nuevo a que alcance el equilibrio térmico. Para todos los sistemas se realizaron las medidas por triplicado. Una vez finalicen las medidas de tiempo en todo el rango de temperaturas estudiado, el viscosímetro es lavado cuidadosamente con acetona seca para eliminar cualquier traza de la muestra anterior y evitar contaminaciones de las siguientes muestras.

3.1.4. Propiedades termofísicas analizadas

Además de las propiedades que se han determinado experimentalmente de manera directa, existen otras propiedades que se obtienen mediante cálculos basados en las anteriores, que proporcionan información de gran relevancia sobre el comportamiento y la estructura de las mezclas. Una de ellas son los coeficientes de actividad, se trata de coeficientes que permiten ajustar las concentraciones de los componentes de una mezcla en ecuaciones termodinámicas, con el objetivo de poder aplicar con mayor precisión estas expresiones para mezclas que presentan desviaciones con respecto a su comportamiento ideal. Permiten relacionar la actividad con las concentraciones reales y de manera general suelen describirse como (Randall, 1927):

$$a_i = \gamma_i C_i \tag{8}$$

Donde:

- a_i: actividad del componente.
- γ_i: coeficiente de actividad.
- C_i: concentración real del componente.

Por otra parte, es posible calcular funciones de exceso, que describen y cuantifican la desviación de las propiedades de la mezcla con respecto al modelo ideal. Los valores obtenidos en las funciones de exceso representan el resultado directo de fenómenos que suceden en los procesos de mezcla como la disminución o generación de interacciones moleculares o los efectos estructurales que surgen a partir de las mezclas de las diferentes formas y tamaños de dichos componentes. Una función de exceso puede describirse de manera general como:

$$M^E = \Delta M_{mezcla} - \Delta M_{mezcla}^{ideal} \tag{9}$$

Para una propiedad M la función de exceso M^E se define como la diferencia que existe entre el valor de dicha propiedad para una disolución real y el valor de esa misma propiedad para una disolución ideal en las mismas condiciones de presión, temperatura y composición, donde ΔM_{mezcla} es el cambio real que se produce en la propiedad M en la mezcla y $\Delta M_{mezcla}^{ideal}$ es el cambio que se produciría si la mezcla se comportase idealmente. A continuación se describen la principales propiedades termofísicas calculadas en el desarrollo del presente trabajo de investigación.

3.1.4.1. Volumen molar de exceso

El volumen molar de exceso (V^E) de una mezcla líquida multicomponentes se calcula utilizando las densidades de los líquidos puros y las densidades de las diversas mezclas, conociendo la composición o fracción molar de cada componente en dichas mezclas. La expresión que se utiliza de manera general es:

$$V^E = V - V^{id} = \frac{\sum_{i=1}^{C} x_i M_i}{\rho} - \sum_{i=1}^{C} x_i \frac{M_i}{\rho_i} \quad (10)$$

Donde V^E es el volumen molar de exceso, Ves el volumen molar de la mezcla real y V^{id} es volumen molar de la mezcla si se comportara en condiciones ideales. Además, x_i, M_i, ρ_i designan respectivamente fracción molar, peso molecular y densidad y la C indica el número de componentes en la mezcla (Caro, 2009).

3.1.4.2. Volumen molar parcial de exceso

Los volúmenes parciales molares de exceso y a dilución infinita son fundamentales para caracterizar el comportamiento de las mezclas. Ayudan a entender cómo los componentes interactúan y cómo estas interacciones afectan las propiedades macroscópicas de la mezcla. El volumen molar parcial de exceso ($V^{\bar{E}}$) de una mezcla líquida multicomponentes describe cómo difiere el volumen molar parcial de un componente dado y el volumen molar parcial del mismo en estado puro.

$$\bar{V}_i^E = \bar{V}_i - V_i \quad (11)$$

El volumen molar parcial de exceso a dilución infinita ($V_\infty^{\bar{E}}$) de una es el valor límite del volumen parcial molar en exceso cuando la concentración de uno de los componentes tiende a cero, representa el efecto de añadir una cantidad infinitesimal de un soluto a un solvente puro (Trenzado, 1999).

3.1.4.3. Viscosidad dinámica y desviación de la viscosidad

Otra de las propiedades más relevantes de las mezclas líquidas es la viscosidad dinámica (η). Una vez determinados experimentalmente los valores de densidad (ρ) y viscosidad cinemática (v), η se calcula a través de la expresión:

$$\eta = v \cdot \rho \tag{12}$$

Cabe señalar que se trata de una propiedad de transporte, esto quiere decir que describe al sistema cuando no está en equilibrio, es decir, cuando se están produciendo fenómenos de transporte de materia o energía. Por lo tanto, por definición no es posible calcular una «viscosidad exceso», así se recurre al término Desviación de la Viscosidad ($\Delta\eta$). Esta propiedad mide la desviación entre un modelo lineal promediado entre las fracciones molares y las viscosidades de los componentes puros (Caro, 2009).

3.1.4.4. Coeficiente de expansión térmica isobárico

La expresión que define el coeficiente de expansión térmica isobárico α de un líquido puro o de una mezcla de composición x es la siguiente (Caro, 2009):

$$\alpha = \frac{1}{V}\left(\frac{\partial V}{\partial T}\right)_{p,x} = -\left[\frac{\partial(ln\rho)}{\partial T}\right]_{p,x} \tag{13}$$

Donde:

- V: volumen de la mezcla.
- T: temperatura a la que se encuentra la mezcla.
- $\left(\frac{\partial V}{\partial T}\right)_{p,x}$: derivada parcial del volumen con respecto a la temperatura.

El coeficiente de expansión térmica isobárico (α) indica cuánto se expande o contrae una sustancia cuando la temperatura cambia a presión constante.

El coeficiente de expansión térmica isobárico en exceso (α^E) se usa para medir en mezclas el cambio en el coeficiente de expansión térmica, en comparación con la suma de los coeficientes de expansión térmica individuales de los componentes puros, que viene dada por la expresión:

$$\alpha^E = \alpha - \alpha^{id} \tag{14}$$

Donde (α) es el coeficiente de expansión térmica isobárico calcula según la expresión (13) y (α^{id}) representa el coeficiente de expansión térmica isobárico de la mezcla como si los componentes individuales se comportaran de manera ideal.

3.1.5. Correlaciones y modelos

Existen en la literatura una cantidad significativa de expresiones que caracterizan las relaciones funcionales entre las propiedades de las mezclas líquidas y su composición, abarcando desde enfoques puramente empíricos hasta aquellos fundamentados en modelos teóricos. Habitualmente estas expresiones o modelos incluyen un conjunto de parámetros que han de determinarse mediante un ajuste con datos experimentales. A continuación, se presentan las correlaciones o modelos utilizados en este estudio.

3.1.5.1. Ecuación de Redlich y Kister

En 1948, Redlich y Kister formularon una ecuación que permite expresar la magnitud de exceso en un sistema multicomponente en función de las fracciones molares de las mezclas en forma de potencias. Esta ecuación se ha convertido en una de las más empleadas para la representación matemática de las propiedades de exceso en mezclas de líquidos no electrolitos, y es la que se aplica en la presente investigación para correlacionar los datos de fracción molar con el volumen molar de exceso y la fracción molar con la desviación de la viscosidad (Redlich et al., 1948).

Los términos de la ecuación de Redlich y Krister para un sistema de N componentes:

$$Y^E = \sum_{i=1}^{N-1}\sum_{j=i+1}^{N} x_i x_j \left[A_{ij} + B_{ij}(x_i - x_j) + C_{ij}(x_i - x_j)^2 + \cdots\right]$$
$$+ \sum_{i=1}^{N-2}\sum_{j=i+1}^{N-1}\sum_{k=j+1}^{N} x_i x_j x_k \left[\begin{array}{c} A_{ijk} + \sum_{q=1}^{p} B_{ijk,q}(x_i - x_j)^q \\ + \sum_{q=1}^{p} C_{ijk,q}(x_i - x_k)^q + \sum_{q=1}^{p} D_{ijk,q}(x_j - x_k)^q \end{array}\right] + \cdots$$

En esta expresión son necesarios datos experimentales para ajustar los parámetros binarios con subíndices i, j, k … En concreto, para las mezclas binarias estudiadas en el presente trabajo de investigación, la ecuación anterior se puede expresar de la siguiente forma:

$$Y^E = x_1 x_2 [A_{12} + B_{12}(x_1 - x_2) + C_{12}(x_1 - x_2)^2 + \cdots] \quad (15)$$

Este ajuste garantiza que las magnitudes de exceso Y^E (V^E o $\Delta\eta$) tengan valor nulo para los componentes puros, esto es en los extremos del intervalo de fracciones molares, ya que todos los términos quedan multiplicados por $x_1 x_2$. Para mezclas binarias $x_1 + x_2 = 1$, si se establece $x_1 = x$ la ecuación (6) podría expresarse como:

$$Y^E = x(1-x)\sum_{i=0}^{m-1} A_i (2x-1)^i \quad (16)$$

Donde *m* representa el número total de parámetros. El coeficiente A_i es posible obtenerlo a través del método de los mínimos cuadrados, suponiendo que las fracciones molares se

encuentran libres de error y que todos los valores de las magnitudes de exceso (Y^E) presentan el mismo peso estadístico (Caro, 2009).

3.1.5.2. Teoría Prigogine – Flory – Patterson.

La teoría de Prigogine – Flory – Patterson (PFP), es ampliamente utilizada para analizar y predecir las propiedades de exceso termodinámicas, como por ejemplo el volumen molar de exceso (V^E), para diferentes mezclas. En esta teoría, las propiedades termodinámicas en exceso de las mezclas líquidas están relacionadas con las propiedades macroscópicas de los componentes puros. La teoría PFP considera que las propiedades termodinámicas en exceso de las mezclas binarias son la suma de tres contribuciones (Zafarani-Moattar et al., 2006):

- **Interacciones moleculares (χ_{12})**: describe cómo interactúan las moléculas entre sí en la mezcla.

- **Volumen libre**: surge a raíz de la diferencia entre los grados de expansión de los dos componentes. Considera el espacio no ocupado por las moléculas, permitiendo entender la distribución y movilidad molecular.

- **Presión (*P**)**: depende de la diferencia entre la presión interna de los componentes puros y el comportamiento de sus volúmenes en la mezcla.

3.1.5.3. Ecuación Vogel – Fulcher – Tamman.

Generalmente, cuando un líquido se enfría a una velocidad suficiente para evitar su cristalización, la viscosidad o el tiempo de relajación del líquido aumentan drásticamente hasta que se produce la transición vítrea. Los mecanismos que rigen esta transición son sumamente complejos, dando lugar a una evolución de la viscosidad en función del tiempo que no se ajusta al modelo habitual de Arrhenius. Una de las expresiones más utilizadas para describir la dependencia de temperatura en estos casos es la ecuación de Vogel – Fulcher – Tamman (VFT), que viene definida como (Ikeda et al., 2013):

$$\eta = \eta_0 exp\left(\frac{\mathrm{B}_{VFT}}{T-T_0}\right) \tag{17}$$

Donde $\eta(T)$ es la viscosidad a una temperatura T, T_0 es una temperatura hipotética por debajo de T_g donde la viscosidad se vuelve infinita, es un parámetro que facilita la descripción matemática del comportamiento de la viscosidad; η_0 es la viscosidad a T_0 y B_{VFT} es una constante relacionada con la energía de activación, representa la sensibilidad de la viscosidad a los cambios de temperatura (Ikeda et al., 2013).

3.2. Métodos computacionales

Los métodos computacionales son herramientas que posibilitan la obtención de información sobre las estructuras de un sistema químico, así como la predicción de sus propiedades y comportamientos, a través del empleo de métodos matemáticos, algoritmos y simulaciones por ordenador. Estos métodos teóricos se fundamentan en diversos modelos o teorías basadas en la mecánica cuántica y la mecánica molecular.

En este capítulo se realiza una breve introducción a la mecánica cuántica y a la mecánica molecular, así como a diversas herramientas y teorías enmarcadas dentro de estos modelos.

3.2.1. Mecánica cuántica (QM)

La mecánica cuántica, QM (del inglés *Quantum Mechanics*) es una teoría física que describe el comportamiento de las partículas a escalas muy pequeñas, nivel atómico y subatómico. De todas las contribuciones relevante realizadas al inicio del siglo XX, una de las más relevantes fue la elaborada por Schrödinger en 1926 (Schrödinger, 1926). Esta ecuación se representa de manera independiente del tiempo para poder considerar al sistema en uno de sus estados estacionarios, y lo describe a través de la expresión:

$$H\Psi(r) = E\Psi(r) \tag{18}$$

Relaciona la función de onda (Ψ), que describe el estado del sistema y contiene toda la información que es posible conocer del mismo; con la energía (E), en un estado cuántico específico del sistema, donde el operador Hamiltoniano (H) describe la energía total de núcleos y electrones (suma de energía cinética y potencial de las partículas) (Magalí, 2013). El objetivo de la mecánica cuántica es resolver con exactitud la ecuación de Schrödinger con el mayor grado de precisión posible, aunque su resolución implica introducir diversas aproximaciones, como la aproximación de Born-Oppenheimer. Esta aproximación consiste en considerar por separado los movimientos de los núcleos y los electrones, teniendo en cuenta que los núcleos tienen una masa miles de veces mayor que la de los electrones y, por lo tanto, se desplazan más lentamente (Magalí, 2013).

Estos métodos son conocidos como *ab initio*, término que proviene del latín y significa «desde el principio», ya que no incorporan ningún parámetro empírico externo, excepto los valores de las constantes físicas fundamentales. Su principal ventaja es su alta precisión, aunque su coste computacional es extremadamente elevado, por lo que solo se aplican a moléculas con un número reducido de átomos, del orden de decenas. Su uso es esencial en el análisis de reacciones que involucran la ruptura y formación de enlaces (Gracia, 2007).

También existen los métodos semiempíricos, basados en la ecuación de Schrödinger, que contienen una parte basada en la teoría (función de onda y Hamiltoniano) y otra en los

experimentos. Estos son más rápidos que los métodos *ab initio* y permiten estudiar moléculas o sistemas de tamaño mediano y grande. No obstante, su principal desventaja es que presentan una fiabilidad baja (Gutiérrez, 2020).

3.2.1.1. Teoría del funcional de la densidad (DFT)

Ante las dificultades que presenta la ecuación de Schrödinger para ser resuelta, Hohenberg y Kohn desarrollan un procedimiento alternativo y conceptualmente distinto para lograr obtener información acerca de un sistema, permitiendo calcular su energía a través de su correlación electrónica (Hohenberg et al., 1964). Estos autores describen la Teoría del Funcional de la Densidad, demostrando que la energía del estado fundamental de un sistema electrónico está definida por su densidad electrónica, considerándolo un procedimiento variacional alternativo a la solución de la ecuación de Schrödinger. La DFT no intenta calcular la función de onda (Ψ), sino que expresa la energía del estado fundamental como un funcional de la densidad electrónica $\rho_0(r)$, reduciendo el problema a una función de solamente 3 variables:

$$\mathrm{E}[\rho] = \mathrm{F}[\rho] + \int \mathrm{dr}\rho(\mathrm{r})\mathrm{v}(\mathrm{r}) + \mathrm{V}_{ee}[\rho] \tag{19}$$

Donde $\mathrm{F}[\rho]$ es el funcional universal que contiene a la energía cinética, $\mathrm{T}[\rho]$, y $\mathrm{V}_{ee}[\rho]$ es la parte no clásica de la interacción electrónica, representando la repulsión electrónica. Esta teoría ha ganado popularidad porque es posible aplicarla a sistemas relativamente grandes, obteniendo resultados con precisión similar a los obtenidos con aproximaciones para la ecuación de Schrödinger, pero con un coste computacional mucho menor. Y aunque esta ecuación sienta las bases de la DFT, el teorema planteado por Hohenberg y Kohn no proporciona la fórmula matemática exacta que relaciona la energía con la densidad electrónica, así que es necesario recurrir a expresiones aproximadas (Gutiérrez, 2020).

Ante la indeterminación de los funcionales, Khon y Sham en 1965 idearon un método que consistía en generar un sistema ficticio constituido por un conjunto de N electrones no interactuantes sometidos únicamente a la acción de un potencial externo $\mathrm{v}_s(r)$, de forma que la densidad electrónica del estado fundamental de referencia $\rho_s(r)$ es igual a la densidad del estado fundamental exacta $\rho_0(r)$ (Kohn et al., 1965).

El sistema se representa por el determinante de Slater, cuyos elementos son funciones que representan a los electrones del sistema (orbitales, φ_i). Así, la energía cinética es igual a la suma de energías cinéticas individuales, y la densidad electrónica a la suma de densidades orbitales (Gutiérrez, 2020):

$$T_s[\rho] = \sum_{i=1}^{N} \int dr \varphi_i^*(r) \left(-\frac{1}{2}\nabla^2\right) \varphi_i(r) \tag{20}$$

$$\rho(r) = \sum_{i=1}^{N} \rho_i(r) = \sum_{i=1}^{N} \varphi_i^*(r)\varphi_i(r) \tag{21}$$

El modelo de Kohn y Sham incluye un elemento adicional, la expresión clásica de la energía de repulsión electrostática interelectrónica, conocida como interacción coulombiana clásica, $J[\rho]$. Con todo esto, el funcional universal se describe como:

$$\mathrm{F}[\rho] = \mathrm{T}[\rho] + \mathrm{V}_{ee}[\rho] = T_s[\rho] + \mathrm{V}_{ee}[\rho] + E_{xc}[\rho] \quad (22)$$

Donde $E_{xc}[\rho]$ es el funcional de intercambio y correlación, que se define como:

$$E_{xc}[\rho] = T[\rho] - T_s[\rho] + V_{ee}[\rho] - J[\rho] \quad (23)$$

De esta manera, resuelven el problema de la indeterminación de $\mathrm{T}[\rho]$. La clave para la aumentar la precisión utilizando el método propuesto por Kohn y Sham, consiste en utilizar expresiones que permitan una buena aproximación a $E_{xc}[\rho]$ (Magalí, 2013).

El principal inconveniente de la DFT se encuentra en el hecho de que para sistemas en que el modelo escogido da resultados erróneos, no propone una forma sistemática de mejorarlos. En los métodos *ab initio*, un cambio de las aproximaciones a órdenes mayores conduce a resultados mejores. Además, cabe resaltar que la DFT trata de forma incorrecta los sistemas con un único electrón (dado que la energía de correlación-intercambio es diferente de cero), los sistemas con enlaces débiles (complejos de Van der Waals y por transferencia de carga) y la disociación de enlaces en especies iónicas en las que la carga y el espín están separados en distintos fragmentos o localizados en el mismo fragmento (Magalí, 2013).

Funcionales de intercambio y correlación

En síntesis, el funcional toma la densidad electrónica como entrada y produce la energía total del sistema como salida, teniendo en cuenta el efecto del intercambio electrónico y la correlación electrónica. Sin embargo, no se trata de una expresión exacta, es necesario utilizar aproximaciones, como es el funcional de intercambio y correlación, $E_{xc}[\rho]$. La diferencia entre la precisión de los métodos utilizados en DFT radica en la elección del funcional de intercambio y correlación, son parámetros únicos contenidos en una expresión matemática válida para todos los sistemas. Estos parámetros pueden asignarse a través de dos estrategias: forzar a que el funcional cumpla con los criterios especificados o ajustar los parámetros basándose en datos empíricos. En la práctica, suele utilizarse una combinación de ambos enfoques y la evaluación de su precisión implica la comparación con observaciones experimentales o cálculos avanzados. Aunque la elección de un funcional de intercambio y correlación óptimo depende del sistema y las propiedades consideradas (Rozas, 2024). Algunos de los funcionales más utilizados son:

- **Aproximación local de la densidad, LDA (del inglés *Local Density Approximation*)**

Es el funcional más simple, en este la densidad puede ser considerada localmente como un gas de electrones uniforme, partiendo de la premisa de que la densidad varía tan lentamente que es localmente uniforme (Rozas, 2024). En estos, los efectos de intercambio y correlación son locales

y dependen exclusivamente del valor de la densidad electrónica en cada punto. En general proporcionan resultados muy buenos, obteniendo buenas geometrías, aunque con distancias subestimadas. No son adecuados para sistemas con enlaces débiles, ya que tienden a incrementar la energía de los enlaces (Magalí, 2013).

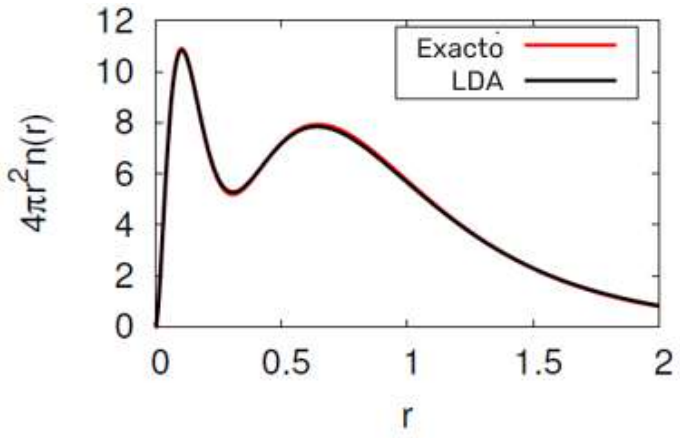

Figura 30. Densidad radial del átomo de Ne exacta y aproximada con funcional LDA. Adaptado de la referencia (Burke et al., 2014).

- **Aproximaciones generalizadas del gradiente, GGA (del inglés *Generalized Gradient Approximation*)**

Se trata de funcionales más complejos que definen con mayor precisión las contribuciones de intercambio y correlación, en los que se considera la densidad electrónica en cada punto y la variación de la misma a su alrededor. Con estos funcionales se mejoran las geometrías, las frecuencias y la densidad con respecto a los LDA, aunque continúan siendo imprecisos en la descripción de complejos de van der Waals (Magalí, 2013).

- **Híbridos**

Incluyen información de la densidad y su gradiente, y la contribución del intercambio de Hartree-Fock (E_x^{HF}) en un radio constante. Son los más utilizados en química cuántica (Gutiérrez, 2020).

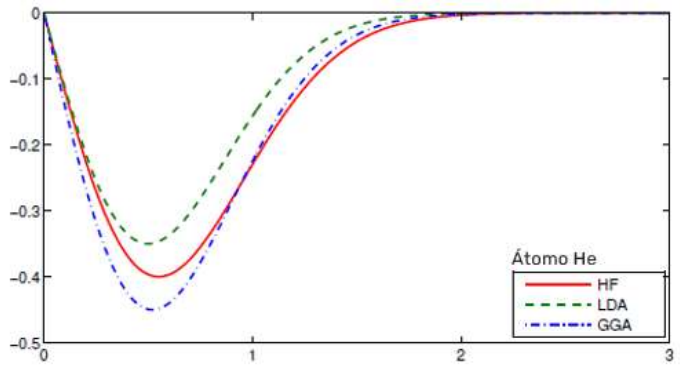

Figura 31. Representación del intercambio promediado de agujeros para el átomo de He definido por funcionales LDA, GGA y sistema exacto. Adaptado de la referencia (Burke et al., 2014).

En el presente trabajo de investigación, los funcionales utilizados durante los cálculos realizados son GGA y de tipo híbrido. En concreto han sido:

- **Funcional B3LYP**

Se trata de un tipo de funcional empleado en química para analizar estructuras y propiedades moleculares, siendo apropiado para la mayoría de los sistemas orgánicos. Este funcional es eficaz en la optimización geométrica de las moléculas y se caracteriza por su rapidez en los cálculos. En este contexto, el número 3 indica que el funcional se fundamenta en tres parámetros (Gutiérrez, 2020).

- **Funcional GGA/PBE**

Se trata de una derivación sencilla de una GGA simple en la que todos los parámetros (distintos de los de la LSD) son constantes fundamentales, mejorando la densidad de espín local (LSD) de átomos, moléculas y sólidos (Perdew et al., 1996). Este funcional utiliza una función racional del gradiente de densidad reducido para el factor de mejora, es de los más empleados y se considera mejorado con respecto a funcionales utilizados anteriormente como PW91 y PW86 (Rozas, 2024).

3.2.1.2. Teoría Cuántica de Átomos en Moléculas (QTAIM)

Desarrollada por Bader en 1990, la Teoría Cuántica de Átomos en Moléculas, QTAIM (*Quantum Theory of Atoms In Molecules*) es una de las herramientas topológicas principales para definir la estructura molecular. La topología es una herramienta matemática dentro de la mecánica cuántica que permite dividir el espacio tridimensional de los sistemas en contribuciones atómicas (Gutiérrez, 2020). QTAIM define una forma intuitiva de dividir las moléculas en átomos basándose en la densidad de carga electrónica, $\rho(r)$, y utiliza los teoremas de la mecánica cuántica para dar cuenta de la noción de enlace químico. Se ha utilizado para el análisis de carga y la comprensión del enlace químico, es ideal para el estudio de interacciones fuertes por puentes de hidrógeno (Alberto et al., 2017).

La definición de átomo de Bader se basa exclusivamente en la densidad de carga electrónica. Utiliza el término «superficie de flujo cero» para referirse al producto escalar de $\rho(\vec{r})$ con $n(\vec{r})$. Esta es una superficie 2D en la que la densidad de carga es un mínimo perpendicular a la superficie. En los sistemas moleculares, la densidad de carga alcanza mínimos entre los átomos y máximos en los núcleos (Rozas, 2024).

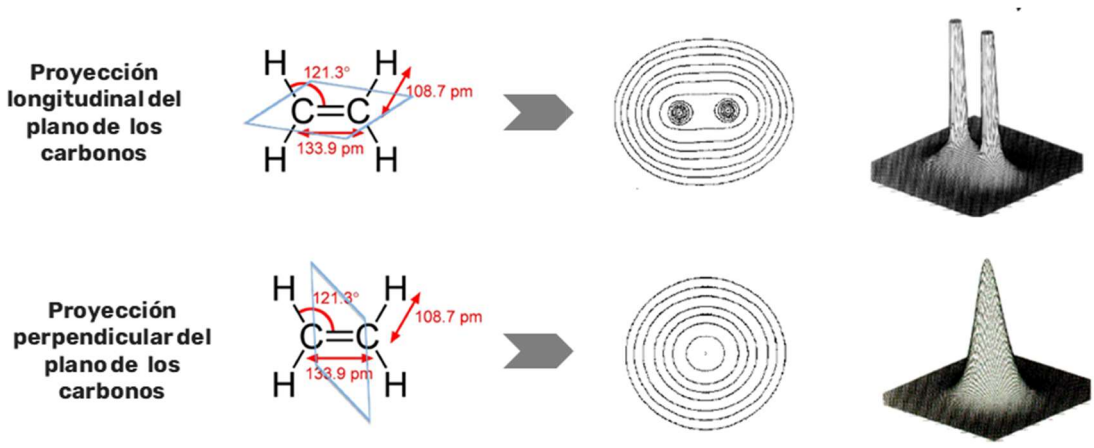

Figura 32. Diferentes proyecciones de ρ(r) sobre el plano en una molécula de etileno, conteniendo solo los dos carbonos. Adaptado de la referencia (Gómez, 2015).

Considerando el gradiente de la densidad de carga electrónica, $\nabla\rho(\vec{r})$, se realiza un análisis cuantitativo de la topología de $\rho(\vec{r})$. Los puntos en los que el gradiente se anula, es decir, la primera derivada de la densidad de carga es cero, se denominan puntos críticos, *CP*, y son clave para definir las propiedades topológicas de un sistema. Existen cuatro tipos diferentes de puntos críticos, los cuales se caracterizan por su rango, ω, que viene determinado por el número de curvas de ρ(r) distintas de cero; y su signatura, σ, que es la suma algebraica de los signos de esas curvas (Matta et al., 2007).

Tabla 9. Descripción de los principales puntos críticos definidos (Matta et al., 2007).

Punto crítico	Elemento de la estructura molecular	Descripción
(3,-1)	Punto crítico de enlace (BCP)	se encuentra entre dos átomos enlazados
(3,+1)	Punto crítico anillo (RCP)	se encuentra dentro de un anillo de átomos enlazados
(3,-3)	Punto crítico nuclear (NCP)	corresponde a máximos locales de *ρ(r)*
(3,+3)	Punto crítico de jaula (CCP)	corresponde a mínimos locales de *ρ(r)*

El Laplaciano $\nabla\rho(\vec{r})$ es fundamental para entender la naturaleza del enlace químico. Además, se establecen relaciones significativas entre el Laplaciano y otros parámetros topológicos, tales como la energía cinética, $G(\vec{r})$, la energía potencial, $V(\vec{r})$, y las densidades de energía total, $H(\vec{r})$. Dentro de la caracterización de enlaces de hidrógeno mediante QTAIM, se observa que mayores valores de densidad electrónica en el BCP están asociados con enlaces de hidrógeno más fuertes. De acuerdo con la clasificación de enlaces de hidrógeno propuesta por Rozas y su equipo, valores positivos del Laplaciano de densidad y de la densidad total de energía electrónica indican enlaces de hidrógeno débiles y moderados; mientras que los valores positivos del

Laplaciano junto con los valores negativos de la densidad total de energía electrónica se relacionan con enlaces de hidrógeno fuertes (Rozas, 2024).

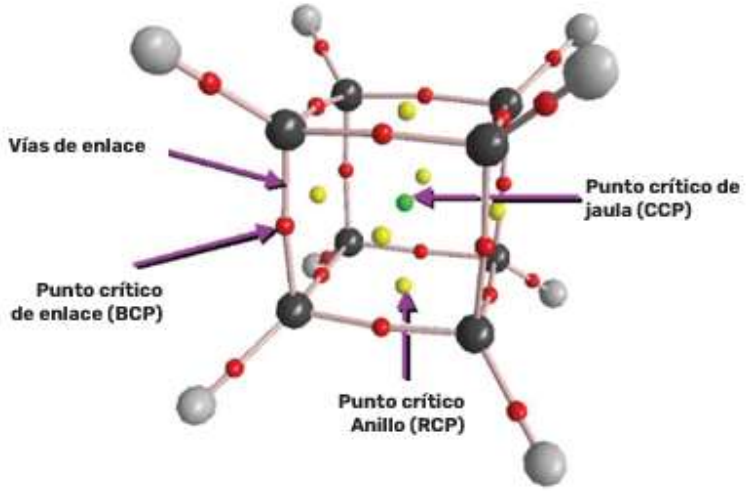

Figura 33. Representación de la molécula de cubano mostrando las trayectorias de enlace (líneas) y los diferentes puntos críticos: nuclear (codificado por colores según el elemento: C= negro, H=gris, F=amarillo), enlace (esferas rojas), anillo (esferas amarillas) y puntos críticos de jaula (esferas verdes). Adaptado de la referencia (Matta et al., 2007).

3.2.1.3. Gradiente de la Densidad electrónica Reducido (RDG)

El Gradiente de Densidad Reducida, RDG (Reduced Density Gradient), permite visualizar isosuperficies de la densidad electrónica existente entre átomos interactuantes. Permite un enfoque más intuitivo que el obtenido con QTAIM de las interacciones de Van der Waals, los enlaces de hidrógeno y las repulsiones estéricas. Además de proporcionar información sobre la naturaleza de los enlaces, permite identificar la presencia de puntos críticos en la densidad electrónica (Boto et al., 2016).

Para distinguir los distintos tipos de interacción, se ha utilizado la función RDG, que se expresa como:

$$RDG(r) = \frac{1}{2(3\pi^2)^{1/3}} \cdot \frac{|\nabla\rho(r)|}{\rho(r)^{4/3}} \quad (24)$$

donde $\rho(r)$ es la densidad electrónica total. Según QTAIM, la relación entre el segundo autovalor de la matriz hessiana de densidad electrónica, λ2, y la densidad electrónica total $\rho(r)$ puede escribirse en la forma:

$$\Omega(r) = sign\big(\lambda_2(r)\big)\rho(r) \quad (25)$$

La cual describe que las interacciones entre los átomos dependen de la densidad de carga electrónica, $\rho(r)$, y del autovalor λ_2 . Estas condiciones se representan a través de la escala de colores que se muestra en la figura X, de tal forma que (Yang et al., 2016):

- **Color azul**: valores de $\rho(r)>0$ y $\lambda_2<0$. Indica presencia de enlaces de hidrógeno.
- **Color verde**: valores de $\rho(r)\approx 0$ y $\lambda_2\approx 0$. Representa interacciones de naturaleza electrostática, tipo Van der Waals.
- **Color rojo**: valores de $\rho(r)>0$ y $\lambda_2>0$. Indica efectos estéricos intramoleculares.

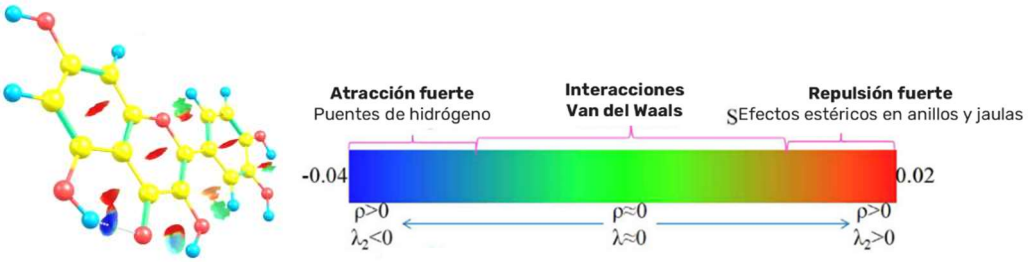

Figura 34. Representación de Iso-superficies RDG y escala de valores. Adaptado de la referencia (Yang et al., 2016).

3.2.1.4. Función de localización de electrones (ELF) e Índice de bifurcación núcleo-valencia (CVB)

La función de localización de electrones, comúnmente referida por sus siglas en inglés ELF (*Electron Localization Function*), es una función local que mide la eficacia de la repulsión de Pauli en un punto específico del espacio molecular. Esta función proporciona una medida de la probabilidad de localizar un electrón en las proximidades de otro electrón de referencia. Asimismo, aporta información relevante sobre la naturaleza de los enlaces químicos, la transferencia de carga y la clasificación de los enlaces químicos en superficies moleculares. Con el objetivo de obtener un índice de localización adimensional, el ELF se compara con el valor correspondiente a un gas de electrones uniforme con una densidad de espín igual a $\rho(\vec{r})$. La relación de estos dos valores, que oscila entre 0 y 1, expresa la localización de electrones para el gas de electrones uniforme, correspondiendo 1 a la localización perfecta y 0,5 al gas de electrones (Rozas, 2024).

Para definir una escala que permite caracterizar los enlaces de hidrógeno débiles y medios basada en criterios topológicos se define el CVB (por sus siglas en inglés, *Core-Valence Bifurcation*). El ELF permite identificar los máximos y sus correspondientes cuencas. Este método delimita dos categorías distintas de cuencas: las cuencas de núcleo, denominadas C, y las cuencas de valencia, denominadas V. Se define el CVB como la diferencia entre el valor mínimo de ELF en el que todas las cuencas de núcleo se diferencian de las cuencas de valencia, y el valor de ELF en el punto de silla que conecta las cuencas. Un valor positivo del índice CVB indica un enlace de hidrógeno débil, mientras que una disminución del índice CVB significa un aumento de la fuerza de la interacción (Fuster et al., 2000).

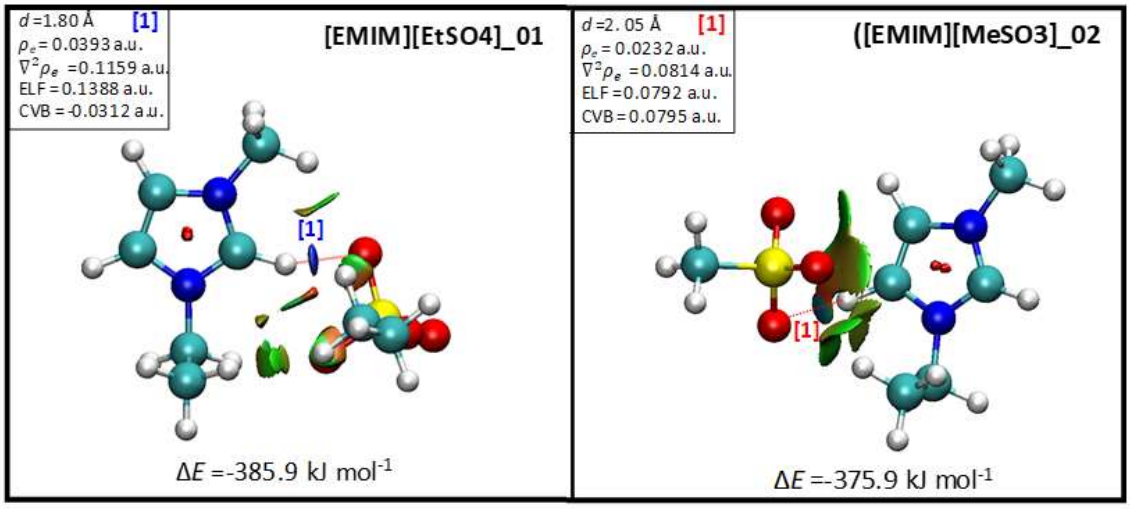

Figura 35. Estructuras optimizadas por DFT para dímeros [EMIM][EtSO4] y [EMIM][MESO3] en agrupaciones 1 : 1 que muestran las configuraciones de menor energía, incluida la energía de enlace, ΔE, las propiedades QTAIM (densidad electrónica, ρe, y Laplaciano de la densidad electrónica, ∇² ρe), la función de localización de electrones (ELF), el índice de bifurcación núcleo-valencia (CVB), todas estas propiedades indicadas en el punto crítico de enlace (BCP).

Programas de cálculo utilizados

Los cálculos DFT se llevan a cabo secuencialmente con el objetivo de resolver la estructura electrónica del sistema. Este proceso consiste en determinar la densidad electrónica y la energía asociada a partir de las posiciones de los átomos. Se inicia con una estimación preliminar de la densidad electrónica, que se ajusta de manera iterativa hasta lograr la autoconsistencia resolviendo las ecuaciones de Kohn-Sham, que se fundamentan en el funcional de energía total. Este proceso iterativo se repite hasta que la densidad electrónica converge hacia una solución estable. En la figura 36 se representa de manera esquemática y simplificada un diagrama de la secuencia.

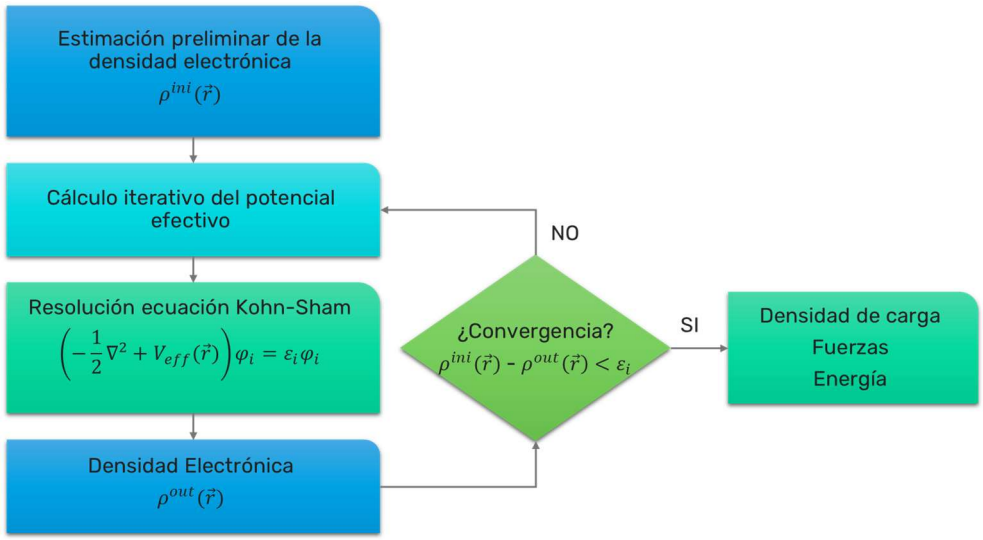

Figura 36. Representación esquemática de simulación DFT. Adaptado de la referencia (Rozas, 2024)

Existe una gran variedad de software para realizar cálculos de mecánica cuántica. A continuación se describen los programas informáticos empleados para realizar los cálculos matemáticos mencionados, así como la visualización de los resultados obtenidos.

- **Avogadro**

Este programa permite construir y optimizar las estructuras de las moléculas y los clusters. Se trata de un software libre que ofrece representaciones de alta calidad y visualizaciones en 3D (figura 37.a).

- **ORCA**

Se trata de un programa general de química cuántica que desde métodos semiempíricos hasta DFT (figura 37.b). Este programa está diseñado para aplicarse en diversos campos: moléculas de gran tamaño, complejos de metales de transición, complejos farmacéuticos, etc. Sus principales aplicaciones son el cálculo y la optimización de geometrías, la búsqueda conformacional, la simulación de espectros vibracionales, así como el cálculo de frecuencias (Neese, 2012).

- **DMol3**

Software del entorno BIOVIA Materials Studio (figura 37.c), se trata de un programa de modelado basado en la DFT para simular procesos químicos y predecir propiedades de materiales con rapidez y precisión. En este trabajo se ha utilizado para la la preoptimización de la geometría y el equilibrio inicial del sistema.

Figura 37. a) Software Avogadro. b) Software ORCA. c) Sofware DMol3

- **MultiWFN**

El análisis topológico basado en QTAIM se llevó a cabo utilizando el software MultiWFN (*Multifunctional Wavefunction Analyzer*) (figura 38.a). MultiWFN es de uso gratuito, fácil de manejar y compatible con casi todos los métodos de análisis de funciones de onda más relevantes (Lu et al., 2012). Sus aplicaciones principales son:

- Determinación de puntos críticos.
- Cálculo de densidades electrónicas (ρ) y Laplacianas ($\nabla 2\rho$).
- Producción de mapas de contorno de $\nabla 2\rho$ de diversos planos moleculares.
- Obtención de gráficos de dispersión e isosuperficies RDG.
- Determinación de las composiciones orbitales fronterizas.

- **VMD**

Con el objetivo de realizar el análisis de las isosuperficies RDG se ha utilizado el programa VMD (*Visual Molecular Dynamics*) (figura 38.b). Se trata de un programa especializado en modelado molecular y visualización de estructuras, con gran número de herramientas y métodos para representar sistemas en tres dimensiones (Humphrey, 1996). Además de la visualización de los perfiles de densidad, permite la identificación de los enlaces de hidrógeno formados y la extracción de otras propiedades.

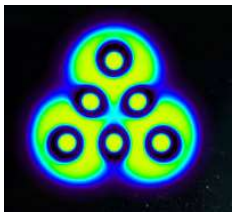

Figura 38. a) Software MultiWFN. b) Software VMD.

3.2.2. Mecánica molecular (MM).

En la Mecánica Molecular, MM, las moléculas son consideradas como un conjunto de esferas (átomos) que están conectados mediante enlaces cuyo movimiento e interacciones se puede describir con la ayuda de las leyes de la física clásica, a través de funciones de energía potencial dependientes tanto de la posición como del tiempo. Ya que las herramientas de la MM presentan un coste computacional bajo en comparación con los métodos cuánticos, se utilizan para analizar el comportamiento de conjuntos de cientos o miles de moléculas, moléculas complejas o análisis de los estados fundamentales de los sistemas. Sin embargo, no pueden ser aplicados a sistemas que impliquen ni una rotura ni una formación de enlaces, al no resolver la ecuación de Schrödinger (Gutiérrez, 2020).

En la MM se realiza una simplificación importante: en las funciones de energía potencial sólo se consideran de manera explícita los núcleos de los átomos, los electrones están considerados implícitamente en los enlaces (Gracia, 2007). Esta asunción tiene su origen en la aproximación de Born-Oppenheimer, en la que se consideran por separado los movimientos de los electrones y del núcleo, ya que la masa de este último es tan superior a la de los electrones que esos pueden

adaptarse rápidamente a los cambios. La función que define la energía de una molécula así considerada se denomina Campo de Fuerzas (Force Field) (Bueren-Calabuig, 2014).

Para realizar un análisis completo de los sistemas también es necesario estudiar las propiedades estructurales y termodinámicas macromoleculares, además del comportamiento de las moléculas en la fase líquida. Dentro de la MM, existen dos técnicas de simulación computacional que permiten obtener una muestra representativa de la configuración de los sistemas a diferentes temperaturas: el método Monte Carlo y las simulaciones de Dinámica Molecular, MD (*Molecular Dynamics*). En el primero se analiza la energía de los sistemas a través de coordenadas generadas al azar. Por el contrario, MD es un método determinista, ya que a partir de un punto de la trayectoria de las partículas es posible generar su evolución con el tiempo (Bueren-Calabuig, 2014).

3.2.2.1. Dinámica Molecular

La dinámica molecular se fundamenta en los principios de la mecánica molecular, donde los núcleos de los átomos son tan pesados que se tratan como partículas clásicas. Debido a esta aproximación, su dinámica puede ser analizada a través de la segunda ley de Newton, cuya forma diferencial se expresa de la siguiente forma (Bueren-Calabuig, 2014):

$$F_{x_i} = m_i \cdot a \rightarrow \frac{d^2y}{dt^2} = \frac{F_{x_i}}{m_i} \tag{26}$$

Donde F_{x_i} es la fuerza aplicada sobre una partícula i en el eje x a un tiempo t. La energía total del sistema se calcula a partir de una velocidad y coordenadas iniciales, que permiten determinar la energía cinética y la energía potencial respectivamente. Para analizar la evolución temporal del sistema se utilizan métodos de integración numérica, que permiten calcular los estados del sistema separados por un intervalo de tiempo fijo δt_i. La derivada de la energía potencial con respecto a las coordenadas nos da la fuerza resultante sobre cada partícula (Gutiérrez, 2020). Se calculan las fuerzas sobre los átomos en cada intervalo, asumiendo que son constantes durante este tiempo, y se combinan con las posiciones y velocidades actuales para generar el nuevo estado.

$$F = -\frac{\delta E_{potencial}}{\delta x} = 0 \tag{27}$$

Cuando los átomos se encuentran en sus nuevas posiciones, se recalculan estas fuerzas. Este proceso se realiza de forma sucesiva hasta que se genere la trayectoria completa de cada átomo. Uno de los métodos más utilizados para integrar estas ecuaciones es el algoritmo de Verlet. Consiste en definir dos aproximaciones de las series de Taylor para las posiciones en la nueva etapa $x(t + \Delta t)$y la etapa previa $x(t - \Delta t)$ (Gracia, 2007):

$$x(t + \Delta t) = x(t) + v(t)\Delta t + \frac{1}{2}a(t)\Delta t^2 + \frac{1}{6}b(t)\Delta t^3 + O(\Delta t^4) \tag{28}$$

$$x(t-\Delta t) = x(t) - v(t)\Delta t + \frac{1}{2}a(t)\Delta t^2 - \frac{1}{6}b(t)\Delta t^3 + O(\Delta t^4) \quad (29)$$

El principal inconveniente de este algoritmo es que no es posible generar la velocidad del sistema directamente, necesaria para calcular la energía cinética del mismo. Aunque en general es un algoritmo fiable, exacto, de fácil implementación y con un coste computacional bajo (Gracia, 2007).

3.2.2.2. Campo de fuerzas

Se denomina campo de fuerza o *force field* a la expresión que define la energía de una molécula en función de sus coordenadas. Cada campo de fuerza es el resultado de la suma de energías potenciales calculadas entre la conformación real de la molécula y la conformación ideal de la misma (Gracia, 2007). Se expresa como la suma de varios términos que considera enlazantes, que describen las tensiones entre los átomos (E_{enl}), sus ángulos (E_{ang}) y torsiones (E_{tor}); y términos no enlazantes, como son las interacciones de Van der Waals (E_{vdw}) y electrostáticas (E_{ele}) (Berkert et al., 1982).

$$\mathrm{E} = \underbrace{\mathrm{E}_{enl} + \mathrm{E}_{ang} + \mathrm{E}_{tor}}_{Enlazantes} + \underbrace{\mathrm{E}_{vdw} + \mathrm{E}_{ele}}_{No\ enlazantes} \quad (30)$$

Interacciones enlazantes

- **Interacción de enlace o tensión (E_{enl})**: definen el cambio de energía potencial que existe cuando un enlace cambia de longitud. Aunque este comportamiento está perfectamente descrito por el Potencial de Morse, se trata de una expresión compleja poco eficiente para llevar a cabo los cálculos en MM sobre partículas que no presentan modificaciones grandes con respecto a sus posiciones de equilibro. Así que la opción más eficiente es utilizar la Ley de Hooke (Torres et al., 2009).

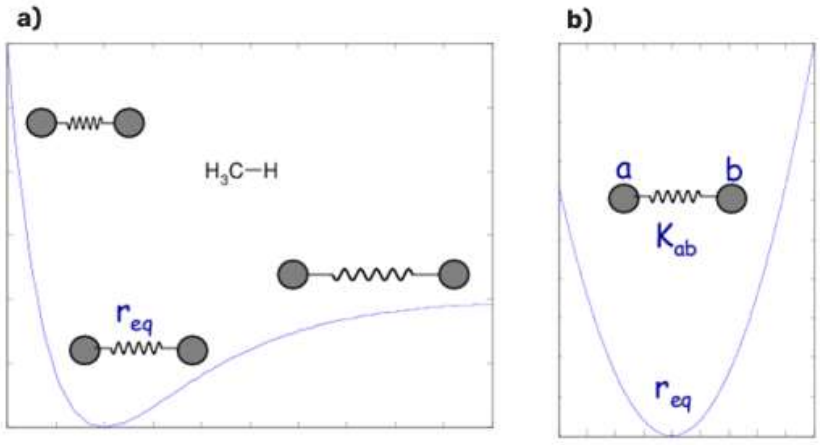

Figura 39. Representación esquemática del comportamiento definido por el potencial de Morse (a) y la ley de Hooke (b) (Torres et al., 2009).

- **Interacción entre sus ángulos ($\mathbf{E}_{ang}$):** esta energía representa la contribución necesaria para modificar un ángulo formado por tres átomos. Cuando alguno de estos átomos se encuentra en un plano diferente, esto suele requerir cierta energía extra, que se define con el término de interacción fuera de plano (E_{oop}) (Rozas, 2024).

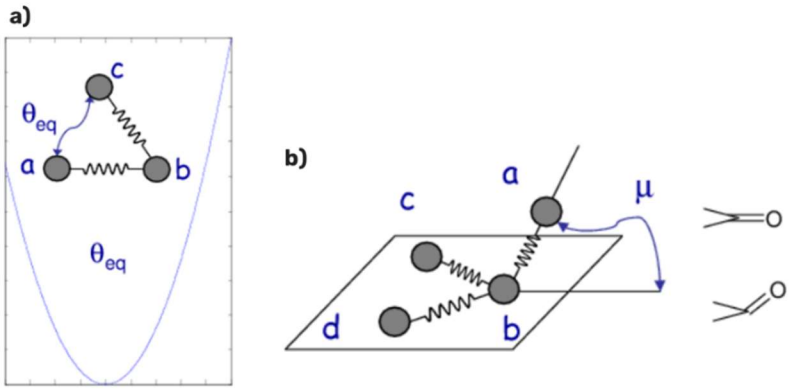

Figura 40. Representación esquemática de las interacciones entre los ángulos de los átomos (a) y el caso particular cuando alguno se encuentra en un plano diferente (Torres et al., 2009).

- **Interacción de torsión ($\mathbf{E}_{tor}$):** esta energía depende del tipo de enlace y representa la energía necesaria para realizar una torsión entre pares de átomos que se encuentran en planos diferentes (Torres et al., 2009).

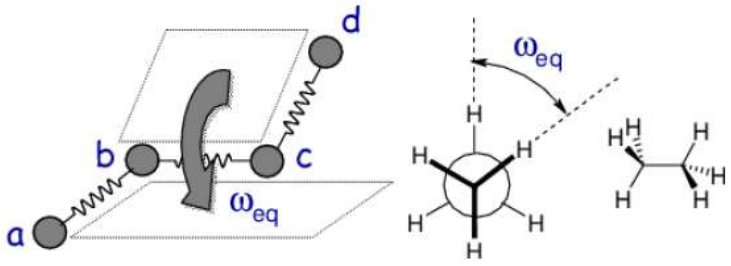

Figura 41. Representación esquemática de las interacciones de torsión (Torres et al., 2009).

Interacciones no enlazantes

- **Interacción de Van der Waals ($\mathbf{E}_{vdw}$):** se encuentra definida por el potencial electrostático de Lennard-Jones y varía en función de la distancia entre los átomos (Bueren-Calabuig, 2014). Cuando estos se aproximan desde el infinito, sus nubes electrónicas comienzan a solaparse hasta alcanzar un estado de atracción debida fundamentalmente a los dipolos inducidos. Sin embargo, si estos continúan aproximándose, se genera una energía de repulsión denominada repulsión de Pauli, que incrementa con mayor rapidez que la energía de atracción (Torres et al., 2009).

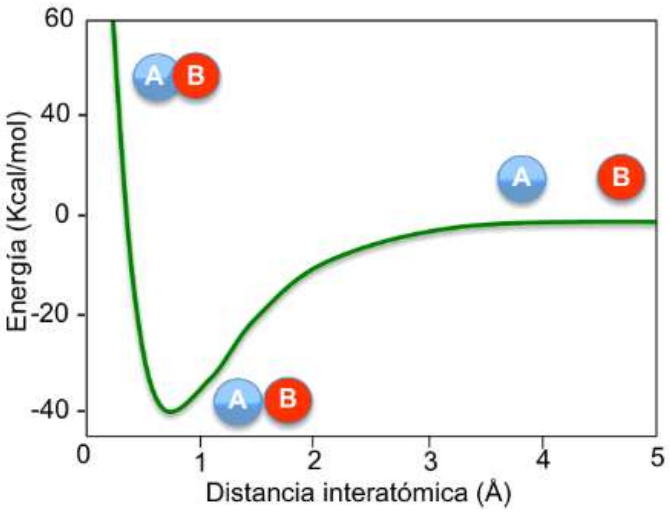

Figura 42. La energía de interacción de Van der Waals viene definida por el potencial electrostático de Lennard-Jones (Bueren-Calabuig, 2014).

- **Interacción electrostática ($\mathbf{E}_{ele}$):** vienen definidas por la fórmula clásica del potencial de Coulomb, que considera las interacciones electrostáticas como la suma de las interacciones entre pares de cargas puntuales (Bueren-Calabuig, 2014).

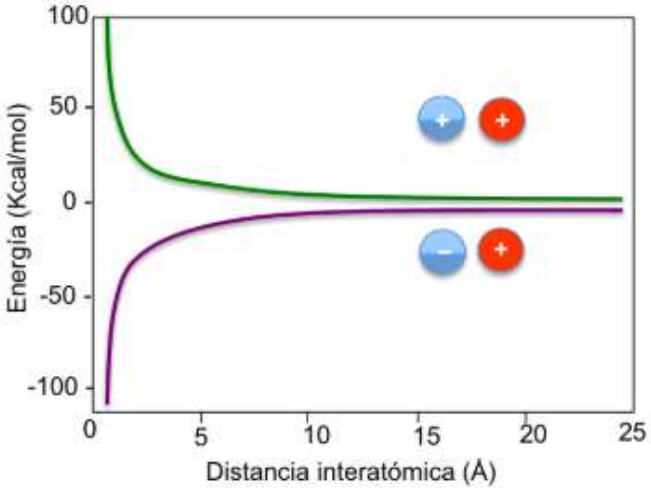

Figura 43. La energía de interacción electrostática viene definida por la forma clásica del potencial de Coulomb (Bueren-Calabuig, 2014).

3.2.2.3. Condiciones de límite periódico

En las simulaciones de MD se consideran sistemas formados por miles de átomos, a escala microscópica este número parece grande, pero a nivel macroscópico es un pequeño conjunto de átomos rodeados en mayor medida de vacío. Los átomos que se encuentran en el límite del área de la simulación podrían presentar comportamientos diferentes al interactuar con vacío y no con otros átomos del sistema, provocando un efecto frontera o boundary effects (Gracia, 2007).

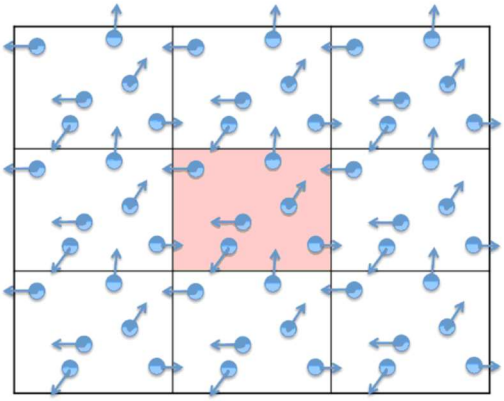

Figura 44. Condiciones de límite periódico en dos dimensiones (Bueren-Calabuig, 2014).

Para evitar este efecto no deseado y poco representativo, se suele aplicarse lo que se conoce como Condiciones de Límite Periódicas, PBC (siglas del inglés *Periodic Boundary Conditions*). En esta condición las moléculas del sistema se confinan dentro de un espacio delimitado normalmente cúbico y a continuación, este volumen se replica en todas las direcciones espaciales, dando lugar a la generación de veintiséis cubos adyacentes idénticos (Figura 45). Estos cubos a su vez, también se encuentran rodeados de réplicas idénticas, simulando así que el sistema sea infinito en extensión, con el objetivo de preservar las características del comportamiento a granel (Rozas, 2024).

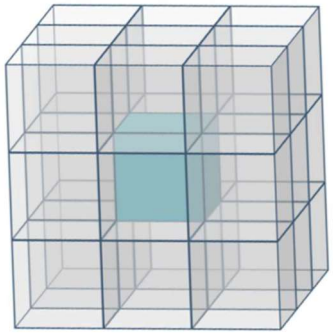

Figura 45. El cubo azul contiene el sistema originario, rodeado de 26 réplicas adyacentes (Rozas, 2024).

Otro método para impedir este efecto son las condiciones límite estocásticas (más conocido por su denominación en inglés *Stochastic Boundary Conditions*). Con este método se restringe el movimiento de los átomos que se encuentran en el límite del espacio definido para el sistema, generando un efecto de repulsión en estos. No obstante, este método es menos utilizado ya que puede conducir a resultados anómalos (Gutiérrez, 2020).

Debido a que el cálculo de las interacciones de largo alcance suele ser costoso computacionalmente hablando, se han establecido métodos para optimizarlo. Para las interacciones de corto alcance, por ejemplo de Van der Waals, el potencial disminuye rápidamente a media que aumenta la distancia entre los átomos, así que no se considera necesario tener en cuenta cierto tipo de interacción de largo alcance. Sin embargo, es necesario

establecer un valor por encima del cual no sea necesario calcular este tipo de interacciones. Este valor se denomina *cut off* y para simulaciones periódicas ha de ser menor que la mitad de la longitud del lado más corto del espacio analizado, suele encontrarse entre 8 y 12 A (Gracia, 2007). No obstante, este límite puede afectar al cálculo de las interacciones de largo alcance, como son las electrostáticas. Para corregir esto se aplica el sumatorio de Ewald. Con este se considera que las partículas electrostáticas interaccionan con las partículas de su espacio definido en la simulación, así como con sus réplicas definidas en un sistema infinito de celdas (Gracia, 2007).

3.2.2.4. Análisis de trayectorias

Al concluir los cálculos se generan un conjunto de trayectorias y energías a partir de las cuales es posible deducir diversas propiedades y calcular su promedio a lo largo del tiempo. Los análisis se pueden dividir en dos categorías principales:

Análisis estructural

Estos análisis se enfocan exclusivamente en la disposición espacial en cada paso de la simulación, sin considerar ningún orden temporal o secuencial. Se obtienen diferentes gráficas e información en función de la dimensionalidad de la característica observada.

Incluyen funciones de distribución radial (RDF), funciones de distribución angular (ADF) o funciones de distribución diédrica (DDF). Las RDF proporcionan información promediada de la distancia entre dos partículas, dando la probabilidad de encontrar una partícula observada a una cierta distancia de una partícula de referencia. Una de las herramientas más utilizadas para esta representación es la matriz de conexión (cmat). En ella se identifican los pares interactuantes relevantes, ejes de la matriz, y se calculan sus correspondientes RDF. Cada espacio en la matriz coloreado corresponde a una distancia e intensidad, dando lugar a una representación visual de las interacciones intermoleculares más significativas dentro de las mezclas.

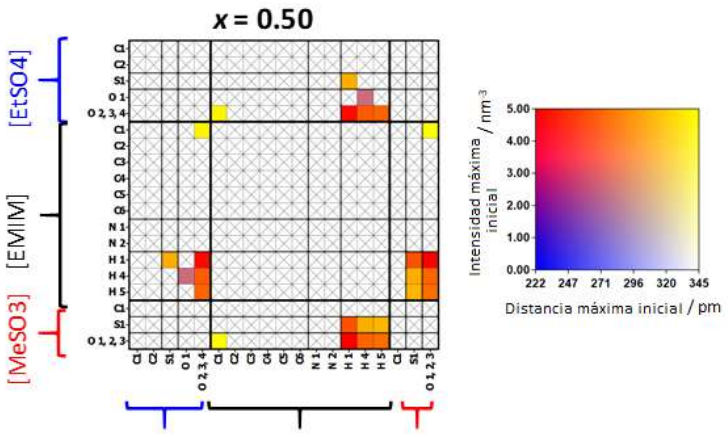

Figura 46. Ejemplo matriz cmat (RDF) en la mezcla equimolar x [EMIM][EtSO4] + (1-x) [EMIM][MeSO3], a partir de simulaciones MD a 303 K y 1 bar.

Al igual que las RDF, las funciones de distribución espacial, SDF (por sus siglas en inglés, *Spatial Distribution Functions*), muestran la probabilidad de encontrar una partícula observada a una cierta distancia de la partícula de referencia. Sin embargo, las SDF proporcionan un histograma tridimensional. Se puede realizar una combinación de las funciones mencionadas para obtener la función de distribución combinada, CDF (siglas procedentes del inglés C*ombined Distribution Function*).

Análisis dinámico

Este tipo de análisis sí considera las características dependientes del tiempo. Entre las herramientas más populares en el ámbito del análisis dinámico se encuentra las funciones de distribución de la velocidad, VDF (por sus siglas en inglés *Velocity Distribution Functions*), que ofrecen una representación interesante de la distribución de las velocidades de cualquier partícula del sistema. Asimismo, el desplazamiento cuadrático medio, MSD (siglas procedentes del término en inglés *Mean Square Displacement*), consiste en una función bidimensional que proporciona información sobre la difusividad de las partículas observadas. La pendiente de la MSD se relaciona directamente con el coeficiente de difusión D de la partícula en cuestión.

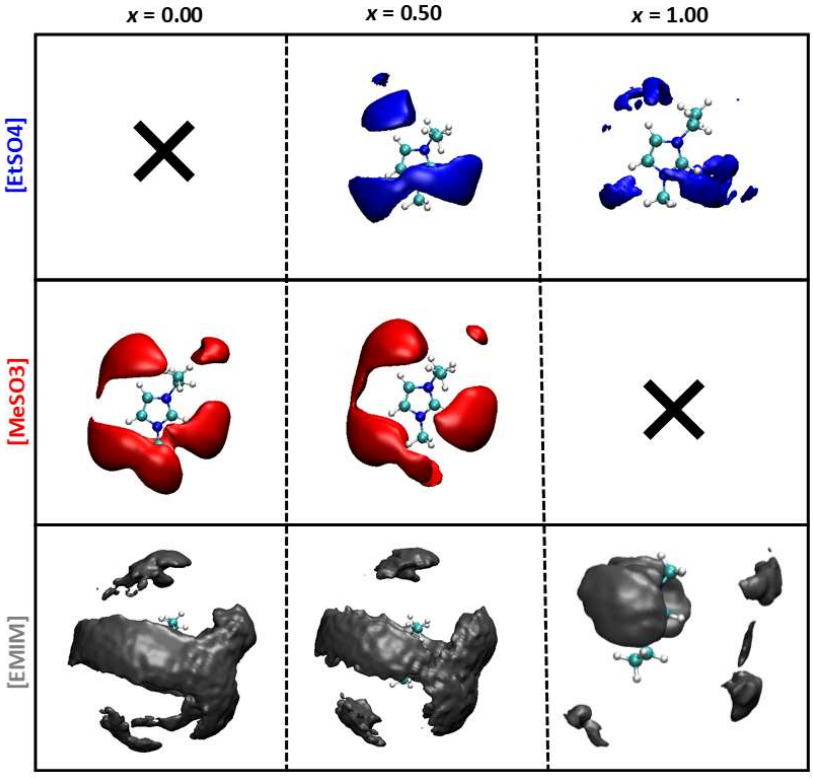

Figura 47. Ejemplo de SDF alrededor del catión central [EMIM] para los iones [EtSO4], [MeSO3] y [EMIM] en mezclas x [EMIM][EtSO4] + (1-x) [EMIM][MeSO3], donde x representa la fracción molar, a partir de simulaciones MD a 303 K y 1 bar.

Programas de cálculo utilizados

En MD es fundamental definir un conjunto de condiciones iniciales en las que se llevará a cabo la simulación. Las condiciones a fijar pueden ser: número total de partículas (N), volumen total (V), energía total (E), presión (P) y temperatura (T). Dependiendo de la combinación de estas variables, se puede clasificar en conjunto microcanónico (NVE), que representa un sistema aislado de su entorno; conjunto canónico (NVT), que representa un sistema en equilibrio térmico a temperatura constante; o conjunto isotérmico-isobárico (NPT), el cual representa un sistema en el que la presión se ajusta ajustando cambiando el volumen de la caja de simulación, es especialmente útil cuando se simulan líquidos o sólidos en contacto con un medio circundante. La elección del conjunto puede influir en los resultados obtenidos, y la elección del conjunto debe basarse en el sistema específico que se está estudiando (Rozas, 2024).

Para comenzar la simulación, es necesario definir el conjunto de partículas seleccionadas y establecer la velocidad de las N partículas. La configuración inicial se logra empaquetando las moléculas en regiones definidas del espacio, diseñando también el tamaño y la forma de la caja de simulación. Esta caja ha de ser lo suficientemente grande como para acomodar el sistema sin interacciones significativas con sus imágenes periódicas. Las velocidades iniciales se asignan en base a una temperatura o una distribución de energía deseada. Durante la fase de equilibrio, el sistema se somete a algoritmos como la minimización de energía y la dinámica molecular, con el fin de ajustar las posiciones y las velocidades (Rozas, 2024).

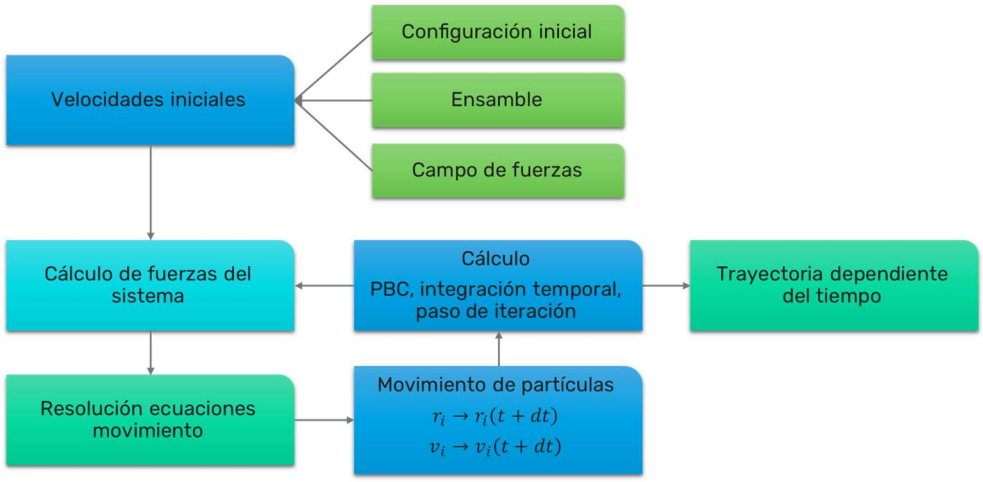

Figura 48. Representación esquemática de simulación MD. Adaptado de la referencia (Rozas, 2024)

Con el objetivo de realizar el análisis estructural y dinámico de las trayectorias, se han utilizado los softwares VMD (mencionado en apartados anteriores), MDynaMix y TRAVIS.

- **MDynaMix**

Este software facilita la simulación de combinaciones de moléculas, utilizando los campos de fuerzas más prevalentes, que se fundamentan en la función de energía potencial. Esto abarca

interacciones electrostáticas y del tipo Lennard-Jones, así como enlaces covalentes, ángulos, y ángulos diédricos de diversas categorías, además de incluir otros términos complementarios. También incorpora condiciones de frontera periódicas y aplica algoritmos para el manejo de interacciones electrostáticas (Lyubartsev & Laaksonen, 2000).

- **TRAVIS**

Permite obtener funciones de distribución conjunta (CDF) de ángulos y distancias, así como los tiempos de relajación (vida útil) de los enlaces de hidrógeno (Brehm & Kirchner, 2011). También permite el cálculo de funciones de distribución radial, espacial y coeficientes de difusión.

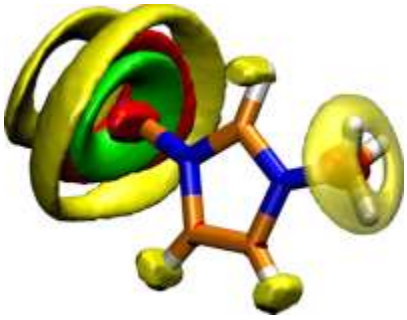

Figura 49. Software TRAVIS.

Capítulo 4

Consistencia de las publicaciones

4.1. Consistencia de las publicaciones

El objetivo de este capítulo se enfoca en analizar la consistencia de las publicaciones recogidas en el marco de esta tesis doctoral. Aunque cada uno explora los comportamientos particulares de diferentes DSILs y NADES, a lo largo de los artículos publicados existe un hilo conductor que apoya el objetivo general de esta investigación: el análisis multiescala de las propiedades fisicoquímicas y la relación entre estructura y propiedades en estos sistemas.

Como ya se ha mencionado, existen una considerable cantidad de artículos sobre ILs y DES, aunque la mayoría de los estudios se orientan hacia los componentes puros o su combinación con otros disolventes. Las publicaciones que analizan el comportamiento de las mezclas binarias DSIL o los disolventes de reciente desarrollo como los NADES todavía son escasos. Además, los artículos que presentan resultados que combinan mediciones experimentales y métodos computaciones también son relativamente infrecuentes. El enfoque multiescala permite obtener una visión más amplia y ajustada entre la relación microscópica de la estructura e interacciones y las propiedades y comportamiento macroscópico. Esta combinación entre mezclas binarias de disolventes y el análisis de sus propiedades y comportamiento a diferentes escalas son el objeto principal de este trabajo.

Los trabajos publicados se clasifican en dos grupos atendiendo a la naturaleza de las mezclas estudiadas, DSIL y NADES. En el caso de los DSIL se han estudiado mezclas que presentan el catión común 1-Etil-3metil-imidazolio ($[EMIM]^+$) , con tres aniones diferentes: tetrafluoroborato ($[BF_4]^-$), etilsulfato ($[EtSO_4]^-$) y metanosulfonato ($[MeSO_3]^-$). Además de estos tres DSIL, desarrollado en un trabajo de investigación elaborado inmediatamente antes de la realización de la tesis, se realizó un estudio equivalente para la mezcla $[EMIM][BF_4]$ + [EMIM][TSFI]. Aunque este último no está recogido en el marco temporal de la tesis, también se refleja dentro del compendio de artículos debido a su importancia como preámbulo a la investigación que se presenta en este trabajo. Analizando las variaciones en las propiedades de estos 4 DSIL es posible determinar el efecto del anión. Además, la diferencia en la naturaleza de los aniones hace posible inferir qué características aniónicas impactan en las propiedades finales de los DSIL.

En los 4 artículos se estudiaron las propiedades de los DSIL en función de la composición y la temperatura de las mezclas. Se analizaron propiedades termofísicas experimentales, así como las desviaciones de la idealidad, que permiten deducir el comportamiento de fase y la miscibilidad del sistema. Estos resultados se integran con los obtenidos a través del uso de diferentes técnicas de simulación molecular (química cuántica y dinámica molecular clásica), que aportan información complementaria sobre la estructura de los DSIL, las interacciones intermoleculares, incluidos los enlaces de hidrógeno, y los efectos específicos de los iones. Igualmente se estudió el mecanismo de difusión de los aniones en las diferentes interfases de los líquidos mediante métodos de dinámica molecular. También se llevó a cabo un estudio computacional de los mecanismos potenciales de interacción entre las moléculas involucradas y

las dianas biológicas, con el fin de deducir las bases de los efectos tóxicos asociados a las mezclas de líquidos iónicos. El conjunto de los resultados permite llevar a cabo una caracterización multiescala de las mezclas, lo que proporciona una nueva metodología para el diseño de disolventes para aplicaciones particulares, eligiendo no solo la identidad de los iones, sino también su proporción.

En relación con los NADES, las combinaciones seleccionadas para realizar los estudios se basaron en la elección de cinco HBA de origen natural, como son Mentol (MEN), Timol (THY), Eucaliptol (CIN), D-Carvone (CAR) y Geraniol (GER). Estos se estudiaron en combinación con tres ácidos grasos saturados (ácido decanóico, ácido mirísitco y ácido esteárico) y dos ácidos grasos insaturados (ácido linoléico y ácido oléico). Para estos NADES se determinaron experimentalmente los ratios molares de trabajo, así como la densidad y la viscosidad de aquellas mezclas cuyo punto eutéctico permitía que permanecieran en estado líquido a temperatura ambiente. De igual manera que para los DSILs, también se realizó un análisis multiescala para los NADES, utilizando métodos y herramientas propios de DFT y simulaciones de dinámica molecular. Adicionalmente, para el NADES THY:CAR se realizó de manera particular un estudio del comportamiento a alta presión de este disolvente. Estas mediciones también proporcionan información crucial sobre las propiedades termodinámicas de la mezcla, lo cual es fundamental para el escalado y el diseño del proceso en operaciones de alta presión.

Los trabajos publicados se encuentran estructurados en dos grupos, atendiendo a la naturaleza de los líquidos. En el momento de depositar la presente tesis doctoral, los artículos 0, I, II y IV ya habían sido publicados en su totalidad, mientras que los artículos III y V se encontraban en proceso de revisión. La información detallada sobre estos se encuentra resumida en el Listado de Publicaciones al inicio de este documento. Estos se detallan en la siguiente tabla:

Tabla 10. Relación de artículos publicados y presentados.

Mezcla	Sistema	Objetivo	Artículo
DSIL	[EMIM][BF_4] + [EMIM][TSFI]	Caracterización multiescala DSIL en función de la composición y la temperatura. Se analizan las propiedades fisicoquímicas experimentales en conjunto con herramientas de simulación molecular, proporcionando una caracterización micro y macroscópica de su estructura, facilitando así el diseño de este tipo de disolventes.	0
	[EMIM][BF_4] + [EMIM][$EtSO_4$]		I
	[EMIM][$EtSO_4$] + [EMIM][$MeSO_3$]		II
	[EMIM][BF_4] + [EMIM][$MeSO_3$]		III
NADES	THY + CAR	Análisis en condiciones de alta presión del comportamiento del NADES THY:CAR, bajo un enfoque que combina métodos experimentales y computacionales. Aporta información valiosa sobre los efectos de la presión en la organización estructural y las propiedades de transporte.	IV
	C10AC/C14AC/C18AC + MEN/THY/CIN/CAR/GER	Caracterización de NADES basados en monoterpenoides y ácidos grasos saturados mediante un enfoque experimental y de modelado molecular. Combina resultados experimentales y computacionales para establecer relaciones robustas entre estructura y propiedades, contribuyendo a la optimización del diseño de solventes sostenibles.	V

Capítulo 5
Publicaciones

5.1. Publicaciones líquidos iónicos

A continuación se detalla la relación de artículos publicados en relación a las mezclas binarias de líquidos iónicos.

5.1.1. Publicación 0

Título:	**Experimental and molecular modeling study on the binary mixtures of [EMIM][BF_4] and [EMIM][TFSI] ionic liquids**				
Autores:	José L. Trenzado [a], Ylenia Rodríguez [a], Alberto Gutiérrez [b], Alberto Cincotti [c], Santiago Aparicio [b]				
Afiliación:	[a]) Departamento de Física, Universidad de Las Palmas de Gran Canaria, 35017 Las Palmas G.C., Spain [b]) Department of Chemistry, University of Burgos, 09001 Burgos, Spain [c]) Department of Mechanical, Chemical and Materials Engineering, University of Cagliari, 09123 Cagliari, Italy				
Revista:	Journal of Molecular Liquids				
Factor impacto (IF):	6.633	**Cuartil (JRC):**	Q1	**Citas:**	22
Editor:	Elsevier	**Fecha de publicación:**	06/04/2021		

Journal of Molecular Liquids 334 (2021) 116049

Contents lists available at ScienceDirect

Journal of Molecular Liquids

journal homepage: www.elsevier.com/locate/molliq

Experimental and molecular modeling study on the binary mixtures of [EMIM][BF_4] and [EMIM][TFSI] ionic liquids

José L. Trenzado [a,*], Ylenia Rodríguez [a], Alberto Gutiérrez [b], Alberto Cincotti [c], Santiago Aparicio [b,*]

[a] Departamento de Física, Universidad de Las Palmas de Gran Canaria, 35017 Las Palmas G.C., Spain
[b] Department of Chemistry, University of Burgos, 09001 Burgos, Spain
[c] Department of Mechanical, Chemical and Materials Engineering, University of Cagliari, 09123 Cagliari, Italy

ARTICLE INFO

Article history:
Received 3 September 2020
Revised 4 March 2021
Accepted 31 March 2021
Available online 6 April 2021

Keywords:
Ionic liquids
Mixtures
Intermolecular forces
Thermodynamics
Molecular simulation

ABSTRACT

The properties of [EMIM][BF_4] + [EMIM][TFSI] double salt ionic liquid (DSIL) were studied as a function of mixtures composition and temperature. Experimental physicochemical properties combined with molecular simulation (quantum chemistry and classical molecular dynamics) were considered, thus providing a micro and macroscopic characterization of fluids' structuring, intermolecular forces and molecular aggregation. The results were analysed in thermodynamics terms considering deviations of ideality and mixing properties as well as from the solvation and interaction between the involved ionic liquids by the developed complex hydrogen bonding networks. Likewise, liquid [EMIM][BF_4] + [EMIM][TFSI] interfaces ($x_{[EMIM][BF4]} = x_{[EMIM][TFSI]} = 0.5$) were also studied using molecular dynamics methods to examine the diffusion of $[BF_4]^-$ and $[TFSI]^-$ anions in the [EMIM][BF_4] + [EMIM][TFSI] liquid interface, and the mechanism of interface crossing. The results allow a multiscale characterization of the considered ionic liquid mixtures thus providing another way of designing IL-type solvents for specific applications, by choosing not only the ion identity but also the ion ratio.

© 2021 Elsevier B.V. All rights reserved.

1. Introduction

Ionic liquids (ILs) have attracted great attention because of their properties such us negligible vapor pressure [1], stability [2] or solvency power for different types of molecules [3,4], which combined with the variety of cation–anion combinations available (10^{18} possible mixed ILs [5]) show the possibility of considering ILs as designer solvents for process specific requirements [6]. Most of the available literature has considered so-called pure ILs, i.e. ILs formed by one type of cation plus one type of anion. However, a better-off structural diversity is achieved by mixing ILs, becoming an alternative "tool" to design tailor-made solvents for required technologies. Through the combination of more than one cation or anion in the mixture, a new concept of "double salt ILs" (DSILs) or blended ILs is obtained [7,8]. This definition allows a fuller consideration of the interactions generated between the mixture of ions and the presence of a new material. Combining ions in an IL may induce a preferential orientation of the ionic species and non-covalent interaction sites that would be markedly different from those possible in the single-component ILs [9,10]. The remarkable advantage of using DSILs depends on a suitable anion-cation combination in order to accomplish more efficient electrochemical devices by designing task-specific IL mixtures. Although DSILs offer significant advantages over classical pure ILs as separation solvents, relevant studies are still scarce and a systematic DSIL selection method is thus highly desirable.

In a first systematic approach, IL mixtures may be studied considering a common cation and then analyse the effect of anion type. Canongia et al. [11] studied the deviation form ideality of IL mixtures (i.e. DSILs) containing [C_4MIm] as common cation, with anions such as PF_6, BF_4 or NTf_2, using the measured excess molar volume. These systems showed small excess molar volumes, i.e. low deviations from ideality, being almost pressure and temperature independent. Stoppa et al. [12] considered [C_2MIm] as common cation and mixtures including BF_4 and dicyanamide anions, also reporting almost linear behaviour with mixture composition for the studied mixtures and several thermophysical properties. Mixtures considering pyridinium – based cations with Tf_2N and dicyanamide anions were considered by Larriba et al. [13] reporting minor deviations from ideality for the reported mixtures. Pyrrolidium – base cations and their mixtures involving NTf_2 and dicyanamide anions were considered by Annat et al.[14] showing in all the cases simple mixing behaviour. The behaviour of systems including a common anion and the effect of cation type was also

* Corresponding authors.
E-mail addresses: jose.trenzado@ulpgc.es (J.L. Trenzado), sapar@ubu.es (S. Aparicio).

https://doi.org/10.1016/j.molliq.2021.116049
0167-7322/© 2021 Elsevier B.V. All rights reserved.

considered in the literature. The IL mixtures with common anions were considered by Navia et al. [15], considering BF_4 anion and alkylimidazolium cations with variable chain length, and considering excess enthalpy and excess volume. These authors reported small deviations from ideality for the considered systems. These results were also confirmed through experimental measurements of viscosity, which show minor deviations from linear behaviour [16]. Mixtures with bis(trifluoromethylsulfonyl)imide as common anion and imidazolium, pyrrolidinium and piperazinium cations were studied by Oliveira et al. [17] considering surface tension and density measurements, thus reporting low deviations from linearity even for the largely different involved cations.

Therefore, the reported results for IL mixtures, both considering common anion or common cation, show minor deviations from linearity or small non-dideality behaviour with mixture composition. The IL mixtures studied in the literature have been reviewed [10], and although in most of the cases the deviations from ideality are minor, there are also systems containing large deviations [18]. Therefore, there is a need to clarify the molecular – level and nanoscopic roots on the behaviour of mixed ILs and their relationship with macroscopic properties. For this purpose, molecular simulation is a suitable approach to obtain the required information. The available studies on simulations for ILs mixtures were recently reviewed by Dhakal et al. [19], showing the prevailing role of the type of developed hydrogen bonds between the considered anions and cations and its role on the deviations from ideality. Nevertheless, the analysis of the local structure around ions is still very scarce and the information on local composition is still almost absent as well as the effect of developed intermolecular forces, specially hydrogen bonding.

Therefore, there is a lack of basic knowledge on the properties and molecular level structuring of DSILs mixtures, which need to be considered systematically to select the most suitable molecular combinations regarding the required properties for industrial applications. The use of DSILs have two notable advantages over two-ion ILs. Firstly, the number of DSILs resulting from the combinations of two-ion ILs is many orders of magnitude larger, so they significantly extend the solvent selection space [20]. Secondly, DSILs offer an easy approach to tune solvent properties. For example, Pinto et al. observed that the viscosity of the "mixture" of $[C_2MIm][NTf_2]$ and $[C_4EIm][EtSO_4]$ varies from 32.6 to 255.2 mPa·S with the molar fraction of $[C_4EIm][EtSO_4]$ increasing from 0 to 1 [21]; Lei et al. found that the solubility of CO_2 in the "mixture" of $[C_8MIm]$ $[NTf_2]$ and $[C_nMIm][BF_4]$ (n = 2, 4) can be adjusted by different IL compositions [22]. Therefore, DSILs open new horizons for the identification of suitable solvents for separation processes. For this, the study DSILs mixtures requires a systematic approach, considering the large number of possible combinations and the mixture composition effects. The main objectives should be, on the one hand, to analyse the intermolecular forces (cation–anion dimers, cation–anion-anion trimer and cation–anion-cation–anion tetramer) and microscopic behaviour [23] as a function of the mixed components and composition and, on the other hand, to infer their effects and relationships with macroscopic physicochemical properties [24] to develop predictive models. The microscopic level information on DSILs systems can be inferred from molecular modelling studies, for which the combined use of density functional theory (DFT) and classical molecular dynamics simulations (MD) could be suitable. In the same way, the macroscopic level vision of DSILs can be inferred from the experimental determination of selected thermophysical properties, with relevance for process design purposes [25]. The combination of both experimental and molecular modelling studies leads to the required micro and macroscopic characterization. The studies as function of mixtures composition, pressure and temperature, allow to characterize the intermolecular forces, deviations from ideality and structural changes upon mixing

Our research group has been developing a systematic theoretical and experimental research for different types of ILs with, for example, molecular solvents (MSs), where starting from ILs based on alkylimidazolium cations and different types of anions the mixtures with relevant MSs such as water, alcohols, acetone, acetonitrile, dimethylformamide, ethylene glycol or dimethylsulfoxide have been considered [26–30]. However, as previously mentioned, in the case of DSILs there is still much to study. Therefore, in this work a study of 1-ethyl-3-methylimidazolium coupled with tetrafluoroborate and bistriflimide ([EMIM][BF_4] and [EMIM][TFSI]) ILs and their binary mixtures containing a common cation (DSILs) has been reported in the full composition range as a function of temperature. For these systems, microstructuring and characterization of intermolecular forces is not available in the literature. Therefore, the reported results allow to infer the mechanism of molecular interaction between [EMIM][BF_4] and [EMIM][TFSI] ILs and their binary constituent mixtures with $[EMIM]^+$ as common cation. Likewise, MD simulations on [EMIM][BF_4] + [EMIM][TFSI] interfaces ($x_{[EMIM][BF4]} = x_{[EMIM][TFSI]} = 0.5$) were carried out, inferring the diffusion of $[BF_4]^-$ and $[TFSI]^-$ anions across the interface and the behaviour at [EMIM][BF_4] + [EMIM][TFSI] liquid interfaces.The selection of these ILs was done considering that the available literature have showed minor deviations from ideality for alkylimidazolium – based cations but the nanoscopic behaviour of these systems is not clarified, neither in the evolution of excess and mixing properties nor in the changes in intermolecular forces upon mixing and the local composition effects. The main novelty of this work stands on the combination of highly accurate thermophysical studies with molecular modelling, as a function of composition and temperature, which may led to the required insights into the mixtures properties.

2. Methods

2.1. Materials

The chemicals used for the experimental study, reported in Table S1 (Supplementary Information), were obtained from commercial suppliers and were used without additional purification. Pure ILs were degassed by ultrasound, handled under inert atmosphere and water content measured. The properties of pure ILs were measured as a function of temperature (283.15 to 313.15 K range) and compared with literature, Table S2 (Supplementary Information), showing minor differences, which can be attributed to water content and different origin of the samples [31], but discards the presence of relevant impurities [32]. The mixture samples (x [EMIM][BF_4]+ (1-x) [EMIM][TFSI], where × stands for mole fraction) were prepared in the full composition range by weighing (Mettler AE240 balance, ± 0.01 mg) to ± 0.00004 estimated mole fraction uncertainty.

2.2. Thermophysical properties

Density (ρ) and kinematic viscosity (ν) were measured in the 283.15 to 313.15 K range, in 5 K steps at atmospheric pressure conditions. Kinematic viscosity data were converted to dynamic viscosity (η) data by using experimental density data and used along the work, eq. (1).

$$\eta = \upsilon \times \rho \tag{1}$$

Density was measured with a vibrating tube densitometer (Anton Paar DMA5000) with cell temperature controlled with Peltier elements and measured to ± 0.01 K. The densimeter was

calibrated with water (Panreac Hiperpur-plus) and n-heptane (Fluka > 99.5%) as reference fluids [33,34], thus leading to ± 0.00002 g cm^{-3} uncertainty. Kinematic viscosity was measured using capillary viscometry (Schott-Gerätte AVS350), with the cell temperature measured with ± 0.01 K uncertainty. Viscometer calibration was carried out with suitable reference oils, thus leading to 0.4% overall uncertainty.

Excess and mixing properties derived properties from experimental data were calculated using well-known thermodynamics equations [35] according to the relationships reported in the Supplementary Information. Density data allowed the calculation of excess molar volume, V^E, as well as the partial molar volumes of each compound in a mixture, $\bar{V}_i$, the corresponding excess value, $\bar{V}_i^E$, and the value at infinite dilution, $\bar{V}_i^{E,\infty}$. Likewise, isobaric expansivity, α_p, was inferred from linear fits of ρ vs temperature ($R^2 \geq 0.99999$) together with the excess property, α_P^E. Regarding viscosity, as it is not possible to define an ideal reference term, the so-called mixing viscosity, Δη, was calculated.

2.3. Molecular modelling

Density Functional Theory Calculations. Initial structures for all the considered molecules and molecular clusters were built with Avogadro program [36] and optimized with ORCA software [37]. DFT calculations were carried out using B3LYP functional [38,39], coupled with van der Waals semiempirical contribution from DFT-D3 method by Grimme [40], and 6–311++G** basis set. The interaction energy (ΔE) for all the considered structures was calculated, considering Basis Set Superposition Error (BSSE) corrected by using counterpoise method [41].

The quantum theory of atoms-in-molecules (Bader's AIM theory [42]) was applied for the topological analysis if intermolecular forces, with particular attention to hydrogen bonding, using the Multiwfn program [43]. AIM analysis characterize interaction regions by so-called bond critical points (BCP, (3,-1) type according to Bader's terminology) and ring critical points (RCP, (3,+1) type) and the corresponding values of electron density, ρ, and Laplacian of electron density, $\nabla^2\rho$ [44]. The analysis of the inferred critical points may be related with the strength and nature of the interactions [45,46] which was complemented by the use of the Reduced Density Gradient analysis (RDG) [47].

Classical Molecular Dynamics Simulations. MD simulations were carried out with MDynaMix v.5.2 [48] for the forcefield parameterizations reported in Table S3 (Supplementary Information) for the systems and conditions included in Figures S1 and S2 and Table S4 (Supplementary Information). MD simulations were carried out for [EMIM][BF_4] with [EMIM][TFSI] mixtures in the full composition range. For the three studied ions, force field parameters were extracted form SwissParam database [49], which considers a Merck Molecular Force Field [50], with the exception of atomic charges which were calculated from DFT (B3LYP-D3/6–311++G**) results for optimized structures of isolated monomers using ChelpG approach [51]. The [EMIM][BF_4] + [EMIM][TFSI] solutions studied using MD, Table S4 (Supporting Information), consider *i*) the full composition range to infer different solvation conditions and *ii*) the diffusion of $[BF_4]^-$ and $[TFSI]^-$ anions at [EMIM][BF_4] + [EMIM][TFSI] liquid interface. Initial simulation boxes for each solution composition were built with PACKMOL [52] program for densities 20% lower than those of the corresponding pure ILs, Figures S1 and S2 (Supplementary Information). A single initial simulation box was prepared for each mixture composition, thus, to avoid dependence with the considered initial configuration heating and quenching steps were developed before production runs. Periodic boundary conditions were applied in the three spatial directions. These pre-equilibration runs were developed as follows: *i*) heating up to 500 K, *ii*) NPT simulations at 500 K and 1 bar for 5 ns, *iii*) quenching to 298 K, *iv*) NPT simulations at 298 K and 1 bar for 5 ns. This heating and quenching procedure was repeated three times per mixture composition with the last configuration used for final MD simulations. The moderate viscosity of the considered ILs (34.69 and 58.46 mPa s for [EMIM][BF_4] and [EMIM][TFSI], respectively, Table S2 in the Supplementary Information) assures negligible dependence of the trajectories with regard to the initial configuration using this procedure. The final simulations, starting from the final one from heating – quenching cycles, were carried out in the NPT ensemble at 298 K and 1 bar considering a 10 ns equilibration step followed by 20 ns production run. For the simulation of IL mixture at vacuum interface, 40 ns of production was launched. The control of pressure and temperature was done using the Nose–Hoover method. Electrostatic interactions were treated with the Ewald method [53] (15 Å for cut-off radius). Lennard-Jones cross terms were calculated using Lorentz-Berthelot mixing rules. The Tuckerman–Berne double time step algorithm [54] (1 and 0.1 fs for long and short-time steps) was applied for the equations of motion. Data analysis and visualization was done with MDynamix – TRANAL [39], VMD [55] and TRAVIS [56] programs (See Fig. 1).

3. Results and discussion

3.1. Experimental study

Experimental density and viscosity data for the studied IL mixtures are reported in Table S5 (Supplementary Information) as well as the derived V^E and Δη. Likewise, density and viscosity data as a function of composition were fitted to polynomials, whereas V^E and Δη were fitted to Redlich-Kister polynomials, with all the fitting coefficients being reported in Table S6 (Supplementary Information). All the properties are reported in the 283.15 to 313.15 K range. Results in Fig. 2a show ρ evolution with mixture composition with ρ vs mole fraction showing a largely non-ideal behavior, with ρ being larger than the linear evolution in the whole composition range. This densification effect upon mixing is maintained in the studied temperature range, thus pointing to strong heteroassociations upon mixing and confirming that the mixture of these two

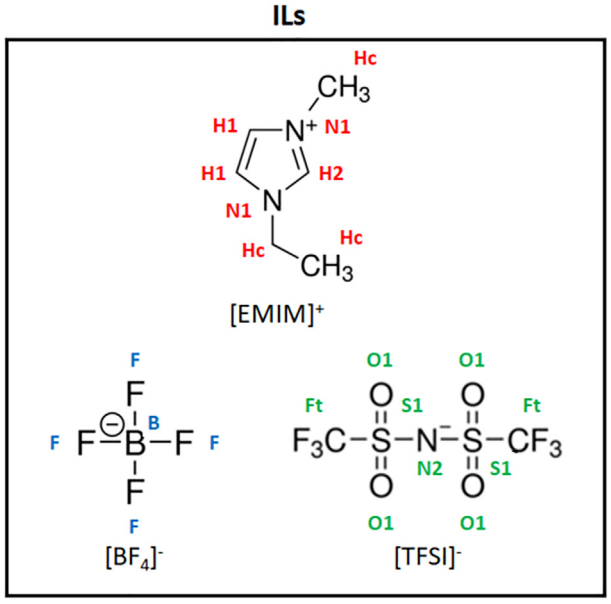

Fig. 1. Molecular structures for ILS studied in this work.

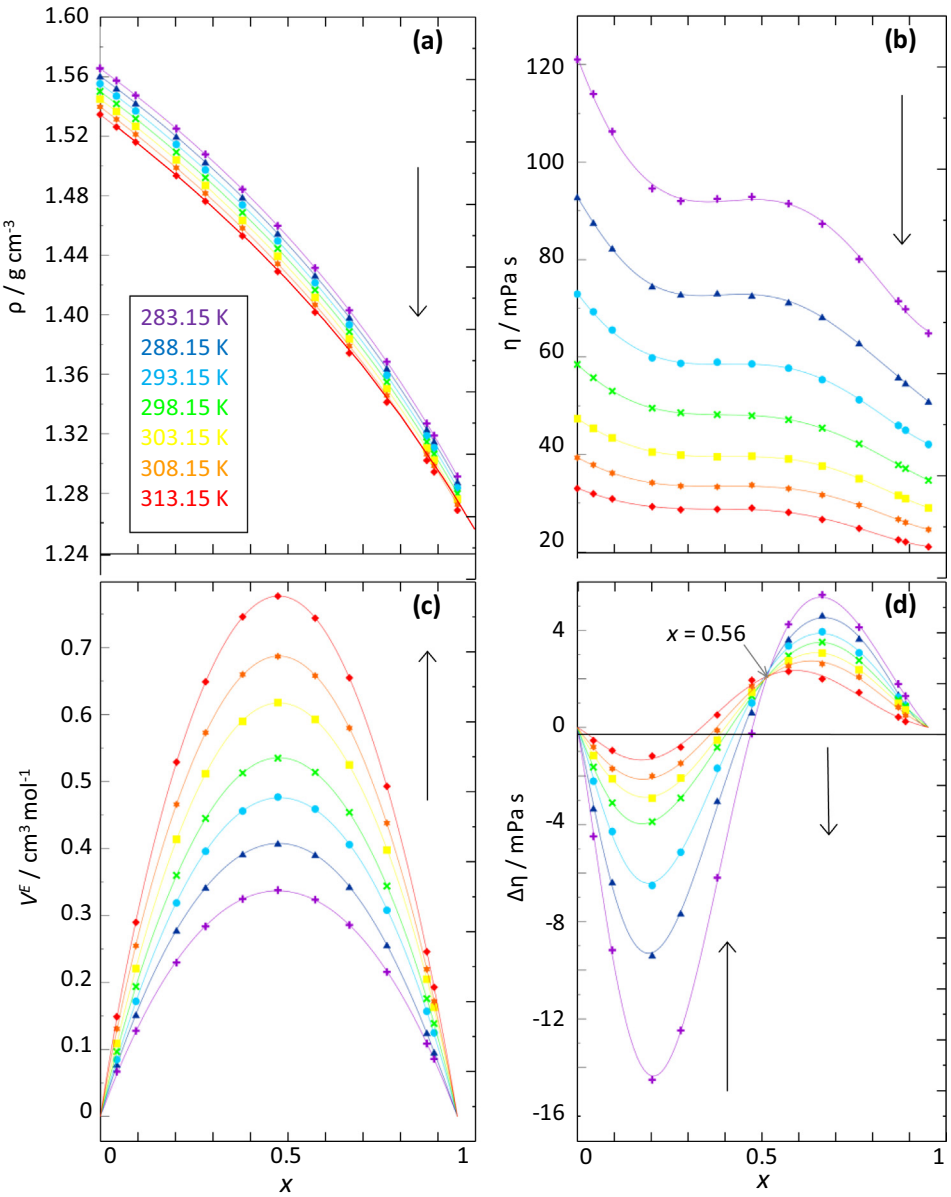

Fig. 2. Experimental thermophysical properties for × [EMIM][BF_4] + (1-x) [EMIM][TFSI], *x* stands for mole fraction, mixtures as a function of temperature. ρ, density, η, dynamic viscosity, V^E, excess molar volume and Δη, mixing viscosity. Black arrows indicate increasing temperature for guiding purposes. Gray arrow in panel d indicates the composition for the intersection point.

ILs, although containing a common cation leads to complex effects beyond the simple ion replacement. It should be remarked that although the mixture [EMIM][BF_4] + [EMIM][TFSI] could be considered as a simple IL with one type of cation ([EMIM]) and two different anions ([BF_4] and [TFSI]), i.e. a double salt IL, the presence of two different types of anions leads to complex intermolecular forces. This is confirmed by the composition evolution of η, Fig. 2b, which is largely non-linear with different behavior as a function of *x*. The viscosity of neat [EMIM][BF_4] is lower than for [EMIM][TFSI], therefore ongoing from neat [EMIM][TFSI] to neat [EMIM][BF_4], i.e. the replacement of [TFSI] anions per [BF_4] ones is accompanied by a decrease in η, but this evolution is not a simple composition effect as showed in Fig. 2b. Three well-defined regions are inferred for the evolution of η vs mole fraction ([BF_4] content): *i*) *x* in 0 to 0.2 range, *ii*) *x* in 0.2 to 0.6 range and *iii*) *x* in 0.6 to 1.0 range. Regions *i* and *iii* are characterized by a decrease in viscosity with increasing [BF_4], thus pointing to an anion replacement interaction mechanism, but region *iii* surprisingly shows constant viscosity. The behavior of region *iii* in terms of viscosity show the development of new intermolecular forces which are not present in the neat ILs and an interaction mechanism different to the simple anion replacement around the central cations. These new intermolecular forces should be strong enough to maintain the high viscosity instead of the decreasing effect because of the presence of [BF_4] anion. Although previous literature studies have claimed almost negligible deviations from ideality for alkylimidazolium based ILs [11,12,15,16,17], results in Fig. 2c and 2d show that mixtures studied in this work are far from an ideal system. This non-ideal behavior indicates the presence of intermolecular effects not present in the neat ILs which determine the properties of the mixed, DSILs. The V^E are remarkably large in the whole composition and temperature range with maxima at equimolar mixture compositions. The behavior of Δη is extremely complex, with negative values below for [TFSI] rich systems and

positive ones for [BF_4] rich mixtures, thus confirming the effect of intermolecular forces on mixtures behavior.

The volumetric properties allowed the calculation of $\bar{V}_i^E$, Fig. 3a and 3b, and the values at infinite dilution, $\bar{V}_i^{E,\infty}$, Fig. 3c. The behaviour of $\bar{V}_i^E$ is very symmetric for both components, with similar positive values in the whole composition range and increasing with temperature. These values of the excess partial molar volumes confirm the strength of intermolecular forces. Likewise, the large values of $\bar{V}_i^{E,\infty}$ show the disrupting effect of one type of anion on the structuring of the other one, thus leading to new intermolecular interactions upon anion replacements. The values of α_p and α_p^E reported in Fig. 4 agree with high non-ideality inferred from the other thermophysical properties. The α_p vs mole fraction evolution, Fig. 4a, is largely non-linear, evolving through maxima around equimolar composition. Therefore, for [TFSI] – rich mixtures the addition of [BF_4] leads to a more compressible fluid, i.e. [BF_4] disrupting effect, which agrees with the behaviour of viscosity, but after this, the increasing [BF_4] content decreases fluids' compressibility, therefore fluids' rearrangements are confirmed again. Nevertheless, α_p^E, Fig. 4b, are positive in the whole composition range, thus confirming the disrupting effect because of the simultaneous presence of both types of anions.

The information obtained from the reported thermophysical properties may be extended through the use of suitable models, which allow to connect the macro with the microscopic information. Therefore, the Prigogine-Flory-Patterson (PFP) [57] has been considered for the prediction of V^E. PFP model allows to infer the different contributions to V^E, thus dividing it as the sum of interactional, free volume and P^* contributions. The excellent performance of PFP model for describing V^E with a single model parameter is confirmed in Fig. 5a for all the studied temperatures. The interactional contribution to total V^E allows to analyse the intermolecular interactions effects, being quantified through the χ_{12} interaction parameter. This interactional contribution, Fig. 5b, is positive in the whole composition range and remarkably larger than the other two ones, Fig. 5c and 5d, being the main contribution to the total V^E, thus confirming the role of the newly developed intermolecular forces on the behaviour of V^E, being on the roots of the large non-ideality of the studied mixtures. Likewise, the linear evolution of χ_{12} with increasing temperature, Fig. 6, confirms that the role of intermolecular forces is maintained in the whole temperature range. The free volume and P^* contributions to the total V^E are negative but remarkably smaller, in absolute value, than the interactional contribution. Thus, packing effects because of the different sizes and shapes of [BF_4] and [TFSI] anions do not have a remarkable effect on V^E being mainly produced because of the newly developed intermolecular forces.

The modelling of viscosity is largely complex considering the complex composition evolution as reported in Fig. 2b. The temperature evolution of viscosity can not be described with a simple Arrhenius equation and thus Vogel – Fulcher – Tamman (VFT) model was considered in the studied temperature range, with the model parameters reported in Fig. 7. The three VFT parameters follow a non-linear evolution with mixture composition, in agreement with behaviour reported tin Fig. 2b, with larger differences

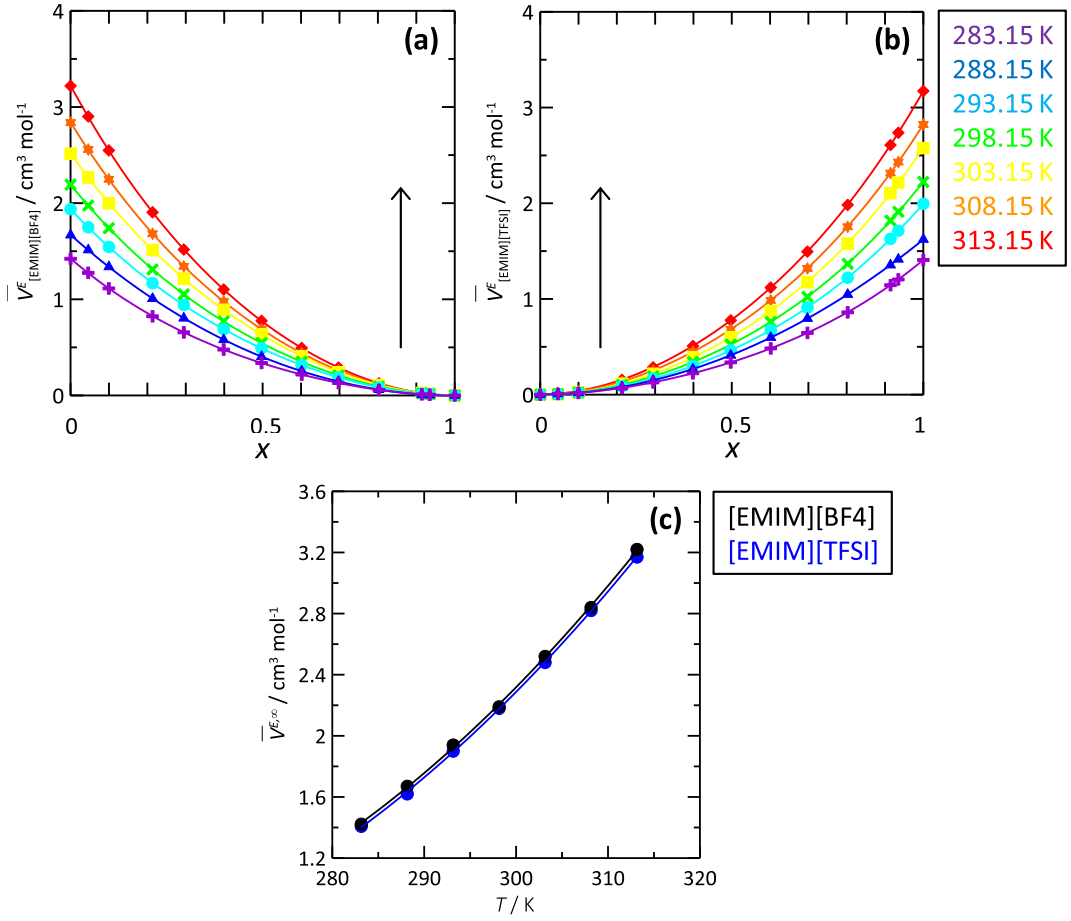

Fig. 3. (a,b) Excess partial molar volume, $\bar{V}^E$, and (c) values at infinite dilution, $\bar{V}^{E,\infty}$, for × [EMIM][BF_4] + (1-x) [EMIM][TFSI], *x* stands for mole fraction, mixtures as a function of temperature. Black arrows indicate increasing temperature for guiding purposes. Values in panels a and show V^E for [EMIM][BF_4] and [EMIM][TFSI], respectively.

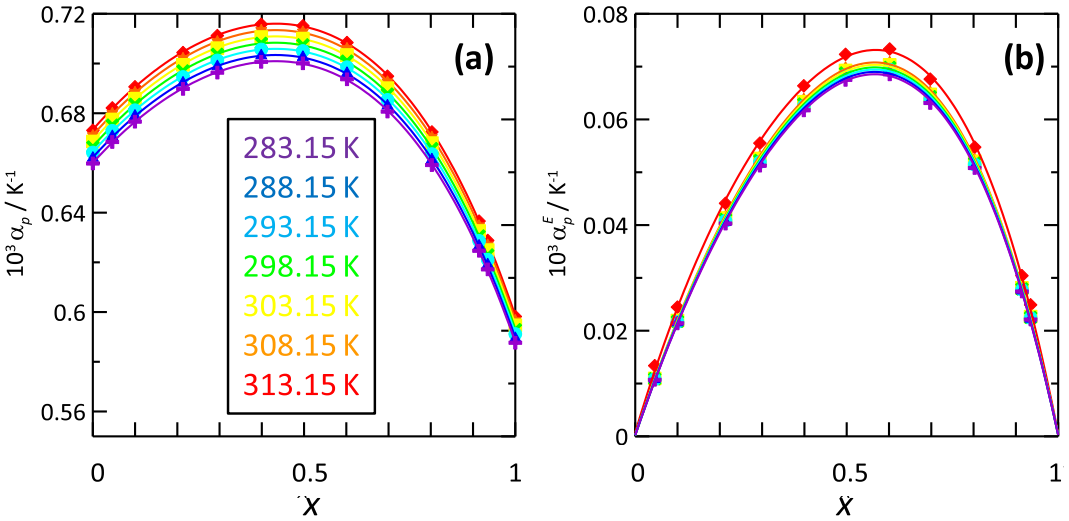

Fig. 4. (a) Isobaric thermal expansion coefficient, and (b) excess isobaric thermal expansion coefficient, for × [EMIM][BF_4] + (1-x) [EMIM][TFSI], *x* stands for mole fraction, mixtures as a function of temperature.

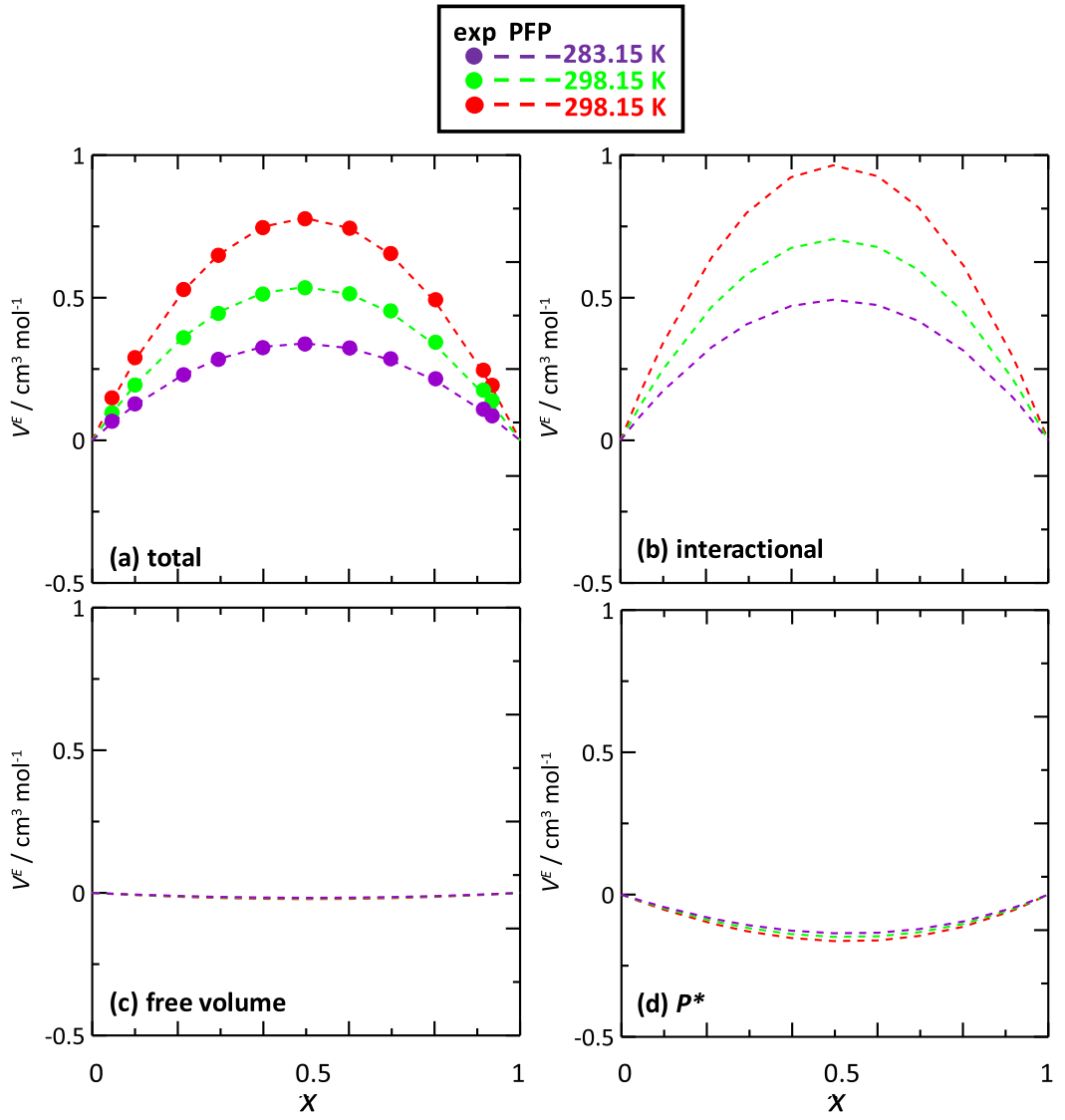

Fig. 5. Comparison of experimental, exp, and Prigogine-Flory-Patterson, *PFP*, excess molar volume, V^E, x [EMIM][BF_4] + (1-x) [EMIM][TFSI], *x* stand for mole fraction, mixtures as a function of temperature. Results in panels b to d show interactional, free volume and P^* PFP contributions to the total V^E.

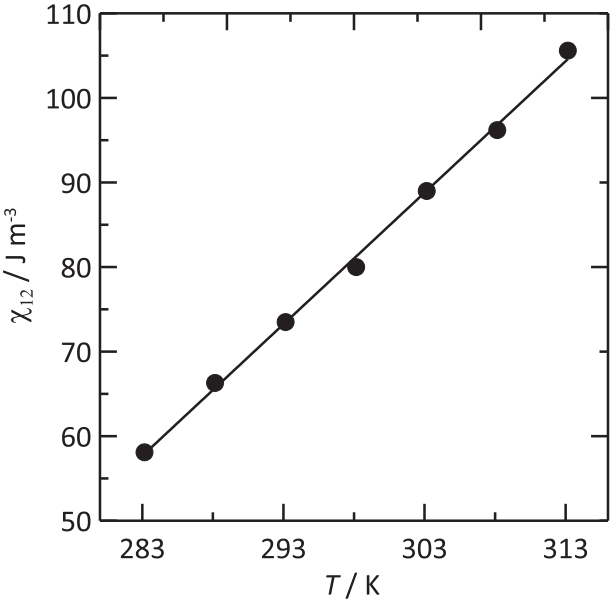

Fig. 6. χ_{12} parameter from the fitting of excess molar volume for × [EMIM][BF_4] + (1-x) [EMIM][TFSI], *x* stand for mole fraction, mixtures as a function of temperature.

for the central composition region around equimolar mixtures. The T_0 parameter, which is close to the glass transition temperature, shows maxima for equimolar mixtures and minima both in [TFSI] and [BF_4] – rich mixtures, thus confirming large structural changes upon anion composition evolution because of the modification of intermolecular forces. Therefore, the reported thermophysical properties show complex behaviour for the studied IL mixtures beyond a simple effect of anion replacement, which can be related to changes in the nature and extension of intermolecular forces. These effects are analysed at the nanoscopic level using molecular modelling tools in sections 3.2 and 3.3.

3.2. DFT modelling of [EMIM][BF_4], [EMIM][TFSI], [EMIM][BF_4] + [TFSI] and [EMIM][BF_4] + [EMIM][TFSI] interactions

In the present study, we analyse the mechanism(s) of [EMIM][BF_4], [EMIM][TFSI], [EMIM][BF_4] + [TFSI] and [EMIM][BF_4] + [EMIM][TFSI] short-range interactions, hydrogen bonding. Different interaction sites were considered, and the structures were geometrically optimized, Fig. 8. The strength of interactions between dimers, trimer and tetramer at different possible interaction sites was quantified through counterpoise corrected binding energies, E_{int}, Table 1. The reported E_{int} are larger (in absolute value) for tetramer than for trimer and dimer, and larger for TFSI dimer than for BF_4 dimer. The mechanism of dimers, trimer and tetramer interactions is depicted in Fig. 8. The presence of hydrogen bond accepting sites (F atoms in $[BF_4]^-$ anion and O/F atoms in $[TFSI]^-$ anion) and donor sites (H atoms in $[EMIM]^+$ cation) in ILs leads to the possibility of developing anion-cation hydrogen bonding. Nevertheless, it is well-know that for the considered [EMIM][BF_4] anion-cation hydrogen bonding between the F atoms of the anion and the CH(2) (carbon atom between both N atoms in imidazolium ring) site in imidazolium is developed [58]. In the case of [EMIM][TFSI] IL, it is also well-known that most of the hydrogen bonds are formed with oxygen atoms as hydrogen acceptors [59] (specifically, the strongest hydrogen bonds are produced between the O(1) atoms of the anion and the CH(2) site in imidazolium). Thus, in the case of the [EMIM][BF_4] + [TFSI] trimer, $[BF_4]^-$/$[TFSI]^-$ anions may compete for this interaction site and also they may develop hydrogen bonding through the CH(1) (the other two CH sites in imidazolium

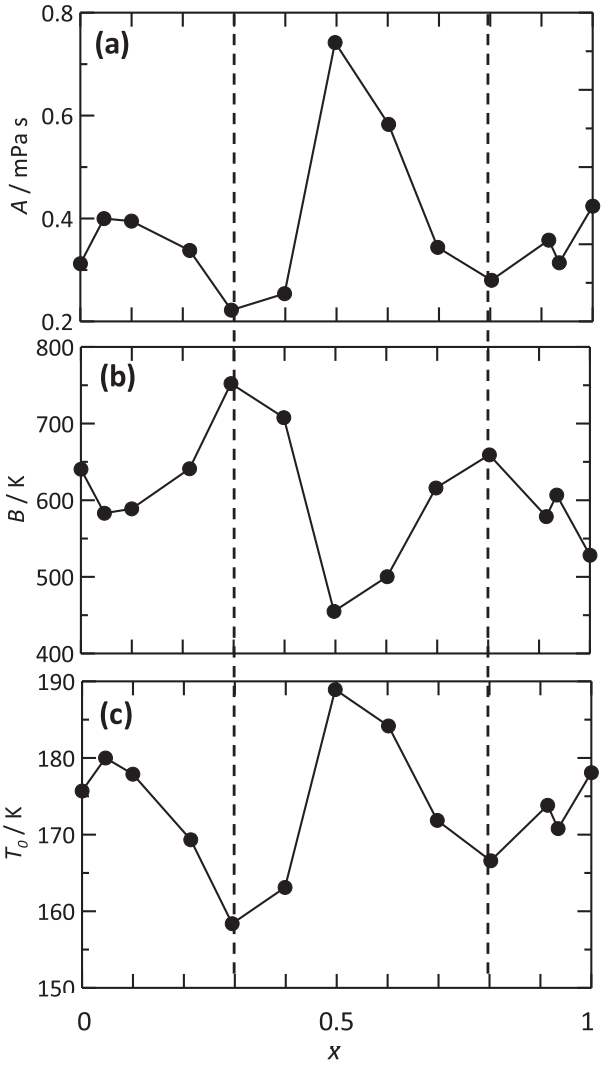

Fig. 7. Fitting parameters of VFT equation for dynamic viscosity for × [EMIM][BF_4] + (1-x) [EMIM][TFSI], *x* stands for mole fraction, mixtures in the 283.15 to 313.15 K temperature range.

ring) sites in imidazolium ring. For the [EMIM][BF_4] + [EMIM][TFSI] tetramer, it is observed that the $[TFSI]^-$ anion interacts through its O(1) atoms with the two $[EMIM]^+$ groups, while the $[BF_4]^-$ anion only interacts through its F atoms with one of the $[EMIM]^+$ groups. The interaction between [EMIM][BF_4] and [TFSI]/[EMIM][TFSI] does not lead neither to large charge transfer toward [TFSI]/[EMIM][TFSI] nor through relevant changes in anion and cation total charges, Fig. 8, thus interaction being van der Waals and hydrogen bonding types.

The dimers, trimer and tetramer interactions were also analysed using the Bader's Atoms in a Molecule (AIM) theory, using the optimized geometries in the Multiwfn code. Hydrogen bonding is topologically analysed in the AIM framework considering the electron density and the formation of bond critical points (BCPs, type (3,-1) in AIMs naming) and additional features like ring critical points (RCPs, type (3,+1)) along the line joining hydrogen donor and acceptor sites. The properties of these critical points (CPs) are quantified with the values of electron density, ρ, and Laplacian of electron density,$\nabla^2\rho$. Likewise, the AIM topological characterization for hydrogen bonding indicates that ρ and$\nabla^2\rho$ must be in the 0.002 to 0.04 a.u. and 0.020 to 0.139 a.u ranges, respectively, with larger values indicating stronger hydrogen bonds [60].

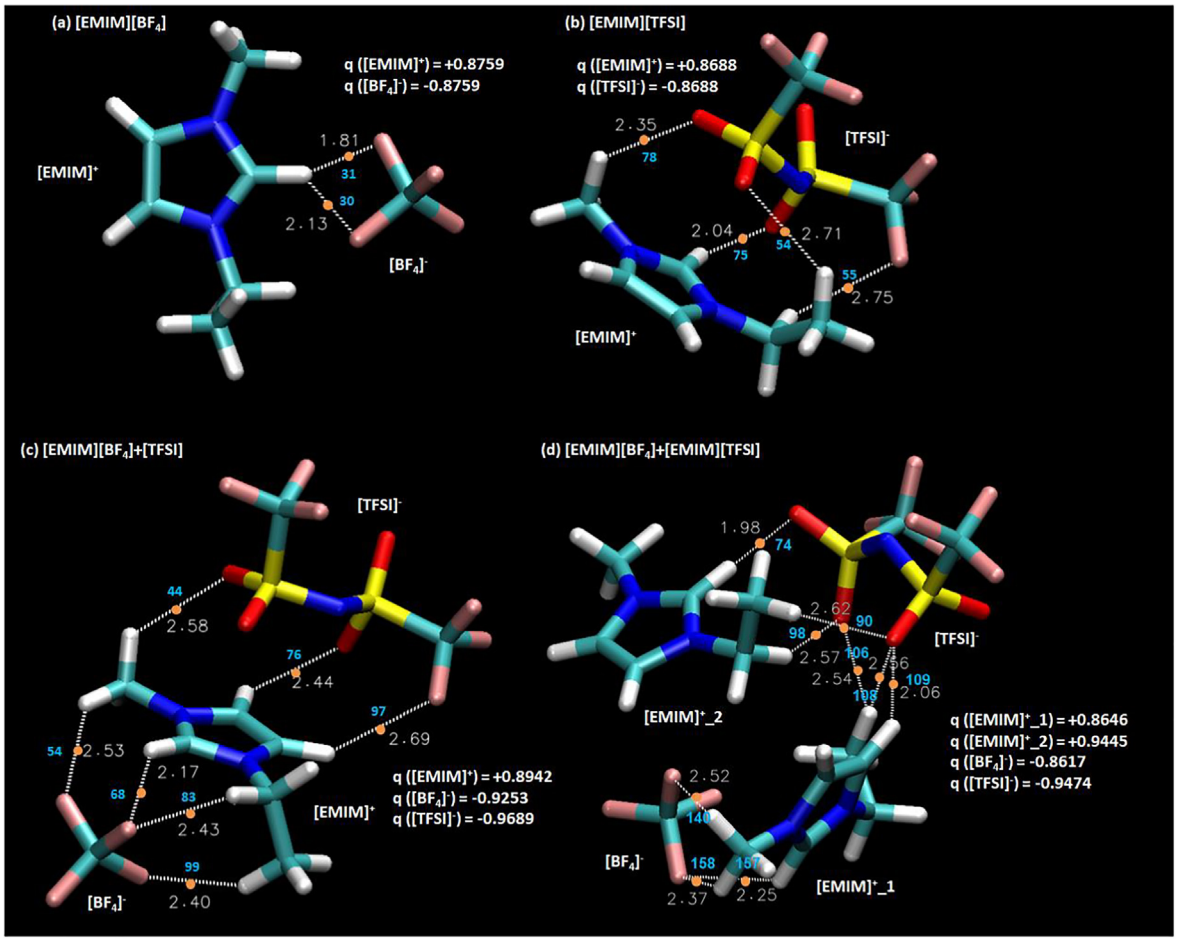

Fig. 8. Atom in molecule (AIM) analysis of interactions, bond critical points (BCPs) and CHELPG charges for (a) [EMIM][BF_4], (b) [EMIM][TFSI], (c) [EMIM][BF_4] + [TFSI], (d) [EMIM][BF_4] + [EMIM][TFSI]. Electron density (ρ) and Laplacian of electron density ($\nabla^2\rho$) for BCPs are reported separately in Table 2.

Table 1
Properties for [$EMIM^+$][BF_4^-], [$EMIM^+$][$TFSI^-$], [$EMIM^+$][BF_4^-] + [$TFSI^-$] and [$EMIM^+$][BF_4^-] + [$EMIM^+$][$TFSI^-$] systems that are calculated at a B3LYP-D3/6–311++G** theory level. Counterpoise corrected interaction energy, (E_{int}); HOMO (E_{HOMO}) and LUMO (E_{LUMO}) energies; HOMO-LUMO energy gap (ΔE_G).

structure	E_{int} / eV	E_{HOMO} / eV	E_{LUMO} / eV	ΔE_G / eV
[$EMIM^+$][BF_4^-]	−3.62	−8.31	−1.48	−6.83
[$EMIM^+$][$TFSI^-$]	−3.64	−7.52	−1.48	−6.04
[$EMIM^+$][BF_4^-] + [$TFSI^-$]	−4.87	−4.89	1.74	−6.63
[$EMIM^+$][BF_4^-] + [$EMIM^+$] [$TFSI^-$]	−8.18	−7.45	−1.27	−6.18

Although dimers, trimer and tetramer interactions are characterized by many CPs, as inferred from the mechanism(s) of interaction in Fig. 8, the most relevant, i.e. stronger, BCPs are reported in Table 2. Results in Table 2 summarize the interactions leading to the stronger BCPs, i.e. CPs with larger ρ and$\nabla^2\rho$, and thus possible hydrogen bond interactions. In all cases, weak hydrogen bonds are formed between [EMIM][BF_4], [EMIM][TFSI], [EMIM][BF_4] + [TFSI] and [EMIM][BF_4] + [EMIM][TFSI]. It should be remarkable that in the case of [EMIM][BF_4] + [TFSI] trimer, larger values are inferred for interaction between the F atom of [BF_4]$^-$ and the CH(2) carbon atom between both N atoms in [EMIM]$^+$ (BCP 68), and also for interaction between the O(1) atom of [TFSI]$^-$and the CH(1) site in [EMIM]$^+$ (BCP 76). In the case of [EMIM][BF_4] + [EMIM][TFSI] tetramer, larger values are inferred for interaction between the F atom of [BF_4]$^-$ and the CH(2) carbon atom between both N atoms in [EMIM]$^+$ (BCP 157), and also for interaction between the O(1) atom of [TFSI]$^-$and the CH(2) site in [EMIM]$^+$ (BCP 74). The large interaction energy reported in Table 1 seems to be justified not by the development of single very strong hydrogen bonds but because of the dimers, trimer and tetramer abilities for developing a large number of interactions, as reported in Fig. 8 and confirmed by the large number of BCPs.

Additional analysis of quantum chemistry results for dimers, trimer and tetramer can be done using the Noncovalent interaction (NCI) analysis [61] according to the Reduced Density Gradient (RDG) surfaces. The RDG scatter plots are reported in Fig. 9 showing that hydrogen bonding characteristics regions are inferred, blue spots. In all cases, these regions are narrow and closer to the lower limit of hydrogen bonding region, thus confirming the minor extension of hydrogen bonding. Additionally, RDG regions corresponding to van der Waals-like interactions, green spots, are inferred, which show that these type of weaker interactions should have a remarkable contribution to the large interaction energies reported in Table 1. This mechanism of interaction is confirmed with the RDG isosurfaces reported in Figure S3 (Supporting Information), in which the green spots for all the interaction sites point

Table 2
Atoms-in-a-molecule analysis of the reported [EMIM$^+$][BF$_4^-$], [EMIM$^+$][TFSI$^-$], [EMIM$^+$][BF$_4^-$] + [TFSI$^-$] and [EMIM$^+$][BF$_4^-$] + [EMIM$^+$][TFSI$^-$] systems calculated at the B3LYP-D3/6–311 ++G** level. Bond critical points (BCP, (3, −1)) are provided in the table. Electron density (ρ) and Laplacian of electron density ($\nabla^2\rho$) at the corresponding BCP are provided as a guide for AIM and RDG figure analysis. The most remarkable interactions are reported in bold.

structure	BCP(s)	ρ / a.u.	$\nabla^2\rho$ / a.u.	Interaction sites
[EMIM$^+$][BF$_4^-$]	30	0.0174	0.0717	[EMIM$^+$](H2)···(F)[BF$_4^-$]
	31	**0.0313**	**0.1229**	**[EMIM$^+$](H2)···(F)[BF$_4^-$]**
[EMIM$^+$][TFSI$^-$]	54	0.0063	0.0212	[EMIM$^+$](Hc)···(O1)[TFSI$^-$]
	55	0.0042	0.0180	[EMIM$^+$](Hc)···(Ft)[TFSI$^-$]
	75	**0.0221**	**0.0809**	**[EMIM$^+$](H2)···(O1)[TFSI$^-$]**
	78	0.0125	0.0442	[EMIM$^+$](Hc)···(O1)[TFSI$^-$]
[EMIM$^+$][BF$_4^-$] + [TFSI$^-$]	44	0.0079	0.0262	[EMIM$^+$](Hc)···(F)[BF$_4^-$]
	54	0.0070	0.0262	[EMIM$^+$](Hc)···(O1)[TFSI$^-$]
	68	**0.0155**	**0.0604**	**[EMIM$^+$](H2)···(F)[BF$_4^-$]**
	76	**0.0109**	**0.0406**	**[EMIM$^+$](H1)···(O1)[TFSI$^-$]**
	83	0.0093	0.0339	[EMIM$^+$](Hc)···(F)[BF$_4^-$]
	97	0.0044	0.0179	[EMIM$^+$](H1)···(Ft)[TFSI$^-$]
	99	0.0093	0.0325	[EMIM$^+$](Hc)···(F)[BF$_4^-$]
[EMIM$^+$][BF$_4^-$] + [EMIM$^+$] [TFSI$^-$]	**74**	**0.0242**	**0.0881**	**[EMIM$^+$](H2)···(O1)[TFSI$^-$]**
	90	0.0077	0.0270	[EMIM$^+$](Hc)···(O1)[TFSI$^-$]
	98	0.0083	0.0248	[EMIM$^+$](Hc)···(O1)[TFSI$^-$]
	106	0.0086	0.0308	[EMIM$^+$](Hc)···(O1)[TFSI$^-$]
	108	0.0083	0.0251	[EMIM$^+$](Hc)···(O1)[TFSI$^-$]
	109	0.0191	0.0786	[EMIM$^+$](H1)···(O1)[TFSI$^-$]
	140	0.0088	0.0366	[EMIM$^+$](Hc)···(F)[BF$_4^-$]
	157	**0.0142**	**0.0550**	**[EMIM$^+$](H2)···(F)[BF$_4^-$]**
	158	0.0108	0.0397	[EMIM$^+$](Hc)···(F)[BF$_4^-$]

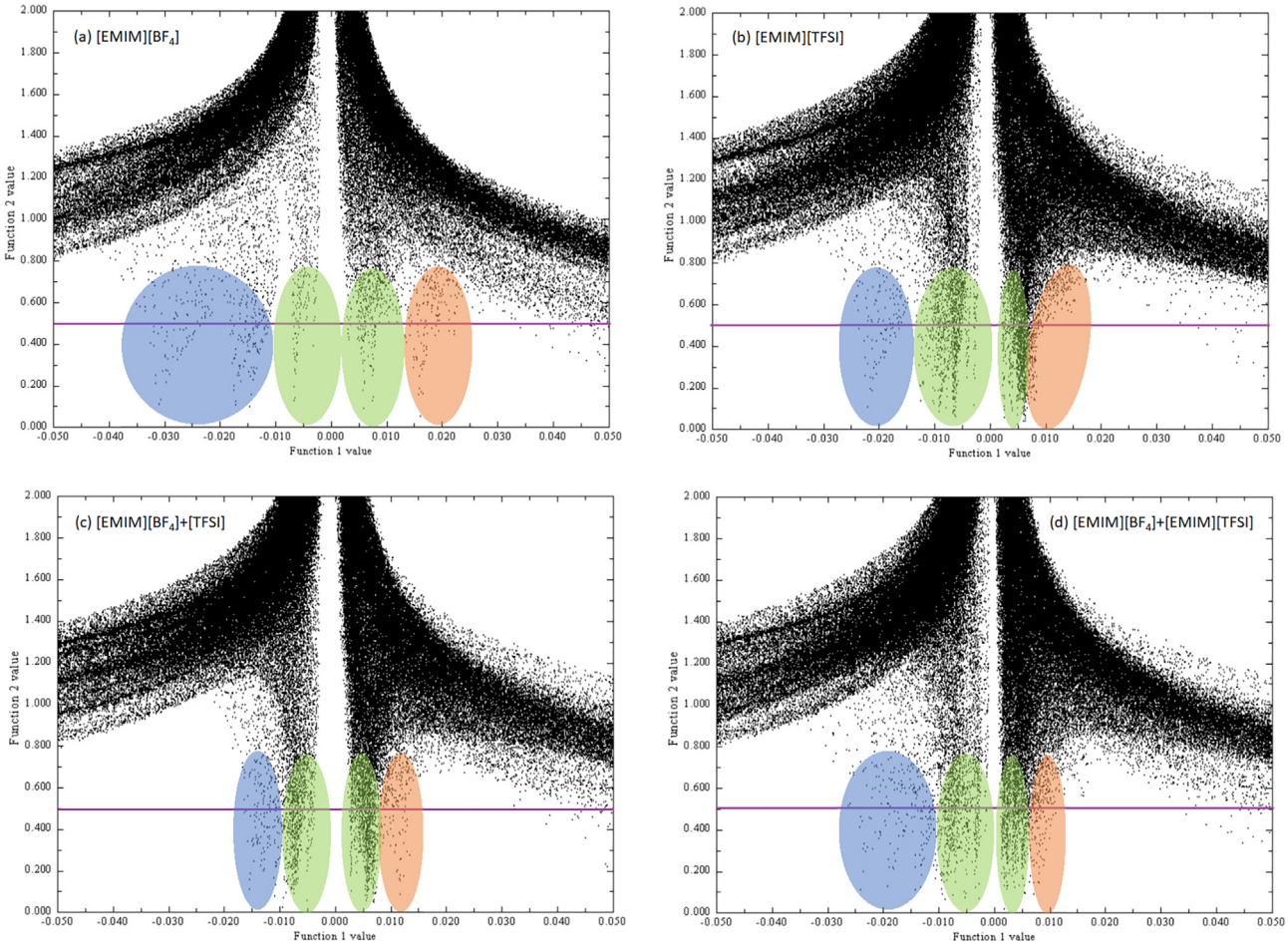

Fig. 9. Reduced density gradient (RDG) scatter plots (function 1 value is sign(λ_2)ρ and function 2 value is RDG functions). Blue shaded area represents hydrogen bonding; green shaded area represents van der Waals interactions and red shaded area represent intra-molecular steric effects.

to van der Waals interactions instead to stronger hydrogen bonding. This mechanism is maintained for the considered dimers, trimer and tetramer.

The associated molecular orbitals for HOMO and LUMO are reported in Fig. 10 as well as the corresponding energy gap in Table 1. The values of energy gaps close to the spectral visible region for all the considered systems are a proof of the stability

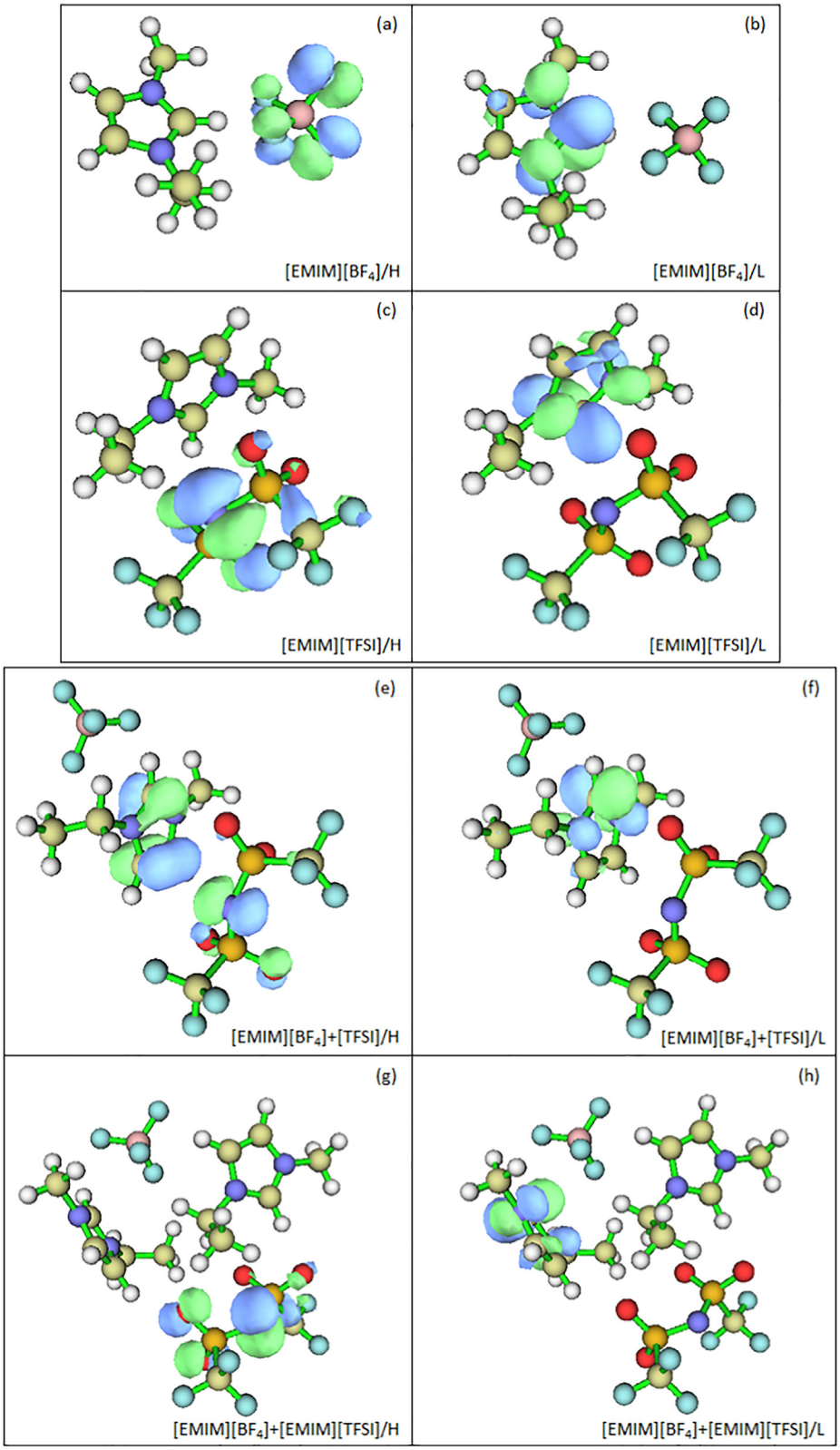

Fig. 10. The HOMO–LUMO graphs for each structure (showing positive (blue) and negative (green) isosurfaces) are embedded in the figures a-h.

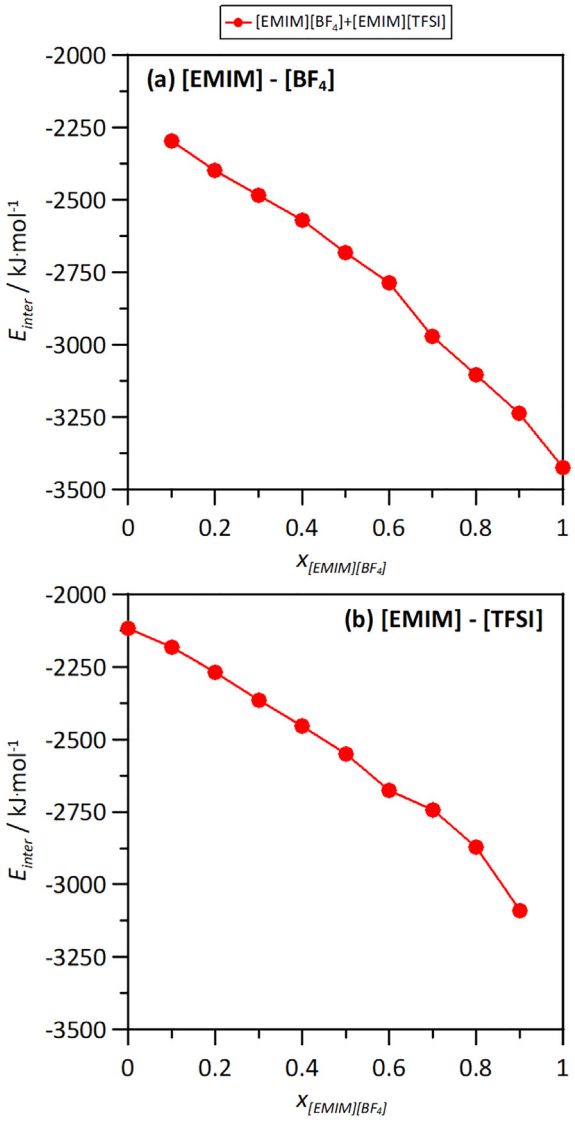

Fig. 11. Intermolecular interaction energy, E_{inter} (sum of Lennard-Jones and coulombic contributions), for the reported interacting pairs in × [EMIM][BF_4] + (1-x) [EMIM][TFSI] mixtures at 298 K and 1 bar.

of the considered dimers, trimer and tetramer interactions in agreement with the large interaction energies reported in Table 1. The HOMO-LUMO energy gaps are practically the same for all the systems, thus showing similar mechanisms of interaction. Likewise, there is not a rule for the molecular location of the HOMO and LUMO orbitals, which can be located both in $[EMIM]^+$ cation or in the corresponding $[BF_4]^-$ or $[TFSI]^-$ anion, depending on the site of interaction.

3.3. MD study of [EMIM][BF_4] + [EMIM][TFSI] liquid structuring

Although DFT results allow a quantification of intermolecular interactions characteristics, only short range effects are considered. Interactions in liquid phases are characterized by longer effects which are theoretically analysed by using MD simulations. The considered force field as reported in Table S3 (Supplementary Information) was validated by the comparison of MD predicted density values and experimental data, Figure S4 (Supplementary Information). The experimental and theoretical values obtained are in suitable agreement), with largely non-ideal behaviour of mixture density predicted by MD. Therefore, we use this approach for inferring molecular level information on the intermolecular interactions and additional nanoscopic effects upon [EMIM][BF_4] + [EMIM][TFSI] mixing.

Anion-cation interactions at the microscopic level are firstly analysed by using intermolecular interaction energies, Fig. 11. E_{inter} provide a quantification of the strength of the different intermolecular interactions in the studied mixtures. Larger values for [EMIM]-[BF_4] interactions are obtained, corresponding to strong electrostatic interactions. The composition evolution of cation–anion interactions energy, increasing (in absolute value) with increasing [EMIM]-[BF_4] content, follows a non-linear pattern, with larger (absolute) values than the corresponding linear evolution with composition.

The structural properties of cation–anion interactions were also analysed using site-site radial distribution functions, RDFs, Fig. 12. It is well-known that prevailing interactions between [EMIM] and [BF_4]/ [TFSI] occur through the imidazolium CH(2) site (placed between the two N atoms in imidazolium ring) acting as donor [62,63] and the ability of [BF_4]/ [TFSI] molecules for acting as acceptors (in the case of [BF_4], through the F site, and in the case of [TFSI], through the O site). [EMIM]-[BF_4] interactions (hydrogen bonding) for the CH-F site show up to three interaction peaks, which are maintained in the whole composition range. The same

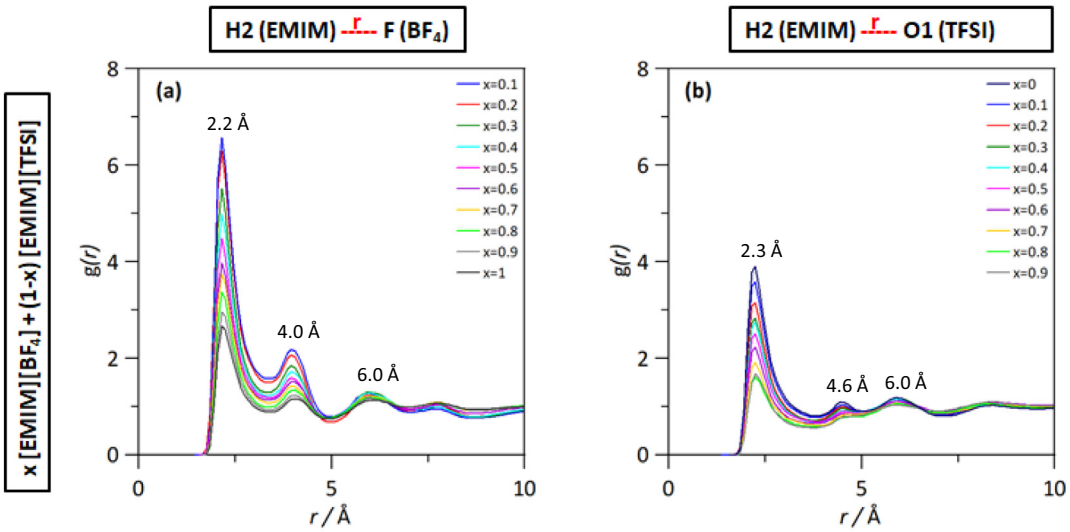

Fig. 12. Site-site radial distribution functions, $g(r)$, for the reported sites in × [EMIM][BF_4] + (1-x) [EMIM][TFSI], x stands for mole fraction, at 298 K and 1 bar.

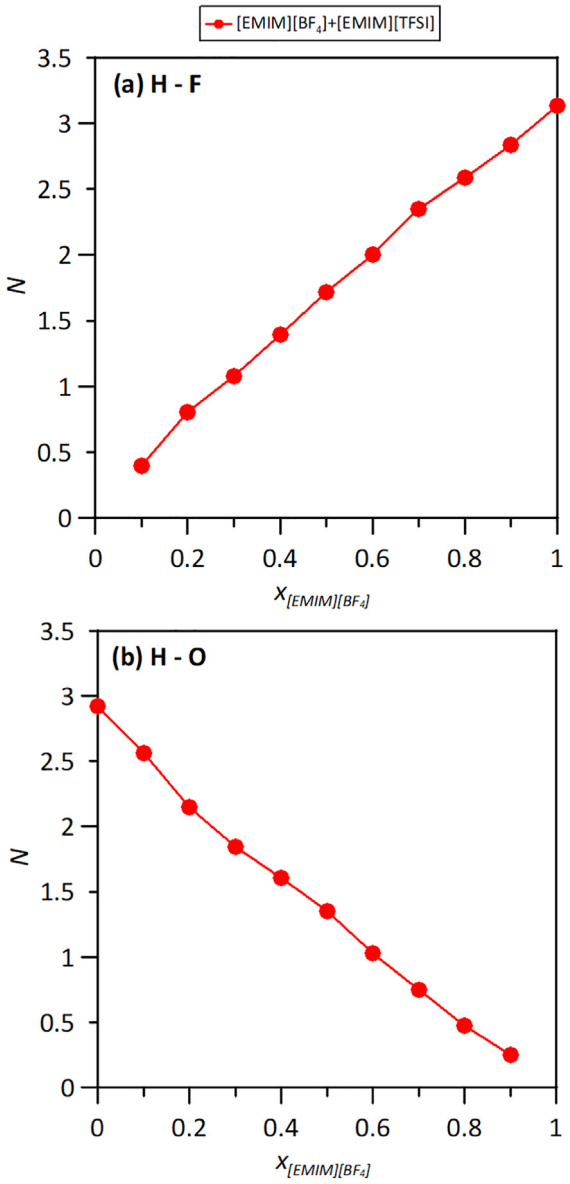

Fig. 13. Solvation numbers, *N*, obtained from the integration of radial distribution functions reported in Fig. 6, corresponding to the first solvation sphere, defined as the first minimum in the corresponding radial distribution function in × [EMIM][BF_4] + (1-x) [EMIM][TFSI], x stands for mole fraction, at 298 K and 1 bar.

behaviour is observed for [EMIM]-[TFSI] interactions, confirming that hydrogen bonding is developed through the CH-O site. However, the [EMIM]-[TFSI] interactions lead to less intense peaks than [EMIM]-[BF_4] interactions, which is in accordance with the values of E_{inter} in Fig. 11 (weaker interactions with the [TFSI] anion, stronger interactions with the [BF_4] anion). The integration of RDFs to obtain solvation numbers, *N*, is reported in Fig. 13, i.e. the number of counterions in the first solvation sphere. In the case of H-F interaction (Fig. 13a), the composition evolution of N follows a non-linear evolution, with values larger than pure dilution effect (i.e. linear evolution), thus confirming the large aggregation trend of [BF_4] anion. In the case of H-O interaction (Fig. 13b), the results show that for [TFSI] rich solutions, many [TFSI] anions are hydrogen bonded to [EMIM], but when [EMIM]-[BF_4] content increases this hydrogen bonding decreases, because of the competing effect of [EMIM]-[BF_4] interactions, Fig. 13a, and thus for [EMIM]-[BF_4] rich mixtures, [TFSI] are less hydrogen bonded to the [EMIM] cation. These competing effects between anions are confirmed by the spatial distribution functions (SDFs) around [EMIM] cation reported in Fig. 14. For all the mixtures and compositions, high density spots of anions around the imidazolium ring are inferred (stronger around the CH site), thus confirming the development of hydrogen bonding through these sites in the whole composition range and both for [BF_4] and [TFSI] anions. Furthermore, [TFSI] anions are placed in closer regions to the CH imidazolium ring (and in minor extension around the other CH groups in the ring), and although showing less localized distributions, these molecules compete for the hydrogen bond donor sites in the [EMIM] cation.

The characteristics of cation–anion hydrogen bonding was also analysed in detail by the so-called combined distribution functions (CDFs, calculated using TRAVIS software[42]) including the corresponding distance and angles for the donor–acceptor sites. CDFs for cation–anion interaction through the CH-F and CH-O sites are reported in Fig. 15, two spots are clearly inferred corresponding to the two peak maxima in RDFs as reported in Fig. 12 (one spot for [EMIM]-[BF_4] interaction, first row, and one spot for [EMIM]-[TFSI] interaction, second row). For [EMIM]-[BF_4] interaction, we observe more intense spots corresponding to an interaction angle of roughly 160°, while for [EMIM]-[TFSI] interaction we observe weaker spots with an interaction angle of roughly 135°. These values, which are maintained in the whole composition range, confirm the hydrogen bonding nature of cation–anion interactions.

The dynamics of hydrogen bonding is analysed by the so-called residence times, *t*, Fig. 16. Larger *t* values were obtained for [TFSI] than for [BF_4], despite the stronger [EMIM]-[BF_4] than [EMIM]-[TFSI] interactions (Fig. 11). Therefore, [TFSI] anion has greater molecular mobility around [EMIM] cation than [BF_4] anion. Like-

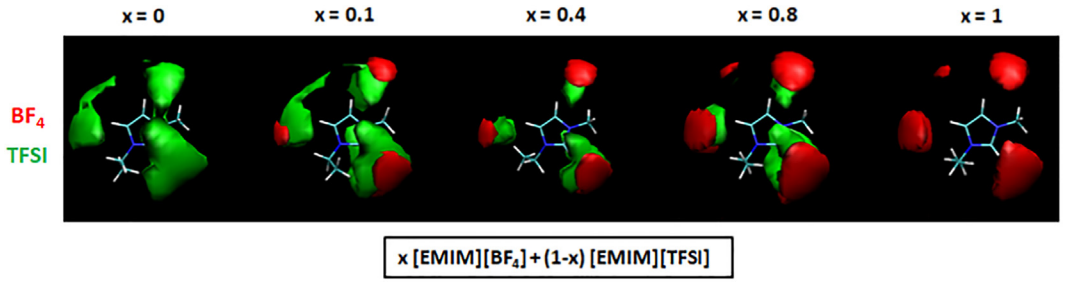

Fig. 14. Spatial distribution functions of the corresponding centers-of-mass around a central [EMIM][BF_4] ion for the reported mixtures at 298 K and 1 bar.

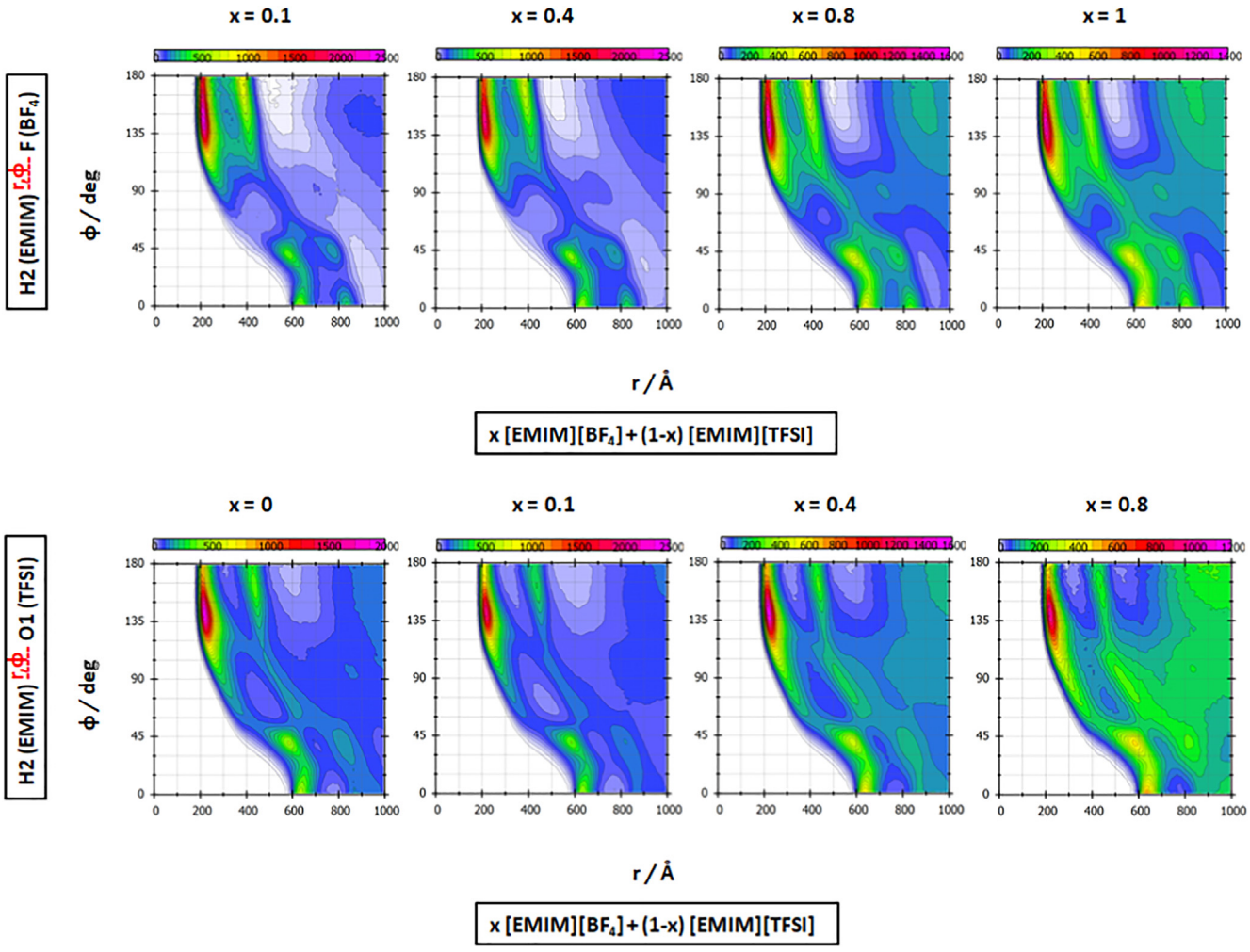

Fig. 15. Combined distribution functions of radial distribution functions (x-axis) and angular distribution functions (y-axis) for the reported distances, r, and angles, φ, (first row, [EMIM]-[BF_4] interactions; second row, [EMIM]-[TFSI] interactions) for × [EMIM][BF_4] + (1-x) [EMIM][TFSI] mixtures at 298 K and 1 bar.

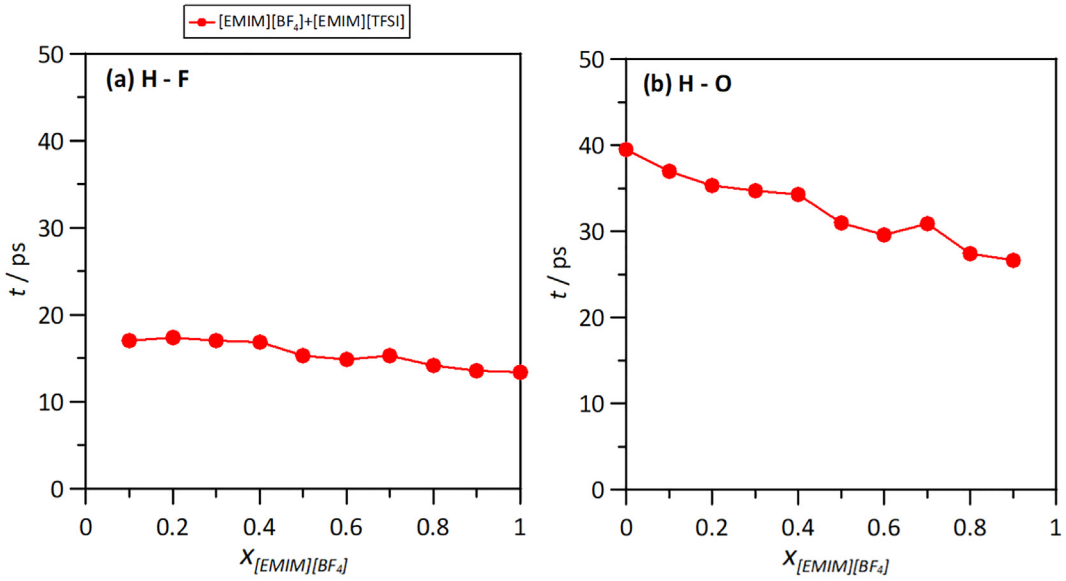

Fig. 16. Residence times, *t*, for selected atom pairs in × [EMIM][BF_4] + (1-x) [EMIM][TFSI] mixtures from MD simulations at 298 K and 1 bar. Residence times are calculated for first solvation layer defined according to the first minima in the corresponding g(r).

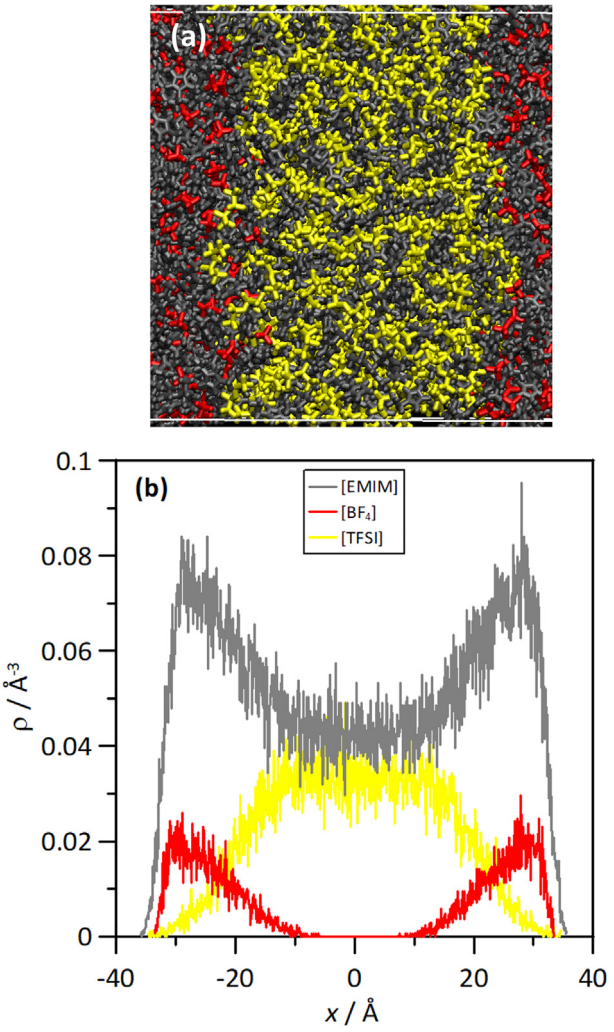

Fig. 17. (a) Snapshot and (b) number density profiles for × [EMIM][BF_4] + (1-x) [EMIM][TFSI] interface, x = 0.5. Values obtained from MD simulations at 298 K and 1 bar.

wise, in the case of [BF_4], the stronger [EMIM]-[BF_4] intermolecular interactions seem to control the dynamics of [EMIM] around [BF_4].

The main properties of [EMIM][BF_4] + [EMIM][TFSI] in liquid phase have been discussed in the previous paragraphs, but the properties of this double salt ionic liquid regarding to [EMIM][BF_4]-[EMIM][TFSI] interface (modelled as in Figure S2, Supplementary Information) were also analysed to infer the structural properties of [BF_4]$^-$ and [TFSI]$^-$ ions at the interface. The [EMIM][BF_4]-[EMIM][TFSI] interface is characterized by a strong adsorption of [BF_4]$^-$ ions leading to a higher dense layer above [TFSI]$^-$ ions, Fig. 17a. Regarding the structure of ions at the interface, results in Fig. 17b show that [BF_4]$^-$ ions penetrate in [EMIM][TFSI] ionic liquid (i.e. starting diffusion toward bulk liquid phase for absorption), which is showed by the widening of the density peaks.

4. Conclusions

The properties of [EMIM][BF_4] + [EMIM][TFSI] mixed ionic liquids were studied using a combined experimental and theoretical approach as a function of composition and temperature. The mixtures are characterized by a largely non-ideal behaviour which is related with the development of new intermolecular forces with changing anionic composition. The reported thermophysical properties, especially excess and mixing functions, confirm non-ideality fort the studied systems. This non-ideality would require complex predictive models for the properties of mixed ionic liquids well beyond the linear mixing rules commonly proposed in the literature. This is even more remarkable for dynamic properties such as viscosity, for which a extremely complex behaviour with mixture composition is reported int his work. The reported molecular modelling studies allowed to quantify the nature, extension and strength of intermolecular forces, confirming the prevailing roles of hydrogen bonding, which determine the cation–anion interactions. These hydrogen bonds being different for the two considered anions are on the basis of the properties of the studied mixtures. Therefore, the considered mixed ILs, containing a common imidazolium cation and two different anion with variable concentration, are complex systems, whose properties cannot be explained with a simple anion replacement mechanism, which is on the roots of the largely non-ideal behaviour from the thermodynamic viewpoint. Thus, ILs containing several types of ions, anions in this work, can be considered for tuning ILs properties, increasing and changing the nature of these fluids, and thus the suitability for different applications. Nevertheless, the large non-ideality of these mixtures should be taken into account for predicting and designing their properties.

Declaration of Competing Interest

The authors declared that there is no conflict of interest.

Acknowledgements

This work was funded Ministerio de Ciencia, Innovación y Universidades (Spain, project RTI2018-101987-B-I00) and by Junta de Castilla y León (Spain, project BU094G18). We acknowledge SCAYLE (Supercomputación Castilla y León, Spain) for providing supercomputing facilities. The statements made herein are solely the responsibility of the authors. Authors declare no competing interests.

Appendix A. Supplementary data

Supplementary data to this article can be found online at https://doi.org/10.1016/j.molliq.2021.116049.

References

[1] R. Ludwig, U. Kragl, Do we understand the volatility of ionic liquids?, Angew. Chem. Int. Ed. 46 (2007) 6582–6584.
[2] B. Wang, L. Qin, T. Mu, Z. Xue, G. Gao, Are ionic liquids chemically stable?, Chem. Rev. 117 (2017) 7113–7131.
[3] J.P. Hallett, T. Welton, Room-temperature ionic liquids: solvents for synthesis and catalysis, Chem. Rev. 111 (2011) 3508–3576.
[4] C.J. Clarke, W.C. Tu, O. Levers, A. Brohl, J.P. Hallett, Green and sustainable solvents in chemical processes, Chem. Rev. 118 (2018) 747–800.
[5] R.D. Rogers, Reflections on ionic liquids, Nature 447 (2007) 917–918.
[6] X. Liu, Y. Huang, Y. Zhao, R. Gani, X. Zhang, S. Zhang, Ionic liquid design and process simulation for decarbonization of shale gas, Ind. Eng. Chem. Res. 55 (2016) 5931–5944.
[7] G. Chatel, J.F.B. Pereira, V. Debbeti, H. Wang, R.D. Rogers, Mixing ionic liquids -"simple mixtures" or "double salts"?, Green Chem. 16 (2014) 2051–2083.
[8] J.F.B. Pereira, P.S. Barber, S.P. Kelley, P. Benton, R.D. Rogers, Double salt ionic liquids based on 1-ethyl-3-methylimidazolium acetate and hydroxylfunctionalized ammonium acetates: strong effects of weak interactions, PCCP 19 (2017) 26934–26943.
[9] R.P. Matthews, I.J. Villar-Garcia, C.C. Weber, J. Griffith, F. Cameron, J.P. Hallett, P.A. Hunt, T. Welton, A Structural Investigation of Ionic Liquid Mixtures, PCCP 18 (2016) 8608–8624.
[10] H. Niedermeyer, J.P. Hallett, I.J. Villar-Garcia, P.A. Hunt, T. Welton, Mixtures of ionic liquids, Chem. Soc. Rev. 41 (2012) 7780–7802.
[11] J.S.N. Canongia-lopes, T.C. Cordeiro, J.M.S.S. Esperanca, H.J.R. Guedes, S. Huq, L. P.N. Rebelo, K.R. Seddon, Deviations from ideality in mixtures of two ionic liquids containing a common ion, J. Phys. Chem. B 109 (2005) 3519–3525.

[12] A. Stoppa, R. Buchner, G. Hefter, How ideal are binary mixtures of room-temperature ionic liquids?, J. Mol. Liq. 153 (2010) 46–51.
[13] M. Larriba, P. Navarro, J. García, F. Rodríguez, Separation of toluene from n-heptane, 2,3-dimethylpentane, and cyclohexane using binary mixtures of [4empy][Tf2N] and [emim][DCA] ionic liquids as extraction solvents, Sep. Purif. Technol. 120 (2013) 392–401.
[14] G. Annat, M. Forsyth, D.R. McFarlane, Ionic Liquid Mixtures—Variations in Physical Properties and Their Origins in Molecular Structure, J. Phys. Chem. B 116 (2012) 8251–8258.
[15] P. Navia, J. Troncoso, L. Romani, Excess magnitudes for ionic liquid binary mixtures with a common ion, J. Chem. Eng. Data 52 (2007) 1369–1374.
[16] P. Navia, J. Troncoso, L. Romaní, Viscosities for ionic liquid binary mixtures with a common ion, J. Sol. Chem. 37 (2008) 677–688.
[17] M.B. Oliveira, M. Dominguez-Perez, O. Cabeza, J.A. López-da-Silva, M.G. Freire, J.A.P. Coutinho, Surface tensions of binary mixtures of ionic liquids with bis (trifluoromethylsulfonyl)imide as the common anion, J. Chem. Thermodyn. 64 (2013) 22–27.
[18] C. Moya, M. Gonzalez, F. Rodríguez, A. Soto, H. Rodríguez, J. Palomar, Non-ideal behavior of ionic liquid mixtures to enhance CO_2 capture, Fluid Phase Equilibr. 450 (2017) 175–183.
[19] P. Dhakal, J.K. Shah, Recent advances in molecular simulations of ionic liquid–ionic liquid mixtures, Curr. Opin. Green Sus. Chem. 18 (2019) 90–97.
[20] B.S. Lee, S.T. Lin, Prediction and screening of solubility of pharmaceuticals in single- and mixed-ionic liquids using COSMO-SAC model, AIChE J. 63 (2017) 3096–3104.
[21] A.M. Pinto, H. Rodríguez, Y.J. Colón, A. Arce, A. Arce Jr., A. Soto, bsorption of carbon dioxide in two binary mixtures of ionic liquids, Ind. Eng. Chem. Res. 52 (2013) 5975–5984.
[22] Z.G. Lei, J. Han, B. Zhang, Q. Li, J. Zhu, B. Chen, Solubility of CO_2 in binary mixtures of room-temperature ionic liquids at high pressures, J. Chem. Eng. Data 57 (2012) 2153–2159.
[23] A.M. Smith, A.A. Lee, S. Perkin, Switching the structural force in ionic liquid solvent mixtures by varying composition, Phys. Rev. Lett. 118 (2017) 096002.
[24] M. Chen, R. Pendrill, G. Widmalm, J.W. Brady, J. Wohlert, Molecular dynamics simulations of the ionic liquid 1-n-Butyl-3-Methylimidazolium chloride and its binary mixtures with ethanol, J. Chem. Theory Comput. 10 (2014) 4465–4479.
[25] V.R. Ferro, C. Moya, D. Moreno, R. Santiago, J. de Riva, G. Pedrosa, M. Larriva, I. Diaz, J. Palomar, Enterprise ionic liquids database [ILUAM] for use in Aspen ONE programs suite with COSMO-based property methods, Ind. Eng. Chem. Res. 57 (2018) 980–989.
[26] A. Gutierrez, M. Atilhan, R. Alcalde, J.L. Trenzado, S. Aparicio, Insights on the mixtures of imidazolium based ionic liquids with molecular solvents, J. Mol. Liq. 255 (2018) 199–207.
[27] R. Alcalde, M. Atilhan, S. Aparicio, Insights on 1-butyl-3-methylimidazolium bis [trifluoromethylsulfonyl] imide + ethanol liquid mixtures: a molecular dynamics approach, J. Chem. Eng. Data 61 (2016) 2729–2737.
[28] C. Herrera, R. Alcalde, M. Atilhan, S. Aparicio, Microscopic characterization of mixtures of amino acid ionic liquids and organic solvents, J. Mol. Liq. 250 (2019) 111–120.
[29] J.L. Trenzado, R. Alcalde, M. Atilhan, S. Aparicio, Molecular dynamics and experimental characterization of [BMIM][BF_4] and [BMIM][PF_6] with ether cosolvent binary mixtures, J. Mol. Liq. 271 (2018) 65–73.
[30] J.L. Trenzado, A. Gutiérrez, R. Alcalde, M. Atilhan, S. Aparicio, Insights on [BMIM][BF_4] and [BMIM][PF_6] ionic liquids and their binary mixtures with acetone and acetonitrile, J. Mol. Liq. 294 (2019) 111632.
[31] S. Aparicio, M. Atilhan, F. Karadas, Thermophysical properties of pure ionic liquids: review of present situation, Ind. Eng. Chem. Res. 49 (2010) 9580–9595.
[32] X. Wang, Y. Chi, T. Mu, A review on the transport properties of ionic liquids, J. Mol. Liq. 193 (2014) 262–266.
[33] W. Wagner, A. Pru, The IAPWS Formulation 1995 for the Thermodynamic Properties of Ordinary Water Substance for General and Scientific Use, J. Phys. Chem. Ref. Data 31 (2002) (1995) 387–535.
[34] E. W. Lemmon, M. L. Huber, M. McLinden, Reference Fluid, Thermodynamic, Transport Properties. NIST Standard Reference Database 23, version 9.0; The National Institute of Standards, Technology: Gaithersburg, MD, 2010.
[35] M.M. Alavianmehr, R. Ahmadi, N. Aguilar, M. El-Shaik, S.M. Hosseini, S. Aparicio, Thermophysical and molecular modelling insights into glycerol + alcohol liquid mixtures, J. Mol. Liq. 297 (2020) 111811.
[36] S. Adams, P. de Castro, P. Echenique, J. Estrada, M.D. Hanwell, P. Murray-Rust, P. Sherwood, J. Thomas, J.A. Townsend, The Quixote project: collaborative and open quantum chemistry data management in the internet age, J. Cheminformatics 3 (2011) 38.
[37] F. Neese, The ORCA program system, WIREs Comput. Mol. Sci. 2 (2012) 73–78.
[38] C. Lee, W. Yang, R.G. Parr, Development of the Colle-salvetti correlation-energy formula into a functional of the electron density, Phys. Rev. B 37 (1988) 785–789.
[39] A.D. Becke, Density-functional exchange-energy approximation with correct asymptotic behavior, Phys. Rev. A 38 (1988) 3098–3100.
[40] S. Grimme, J. Antony, S. Ehrlich, H.A. Krieg, Consistent and accurate ab initio parametrization of density functional dispersion correction (DFT-D) for the 94 elements H-Pu, J. Chem. Phys. 132 (2010) 154104.
[41] S. Simon, M. Duran, J.J. Dannenberg, How does basis set superposition error change the potential surfaces for hydrogen-bonded dimers?, J. Chem. Phys. 105 (1996) 11024–11031.
[42] R.F.W. Bader, Atoms in Molecules: a Quantum Theory, Oxford University Press, 1990.
[43] T. Lu, F. Chen, Multiwfn: A multifunctional wavefunction analyzer, J. Comput. Chem. 33 (2012) 580–592.
[44] S. Aparicio, C.T. Yavuz, M. Atilhan, Molecular insights into benzimidazole-linked polymer interactions with carbon dioxide and nitrogen, ChemistrySelect 3 (2018) 3691–3701.
[45] J. Xiao, Y.P. Zhao, X. Fan, J.P. Cao, G.J. Kang, W. Zhao, X.Y. Wei, hydrogen bonding interactions between the organic oxygen/nitrogen monomers of lignite and water molecules: A DFT and AIM study, Fuel Process. Technol. 168 (2017) 58–64.
[46] V. Anbu, K.A. Vijayalakshmi, R. Karunathan, A.D. Stephen, P.V. Nidhin, Explosives properties of high energetic trinitrophenyl nitramide molecules: A DFT and AIM analysis, Arab. J. Chem. 12 (2019) 621–632.
[47] E.R. Johnson, S. Keinan, P. Mori-Sanchez, J. Contreras-García, A.J. Cohen, W. Yang, Revealing non-covalent interactions, J. Am. Chem. Soc. 132 (2010) 6498–6506.
[48] A.P. Lyubartsev, A. Laaksonen, MDynaMix - a scalable portable parallel MD smulation package for arbitrary molecular mixtures, Comput. Phys. Commun. 128 (2000) 565–589.
[49] V. Zoete, M.A. Cuendet, A. Grosdidier, O. Michielin, SwissParam, A fast force field generation tool for small organic molecules, J. Comput. Chem. 32 (2011) 2359–2368.
[50] T.A. Halgren, Merck molecular force field. I. Basis, form, scope, parameterization, and performance of MMFF94, J. Comput. Chem. 17 (1996) 490–519.
[51] C.M. Breneman, K.B. Wiberg, Determining atom-centered monopoles from molecular electrostatic potentials. The need for high sampling density in formamide conformational analysis, J. Comput. Chem. 11 (1990) 361–373.
[52] L. Martínez, R. Andrade, E.G. Birgin, J.M. Martínez, Packmol: A package for building initial configurations for molecular dynamics simulations, J. Comput. Chem. 30 (2009) 2157–2164.
[53] U.L. Essmann, M.L.; Perera, T. Berkowitz, H. Darden, H. Lee, L.G. Pedersen, A smooth particle mesh Ewald method. J. Chem. Phys. 103 (1995) 8577-8593.
[54] M. Tuckerman, B.J. Berne, G.J. Martyna, Reversible multiple time scale molecular dynamics, J. Chem. Phys. 97 (1992) 1990–2001.
[55] W. Humphrey, A. Dalke, K. Schulten, VMD - Visual molecular dynamics, J. Molec. Graphics 14 (1996) 33–38.
[56] M. Brehm, B. Kirchner, TRAVIS - A free analyzer and visualizer for Monte Carlo and molecular dynamics trajectories, J. Chem. Inf. Model. 51 (2011) 2007–2023.
[57] H. Shekaari, M.T. Zafarani-Moattar, M. Mokhtarpour, S. Faraji, Volumetric and compressibility properties for aqueous solutions of choline chloride based deep eutectic solvents and Prigogine–Flory–Patterson theory to correlate of excess molar volumes at T = (293.15 to 308.15) K, J. Mol. Liq. 289 (2019) 111077.
[58] K. Dong, S. Zhang, D. Wang, X. Yao, Hydrogen bonds in imidazolium ionic liquid mixtures, J. Phys. Chem. A 110 (2006) 9775–9782.
[59] M.Z. Brela, P. Kubisiak, A. Eilmes, Understanding the structure of the hydrogen bond network and its influence on vibrational spectra in a prototypical aprotic ionic liquid, J. Phys. Chem. B 122 (2018) 9527–9537.
[60] H. Roohi, A.R. Nowroozi, E. Anjomshoa, H-bonded complexes of uracil with parent nitrosamine: a quantum chemical study, Comput. Theor. Chem. 965 (2011) 211–220.
[61] E.R. Johnson, S. Keinan, P. Mori-Sanchez, J. Contreras-García, A.J. Cohen, W. Yang, Revealing noncovalent interactions, J. Am. Chem. Soc. 132 (2010) 6498–6506.
[62] K. Dong, S. Zhang, D. Wang, X. Yao, Hydrogen bonds in imidazolium ionic liquids, J. Phys. Chem. A 110 (2006) 9775–9782.
[63] K. Dong, S. Zhang, J. Wang, Understanding the hydrogen bonds in ionic liquids and their roles in properties and reactions, Chem. Comm. 52 (2016) 6744–6764.

5.1.1.1. Información experimental 0

Tabla 11. Comparación de los datos experimentales con la literatura citada, tanto de las densidades, ρ (g cm^{-3}), como de las viscosidades cinemáticas, η (mPa s), de los compuestos puros a las temperaturas de trabajo.

	ρ / g cm^{-3}		ν / mm^2 s^{-1}		ρ / g cm^{-3}		ν / mm^2 s^{-1}	
T / K	exp.	lit.	exp.	lit.	exp.	lit.	exp.	lit.
	[EMIM][BF$_4$]				[EMIM][TSFI]			
283.15	1.29151	1.29704[a]	50.220	57.362[g]	1.56559	1.24691[i]	77.331	56.2[k]
288.15	1.28766	1.29321[a]	39.534	55.5[e]	1.56042	1.24348[i]	59.506	49.4[l]
		1.28803[b]		-		-		-
293.15	1.28384	1.28389[c]	32.746	38.208[g]	1.55523	1.24009[i]	46.876	41.6[m]
		1.28390[d]		-		-		-
298.15	1.28005	1.28007[b]	27.100	35.8[h]	1.55006	1.23689[i]	37.715	33.9[m]
		1.27990[e]		-		-		-
303.15	1.27626	1.27626[c]	22.738	27.083[g]	1.54489	1.23678[i]	30.637	28.35[l]
		1.27612[f]		-		-		-
308.15	1.27249	1.27248[b]	19.315	25.54[h]	1.53974	1.23346[j]	25.547	24.15[l]
		1.27240[d]		-		-		-
313.15	1.26873	1.26857[f]	16.562	20.008[g]	1.53460	1.23332[k]	21.504	20.76[l]

(a) Sanmamed et al.. 2010
(b) Stoppa et al.. 2010
(c) Bhagour et al.. 2013
(d) Song and Chen. 2014
(e) Rilo et al.. 2010
(f) Rao et al.. 2017
(g) Shamsipur et al.. 2010
(h) Navia et al.. 2008
(i) Rocha et al.. 2013
(j) Safarov et al.. 2011
(k) Yadav et al.. 2018
(l) Liu et al.. 2018
(m) Hofmann et al.. 2016

Bhagour, S., Solanki, S., Hooda, N., Sharma, D., (2018) Journal of Chemical Thermodynamics, 60, 76-86.

Hofmann, A., Migeot, M., Hanemann, T. (2016) Journal of Chemical and Engineering Data, 61, 114−123.

Liu, Q., Zhao, L., Zheng, Q., Mou, L., Zhang, P. (2018) Journal of Chemical and Engineering Data, 63, 4484-4496.

Navia, P., Troncoso, J., Romani, L. (2008) Journal of Solution Chemistry, 37, 677-688.

Rao, V.S., Krishna, T.V., Mohan, T.M., Rao, P.M. (2017) Journal of Chemical Thermodynamics, 104, 150-161.

Rilo, E., Vila, J., Pico, J., García-Garabal, S., Segade, L., Varela, L. M., & Cabeza, O. (2010). Journal of Chemical and Engineering Data, 55(2), 639–644.

Rocha, M., Neves, C., Freire, M, Russina, O., Triolo, A., Coutinho, A. (2013) Journal of Physical Chemistry B, 117, 10889-10897.

Safarov, J., El-Awady, W., Shahverdiyev, A., Hassel, E. (2011) Journal of Chemical and Engineering Data, 56, 106-112.

Sanmamed, Y. A., González-Salgado, D., Troncoso, J., Romani, L., Baylaucq, A., & Boned, C. (2010). Journal of Chemical Thermodynamics, 42(4), 553–563.

Shamsipur, M., Beigi, A.A.M., Teymouri, M., Pourmortazavi, S.M. (2010) Journal of Molecular Liquids, 157, 43−50.

Song, D., & Chen, J. (2014). Journal of Chemical and Engineering Data, 59(2), 257–262.

Stoppa, A., Zech, O., Kunz, W., Buchner, R. (2010) Journal of Chemical and Engineering Data, 55, 1768-1773.

Yadav, A., Guha, A., Pandey, A., Pal, M., Trivedi, A., Pandey, S. (2018) Journal of Chemical Thermodynamics, 116, 67-75.

Tabla 12. Densidades (ρ), viscosidades cinemáticas (ν), viscosidades dinámicas (η), volúmenes molares de exceso (VE) y desviaciones en la viscosidad ($\Delta\eta$) del sistema {(x) [EMIM][B$_4$] + (1-x) [EMIM][TSFI]} a diferentes temperaturas.

x	ρ / g cm^{-3}	ν / mm^2 s^{-1}	η / mPa s	V^E / cm^3 mol^{-1}	$\Delta\eta$ / mPa s
		283.15 K			
0.04600	1.55731	73.203	114.000	0.067	-4.4836
0.09965	1.54737	68.690	106.289	0.128	-9.1784
0.21336	1.52502	62.006	94.560	0.230	-14.5158
0.29467	1.50782	61.034	92.028	0.284	-12.4774
0.39849	1.48420	62.307	92.476	0.325	-6.1939
0.49711	1.45979	63.621	92.873	0.338	-0.2535
0.60158	1.43149	63.917	91.497	0.324	4.2429
0.69740	1.40297	62.247	87.331	0.286	5.4627
0.80242	1.36839	58.529	80.090	0.216	4.1249
0.91417	1.32704	53.858	71.472	0.109	1.7887
0.93468	1.31887	52.940	69.821	0.086	1.2906
		288.15 K			
0.04600	1.55211	56.436	87.595	0.078	-3.3305
0.09965	1.54214	53.372	82.307	0.152	-6.3676
0.21336	1.51974	49.040	74.528	0.278	-9.3766
0.29467	1.50255	48.479	72.842	0.342	-7.6518
0.39849	1.47898	49.436	73.115	0.392	-3.0237
0.49711	1.45465	49.926	72.625	0.408	0.6233
0.60158	1.42650	49.948	71.251	0.391	3.6317
0.69740	1.39817	48.793	68.221	0.343	4.6211
0.80242	1.36388	46.090	62.861	0.256	3.6666
0.91417	1.32291	42.221	55.855	0.125	1.3487
0.93468	1.31482	41.541	54.619	0.096	0.9730
		293.15 K			
0.04600	1.54692	44.779	69.270	0.085	-2.2125
0.09965	1.53692	42.643	65.539	0.172	-4.2876
0.21336	1.51450	39.488	59.805	0.319	-6.5124
0.29467	1.49731	39.182	58.668	0.396	-5.1401
0.39849	1.47378	39.981	58.923	0.456	-1.6812
0.49711	1.44953	40.402	58.564	0.477	1.0033
0.60158	1.42151	40.583	57.689	0.459	3.3524
0.69740	1.39335	39.702	55.319	0.406	3.9394
0.80242	1.35929	37.675	51.211	0.308	3.0724
0.91417	1.31866	34.829	45.928	0.157	1.2383
0.93468	1.31063	34.303	44.959	0.125	0.9023
		298.15 K			
0.04600	1.54172	36.150	55.733	0.097	-1.6336
0.09965	1.53171	34.592	52.985	0.194	-3.1061
0.21336	1.50928	32.798	49.501	0.360	-3.8871
0.29467	1.49212	32.536	48.548	0.445	-2.9073
0.39849	1.46865	32.793	48.161	0.513	-0.8265
0.49711	1.44451	33.185	47.936	0.535	1.2928
0.60158	1.41664	33.257	47.113	0.514	2.9532
0.69740	1.38866	32.690	45.395	0.454	3.5128
0.80242	1.35485	31.110	42.149	0.344	2.7633
0.91417	1.31455	28.798	37.856	0.176	1.1268
0.93468	1.30660	28.404	37.113	0.139	0.8714

Tabla 12. Continuación.

x	ρ / g cm^{-3}	ν / mm^2 s^{-1}	η / mPa s	V^E / cm^3 mol^{-1}	$\Delta\eta$ / mPa s
		303.15 K			
0.04600	1.53652	29.503	45.332	0.109	-1.1558
0.09965	1.52647	28.424	43.388	0.221	-2.1172
0.21336	1.50399	26.932	40.505	0.414	-2.9181
0.29467	1.48683	26.805	39.854	0.512	-2.0802
0.39849	1.46340	27.000	39.512	0.590	-0.5212
0.49711	1.43933	27.562	39.671	0.618	1.4436
0.60158	1.41161	27.669	39.058	0.593	2.7435
0.69740	1.38382	27.187	37.622	0.525	3.0620
0.80242	1.35029	25.931	35.014	0.398	2.3771
0.91417	1.31037	24.100	31.580	0.205	0.9894
0.93468	1.30249	23.753	30.938	0.163	0.7230
		308.15 K			
0.04600	1.53128	24.717	37.849	0.131	-0.8072
0.09965	1.52121	23.774	36.165	0.255	-1.6994
0.21336	1.49873	22.810	34.186	0.466	-2.0004
0.29467	1.48159	22.616	33.508	0.573	-1.4785
0.39849	1.45822	22.859	33.333	0.660	-0.1215
0.49711	1.43426	23.495	33.698	0.687	1.6989
0.60158	1.40670	23.446	32.981	0.658	2.5235
0.69740	1.37911	22.959	31.663	0.580	2.6195
0.80242	1.34585	21.972	29.571	0.438	2.0773
0.91417	1.30631	20.423	26.679	0.220	0.8345
0.93468	1.29852	20.044	26.028	0.172	0.4861
		313.15 K			
0.04600	1.52608	20.910	31.910	0.149	-0.5386
0.09965	1.51596	20.353	30.854	0.290	-0.9513
0.21336	1.49342	19.595	29.264	0.529	-1.1782
0.29467	1.47628	19.407	28.650	0.649	-0.8175
0.39849	1.45295	19.779	28.738	0.746	0.5151
0.49711	1.42908	20.282	28.985	0.777	1.9444
0.60158	1.40167	20.042	28.092	0.744	2.3038
0.69740	1.37428	19.381	26.635	0.655	1.9954
0.80242	1.34132	18.501	24.816	0.493	1.4354
0.91417	1.30218	17.255	22.469	0.246	0.4281
0.93468	1.29447	17.024	22.037	0.193	0.2420

Tabla 13. Parámetros (A_k) obtenidos para un ajuste polinómico en el caso de las propiedades ρ, ν, y con la ecuación de Redlich y Kister (6) para V^E, Δη, así como las desviaciones estándar (s) para el sistema binario (x)[EMIM][BF_4]+(1-x)[EMIM][TSFI].

Propiedad	A_0	A_1	A_2	A_3	A_4	A_5	A_6	s
				283,15 K				
ρ (g/cm^3)	1.566	-0.175	-0.069	-0.0004	-0.031	-	-	0.00003
ν (mm^2·s^{-1})	77.703	-115.772	200.219	155.986	-566.315	298.674	-	0.490
V^E (cm^3·mol^{-1})	1.348	-0.016	0.085	-	-	-	-	0.002
Δη (mPa·s)	0.303	109.642	-118.283	-23.499	84.900	-36.481	-	0.173
				288,15 K				
ρ (g/cm^3)	1.561	-0.176	-0.067	0.0009	-0.031	-	-	0.0002
ν (mm^2·s^{-1})	59.693	-82.744	169.802	17.117	-292.992	168.744	-	0.261
V^E (cm^3·mol^{-1})	1.632	-0.003	0.023	-0.105	-	-	-	0.001
Δη (mPa·s)	3.662	70.401	-71.595	11.210	37.066	-48.894	-	0.191
				293,15 K				
ρ (g/cm^3)	1.555	-0.176	-0.066	0.001	-0.030	-	-	0.00003
ν (mm^2·s^{-1})	47.029	-57.322	109.334	50.843	-256.405	139.357	-	0.217
V^E (cm^3·mol^{-1})	1.904	0.018	0.074	0.053	-	-	-	0.001
Δη (mPa·s)	5.145	53.088	-53.960	3.168	31.843	-33.356	-	0.170
				298,15 K				
ρ (g/cm^3)	1.550	-17.698	-0.064	0.001	-0.030	-	-	0.000
ν (mm^2·s^{-1})	37.744	-39.600	80.834	14.400	-149.856	83.592	-	0.037
V^E (cm^3·mol^{-1})	2.142	0.003	-0.011	0.057	0.162	-	-	0.001
Δη (mPa·s)	5.353	39.371	-20.456	-10.329	21.603	-4.247	25.798	0.016

Tabla 13. Continuación.

Propiedad	A_0	A_1	A_2	A_3	A_4	A_5	A_6	s
				303,15 K				
ρ (g/cm^3)	1.545	-0.178	-0.006	0.002	-0.030	-	-	0.00003
ν (mm^2·s^{-1})	30.665	-27.767	42.207	71.440	-186.758	92.983	-	0.061
V^E (cm^3·mol^{-1})	2.470	0.008	-0.010	0.116	0.175	-	-	0.001
Δη (mPa·s)	5.781	33.272	-23.414	-15.845	9.092	-	-	0.066
				308,15 K				
ρ (g/cm^3)	1.540	-0.178	-0.061	0.002	-0.030	-	-	0.00003
ν (mm^2·s^{-1})	25.583	-21.884	35.098	57.951	-156.818	79.403	-	0.090
V^E (cm^3·mol^{-1})	72.750	-0.0003	-0.024	-0.060	0.231	-	-	0.001
Δη (mPa·s)	6.246	26.569	-21.178	-13.634	8.533	-	-	0.122
				313,15 K				
ρ (g/cm^3)	1.534	-0.180	-0.059	0.003	-0.030	-	-	0.00003
ν (mm^2·s^{-1})	21.482	-9.887	-45.085	355.409	-726.246	593.389	-1.725	0.093
V^E (cm^3·mol^{-1})	3.109	-0.006	-0.022	-0.106	0.244	-	-	0.001
Δη (mPa·s)	7.153	18.388	-25.540	-12.442	16.108	-	-	0.134

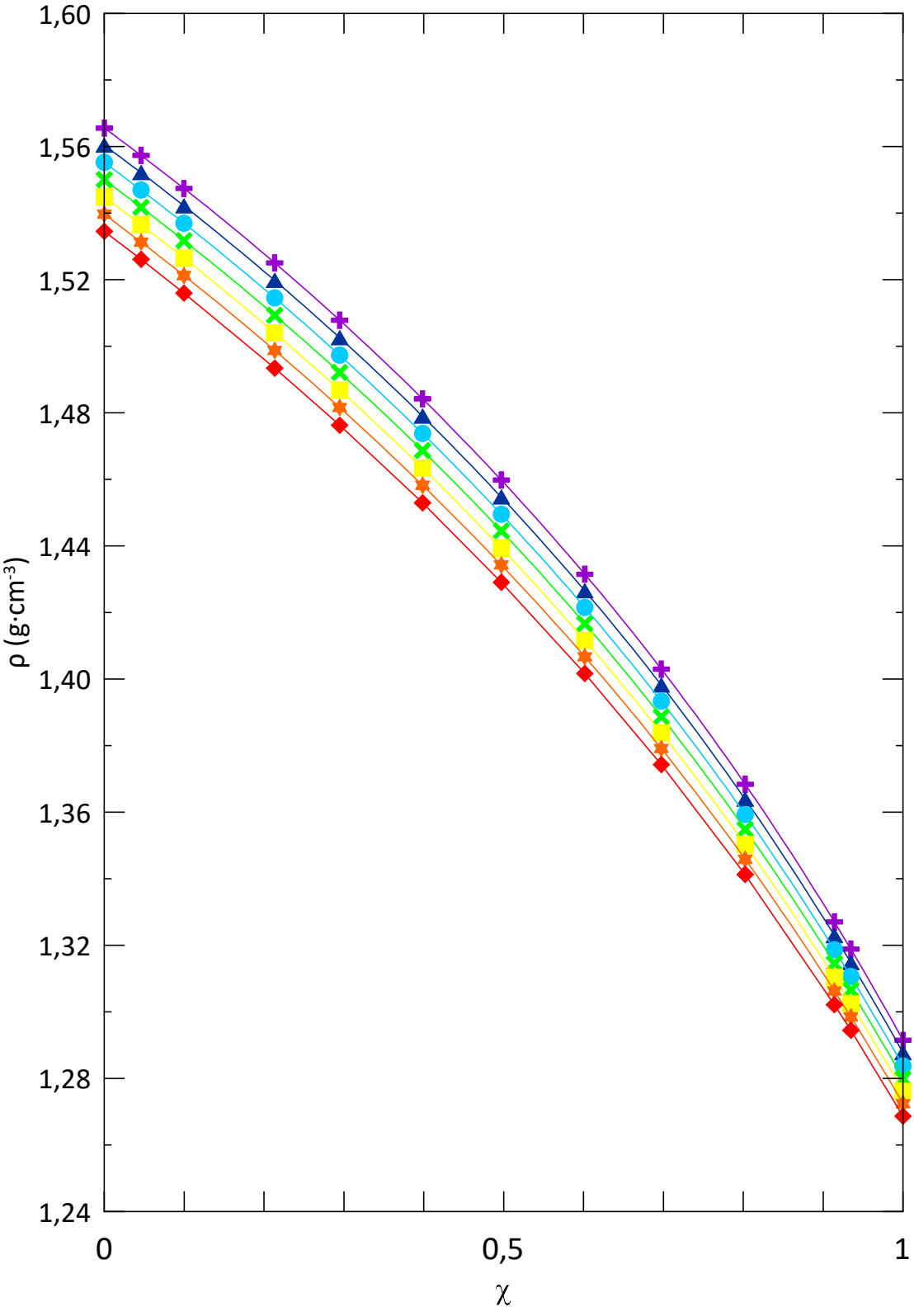

Figura 50. Variación de la densidad del sistema (x)[EMIM][BF_4]+(1-x)[EMIM][TSFI] en función de la temperatura: (+)283,15K, (▲)288,15K, (●)293,15K, (x)298,15K, (■)303,15K, (*)308,15K, (♦)313,15K.

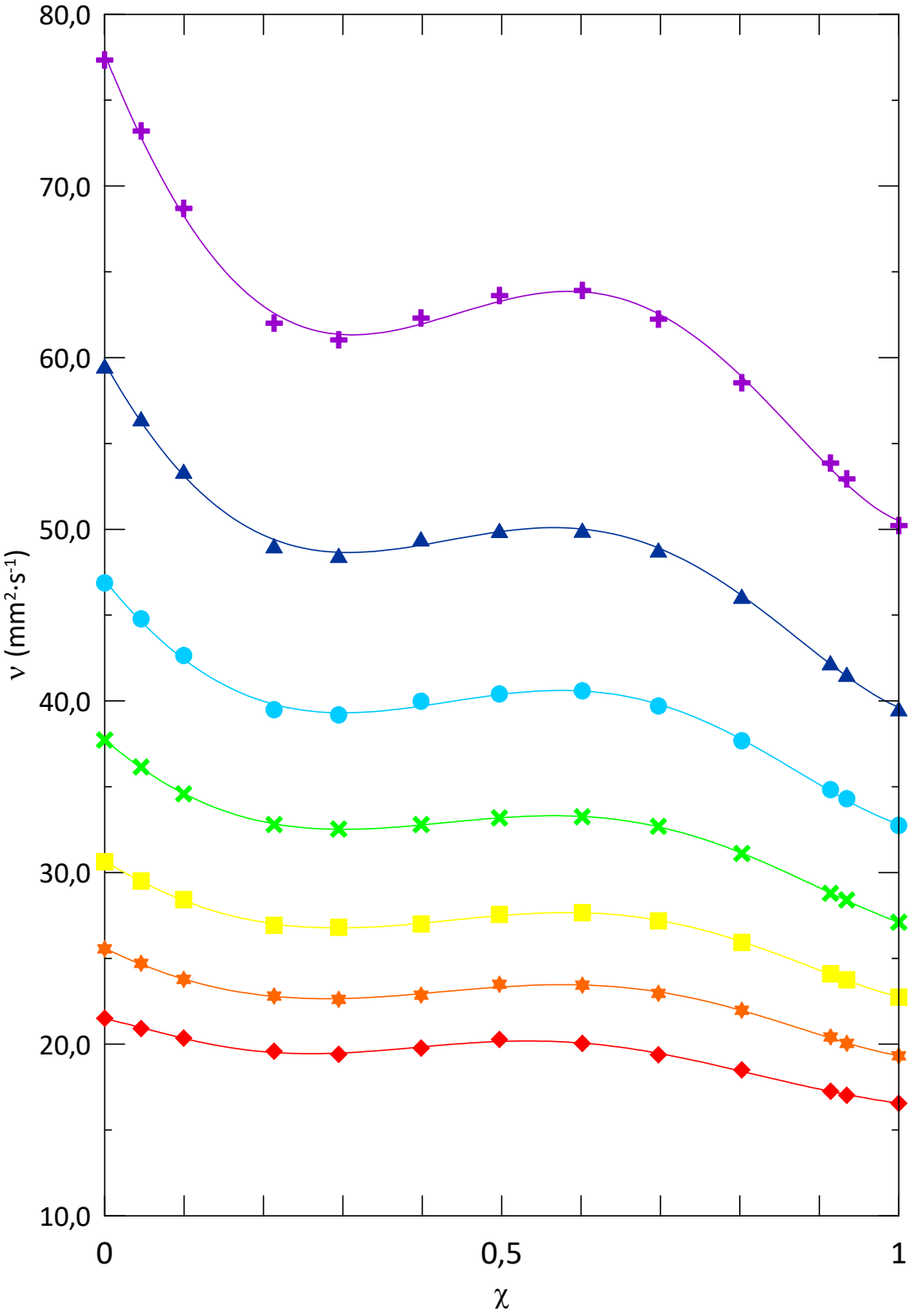

Figura 51. Variación de la viscosidad cinemática del sistema (x)[EMIM][BF_4]+(1-x)[EMIM][TSFI] en función de la temperatura: (+)283,15K, (▲)288,15K, (●)293,15K, (x)298,15K, (■)303,15K, (*)308,15K, (♦)313,15K.

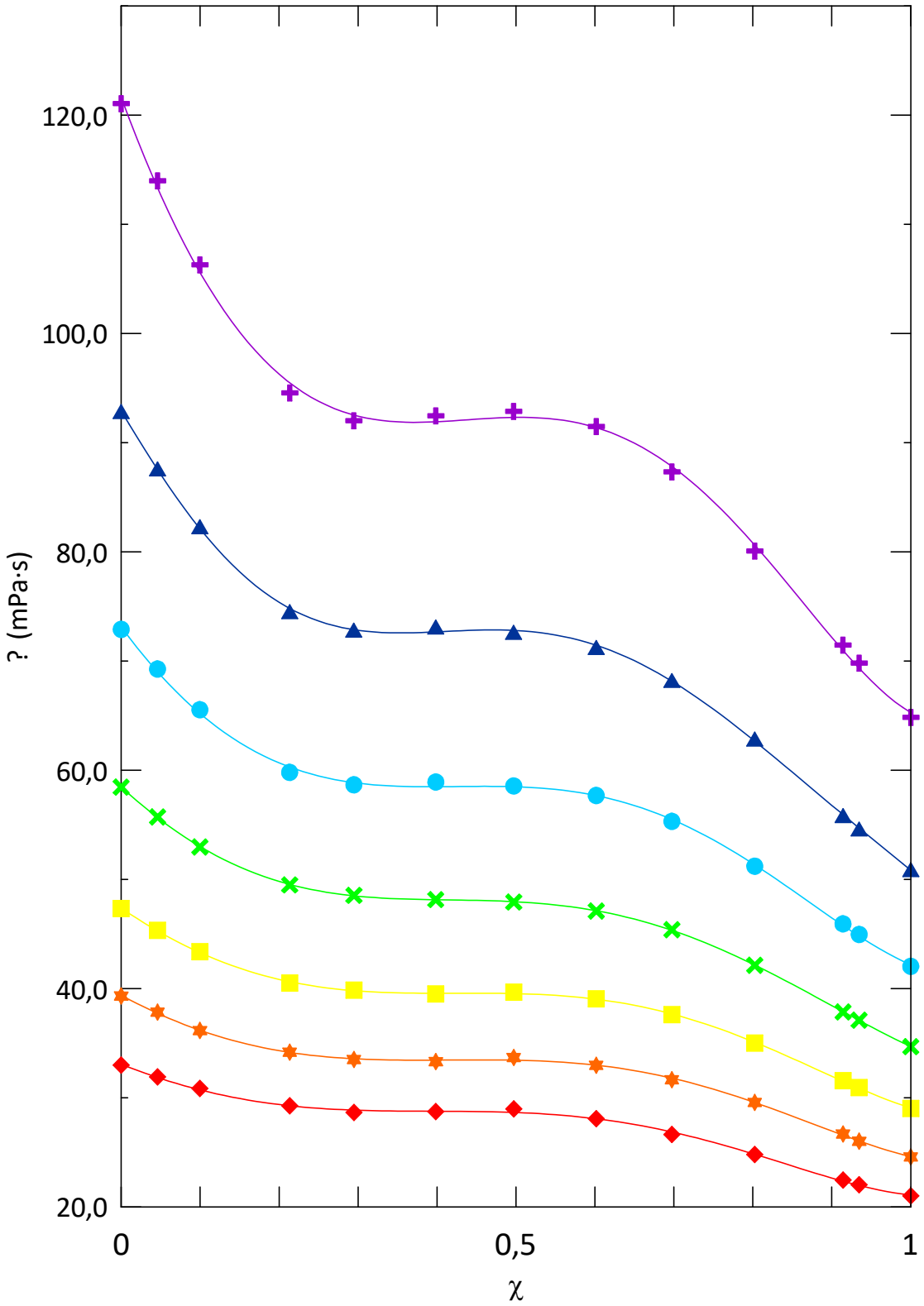

Figura 52. Variación de la viscosidad dinámica del sistema (x)[EMIM][BF_4]+(1-x)[EMIM][TSFI] en función de la temperatura: (+)283,15K, (▲)288,15K, (●)293,15K, (x)298,15K, (■)303,15K, (*)308,15K, (♦)313,15K.

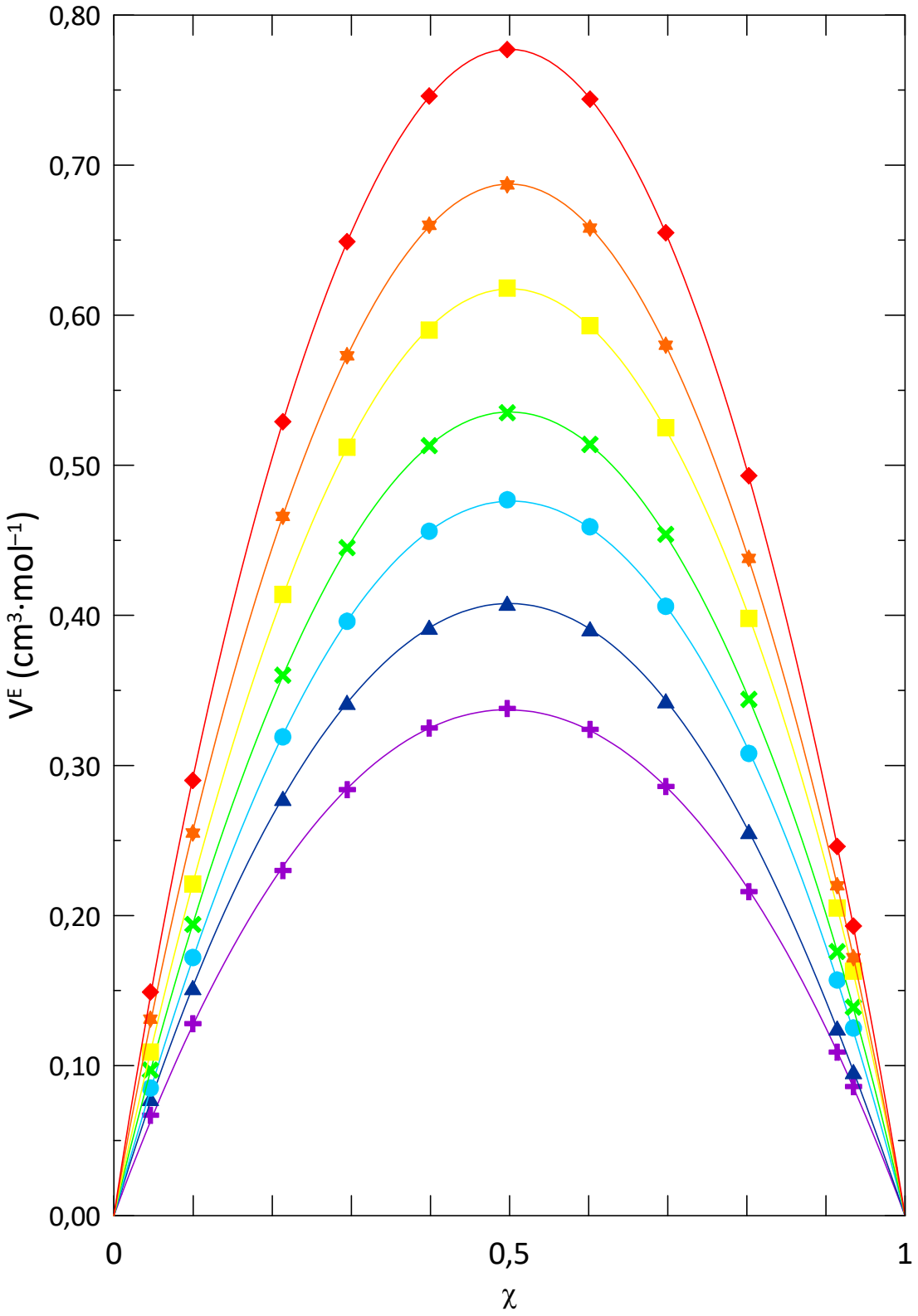

Figura 53. Volumen molar de exceso del sistema (x)[EMIM][BF_4]+(1-x)[EMIM][TSFI] en función de la temperatura: (+)283,15K, (▲)288,15K, (●)293,15K, (x)298,15K, (■)303,15K, (*)308,15K, (♦)313,15K.

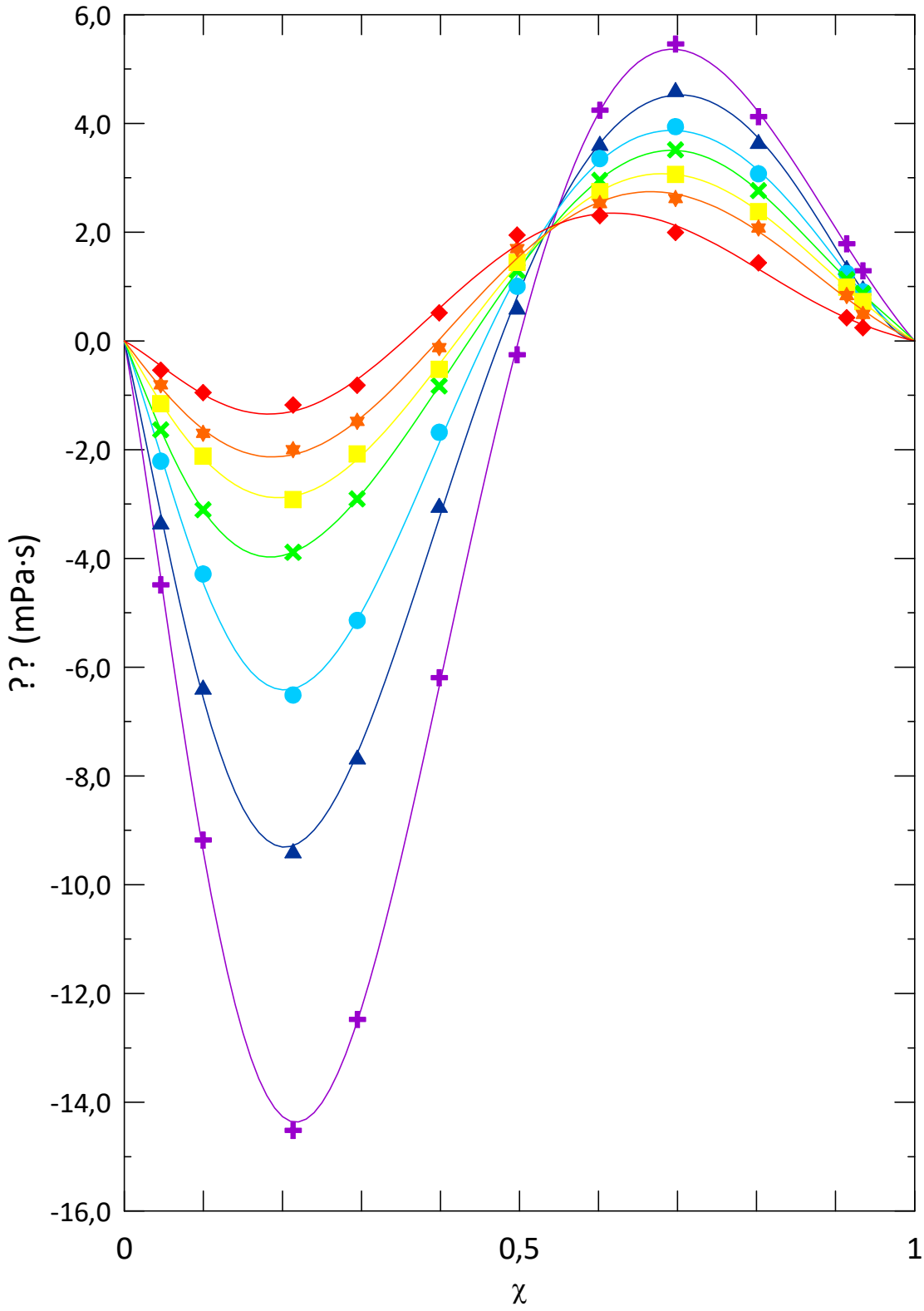

Figura 54. Desviaciones de la viscosidad del sistema (x)[EMIM][BF_4]+(1-x)[EMIM][TSFI] en función de la temperatura: (+)283,15K, (▲)288,15K, (●)293,15K, (x)298,15K, (■)303,15K, (*)308,15K, (♦)313,15K.

5.1.2. Publicación I

Título:	**On the properties and intermolecular forces of ionic liquid mixtures: the archetypical case of [EMIM][BF_4] + [EMIM][$EtSO_4$]**
Autores:	Ylenia Rodríguez [a], Santiago Aparicio [b], José L. Trenzado [a]
Afiliación:	[a]) Departamento de Física, Universidad de Las Palmas de Gran Canaria, 35017 Las Palmas G.C., Spain [b]) Department of Chemistry, University of Burgos, 09001 Burgos, Spain
Revista:	Industrial & Engineering Chemistry Research
Factor impacto (IF): 3.8	**Cuartil (JRC):** Q2 **Citas:** 0
Editor: American Chemical Society	**Fecha de publicación:** 10/01/2025

I&EC research
Industrial & Engineering Chemistry Research

Open Access
This article is licensed under CC-BY 4.0

pubs.acs.org/IECR
Article

Properties and Intermolecular Forces of Ionic Liquid Mixtures: The Archetypical Case of [EMIM][BF_4] + [EMIM][$EtSO_4$]

Ylenia F. Rodríguez, Santiago Aparicio,* and Jose L. Trenzado*

Cite This: *Ind. Eng. Chem. Res.* 2025, 64, 1774−1791
Read Online

ACCESS | Metrics & More | Article Recommendations | Supporting Information

ABSTRACT: The properties and nanostructure of the Double Salt−Ionic Liquid formed by the combination of [1-ethyl-3-methylimidazolium][BF_4] and [1-ethyl-3-methylimidazolium][$EtSO_4$] in the whole composition range are studied by a combined experimental and molecular simulation approach. The measured physicochemical properties were analyzed in terms of deviations of ideality and its relationships with intermolecular forces. Quantum chemistry calculations of model clusters were carried out to infer nanoscopic aggregations, considering several mechanisms of interactions. Classical molecular dynamics simulations were carried out as a function of mixture composition, pressure, and temperature, allowing one to characterize structural, dynamic, and energetic properties of the considered mixed ionic liquids. The possible mechanisms of interaction of the involved molecules with biological targets, proteins, and model cell membranes were also computationally studied to infer molecular level roots of toxicological effects of mixtures of ionic liquids. This multiapproach−multiscale study provides for the first time a global characterization of mixtures of ionic liquids.

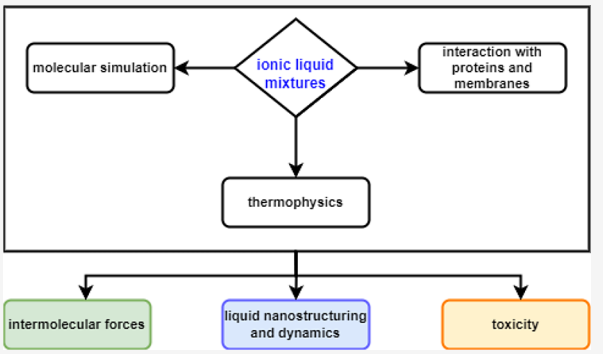

Downloaded via UNIV DE BURGOS on February 6, 2025 at 07:49:58 (UTC).
See https://pubs.acs.org/sharingguidelines for options on how to legitimately share published articles.

1. INTRODUCTION

Ionic liquids (ILs) have received special attention in recent decades, although they have been studied since the last century. The history of ILs started in 1914 when Walden prepared the first ionic liquid, ethylammonium nitrate (EAN),[1] which evolved when 40 years later, Hurley and Wier reported the second generation of ionic liquids by mixing alkylpyridinium chlorides with $AlCl_3$. Unfortunately, most of those initial ILs were not stable in the presence of humidity and it was not easy to regulate their acidity/basicity.[2] The evolution of IL research led to the last two decades, with the number of ILs published papers exponentially increasing from a few in 1996 to more than 5000 in 2016,[3] and the interest being maintained up to now with 6457 research documents containing the term ionic liquid indexed in the SCOPUS database. This maintained interest in IL properties, synthesis and technologies rises from all the proposed advantages ILs offer, in terms of their physicochemical properties, which indicate to be a future growing and continuing successful field.[4]

It should be mentioned that also certain criticism has been considered on the possible large-scale application of ILs, based on concerns about unsuitable physicochemical properties (e.g., large viscosity), toxicity, or poor biodegradation.[5−7] Nevertheless, many of these possible drawbacks may be avoided via the proper selection of suitable ions, leading to ILs among the plethora of possible compounds.

What makes Ionic liquids so particular is their exclusively composed ions structure, not like usual solvents composed of neutral molecules, and remaining in liquid state at room temperature. Combinations of cations and anions of different characteristics and sizes cause ionic liquids properties to vary in one direction or another, allowing adapting their properties to the needs required (*tailor-made solvents*). Physicochemical properties may be fine-tuned via regulation of the molecular structures of the involved ions, e.g. Dong et al. observed that the viscosity increases with increasing cation alkyl chain length (e.g., imidazolium and pyridinium)[4] Density is also another property strongly affected by ion characteristics, for example, it usually increases with anion molecular mass.[8] Their exceptional range of tunable properties is one of the key reasons behind the growing interest in ionic liquids, and the development and understanding of the structure−property relationship is fundamental to understanding IL behavior. The capacity to tune their properties made them a perfect tool, allowing the design of tailor-solvents for the required technologies and offering a replacement for traditional volatile organic compounds (VOCs).

There are multiple studies that broadly analyze the potential applications for ILs, including remarkable catalytic perform-

Received: July 31, 2024
Revised: October 16, 2024
Accepted: October 23, 2024
Published: January 10, 2025

© 2025 The Authors. Published by American Chemical Society

ance,[9] good behavior as gas adsorbents or extractant agents[10−12] and excellent lubricant properties.[13−15] In addition, researchers continue to explore the broad potential of ILs in new and unexplored fields. Khupse and Kumar studied ionic liquid utilization in electrochemical devices such as supercapacitors, lithium-ion batteries, or polymer-electrolyte fuel cells. Two main advantages of using ionic liquids include nonvolatility and prevention of electrolytes.[16] The concept of *IoNanofluids* was proposed by Nieto de Castro and co-workers; it represents a new class of heat transfer fluids where nanomaterials like particles, tubes, and rods are dispersed in ionic liquids. IoNanofluids are one of the most recent applications of complex systems of ionic liquids and nanomaterials, they could be used for heat transfer to catalysis, lubricants, or luminescent materials.[17] Due to the unique properties of ILs, their application in the pharmaceutical field has been extended in numerous processes, from drug synthesis to the development of new solubilization and dosage forms of active pharmaceutical ingredients (API-ILs), with research also being carried out at other stages of drug development and delivery. Research has shown that the proper selection of anion/cation combinations has a significant impact on the solubilization mechanism of poorly water-soluble APIs.[18]

The combination of more than two types of ions is known to possibly exhibit unexpected associations that yield nonideal properties. Double salt ionic liquids (DSILs) are thus defined as ionic liquids containing more than one cation or anion and presenting different physicochemical properties than their component single salts. Many properties of DSILs, such as solubility, are dependent on chemical associations between the ions, and altering the ionic ratios can induce different chemical interactions leading to new properties.[19] The combination of ions can induce preferential orientation of ionic species and noncovalent interaction. The advantage of using DSILs depends on a suitable anion−cation combination to accomplish more efficiently by designing task-specific IL mixtures. Although DSILs offer significant advantages over classical pure ILs, relevant studies are still scarce, and a systematic DSIL selection method is thus highly desirable.[20] Therefore, the aim of this work was to study the physicochemical properties, nanostructuring, and biological effects of DSILs formed by the combination of 1-ethyl-3-methylimidazolium cation coupled with bistriflimide and ethylsulfate ([EMIM][BF_4] and [EMIM][$EtSO_4$]), leading to IL binary mixtures containing a common cation (DSILs), as shown in Figure 1. All physicochemical properties were reported in the full composition range as a function of temperature. Microstructuring and characterization of intermolecular forces allow us to infer the mechanism of molecular interaction between [EMIM][BF_4] and [EMIM][$EtSO_4$] ILs and their binary constituent mixtures with $[EMIM]^+$ as a common cation. The selection of these ILs to be mixed was done considering that the available literature has shown minor deviations from ideality but the nanoscopic behavior of these systems has not been extensively studied, neither the evolution of excess and mixing properties nor in the changes in intermolecular forces upon mixing and the local composition effects. Likewise, the possible biological effects of the considered DSILs were in silico studied through the consideration of their interaction with target biomolecules as well as with model cell membranes. The main innovation of this work consists in the combination of thermophysical studies with molecular modeling, which can provide the necessary knowledge about the properties of the mixture considering a multiscale approach.[20]

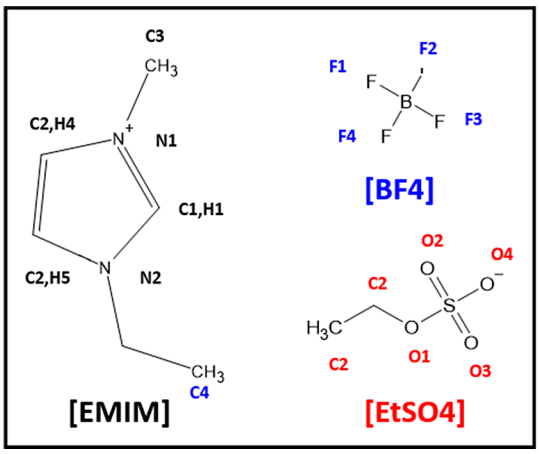

Figure 1. Ions forming ILs considered in this work as well as labeling for relevant atoms.

2. METHODS

2.1. Chemicals. The studied ionic liquids [EMIM][BF_4] and [EMIM][$EtSO_4$] used for the experimental study were supplied by a commercial provider (Sigma-Aldrich) and were used without additional purification, Table S1 (Supporting Information). Pure ILs were degassed by ultrasound and stored under suitable conditions. All the properties of pure ILs were measured as a function of temperature in the 283.15−313.15 K range, in 5 K steps at atmospheric pressure, and compared with literature (Table S2, Supporting Information), showing minor differences. The presence of relevant impurities was discarded, differences can be attributed to water content and different origins of the samples. The mixture samples (x [EMIM][BF_4]+ $(1 - x)$ [EMIM][$EtSO_4$], where x stands for mole fraction) were prepared in the full composition range by weighing (Mettler AE240 balance, ± 0.01 mg) to ±0.00004 estimated mole fraction uncertainty.

2.2. Apparatus and Procedures. Density (ρ) and kinematic viscosity (ν) were measured for x [EMIM][BF_4] + $(1 - x)$ [EMIM][$EtSO_4$] liquid mixtures, where x stands for mole fraction, in the full composition range, at atmospheric pressure and temperature in the 283.15−313.15 K range in 5 K steps. ρ was measured with a vibrating tube densimeter (Anton Paar DMA5000, uncertainty 1×10^{-4} g cm^{-3}), with Peltier control for the cell temperature (uncertainty 0.01 K). The thermal expansion coefficient, α_p, was calculated according to its thermodynamic definition:

$$\alpha_p = -\frac{1}{\rho}\left(\frac{\partial \rho}{\partial T}\right)_p = -\frac{1}{\rho}a \quad (1)$$

where a is the slope of the corresponding ρ vs temperature linear fit.

ν was measured using various Ubbelohde viscometers according to the required viscosity range, in an external circulating bath with a cell temperature measured with ±0.01 K uncertainty (CT-52, Schott Instruments) and an automatic control unit AVS350 (Schott, ViscoSystem) with ±0.01 s uncertainty. Dynamic viscosity (η) was calculated as in eq 2.

$$\eta = \nu\rho \quad (2)$$

The expanded uncertainties of the experimental properties (0.95 confidence level) are as follows: $Uc(T)$ = ± 0.01 K. $Uc(x)$ = ±

https://doi.org/10.1021/acs.iecr.4c02839
Ind. Eng. Chem. Res. 2025, 64, 1774−1791

0.00001. $Uc(\rho) = \pm 0.00001$ g cm^{-3}. $Uc(\nu) = \pm 0.01$ mm^2 s^{-1}; $Uc(\eta) = \pm 0.01$ mPa s.

The viscosity versus temperature evolution was described according to the Vogel−Fulcher−Taman (VFT) model:

$$\eta = \eta_0 \exp\left(\frac{B}{T - T_0}\right) \tag{3}$$

VFT fitting parameters were used for the calculation of Angell's strength (fragility measurement) parameter, D_f.

$$D_f = \frac{B}{T_0} \tag{4}$$

Experimental density data were considered for the calculation of excess molar volume, V^E:

$$V^E = \frac{\sum_{i=1}^{2} x_i M_i}{\rho} - \sum_{i=1}^{2} x_i \frac{M_i}{\rho_i} \tag{5}$$

where M_i is the molar mass of the component i, ρ_i and ρ the densities of the pure compound i and for the corresponding mixture, respectively. Likewise, the excess thermal expansion coefficient, α_p^E, was calculated as follows:

$$\alpha_p^E = \alpha_p - \sum_{i=1}^{2} \varphi_i \alpha_{p,i} \tag{6}$$

where α_p and $\alpha_{p,i}$ are the thermal expansion coefficients of the mixture and pure component i, respectively; φ_i stands for the volume fraction of component i, φ_i:

$$\varphi_i = \frac{x_i V_i^*}{\sum_{i=1}^{2} x_i V_i^*} \tag{7}$$

where x_i stands for the mole fraction of i component and V_i^* for the molar volume of pure i compound. For the case of viscosity, as the ideal state reference term cannot be defined and thus excess property could not be considered, the so-called mixing viscosity, $\Delta\eta$, was calculated:

$$\Delta\eta = \eta - \sum_{i=1}^{2} x_i \eta_i \tag{8}$$

Additionally, excess and mixing properties were fitted to an isothermal Redlich−Kister type polynomial equation as a function of mole fraction, x:

$$Y^E = x(1 - x) \sum_{i=0}^{n} A_i (1 - 2x)^i \tag{9}$$

Likewise, the partial molar volume $\overline{V}_i$ of each component i was calculated:

$$\overline{V}_i = V_m^E + V_i^* + (1 - x_i)\left(\frac{\partial V^E}{\partial x_i}\right)_{T,P} \tag{10}$$

where V_i^* stands for the molar volume of pure component i, with the partial derivative of the excess volume calculated from the corresponding Redlich−Kister coefficients. Excess partial molar volumes, $\overline{V}_i^E$, were defined as

$$\overline{V}_i^E = \overline{V}_i - V_i^* \tag{11}$$

The excess partial molar volumes at infinite dilution, $\overline{V}_i^{E,\infty}$ were calculated:

$$\overline{V}_i^{E,\infty} = \overline{V}_i^{\infty} - V_i^* \tag{12}$$

where the partial molar volume at infinite dilution, $\overline{V}_i^{\infty}$, is defined as the corresponding limiting value when $x_i \to 0$. All the relevant thermophysical properties and the corresponding fitting parameters are reported in Tables S3−S5 (Supporting Information).

Parameters for the modeling of excess volume according to the Prigogine−Flory−Patterson (PFP)[21] model are reported in Table S6 (Supporting Information).

2.3. Density Functional Theory Calculations. Intermolecular interactions between involved anions and cations were analyzed considering different ionic clusters (dimmers and tetramers), whose structures were optimized through density functional theory (DFT) calculations carried out with Dmol3[22] software. The main objective of DFT calculations is to analyze the nature of intermolecular forces in the considered IL mixtures, in particular, for the characteristics of hydrogen bonding. For that purpose, dimmers and higher aggregates were built, and their geometries were optimized through energy minimization. All the calculations were carried out at the GGA/PBE plus Grimme's D3[23] dispersion contribution theoretical level. The optimized geometries for the considered clusters were used for the calculation of the interaction energy, ΔE, as the difference between the energy of the corresponding cluster and the sum of the corresponding monomers. All the ΔE were corrected for the basis set superposition error (BSSE) using the counterpoise method.[24] Regarding the accuracy of calculated ΔE, it is estimated to be in the 8−13 kJ mol^{-1},[25] which is well beyond the large ΔE values for anion−cation interactions in ILs (roughly 1%).

The topological properties of the clusters were analyzed considering the quantum theory of atoms in molecule (Bader's QTAIM theory)[26] as in MultiWFN software,[27] considering electron density (ρ_e) and Laplacian of the electron density ($\nabla^2\rho_e$), of bond (BCPs, type (3,−1) in QTAIM) and Ring (RCPs, type (3,−1) in QTAIM) critical points. and electron localization function (ELF) using core−valence bifurcation index (CVB[28]) were also considered as well as Interaction Region Indicator (IRI) analysis.[27]

2.4. Classical Molecular Dynamics Simulations. Classical MD simulations were carried out using the MDynaMix v.5.2 program.[29] The force field parametrizations for the three types of ions considered in this work ($[EMIM]^+$,$[BF_4]^-$ and $[EtSO_4]^-$) (Table S7, Supporting Information) were obtained from SwissParam database (Merck Molecular Force Field[30]), except atomic charges which were computed from DFT calculations of ions using ChelpG method. Simulation boxes were built as indicated in Table S8 (Supporting Information) for covering the whole mixture composition range, as well as for different pressure and temperature conditions to analyze their effect on mixture properties. Initial cubic simulation boxes were prepared with the Packmol program.[31] All MD simulations were carried out according to a two-stage procedure: (i) NVT simulations at the considered conditions for 10 ns, followed by (ii) NPT simulations at the considered pressure and temperature conditions for 200 ns, which were used for the analysis of mixtures properties.

All MD simulations were performed by considering periodic boundary conditions along the three space directions. The equations of motion were solved considering the Tuckerman−Berne double-time step algorithm[32] with 1.0 and 0.1 fs for long and short-time steps. Electrostatic interactions were treated with

https://doi.org/10.1021/acs.iecr.4c02839
Ind. Eng. Chem. Res. 2025, 64, 1774−1791

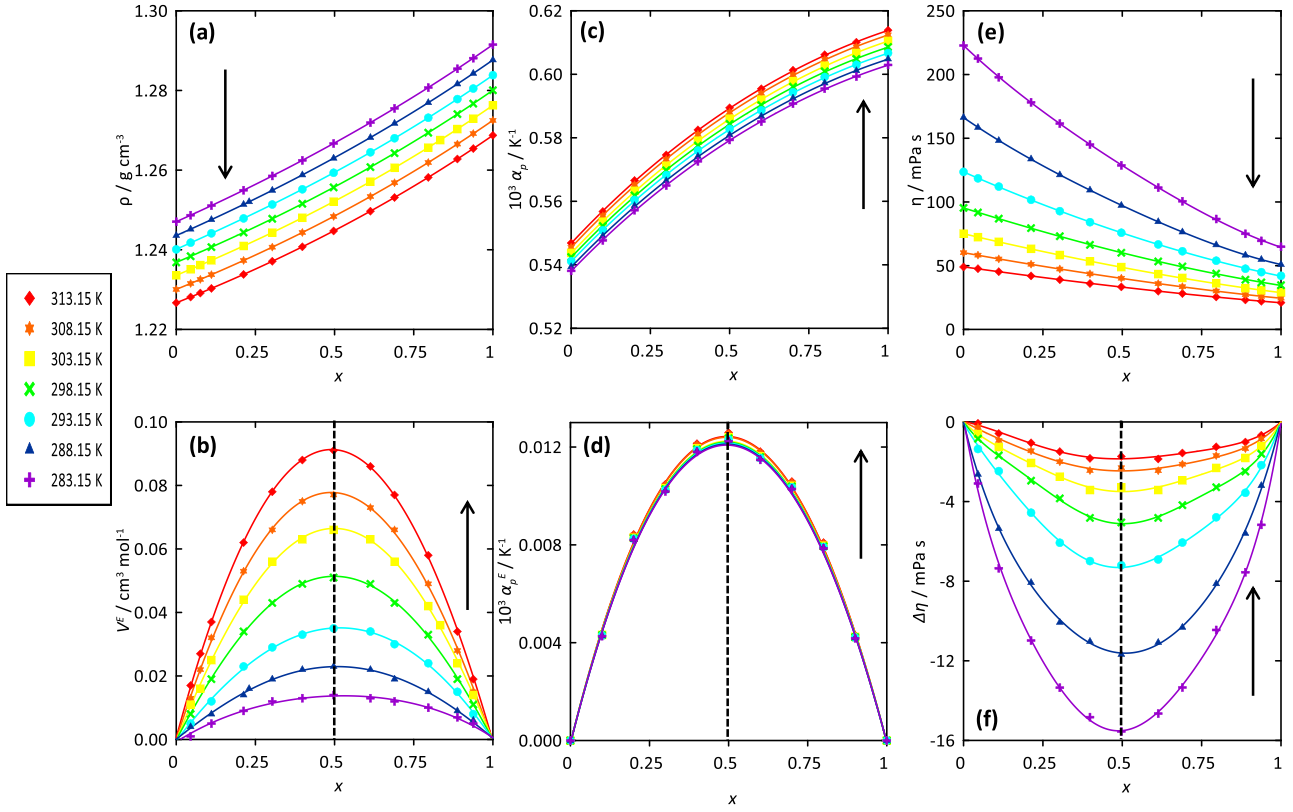

Figure 2. Experimental thermophysical properties for x [EMIM][BF4] + $(1 - x)$ [EMIM][EtSO4], where x stands for mole fraction, as a function of temperature. (a) Density (ρ), (b) excess molar volume (V^E), (c) isobaric thermal expansion coefficient (α_p), (d) excess isobaric thermal expansion coefficient (α_p^E), (e) dynamic viscosity (η), and (f) mixing viscosity ($\Delta\eta$). Black arrows indicate an increasing temperature for guiding purposes. Dashed lines in panels b,d and f show equimolar composition to show position of the maxima in the corresponding excess or mixing property.

the Ewald method[33] (15 Å for cutoff radius). Lennard−Jones potential was considered (15 Å cutoff distance) with Lorentz−Berthelot mixing rules for cross terms. Temperature and pressure were controlled with the Nose−Hoover method.[34] The visualization and analysis of MD trajectories were carried out with VMD[35] and TRAVIS.[36]

2.5. Coarse-Grained Classical Molecular Dynamics Simulations of Ionic Liquid−Lipid Bilayer Interactions. The possible biological negative effects of the considered IL mixture may be studied using the concept of adverse outcome pathways (AoPs), i.e. the sequence of events, from molecular to cellular to organ levels, which leads to a toxic effect of a substance on a living organism.[37] The series of complex processes leading to final toxicity is proposed to be initiated from a so-called molecular initiating event (MiE).[38] A particularly well-known MiE is the interaction of chemicals with plasma (cell) membranes.[39] For this purpose, the mechanism(s) of interaction of the considered IL mixtures with a model cell membrane, formed by a DPPC lipid bilayer, and the changes in the membrane properties in the presence of ILs in an aqueous solution were analyzed using Coarse Grained Molecular Dynamics (CG-MD) simulations. The reason to study the IL−lipid bilayers interactions using CG-MD simulations instead of All Atom simulations (as indicated in Section 2.4 for liquid phase properties) stands on the size of the considered systems (water + IL + lipid bilayer with a large number of atoms) as well as considering the time scale required to infer lipid bilayer changes; therefore, CG-MD provides a suitable solution to provide results at a reasonable computational cost.

CG-MD simulations were carried out considering IL mixtures in aqueous solutions at different concentrations (Table S9, Supporting Information). The beading of the ions, water, and DPPC molecules is explained in Figure S1 (Supporting Information). CG force field parametrization was done according to the Martini3 CG force field[40] (Figure S1, Supporting Information). The suitability of the Martini force field for describing ILs has been recently probed,[41] and thus, the CG-MD approach is a suitable option for describing the behavior of the considered IL mixtures at model plasma membranes. Water solutions in contact with DPPC bilayer for 17−20 wt % content of IL mixtures were considered, with these IL mixtures corresponding to x [EMIM][BF_4] + $(1 - x)$ [EMIM][$EtSO_4$] with 0, 0.25, 0.50, 0.75, and 1.00 mole fraction.

CG-MD simulations were carried out with the MESOCITE/Materials Studio software. Simulations were carried out in a three stages procedure: (i) energy minimization through geometry optimization using the conjugated gradient method, (ii) 1 ns NVT simulations at 318 K with the Velocity Scale method for temperature control, and (iii) 500 ns NPT simulations at 318 K (Nose thermostat) and 1 bar (Berendsen barostat); 1.0 ps was used for coupling constants of the thermostat and barostat along all the simulations, and a 20 fs time step was used for all the simulations. Electrostatics (i.e., Coulombic interactions) were handled with the Ewald method and van der Waals with a group (bead) based cutoff method, 15.0 Å cutoffs.

2.6. Interaction of the Ionic Liquid with Model Biomolecules. Additional studies on the possible negative biological effects of the considered IL mixtures were in silico

https://doi.org/10.1021/acs.iecr.4c02839
Ind. Eng. Chem. Res. 2025, 64, 1774−1791

conducted through the analysis of the interaction of the involved IL molecules with target biomolecules. For this purpose, four biomolecules were selected: 1BNA (B-DNA dodecamer), 1AO6 (human serum albumin), 1QZR (ATPase region of *Saccharomyces cerevisiae* topoisomerase), and (cyclooxygenase-2 (prostaglandin synthase-2). Docking calculations for IL molecular clusters corresponding to ten different arrangements inferred from results in Section 2.3 on the four selected biomolecules were carried out. The biomolecule structures were obtained from the Protein Databank and prepared using Autodock Tools with docking regions containing the whole biomolecules (i.e., not−guided docking). Docking studies were carried out using Autodock Vina[42] with the obtained docked structures being ranked through the corresponding affinities (scores).

3. RESULTS AND DISCUSSION

3.1. Macroscopic and Thermodynamic Characterization. Density and kinematic viscosity values for pure ILs [EMIM][BF4] and [EMIM][EtSO4] and their binary mixtures in the full composition range have been experimentally measured in the 283.15−313.15 K range. These properties, as well as the derived ones, are reported in Figure 2. For the analysis of density data reported in Figure 2a, it should be initially remarked that although both pure ILs are largely dense fluids, [EMIM][BF4] is denser than [EMIM][EtSO4], 3.5% denser on average in the considered temperature range. The usual trend on the density for ILs showing a common cation (in this case [EMIM]) is the increase of density with the molar mass of the anion,[8] but an opposite behavior is inferred for [BF4] and [EtSO4], in which the lightest anion ([BF4], M = 86.80 g mol^{-1}) is denser than the heaviest one ([EtSO4], M = 125.12 g mol^{-1}), and thus, further effects need to be considered. Considering the relevance of anion−cation interactions on the ILs properties, the structures of [EMIM][BF4] 1:1 and [EMIM][EtSO4] 1:1 dimer clusters were optimized using DFT and their properties, analyzed to infer relationships with fluids' density. The volume of the optimized dimers, in which cations and anions are hydrogen-bonded, was calculated and from that, an estimation of the density was inferred via the ratio of this volume and the dimer molar mass of the cluster, which, although neglecting additional effects present in the liquid phase, provide a rough estimation of fluids density. The inferred densities are 1.12 and 1.08 g cm^{-3}, for [EMIM][BF4] and [EMIM][EtSO4], respectively, although being roughly 13% lower than the experimental values reported in Figure 2a, confirm that [BF4]−containing IL is roughly 3.5% denser than IL containing [EtSO4], and it shows the pivotal role of the nature of the developed [EMIM]−anion hydrogen-bonded cluster on the properties of the bulk fluid. The evolution of density with mixture composition as reported in Figure 2a is slightly nonlinear, which leads to positive V^E, i.e. expansion upon mixing, although V^E are not too large and decrease upon heating, thus indicating low deviations from ideality. The low values for excess properties have been previously reported for different types of ILs.[43−45] Chakraborty et al.[45] proposed that [alkylimidazolium]−based IL mixtures with a common cation usually showed positive V^E because of the excess molar volume for imidazolium-based IL−IL mixtures may be linked to the free volume created by the alkyl chain, although negative V^E has also been reported for [alkylimidazolium]−containing mixtures.[42] The results obtained in this work for [EMIM][BF4]−[EMIM]-[EtSO4] mixtures may be compared with those from Navia et al.[43] for [1-butyl-3-methylimidazolium][BF4] ([BMIM][BF4]) - [1-butyl-3-methylimidazolium][methylsulfate] ([BMIM]-[MeSO4]). In the case of [BMIM][BF4]−[BMIM][MeSO4] with a minima for V^E of roughly -0.06 cm^3 mol^{-1} at equimolar mixture composition and 303 K in contrast with a maxima of 0.065 cm^3 mol^{-1} for [EMIM][BF4]−[EMIM][EtSO4]. This behavior confirms the role of the size of cation alkyl chains on the development of free space to fit cations; in the case of [BMIM] larger free space is produced than for [EMIM], which allows the proper fitting of the smaller [MeSO4] anions in comparison with the larger [EtSO4] ones. Nevertheless, in both cases deviations from ideality are very low (positive or negative), thus pointing to an effect of free space rearrangement upon mixing with negligible disruption in the established intermolecular forces.

The calculated α_p values are reported in Figure 2c. Pure [EMIM][BF4] is more compressible than [EMIM][EtSO4], in agreement with the literature.[46,47] The α_p evolution with mixture composition shows a nonlinear behavior, which leads (Figure 2d) to positive α_p^E (i.e., more compressible fluids upon mixing) with maxima at equimolar composition and almost negligible effect of the temperature. Nevertheless, the reported positive α_p^E values are very low (roughly 0.012 × 10^{-3} K^{-1}), thus leading to almost ideal mixtures considering this property and pointing again to very minor restructuring effects rising from the available free space as the main effect upon mixing in terms of compressibility.

The dynamic properties of the considered IL mixtures were macroscopically analyzed through the dynamic viscosity (Figure 2e). First, it should be remarked that pure [EMIM][EtSO4] is roughly three times more viscous than [EMIM][BF4]. The viscosity evolution with temperature for both pure ILs as well as for the studied mixtures cannot be described according to an Arrhenius model, and thus VFT fitting was considered for all the systems. The calculated VFT parameters allowed us to infer the D_f (fragility) parameter. The D_f values for pure ILs are 3.19 and 3.04 for [EMIM][EtSO4] and [EMIM][BF4], respectively, and thus, although [EMIM][EtSO4] is more fragile, both fluids may be considered fragile ones. In spite of the small differences in the pure fluids' fragility, the large differences between the viscosities of both ILs lead to a nonlinear evolution of viscosity upon mixing and, thus, to negative non-negligible $\Delta\eta$ (Figure 2f). The negative $\Delta\eta$ are usually assigned to factors such as fewer surfaces available for friction,[48] or mainly to the weakening of intermolecular forces between molecules.[49] The case of negative non-negligible $\Delta\eta$ for [EMIM][BF4]−[EMIM][EtSO4] does not seem to be produced from large variations of intermolecular forces, as discarded from the very low excess properties reported in Figure 2b,d. Although $\Delta\eta$ is not an excess property, in the thermodynamic sense (ideal state is not possible to define), the decrease in viscosity upon mixing should rely on the rearrangement of molecular clusters upon mixing. It has been reported that large negative $\Delta\eta$ is obtained when mixing ILs with dissimilar structures,[50] which is confirmed for [BF4] and [EtSO4] anions. This is also inferred from the large differences between the viscosities of pure ILs ([EtSO4] > [BF4]), which may be also related to the differences among the intermolecular forces in each pure IL. This effect is confirmed by literature results showing the large cation effect,[49] for [EMIM][NTf2]−[EMIM][EtSO4] showed very small $\Delta\eta$ (<4 mPa s) in contrast with [EMIM][NTf2]−[BMIM][EtSO4] ($\Delta\eta$ maximum of 60 mPa s). In the case of [EMIM][BF4]−[EMIM][EtSO4] the anion type effect rises from the type of anion−cation

https://doi.org/10.1021/acs.iecr.4c02839
Ind. Eng. Chem. Res. 2025, 64, 1774−1791

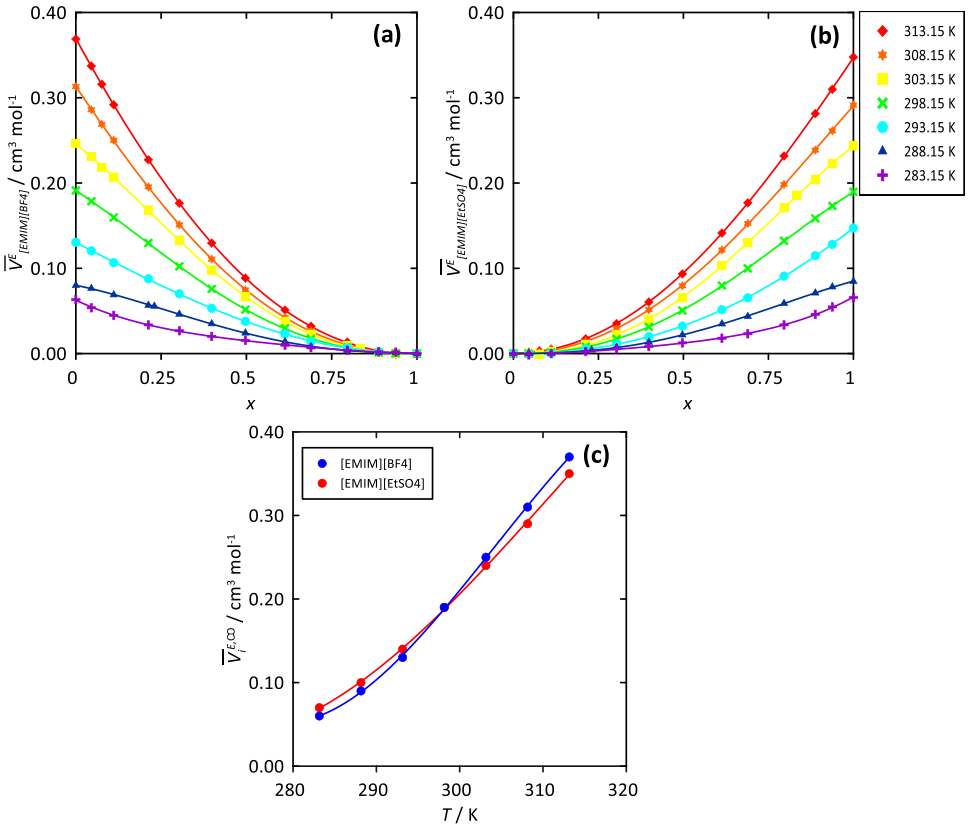

Figure 3. (a, b) Excess partial molar volume of component i, $\overline{V}_i^{E}$, and (c) values at infinite dilution, $\overline{V}_i^{E,\infty}$, for x [EMIM][BF4] + $(1 - x)$ [EMIM][EtSO4], where stands for mole fraction, as a function of temperature. Black arrows indicate increasing temperature for guiding purposes. Panels a and b show the results for [EMIM][BF_4] and [EMIM][TFSI], respectively.

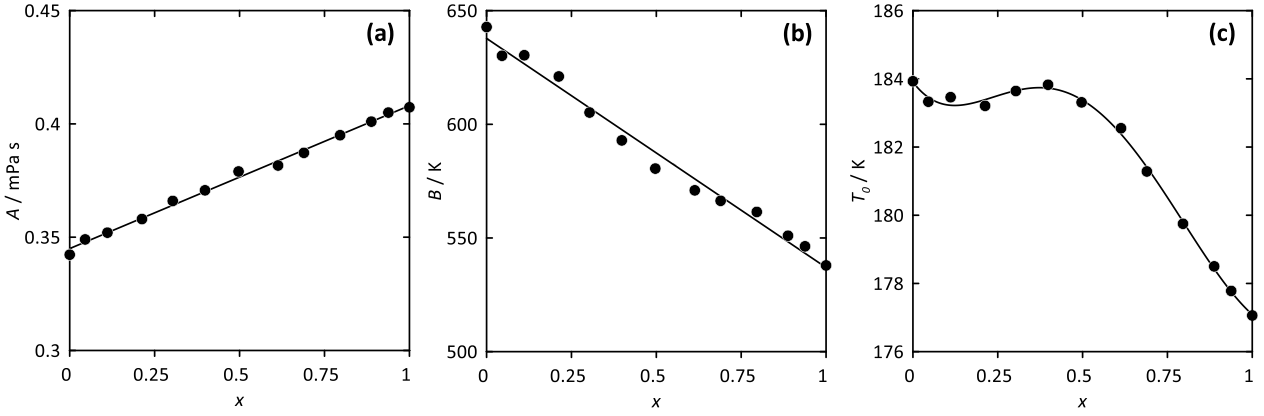

Figure 4. Fitting parameters of VFT equation for experimental dynamic viscosity of x [EMIM][BF4] + $(1 - x)$ [EMIM][EtSO4], where stands for mole fraction, in the 283.15−313.15 K temperature range.

intermolecular forces (hydrogen bonding), being C(H)−F (for [BF4]) in contrast with C(H)−O (for [EtSO4]), and thus, although the effect of anion on viscosity is less remarkable than the cation one, it is the main reason for the negative $\Delta\eta$. Nevertheless, large changes in intermolecular forces are not produced but the differences in those upon mixing should be noted.

Further analysis of the mixed IL structuring is carried out by considering the excess partial molar volumes reported in Figure 3a,b for each IL mixture component. The reported $\overline{V}_i^{E}$, and the values at infinite dilution, $\overline{V}_i^{E,\infty}$, Figure 3c, show symmetric behavior for both mixture components, i.e., minor disruption of each IL structuring upon mixing, leading to low positive $\overline{V}_i^{E}$ in agreement with the low V^E values (Figure 2b). The low and positive $\overline{V}_i^{E,\infty}$ values indicate a proper fitting of each type of IL into the structure of the second one with almost negligible disruption. These results confirm that the mixing is produced by the fitting of each IL into the other one structuring with negligible disruptions of intermolecular forces, thus resulting in small excess properties.

The behavior of $\overline{V}_i^{E}$ is very symmetric for both components, with similar positive values in the whole composition range and increasing with temperature. These values of the excess partial molar volumes confirm the strength of intermolecular forces. Likewise, the large values of $\overline{V}_i^{E,\infty}$ show the disrupting effect of

https://doi.org/10.1021/acs.iecr.4c02839
Ind. Eng. Chem. Res. 2025, 64, 1774−1791

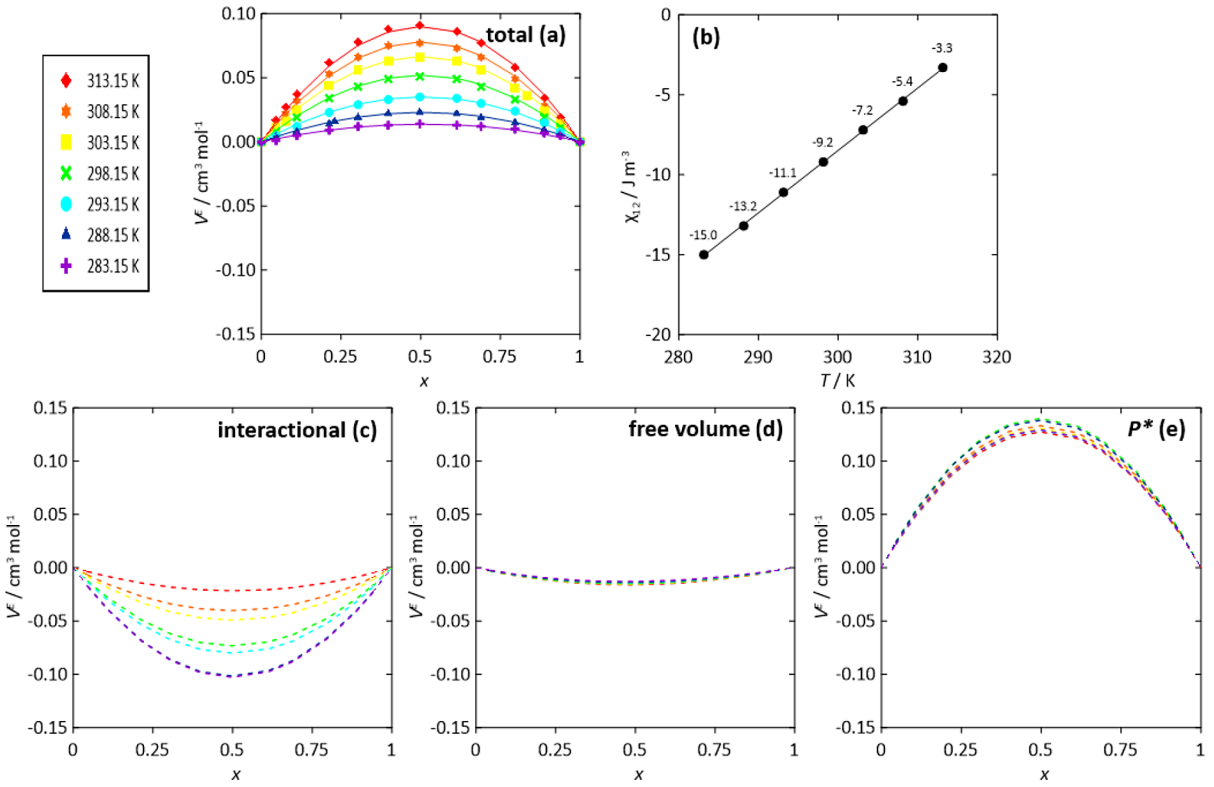

Figure 5. (a) Comparison of experimental, symbols, and PFP (lines) excess molar volume, V^E, with the PFP interaction coefficient, χ_{12}, reported in (b) x [EMIM][BF4] + $(1-x)$ [EMIM][EtSO4], where stands for mole fraction, as a function of temperature. Results in panels c-e show interactional, free volume, and P^* PFP contributions to the total V^E.

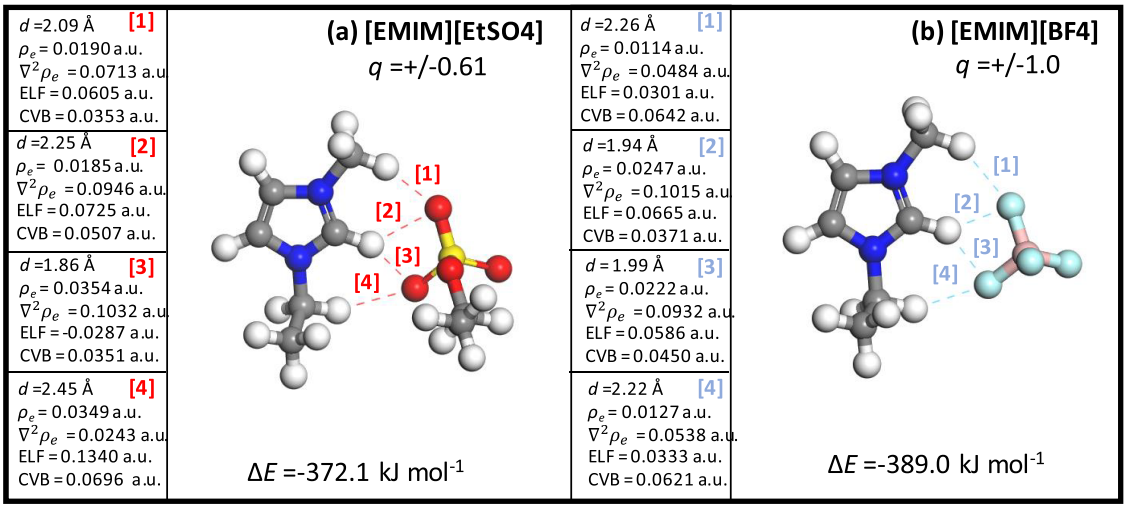

Figure 6. DFT optimized structures of [EMIM]−[EtSO4] and [EMIM]−[BF4] 1:1 clusters showing the lowest energy configurations including binding energy, ΔE, QTAIM properties (electronic density, ρ_e, and Laplacian of electron density, $\nabla^2\rho_e$), electron localization function (ELF), core valence bifurcation index (CVB), all these properties reported at the bond critical point (BCP) and region corresponding to the reported hydrogen bonds (dashed lines). Total cation and anion (ChelpG) charges are also reported, q.

one type of anion on the structuring of the other, thus leading to new intermolecular interactions upon anion replacements.

The small changes in intermolecular forces upon mixing are confirmed by the mixture composition evolution of the calculated VFT parameters. The VFT A and B parameters (Figure 4a,b) follow a linear trend with mixture mole fraction, and the T_0 parameter (Figure 4c), which is related to the glass transition temperature, evolves through a nonlinear relationship, remaining constant from neat [EMIM][EtSO4] to almost equimolar mixtures. Nevertheless, it should be remarked that the difference between the T_0 of both pure ILs is just 7 K. Therefore, these VFT parameters indicate that the changes in intermolecular forces arise just from the dilution of each type of IL in the second one upon concentration changes, without large changes in the nature of each cation−anion interaction.

Further details on the intermolecular forces in the considered IL mixtures may be inferred from the information obtained from the PFP[21] modeling of V^E (Figure 5), which allows to

https://doi.org/10.1021/acs.iecr.4c02839
Ind. Eng. Chem. Res. 2025, 64, 1774−1791

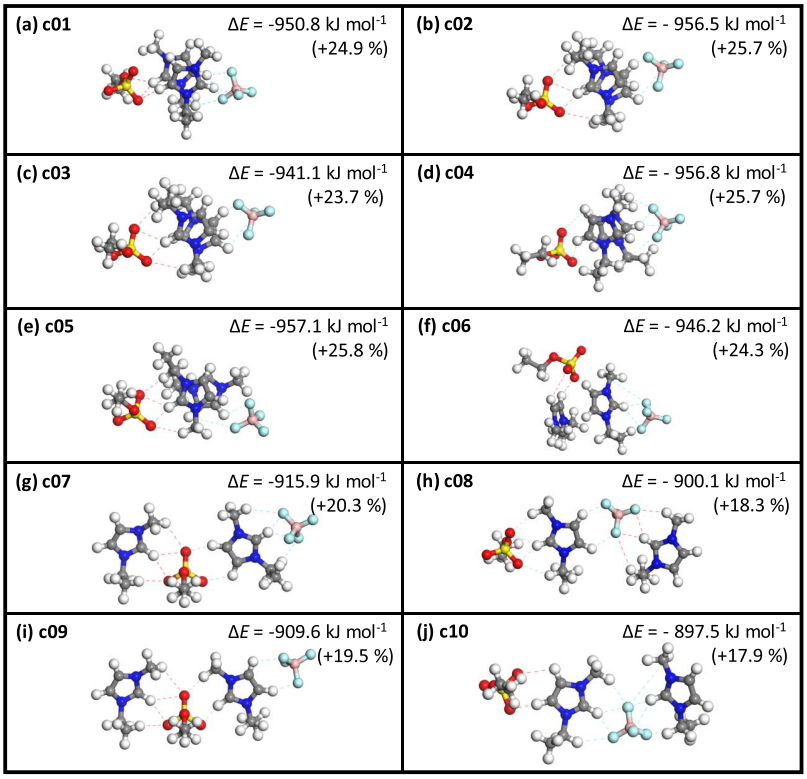

Figure 7. DFT optimized structures and binding energy, ΔE, for (1) [EMIM] − (1) [EtSO4] + (1) [EMIM] − (1) [BF4] clusters, considering different molecular orientations. Parenthesized percentage values indicate the difference between the binding energy per cluster and the sum of each dimer from the results in Figure 6.

connection of the macro and microscopic information. Results in Figure 5A show that the PFP model is able to describe V^E with a single fitting parameter, χ_{12} (Figure 5b). The small values for χ_{12}, linearly decreasing with temperature, show again the minor changes in intermolecular forces upon mixing.[51,52] The PFP analysis of V^E allows us to infer three contributions: interactional, free volume, and P^* contributions. It is remarkable that free volume contribution is almost negligible, with the interaction being negative and P^* being positive and slightly larger leading to the minor positive V^E. Therefore, the newly developed intermolecular forces developed upon mixing (negative χ_{12}, Figure 5b) are produced in minor extension (small negative interactional contribution, Figure 5c) and are mostly balanced by the positive P^* contributions paired with almost negligible free volume contribution (Figure 5d). The P^* contribution stands on the differences in internal pressures and reduced volumes of the components upon mixing,[53] this positive effect reported in Figure 5e confirms that changes upon mixing rise in the reorganization of molecules with the minor extension of new interactions (Figure 5b,c).

3.2. On the Nature of Hydrogen Bonding. Experimental thermophysical properties reported in the previous section allowed us to characterize the macroscopic behavior from the thermodynamic viewpoint and also infer pivotal features of the fluids' nanoscopic properties. Further analysis of the nature of the mixed fluids was carried out through the consideration of intermolecular forces (hydrogen bonding) via DFT calculations, considering model molecular clusters for neat ILs and mixed ILs. In the first stage, dimers formed by [EMIM]: [EtSO4] and [EMIM]: [BF4] in 1:1 combinations were considered, with their main properties reported in Figure 6. Although the dimer model is a limited representation of ILs, it provides relevant information on the short-range cation−anion interactions mainly via neat Coulombic and hydrogen bonding. The ΔE values reported in Figure 6 indicate strong cation−anion interactions for both anions, with a very minor effect on the type of anion. The similar strength of interaction with [EMIM] both for [EtSO4] and [BF4] would be on the root of the minor changes in ideality, as reported in the previous section, i.e., the binary mixed IL in which the concentration of one type of anion decreases whereas the concentration for the other one increase does not lead to remarkable changes in the anion−cation interaction energy, thus, minor changes in energy-related properties of the fluid as a function of composition. The main anion-[EMIM] interaction is developed via hydrogen bonding through the C(1) site in the imidazolium ring (the −CH site between the two N atoms) but also the anions are able to interact with the hydrogen atoms in the neighbor alkyl sites, thus leading to very strong anion−cation interactions through the four interacting sites, Figure 6. Regarding the Coulombic interaction, results for [EMIM]−[EtSO4] show lower ionic charges than for [EMIM]−[BF4], i.e., stronger Coulombic interactions for the spherical [BF4] anion. This also leads to slightly shorter hydrogen bonds with the cation for [BF4], interactions [2] and [3] in Figure 6.

The QTAIM analysis of cation−anion interactions via ρ_e and $\nabla^2\rho_e$ for the type (3,−1) BCPs developed in the hydrogen bonding paths ([2] and [3] interactions in Figure 6) and for the interaction with the alkyl groups ([1] and [4] in Figure 6). It should be remarked that 0.002 au < ρ_e < 0.04 au and 0.02 au < $\nabla^2\rho_e$ < 0.139 au ranges correspond to interactions that can be classified as shared-based interactions or H-bond established between the attraction sites, with larger values indicating stronger interactions.[54] The ρ_e and $\nabla^2\rho_e$ for H-bond interactions

https://doi.org/10.1021/acs.iecr.4c02839
Ind. Eng. Chem. Res. 2025, 64, 1774−1791

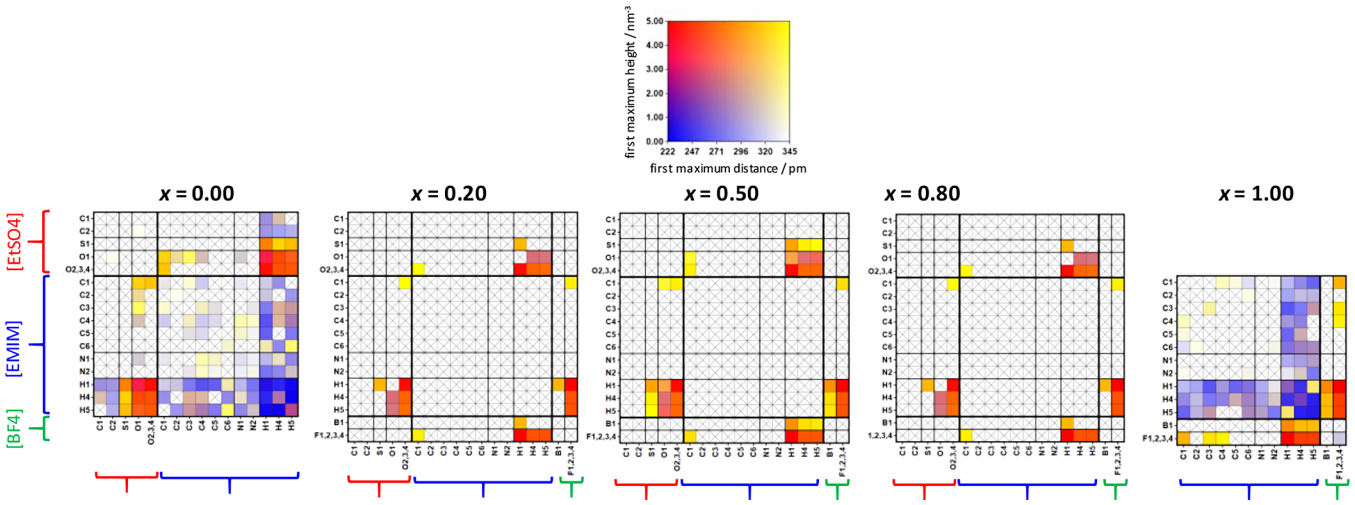

Figure 8. Connection matrix analysis of interactions in x [EMIM][BF4] + $(1 - x)$ [EMIM][EtSO4] mixtures, where et is for mole fraction, from MD simulations at 303 K and 1 bar. Atom labeling as in Figure 1.

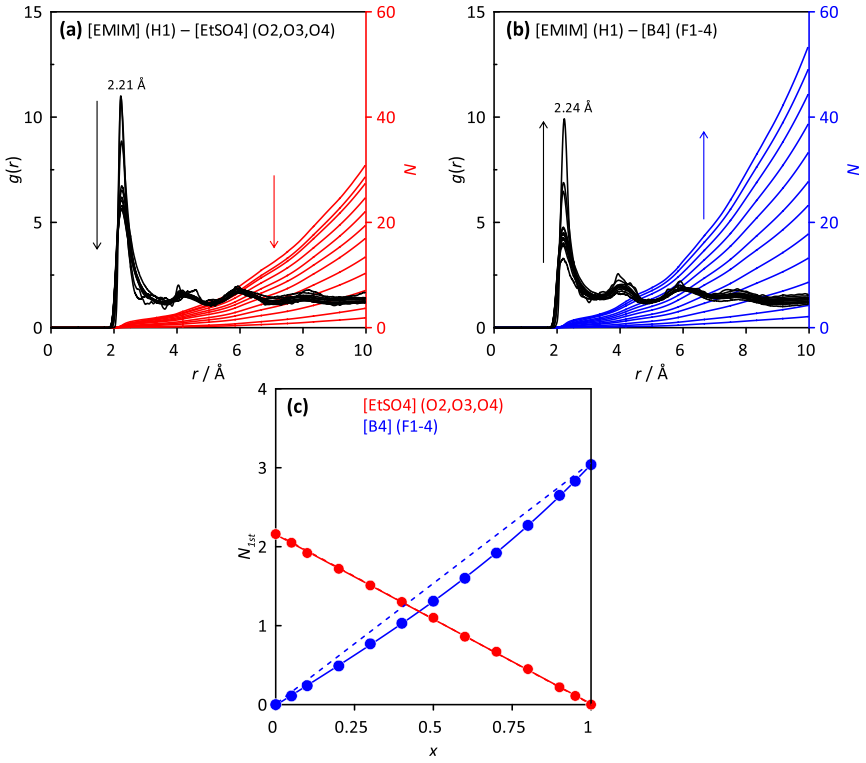

Figure 9. (a, b) Center-of-mass radial distribution function, $g(r)$, and the corresponding solvation number, N, in x [EMIM][BF4] + $(1 - x)$ [EMIM][EtSO4] mixtures, where m stands for mole fraction, from MD simulations at 303 K and 1 bar. Arrows indicate increasing mole fraction for the compositions reported in Table S8 (Supporting Information). (c) N values for the radial distribution function first peak ($r < 3.60$ Å). In panel c, dashed lines indicate linear behavior for comparison purposes. Atom labeling as in Figure 1.

([2] and [3] in Figure 3) indicate the formation of strong interactions for both anions and the presence of two simultaneous interactions on the C(1) [EMIM] site contributes to large anion−cation interactions. Likewise, anion−cation interactions through the alkyl sites in [EMIM] ([1] and [4]) although weaker than those through C(1) are also strong, thus contributing to the stabilization of cation−anion pairs. The strength of anion−cation intermolecular interactions is also quantified via CVB and ELF, which indicate moderately strong interactions.

Beyond the minimal anion−cation dimers considered as initial models of isolated clusters, the effect of mixing in the considered H-bonding was analyzed via DFT considering tetramers formed by the association of dimers reported in Figure 6 considering different mechanisms of interaction, i.e., spatial arrangements with particular orientations. These tetramers, resembling equimolar [EMIM][EtSO4] + [EMIM]-[BF4] clusters, were considered in ten different orientations, the optimized structures of which are reported in Figure 7. For all the cases, large ΔE values are inferred in all the cases, with the values for the tetramer being larger than the addition of those for

https://doi.org/10.1021/acs.iecr.4c02839
Ind. Eng. Chem. Res. 2025, 64, 1774−1791

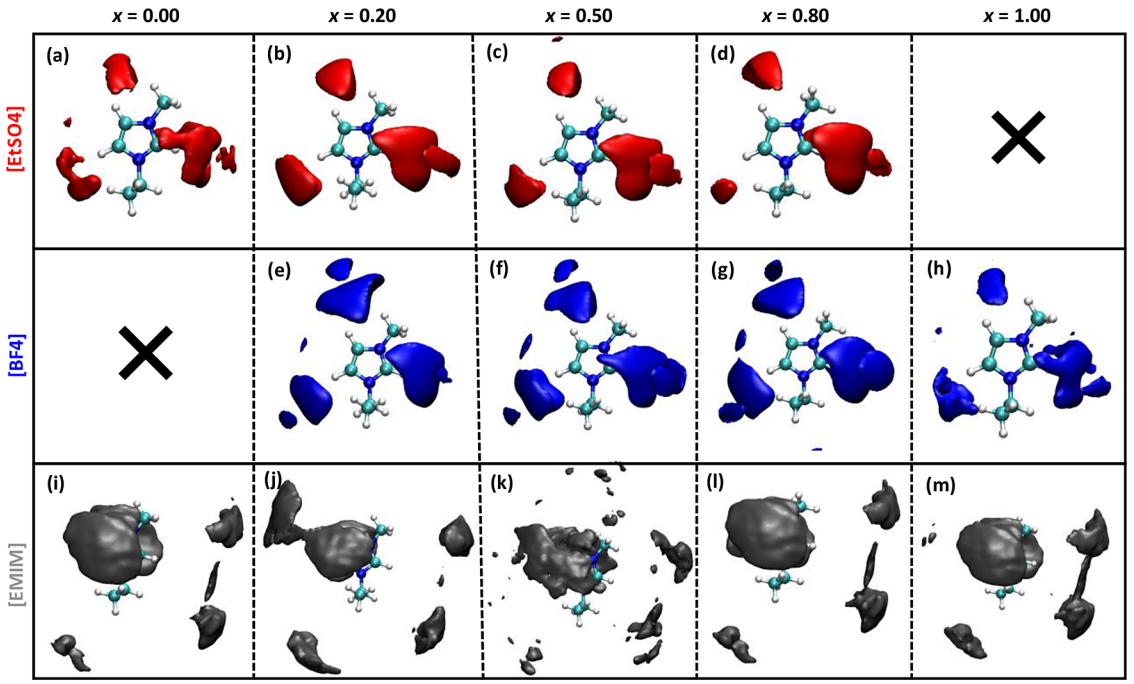

Figure 10. Spatial Distribution Functions around central [EMIM] cation for the reported molecules: [EtSO4] (O2−4 atoms), [BF4] (F1−4 atoms) and [EMIM] (C1 atoms) in x [EMIM][BF4] + (1 − x) [EMIM][EtSO4] mixtures, where stands for mole fraction, from MD simulations at 303 K and 1 bar.

the dimers, i.e. new intermolecular forces are formed upon tetramer formation leading to increases in ΔE values in the range of 18−26%. Therefore, the formation of larger clusters of the replacement of a type of anion for another one in the neighbor cluster does not lead either to a disrupting effect or to a decrease in the cluster (H-bonding) stability but, on the contrary, to additional stabilization. Likewise, the ten different orientations reported in Figure 7 show ΔE with minor differences between them (∼58 kJ mol^{-1}), thus confirming a large versatility of the arrangements between neighbor ionic pairs leading to stable configurations, which would be on the roots of the thermodynamics macroscopic behavior.

3.3. Nanoscopic Characterization of Mixed Liquid Phases. The model clusters reported in the previous section provide information on the nature of H-bonding in the considered systems, but liquid structuring is also characterized by additional effects like long-range interactions, molecular packing, and dynamic evolution, which require considering larger model systems being studied using MD simulations. The suitability of the considered force field used for MD simulations is analyzed via the comparison of (relevant) experimental properties (density and dynamic viscosity; Figure S1, Supporting Information). The MD-predicted density and viscosity data are lower than the experimental ones, but the deviations for density (1.2% on average) and viscosity (19.1% on average) are reasonable considering the purely predictive nature of the MD approach. Likewise, the evolution of density and viscosity with mixture composition is in reasonable agreement with experimental behavior, and thus, the considered MD approach may be considered as a suitable representation of the considered mixed fluid properties and structuring.

The first analysis of the studied IL mixtures was carried out considering structuring. The possible donor−acceptor sites were analyzed via Radial Distribution Functions (RDFs), which were systematically arranged considering the so-called connection matrix (*cmat*), in which RDFs for relevant interacting pairs are calculated, the first RDF peak being calculated in terms of its distance and intensity and assigned a color code, thus inferring the most relevant intermolecular interactions, Figure 8. The reported *cmat* results discard [EMIM]−[EMIM] self-association and confirm cation−anion interaction. The cation−anion interaction is mainly developed (red spots in Figure 8) through the cation C(1) sites, whereas interactions through the [EMIM] C(2) sites (opposite sites in imidazolium ring) also being present are produced in lower extension (orange spots in Figure 8). This pattern of interaction is maintained in the whole composition range, and when both anions are present in the mixture they provide the same mechanism of interaction being a combination of those of neat ILs, thus proving that the model clusters considered for DFT studies (Figure 7) are representative of the mechanism of interaction and that the liquid mixture structure is mainly characterized by a continuous replacement of one type of anion by the other one, without large disruptions of the liquid phase structuring and thus leading to minor deviations of thermodynamic ideality.

Particular details of the cation−anion interactions via the main interaction site C(1) in the imidazolium ring are reported in Figure 9 considering RDFs. The RDFs are almost equivalent for both types of anions (Figure 9a,b) following a first very intense RDF peak corresponding to H-bonding followed by weak peaks at larger distances, i.e., cluster models in Figures 6 and 7 represent the mechanism of H-bonding. The maximum of the first RDF peak appears at the same distance for both anions and their intensity changes upon changing anion concentration without changes in the position, i.e., indicating again an anionic replacement mechanism. The integration of the first peak of RDFs leads to the number of anions around the [EMIM], N_{first}, which are plotted as a function of mixture composition in Figure 9c. In the case of [EtSO4], N_{first} evolves in a linear way with composition, and for the case of [BF4] N_{first} evolves in a

https://doi.org/10.1021/acs.iecr.4c02839
Ind. Eng. Chem. Res. 2025, 64, 1774−1791

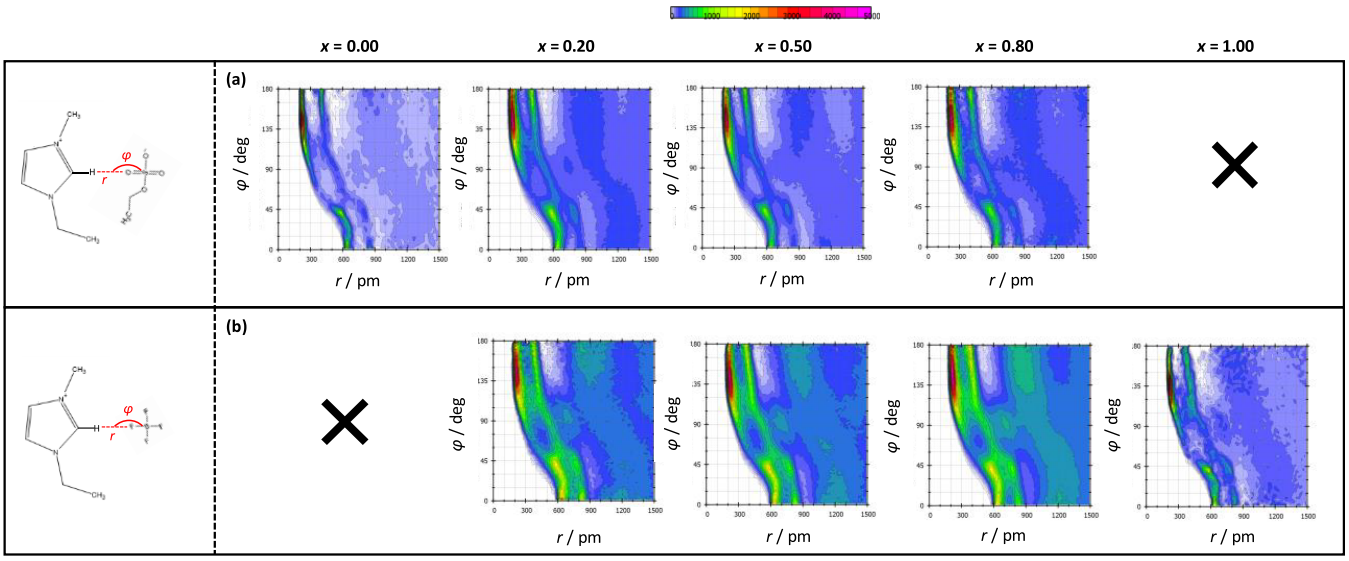

Figure 11. Combined Distribution Functions for the distance and angles between relevant sites in x [EMIM][BF4] + $(1 - x)$ [EMIM][EtSO4] mixtures, where the asterisk stands for mole fraction, from MD simulations at 303 K and 1 bar.

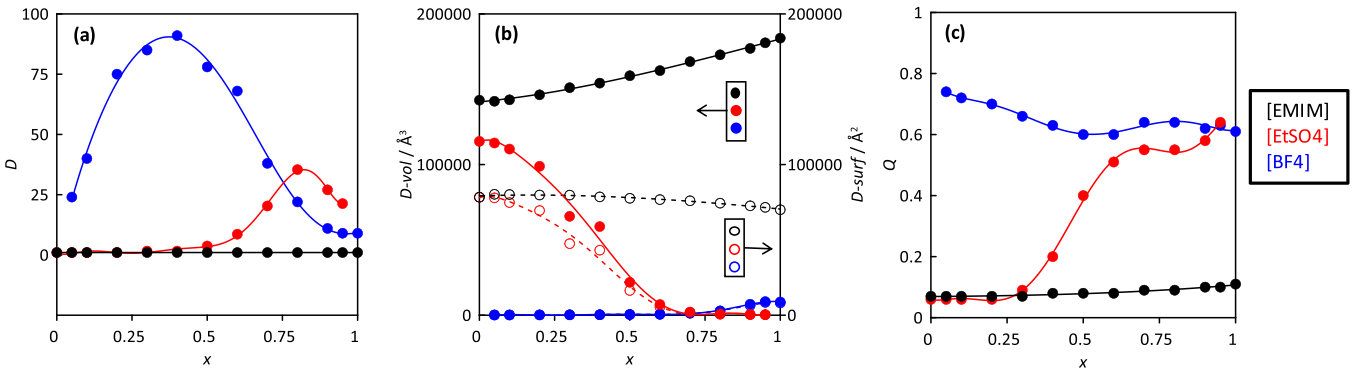

Figure 12. Domain analysis in x [EMIM][BF4] + $(1 - x)$ [EMIM][EtSO4] mixtures, where "Mole fraction" stands for, from MD simulations at 303 K and 1 bar. Number of domains, *D*, average domain area, *D-surf*, volume, *D-vol*, and isoperimetric index, *Q*, are reported. Atom labeling as in Figure 1.

nonlinear way with a lower number of [BF4] anions than expected from composition; this deviation is not too large and confirms the replacement of one type of anion by the other one around the cation upon mixing in a ratio corresponding to the mixture composition.

The distribution of anions around the [EMIM] cation is analyzed via spatial distribution functions (SDFs), Figure 10. SDFs indicate that both anions are mainly placed around the C(1) site of [EMIM] and non-negligible distributions are also produced around the C(2) sites, corresponding to the interaction between neighbor anion−cation clusters. It is remarkable that both anions show an analogous distribution around the cation, which is maintained throughout the whole composition range. Likewise, the interaction between neighbor [EMIM] cations is characterized by a distribution on top of the imidazolium ring, in this way allowing anion−cation effective interactions as well as ring−ring interactions between neighbor [EMIM] cations leading to additional stabilization factors in terms of van der Waals interactions as well as to more effective molecular packing, and thus densification.

The geometrical nature of the developed H-bonds is analyzed via the combined distribution functions (CDFs) considering interatomic separation and angle between relevant sites (around C(1) in [EMIM]), Figure 11. It is remarkable that the hydrogen bonding is confirmed considering a geometrical criterion (red spot in Figure 11) and exactly the same pattern for CDFs is inferred for the considering anions and the whole concentration range, i.e. almost negligible effect of mixture composition is inferred in the hydrogen bonding and interionic orientation.

Beyond the anion−cation intermolecular forces, analysis of the liquid phase properties is carried out considering long-range molecular distribution and clustering on the considered mixtures through the domain analysis reported in Figure 12. Although negligible changes upon mixing are inferred from the analysis of intermolecular forces previously discussed, results for domains reported in Figure 12 show subtle changes. In the case of [EMIM] domains, the domain count shows a single domain along the whole fluid, indicating a large interconnection between cations in agreement with the spatial distribution reported in Figure 10i−m, which showed cation to cation (top on top) orientation. The size of this [EMIM] domain increases with [BF4] content, which corresponds to an increase in density on going from [EtSO4] to [BF4] (Table S1, Supporting Information). Regarding anion domains, results for [EtSO4] show a lower number of domains than for [BF4] in the [EtSO4]−rich region (low x) and vice versa for the [BF4] rich region. Nevertheless, the size of [EtSO4] domains is mostly lower than those for [BF4], mainly because of the large anion

https://doi.org/10.1021/acs.iecr.4c02839
Ind. Eng. Chem. Res. 2025, 64, 1774−1791

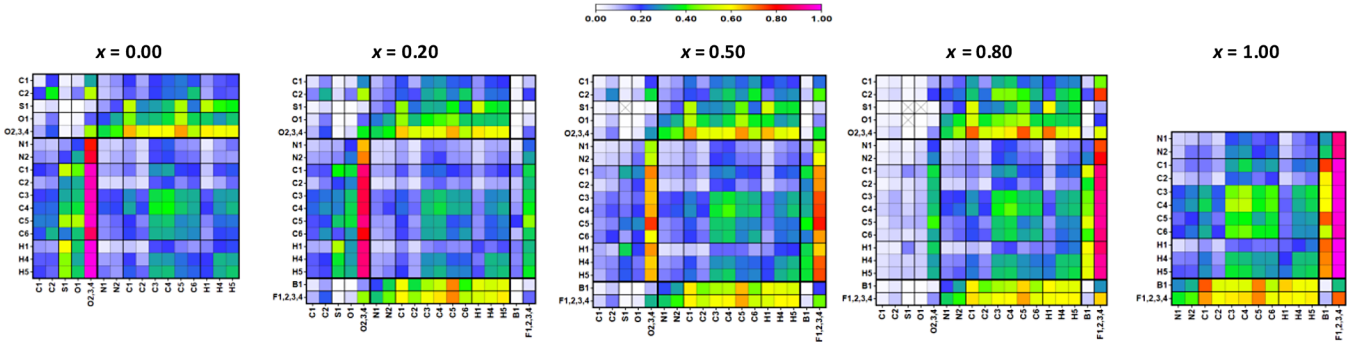

Figure 13. Neighbor probability matrix from Voronoi analysis in x [EMIM][BF4] + $(1 - x)$ [EMIM][EtSO4] mixtures, where the letter "Et" stands for mole fraction, from MD simulations at 303 K and 1 bar. Atom labeling as in Figure 1.

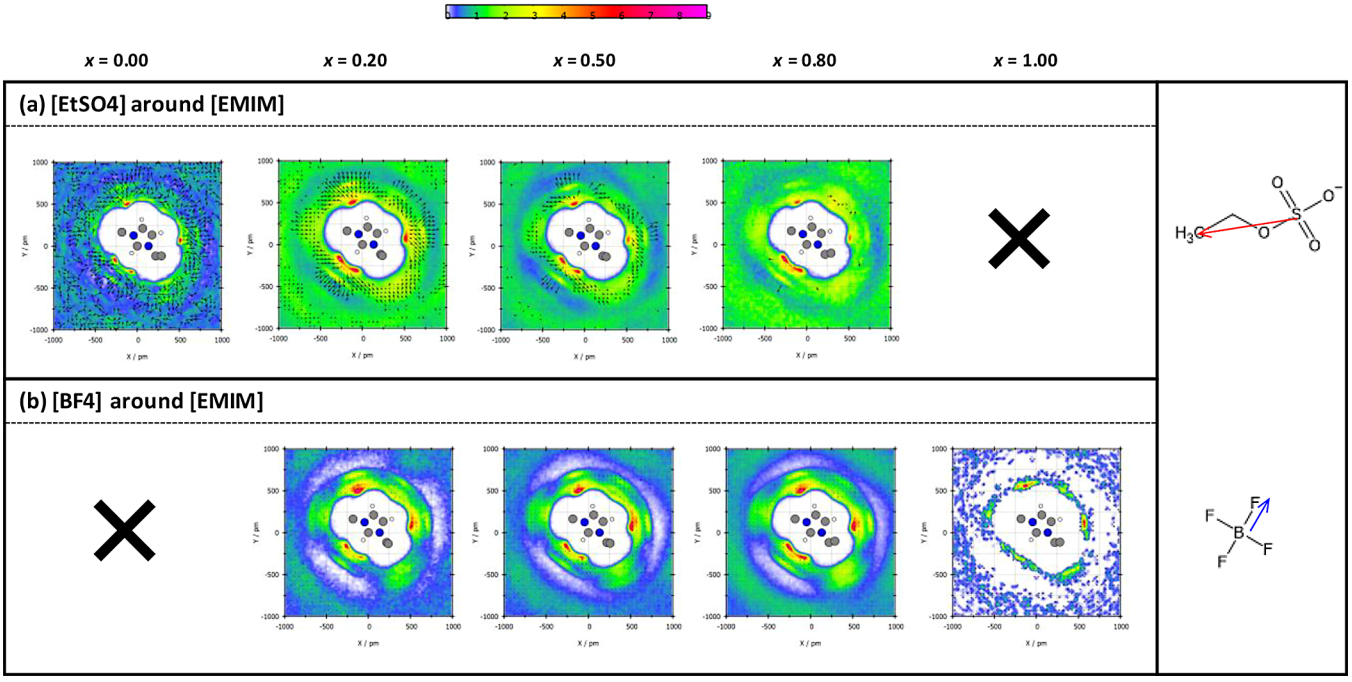

Figure 14. Average particle density of the reported molecules around a central [EMIM] molecule in x [EMIM][BF4] + $(1 - x)$ [EMIM][EtSO4] mixtures, where the "mean atomic mass" stands for mole fraction, from MD simulations at 303 K and 1 bar. Average orientation of the reported vectors is also indicated.

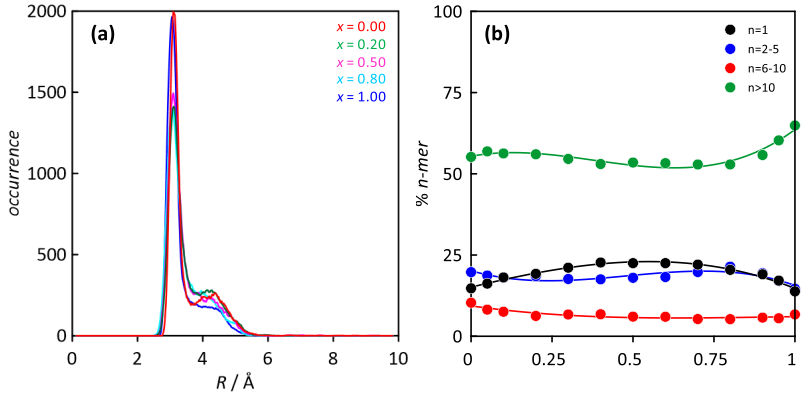

Figure 15. Cluster analysis for cation - anion aggregation in x [EMIM][BF4] + $(1 - x)$ [EMIM][EtSO4] mixtures, where stands for mole fraction, from MD simulations at 303 K and 1 bar. (a) Results show occurrence of possible clusters as a function of distance, R. (b) Percentage distribution of the cluster composed of n molecules (n-mers).

size. The evolution of anion domains follows a nonlinear trend increasing up to a value, i.e., declustering, and then decreasing reclustering. These effects point to a mechanism of anionic replacement which forces the connection of anion domains of

https://doi.org/10.1021/acs.iecr.4c02839
Ind. Eng. Chem. Res. 2025, 64, 1774−1791

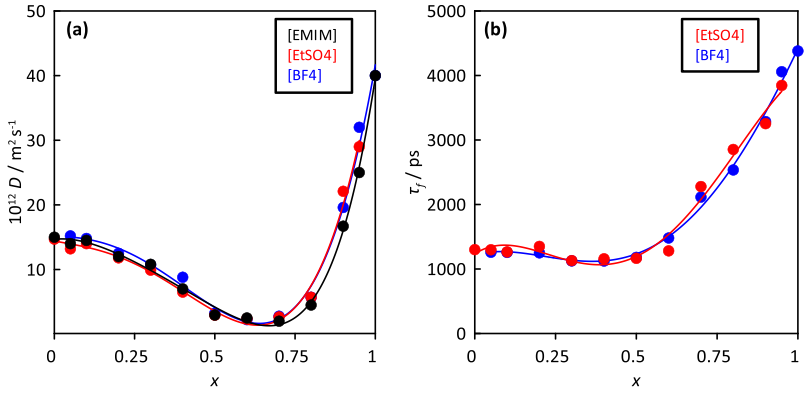

Figure 16. (a) Center-of-mass self-diffusion coefficient, D, and (b) living times of ion pairs, τ_f, for the considered ions in x [EMIM][BF4] + (1 − x) [EMIM][EtSO4] mixtures, where the word "mole fraction" stands for mole fraction, from MD simulations at 303 K and 1 bar.

the same type when the other anion prevails, i.e., anion microdomains leading to certain nanoscopic heterogeneity. Likewise, a relevant structural feature appears from the cationic interconnection, which determines the fluids' structure in which anions are distributed in the available sites around the C(1) imidazolium sites. The anionic domains show a certain degree of sphericity, especially changing the shape for those involving [BF4] anion, Figure 12c. Further analysis of the possible clustering is carried out through the neighbor probability matrix reported in Figure 13. These matrices show a similar interatomic distribution function in the whole considered composition range, and they may be considered as a fingerprint of the atom-to-atom distribution in the liquid phases, i.e. confirming analogous site-to-site distribution independently of the type of anion, thus pointing again to the anion per anion replacement mechanism for describing mixture properties.

The orientation of anions in the solvation shells around the [EMIM] cation is analyzed in Figure 14. Both types of anions show similar orientation around the cation C−H imidazolium sites (red spots). Likewise, anion vectors are highly oriented around the H-bonding imidazolium sites, especially for the [EtSO4] anion, in which the sulfate group is totally oriented toward the ring whereas the spherical shape of [BF4] provides a larger flexibility around the cation. This effect would be on the root of the lower density for [EtSO4] than for [BF4].

The anion−cation clustering is analyzed in Figure 15. Results in Figure 15a report cluster size distribution as a function of mixture composition, showing almost the same distribution in the whole composition range, i.e. changing the type of anion does not remarkably change the size of clusters, and only one type of anion is replaced by the other one. The two main peaks in Figure 15a correspond to clusters with 3.1 and 4.4 Å radii, being an anion−cation dimer (n = 1) or tetramer (n = 2). The first peak corresponding to n = 1 shows almost negligible changes upon mixing, whereas the second (weaker) one slightly decreases with increasing [BF4], but the most relevant features of cluster size are maintained in the whole composition range. Further analysis was carried out considering the percentage distribution of each type of cluster starting from n = 1 (1:1 anion−cation pair), as the simplest and smallest association, and increasing the number of ions in the cluster, Figure 15b. The first relevant conclusion stands on the large percentage of clusters with n > 10, which agreed with the domain distribution reported in Figure 14a, considering the interconnection between the cations. Therefore, liquid structuring is characterized by large clusters connected anion to cation via hydrogen bonding and through additional interactions among neighbor pairs (Figure 7). The cluster distribution shows subtle changes with mixture composition, but the most relevant features are analogous in the whole composition range, i.e., the mechanism of ionic aggregation and distribution remaining almost constant when one type of anion is gradually replaced by the other one.

The dynamic properties of the mixed ILs were first analyzed considering the self-diffusion coefficients, D, as calculated from the mean square displacement (MSD) and Einstein's equation, Figure 16a. The first remarkable result stands for the equal D values for the cation and anions at each fixed composition. This pairing of ionic movement comes from the development of anion−cation interactions, clustering, and through the replacement of a type of anion by the other one, leading to paired [EtSO4] and [BF4] diffusion. The composition evolution of D is largely nonlinear, in agreement with the experimental behavior of viscosity, Figure 2e,f. The D values for pure [EMIM][EtSO4] are lower than those for pure [EMIM][BF4], corresponding to larger viscosities for [EtSO4] containing fluids. These lower diffusion could be explained considering that [EtSO4] participates in larger domains than [BF4], Figure 12, and although anion−cation interactions have almost the same strength for both types of anions, Figures 6 and 7, the larger domains hinder ionic diffusion, thus leading to larger viscosity. The nonlinear evolution of D with mixture composition evolves through a minimum at [BF4] rich composition and then a sharp increase up to neat [EMIM][BF4]. The initial decrease of D for the [EtSO4] rich region with [BF4] increasing concentration may rise by the dispersion of [BF4] anions in the large [EtSO4] domains, Figure 12a. This increasing concentration of isolated [BF4] domains will decrease ionic mobility for all the considered ions. As the [BF4] rich region is reached, larger [BF4] prevailing domains are formed, which move faster, i.e. increasing global ionic motion. Therefore, ionic mobility and domains and clustering evolution with composition evolution are largely correlated.

Additionally, the dynamic properties of H-bonding are analyzed considering reactive flux analysis,[55] which leads to the hydrogen bonding lifetime (so-called forward process, τ_f), Figure 16b. This analysis shows very stable H-bonds with longer lifetimes for [BF4]−rich mixtures. Likewise, for each fixed composition, the lifetimes of each type of hydrogen bond are the same, which again points to the replacement mechanism as the feature controlling the nanoscopic structuring. Almost negligible changes in lifetimes are produced up to equimolar compositions, i.e., [EtSO4]−rich mixtures, and then a further increase in

https://doi.org/10.1021/acs.iecr.4c02839
Ind. Eng. Chem. Res. 2025, 64, 1774−1791

lifetimes with [BF4] enrichment. This effect can be justified considering the domain distribution reported in Figure 12a; for the [EtSO4]-rich region, almost a continuous domain is produced connecting cations and anions (domain count close to unity), and this facilitates H-bonding breaking and reforming. Upon the increase of the [BF4] content, the number of anion domains increases, thus hindering H-bonding reforming. Nevertheless, these dynamic features agree with experimental behavior and show how structuring and dynamic properties are intimately connected, and thus not only is the mechanism of interionic interaction relevant but also the long-range ionic distribution pivotal for determining ionic mobility, although intermolecular forces remain almost constant upon mixing.

3.4. Interaction with Biomolecules and Cell Membranes. The possible biological effects (i.e., toxicity) of the considered ILs and IL mixtures are first analyzed considering their interaction with a model lipid bilayer formed by DPPC lipids to mimic the interaction of the considered ILs with cell walls. Literature studies on the interaction of ILs with lipid bilayers are scarce, Yoo et al.[56] probed via MD simulations imidazolium cationic insertion into model POPC bilayers leading to surface roughening as the precursor of bilayer disruption, and additional perturbation effects have been reporting being indicative of toxic effect of mainly imidazolium−based ILs.[57,58] Nevertheless, these studies considered neat ILs not mixed ILs, and, in most of the cases, low IL concentration. Results in Figure 17 show DPPC bilayer structuring in the presence of the considered IL mixtures. Both for pure ILs as well as for the considered mixtures, large bilayer roughness is induced, which confirms the roughness previously reported[54] being exacerbated by the larger concentration considered in this work. Although the bilayer integrity is maintained upon interaction with ILs, the roughening is induced by the adsorption of ions on the outer polar region of the lipids. Likewise, there is a clearly different preferential adsorption arrangement with [BF4] anions placed in outer regions close to the head choline groups, whereas [EtSO4] and mainly [EMIM] cations penetrate inside the bilayer remaining closer to the phosphate and glycerol groups, respectively. All of the considered ions remain in the top polar region of the bilayer surface without staying in the apolar central region. Surface roughening is maintained and shows similar characteristics for all the considered composition effects, with the anion exchange scheme pointing to a larger amount of ions on the outer layer for [BF4]-rich mixtures, whereas for [EtSO4]-rich mixtures, a larger ionic concentration is inferred in inner regions of the polar heads. In all the cases, the presence of [EMIM] inside the polar region leads to a largely disruptive effect on the surface roughness. This increase in the surface curvature is produced by the large affinity of the considered ions for the polar head groups of the lipids, which through increasing roughness leads to an improvement of ion−lipid interactions both in terms of extension and strength. The perturbation of bilayer properties is quantified considering bilayer width and Area Per Lipid (APL) taking as reference the calculated bilayer properties in the absence of ILs; Figure 18a. In most of the cases, the presence of the ILs leads to a bilayer expansion (with the exception of neat [EMIM][BF4] in the three space directions (increase of width and APL), which is produced for the accommodation of strongly interacting ions. There is not a clear effect on the content of anions, although the presence of [BF4] seems to decrease the perturbative effects because the spherical symmetry and size of these anions allow better surface accommodation with lower

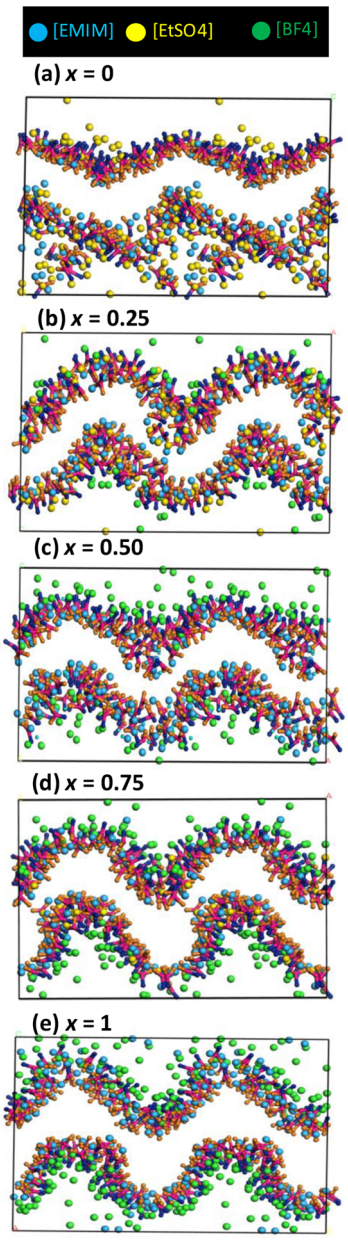

Figure 17. Results of Coarse Grained MD simulations of x [EMIM][BF4] + $(1 - x)$ [EMIM][EtSO4] mixtures in aqueous solution (Table S9, Supporting Information) in contact with the DPPC lipid bilayer at 313 K. Snapshots at the end of the simulations are reported. Lipid alkyl chains as well as water molecules are omitted for the sake of visibility.

bilayer disruption. The strong ion−(polar head) lipid interactions decrease lipid mobility, as probed by the decrease in lateral diffusion reported in Figure 18c, i.e., ions adsorption on the surface modifies both the structural and dynamic properties (fluidity) of the bilayer, which indicate a large disrupting effect. Nevertheless, considering that ion interaction is produced in the polar head regions of the bilayer, perturbations on the apolar regions are almost negligible as probed by the minor changes in lipid extension and internal angle reported in Figure 19. The mechanism of ion-polar head interactions is quantified through the corresponding RDFs reported in Figure 20, where it is clearly proved that the [EMIM] cation interacts mainly with internal phosphate and glycerol, [BF4] with external choline, and

https://doi.org/10.1021/acs.iecr.4c02839
Ind. Eng. Chem. Res. 2025, 64, 1774−1791

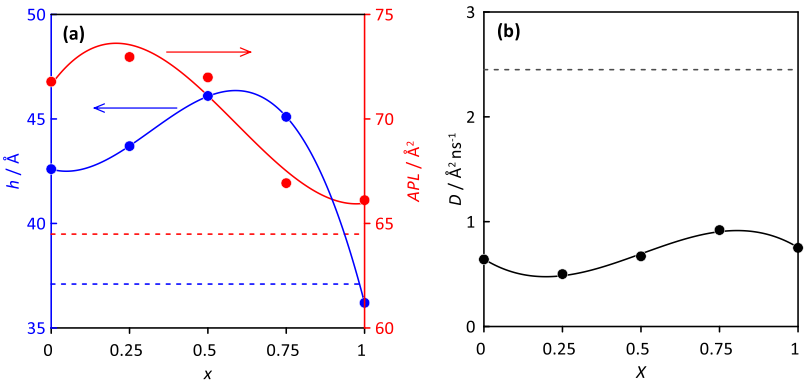

Figure 18. Results of Coarse Grained MD simulations of x [EMIM][BF4] + $(1 - x)$ [EMIM][EtSO4] mixtures in aqueous solution (Table S9, Supporting Information) in contact with DPPC lipid bilayer at 313 K. (a) Lipid bilayer width, h, defined as the distance between NC groups (choline group) in top and bottom layers and APL standing as Area per Lipid; (b) lateral self-diffusion coefficients, D, for DPPC lipids. Dashed lines in each panel show the values for the DPPC bilayer in contact with the water layer in the absence of ILs.

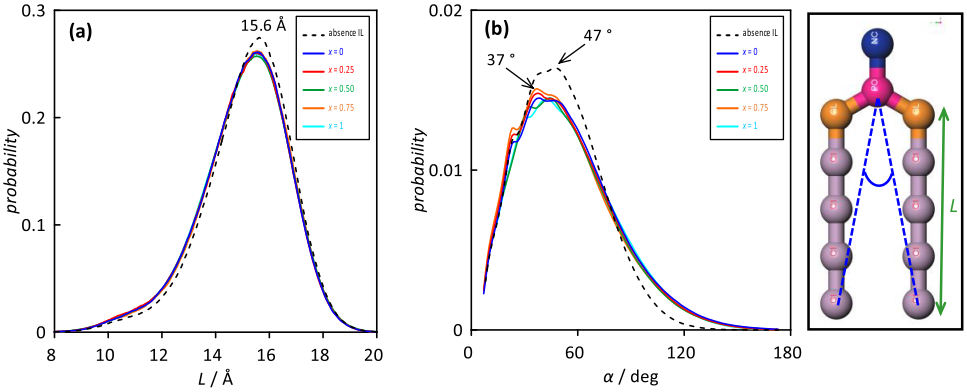

Figure 19. Results of Coarse Grained MD simulations of x [EMIM][BF4] + $(1 - x)$ [EMIM][EtSO4] mixtures in aqueous solution (Table S9, Supporting Information) in contact with the DPPC lipid bilayer at 313 K. Results indicate probability distributions of geometrical properties of DPPC lipid in the bilayers.

[EtSO4] remaining in a central region being able to interact with all the groups. These results indicate that for a mixed IL containing [BF4] and [EtSO4] anions, both types of anions do not compete for the adsorption regions on the lipid polar surfaces, whereas they adsorbed in different regions, being also different from those of [EMIM] cation, and thus, the anionic effect on lipid bilayer disruption would be additive and synergistic, leading to larger toxic effects.

Additional possible toxic effects of the considered ILs were analyzed by doing docking studies on four model proteins for ion clusters reported in Figure 7, as models of mixed ILs interacting with different biological targets. The results in Figure 21 provide the biomolecule−cluster interaction energies. Docking interaction energies are in the −6 to −21 kcal mol^{-1}, which indicates favorable ionic cluster−biomolecule interaction, i.e. non-negligible biological effects that may be related, at least qualitatively with possible toxic effects. For a fixed cluster configuration, there is not a remarkable effect on the type of biomolecule, indicating that ion pairs are able to reach the most stable configuration independently of the biomolecule. Nevertheless, results indicate that there is a large effect on the type of considered clusters leading to very different interactions with the biomolecule both in terms of mechanism(s) and strength. Therefore, these results combined with those for the interaction with lipid bilayers point to aremarkable interaction of the considered mixed ILs with biosystems, pointing to non-negligible toxic effects, exacerbated through synergistic effects by the presence of different types of anions, which should be taken into account for the large-scale application of complex multicomponent IL mixtures.

4. CONCLUSIONS

In this research, our primary focus was the comprehensive examination of [EMIM][BF4] and [EMIM][EtSO4] ionic liquids and their binary mixtures from macroscopic to nanoscopic scales as well as their potential biological implications. Beginning with macroscopic investigations, density and viscosity measurements unveiled a remarkable trend attributed to the presence of hydrogen-bonded cluster structures. Analysis of excess properties provided valuable insights into the mixing behavior of these ILs, revealing minor deviations from ideality primarily driven by the rearrangement of molecular clusters within the available free space. Moreover, the study of excess partial molar volumes demonstrated symmetric behavior, affirming the minimal disruption of the IL structuring upon mixing. Our research also delved into the behavior of intermolecular forces, demonstrating that changes in these forces were predominantly a result of dilution effects, with little alteration in cation−anion interactions. Collectively, these findings significantly contribute to our understanding of IL behavior, offering valuable insights into its potential applications in the fields of chemistry and materials science.

Moving to the nanoscopic realm, molecular dynamics (MD) simulations enabled the exploration of mixed liquid phases. The

https://doi.org/10.1021/acs.iecr.4c02839
Ind. Eng. Chem. Res. 2025, 64, 1774−1791

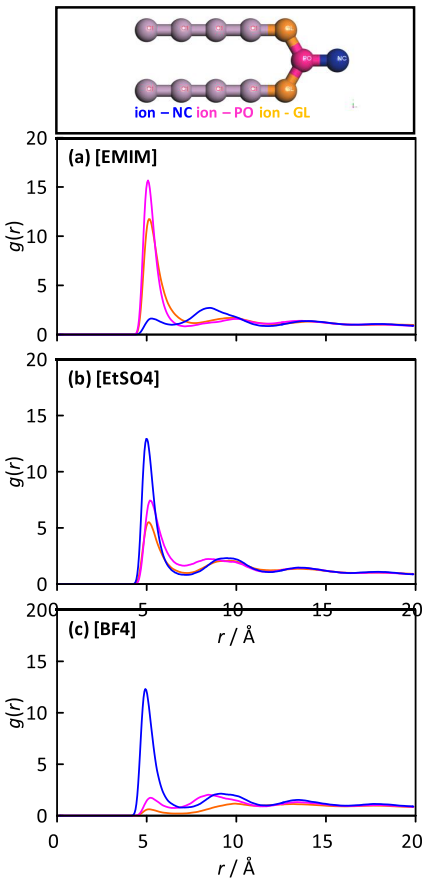

Figure 20. Results of Coarse Grained MD simulations of x [EMIM][BF4] + $(1 - x)$ [EMIM][EtSO4] (x = 0.5) mixture in aqueous solution (Table S9, Supporting Information) in contact with the DPPC lipid bilayer at 313 K. Results indicate radial distribution functions between the indicated ions and polar head groups in DPPC lipid in the bilayer.

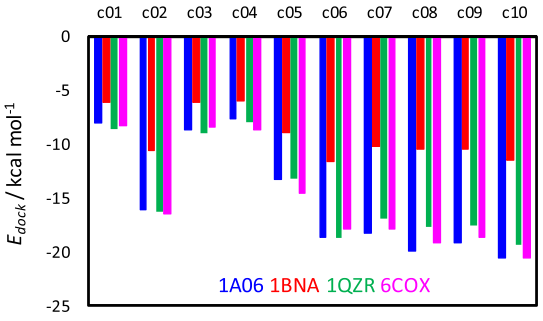

Figure 21. Results for the docking of IL clusters (Figure 7) into the reported biomolecules indicating IL−biomolecule affinity quantified as docking (interaction) energy, E_{dock}. E_{dock} values for the strongest interaction pose are reported in each case.

analysis uncovered robust cation−anion interactions at the C(1) and C(2) sites of [EMIM], with anion−cation replacement being the predominant structural mechanism. Spatial Distribution Functions illustrated consistent anion−cation interactions, substantiating structural stabilization and densification within these mixed liquid phases. Combined Distribution Functions further verified uniform hydrogen bonding geometry across anions and compositions, while domain analysis unveiled subtle nanoscale heterogeneity in anion domains. The study of cation−anion clustering revealed the enduring presence of large, hydrogen-bonded clusters, which remained consistent through various compositional variations. Additionally, dynamic properties, including self-diffusion coefficients and hydrogen bonding lifetimes, exhibited correlations with the observed viscosity behavior, demonstrating the interconnected nature of intermolecular forces, structural dynamics, and ionic mobility within these mixed liquid phases. These nanoscopic insights deepen our understanding of these systems, providing valuable knowledge for potential applications.

Expanding our scope to examine the potential biological effects, interactions with a model lipid bilayer, and docking studies on model proteins were conducted. Simulations uncovered the disruptive influence of both pure ILs and mixed ILs on the lipid bilayer, which induces significant roughening. Preferential adsorption of [BF4] anions near the choline groups and deeper penetration of [EtSO4] and [EMIM] cations into the bilayer were observed, underscoring the distinct behaviors of different ion types. Docking studies with model proteins indicated favorable interactions between ionic clusters and biomolecules, hinting at the potential biological effects. Importantly, the configuration of ion clusters played a crucial role in determining the nature and strength of these interactions, pointing to non-negligible toxic effects, possibly exacerbated by synergistic effects arising from the presence of various anion types.

This research not only advances our understanding of the fundamental behavior of ILs but also underscores the importance of considering the toxicological implications of complex multicomponent IL mixtures, particularly when they are employed on a large scale in diverse applications. The interactions observed with lipid bilayers and biomolecules emphasize the necessity for a comprehensive assessment of the biological effects of ILs in real-world scenarios, bridging the gap between fundamental research and practical applications.

From the viewpoint of industrial and technological relevance, this comprehensive study of [EMIM][BF4] and [EMIM][EtSO4] ionic liquids and their mixtures has significant implications. The insights gained into their macroscopic and nanoscopic properties can guide the development of tailored ILs for specific applications in chemistry and materials science. For instance, an understanding of viscosity trends and mixing behavior can inform the design of IL-based lubricants, electrolytes, and heat transfer fluids. The nanoscopic analysis of ion interactions and clustering behavior is crucial for optimizing ILs for use in catalysis, gas capture, and electrochemical devices. Furthermore, the revealed biological interactions are vital for assessing the environmental impact and safety of ILs in large-scale industrial processes. This knowledge can drive the development of safer, more efficient IL formulations for applications in pharmaceuticals, biomass processing, and green chemistry. Overall, this research provides a solid foundation for advancing IL technology across various sectors, balancing performance with safety considerations.

■ ASSOCIATED CONTENT

Supporting Information

The Supporting Information is available free of charge at https://pubs.acs.org/doi/10.1021/acs.iecr.4c02839.

Additional experimental and computational details, including thermophysical properties and molecular dynamics results (PDF)

https://doi.org/10.1021/acs.iecr.4c02839
Ind. Eng. Chem. Res. 2025, 64, 1774−1791

AUTHOR INFORMATION

Corresponding Authors

Santiago Aparicio − *Department of Chemistry, University of Burgos, 09001 Burgos, Spain;* orcid.org/0000-0001-9996-2426; Email: sapar@ubu.es

Jose L. Trenzado − *Department of Physics, University of Las Palmas de Gran Canaria, 35017 Las Palmas G.C., Spain;* Email: jose.trenzado@ulpgc.es

Author

Ylenia F. Rodríguez − *Department of Physics, University of Las Palmas de Gran Canaria, 35017 Las Palmas G.C., Spain*

Complete contact information is available at: https://pubs.acs.org/10.1021/acs.iecr.4c02839

Notes

The authors declare no competing financial interest.

ACKNOWLEDGMENTS

We acknowledge SCAYLE (Supercomputación Castilla y León, Spain) for providing supercomputing facilities. The statements made herein are solely the responsibility of the authors.

REFERENCES

(1) Walden, P. *Eber die Molekulargrösse und ElektrischeLeitfähigkeit Einiger Geschmolzenen Salze*; Benrath und Wainoff: 1914.

(2) Hurley, F. H.; Wier, T. P. The electrodeposition of aluminum from nonaqueous solutions at room temperature. *J. Electrochem. Soc.* **1951**, *98*, 207−212.

(3) Lei, Z.; Chen, B.; Koo, Y. M.; Macfarlane, D. R. Introduction: Ionic Liquids. *Chem. Rev.* **2017**, *117*, 6633−6635.

(4) Dong, K.; Liu, X.; Dong, H.; Zhang, X.; Zhang, S. Multiscale studies on ionic liquids. *Chem. Rev.* **2017**, *117*, 6636−6695.

(5) Philippi, F.; Rauber, D.; Eliasen, K. L.; Bouscharain, N.; Niss, K.; Kay, C. W.; Welton, T. Pressing matter: why are ionic liquids so viscous? *Chem. Sci.* **2022**, *13*, 2735−2743.

(6) Chen, Y.; Mu, T. Revisiting greenness of ionic liquids and deep eutectic solvents. *Green Chem. Eng.* **2021**, *2*, 174−186.

(7) Binnemans, K.; Jones, P. T. Ionic Liquids and Deep-Eutectic Solvents in Extractive Metallurgy: Mismatch Between Academic Research and Industrial Applicability. *J. Sustain. Metallurgy* **2023**, *9*, 423−428.

(8) Yadav, A.; Guha, A.; Pandey, A.; Pal, M.; Triveti, S.; Pandey, S. Densities and dynamic viscosities of ionic liquids having 1-butyl-3-methylimidazolium cation with different anions and bis-(trifluoromethylsulfonyl)imide anion with different cations in the temperature range (283.15 to 363.15) K. *J. Chem. Thermodyn.* **2018**, *116*, 67−75.

(9) Zhang, Q.; Zhang, S.; Deng, Y. Recent advances in ionic liquid catalysis. *Green Chem.* **2011**, *13*, 2619−2637.

(10) Macfarlane, D. R.; et al. Energy applications of ionic liquids. *Energy Environ. Sci.* **2014**, *7*, 232−250.

(11) Wang, M.; Zhang, L.; Gao, L.; Pi, K.; Zhang, J.; Zheng, C. Improvement of the CO2 absorption performance using ionic liquid [NH2emim][BF4] and [emim][BF4]/[bmim][BF4] mixtures. *Energy Fuels* **2013**, *27*, 461−466.

(12) Ventura, S. P. M.; Silva, F. A.; Quental, M. V.; Mondal, D.; Freire, M. G.; Coutinho, J. A. P. Ionic-liquid-mediated extraction and separation processes for bioactive compounds: past, present, and future trends. *Chem. Rev.* **2017**, *117*, 6984−7052.

(13) Zhou, Y. Ionic Liquids as Lubricant Additives-a Review. *ACS Appl. Mater. Interfaces* **2017**, *9*, 3209−3222.

(14) Zhou, F.; Liang, Y.; Liu, W. Ionic liquid lubricants: Designed chemistry for engineering applications. *Chem. Soc. Rev.* **2009**, *38*, 2590−2599.

(15) Xiao, H. Ionic Liquid Lubricants: Basics and Applications. *Tribol. Trans.* **2017**, *60*, 20−30.

(16) Zhou, W.; Zhang, M.; Kong, X.; Huang, W.; Zhang, Q. Recent advance in ionic-liquid-based electrolytes for rechargeable metal-ion batteries. *Adv. Sci.* **2021**, *8*, No. 2004490.

(17) de Castro, C. N. et al. Synthesis, properties and physical applications of ionanofluids. In *Ionic Liquids - New Aspects for the Future*; InTech, 2013.

(18) Pedro, S. N.; Freire, C. S. R.; Silvestre, A. J. D.; Freire, M. G. The role of ionic liquids in the pharmaceutical field: An overview of relevant applications. *Int. J. Mol. Sci.* **2020**, *21*, 8298.

(19) Chatel, G.; Pereira, J. F. B.; Debbeti, V.; Wang, H.; Rogers, R. D. Mixing ionic liquids-simple mixtures or "double salts"? *Green Chem.* **2014**, *16*, 2051−2083.

(20) Trenzado, J. L.; Rodríguez, Y.; Gutiérrez, A.; Cincotti, A.; Aparicio, S. Experimental and molecular modeling study on the binary mixtures of [EMIM][BF4] and [EMIM][TFSI] ionic liquids. *J. Mol. Liq.* **2021**, *334*, No. 116049.

(21) Shekaari, H.; Zafarani-Moattar, M. T.; Mokhtarpour, M.; Faraji, S. Volumetric and compressibility properties for aqueous solutions of choline chloride based deep eutectic solvents and Prigogine−Flory−Patterson theory to correlate of excess molar volumes at T = (293.15 to 308.15) K. *J. Mol. Liq.* **2019**, *289*, No. 111077.

(22) BIOVIA Dassault Systèmes. *Dmol3*; Dassault Systèmes: San Diego, 2022.

(23) Grimme, S.; Antony, J.; Krieg, H. A consistent and accurate ab initio parametrization of density functional dispersion correction (DFT-D) for the 94 elements H-Pu. *J. Chem. Phys.* **2010**, *132*, 154104.

(24) Simon, S.; Duran, M.; Dannenberg, J. How does basis set superposition error change the potential surfaces for hydrogen-bonded dimers? *J. Chem. Phys.* **1996**, *105*, 11024.

(25) Bogojeski, M.; Vogt-Maranto, L.; Tuckerman, M. E.; Müller, K. R.; Burke, K. Quantum chemical accuracy from density functional approximations via machine learning. *Nat. Commun.* **2020**, *11*, 5223.

(26) Bader, R. F. W. Atoms in molecules. *Acc. Chem. Res.* **1985**, *18*, 9−15.

(27) Lu, T.; Chen, F. Multiwfn: A multifunctional wavefunction analyzer. *J. Comput. Chem.* **2012**, *33*, 580−592.

(28) Fuster, F.; Silvi, B. Does the topological approach characterize the hydrogen bond? *Theor. Chem. Acc.* **2000**, *104*, 13−21.

(29) Lyubartsev, A. P.; Laaksonen, A. MdynaMix−A Scalable Portable Parallel MD Simulation Package for Arbitrary Molecular Mixtures. *Comput. Phys. Commun.* **2000**, *128*, 565−589.

(30) Zoete, V.; Cuendet, M. A.; Grosdidier, A.; Michielin, O. SwissParam. A fast force field generation tool for small organic molecules. *J. Comput. Chem.* **2011**, *32*, 2359−2368.

(31) Martínez, L.; Andrade, R.; Birgin, E. G.; Martínez, J. M. Packmol: a package for building initial configurations for molecular dynamics simulations. *J. Comput. Chem.* **2009**, *30*, 2157−2164.

(32) Tuckerman, M.; Berne, B. J.; Martyna, G. J. Reversible multiple time scale molecular dynamics. *J. Chem. Phys.* **1992**, *97*, 1990−2001.

(33) Essmann, U. L.; Perera, M. L.; Berkowitz, T.; Darden, H.; Lee, H.; Pedersen, L. G. A smooth particle mesh ewald method. *J. Chem. Phys.* **1995**, *103*, 8577−8593.

(34) Hoover, W. G. Canonical dynamics: Equilibrium phase-space distributions. *Phys. Rev. A* **1985**, *31*, 1695.

(35) Humphrey, W.; Dalke, A.; Schulten, K. VMD−Visual molecular dynamics. *J. Mol. Graphics* **1996**, *14*, 33−38.

(36) Brehm, M.; Kirchner, B. TRAVIS−A free analyzer and visualizer for Monte Carlo and molecular dynamics trajectories. *J. Chem. Inf. Model.* **2011**, *51*, 2007−2023.

(37) Halappanavar, S.; van der Bruel, S.; Nymark, P.; Gaté, L.; Seidel, C.; Valentino, S.; Zhernovkov, V.; Danielsen, P. H.; de Vizcaya, A.; Wolff, H.; Stoger, T.; Boyadziev, A.; Poulsen, S. S.; Sorli, J. B.; Vogel, U. Adverse outcome pathways as a tool for the design of testing strategies to support the safety assessment of emerging advanced materials at the nanoscale. *Part. Fib. Toxicol.* **2020**, *17*, 16.

(38) Allen, T. E. H.; Goodman, J. M.; Gutsell, S.; Russell, P. J. A History of the Molecular Initiating Event. *Chem. Res. Toxicol.* **2016**, *19*, 2060−2070.
(39) Halappanavar, S.; Sharma, M.; Wallin, H.; Vogel, U.; Sullivan, K.; Clippinger, A. J. *Substance interaction with the lung resident cell membrane components leading to lung fibrosis*. https://aopwiki.org/aops/173 (accessed November 11, 2022).
(40) Marrink, M. A.; Risselada, H. J.; Yefimov, S.; Tieleman, D. P.; de Vries, A. H. The MARTINI force field: coarse grained model for biomolecular simulations. *J. Phys. Chem. B* **2007**, *111*, 7812−7824.
(41) Vazquez-Salazar, L. I.; Selle, M.; de Vries, A. H.; Marrink, S. J.; Souza, P. C. T. Martini coarse-grained models of imidazolium-based ionic liquids: from nanostructural organization to liquid−liquid extraction. *Green Chem.* **2020**, *22*, 7376−7386.
(42) Trott, O.; Olson, A. J. AutoDock Vina: improving the speed and accuracy of docking with a new scoring function, efficient optimization and multithreading. *J. Comput. Chem.* **2010**, *31*, 455−461.
(43) Navia, P.; Troncoso, J.; Romani, L. Excess magnitudes for ionic liquid binary mixtures with a common ion. *J. Chem. Eng. Data* **2017**, *52*, 1369−1374.
(44) Clough, M. T.; Crick, C. R.; Grasvik, J.; Hunt, P. A.; Niedermeyer, H.; Welton, T.; Whitaker, O. R. A physicochemical investigation of ionic liquid mixtures. *Chem. Sci.* **2015**, *6*, 1101−1114.
(45) Chakraborty, M.; Barik, S.; Mahapatra, A.; Sarkar, M. Binary mixtures of ionic liquids: Ideal, non-ideal, or quasi-ideal? *J. Chem. Phys.* **2021**, *154*, 224507.
(46) Gomez, E.; Gonzalez, B.; Calvar, N.; Tojo, E.; Dominguez, A. Physical properties of pure 1-ethyl-3-methylimidazolium ethylsulfate and its binary mixtures with ethanol and water at several temperatures. *J. Chem. Eng. Data* **2006**, *51*, 2096−2102.
(47) Zarei, H.; Keley, V. Density and speed of sound of binary mixtures of ionic liquid 1-ethyl-3-methylimidazolium tetrafluoroborate, N,N-dimethylformamide, and N,N-dimethylacetamide at temperature range of 293.15−343.15 K: Measurement and PC-SAFT modeling. *J. Chem. Eng. Data* **2017**, *62*, 913−923.
(48) Živković, E. M.; Živković, N. V.; Majstorović, D. M.; Stanimirović, A. M.; Kijevčanin, M. L. Volumetric and transport properties of binary liquid mixtures with 1-ethyl-3-methylimidazolium ethyl sulfate as candidate solvents for regenerative flue gas desulfurization processes. *J. Chem. Thermodyn.* **2018**, *119*, 135−154.
(49) Liu, Q.; Ma, L.; Wang, S.; Fu, X.; Wang, J.; Zheng, Q. Study on the properties of density, viscosity, excess molar volume, and viscosity deviation of [C2mim][NTf2], [C2mmim][NTf2], [C4mim][NTf2], and [C4mmim][NTf2] with PC binary mixtures. *J. Mol. Liq.* **2021**, *325*, No. 114573.
(50) Pinto, A. M.; Rodriguez, H.; Colon, Y. J.; Arce, A.; Arce, A.; Soto, A. Absorption of Carbon Dioxide in two binary mixtures of ionic liquids. *Ind. Eng. Chem. Res.* **2013**, *52*, 5975−5984.
(51) Shekaari, H.; Zafarani-Moattar, M. T.; Mokhtarpour, M.; Faraji, S. Compatibility of sustainable solvents ionic liquid, 1-ethyl-3-methylimidazolium ethyl sulfate in some choline chloride based deep eutectic solvents: thermodynamics study. *J. Chem. Thermodyn.* **2020**, *141*, No. 105961.
(52) Anwar, N.; Riyazuddeen; Yasmeen, S. Volumetric, compressibility and viscosity studies of binary mixtures of [EMIM][NTf2] with ethylacetate/methanol at (298.15−323.15) K. *J. Mol. Liq.* **2016**, *224*, 189−200.
(53) Ilokhani, H.; Almasi, M. Densities, viscosities, excess molar volumes, and refractive indices of acetonitrile and 2-alkanols binary mixtures at different temperatures: Experimental results and application of the Prigogine−Flory−Patterson theory. *Thermochim. Acta* **2009**, *495*, 139−148.
(54) Koch, U.; Popelier, P. L. Characterization of C-H-O Hydrogen bonds on the basis of the charge density. *J. Phys. Chem.* **1995**, *99*, 9747−9754.
(55) Luzar, A. Resolving the hydrogen bond dynamics conundrum. *J. Chem. Phys.* **2000**, *113*, 10663−10675.
(56) Yoo, B.; Shah, J. K.; Zhu, Y.; Maginn, E. J. Amphiphilic interactions of ionic liquids with lipid biomembranes: a molecular simulation study. *Soft Matt.* **2014**, *10*, 8641−8651.
(57) Jing, B.; Lan, N.; Qiu, J.; Zhu, Y. Interaction of ionic liquids with a lipid bilayer: a biophysical study of ionic liquid cytotoxicity. *J. Phys. Chem. B* **2016**, *120*, 2781−2789.
(58) Galluzzi, M.; Marfori, L.; Asperti, S.; De Vita, A.; Giannangeli, M.; Caselli, A.; Milani, P.; Podesta, A. Interaction of imidazolium-based ionic liquids with supported phospholipid bilayers as model biomembranes. *Phys. Chem. Chem. Phys.* **2022**, *24*, 27328−27342.

https://doi.org/10.1021/acs.iecr.4c02839
Ind. Eng. Chem. Res. 2025, 64, 1774−1791

5.1.2.1. Información experimental I

Tabla 14. Comparación de los datos experimentales con la literatura citada, tanto de las densidades, ρ (g cm^{-3}), como de las viscosidades dinámicas, η (mPa s), de los compuestos puros a las temperaturas de trabajo.

	ρ / g cm^{-3}		η / mPa s		ρ / g cm^{-3}		η / mPa s	
T / K	exp.	Lit.	exp.	Lit.	exp.	Lit.	exp.	Lit.
	[EMIM][BF$_4$]				[EMIM][EtSO$_4$]			
283.15	1.29151	1.29704[a]	64.86	67.8[a]	1.24704	1.24691[k]	222.78	224.00[k]
		1.29200[b]		-		1.24730[l]		218.56[t]
		1.29089[®]		-		1.24640[m]		-
288.15	1.28766	1.28803[d]	50.91	54.1[p]	1.24357	1.24348[k]	166.34	161.56[t]
		1.28820[b]		55.5[q]		1.24370[l]		-
		1.28674[®]		-		1.24310[m]		-
293.15	1.28384	1.28390[f]	42.04	43.4[a]	1.24019	1.24009[k]	123.58	122.31[t]
		1.28390[g]		44.19[p]		1.24010[l]		122.07[u]
		1.28389[h]		-		1.24021[n]		-
298.15	1.28005	1.27990[f]	34.69	36.17[p]	1.23682	1.23689[o]	95.34	94.64[t]
		1.28000[g]		36.93[g]		1.23678[n]		96.21[v]
		1.28007[d]		-		1.23670[l]		-
303.15	1.27626	1.27626[g]	29.02	30.13[p]	1.23358	1.23346[o]	75.09	75.10[u]
		1.27630[f]		30.54[®]		1.23336[n]		74.72[t]
		1.27626[h]		-		1.23332[k]		75.89[v]
308.15	1.27249	1.27240[g]	24.58	25.557[s]	1.23005	1.23006[o]	60.17	60.01[t]
		1.27248[d]		26.0[q]		1.22996[n]		30.73[v]
		1.27260[i]		-		1.22994[k]		-
		1.26860[g]		22.61[g]		1.22657[n]		49.38[v]
		1.26857[j]		-		1.22656[k]		-

(a) Sanmamed et al.. 2010
(b) Seiki et al.. 2012
® Gutiérrez et al.. 2018
(d) Stoppa et al.. 2010
® Ayranci & Sahin. 2018
(f) Gupta et al.. 2020
(g) Song and Chen. 2014
(h) Sharma et al.. 2014
(i) Darolia et al.. 2022
(j) Srinivasa Rao et al.. 2017
(k) Hasse et al.. 2009
(l) Dakkach et al.. 2018
(m) Mohan et al.. 2022
(n) Rajendran et al.. 2020
(o) Singh et al.. 2014
(p) Schreiner et al.. 2010
(q) Rilo et al.. 2010
® Narsimlu et al.. 2019
(s) Zhang et al.. 2004
(t) Tariq et al.. 2021
(u) Larriba et al.. 2011
(v) Anwar et al.. 2017

Anwar, N., & Riyazuddeen. (2017). Fluid Phase Equilibria, 437, 127–139.

Ayranci, E., & Sahin, E. M. (2018). Journal of Solution Chemistry, 47(2), 246–261.

Dakkach, M., Gaciño, F., Guimarey, M. J. G., Mylona, S. K., Paredes, X., Comuñas, M. J. P., Fernández, J., & Assael, M. J. (2018). Journal of Chemical Thermodynamics, 121, 27–38.

Darolia, P. J., Malik, S., Garg, S., & Sharma, V. K. (2022). Chemical Data Collections, 41.

Gupta, H., Malik, S., Sharma, D., & Sharma, V. K. (2020). Chemical Data Collections, 28.

Gutiérrez, A., Atilhan, M., Alcalde, R., Trenzado, J. L., & Aparicio, S. (2018). Journal of Molecular Liquids, 255, 199–207.

Hasse, B., Lehmann, J., Assenbaum, D., Wasserscheid, P., Leipertz, A., & Fröba, A. P. (2009). Journal of Chemical and Engineering Data, 54(9), 2576–2583.

Larriba, M., García, S., García, J., Torrecilla, J. S., & Rodríguez, F. (2011). Journal of Chemical and Engineering Data, 56(9), 3589–3597.

Mohan, M., Kumar, N., Goud, V. V., Simmons, B. A., Sale, K. L., Gladden, J. M., Singh, S., & Banerjee, T. (2022). Fluid Phase Equilibria, 562.

Narsimlu, V., Reddy, K. C. S., Krishna, T. V., Mohan, T. M., & Rao, V. S. (2019). Journal of Chemical Thermodynamics, 139.

Rajendran Startha Christabel, A., Ramalingam, A., Reji, D. J. P. M., Nagaraj, S., & Ravichandran, S. (2020). Journal of Chemical and Engineering Data, 65(2), 446–476.

Rilo, E., Vila, J., Pico, J., García-Garabal, S., Segade, L., Varela, L. M., & Cabeza, O. (2010). Journal of Chemical and Engineering Data, 55(2), 639–644.

Sanmamed, Y. A., González-Salgado, D., Troncoso, J., Romani, L., Baylaucq, A., & Boned, C. (2010). Journal of Chemical Thermodynamics, 42(4), 553–563.

Schreiner, C., Zugmann, S., Hartl, R., & Gores, H. J. (2010). Journal of Chemical and Engineering Data, 55(5), 1784–1788.

Seki, S., Tsuzuki, S., Hayamizu, K., Umebayashi, Y., Serizawa, N., Takei, K., & Miyashiro, H. (2012). Journal of Chemical and Engineering Data, 57(8), 2211–2216.

Sharma, V. K., Solanki, S., & Bhagour, S. (2014). Journal of Chemical and Engineering Data, 59(4), 1140–1157.

Singh, M. P., Mandal, S. K., Verma, Y. L., Gupta, A. K., Singh, R. K., & Chandra, S. (2014). Journal of Chemical and Engineering Data, 59(8), 2349–2359.

Song, D., & Chen, J. (2014). Journal of Chemical and Engineering Data, 59(2), 257–262.

Srinivasa Rao, V., Vijaya Krishna, T., Madhu Mohan, T., & Madhusudana Rao, P. (2017). Journal of Chemical Thermodynamics, 104, 150–161.

Tariq, M., Esperança, J. M. S. S., Rebelo, L. P. N., Paredes, X., Santos, F. J. V., & Nieto de Castro, C. A. (2021). Journal of Molecular Liquids, 337.

Zech, O., Stoppa, A., Buchner, R., & Kunz, W. (2010). Journal of Chemical and Engineering Data, 55(5), 1774–1778.

Zhang, S., Li, X., Chen, H., Wang, J., Zhang, J., & Zhang, M. (2004). Journal of Chemical and Engineering Data, 49(4), 760–764.

Tabla 15. Densidades (ρ), viscosidades cinemáticas (ν), viscosidades dinámicas (η), volúmenes molares de exceso (VE) y desviaciones en la viscosidad ($\eta\Delta$) del sistema {(x) [EMIM][BF_4] + (1-x) [EMIM][$EtSO_4$]} a diferentes temperaturas.

X	ρ / g cm^{-3}	ν / mm^2 s^{-1}	η / mPa s	V^E / cm^3 mol^{-1}	$\Delta\eta$ / mPa s
		283.15 K			
0.04543	1.24868	170.19	212.52	0.001	-3.09
0.11104	1.25109	158.18	197.89	0.005	-7.35
0.21268	1.25495	142.01	178.21	0.009	-10.98
0.30328	1.25854	128.35	161.53	0.012	-13.35
0.39825	1.26245	114.90	145.06	0.013	-14.83
0.49701	1.26669	101.64	128.74	0.014	-15.55
0.61322	1.27193	87.50	111.29	0.013	-14.65
0.68937	1.27551	78.85	100.58	0.012	-13.34
0.79589	1.28073	67.66	86.65	0.010	-10.45
0.88785	1.28545	58.36	75.02	0.007	-7.55
0.93801	1.28811	53.94	69.48	0.005	-5.17
		288.15 K			
0.04543	1.24518	127.26	158.46	0.004	-2.63
0.11104	1.24756	118.76	148.16	0.008	-5.36
0.21268	1.25138	106.86	133.72	0.014	-8.07
0.23016	1.25205	-	-	0.016	-
0.30328	1.25492	96.63	121.27	0.019	-10.07
0.39825	1.25879	86.86	109.34	0.022	-11.03
0.49701	1.26299	77.03	97.29	0.023	-11.68
0.61322	1.26818	66.61	84.48	0.022	-11.08
0.68937	1.27174	60.11	76.44	0.019	-10.32
0.79589	1.27693	51.95	66.34	0.015	-8.13
0.88785	1.28163	45.45	58.25	0.009	-5.60
0.93801	1.28428	42.72	54.86	0.006	-3.20
		293.15 K			
0.04543	1.24178	95.44	118.52	0.005	-1.36
0.11104	1.24412	90.07	112.06	0.012	-2.47
0.21268	1.24787	81.49	101.69	0.023	-4.56
0.30328	1.25136	74.16	92.78	0.029	-6.07
0.39825	1.25518	67.02	84.12	0.033	-6.99
0.49701	1.25933	60.23	75.85	0.035	-7.20
0.61322	1.26447	52.73	66.67	0.034	-6.91
0.68937	1.26800	48.35	61.31	0.030	-6.06
0.79589	1.27315	42.33	53.90	0.024	-4.79
0.88785	1.27783	37.27	47.62	0.015	-3.56
0.93801	1.28048	35.08	44.92	0.008	-2.17
		298.15 K			
0.04543	1.23837	74.08	91.74	0.008	-0.84
0.11104	1.24066	70.06	86.92	0.019	-1.68
0.21268	1.24434	63.88	79.49	0.034	-2.95
0.30328	1.24778	58.59	73.11	0.043	-3.84
0.39825	1.25155	53.02	66.36	0.049	-4.82
0.49701	1.25566	47.90	60.15	0.051	-5.05
0.61322	1.26075	42.30	53.33	0.049	-4.82
0.68937	1.26426	39.03	49.35	0.043	-4.18
0.79589	1.26939	34.49	43.78	0.033	-3.28
0.88785	1.27406	30.61	39.00	0.019	-2.49
0.93801	1.27670	28.86	36.85	0.011	-1.60

Tabla 15. Continuación.

X	ρ / g cm^{-3}	ν / mm^2 s^{-1}	η / mPa s	V^E / cm^3 mol^{-1}	$\Delta\eta$ / mPa s
		303.15 K			
0.04543	1.23510	58.61	72.39	0.011	-0.61
0.07610	1.23615	-	-	0.016	-
0.11104	1.23734	55.53	68.71	0.025	-1.26
0.21268	1.24095	50.95	63.23	0.044	-2.06
0.30328	1.24432	46.90	58.36	0.056	-2.75
0.39825	1.24803	42.73	53.32	0.063	-3.42
0.49701	1.25208	39.06	48.90	0.066	-3.29
0.61322	1.25711	34.54	43.42	0.063	-3.42
0.68937	1.26058	32.04	40.39	0.056	-2.94
0.79589	1.26567	28.53	36.11	0.042	-2.31
0.83359	1.26754	-	-	0.036	-
0.88785	1.27031	25.49	32.38	0.024	-1.81
0.93801	1.27293	24.09	30.67	0.014	-1.21
		308.15 K			
0.04543	1.23154	47.33	58.29	0.013	-0.27
0.07610	1.23256	-	-	0.022	-
0.11104	1.23374	44.81	55.29	0.032	-0.93
0.21268	1.23731	41.34	51.16	0.053	-1.45
0.30328	1.24066	38.19	47.38	0.066	-2.00
0.39825	1.24433	35.00	43.56	0.075	-2.44
0.49701	1.24836	32.19	40.18	0.077	-2.30
0.61322	1.25337	28.64	35.90	0.073	-2.45
0.68937	1.25682	26.67	33.52	0.066	-2.12
0.79589	1.26190	23.90	30.15	0.049	-1.69
0.88785	1.26654	21.50	27.23	0.028	-1.34
0.93801	1.26917	20.43	25.93	0.015	-0.85
		313.15 K			
0.04543	1.22813	38.80	47.65	0.017	-0.07
0.07610	1.22913	-	-	0.027	-
0.11104	1.23030	36.82	45.30	0.037	-0.58
0.21268	1.23381	34.04	41.99	0.062	-1.05
0.30328	1.23711	31.54	39.02	0.078	-1.49
0.39825	1.24074	29.03	36.02	0.088	-1.83
0.49701	1.24472	26.80	33.36	0.091	-1.73
0.61322	1.24969	23.98	29.97	0.086	-1.86
0.68937	1.25312	22.46	28.14	0.077	-1.56
0.79589	1.25817	20.24	25.47	0.058	-1.25
0.88785	1.26279	18.33	23.14	0.034	-1.01
0.93801	1.26541	17.45	22.08	0.019	-0.67

Tabla 16. Parámetros (A_k) obtenidos para un ajuste polinómico en el caso de las propiedades ρ, ν, y con la ecuación de Redlich y Kister (6) para V^E, Δη, así como las desviaciones estándar (s) para el sistema binario (x)[EMIM][BF_4]+(1-x)[EMIM][$EtSO_4$].

Propiedad	A_0	A_1	A_2	A_3	A_4	A_5	A_6	s
				283,15 K				
ρ (g/cm^3)	1.247	0.036	0.007	0.002	-	-	-	0.00001
ν (mm^2·s^{-1})	178.18	-179.10	50.502	-	-	-	-	0.47
η (mPa·s)	222.23	-217.60	59.364	-	-	-	-	0.59
V^E (cm^3·mol^{-1})	0.055	-0.008	0.003	0.039	-	-	-	0.000
Δη (mPa·s)	-62.177	0.949	6.736	-9.520	-54.035	65.973	15.469	0.13
				288,15 K				
ρ (g/cm^3)	1.244	0.035	0.007	0.002	-	-	-	0.00001
ν (mm^2·s^{-1})	133.41	-132.93	38.684	-	-	-	-	0.28
η (mPa·s)	165.93	-161.10	45.566	-	-	-	-	0.35
V^E (cm^3·mol^{-1})	0.092	0.002	-0.019	-0.002	0.026	0.019	-	0.000
Δη (mPa·s)	-46.451	-1.747	-4.849	2.348	-13.404	-	-	0.14
				293,15 K				
ρ (g/cm^3)	1.240	0.035	0.007	0.002	-	-	-	0.00000
ν (mm^2·s^{-1})	99.702	-91.409	24.172	-	-	-	-	0.19
η (mPa·s)	123.67	-110.19	28.186	-	-	-	-	0.24
V^E (cm^3·mol^{-1})	0.140	0.003	0.006	0.016	-0.026	-	-	0.000
Δη (mPa·s)	-29.005	2.458	0.951	-17.328	13.044	7.420	-29.134	0.15
				298,15 K				
ρ (g/cm^3)	1.237	0.034	0.007	0.002	-	-	-	0.00001
ν (mm^2·s^{-1})	77.191	-66.969	16.624	-	-	-	-	0.17
η (mPa·s)	95.481	-80.384	19.257	-	-	-	-	0.22
V^E (cm^3·mol^{-1})	0.204	0.000	0.016	-0.013	-0.057	0.021	-	0.000
Δη (mPa·s)	-20.487	-0.488	13.677	-5.930	-28.451	-1.078	7.597	0.09

Tabla 16. Continuación.

Propiedad	A_0	A_1	A_2	A_3	A_4	A_5	A_6	s
				303,15 K				
ρ (g/cm^3)	1.234	0.033	0.007	0.002	-	-	-	0.00001
ν (mm^2·s^{-1})	60.912	-49.901	11.502	-	-	-	-	0.13
η (mPa·s)	75.146	-59.640	13.222	-	-	-	-	0.17
V^E (cm^3·mol^{-1})	0.263	-0.004	0.015	0.004	-0.070	-	-	0.000
Δη (mPa·s)	-13.986	-0.324	5.686	-3.252	-12.785	-2.612	-	0.13
				308,15 K				
ρ (g/cm^3)	1.230	0.032	0.008	0.002	-	-	-	0.00001
ν (mm^2·s^{-1})	48.992	-38.208	8.361	-	-	-	-	0.11
η (mPa·s)	60.266	-45.462	9.556	-	-	-	-	0.13
V^E (cm^3·mol^{-1})	0.308	-0.001	0.034	-0.034	-0.084	-	-	0.000
Δη (mPa·s)	-9.652	0.153	-1.394	-5.070	-	-	-	0.12
				313,15 K				
ρ (g/cm^3)	1.227	0.032	0.008	0.002	-	-	-	0.00001
ν (mm^2·s^{-1})	40.059	-30.016	6.386	-	-	-	-	0.0
η (mPa·s)	49.142	-35.581	7.282	-	-	-	-	0.12
V^E (cm^3·mol^{-1})	0.365	-0.003	0.006	-0.038	-0.025	-	-	0.000
Δη (mPa·s)	-7.317	0.493	-0.048	-5.870	-	-	-	0.10

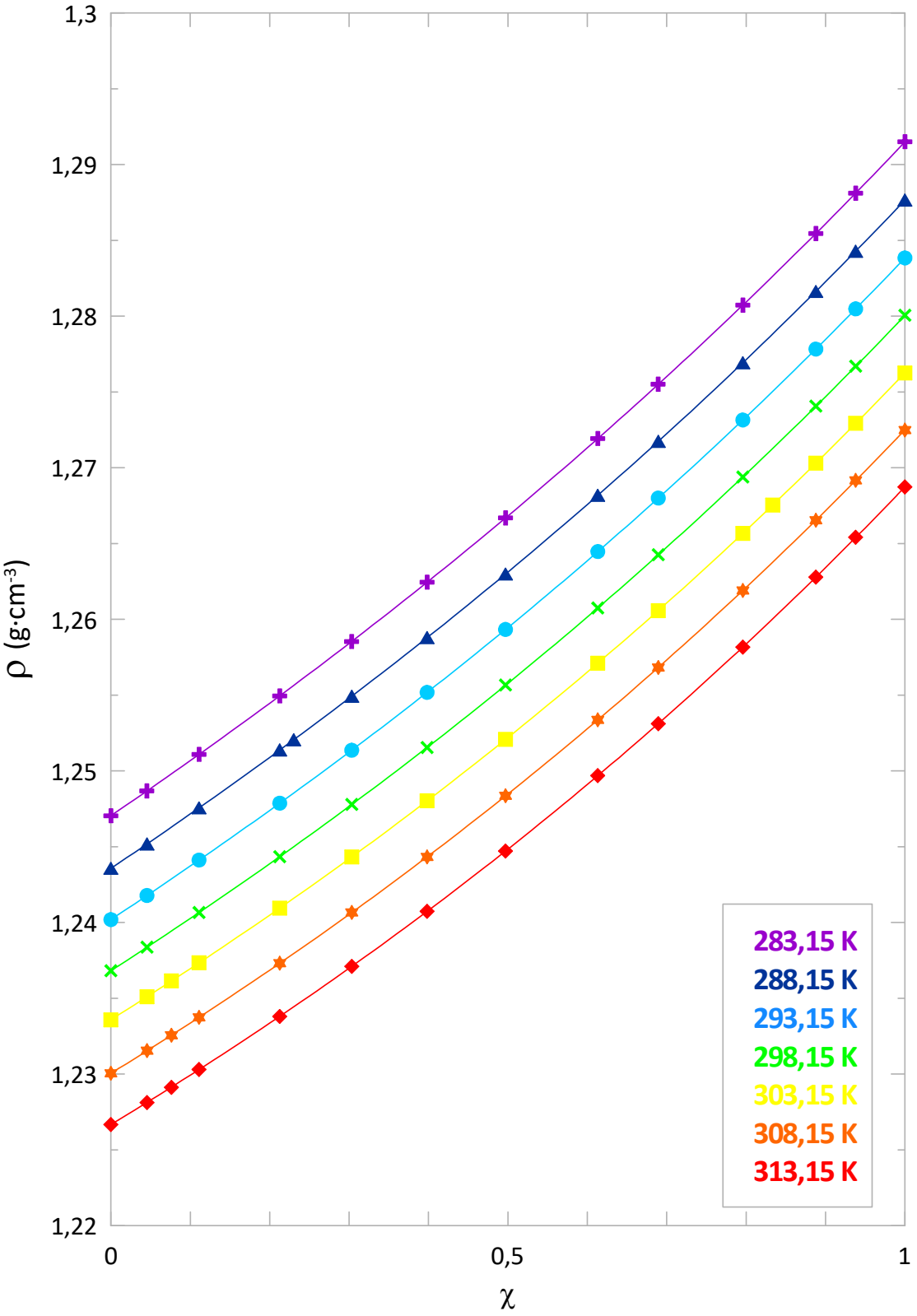

Figura 55. Variación de la densidad del sistema (x)[EMIM][BF_4]+(1-x)[EMIM][$EtSO_4$] en función de la temperatura: (+)283,15K, (▲)288,15K, (●)293,15K, (x)298,15K, (■)303,15K, (*)308,15K, (♦)313,15K.

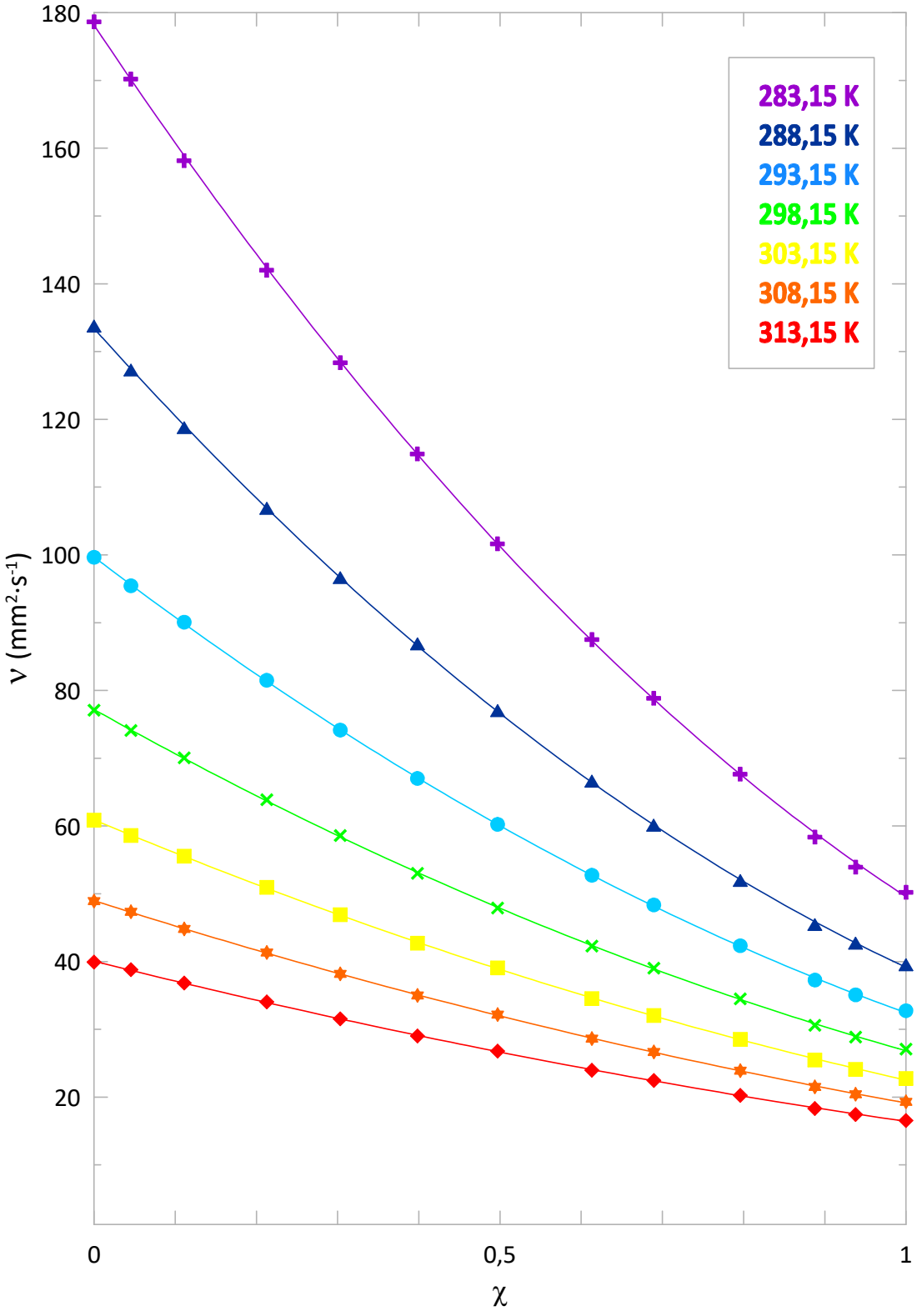

Figura 56. Variación de la viscosidad cinemática del sistema (x)[EMIM][BF_4]+(1-x)[EMIM][$EtSO_4$] en función de la temperatura: (+)283,15K, (▲)288,15K, (●)293,15K, (x)298,15K, (■)303,15K, (*)308,15K, (♦)313,15K.

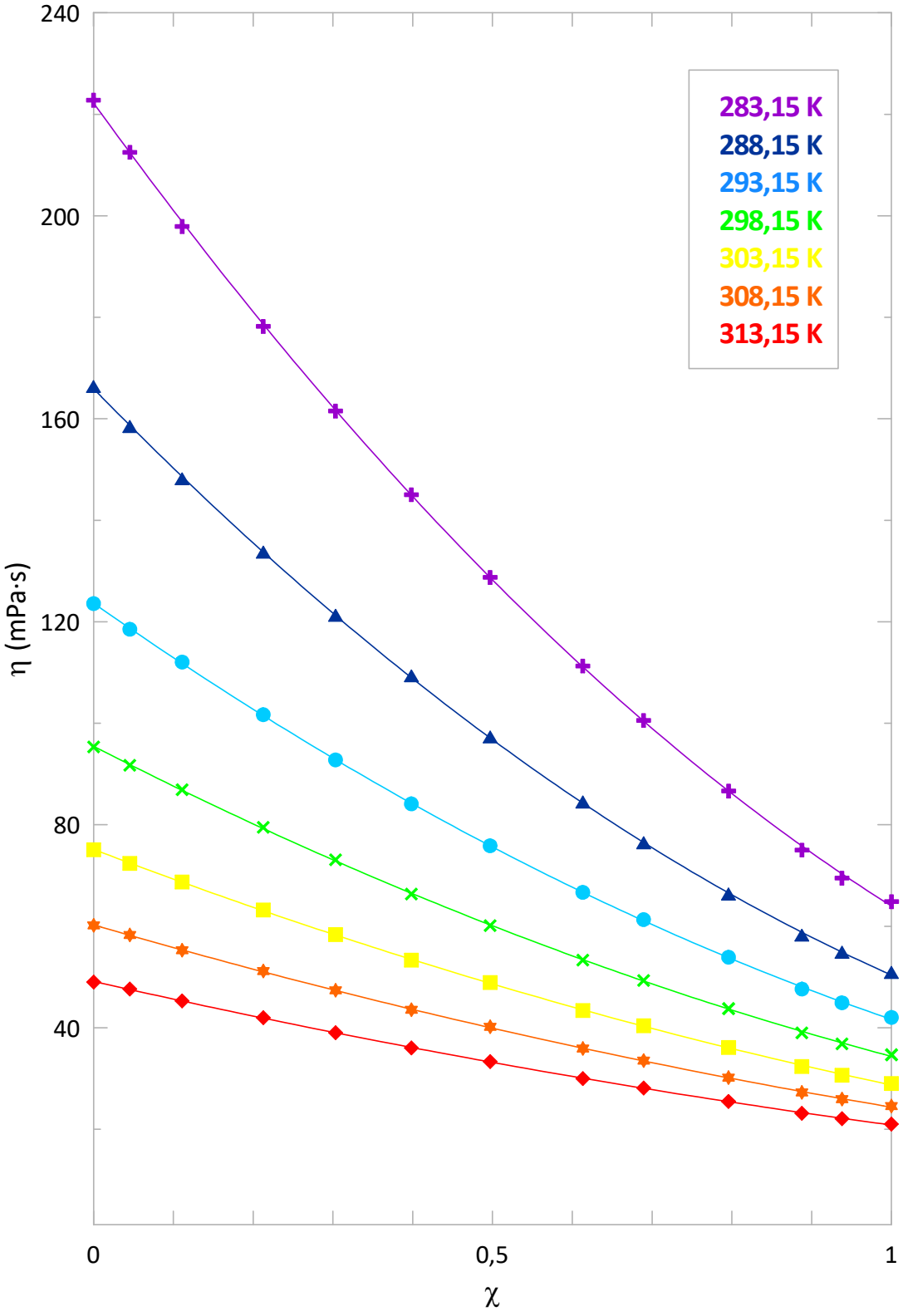

Figura 57. Variación de la viscosidad dinámica del sistema (x)[EMIM][BF_4]+(1-x)[EMIM][$EtSO_4$] en función de la temperatura: (+)283,15K, (▲)288,15K, (●)293,15K, (x)298,15K, (■)303,15K, (*)308,15K, (♦)313,15K.

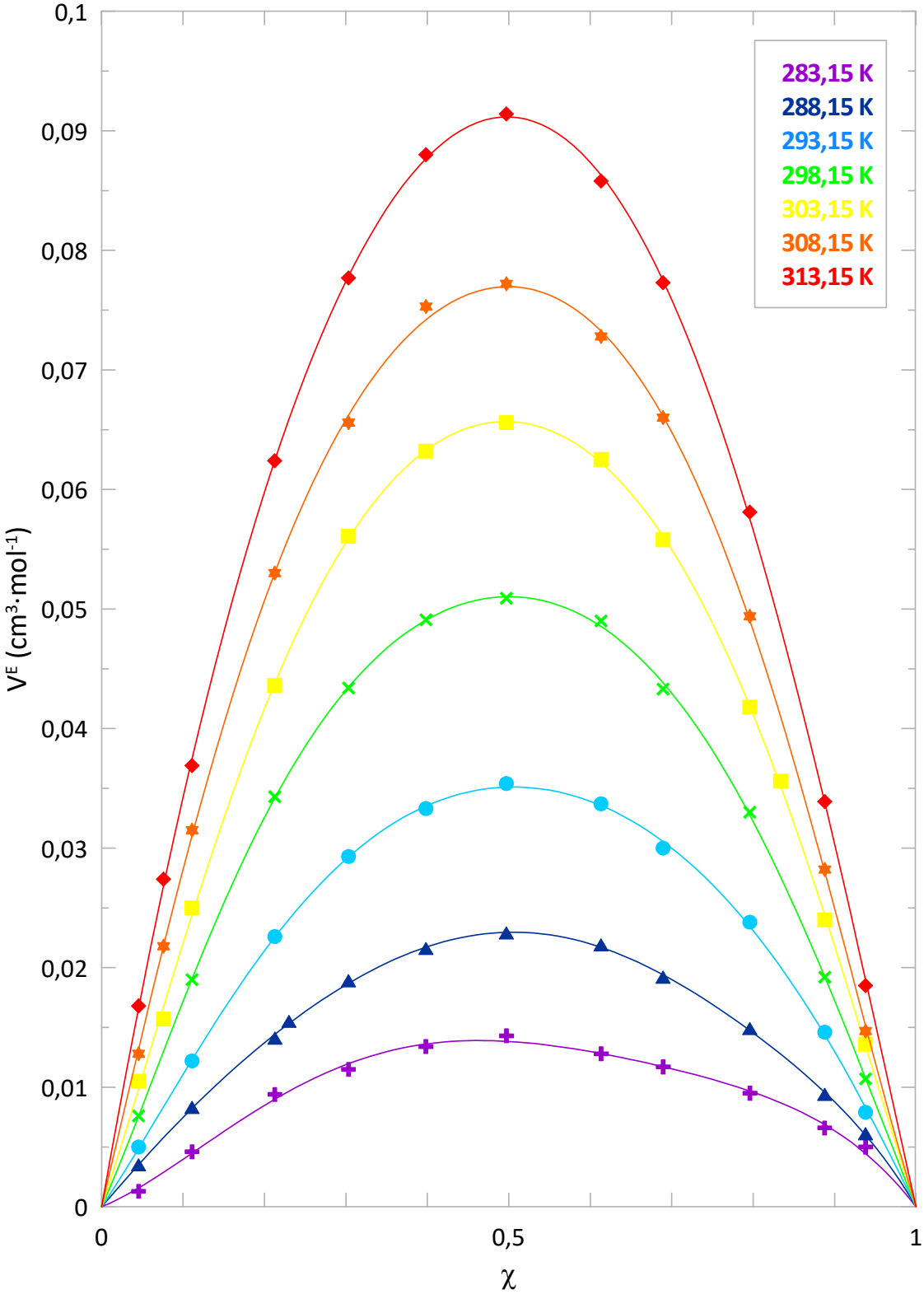

Figura 58. Volumen molar de exceso del sistema (x)[EMIM][BF_4]+(1-x)[EMIM][$EtSO_4$] en función de la temperatura: (+)283,15K, (▲)288,15K, (●)293,15K, (x)298,15K, (■)303,15K, (*)308,15K, (♦)313,15K.

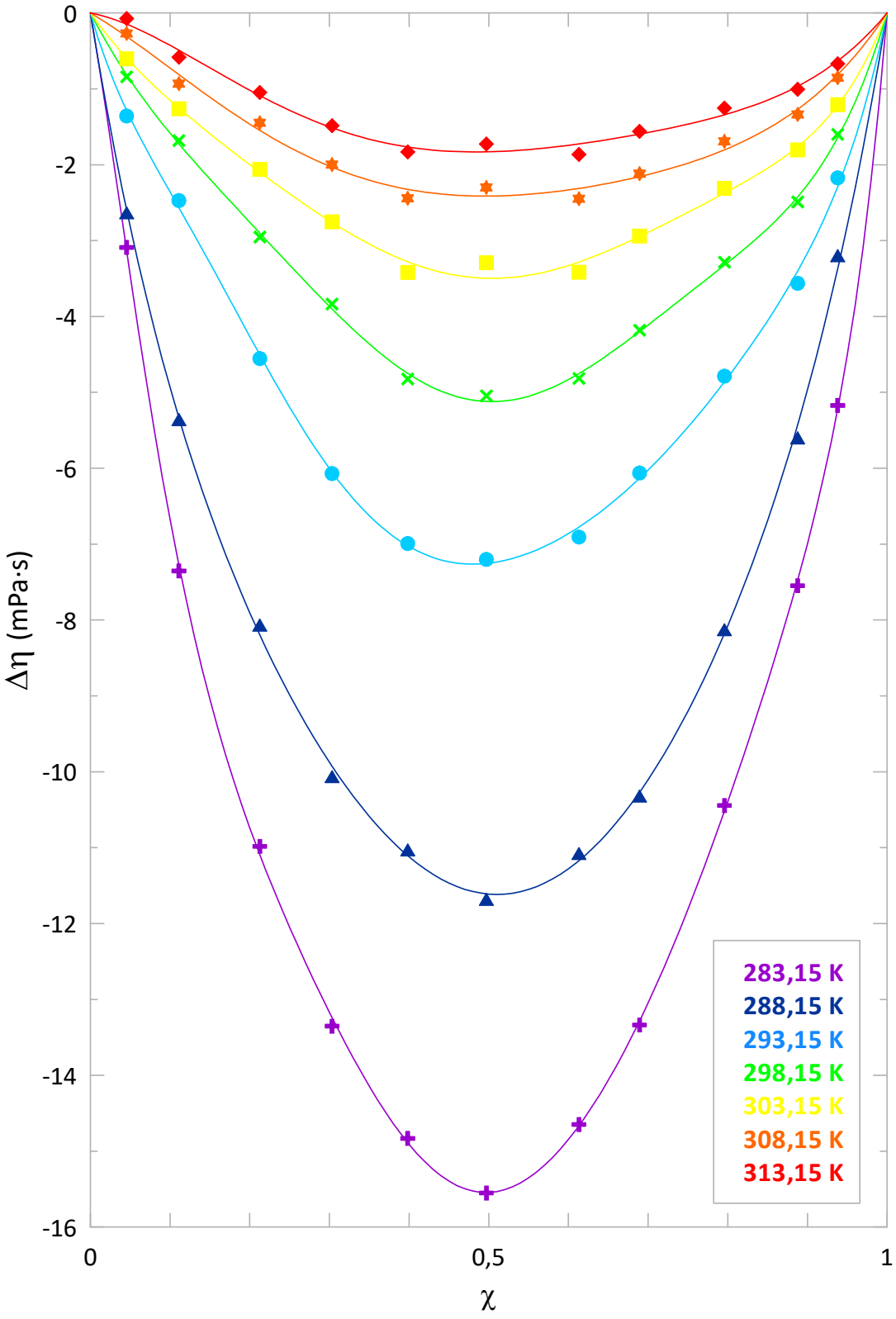

Figura 59. Desviaciones de la viscosidad del sistema (x)[EMIM][BFO₄]+(1-x)[EMIM][EtSO₄] en función de la temperatura: (+)283,15K, (▲)288,15K, (●)293,15K, (x)298,15K, (■)303,15K, (*)308,15K, (♦)313,15K.

5.1.3. Publicación II

Título:	**Unveiling the Intermolecular Forces and Unique Properties of [EMIM][$EtSO_4$] + [EMIM][$MeSO_3$]**				
Autores:	Ylenia Rodríguez [a], Santiago Aparicio [b], José L. Trenzado [a]				
Afiliación:	[a]) Departamento de Física, Universidad de Las Palmas de Gran Canaria, 35017 Las Palmas G.C., Spain [b]) Department of Chemistry, University of Burgos, 09001 Burgos, Spain				
Revista:	Journal of Molecular Liquids				
Factor impacto (IF):	6.633	**Cuartil (JRC):**	Q1	**Citas:**	0
Editor:	Elsevier	**Fecha de publicación:**	10/12/2024		

Journal of Molecular Liquids 418 (2025) 126395

Contents lists available at ScienceDirect

Journal of Molecular Liquids

journal homepage: www.elsevier.com/locate/molliq

Unveiling the intermolecular forces and unique properties of [EMIM][$EtSO_4$] + [EMIM][$MeSO_3$]

Ylenia F. Rodríguez [a], Santiago Aparicio [b,*], Jose L. Trenzado [a,*]

[a] Department of Physics, University of Las Palmas de Gran Canaria, 35017 Las Palmas, G.C., Spain
[b] Department of Chemistry, University of Burgos, 09001 Burgos, Spain

ARTICLE INFO

Keywords:
Ionic liquids
Mixtures
Double salts
Physicochemical properties
Intermolecular forces
Molecular dynamics
Cell membranes
Proteins

ABSTRACT

This study delves into the intricate interplay of intermolecular forces governing the archetypal ionic liquid mixture [EMIM][$EtSO_4$] + [EMIM][$MeSO_3$] through a synergistic integration of experimental and computational techniques. High-precision measurements of density, viscosity, and thermal conductivity across a temperature and compositional landscape unveil the system's phase behavior and miscibility. Complementary insights into the microscopic interactions, including hydrogen bonding and ion-specific effects, are gleaned from molecular dynamics simulations and quantum mechanical calculations. This multipronged approach fosters a comprehensive understanding of the underlying forces dictating the observed thermophysical properties, propelling fundamental knowledge in the realm of ionic liquid mixtures and paving the way for the rational design of tailor-made ionic liquids with targeted properties for diverse fields, ranging from chemical engineering to energy storage.

1. Introduction

Ionic liquids (ILs) have emerged as a remarkable class of solvents, capturing the attention of researchers across diverse scientific disciplines with their unique blend of physical and chemical properties. Although one of the most popular origins of ionic liquids dates to 1914 [1,2], it was not until the last years of the twentieth century when the interest in this type of solvent was grown. In 1998 Michael Freemantle started to write some reports in *Chemical & Engineering News*, where introduced the idea of "design solvent". This concept was grounded on the notion that vast collection of cation–anion combinations is available to generate a huge number of ionic liquids, allowing the selection of an ionic liquid with ideal properties for any given application [1,2]. It is estimated that there are 10^{19} ILs potentially available, while less than 1600 have been already characterized [3].

Among the general features that can be pointed out about the properties of these solvents included low vapor pressure or non-volatility under ambient conditions, wide liquid temperature ranges or long-range thermal stability [3]. However, the potential of these solvents is not found only in their general characteristics, but also the capacity to adapt their properties modifying the cation–anion combination. The structures of ILs are determined by different intermolecular interactions, such as Coulombic forces, dispersion interactions, H-bonding and p-interactions. Understanding the molecular-level arrangement in a mixture of different ILs is challenging, but it can be very important for designing this solvent [4,5]. Viscosity is one of the most important and studied property of ILs, it was observed that the anion structures have more effect on the viscosity than cation structure [6,7]. Regarding other pivotal property as IL melting point, it has been reported that it tends to decrease when increasing alkyl chain lengths for short chains (up to C4) and increasing the anion size, but increases again for long chains (more than C10) [8–10]. In general, the alkyl chain length in imidazolium cation has a large effect on ILs liquids [11], both in their physicochemical properties as well in the anion-cation hydrogen bonding leading to the formation of ionic pairs. Likewise, long hydrocarbon chain lead to remarkable hydrophobic character [12].

Related with ILs vaporization, although ILs vapor pressure may be considered as negligible in comparison with Volatile Organic Compounds [13], some groups observed that vapor pressure to increase with increasing alkyl chain length in the cations [14,15].

But in the real benefit of understanding how the cation–anion combination impact in their properties, is the ability to be tunable according to their field of application. This unique property has made ILs interesting materials for multiple applications in very diverse areas, such as

* Corresponding authors.
E-mail addresses: sapar@ubu.es (S. Aparicio), jose.trenzado@ulpgc.es (J.L. Trenzado).

https://doi.org/10.1016/j.molliq.2024.126395
Received 13 February 2024; Received in revised form 5 September 2024; Accepted 28 October 2024
Available online 1 November 2024
0167-7322/© 2024 Published by Elsevier B.V.

polymer for gas separation membranes, carbon dioxide adsorbents and separation, stationary phase in gas–liquid chromatography, electrolytes for batteries, electrolytes for electrochemical supercapacitors, catalysts and catalyst supports, lubricants or additives, based antimicrobial additives, separation agents to break azeotropic mixtures, and recently int the development of pharmaceuticals [2,5,16]. In catalysis, ILs have emerged as green alternatives to conventional organic solvents, often employed in reactions that were traditionally carried out under hazardous conditions [17]. Their ability to dissolve a wide range of compounds, coupled with their low volatility, enhances the efficiency and sustainability of various catalytic processes. Furthermore, ILs have shown immense potential in electrochemical applications, such as electrolytes in batteries and supercapacitors, owing to their wide electrochemical windows and low flammability [18].

Among the vast array of ILs, those based on the 1-ethyl-3-methylimidazolium ([EMIM]) cation have garnered significant attention. The versatility of the [EMIM] cation, combined with a diverse range of anions, offers a rich palette for tailoring IL properties [19,20]. Likewise, the general class of imidazolium-ILs have been considered for a plethora of technological applications such as CO_2 capture [21], catalysis [22], polymers [23], petrochemical for oil–water separation operations [24], batteries [25], or pharmaceutical applications [26], among others.

In this paper, we delve into the investigation of a binary IL mixture, [EMIM][EtSO4] + [EMIM][MeSO3], to unravel the intricate interplay of molecular forces and thermophysical properties within this specific system. Although there are many articles published on the study of ionic liquids individually, very few authors have analyzed the behavior of combinations of ILs [27,28]. The choice of [EMIM][EtSO4] + [EMIM][MeSO3] as the subject of this study is driven by its relevance to both industrial and technological applications. In particular, [EMIM][EtSO4] have been considered for extraction of natural compounds from vegetal sources [29], catalysis [30], protein engineering [31], or energy storage applications [32]. For [EMIM][MeSO3], technological application such as gas treatment operations [33], aromatics separation [34], or dehydrogenation operations [35].

The subtle variation introduced by the combination of ethyl sulfate ([EtSO4]) and methyl sulfonic acid ([MeSO3]) anions in this binary mixture may yield unique properties, influencing its behavior in unanticipated ways. Comprehending the thermodynamic and structural aspects of this binary IL system is essential for harnessing its potential in practical applications, such as energy storage devices, gas separations, and green solvents.

The significance of IL mixtures lies in the emergence of novel properties arising from the combination of different ILs [19]. Binary or ternary mixtures can exhibit synergistic effects, leading to enhanced or novel properties not exhibited by the individual components. This paper's focus on [EMIM][EtSO4] + [EMIM][MeSO3] aims to contribute to the understanding of how specific combinations of cations and anions influence the overall behavior of IL mixtures by using a combined experimental and molecular modelling approach for the study of [EMIM][EtSO4] + [EMIM][MeSO3] IL mixtures (*double salt* ILs) in the whole composition range. The main novelty of the considered work stands on the combination of experimental and computational studies for the complex IL mixture to provide: (i) accurate thermophysical properties required for process design purpose, (ii) characterize anion – cation hydrogen bonding in the mixture(s) via quantum chemistry studies, (iii) study nanoscopic structuring and dynamics via Molecular Dynamics (MD) Simulations, and (iv) analyzed the safety of the considered systems vis simulations of the interaction with target biological molecules. This wide range approach allows a multiscale characterization of the considered mixed ILs, studying their functionality, properties and safety.

2. Methods

2.1. Chemicals

Pure ILs used for the experimental study, [EMIM][EtSO4] and [EMIM][MeSO3], were used without further purification. The sources of ILs, their CAS number, purities, and molar mass are listed in Table S1 (Supplementary Information). Prior to use ILs were degassed by ultrasound and they were kept in a dry, dark place in delivery bottles. The preparation of the binary mixtures was carried out in the full composition range (x [EMIM][EtSO4]+ $(1-x)$ [EMIM][MeSO3], where x stands for mole fraction) into airtight glass vials and the appropriate masses were measured gravimetrically using Mettler Toledo balance (Model AE240, ±0.01 mg) with a stated accuracy to $\pm 4 \cdot 10^{-4}$ g cm^{-3}. Density, ρ, and kinematic viscosity, ν, measurements for pure ILs and binary mixtures were performed as a function of temperature in the 283.15–313.15 K range, in 5 K steps at atmospheric pressure, and compared with literature (Table S2, Supplementary Information), showing suitable agreement. Therefore, the presence of relevant impurities was discarded; differences can be attributed to water content and different origin of the samples.

2.2. Apparatus and procedures

The experimental properties (Table S3, Supplementary Information) ere density and dynamic viscosity. Density measurements were performed with a vibrating tube densimeter model DMA5000 (Anton Paar, uncertainty $1 \cdot 10^{-4}$ g cm^{-3}), with Peltier control for the cell temperature (uncertainty 0.01 K). Prior to performed the assays, the densimeter was calibrated with suitable reference standards. Approximately 1 mL of sample were necessary to fill the tube, which was carefully introduced using a syringe to prevent the formation of bubbles. The thermal expansion coefficient, α_p, was calculated according to its thermodynamic definition:

$$\alpha_p = -\frac{1}{\rho}\left(\frac{\partial \rho}{\partial T}\right)_p = -\frac{1}{\rho}a \tag{1}$$

where a is the slope of the corresponding ρ vs temperature linear fit.

Kinematic viscosity was measured at atmospheric pressure using several Ubbelohde viscometers. The viscometer was immersed in a circulating water bath with a cell temperature (CT-52, Schott Instruments, ± 0.01 K uncertainty) and an automatic control unit (AVS350, Schott, ViscoSystem®, ± 0.01 s uncertainty). Experiments were repeated three times at each temperature for all compositions and the results were averaged. Dynamic viscosity (η) of the mixtures were calculated as in Eq. (2).

$$\eta = \nu\rho \tag{2}$$

The evolution of viscosity with temperature was described according to the Vogel-Fulcher-Taman (VFT) model as in Eq. (3), Table S4 (Supplementary information). VFT fitting parameters were used for the calculation of Angell's strength (fragility measurement) parameter, D_f, according to expression (4).

$$\eta = \eta_0 exp\left(\frac{B}{T - T_0}\right) \tag{3}$$

$$D_f = \frac{B}{T_0} \tag{4}$$

The excess molar volume, V^E, for a binary mixture was calculated as:

$$V^E = \frac{\sum_{i=1}^{2} x_i M_i}{\rho} - \sum_{i=1}^{2} x_i \frac{M_i}{\rho_i} \tag{5}$$

where M_i is the molar mass of the component i, ρ_i and ρ the densities of the pure compound i and for the corresponding mixture, respectively.

Excess thermal expansion coefficient, α_p^E, was defined as:

$$\alpha_p^E = \alpha_p - \sum_{i=1}^{2} \varphi_i \alpha_{p,i} \tag{6}$$

where α_p and $\alpha_{p,i}$ are the thermal expansion coefficients of the mixture and pure component i, respectively; φ_i stands for the volume fraction of component i, φ_i:

$$\phi_i = \frac{x_i V_i^*}{\sum_{i=1}^{2} x_i V_i^*} \tag{7}$$

where x_i stands for the mole fraction of i component and V_i^* for the molar volume of pure i compound. Regarding viscosity, it is no possible to defined an ideal reference state, so excess property could not be considered, the so-called mixing viscosity, $\Delta\eta$, was calculated according to:

$$\Delta\eta = \eta - \sum_{i=1}^{2} x_i \eta_i \tag{8}$$

Experimental density, ρ, kinematic viscosity, ν, dynamic viscosity, η, excess molar volume, V^E, and mixing viscosity, $\Delta\eta$, are reported in Table S3 (Supplementary Information). The excess properties and changes of mixing were correlated at each temperature as a function of mole fraction by means of empirical Redlich–Kister polynomials:

$$Y^E = x(1-x)\sum_{i=0}^{n} A_i (1-2x)^i \tag{9}$$

Additionally, the partial molar volume $\overline{V}_i$ of each i – component was calculated:

$$\overline{V}_i = V_m^E + V_i^* + (1-x_i)\left(\frac{\partial V^E}{\partial x_i}\right)_{T,P} \tag{10}$$

where V_i^* stands for the molar volume of pure component i, with the partial derivative of excess volume calculated from the corresponding Redlich-Kister coefficients. Excess partial molar volumes, $\overline{V}_i^E$, were calculated:

$$\overline{V}_i^E = \overline{V}_i - V_i^* \tag{11}$$

The partial molar volumes at infinite dilution, $\overline{V}_i^{E,\infty}$ were defined as:

$$\overline{V}_i^{E,\infty} = \overline{V}_i^{\infty} - V_i^* \tag{12}$$

The partial molar volume at infinite dilution, $\overline{V}_i^{\infty}$, is defined as the corresponding limiting value when $x_i \to 0$. Correlation of relevant thermophysical properties and the fit coefficient to a polynomial model or to Redlich-Kister function are reported in Tables S5 (Supplementary Information). Likewise, modelling of volumetric properties of the mixtures (excess volume) was carried out according to the Prigogine – Flory – Patterson (PFP) [36] (parameters in Table S6, Supplementary Information).

2.3. Density functional theory calculations

Density functional theory (DFT) calculations using Dmol3 software [37] were employed to investigate intermolecular interactions, particularly hydrogen bonding, within anion-cation clusters in the IL mixtures. Different types of clusters were studied and their geometries optimized via energy minimization considering Double Numerical with Polarization (DNP) basis set with with GGA/PBE functional and Grimme's D3 dispersion correction level [38]. Interaction energies (ΔE) were calculated as the difference between cluster and monomer energies, corrected for basis set superposition error (BSSE) using the counterpoise method [39].

Topological analyses of optimized clusters were performed using Bader's QTAIM theory [40] implemented in MultiWFN software [41]. The electron density (ρ_e) and Laplacian of the electron density ($\nabla^2\rho_e$), of bond (BCPs, type (3,-1) in QTAIM) and Ring (RCPs, type (3,-1) in QTAIM) critical points were considered. Additionally, electron localization function (ELF) with Core-valence bifurcation index (CVB) [42]) were utilized as well as Natural Bond Orbital (NBO) analysis of interionic interacting regions.

2.4. Classical molecular dynamics simulations

Classical MD simulations were performed using MDynaMix v.5.2 software [43]. Force field parameters for the three ion types: $[EMIM]^+$, $[BF4]^-$, and $[EtSO4]^-$ (Table S7, Supplementary Information), were sourced from the SwissParam database (Merck Molecular Force Field [44])), except for atomic charges. These were computed via DFT calculations using the ChelpG method. Simulation boxes (Table S8, Supplementary Information) covered the entire mixture composition range and various pressure–temperature conditions to analyze their impact on mixture properties. Initial cubic boxes were prepared with Packmol software [45]. All MD simulations followed a two-step procedure: *i*) NVT simulations: Performed at 303 K for 10 ns, followed by *ii*) NPT simulations: Performed at 303 K and 1 bar for 200 ns, used for property analysis. Periodic boundary conditions were applied in all three spatial directions. The equations of motion were solved using the Tuckerman–Berne double time step algorithm [46] with 1.0 and 0.1 fs for long and short steps, respectively. Electrostatic interactions were treated with the Ewald method [47] using a 15 Å cutoff radius. Lennard-Jones potential (15 Å cutoff) with Lorentz-Berthelot mixing rules was used for cross terms. Temperature and pressure were controlled with the Nose-Hoover method [48]. VMD [49] and TRAVIS [50] softwares were used for trajectory visualization and analysis.

2.5. COSMO calculations

The DFT optimized structures for isolated ions, cation – anion dimers, and cation – anion larger aggregates were considered for the calculations of COSMO files at BP86/def-TZVP theoretical level for COSMOtherm and COSMOperm calculations using COSMOthermX software [51]. The use of BP86/def-TZVP theoretical level for COSMO instead of DNP/GGA/PBE-D3 used for DFT calculations in Section 2.3 is a requirement of the considered COSMO parameterization, which is developed for exactly that theoretical level.

Possible biological effects of the developed IL clusters were studied analyzing their cell membrane permeability was studied considering COSMOperm [52]. The lipid Dipalmitoylphosphatidylcholine (DPPC) was considered as a simplified model for lipid bilayers composition and thus, the permeability of the considered ionic clusters as well as free energy profiles for the permeation in the bilayer was calculated.

2.6. Protein docking

A set of 102 human proteins (Table S9, Supplementary Information), covering different families to infer possible mechanisms of interactions, were selected for docking calculations. All the protein structures were obtained from the Protein Databank, with the structure for both proteins and nanoparticles, were prepared with PlayMolecule – ProteinPrepare: a protein preparation app for MD simulations – [53] and Autodock Tools with Gasteiger charges considered for all the aforementioned systems. The *rigid ligand* and *rigid receptor docking* calculations were carried out with Autodock Vina [54].

3. Results and discussion

3.1. Macroscopic and thermodynamic characterization

Experimental density and kinematic viscosity were measured for pure $[EMIM][EtSO_4]$ and $[EMIM][MeSO_3]$ and all composition range of their binary mixtures, between temperatures from 283.15 to 313.15 K.

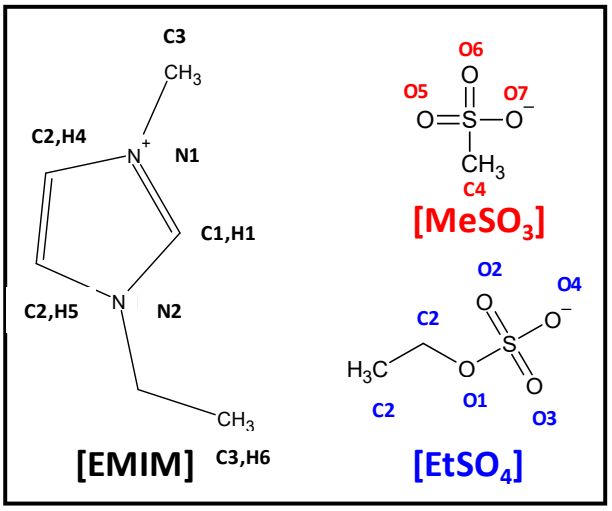

Fig. 1. Ions forming ILs considered in this work as well as labelling for relevant atoms.

Likewise, derived thermodynamics properties (V^E, $\Delta\eta$, α_p and $\overline{V}_i^E$) were calculated. The results of experimental study and derived properties are reported in Figs. 2–5.

Results in Fig. 2a show the behavior of density as a function of temperature and IL mixture composition. Although both pure ILs exhibit close density values (1.23682 and 1.24078 g cm^{-3} at 298.15 K, for [EMIM][EtSO$_4$] and [EMIM][MeSO$_3$], respectively, Table S2, Supplementary Information), mixture density values do not change linearly with the mole fraction (i.e. non-ideal mixtures from the thermodynamic viewpoint), following a s-shaped evolution, Fig. 2a. In spite of the proximity of the densities for the two pure ILs (0.3 % difference), the density vs mixture mole fraction shows a complex pattern characterized by a maximum at low [MeSO$_3$] ($x = 0.07$) and a minimum at high [EtSO$_4$] content (x = 0.91), thus showing an intricate mixing behavior from the volumetric viewpoint. The density vs mixture composition evolution shows slightly higher density values than linear evolution at [EMIM][MeSO$_3$] rich molar fractions ($x < 0.25$) and lower values than linear evolution at [EMIM][EtSO$_4$] rich mixtures, thus leading to the complex V^E behavior reported in Fig. 2c indicating non-ideal mixing behavior. A sinusoidal V^E behavior being negative for [EMIM][MeSO$_3$] rich mixtures (minimum at $x = 0.14$), and positive for [EMIM][EtSO$_4$] rich molar fractions (maximum at $x = 0.78$) with null V^E from $x = 0.25$ to $x = 0.40$ in function of temperature. Molecular weight and more importantly, the volume occupied by each anion seems to motivate of some deviation. Voluminous and heavy anions only weakly interact, whereas small and light anions provide strong interaction potential due to their higher surface charge density [55,56]. Densification effect and V^E negative values at [EMIM][MeSO$_3$] rich mixtures suggest a higher degree of packing compared to [EtSO$_4$] anions, larger and heavier than [MeSO$_3$] anions. Also, V^E negative values would indicate the presence of stronger molecular interactions [57].

The values of α_p and α_P^E are reported in Fig. 2c and d. The α_p values for pure ILs are very similar ($0.554{\cdot}10^{-3}$ and $0.547{\cdot}10^{-3}$ K^{-1} for [EMIM][MeSO$_3$] and [EMIM][EtSO$_4$] at 298.15 K, respectively), being ILs with [EtSO$_4$] slightly less compressible, due to the larger size of the considered anion. Nevertheless, the α_p vs mixture composition evolution

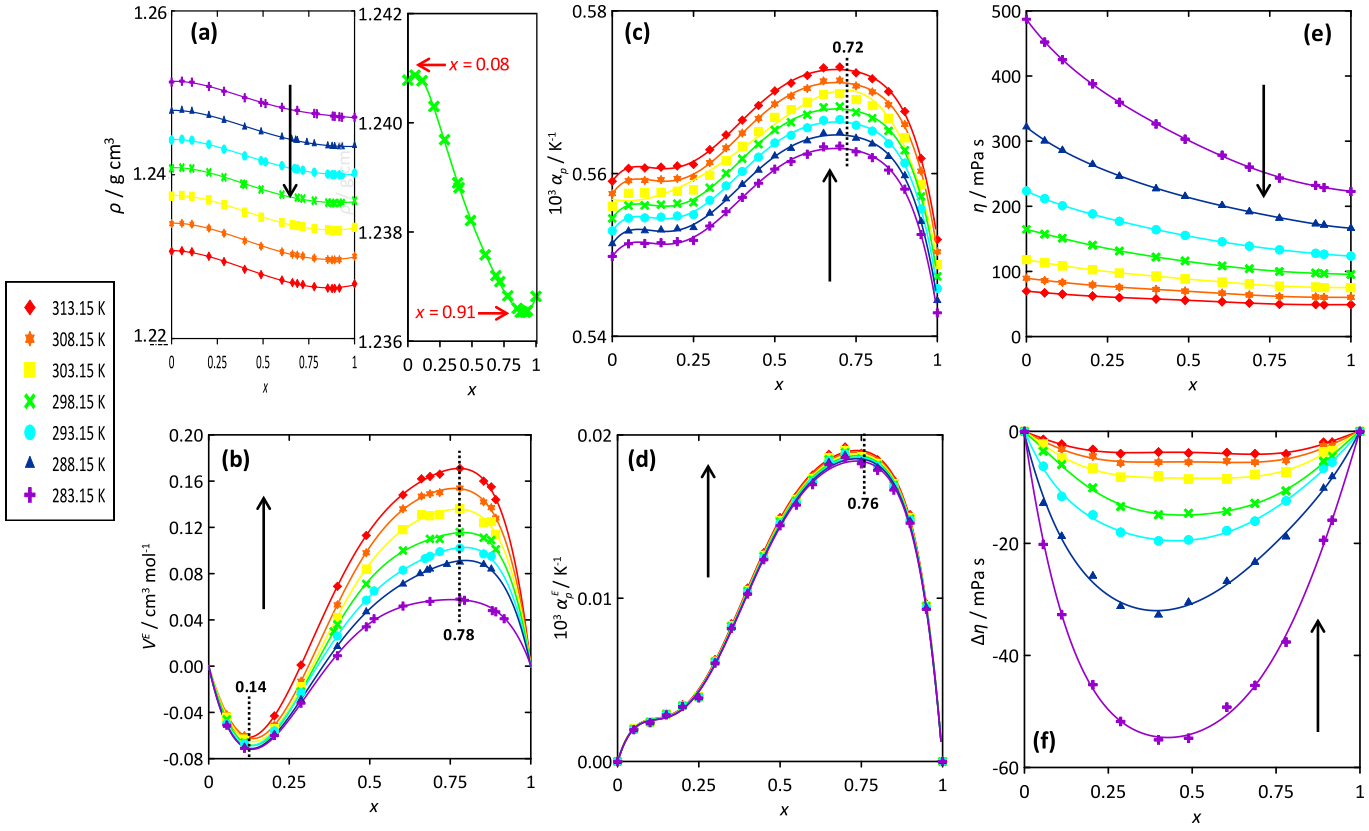

Fig. 2. Experimental thermophysical properties for x [EMIM][EtSO$_4$] + (1 − x) [EMIM][MeSO$_3$], where x stands for mole fraction, as a function of temperature. (a) Density (ρ), (b) excess molar volume (V^E), (c) isobaric thermal expansion coefficient (α_p), (d) excess isobaric thermal expansion coefficient (α_P^E), (e) dynamic viscosity (η), and (f) mixing viscosity ($\Delta\eta$). Black arrows indicate increasing temperature for guiding purposes. Dashed lines in panels b, c, d show equimolar composition to show position of the maxima in the corresponding excess or mixing property. Panel a is divided into two subpanels, to show the non-linear evolution of density with mixture composition.

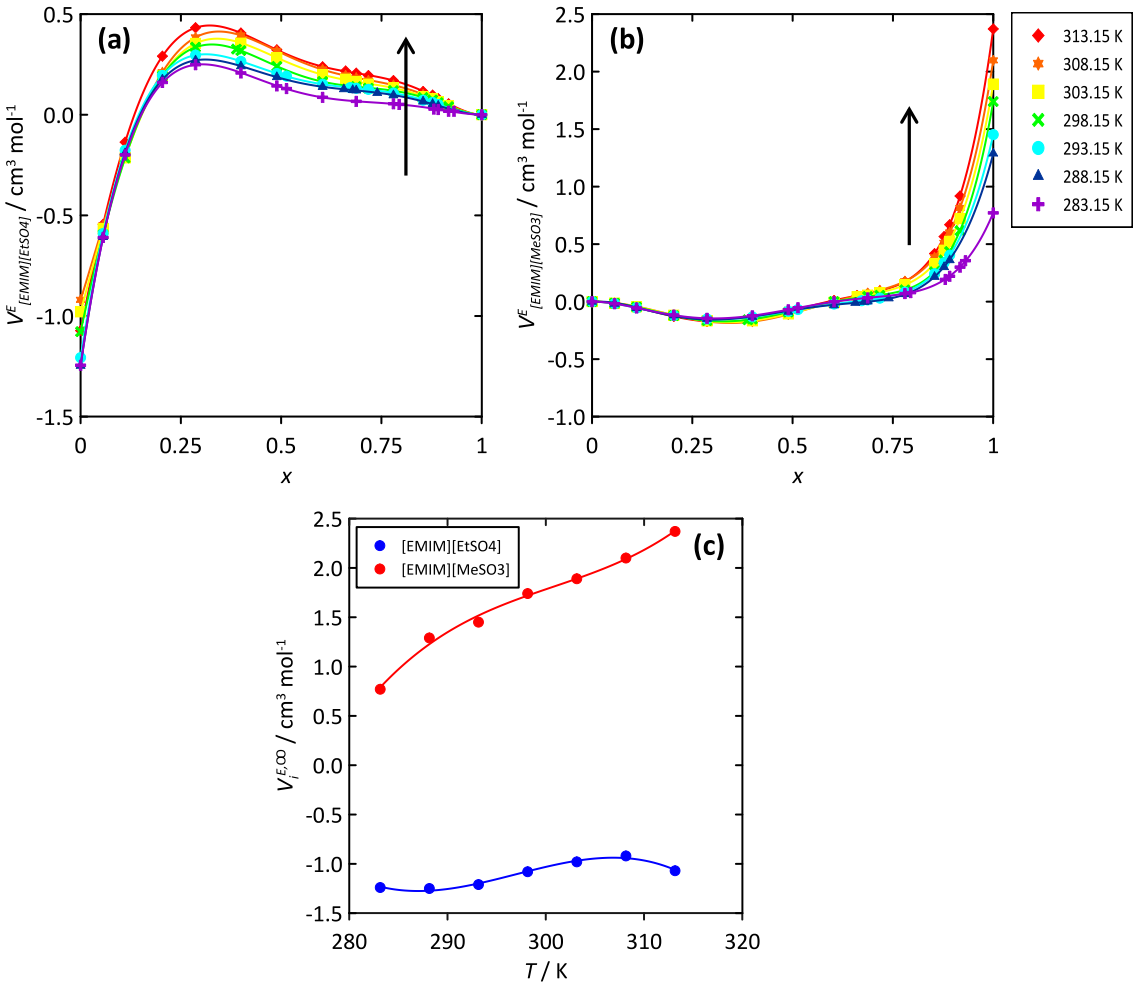

Fig. 3. (a,b) Excess partial molar volume of component *i*, $\overline{V}_i^E$, and (c) values at infinite dilution, $\overline{V}_i^{E,\infty}$, for *x* [EMIM][$EtSO_4$] + (1 − *x*) [EMIM][$MeSO_3$], where stands for mole fraction, as a function of temperature. Black arrows indicate increasing temperature for guiding purposes. Panels a and b show results for [EMIM][$EtSO_4$] and [EMIM][$MeSO_3$], respectively.

evolves through a maximum at $x = 0.72$, [$EtSO_4$] – rich mixtures, which leads to positive α_P^E in the whole composition range, i.e. more compressible mixed fluids confirming the disrupting effect because of the simultaneous presence of both types of anions. Although α_P^E shows very low values, it is almost independent of the temperature. It could be inferred that for [$MeSO_3$] rich mixtures, the addition of [$EtSO_4$] leads to a more compressible liquid.

The viscosity evolution with mixture composition in function of temperature is represented in Fig. 2e. Viscosity temperature changes for both pure ILs and the mixtures do not follow Arrhenius behavior. It should be notice that pure [EMIM][$MeSO_3$] viscosity values are twice higher than [EMIM][$EtSO_4$] values, Table S2 (Supplementary Information). The $\Delta\eta$ are negative and very large in the whole composition and temperature range and decrease upon heating (Fig. 2f). However, the behavior shows some differences according to the temperature ranges studied. For higher temperatures, from 313.15 K to 303.15 K, $\Delta\eta$ values move in narrow scale with slight difference between concentrations. Nevertheless, for temperatures range between 298.15 K and 283.15 K, $\Delta\eta$ become larger, with minimum near to 0.40 mol fraction at the lowest temperature. The viscosity deviations are closely related to the intermolecular interactions, negative viscosity deviation pointing to the weakening of intermolecular forces upon mixing [58], which is a results of the differences in strength for the anion – cation interactions for the two considered anions. The calculated excess partial volumes, $\overline{V}_i^E$, are reported if Fig. 3a and b, and the values at infinite dilution, $\overline{V}_i^{E,\infty}$, Fig. 3c.

$\overline{V}_i^E$ for both ILs present very dissimilar behaviours. The excess partial volume corresponding to [EMIM][$EtSO_4$] shows negative values for mole fraction under approximately $x = 0.20$ regardless of the temperature. These results would indicate that the strong anion-cation coulombic interactions lead to very dense packings with small spaces, allowing efficient packing of [$EtSO_4$] anions into a [$MeSO_3$] – dominated fluid, which agrees with negative V^E [18]. However, for higher concentrations ranges, the values become positive but remain relatively small. Moreover, IL [EMIM][$MeSO_3$] excess partial volume remains near to zero values almost $x = 0.75$ mol fraction in all the temperature range but increase rapidly for higher concentrations of [EMIM][$EtSO_4$], resulting in larger values. This dissimilar behavior for the high dilution mixing region is quantified through $\overline{V}_i^{E,\infty}$ show the disrupting effect of one type of anion on the structuring of the other one. IL [EMIM][$MeSO_3$] presents positive and increasing excess partial volumes according to temperature, but IL [EMIM][$EtSO_4$] shows negative $\overline{V}_i^{E,\infty}$ values in all the temperature range. Therefore, whereas [EtSO4] are able to fit into the holes of [EMIM][$MeSO_3$] rich fluid the opposite behaviour is inferred for [$MeSO_3$], which agrees on the sign of V^E. The poor fitting of [$MeSO_3$] anions into [$EtSO_4$] – rich fluid is even worse upon heating, whereas almost negligible effect for [$EtSO_4$] into [$MeSO_3$] fluid is inferred, Fig. 3c.

In addition, the VFT approach was employed to analyze the viscosity evolution with temperature and mixture composition. The non-linear evolution of the three VFT parameters (Fig. 4a, b and c) is consistent

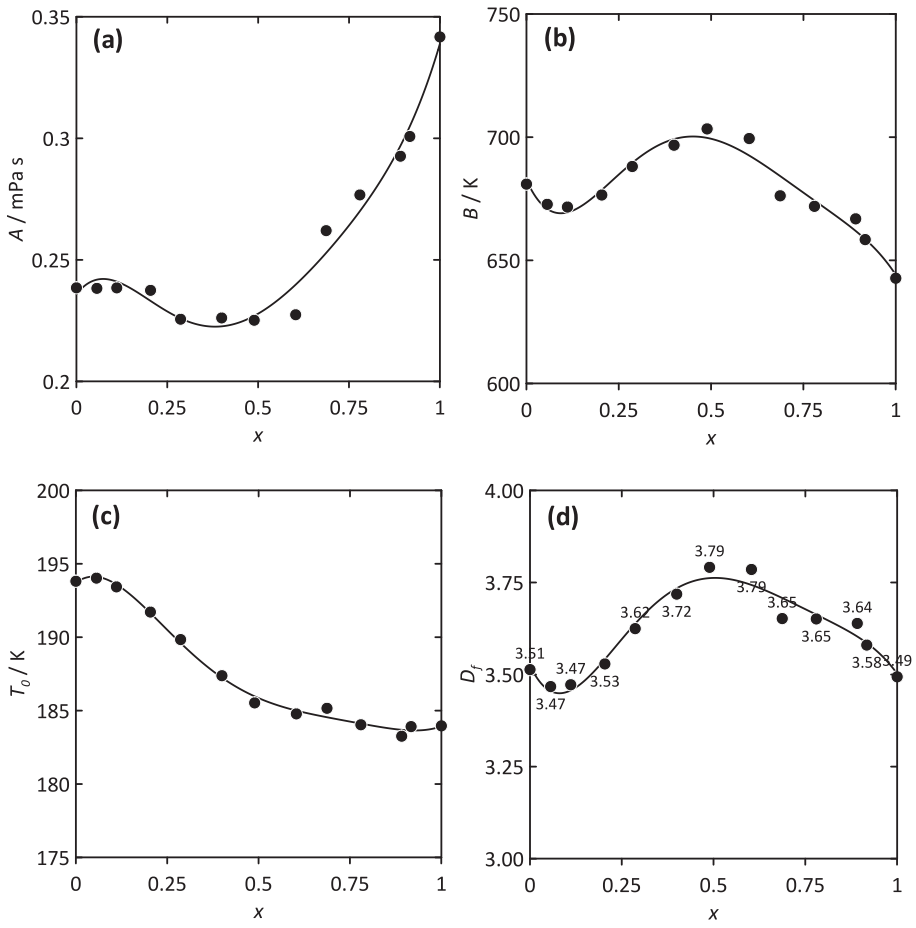

Fig. 4. Fitting parameters of VFT equation for experimental dynamic viscosity, and Angell's fragility parameter, D_f, for x [EMIM][$EtSO_4$] + (1 − x) [EMIM][MeSO3] where stands for mole fraction, in the 283.15 to 313.15 K temperature range.

with other parameters behavior findings reported. The T_0 parameter, which is related to the glass transition temperature, shows maxima close to pure IL [EMIM][$MeSO_3$] and minima near to pure IL [EMIM][$EtSO_4$]. The calculated VFT parameters allowed to infer D_f parameter. For pure ILs are 3.49 and 3.51 for [EMIM][EtSO4] and [EMIM][$MeSO_3$], respectively, so both ILs are fragile ones, with very minor changes upon mixing.

The description of V^E according to PFP model has been carried out using a composition and temperature dependent χ_{12} interaction parameter. The composition dependence of χ_{12}, in contrast with the usual approach in the literature which considers constant χ_{12} [59], rises from the complex shape of V^E which can not be described using a single constant interaction parameter, Fig. 5a. It should be remarked that the interactional contribution, Fig. 5b, is the main one to the total V^E with close to zero free volume contribution. Therefore, V^E is produced by the ionic rearrangements upon mixing to fulfil the most suitable intermolecular forces. The composition evolution of χ_{12} is reported in Fig. 5c, being negative for [$MeSO_3$] – rich mixtures and positive for [$EtSO_4$] ones, i.e. pointing to stronger intermolecular forces for [$MeSO_3$] containing ionic liquids, which also would agree with larger viscosity. The linear temperature evolution of χ_{12} is reported in Fig. 5d, confirming the weakening of intermolecular interactions upon mixing.

3.2. On the nature of hydrogen bonding

DFT was applied to analyze the nature of intermolecular forces, in particular hydrogen bonding, which are present in the considered mixed fluids. For this purpose, two types of clusters were considered: *i*) dimers, i.e. [EMIM]-[$EtSO_4$] and [EMIM]-[$MeSO_3$], as the minimal model for describing anion – cation interactions, and *ii*) large aggregates composed of four anion – cation pairs, i.e. 4 [EMIM] + a [$MeSO_3$] + b [$EtSO_4$], labelled as 4*ab* clusters: 440 (to mimic large clusters in pure [EMIM][$MeSO_3$]), 431 (to mimic x = 0.25 mixtures), 422 (to mimic x = 0.50), 414 (x = 0.75) and 404 (x = 1, pure [EMIM][$EtSO_4$]). The optimized structures of the optimized clusters are reported in Fig. 6. The ΔE values reported in Fig. 6a for anion – cation dimers indicate stronger interactions when [$MeSO_3$] anion is involved. Likewise, hydrogen bonding through H1-imidazolium donor site is stronger than through H4,H5-imidazolium, Fig. 1, although in both cases the QTAIM properties as well as CVB / ELF indicate the formation of strong hydrogen bonds. The formation of 4*ab* clusters leads to an increase of ΔE as quantified per number of hydrogen bond donor, e.g. in the case of neat [EMIM]-[$MeSO_3$] ΔE being −408 kJ/mol evolving to −494.7 kJ/mol in the 400 cluster, i.e. developing of cooperative effects in larger clusters as the formation of additional hydrogen bonds and van der Waals like interactions. In the case of 4*ab* cluster the different content of anions mimic the mixture composition, the corresponding ΔE decreases on going from neat [EMIM][$MeSO_3$] (400 cluster) to neat [EMIM][$EtSO_4$] (440) in a close to linear evolution, Fig. 6a. Therefore, anion – cation interactions beyond simplified dimer structures are characterized by a large network of hydrogen bonds as well as per the development of van der Waals like interactions.

3.3. Nanoscopic characterization of mixed liquid phases

The analysis of mixed ILs liquid structuring at the nanoscopic level considering additional large range effects beyond those interactions studied in the previous section was carried using MD simulation in the

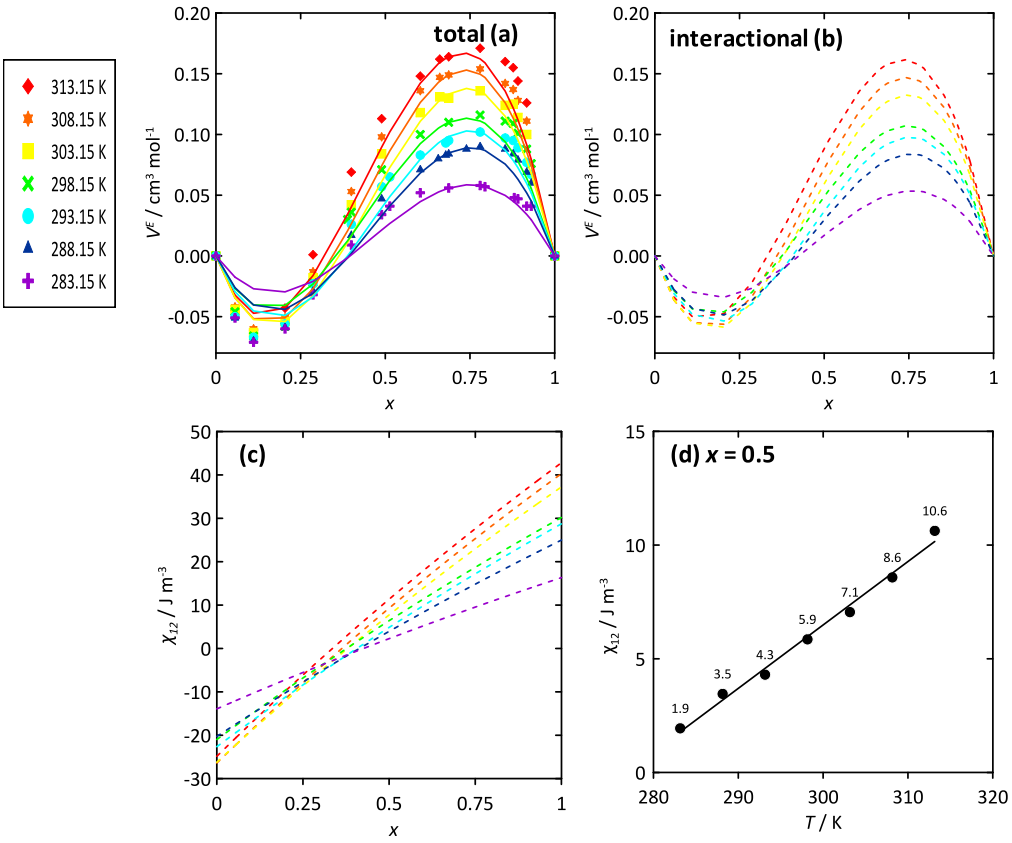

Fig. 5. (a) Comparison of experimental, symbols, and PFP (lines) excess molar volume, V^E, for x [EMIM][EtSO4] + (1 − x) [EMIM][MeSO3]where stands for mole fraction, in the 283.15–313.15 K temperature range. Panel b shows PFP interactional contribution to total excess molar volume. Panel c shows χ_{12} PFP interaction parameter as a function of composition. Panel d shows χ_{12} PFP interaction parameter at equimolar composition as a function of temperature. Parameters required for PFP calculations reported in Table S6 (Supplementary Information).

whole composition range. MD simulations results were firstly analyzed from the structural viewpoint to infer the (ionic) molecular arrangements in the liquid state and the changes with mixture composition. The suitability of the model is analyzed via the comparison of experimental density data with those obtained from MD (Fig. S1, Supplementary Information). MD leads to a slight underprediction of density but deviations with experimental results (−0.8 % on average) as well as the shape of the predicted density vs mixture composition evolution, confirms the model ability to describe the mixed fluids' properties.

The structural analysis of the IL mixtures employed Radial Distribution Functions (RDFs) to probe potential donor–acceptor interactions considering the relevance of hydrogen bonding for IL mixtures in terms of pairing and clustering [60]. A systematic approach based on a connection matrix (*cmat*) was adopted, where relevant interacting pairs were identified and their corresponding RDFs calculated. The first peak of each RDF was characterized by its distance and intensity and assigned a distinct color code, providing a visual representation of the most significant intermolecular interactions within the mixtures, Fig. 7. Hydrogen bonding with [EMIM] may be carried out, Fig. 6, through two C—H sites in the imidazolium ring: (*i*) H1 site (Fig. 1) and (*ii*) H4,H5 sites (Fig. 1), with DFT results showing, Fig. 6, how anion – [EMIM] hydrogen bonds are stronger for the H1 site (C-H1 being the site among the two nitrogen atoms in the imidazolium ring). The *cmat* results confirms that both types of anions are hydrogen bonded via the oxygen atoms both to H1 and H4/H5 donor sites, although the intensity of the (red) spots for interactions with H1 site is larger than for H4/H5, thus confirming a larger number of hydrogen bonds via the H1 site. This mechanism of hydrogen bonding is maintained in the full composition range. The absence of additional relevant spots in the reported *cmats* shows that hydrogen bonding is the driving force for the ion pairing in the studied mixtures with competing effects among the two types of anions. The relevant RDFs for [EMIM]-anion interactions via the H1 ([EMIM]) site are reported in Fig. 8a and b for both types of anions. RDFs are very similar for both anions: a first narrow and intense peak at 2.2 Å (oxygen to hydrogen) separation, corresponding to the hydrogen bonded pairs, followed by a second wider and weaker bang at 6 Å corresponding to cations in the second solvation shell, in agreement with the 4*ab* clusters models proposed in DFT section, indicating alternating cation–anion interacting pairs. The intensity of each peak decreases as the concentration of each anion decreases, pointing to an anion replacement mechanism in the solvation, hydrogen bonded, shells around central [EMIM] donor sites. The integration of RDFs for the first peak, corresponding to the first solvation shell, i.e. anions hydrogen bonded to [EMIM], leads to the solvation shell content, N_{1st}, Fig. 8c. The composition evolution of N_{1st} follows a non-linear evolution for both anions but with a completely different evolution: *i*) for [$MeSO_3$] N_{1st} is larger than the linear evolution, whereas *ii*) for [$EtSO_4$] it is lower, i.e. there is larger number of [$MeSO_3$] anions around [EMIM] than [$EtSO_4$], thus pointing to [$MeSO_3$] enrichment, because of stronger hydrogen bonds, Fig. 6, and leading to the behavior of V^E: negative for [$MeSO_3$] rich region and positive for [$EtSO_4$], as well as for the $\overline{V}_i^{E,\infty}$. This preferential solvation mechanism would be the reason of the complex deviations of ideality reported in Figs. 2 and 3.

Spatial Distribution Functions (SDFs) reported around [EMIM] cation shows further details on the exact solvation mechanism(s), Fig. 9. [$EtSO_4$] and [$MeSO_3$]a re placed around central [EMIM] following slightly different patterns, whereas [$EtSO_4$] follows a more localized distribution around H1 and H5 sites, [$MeSO_3$] shows wider distribution ranges, which would justify the larger number of [$MeSO_3$] in the shell around [EMIM] reported in Fig. 8c. Additionally, [EMIM] cations

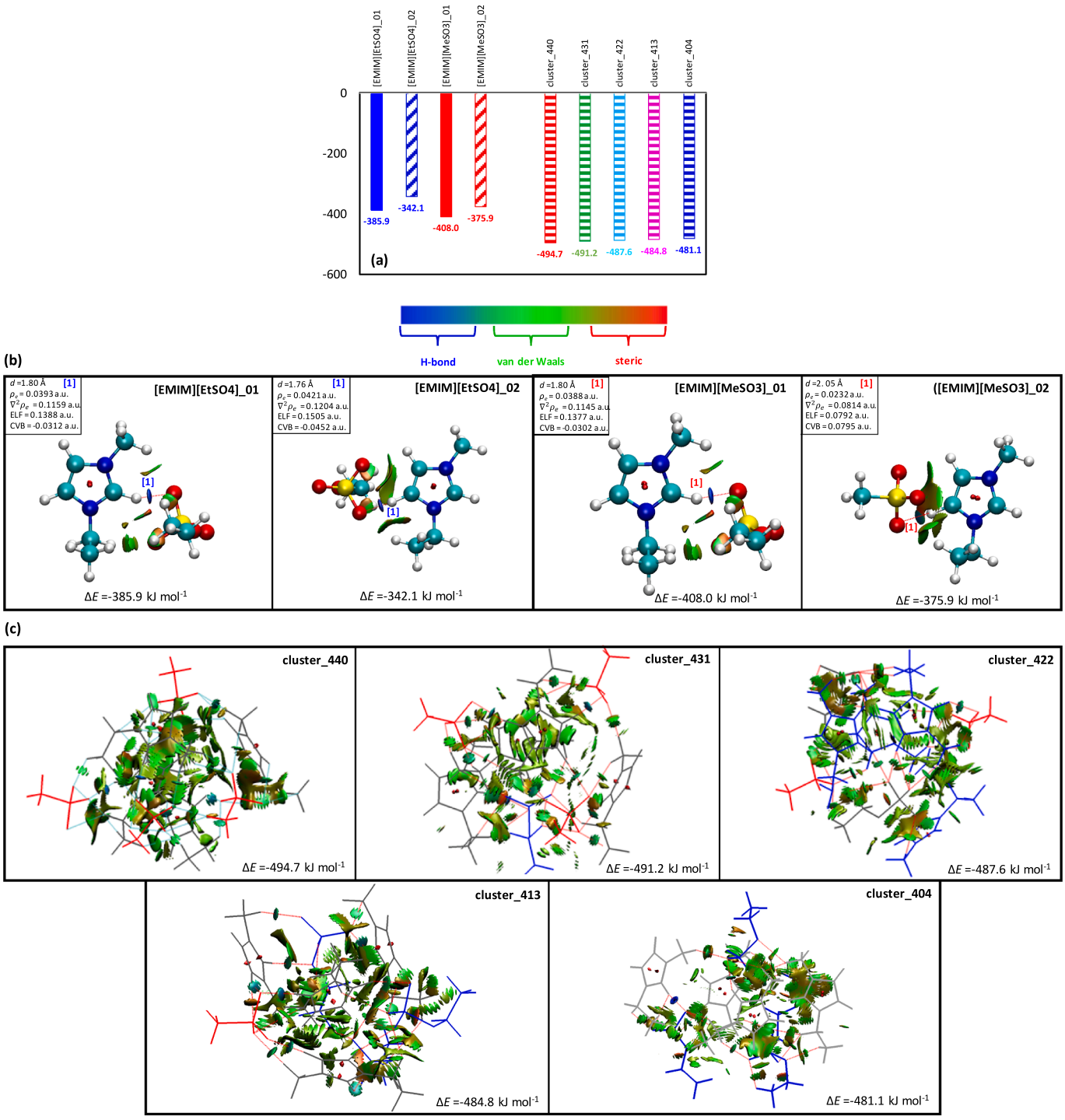

Fig. 6. DFT optimized structures of (a) [EMIM] – [EtSO4] and [EMIM] – [MESO3] 1:1 clusters showing the lowest energy configurations including binding energy, Δ*E*, QTAIM properties (electronic density, ρ_e, and Laplacian of electron density, $\nabla^2\rho_e$), Electron Localization Function (ELF), Core Valence Bifurcation index (CVB), all these properties reported at the Bond Critical Point (BCP) and region corresponding to the reported hydrogen bonds (dashed lines). (b)DFT optimized structures and binding energy, Δ*E*, for (4) [EMIM] + {(*a*) [EtSO4] + (*b*) [BF4]} clusters, labelled as 4*ab*. Δ*E* for 4*ab* cluster is reported per number of [EMIM], i.e. total divided per four. Panel b color code: (gray) [EMIM], (blue) [EtSO4] and (red) [MeSO3]. (For interpretation of the references to color in this figure legend, the reader is referred to the web version of this article.)

occupy free regions not occupied by the anions allowing an efficient packing in agreement with model clusters in Fig. 6.

The geometrical properties of the developed hydrogen bonds are studied in Fig. 10 using Combined Distributed Functions (CDFs) reporting relevant intermolecular distances and orientations for the two anion – cation interactions. Hydrogen bonding is confirmed for both ions both via donor – acceptor separation, as for RDFs in Fig. 8a and b, as well as for the orientation, with a donor – acceptor angle maxima at 165°. Almost negligible changes in this interacting pattern with mixture content are inferred, i.e. confirming the ionic replacement mechanism around the [EMIM] hydrogen bond donor sites.

The formation of large aggregation clusters is analysed via the

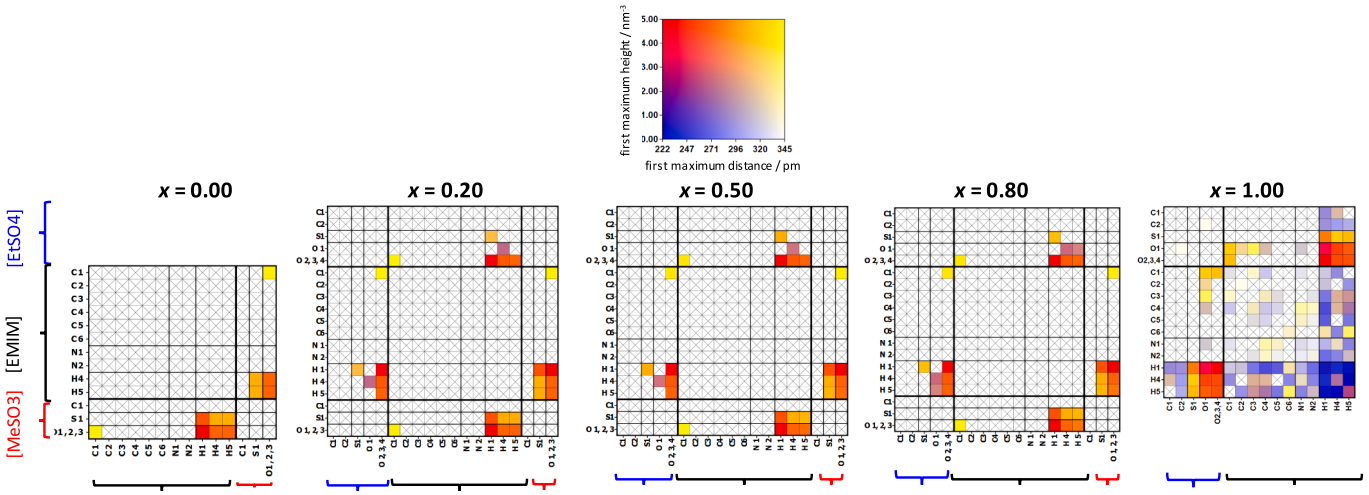

Fig. 7. Connection matrix analysis of interactions in x [EMIM][EtSO4] + (1 − x) [EMIM][MeSO3] mixtures, where stands for mole fraction, from MD simulations at 303 K and 1 bar. Atom labelling as in Fig. 1.

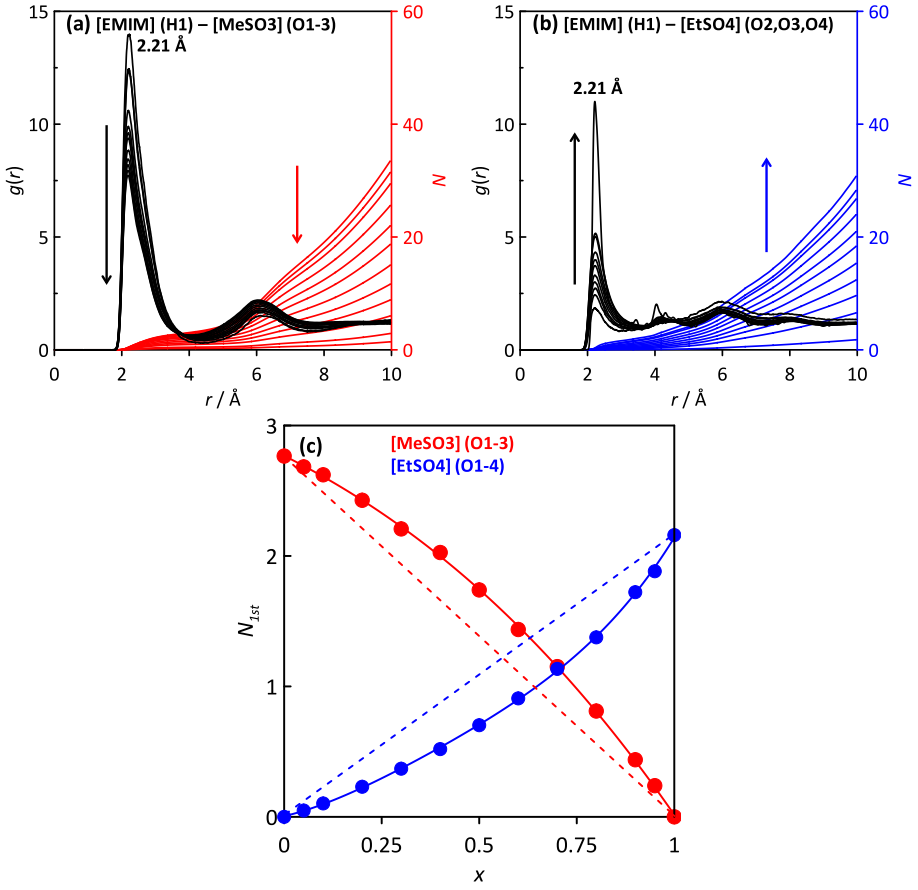

Fig. 8. (a,b) Site − site Radial Distribution Function, $g(r)$, and the corresponding solvation number, N, in x [EMIM][EtSO4] + (1 − x) [EMIM][MeSO3] mixtures, where stands for mole fraction, from MD simulations at 303 K and 1 bar. Arrows indicate increasing mole fraction for the compositions reported in Table S8 (Supplementary Information). (c) N values for the Radial Distribution Function first peak (r < 3.60 Å), N_{1st}. In panel c, dashed lines indicate linear behavior for comparison purposes. Atom labelling as in Fig. 1.

domain analysis reported in Fig. 11. The [EMIM] cations are characterized by the development of a single domain along the fluids, in the whole composition range, Fig. 11a, in agreement with the stacking of cations inferred from SDFs in Fig. 9. This leads to large, Fig. 11b, and non-spherical [EMIM] domains, Fig. 11c (low isoperimetric indices). For the anion-domains, the studied anions show very different behaviour, whereas [$MeSO_3$] shows larger number of domains, i.e. small non-spherical anionic domains, for [$EtSO_4$] larger domains are produced, specially for [$EtSO_4$] rich mixtures.

To further investigate potential clustering phenomena, the neighbor probability matrices are presented in Fig. 12. These matrices reveal a remarkably consistent interatomic distribution function across the

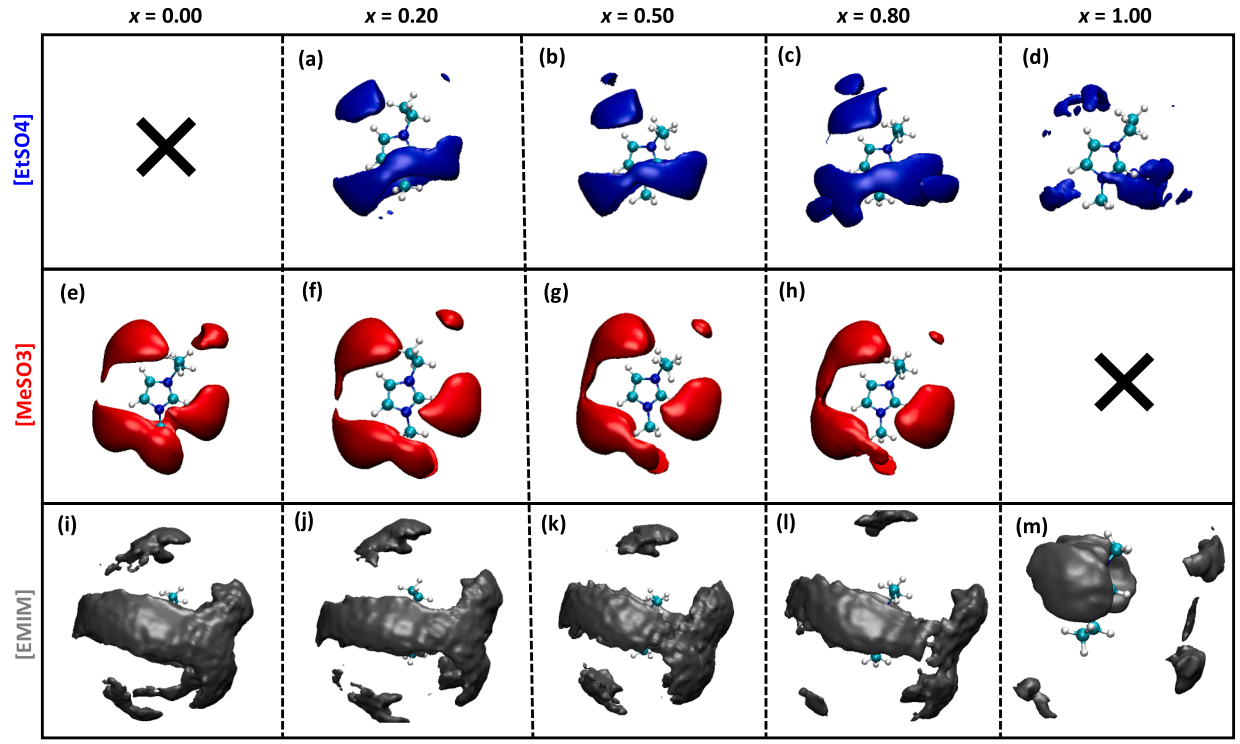

Fig. 9. Spatial Distribution Functions around central [EMIM] cation for the reported molecules: [EtSO4] (O2-4 atoms), [MeSO3] (O1-3 atoms), and [EMIM] (C1 atom) in x [EMIM][EtSO4] + (1 − x) [EMIM][MeSO3] mixtures, where stands for mole fraction, from MD simulations at 303 K and 1 bar.

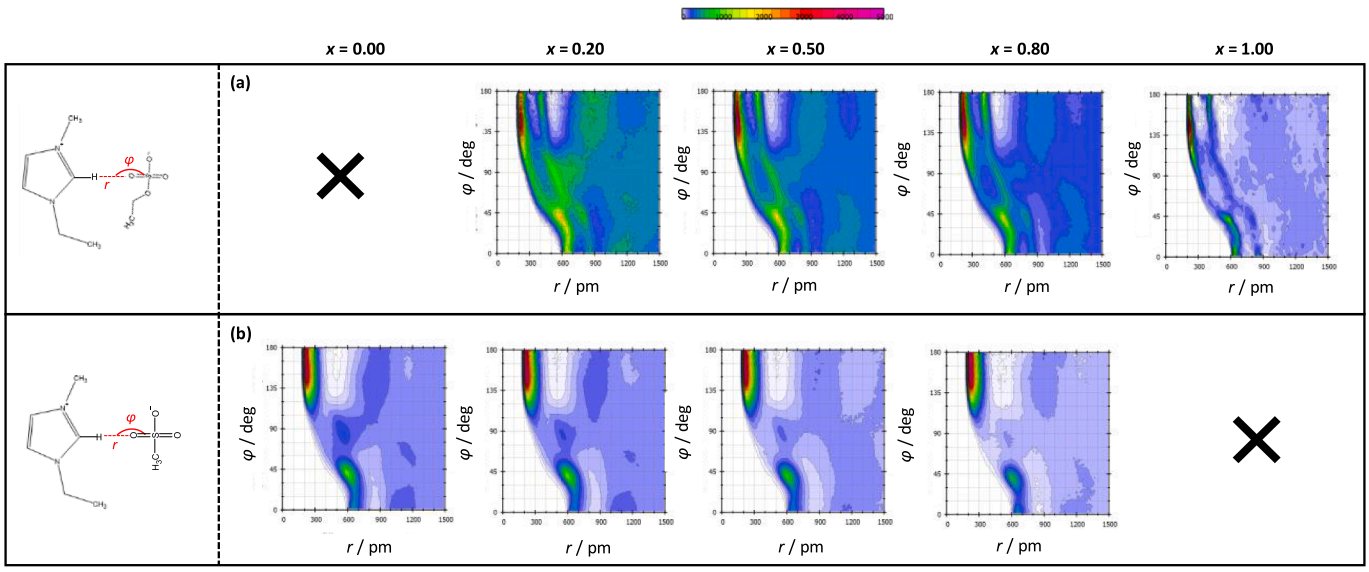

Fig. 10. Combined Distribution Functions for the distance and angles between relevant sites in x [EMIM][EtSO4] + (1 − x) [EMIM][$MeSO_3$] mixtures, where stands for mole fraction, from MD simulations at 303 K and 1 bar.

entire investigated composition range. This consistency suggests that the matrices can be interpreted as "fingerprints" of the atom-to-atom distribution within the liquid phases. In other words, the data indicates that the specific site-to-site distribution remains largely independent of the anion type, with the anion – cation hydrogen bonding as the prevailing driving force, further supporting the anion-per-anion replacement mechanism as a valid approach for describing the properties of these mixtures. Additionally, Fig. 13 examines the solvation shell structure around the [EMIM] cation, specifically focusing on the anion orientation. Both anions, [$EtSO_4$] and [$MeSO_3$], exhibit similar preferential orientations around the C—H imidazolium (donor) sites, red hot spots. However, distinct behavior is observed for the H-bonding imidazolium sites. The larger [$EtSO_4$] anion displays directional alignment with the ring due to the well-defined orientation of its sulfate group and this is even reinforced for [$MeSO_3$] anion, which is on the root of the volumetric properties reported in Fig. 2.

Anion-cation clustering within the IL mixtures was investigated using the data presented in Fig. 14. The cluster size distribution, displayed in Fig. 14a, remains remarkably consistent across the entire composition range: small prevailing clusters formed via anion-cation

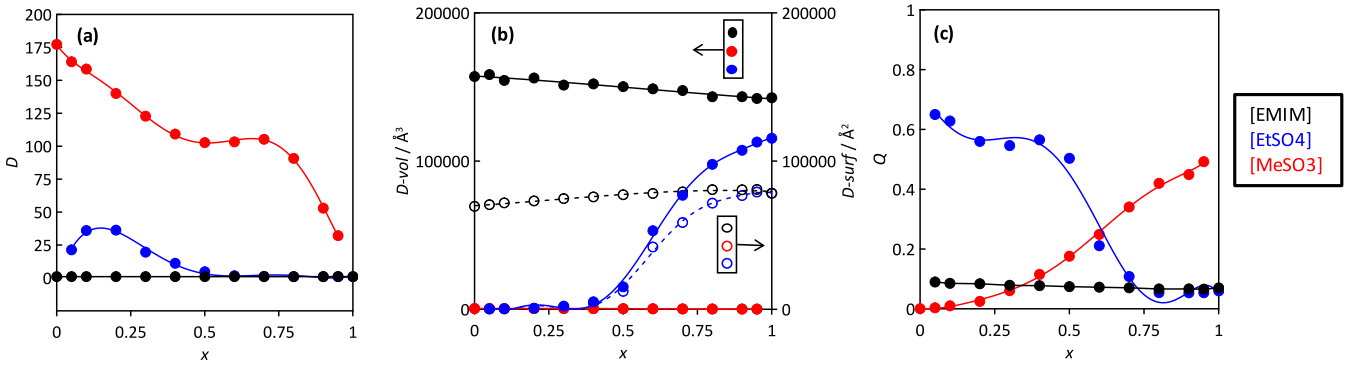

Fig. 11. Domain analysis in x [EMIM][$EtSO_4$] + (1 − x) [EMIM][$MeSO_3$] mixtures, where stands for mole fraction, from MD simulations at 303 K and 1 bar. Number of domains, *D*, average domain area, *D-surf*, and volume, *D-vol*, and isoperimetric index, *Q*, are reported. Atom labelling as in Fig. 1.

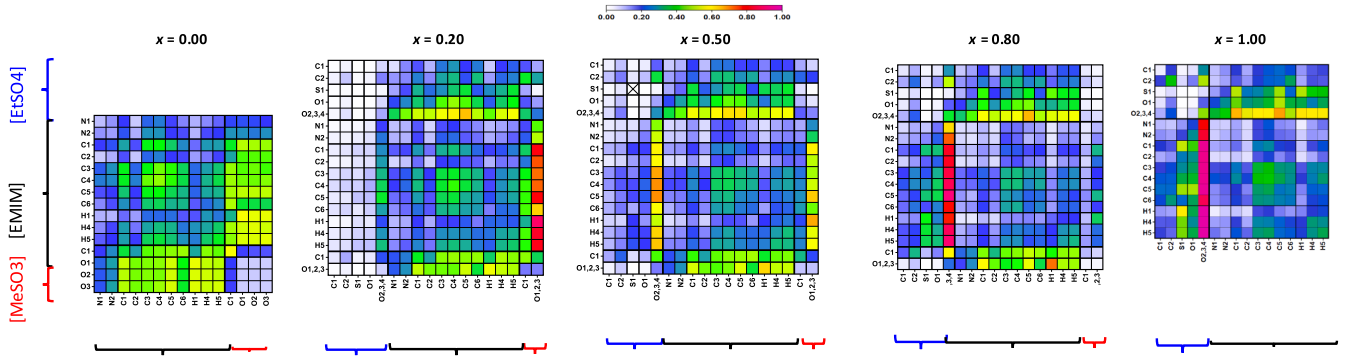

Fig. 12. Neighbor probability matrix from Voronoi analysis in x [EMIM][$EtSO_4$] + (1 − x) [EMIM][$MeSO_3$] mixtures, where stands for mole fraction, from MD simulations at 303 K and 1 bar. Atom labelling as in Fig. 1.

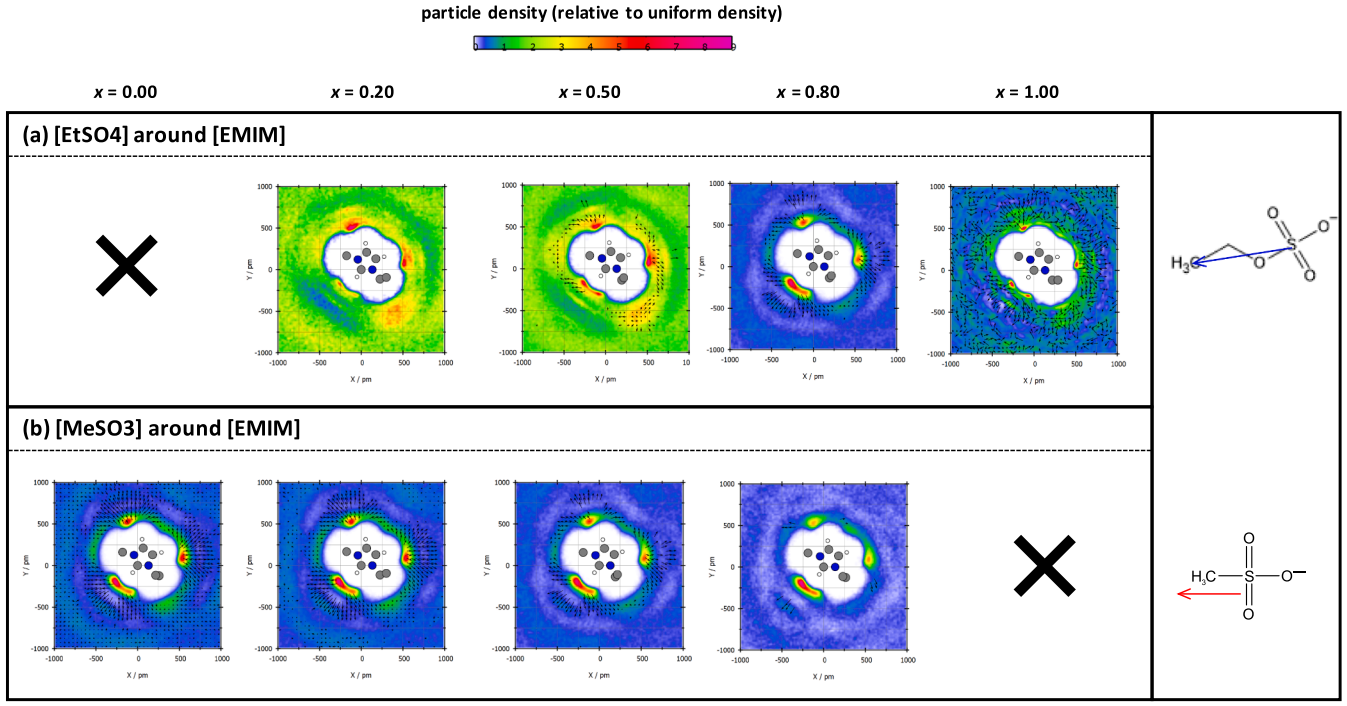

Fig. 13. Average particle density of the reported molecules around a central [EMIM] molecule in x [EMIM][$EtSO_4$] + (1 − x) [EMIM][MeSO3] mixtures, where stands for mole fraction, from MD simulations at 303 K and 1 bar. Average orientation of the reported vectors is also indicated.

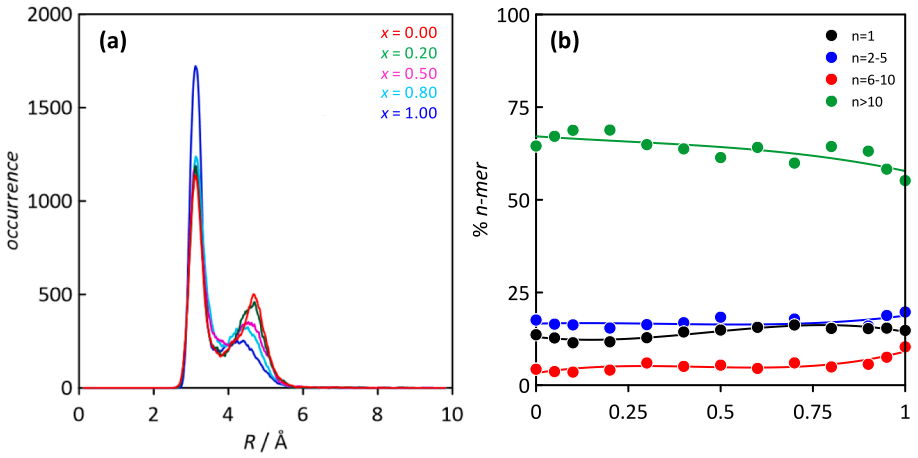

Fig. 14. Cluster analysis for cation – anion aggregation in x [EMIM][$EtSO_4$] + (1 − x) [EMIM][$MeSO_3$] mixtures, where stands for mole fraction, from MD simulations at 303 K and 1 bar. (a) Results show occurrence of possible clusters as a function of distance, R. (b) Percentage distribution of cluster composed of n molecules (*n-mers*).

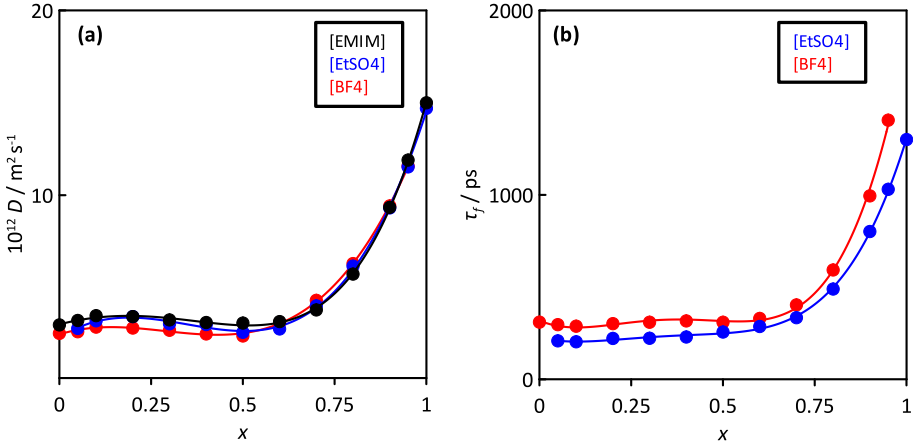

Fig. 15. (a) Center-of-mass self-diffusion coefficient, D, and (b) living times of ion pairs (cation – anion), τ_f, for the considered ions in in x [EMIM][$EtSO_4$] + (1 − x) [EMIM][$MeSO_3$] mixtures, where stands for mole fraction, from MD simulations at 303 K and 1 bar.

hydrogen bonding. This implies that replacing one anion type with another does not significantly alter the cluster size, suggesting an anion-per-anion replacement mechanism. The primary peaks in Fig. 14a correspond to clusters with radii of 3.2 Å and 4.6 Å, likely representing anion-cation dimers ($n = 1$) and tetramers ($n = 2$), respectively. While the $n = 1$ peak decreases its intensity with increasing [$MeSO_3$] content, the $n = 2$ peak shows a reverse evolution, i.e. the stronger nature of [EMIM] – [$MeSO_3$] leads to slightly larger populations of bigger clusters. Nevertheless, the overall cluster size distribution remains qualitatively similar across the composition range. Further analysis, presented in Fig. 14b, examines the percentage distribution of clusters with increasing n (number of anion-cation pairs). Notably, clusters with n > 11 constitute a significant portion, reflecting the domain distribution observed in Fig. 14a for [EMIM] and suggesting interconnected cation chains. Therefore, the liquid structure is characterized by large clusters primarily linked through anion-cation hydrogen bonds and additional inter-pair interactions While subtle changes in cluster distribution are observed with changing composition, the underlying aggregation mechanism and overall distribution remain largely unaffected. This finding supports the anion-per-anion replacement approach for describing mixture properties.

The dynamic behavior of the considered IL mixtures are quantified via the Self-diffusion coefficients (D) both for cations and anions. Results in Fig. 15a indicate anion – cation coupled diffusion, which is consistent with the clustering reported in previous sections and the anion-per-anion replacement mechanism. D exhibited non-linear composition dependence with lower values for [$MeSO_3$] rich mixtures, reflecting higher viscosities, Fig. 2e, correlated with larger [$EtSO_4$]-based domains (Fig. 11b). Likewise, D values for all the involved ions are almost constant for [$MeSO_3$] – rich mixtures, up to roughly equimolar compositions, and thus they increase as a result of the formation of larger [$EtSO_4$] – dominated diffusion domains. Therefore, ionic mobility strongly correlated with domain and clustering evolution. Reactive flux analysis revealed hydrogen bonds lifetimes, τ_f, Fig. 15b. The τ_f shows an analogous pattern to D, [EMIM] – [$MeSO_3$] being more labile than [EMIM] – [$EtSO_4$] hydrogen bonds, with almost constant τ_f for [$MeSO_3$] mixtures up to equimolar composition. This behavior arose from the domain distribution (Fig. 11a), in [$EtSO_4$]-rich mixtures, continuous cation–anion domains facilitated H-bond breaking and reforming whereas for [$MeSO_3$] – rich mixtures, fragmented domains hindered hydrogen bonding reforming, leading to lower lifetimes. Notably, these dynamic features corroborated experimental findings and highlighted the intimate connection between structure and dynamics. While intermolecular forces remained relatively constant upon mixing, both the interaction mechanism and long-range ionic distribution, formed domains played crucial roles in determining ionic mobility.

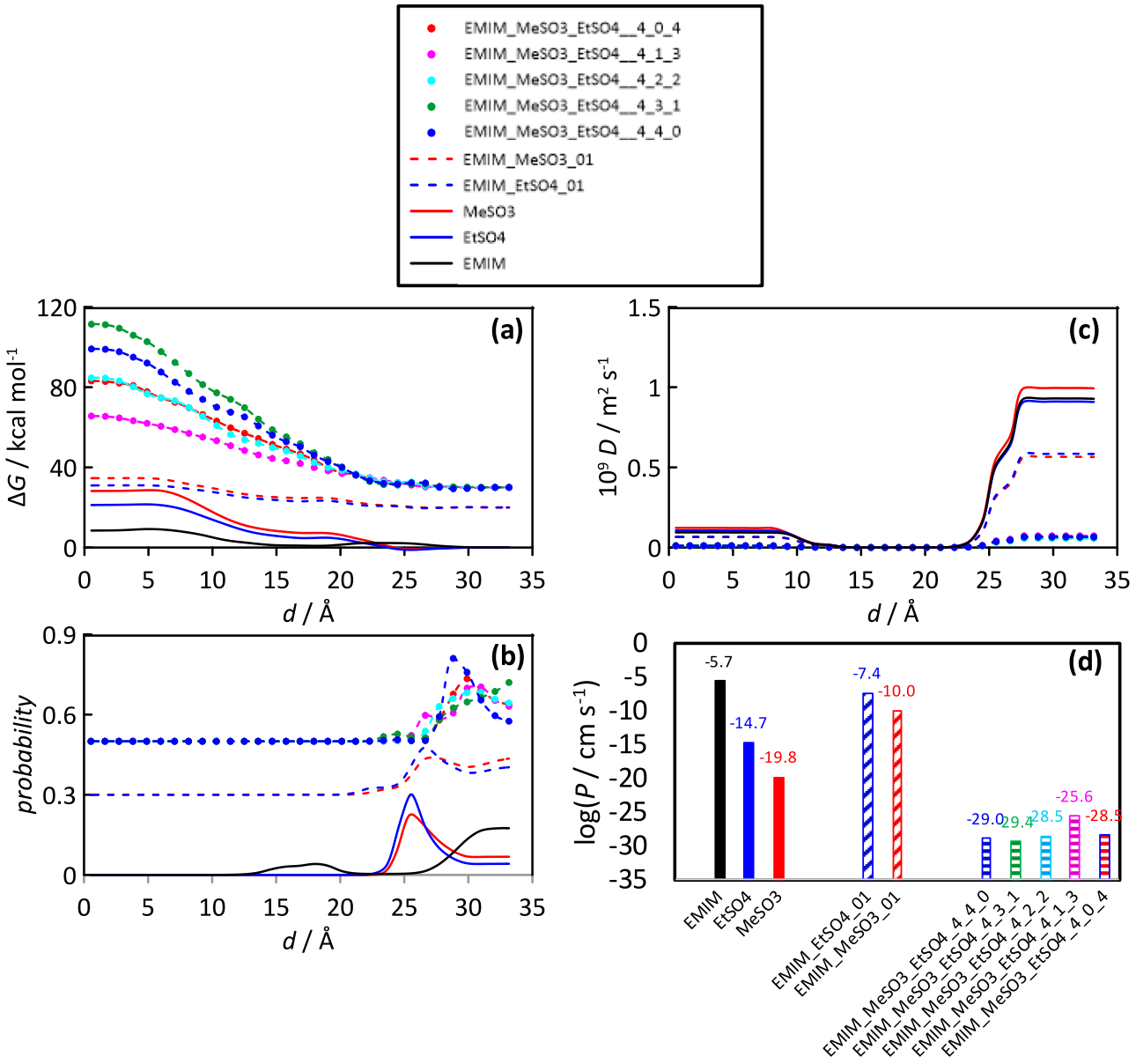

Fig. 16. COSMOperm results for the interaction between the considered systems and DPPC lipid bilayer at 303 K. (a) Free energy, Δ*G*, (b) probability distribution across the bilayer (*d* = 0 standing for bilayer center), (c) self-diffusion coefficient across the membrane, *D*, and (d) permeability, *P*.

3.4. Interaction with biomolecules and cell membranes

The results for the study on the interaction of model IL clusters with DPPC lipid bilayer as inferred from COSMOperm are reported in Fig. 16. The molecular models considered monomers (isolated ions), anion – cation pairs (dimers), and 4*ab* clusters (as described in Section 3.2). The free energy across the membrane shows how large barriers for all the considered ionic clusters because of the presence of the apolar alkyl chain region in the center of the bilayer. It is known the close to null permeability of phospholipid membranes for ions [61], and thus the large energy barriers reported in Fig. 16a. It is also remarkable that the energy barriers are large for isolated ions whereas they decrease as the anion – cation dimers are formed, probably because the formation of the pair upon hydrogen bonding leads to a masking of the charges allowing a better interaction with the membrane. Nevertheless, as the cluster sizes increases to 4*ab* models barriers remain large. Likewise, the presence of [$MeSO_3$] anion leads to larger barriers in comparison with [$EtSO_4$]. This poor ability to cross the membranes is confirmed in the distribution plots reported in Fig. 16b, where in all the cases the most probable location of ions and clusters is in the vicinity of the outer polar regions of the DPPC bilayers, with increasing size of the ionic cluster leading to placing in more external regions. This behavior is confirmed by the reported self-diffusion coefficients, Fig. 16b, which shows lower molecular mobility as the cluster size increases. Therefore, the permeability of the considered ionic clusters across the DPPC model bilayer (Fig. 16d) is almost negligible, even decreasing with increasing cluster size. Thus, the considered mixed ILs would not be able to penetrate into the lipid bilayers but they show affinity for the head polar regions, thus leading to perturbations in the properties of the bilayers at this areas, decreasing their fluidity.

To further investigate potential toxicological effects, docking studies were performed on 100 model proteins, select considering different relevant groups of target proteins, and using the ion dimers (hydrogen bonded pairs) identified in Fig. 6 as surrogates for mixed IL interactions with diverse biological targets. The results, presented in Fig. 17, reveal biomolecule-cluster interaction energies ranging from −4 to −7 kcal/mol, suggesting moderate attractive interactions but potentially non-negligible biological consequences, potentially linked to adverse

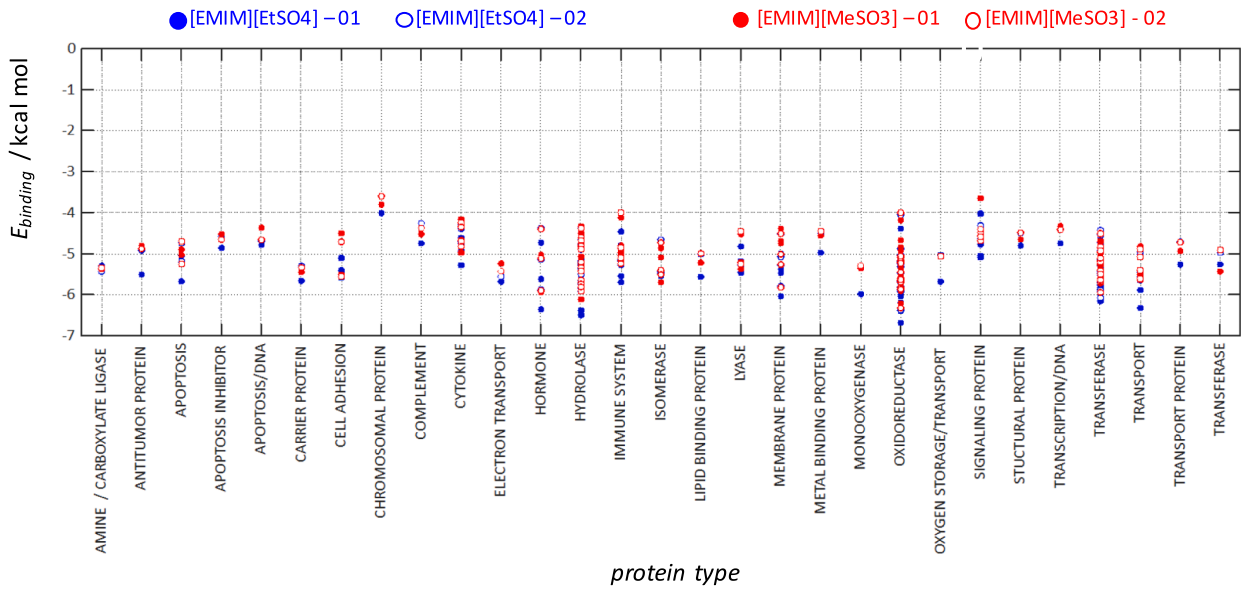

Fig. 17. Docking results for the reported cation – anion pairs in the selected proteins, reporting average binding energy ($E_{binding}$), as obtained from the 9-largest binding poses for each protein. Proteins are classified per type (Table S9, Supplementary Information).

effects. Interestingly, minimal influence of the biomolecule type is observed for a given cluster configuration, indicating an inherent capacity of ion pairs to attain their most stable arrangement irrespective of the target. However, significant variations are observed based on the specific cluster type, leading to diverse interaction mechanisms and strengths with the biomolecules. Collectively, these findings, along with previous results regarding lipid bilayer interactions, highlight the pronounced potential of the investigated mixed ILs to interact with biological systems, raising concerns about potential toxic effects. Notably, the possibility of synergistic toxicity due to the presence of different anions necessitates careful consideration, particularly when contemplating large-scale applications of complex multicomponent IL mixtures.

4. Conclusions

This study delved into the mixing behavior of [EMIM][EtSO4] and [EMIM][MeSO3] across various compositions, employing both experimental and computational methods. Non-ideal mixing behavior was inferred in density, excess molar volume, and viscosity, attributable to the differing sizes and intermolecular interactions of the anions. Anion-cation coupled diffusion was observed with a non-linear composition dependence, correlating with domain formation. Interestingly, hydrogen bonding emerged as a critical player in structuring and dynamics, with [MeSO3] leading to stronger interactions and consequently lower mobility.

Moving to the nanoscale realm, we found an anion-per-anion replacement mechanism governing both solvation shells and clustering. This led to the formation of large, non-spherical cation domains and composition-dependent anion domains. While cluster size distribution primarily featured small units, subtle changes were observed with varying composition. Further analysis revealed that dynamic features were heavily influenced by domain distribution and hydrogen bonding lifetimes.

The investigation of interaction with biomolecules and cell membranes revealed negligible permeability across the model DPPC lipid bilayer due to electrostatic barriers, with larger clusters displaying lower mobility. However, the clusters did exhibit a preference for interaction with the polar head regions, potentially impacting the bilayer's fluidity. Docking studies with protein models yielded moderate biomolecule-cluster interactions, raising concerns about potential toxicological effects. Notably, the possibility of synergistic toxicity due to the presence of different anions necessitates further scrutiny, particularly when contemplating large-scale applications of complex multicomponent ionic liquid mixtures.

This comprehensive study not only unveils the mixing behavior of these mixed ionic liquids but also sheds light on their potential biological effects. The findings underscore the importance of considering interaction mechanisms and long-range ionic distributions when evaluating their suitability for various applications.

CRediT authorship contribution statement

Ylenia F. Rodríguez: Writing – review & editing, Writing – original draft, Visualization, Validation, Methodology, Investigation, Formal analysis, Data curation, Conceptualization. **Santiago Aparicio:** Writing – review & editing, Writing – original draft, Validation, Supervision, Software, Resources, Project administration, Methodology, Investigation, Funding acquisition, Formal analysis, Data curation, Conceptualization. **Jose L. Trenzado:** Writing – review & editing, Writing – original draft, Validation, Supervision, Software, Resources, Project administration, Methodology, Investigation, Funding acquisition, Formal analysis, Data curation, Conceptualization.

Declaration of competing interest

The authors declare that they have no known competing financial interests or personal relationships that could have appeared to influence the work reported in this paper.

Acknowledgements

We acknowledge SCAYLE (Supercomputación Castilla y León, Spain) for providing supercomputing facilities. The statements made herein are solely the responsibility of the authors.

Appendix A. Supplementary data

Specifications of ionic liquids used for experimental studies (Table S1); experimental thermophysical properties of pure ionic liquids as a function of temperature and comparison with literature (Table S2); experimental thermophysical properties of [EMIM][BF4] + [EMIM][EtSO4] mixtures as a function of composition and temperature

(Table S3); fitting parameters for viscosity according to VFT model (Table S4); fitting parameters for experimental thermophysical properties of [EMIM][BF4] + [EMIM][EtSO4] mixtures as a function of composition and temperature (Table S5); pure component parameters used for PFP modelling of experimental excess molar volume (Table S6); all atom force field parameterizations (Table S7); systems for all atom MD simulations of ionic liquid mixtures (Table S8); proteins considered for docking studies (Table S9); Fig. S1 (comparison among experimental and MD predicted density data). Supplementary data to this article can be found online at https://doi.org/10.1016/j.molliq.2024.126395.

Data availability

Data will be made available on request.

References

[1] P. Walden, Lorenz und Kaufler, Elektrochemie geschmolzener Salze. Leipzig, 1909.
2) K Arndt, Benrath und Wainoff, 1905.
[2] T. Welton, Ionic liquids: a brief history, Biophys. Rev. 10 (2018) 691–706.
[3] H.D.B. Jenkins, Ionic liquids-an overview, Sci. Prog. 94 (2011) 265–297.
[4] R.P. Matthews, I.J. Villar-Garcia, C.C. Weber, J. Griffith, F. Cameron, J.P. Hallett, P.A. Hunt, T. Welton, A structural investigation of ionic liquid mixtures, Phys. Chem. Chem. Phys. 18 (2016) 8608–8624.
[5] P. Sappidi, J.E. Bara, C.H. Turner, Molecular-level behavior of imidazolium-based ionic liquid mixtures, Chem. Eng. Sci. 229 (2021).
[6] K. Ghandi, A review of ionic liquids, their limits and applications, Green Sus. Chem. 04 (2014) 44–53.
[7] E.I. Izgorodina, Towards large-scale, fully ab initio calculations of ionic liquids, Phys. Chem. Chem. Phys. 13 (2011) 4189–4207.
[8] I. Krossing, J.M. Slattery, C. Daguenet, P.J. Dyson, A. Oleinikova, H. Weingärtner, Why are ionic liquids liquid? A simple explanation based on lattice and solvation energies, J. Am. Chem. Soc. 128 (2006) 13427–13434.
[9] Y. Marcus, Ionic liquid properties. from molten salts to RTILs, Ed. Springer (2016).
[10] Y. Zhang, E.J. Maginn, Molecular dynamics study of the effect of alkyl chain length on melting points of [CnM IM][PF6] ionic liquids, Phys. Chem. Chem. Phys. 16 (2014) 13489–13499.
[11] P. Sanchora, D.K. Pandey, H.L. Kagdada, A. Mateny, D.K. Singh, Impact of alkyl chain length and water on the structure and properties of 1-alkyl-3-methylimidazolium chloride ionic liquids, Phys. Chem. Chem. Phys. 22 (2020) 17687–17704.
[12] R.F. Rodriguez, A.A. Freitas, H.M. Canongia-Lopes, K. Shimizu, Ionic liquids and water: hydrophobicity vs hydrophilicity, Molecules 26 (2021) 7159.
[13] S. Ravula, N.R. Larm, M.A. Mottaleb, M.P. Heitz, G.A. Baker, Vapor pressure mapping of ionic liquids and low-volatility fluids using graded isothermal thermogravimetric analysis, ChemEngineering 3 (2019) 42.
[14] M.A.A. Rocha, C.F.R.A.C. Lima, L.R. Gomes, B. Schröder, J.A.P. Coutinho, I. M. Marrucho, J.M.S.S. Esperança, L.P.N. Rebelo, K. Shimizu, J.N.C. Lopes, L.M.N.B. F. Santos, High-accuracy vapor pressure data of the extended [CnC1im][Ntf2] ionic liquid series: trend changes and structural shifts, J. Phys. Chem. B 115 (2011) 10919–10926.
[15] L.M.N.B.F. Santos, J.N. Canongia Lopes, J.A.P. Coutinho, J.M.S.S. Esperança, L. R. Gomes, I.M. Marrucho, L.P.N. Rebelo, Ionic liquids: first direct determination of their cohesive energy, J. Am. Chem. Soc. 129 (2007) 284–285.
[16] S.K. Singh, A.W. Savoy, Ionic liquids synthesis and applications: an overview, J. Mol. Liq. 297 (2020) 112038.
[17] L. Zhang, L. Wang, M. Li, J. Xu, Y. Yang, A critical review on recent advances in sustainable homogeneous catalysis using ionic liquids, Cat. Sci. Technol. 13 (2023) 8491–8529.
[18] H. Kim, D. Jeong, J. Bae, J.-M. Lee, Ionic liquids for next-generation electrochemical energy storage devices, Chem. Soc. Rev. 52 (2023) 9054–9105.
[19] S. Chowdhury, S. Mandal, T. Banerjee Green Chemistry with Ionic Liquids, Eds., CRC Press, 2018.
[20] L. Zhang, L. Luo, M. Li, L. Wang, H. Liu, Ionic Liquids in Lithium-Sulfur Batteries: Challenges and Advances, Chem. Eng. J. 460 (2023) 460, 140085.
[21] S. Balchandani, B. Mandal, S. Dharaskar, Measurements and modeling of vapor liquid equilibrium of CO_2 in amine activated imidazolium ionic liquid solvents, Fluid Phase Equilbr. 521 (2020) 112643.
[22] P. Migowski, P. Lozano, J. Dupont, Imidazolium based ionic liquid-phase green catalytic reactions, Green Chem. 25 (2023) 1237–1260.
[23] N.A. Noorhisham, D. Amri, A.H. Mohamed, N. Yahaya, N.M. Ahmad, S. Mohamad, S. Kamaruzaman, H. Osman, J. Mol. Liq. 326 (2021) 115340.
[24] S.M.S. Hussain, A.A. Adewunni, O.S. Alade, M. Murtaza, A. Mahboob, H.J. Khan, M. Mahmoud, M.S. Kamal, A review of ionic liquids: Recent synthetic advances and oilfield application, J. Taiwan Inst. Chem. Eng. 153 (2023) 105195.
[25] S. Papovic, N. Cvticanin, S. Gadzuric, M. Bester-Rogac, M. Vranes, Physicochemical and electrochemical characterisation of imidazolium based IL + GBL mixtures as electrolytes for lithium-ion batteries, Phys. Chem. Chem. Phys. 19 (2017) 28139–28152.
[26] C.C.P. da Silva, B.C.F. Owoyemi, B.R. Alvarenga, N. Alvarez, J. Ellena, R. L. Carneiro, Synthesis and solid-state characterization of diclofenac imidazolium monohydrate: an imidazolium pharmaceutical ionic liquid, CryEngComm. 22 (2020) 5345–5354.
[27] M. Galiński, M.A. Noor Afiqah, A.M. Szymczak, M.R. Lovrić, Recent advances in ionic liquid mixtures, J Chem. Rev. 122 (2022) 8372–8449.
[28] J.L. Urzua, M.L. Valenzuela, J. Cavieres, M.J. Inestrosa, Ionic liquid mixtures as energy storage materials: a preliminary and comparative study based on thermal storage density, RSC Adv. 13 (2023) 19412–19419.
[29] J.S. Laso, A. Piera, G. Vicente, L.F. Batista, R. Rodríguez, J.J. Espada, A successful method for phycocyanin extraction from Arthrospira platensis using [Emim][$EtSO_4$] ionic liquid, Biofuels Biop. Bioref. 15 (2021) 1638–1649.
[30] Z. Wang, C. Luo, B. Wang, T. Lai, Y. Hong, G. Gao, Synergistic catalysis of sulfate ionic liquids and $FeCl_3$ for the dehydration of 1,4-butanediol to tetrahydrofuran, Fuel 363 (2024) 130806.
[31] O. Singh, P.Y. Lee, S. Matysiak, H. Bermudez, Dual mechanism of ionic liquid-induced protein unfolding, Phys. Chem. Chem. Phys. 22 (2020) 19779–19786.
[32] J. Gao, Z. Xu, Performance evaluation of absorption thermal energy storage/transmission using ionic liquid absorbents, Energy Built Environ. 4 (2023) 259–269.
[33] F.R. Radakovitsch, A. Jess, Gas dehydration using the ionic liquid [EMIM][$MeSO_3$] supported on silica gel – structural and water vapor sorption properties, Chem. Eng. J. 398 (2020) 124689.
[34] Y. Guo, F. Shi, Q. Shu, X. Yue, C. Wang, L. Tao, J. Li, Liquid-liquid equilibrium for n-hexane + benzene + sulfolane, + 1-ethyl-3-methylimidazolium bis (trifluoromethylsulfonyl)imide ([EMIM][NTf2]), + 1-ethyl-3-methylimidazolium ethylsulfate ([EMIM][EtSO4]) and + the mixtures of [EMIM][NTf2] and [EMIM][EtSO4], Fluid Phase Equilibr. 529 (2021) 112882.
[35] D.K. Mishra, G. Pugazhenthi, T. Berneeje, Ionic liquid-based deep eutectic solvent as reaction media for the thermal dehydrogenation of ethylene diamine-bis-borane, ACS Sust. Chem. Eng. 8 (2020) 4910–4919.
[36] S. Prathipati, S. Rao, S.R. Munnanagi, R.S. Gopisetti, M.M. Alam, H.B. Bollikolla, The study of intermolecular interactions in [Bmim][PF6] + 1-octyl-2-pyrrolidone binary mixtures from volumetric, acoustic, optical and spectroscopic measurements, J. Cehm. Thermodyn. 179 (2023) 106952.
[37] BIOVIA, Dassault Systèmes,Dmol3, San Diego, Dassault Syst. (2022).
[38] S. Grimme, J. Antony, H. Krieg, A consistent and accurate ab initio parametrization of density functional dispersion correction (DFT-D) for the 94 elements H-Pu, J. Chem. Phys. 132 (2010) 154104.
[39] S. Simon, M. Duran, J. Dannenberg, How does basis set superposition error change the potential surfaces for hydrogen-bonded dimers? J. Chem. Phys. 105 (1996) 11024.
[40] R.F.W. Bader, Atoms in molecules, Acc. Chem. Res. 18 (1985) 9–15.
[41] Lu Tian, F. Chen, Multiwfn: a multifunctional wavefunction analyzer, J. Comput. Chem. 33 (2012) 580–592.
[42] F. Fuster, B. Silvi, Theor. Does the topological approach characterize the hydrogen bond? Chem. Acc. 104 (2000) 13–21.
[43] A.P. Lyubartsev, A. Laaksonen, MdynaMix – a scalable portable parallel MD simulation package for arbitrary molecular mixtures, Comput. Phys. Commun. 128 (2000) 565–589.
[44] V. Zoete, M.A. Cuendet, A. Grosdidier, O. Michielin, SwissParam. A fast force field generation tool for small organic molecules, J. Comput. Chem. 32 (2011) 2359–2368.
[45] L. Martínez, R. Andrade, E.G. Birgin, J.M. Martínez, Packmol: a package for building initial configurations for molecular dynamics simulations, J. Comput. Chem. 30 (2009) 2157–2164.
[46] M. Tuckerman, B.J. Berne, G.J. Martyna, Reversible multiple time scale molecular dynamics, J. Chem. Phys. 97 (1992) 1990–2001.
[47] U.L. Essmann, M.L. Perera, T. Berkowitz, H. Darden, H. Lee, L.G. Pedersen, A smooth particle mesh ewald method, J. Chem. Phys. 103 (1995) 8577–8593.
[48] W.G. Hoover, Canonical dynamics: equilibrium phase-space distributions, Phys. Rev. A. 31 (1985) 1695.
[49] W. Humphrey, A. Dalke, K. Schulten, VMD – visual molecular dynamics, J. Molec. Graph. 14 (1996) 33–38.
[50] M. Brehm, B. Kirchner, TRAVIS – a free analyzer and visualizer for Monte Carlo and molecular dynamics trajectories, J. Chem. Inf. Model. 51 (2011) 2007–2023.
[51] BIOVIA COSMOtherm, Release 2021; Dassault Systèmes. http://www.3ds.com.
[52] J. Schwöbel, A. Ebert, K. Bitterman, K.U. Goss, A. Klamt, COSMOperm: mechanistic prediction of passive membrane permeability for neutral compounds and ions and its pH dependence, J. Phys. Chem. B 124 (2020) 3343–3354.
[53] G. Martínez-Rosell, T. Giorgino, G. De Fabritiis, PlayMolecule ProteinPrepare: a web application for protein preparation for molecular dynamics simulations, J. Chem. Inf. Model. 57 (2017) 1511–1516.
[54] O. Trott, A.J. Olson, AutoDock Vina: improving the speed and accuracy of docking with a new scoring function, efficient optimization, and multithreading, J. Comput. Chem. 31 (2010) 455–461.
[55] G. Chatel, J.F.B. Pereira, V. Debbeti, H. Wang, R.D. Rogers, Mixing ionic liquids-"simple mixtures" or "double salts"? Green Chem. 16 (2014) 2051–2083.
[56] K. Fumino, R. Ludwig, Analyzing the interaction energies between cation and anion in ionic liquids: the subtle balance between Coulomb forces and hydrogen bonding, J. Mol. Liq. 192 (2014) 94–102.
[57] E.M. Živković, N.V. Živković, D.M. Majstorović, A.M. Stanimirović, M. L. Kijevčanin, Volumetric and transport properties of binary liquid mixtures with 1- ethyl-3-methylimidazolium ethyl sulfate as candidate solvents for regenerative flue gas desulfurization processes, J. Chem. Thermodyn. 119 (2018) 135–154.
[58] Q. Liu, L. Ma, S. Wang, Z. Ni, X. Fu, J. Wang, Q. Zheng, Study on the properties of density, viscosity, excess molar volume, and viscosity deviation of [C2mim][NTf2],

[C2mmim][NTf2], [C4mim][NTf2], and [C4mmim][NTf2] with PC binary mixtures, J. Mol. Liq. 325 (2021) 114573.
[59] U. Fatima, H. Riyazuddeen, L.M.V. Montes-Cortes, Experimental and MD simulation investigation on thermophysical properties of binary/ternary mixtures of 1-butyl-3-methylimidazolium trifluoromethanesulfonate with molecular solvents, J. Mol. Liq. 302 (2020) 112481.
[60] K. Dong, S. Zhang, J. Wang, Understanding the hydrogen bonds in ionic liquids and their roles in properties and reactions, Chem. Comm. 52 (2016) 6744–6764.
[61] J.A.H. Schwöbel, A. Ebert, U. Huniar, A. Klamt, COSMOperm: mechanistic prediction of passive membrane permeability for neutral compounds and ions and its pH dependence, J. Phys. Chem. B 124 (2020) 3343–3354.

5.1.3.1. Información experimental II

Tabla 17. Comparación de los datos experimentales con la literatura citada, tanto de las densidades, ρ (g cm-3), como de las viscosidades dinámicas, η (mPa s), de los compuestos puros a las temperaturas de trabajo.

	P / g cm^{-3}		η / mPa s		ρ / g cm^{-3}		η / mPa s	
T / K	exp.	Lit.	exp.	Lit.	exp.	Lit.	exp.	Lit.
	[EMIM][$EtSO_4$]				[EMIM][$MeSO_3$]			
283.15	1.24704	1.24691[(a)]	222.78	224.00[(a)]	1.25132	1.25140[®]	487.18	450[(n)]
		1.24730[(b)]		218.56[(f)]		1.25200[(i)]		439.7[(o)]
		1.24640[I]		-		1.25204[(i)]		-
288.15	1.24357	1.24348[(a)]	166.34	161.56[(f)]	1.24777	1.24810[I]	321.98	337.6[(p)]
		1.24370[(b)]		-		1.24840[(i)]		-
		1.24310[I]		-		1.24849[(i)]		-
293.15	1.24019	1.24009[(a)]	123.58	122.31[(f)]	1.24422	1.24440[(k)]	223.54	233.1[(p)]
		1.24010[(b)]		122.07[(g)]		1.24440[(j)]		210.91[(q)]
		1.24021[(d)]		-		1.24400[(l)]		-
298.15	1.23682	1.23689[I]	95.34	94.64[(f)]	1.24078	1.24090[(j)]	164.56	166.8[(p)]
		1.23678[(d)]		96.21[(h)]		1.24110[(k)]		155[(n)]
		1.23670[(b)]		-		1.24140[®]		-
303.15	1.23358	1.23346[I]	75.09	75.10[(g)]	1.23740	1.23740[(j)]	118.04	117[(n)]
		1.23336[(d)]		74.72[(f)]		1.23780[(k)]		113.17[(q)]
		1.23332[(a)]		75.89[(h)]		1.23700[(l)]		120[®]
308.15	1.23005	1.23006[I]	60.17	60.01[(f)]	1.23402	1.23390[(j)]	89.63	87[®]
		1.22996[(d)]		30.73[(h)]		1.23440[(k)]		93.58[(p)]
		1.22994[(a)]		-		1.23280[(m)]		84.98[(o)]
313.15	1.22668	1.22667[I]	48.99	48.97[(f)]	1.23065	1.23100[(k)]	69.76	69[(i)]
		1.22657[(d)]		49.38[(h)]		1.23000[(l)]		67.31[(q)]
		1.22656[(a)]		-		1.23050[(j)]		72,8[(p)]

(a) Hasse et al., 2009
(b) Dakkach et al., 2018
® Mohan et al., 2022
(d) Rajendran et al., 2020
® Singh et al., 2014
(f) Tariq et al., 2021
(g) Larriba et al., 2011
(h) Anwar et al., 2017
(i) Seki et al., 2012
(i) Hasse et al., 2009
(j) Rabari et al., 2014
(k) Bioucas et al., 2022
(l) Krannich et al., 2016
(m) Marium et al., 2017
(n) Tenney et al., 2014
(o) Vallejo et al., 2020
(p) Vatascin et al., 2021
(q) Bioucas et al., 2018
I Singh et al., 2014

Anwar, N., & Riyazuddeen. (2017). Fluid Phase Equilibria, 437, 127–139.

Bioucas, F. E. B., Queirós, C. S. G. P., Lozano-Martín, D., Ferreira, M. S., Paredes, X., Santos, Â. F., Santos, F. J. V., Lopes, M. L. M., Lampreia, I. M. S., Lourenço, M. J. V., de Castro, C. A. N., & Massonne, K. (2022). Industrial and Engineering Chemistry Research, 61(5), 2280–2305.

Bioucas, F. E. B., Vieira, S. I. C., Lourenço, M. J. V., Santos, F. J. V., Nieto De Castro, C. A., & Massonne, K. (2018). Industrial and Engineering Chemistry Research, 57(25), 8541–8551.

Dakkach, M., Gaciño, F., Guimarey, M. J. G., Mylona, S. K., Paredes, X., Comuñas, M. J. P., Fernández, J., & Assael, M. J. (2018). Journal of Chemical Thermodynamics, 121, 27–38.

Hasse, B., Lehmann, J., Assenbaum, D., Wasserscheid, P., Leipertz, A., & Fröba, A. P. (2009). Journal of Chemical and Engineering Data, 54(9), 2576–2583.

Krannich, M., Heym, F., & Jess, A. (2016). Journal of Chemical and Engineering Data, 61(3), 1162–1176.

Larriba, M., García, S., García, J., Torrecilla, J. S., & Rodríguez, F. (2011). Journal of Chemical and Engineering Data, 56(9), 3589–3597.

Marium, M., Auni, A., Rahman, M. M., Mollah, M. Y. A., & Susan, M. A. B. H. (2017). Journal of Molecular Liquids, 225, 621–630.

Mohan, M., Kumar, N., Goud, V. V., Simmons, B. A., Sale, K. L., Gladden, J. M., Singh, S., & Banerjee, T. (2022). Fluid Phase Equilibria, 562.

Rabari, D., Patel, N., Joshipura, M., & Banerjee, T. (2014). Journal of Chemical and Engineering Data, 59(3), 571–578.

Rajendran Startha Christabel, A., Ramalingam, A., Reji, D. J. P. M., Nagaraj, S., & Ravichandran, S. (2020). Journal of Chemical and Engineering Data, 65(2), 446–476.

Seki, S., Tsuzuki, S., Hayamizu, K., Umebayashi, Y., Serizawa, N., Takei, K., & Miyashiro, H. (2012). Journal of Chemical and Engineering Data, 57(8), 2211–2216.

Singh, M. P., Mandal, S. K., Verma, Y. L., Gupta, A. K., Singh, R. K., & Chandra, S. (2014). Journal of Chemical and Engineering Data, 59(8), 2349–2359.

Tariq, M., Esperança, J. M. S. S., Rebelo, L. P. N., Paredes, X., Santos, F. J. V., & Nieto de Castro, C. A. (2021). Journal of Molecular Liquids, 337.

Tenney, C. M., Massel, M., Mayes, J. M., Sen, M., Brennecke, J. F., & Maginn, E. J. (2014). Journal of Chemical and Engineering Data, 59(2), 391–399.

Vallejo, J. P., Liñeira del Río, J. M., Fernández, J., & Lugo, L. (2020). Journal of Molecular Liquids, 319.

Vataščin, E., Havlová, M., & Dohnal, V. (2021). Fluid Phase Equilibria, 548.

Tabla 18. Densidades (ρ), viscosidades cinemáticas (ν), viscosidades dinámicas (η), volúmenes molares de exceso (VE) y desviaciones en la viscosidad ($\Delta\eta$) del sistema {(x) [EMIM][EtSO$_4$] + (1-x) [EMIM][MeSO$_3$]} a diferentes temperaturas.

X	ρ / g cm^{-3}	ν / mm^2 s^{-1}	η / mPa s	V^E / cm^3 mol^{-1}	$\Delta\eta$ / mPa s
		283.15 K			
0.05622	1.25143	361.29	452.13	-0.051	-20.19
0.11098	1.25131	339.75	425.13	-0.071	-32.71
0.20389	1.25079	310.25	388.06	-0.060	-45.22
0.28652	1.25020	287.67	359.64	-0.032	-51.79
0.39956	1.24940	261.31	326.48	0.009	-55.06
0.48912	1.24884	242.69	303.08	0.034	-54.78
0.51326	1.24869	-	-	0.041	-
0.60317	1.24824	223.09	278.47	0.052	-49.23
0.68702	1.24787	208.50	260.18	0.056	-45.35
0.77977	1.24749	195.12	243.40	0.058	-37.61
0.79412	1.24744	-	-	0.057	-
0.88043	1.24717	-	-	0.048	-
0.89139	1.24714	186.07	232.05	0.047	-19.45
0.91719	1.24708	183.48	228.81	0.041	-15.86
0.93069	1.24703	-	-	0.041	-
		288.15 K			
0.05622	1.24788	240.72	300.39	-0.051	-12.84
0.11098	1.24776	229.18	285.96	-0.070	-18.74
0.20389	1.24725	212.01	264.43	-0.059	-25.82
0.28652	1.24665	197.45	246.15	-0.029	-31.23
0.39956	1.24583	182.24	227.04	0.017	-32.75
0.48912	1.24524	172.93	215.34	0.047	-30.52
0.60317	1.24461	161.75	201.32	0.071	-26.79
0.65614	1.24434	-	-	0.080	-
0.67832	1.24423	-	-	0.083	-
0.68702	1.24419	154.09	191.71	0.084	-23.34
0.73941	1.24396	-	-	0.088	-
0.77977	1.24379	146.17	181.80	0.090	-18.81
0.85366	1.24353	-	-	0.088	-
0.87738	1.24347	-	-	0.084	-
0.89139	1.24345	139.21	173.11	0.079	-10.14
0.91719	1.24342	137.65	171.15	0.069	-8.075
0.93299	1.24342	-	-	0.060	-
		293.15 K			
0.05622	1.24433	170.11	211.68	-0.050	-6.246
0.11098	1.24421	161.41	200.83	-0.067	-11.62
0.20389	1.24371	151.35	188.24	-0.056	-14.92
0.28652	1.24311	142.29	176.88	-0.023	-18.02
0.39956	1.24229	132.05	164.05	0.026	-19.55
0.48912	1.24171	125.05	155.28	0.057	-19.37
0.51326	1.24156	-	-	0.065	-
0.60317	1.24109	117.24	145.51	0.083	-17.74
0.67176	1.24076	-	-	0.093	-
0.68702	1.24069	111.89	138.82	0.095	-16.04
0.71731	1.24055	-	-	0.099	-
0.77977	1.24030	107.38	133.18	0.102	-12.42
0.85366	1.24007	-	-	0.097	-
0.87738	1.24000	-	-	0.095	-
0.89139	1.23999	103.07	127.80	0.089	-6.635
0.91719	1.23998	101.88	126.33	0.077	-5.531

Tabla 18. Continuación.

X	ρ / g cm^{-3}	ν / mm^2 s^{-1}	η / mPa s	V^E / cm^3 mol^{-1}	$\Delta\eta$ / mPa s
		298.15 K			
0.05622	1.24087	126.62	157.13	-0.046	-3.547
0.11098	1.24077	121.66	150.95	-0.066	-5.930
0.20389	1.24030	113.17	140.36	-0.058	-10.09
0.28652	1.23969	105.92	131.31	-0.022	-13.42
0.38846	1.23890	-	-	0.030	-
0.39956	1.23881	98.496	122.02	0.036	-14.89
0.48912	1.23821	93.752	116.09	0.071	-14.62
0.60317	1.23758	87.683	108.51	0.100	-14.29
0.68702	1.23720	84.181	104.15	0.110	-12.86
0.71731	1.23709	-	-	0.110	-
0.77977	1.23683	80.799	99.935	0.116	-10.65
0.85366	1.23660	-	-	0.111	-
0.87738	1.23653	-	-	0.109	-
0.89139	1.23654	78.852	97.504	0.101	-5.353
0.91719	1.23653	78.148	96.632	0.088	-4.439
0.93299	1.23656	-	-	0.076	-
		303.15 K			
0.05622	1.23748	91.609	113.36	-0.044	-2.26
0.11098	1.23738	87.744	108.57	-0.063	-4.70
0.20389	1.23692	83.056	102.73	-0.054	-6.55
0.28652	1.23632	78.893	97.537	-0.018	-8.20
0.39956	1.23545	75.210	92.918	0.042	-7.97
0.48912	1.23482	71.677	88.508	0.084	-8.53
0.60317	1.23417	67.780	83.652	0.118	-8.48
0.66057	1.23388	-	-	0.131	-
0.68702	1.23379	65.522	80.840	0.130	-7.69
0.71731	1.23368	-	-	0.131	-
0.77977	1.23343	62.652	77.277	0.136	-7.27
0.85366	1.23326	-	-	0.124	-
0.87738	1.23318	-	-	0.125	-
0.89139	1.23320	61.700	76.088	0.114	-3.67
0.91719	1.23321	60.996	75.221	0.100	-3.42
		308.15 K			
0.05622	1.23407	69.685	85.996	-0.042	-1.97
0.11098	1.23396	67.382	83.147	-0.060	-3.21
0.20389	1.23348	64.207	79.198	-0.051	-4.42
0.28652	1.23286	61.255	75.519	-0.013	-5.67
0.39956	1.23193	58.733	72.355	0.053	-5.50
0.48912	1.23127	56.620	69.715	0.098	-5.50
0.60317	1.23058	54.095	66.568	0.136	-5.29
0.66057	1.23029	-	-	0.147	-
0.68702	1.23018	51.919	63.870	0.149	-5.52
0.71731	1.23007	-	-	0.150	-
0.77977	1.22982	49.966	61.449	0.154	-5.21
0.85366	1.22964	-	-	0.142	-
0.87738	1.22959	-	-	0.137	-
0.89139	1.22960	49.443	60.795	0.128	-2.58
0.91719	1.22962	48.860	60.079	0.111	-2.5321

Tabla 18. Continuación.

X	ρ / g cm^{-3}	ν / mm^2 s^{-1}	η / mPa s	V^E / cm^3 mol^{-1}	$\Delta\eta$ / mPa s
		313.15 K			
0.05622	1.23072	54.557	67.144	-0.045	-1.45
0.11098	1.23059	52.941	65.149	-0.061	-2.31
0.20389	1.23005	50.639	62.289	-0.043	-3.24
0.28652	1.22939	48.662	59.825	0.001	-3.99
0.39956	1.22845	47.024	57.767	0.069	-3.69
0.48912	1.22780	45.384	55.722	0.113	-3.88
0.60317	1.22713	43.536	53.424	0.148	-3.81
0.66057	1.22683	-	-	0.162	-
0.68702	1.22672	41.972	51.488	0.164	-4.00
0.71731	1.22660	-	-	0.166	-
0.77977	1.22634	40.382	49.522	0.171	-4.04
0.85366	1.22616	-	-	0.160	-
0.87738	1.22611	-	-	0.155	-
0.89139	1.22613	40.195	49.284	0.144	-1.96
0.91719	1.22616	39.804	48.806	0.126	-1.91

Tabla 19. Parámetros (Ak) obtenidos para un ajuste polinómico en el caso de las propiedades ρ, ν, y con la ecuación de Redlich y Kister (6) para VE, Δη, así como las desviaciones estándar (s) para el sistema binario (x)[EMIM][EtSO$_4$]+(1-x)[EMIM][MeSO$_3$].

Propiedad	A_0	A_1	A_2	A_3	A_4	A_5	A_6	s
				283,15 K				
ρ (g/cm^3)	1.251	0.005	-0.056	0.115	-0.105	0.036	-	9.70E-06
ν (mm^2·s^{-1})	389.10	-536.80	992.33	-1584.6	1335.6	-416.86	-	0.8298
η (mPa·s)	486.89	-670.29	1224.1	-1942.9	1633.9	-508.87	-	1.0351
V^E (cm^3·mol^{-1})	0.147	0.419	-0.486	0.482	0.100	0.160	-	0.0014
Δη (mPa·s)	-215.48	59.033	-97.796	-94.102	12.794	204.20	-	0.6496
				288,15 K				
ρ (g/cm^3)	1.248	0.005	-0.058	0.122	-0.117	0.043	-	6.33E-06
ν (mm^2·s^{-1})	257.39	-293.96	388.66	-354.31	136.00	-	-	0.7727
η (mPa·s)	321.19	-366.70	480.18	-435.24	166.93	-	-	0.9609
V^E (cm^3·mol^{-1})	0.197	0.527	-0.342	0.720	0.165	0.025	-	5.27E-04
Δη (mPa·s)	-120.80	68.717	-89.521	-137.19	242.16	185.65	-274.88	0.1969
				293,15 K				
ρ (g/cm^3)	1.244	0.005	-0.059	0.126	-0.122	0.045	-	0.00001
ν (mm^2·s^{-1})	179.28	-170.40	182.18	-154.21	62.980	-	-	0.5227
η (mPa·s)	223.08	-211.96	223.35	-187.15	76.490	-	-	0.6421
V^E (cm^3·mol^{-1})	0.242	0.550	-0.396	0.788	0.416	-0.022	-0.194	9.30E-04
Δη (mPa·s)	-77.752	11.376	-5.415	22.799	-25.857	-	-	0.5689
				298,15 K				
ρ (g/cm^3)	1.241	0.006	-0.062	0.131	-0.126	0.047	-	0.00003
η (mPa·s)	164.66	-133.44	70.193	-6.051	-	-	-	0.4600
ν (mm^2·s^{-1})	132.69	-107.31	57.247	-5.522	-	-	-	0.3700
V^E (cm^3·mol^{-1})	0.304	0.615	-0.650	0.885	1.020	-0.151	-0.457	0.0015
Δη (mPa·s)	-58.558	9.805	-54.891	-36.278	187.12	37.887	-158.18	0.2201

Tabla 19. Continuación.

Propiedad	A_0	A_1	A_2	A_3	A_4	A_5	A_6	s
				303,15 K				
ρ (g/cm^3)	1.237	0.005	-0.057	0.117	-0.110	0.041	-	0.00003
ν (mm^2·s^{-1})	95.474	-79.061	111.34	-131.27	64.582	-	-	0.4067
η (mPa·s)	118.14	-97.739	135.67	-159.61	78.858	-	-	0.4994
V^E (cm^3·mol^{-1})	0.353	0.760	-0.510	0.559	0.612	0.181	-	0.0022
Δη (mPa·s)	-33.519	-1.091	-27.764	7.047	5.628	-2.514	20.067	0.4683
				308,15 K				
ρ (g/cm^3)	1.234	0.002	-0.026	-0.015	0.141	-0.179	0.072	0.00001
ν (mm^2·s^{-1})	72.618	-55.977	88.420	-111.71	55.691	-	-	0.2700
η (mPa·s)	89.614	-69.017	107.47	-135.71	67.957	-	-	0.3307
V^E (cm^3·mol^{-1})	0.411	0.817	-0.527	0.692	0.703	-	-	0.0012
Δη (mPa·s)	-21.716	4.229	-31.079	-32.909	24.689	45.192	-	0.2935
				313,15 K				
ρ (g/cm^3)	1.231	0.006	-0.066	0.145	-0.143	0.055	-	0.00003
ν (mm^2·s^{-1})	56.676	-40.908	71.724	-96.639	49.214	-	-	0.2276
η (mPa·s)	69.752	-50.314	86.977	-117.24	59.969	-	-	0.2775
V^E (cm^3·mol^{-1})	0.472	0.775	-0.449	0.947	0.634	-	-	0.0014
Δη (mPa·s)	-14.981	1.242	-27.960	-21.699	22.931	32.388	-	0.2311

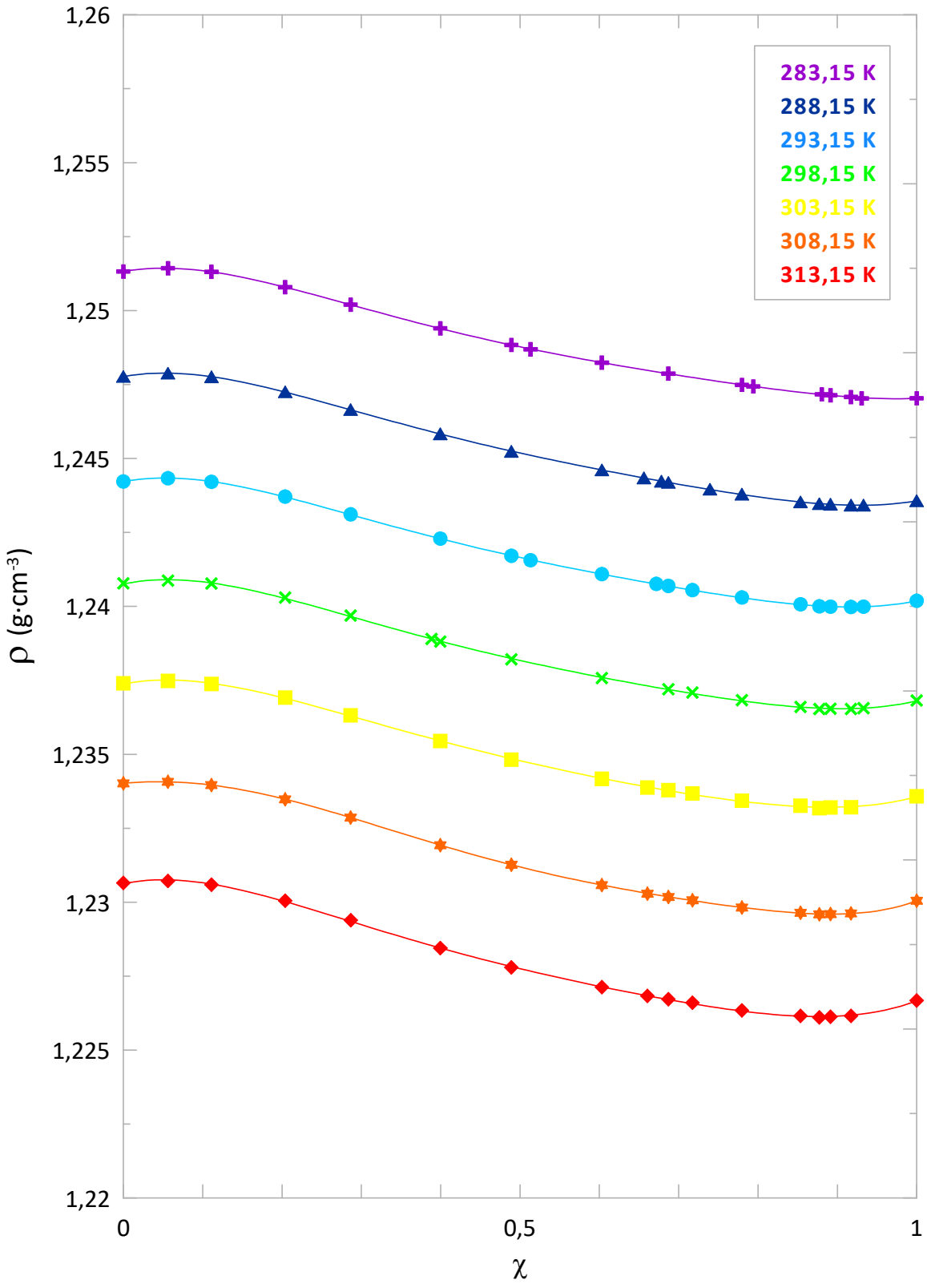

Figura 60. Variación de la densidad del sistema (x)[EMIM][EtSO₄]+(1-x)[EMIM][MeSO₃] en función de la temperatura: (+)283,15K, (▲)288,15K, (●)293,15K, (x)298,15K, (■)303,15K, (*)308,15K, (♦)313,15K.

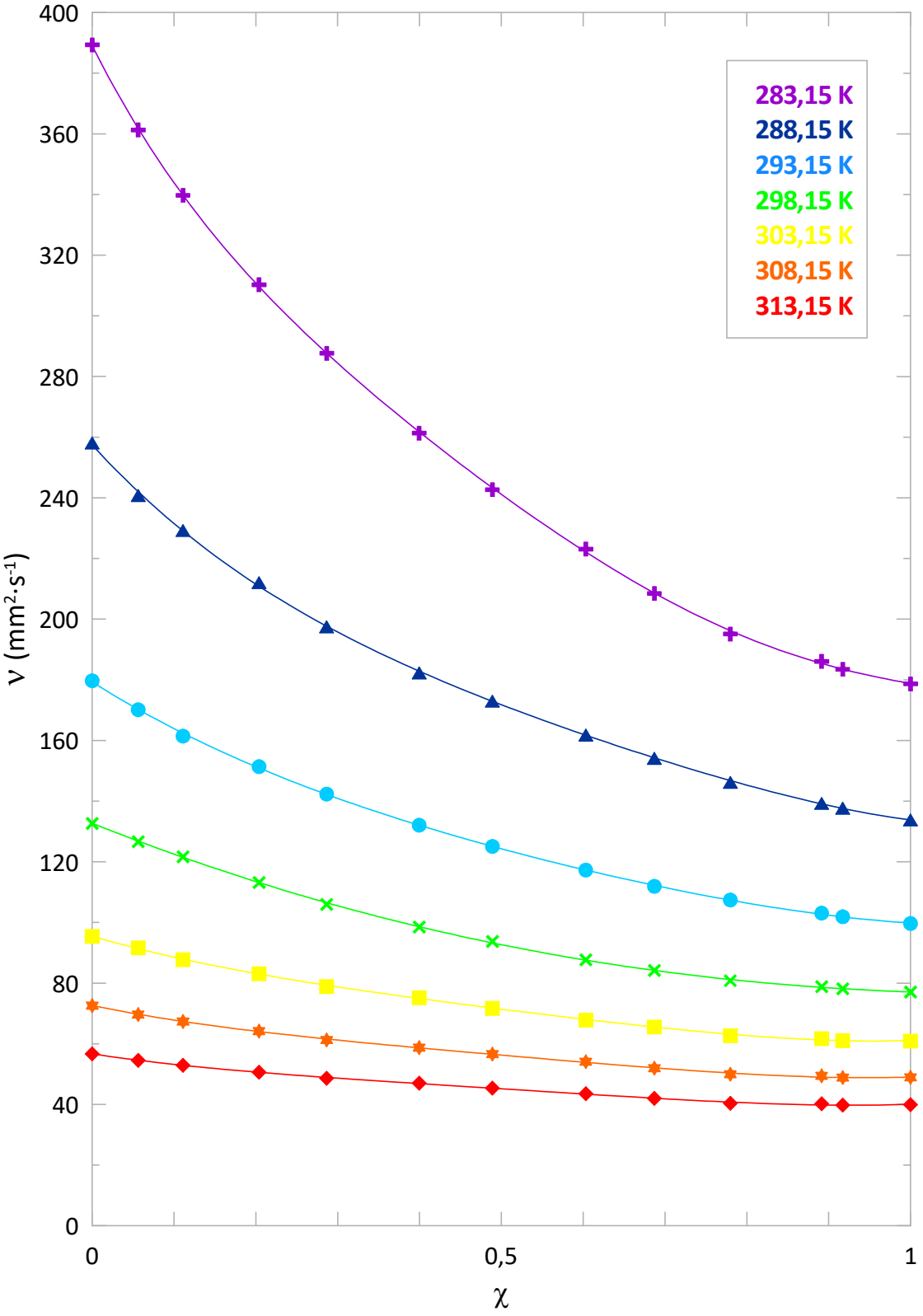

Figura 61. Variación de la viscosidad cinemática del sistema (x)[EMIM][EtSO₄]+(1-x)[EMIM][MeSO₃] en función de la temperatura: (+)283,15K, (▲)288,15K, (●)293,15K, (x)298,15K, (■)303,15K, (*)308,15K, (♦)313,15K.

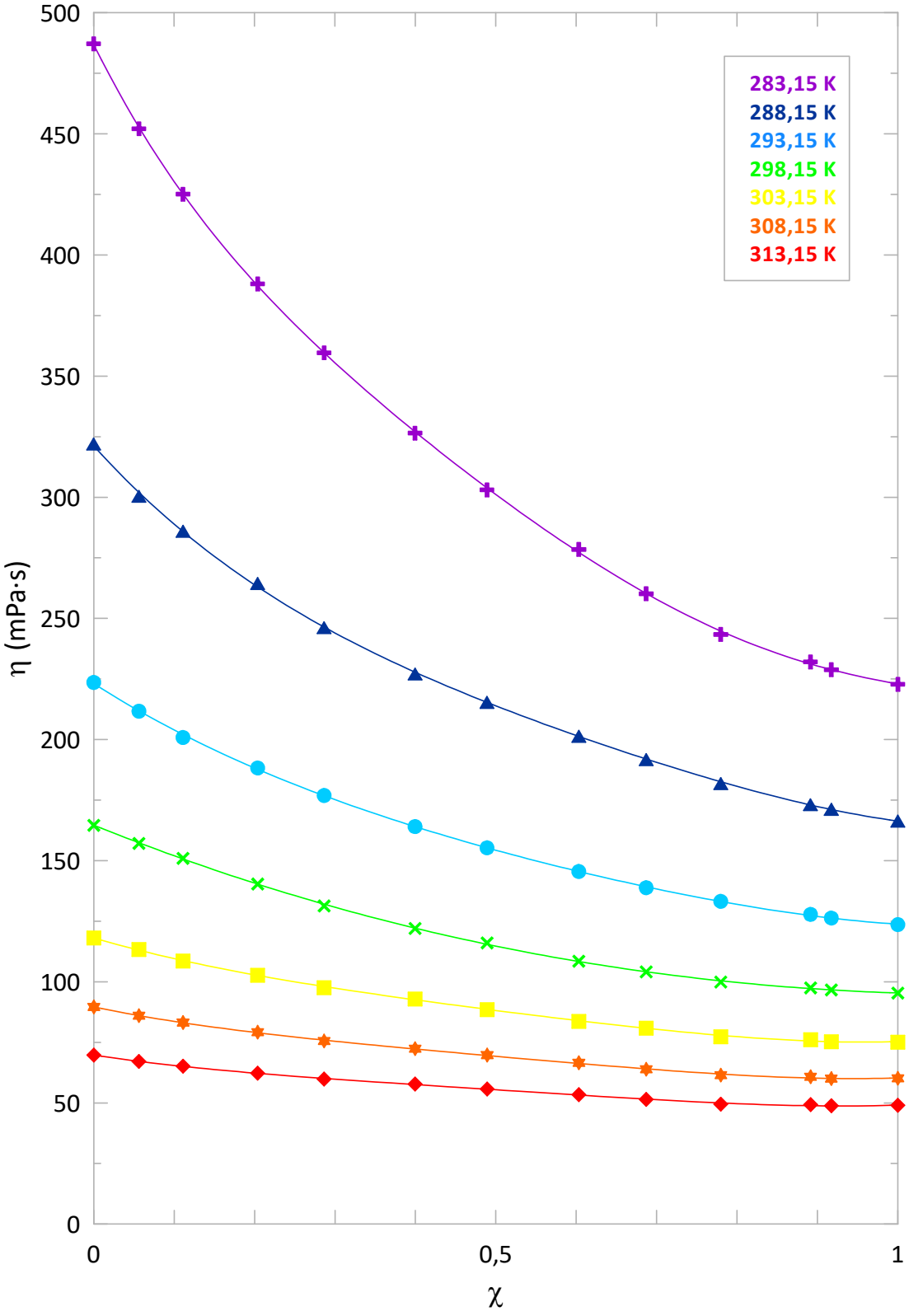

Figura 62. Variación de la viscosidad dinámica del sistema (x)[EMIM][EtSO₄]+(1-x)[EMIM][MeSO₃] en función de la temperatura: (+)283,15K, (▲)288,15K, (●)293,15K, (x)298,15K, (■)303,15K, (*)308,15K, (♦)313,15K.

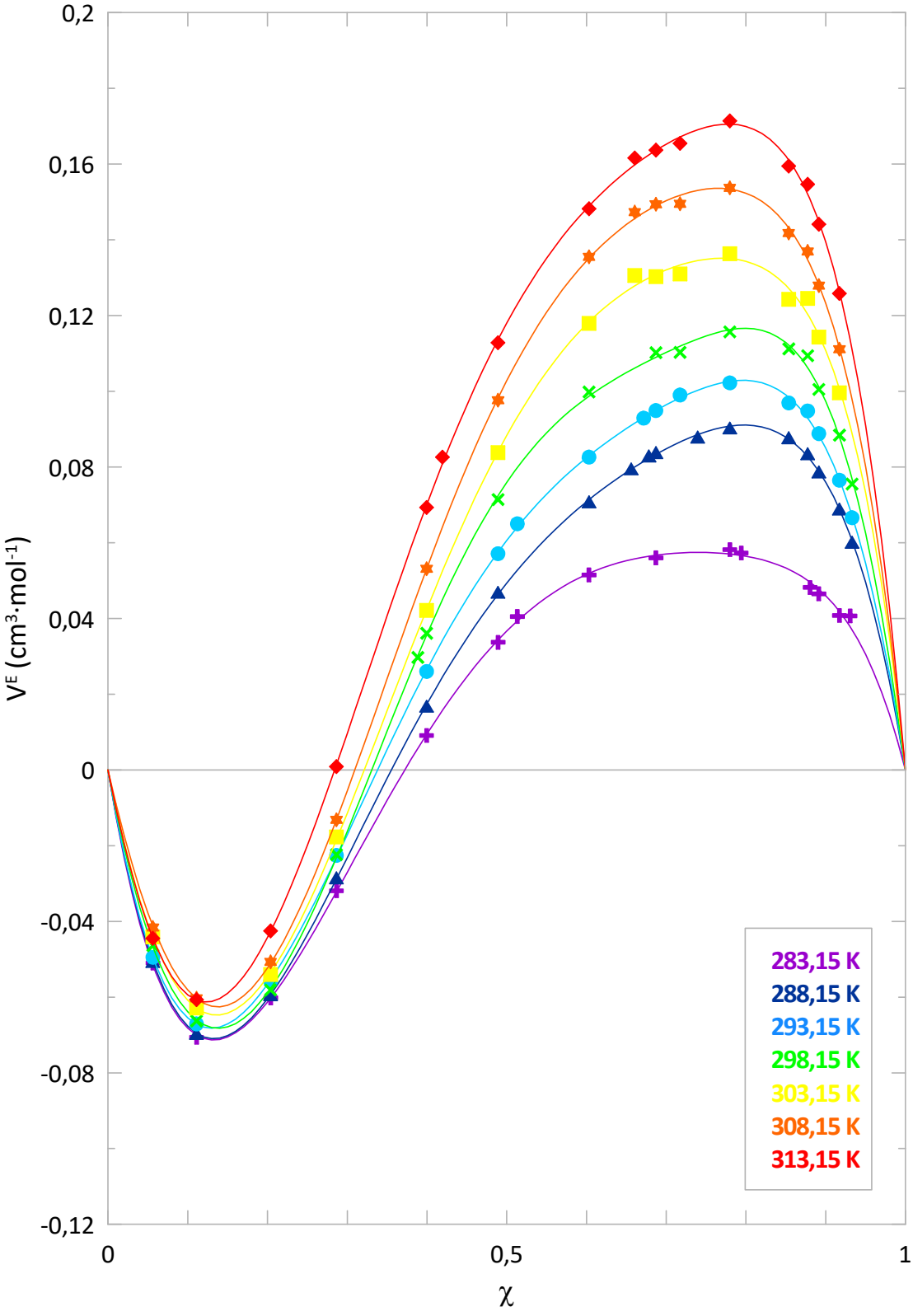

Figura 63. Volumen molar de exceso del sistema (x)[EMIM][EtSO₄]+(1-x)[EMIM][MeSO₃] en función de la temperatura: (+)283,15K, (▲)288,15K, (●)293,15K, (x)298,15K, (■)303,15K, (*)308,15K, (♦)313,15K.

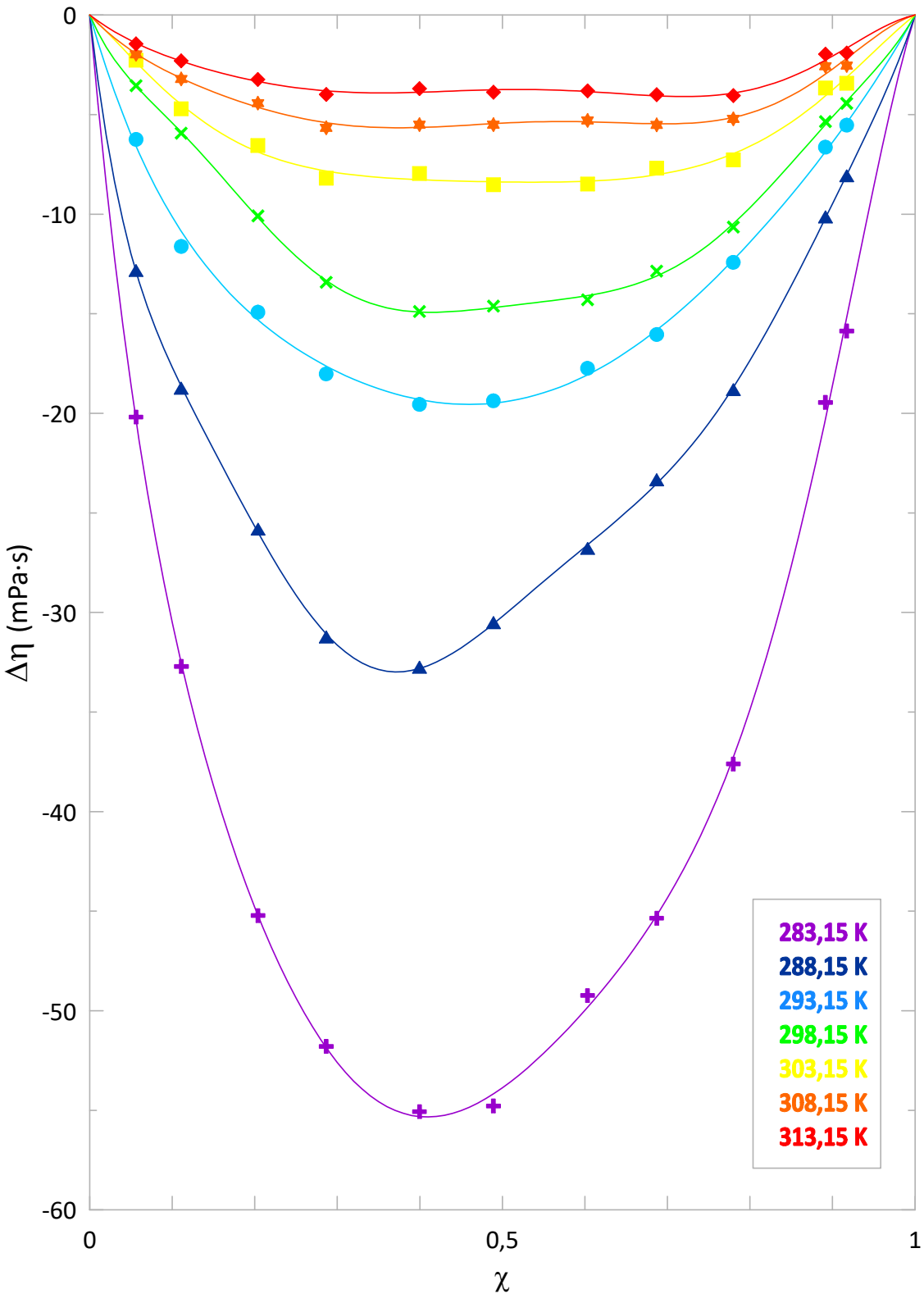

Figura 64. Desviaciones de la viscosidad del sistema (x)[EMIM][EtSO$_4$]+(1-x)[EMIM][MeSO$_3$] en función de la temperatura: (+)283,15K, (▲)288,15K, (●)293,15K, (x)298,15K, (■)303,15K, (*)308,15K, (♦)313,15K.

5.1.4. Publicación III

Título:	**Alkylimidazolium-based Ionic Liquid Mixtures: the case of [EMIM][BF_4] + [EMIM][$MeSO_3$]**				
Autores:	Ylenia Rodríguez [a], Santiago Aparicio [b], José L. Trenzado [a]				
Afiliación:	[a]) Departamento de Física, Universidad de Las Palmas de Gran Canaria, 35017 Las Palmas G.C., Spain [b]) Department of Chemistry, University of Burgos, 09001 Burgos, Spain				
Revista:	Journal of Molecular Liquids				
Factor impacto (IF):	6.633	**Cuartil (JRC):**	Q1	**Citas:**	-
Editor:	Elsevier	**Fecha de publicación:**	*En revisión*		

Alkylimidazolium-based Ionic Liquid Mixtures: the case of [EMIM][BF_4] + [EMIM][$MeSO_3$]

Ylenia F. Rodríguez,[a] Santiago Aparicio[b*] Jose L. Trenzado[a*]

[a] Department of Physics, University of Las Palmas de Gran Canaria, 35017 Las Palmas G.C., Spain

[b] Department of Chemistry, University of Burgos, 09001 Burgos, Spain

[*]Corresponding authors: jose.trenzado@ulpgc.es (J.L.T) and sapar@ubu.es (S. A.)

ABSTRACT

Ionic liquids (ILs) have emerged as a promising class of materials due to their unique properties compared to conventional (volatile) organic solvents. This research explores the potential and properties of binary ionic liquid mixtures, also known as double salt ionic liquids (DSILs), obtained through the combination of two ILs, leading to mixtures containing a single type of cation and two types of anions. The focus of this study is the investigation of a specific (archetypical) DSIL system composed of 1-ethyl-3-methylimidazolium cation ($[EMIM]^+$) combined with tetrafluoroborate ($[BF4]^-$) and methanesulfonate ($[MeSO3]^-$) anions, experimentally obtained as a liquid mixture of [EMIM][BF_4] + [EMIM][$MeSO_3$]. A multiscale approach integrating thermophysical measurements and molecular modeling (Molecular Dynamics simulations) is employed to achieve a comprehensive understanding of the DSIL's properties. The properties of the systems are analyzed in terms of their deviations of ideality when considered as a mixture of two compounds, and its relationships with the developed intermolecular forces, considering their role in the mixed liquid (nano)structuring, ionic clustering and fluid's dynamics. This knowledge is crucial for unlocking the potential applications of ILs beyond those containing just and anion and a cation, through the possibility of tuning their properties including several types of ions, thus leading to fluids with more complex structures which can in various technological fields.

Keywords: Double salt ionic liquids; Multiscale approach; imidazolium; Thermophysical properties; molecular dynamics; intermolecular forces.

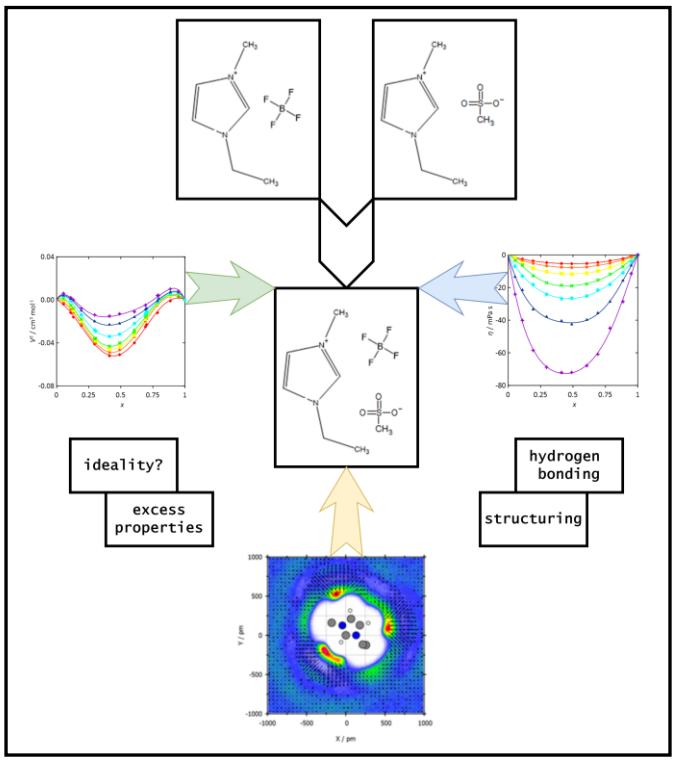

Graphical Abstract

1. INTRODUCTION

Over the past century, ionic liquids (ILs) have emerged as a captivating research area due to their unique properties [1]. Unlike conventional (volatile) solvents, which are composed of neutral molecules, the ionic character of ILs (with melting points typically below 100 °C) leads to negligible volatilities, vanishing atmospheric pollution from their industrial use. ILs are usually classified in three generations [1]: *i*) first generation: ILs with unique physicochemical properties, e.g. alkylimidazolium, as cations, combined with anions such chloroaluminate and metal halides, *ii*) ILs with targeted physicochemical properties, e.g. alkylimidazolium cations combined with anions such as Cl^-, Br^-, I, PF_6^-, BF_4^-, and *iii*) ILs with targeted biological (toxicity), e.g. cations such as choline, combined with anions as amino acids, alkylphosphates or alkylsulfates. This classification of ILs follows the historical evolution of their development since the discovery of ethylammonium nitrate in 1914 by Paul Walden, which marked the birth of ionic liquids [2]. The initial (first) generation of ILs faced limitations due to air and water sensitivity, hindering their early development and technological scaling up [3]. A breakthrough came in the 1990s with the introduction of air and water-stable ILs by Wilkes and Zaworotko, exemplified by 1-ethyl-3-methylimidazolium tetrafluoroborate [4], which paved the way for the second generation of ILs. The surge in popularity of the third generation, or "task-specific" – biologically target, low toxic ILs, underlines their remarkable tunability for specific applications paired with their sustainability as design criteria [5]. Therefore, reflecting their growing importance, the number of scientific publications on ILs has witnessed an exponential rise, reaching over 96,765 by 2022 [6], thus, based on their history over the last century, ILs appear to be one of the most promising fields of research in the area of solvents and related technologies.

ILs are usually formed by an organic cation and an organic or inorganic anion, and thus, the extensive number of possible combinations of known cations and anions (10^6–10^{18}), results in different and unique physicochemical properties which can be fine-tuned and designed for the required technological applications [7]. Due to this huge number of possible combinations, understanding the molecular-level organization of anions and cations in the fluids and the identification of structure−properties correlations, becomes vital for a proper technological development [8]. Therefore, a close integration of experimental, theoretical, and computational

methods is required for a multiscale fluid phase characterization, thus allowing the development of predictive tools to facilitate the design of new ILs. However, the complexity nature of their intermolecular interactions sets a significant challenge to achieve this goal [9]. However, regardless the cation or anion combination, ionic liquids have common unique properties such as extremely low vapor pressure or non-volatility under ambient conditions, large liquid range, tuneable polarity, conductivity, wide solubility, and long-range thermal stability [10]. All these properties can be modified changing the choice of anion or cation. For instance, ionic conductivity, which depends on the available charge carriers and their mobility, decreases by increasing the size of the cation (i.e. longer alkyl chains) [11]. On the other hand, the physical characteristics of the anion can modify properties such as density (increasing as its molecular mass increases) or thermal stability (increasing as its size increases) [12]. The relation between anions and cations also impacts the final properties of ionic liquids, i.e., the lack of symmetry in ions impede the process of crystallization and resulting in lower melting point; or the difference in size between ions may influence in viscosity [13,14].

Most of the reported literature has focused on pure ILs, composed of a single type of cation and a single type of anion, in combination with other solvent. Nevertheless, a greater structural variety can be achieved by mixing ILs, becoming an alternative to design tailor-made solvents for specific applications. By incorporating multiple cations or anions, a novel concept of "double salt ILs" (DSILs) emerges, this mixtures of ILs show interesting and often unpredictable properties [15,16]. Since the structures and behavior of ionic liquids is controlled by a range of intermolecular interactions, which include Coulombic forces, dispersion interactions, hydrogen bonding, and pi-interactions; combining ions in an DSIL can induce a preferential orientation of the ionic species and non-covalent interaction sites that change significantly from those found in single-component ILs [17,18]. DSILs offer significant advantages for the development of ILs and their possible technological applications. Firstly, ILs containing multiple cations and / or anion constitutes a large portion of the proposed 10^{18} ILs [19]. Secondly, the physicochemical properties of the IL phase may be fine-tuned through suitable selection and combination of ions as well as considering the mixture composition [18]. Thirdly, the simplicity of their preparation (with a degree of complexity comparable to ILs containing just one cation and anion [20]), and

thus, possible technological applications of ILs is largely extended. Therefore, DSILs, and in general ILs mixtures, have been considered for applications such as CO_2 capture [21], herbicides development [22], electrochemistry [23], or solvents for complex separation processes [24]. Several literature studies have considered the properties od DSILs from the viewpoint of intermolecular forces and deviations from ideality [17,18]. Intermolecular forces in the DSILs were analyzed via experimental studies (e.g. SAXS measurements) and Molecular Dynamics (MD) simulations [25,26]. Large relevant effects on DSILs structuring have been reported in the mesoscale probing the complexity of intermolecular forces and ionic arrangements [27]. This complexity in DSILs properties and structuring requires a systematic selection method for the considered involved ions [28], thus, allowing to separate the complex factors and thus contributing to the advance in the understanding of properties of DSILs, as mixtures of ILs. Therefore, this work considers an approach to DSILs by integrating thermophysical investigations with molecular modelling (MD) for the archetypical system formed by the specific binary [EMIM][BF_4] + [EMIM][$MeSO_3$], [EMIM] standing for 1-ethyl-3-methylimidazolium cation coupled with tetrafluoroborate and methanesulfonate, Figure 1. This multiscale approach provides a comprehensive understanding of the physicochemical properties and nanostructuring of the studied system aiming to unlock its full potential in various practical applications [2].

2. METHODS

2.1 Chemicals

The ionic liquids [EMIM][BF_4] and [EMIM][$MeSO_3$] were used for the experimental study. They were provided by a commercial supplier (Sigma-Aldrich) and were employed without further purification, Table S1 (Supplementary Information) reported additional information about pure ILs. Prior to use ILs were degassed by ultrasound and stored at suitable conditions, in their delivery bottles in a dry and dark place. The properties of pure ILs were measured as a function of temperature from 283.15 to 313.15 K range, in 5 K steps at atmospheric pressure, and compared with literature, Table S2 (Supplementary Information). The observed minor variations between experimental results and literature can be attributed to slight differences in water content (0.08 and 0.40 wt % for [EMIM][$MeSO_3$] and [EMIM][BF_4], respectively, for the

samples considered in this work, Table S1, Supplementary Information) and their distinct origins. The purity of the considered ILs for mixtures preparation (> 99 %) as well as the low water content assures reliable results for the studied IL mixture. Likewise, the suitable agreement among experimental properties and those reported in the literature (Table S2, Supplementary Information), specially for viscosity, which is largely sensitive to purity [29], confirms the suitability of the considered IL sources. Therefore, it is important to note that presence of significant impurities was discarded. Binary mixtures were prepared in the full composition range, *x* [EMIM][BF_4] + (1-*x*) [EMIM][$MeSO_3$] (where *x* stands for mole fraction), by weighing (Mettler AE240 balance, ± 0.01 mg) to ± 0.00004 estimated mole fraction uncertainty.

2.2 Apparatus and procedures

Density (ρ) and kinematic viscosity (ν) were measured for binary mixtures *x* [EMIM][BF_4] + (1-*x*) [EMIM][$MeSO_3$], where *x* stands for mole fraction, in the full composition range, at atmospheric pressure and temperature in the 283.15 to 313.15 K range. ρ was measured with a vibrating tube densimeter (Anton Paar DMA5000, uncertainty $1 \cdot 10^{-4}$ g cm^{-3}) with cell temperature controlled with Peltier elements and measured to ± 0.01 K. ν was measured using capillary Ubbelohde viscometers. The viscometer was submerged in an external circulating bath with a cell temperature measured with ± 0.01 K uncertainty (CT-52, Schott Instruments) and an automatic control unit AVS350 (Schott, ViscoSystem®) with ± 0.01 s uncertainty. Dynamic viscosity (η) was calculated as in eq. (1).

$$\eta = \nu \, \rho \tag{1}$$

The procedures for calculating derived properties such as thermal expansion coefficient, α_p, as well as excess (excess volume, V^E, and excess thermal expansion coefficient, α_p^E,) and mixing properties (mixing viscosity, $\Delta\eta$) is explained in the Supplementary Information. Additionally, ρ and η were fitted to a polynomial equation, whereas excess and mixing properties were fitted to o an isothermal Redlich–Kister (RK) type polynomial equation as a function of mole fraction, *x*. From the RK fits of V^E, the partial molar volume $\bar{V}_i$ of each i - component was calculated, as well as the excess partial molar volumes, $\bar{V}_i^E$, and the excess partial molar volumes at infinite dilution, $\bar{V}_i^{E,\infty}$, Supplementary Information. Experimental η vs temperature data followed a non-Arrhenius behavior. ILs not obeying Arrhenius law are typically formed by small and symmetrical

ions with low molar mass [30], as those considered in this work. Symmetric and small ions form extended ionic networks, inhibiting laminar flow and thus departing from Arrhenius behavior. Therefore, the Vogel-Fulcher-Taman (VFT) model was applied:

$$\eta = \eta_0 exp\left(\frac{B}{T-T_0}\right) \quad (2)$$

VFT fitting parameters were used for the calculation of Angell's strength (fragility measurement) parameter, D_f:

$$D_f = \frac{B}{T_0} \quad (3)$$

Results for experimental thermophysical properties are reported in Table S3 (Supplementary Information). VFT fit results and D_f parameters are reported in Table S4 (Supplementary Information), with RK fits in Table S5 (Supplementary Information). Additionally, V^E was analysed in terms of the Prigogine – Flory – Patterson (PFP) model [31], for which the required parameters are reported in Table S6 (Supplementary Information).

2.3 Thermodynamics calculations with COSMO

Structures for isolated ions were optimized in gas phase at BP86/def-TZVP plus Grimme's D3 [32] theoretical level using Turbomole software [33], from which the corresponding COSMO files were calculated an used for COSMOtherm calculations with COSMOthermX software [34].

2.4 Classical Molecular dynamics simulations

Software, Molecular Model and Force Field: MD simulations were carried out using MDynaMix v.5.2 software [35]. Force field parameters for the three ion types: $[EMIM]^+$, $[BF_4]^-$, and $[MeSO_3]^-$ (Table S7, Supplementary Information), were obtained from the SwissParam database (Merck Molecular Force Field, MMFF [36])), except for atomic charges. These charges were calculated from calculations of ions (optimized as explained in section 2.3) using ChelpG method.

Simulation Setup: cubic simulation boxes with 1000 total ions (500 [EMMIM] cations and 500 anions, sum of $[BF_4]$ + $[MeSO_3]$ depending on the mixture composition were considered; Table S8, Supplementary Information) were prepared using Packmol software [37], in agreement with experimental density data (Table S3, Supplementary Information). Periodic boundary conditions were applied in all directions for all simulated systems. **Systems preparation and equilibration**: initial simulation boxes were subjected to *i*) NVT simulations (equilibration runs):

performed at 298.15 K for 10 ns, followed by *ii*) NPT simulations (production runs): performed at 298.15 K and 1 bar for 200 ns, used for analysis. All the simulations with a timestep of 1 fs. The Nose-Hoover method [38] was employed for temperature and pressure control. **Non-bonded Interactions:** Electrostatic interactions were treated with the Ewald method [39] using a 15 Å cutoff radius. Lennard-Jones potential (15 Å cutoff) with Lorentz-Berthelot (LB) mixing rules was used for cross terms. Although parameters for MMFF for cross terms are not usually described using LB mixing rules [40], these are a simplified version which can be used with the parameters reported in Table S8 (Supplementary Information). **Data Analysis:** visualization, analysis, and post-processing of the MD trajectories were performed using VMD [41] and TRAVIS [42].

3. RESULTS AND DISCUSSION

3.1 Macroscopic and thermodynamic characterization

Physical properties, ρ and η, values for pure ILs [EMIM][BF_4] and [EMIM][$MeSO_3$], and their binary mixtures in the full composition range have been experimentally measured in the range from 283.15 to 313.15 K. These experimental properties as well as excess / mixing calculated ones, are reported in Figures 2 to 3. Density versus mole fraction as a function of temperature experimental data are show in Figure 2a showing linear behaviour (R^2 = 0.9999, for linear fitting equation). Despite the linearity of the densities, the V^E vs mixture mole fraction (Figure 2b) shows a complex pattern characterized by a minimum almost at equimolar fraction [EMIM][BF_4] (x = 0.44) and two maxima, at [EMIM][$MeSO_3$] rich mixtures (x = 0.06) and [EMIM][BF_4] rich molar fraction (x = 0.92). Nevertheless, V^E values are not too large, increasing in absolute value upon heating (largest value of -0.05 $cm^3\,mol^{-1}$ at 313.15 K), results suggested slight deviations from ideality. The complex V^E pattern for ILs mixture as reported in Figure 2b is a sign of subtle mixed fluid behaviour, largely dependent on the mixture composition. Navia et al. [43] reported V^E for the system [1-butyl-3-methylimidazolium][BF_4] + [1-butyl-3-methylimidazolium][methylsulfate] ([BMIM][BF_4]+[BMIM][$MeSO_4$]), which is similar to the one considered in this work. Their results show $V^E < 0$, with a minima of -0.06 $cm^3\,mol^{-1}$ at 303.15 K for roughly equimolar mixtures, which agrees with results reported in this work. Although values

in [43] does not show the complex pattern as in Figure 2b, their results are reported from x>0.12 and values at high [BMIM][BF_4] are close to zero, thus indicating a similar behaviour to that in Figure 2b. Additionally, IL mixtures containing [EMIM] cation with aminoacid-based anions have also reported complex V^E patterns as those in Figure 2b [44,45]. The small minima at roughly equimolar composition reported in Figure 2b, which (in absolute value) increases upon heating indicates minor changes in intermolecular forces (hydrogen bonding) upon mixing, being the steric factors the most relevant feature. Likewise, the slightly $V^E > 0$ in both composition extremes, i.e. the disrupting effect of [BF_4] anions in [$MeSO_3$] – rich IL, and viceversa, clearly indicates that the differences between the sizes and shapes of both anions determine the volumetric properties upon mixing, with minor changes in hydrogen bonding. This behaviour agrees with literature studies showing as the difference between the sizes of the two ions (cations or anions) increases, the V^E values become larger [18,46,47]. Accordingly, it is possible to infer from the mixture analysed that at equimolar fractions there seems to be a higher degree of efficient packing for both types of anions.

Regarding energy evolution upon mixing, Navia et al. [43] reported exothermic mixing for [BMIM][BF_4]+[BMIM][$MeSO_4$], with a minima of -0.36 kJ mol^{-1} also for equimolar mixtures. For [EMIM][BF_4] and [EMIM][$MeSO_3$], COSMO calculations, using isolated ions approach, led to the excess enthalpy, H^E, reported in Figure 3a, also indicating exothermic mixing with a minima of -0.87 kJ mol^{-1} close to equimolar conditions. This non-negligible H^E also shows the non-ideal character of the considered mixtures. Additional COSMO calculations led to excess entropy, S^E (Figure 3a), being positive and comparable to H^E. Golub et al. [48] showed that for a mixture of ILs sharing a common cation, as in this work, $S^E < 0$ rising from hydrogen bonding redistribution upon mixing may overcompensate the (ideal) positive entropy contribution rising from the distribution of ions in the IL mixture, and also pointing to an enthalpic driven mixing process. In the case of results in Figure 3a, the $S^E > 0$ does not point to hydrogen bonding redistribution, on the contrary an ideal mixing process from the entropy viewpoint, which can be caused by the very different nature of the considered anions ([BF_4] and [$MeSO_3$]) whereas in [48] both considered anions belong to the methanesulphonate family. Nevertheless, the $G^E < 0$ in the whole composition range, indicates enthalpy driven mixing without phase separation. The non-ideal

behaviour of the considered IL mixture is inferred from the COSMO calculated activity coefficients, γ_i (Figure 3b), showing almost symmetric curves for both ILs, which agrees with the indicated minor changes in intermolecular forces upon mixing, in which both ILs show similar affinities. The activity coefficients at infinite dilution, γ_i^{∞}, being almost equal for both compounds also indicate proper fitting of each compound into the hydrogen bonded network developed by the other compound, Figure 3b.

The obtained α_p and α_P^E are show in Figures 2c and 2d respectively. The α_p evolution with mixture composition shows a non-linear behavior, which leads negative α_P^E with minimum nearly at equimolar fraction [EMIM][BF_4] (x = 0.44) and practically negligible effect of the temperature. Although their values are close to zero, negative α_P^E reveal that the mixture of both anion leads a less compressible liquid. The reported minima in α_P^E of -0.007 10^{-3} K^{-1} is slightly lower than those reported in the literature for mixtures of ionic liquids with a common cation (e.g. -0.014 10^{-3} K^{-1} [49]).

Figure 2e show the composition evolution of η, with mixture composition and temperature, which exhibit largely non-linear behaviour, especially as the temperature decreases. Pure viscosity values for [EMIM][$MeSO_3$] are three times those of [EMIM][BF_4] at high temperatures, but at the lowest temperatures studied they are in the order of 8 times higher (Table S2, supplementary Information), therefore the η vs temperature behaviour cannot be described according to Arrhenius model and VFT model was calculated for all the systems (Table S4, supplementary Information). All the VFT fitting parameters, including T_0 which is closely related with the glass transition temperature [50], follow a non – linear evolution with temperature, Figures 4a – 4c, thus pointing to non-negligible effects upon mixing. Also, the D_f parameter was inferred from the calculated VFT parameters. The D_f parameter for neat [EMIM][BF_4] (3.04) is slightly lower than the value previously reported in the literature (4.44 [51]), but confirm that this IL as well as [EMIM][$MeSO_3$] (D_f = 3.51) are largely fragile fluids. The D_f vs mixture composition shows increase of fragility up to roughly equimolar mixtures with almost constant fragility for [BF_4] – rich mixtures (Figure 4d). The behaviour of $\Delta\eta$ vs composition and temperature range exhibit substantial negative values, which are remarkably large for low temperature and (in absolute value) decreases as the temperature increases, with minima close

to equimolar composition for the whole temperature range. These negative values of $\Delta\eta$ are related with certain degree of packing, in agreement with $V^E < 0$ (Figure 2a), resulting in less surface area available for friction and lower viscosity of the mixtures [45,47]. Negative $\Delta\eta$ is a common feature for mixtures of ILs containing [EMIM] as the common cation, e.g. for anions as [BF_4] + [dicyanamide] [52], [bis(trifluoromethanesulfonyl)imide] + [ethylsulphate] [53], or [bis(trifluoromethanesulfonyl)imide] + [acetate] [54]. It has been showed that the decrease in viscosity upon mixing rises from the differences for the cation – anion interactions, in the case of [BF_4] and [$MeSO_3$], their hydrogen bonding with the [EMIM] cation are quite dissimilar (as the viscosity of the neat ILs are, Table S2, Supplementary Information), thus upon mixing leading to the $\Delta\eta < 0$.

Additional investigation into the structuring of mixed ionic liquids involves the calculation of excess partial volumes, $\bar{V}_i^E$, reported in Figures 5a and 5b, and the values at infinite dilution, $\bar{V}_i^{E,\infty}$, Figure 5c. $\bar{V}_i^E$ shows symmetric general behavior for both components, which agrees with the shape of V^E vs mixture composition curves (Figure 2a). $\bar{V}_i^E$ exhibit negative values for each IL when being the solute in a solution where the other IL act as solvent, increasing with temperature. From equimolar point to the mole fractions comprising the other anion pure IL, regardless of the temperature, $\bar{V}_i^E$ shows near zero values. Negatives $\bar{V}_i^E$ results would indicate dense packing between ions. $\bar{V}_i^{E,\infty}$ indicate the disrupting effect of one type of anion on the structuring of the other one. [EMIM][$MeSO_3$] shows positive values decreasing with increasing temperature, while [EMIM][BF_4] exhibit the same decreasing behaviour except from 303.15 K, whose values become negatives, but in both cases the values are very small indicate proper fitting of each anion in the IL formed by the other ion, except for largely diluted mixtures, which would form the very small $V^E > 0$ (Figure 2a). Likewise, there is close to linear correlation between . $\bar{V}_i^{E,\infty}$ and γ_i^{∞}, Figure 5d, thus probing how steric effects control the mixing properties as a consequence of the dissimilarities among the sizes, shapes and mechanism of hydrogen bonding with [EMIM] for the considered anions.

The Prigogine-Flory-Patterson (PFP) has been considered for the prediction of V^E (Table S6, supplementary Information; Figure 6a) to analyse the possible different contributions to the volumetric properties of the considered mixtures, using a single temperature dependent

interaction parameter, X_{12}. The X_{12} was obtained at each temperature from the fitting of experimental excess volume data, as done in the literature for IL mixtures [31]. PFP model allows to infer V^E as the sum of different contributions: interactional (Figure 6b), free volume and P^* contributions. The first relevant result is the moderately predictive ability of PFP for the complex pattern of V^E, and although the model is able to predict the property sign as well as the low values, the shape of the curves is not properly captured. Figure 6a. Nevertheless, the model allows to show, at least in a semi-quantitative way, the intermolecular interactions through the χ_{12} interaction parameter (Figures 6c and 6d) [16,17]. It could be inferred from results in Figure 6c that the strongest interactions take place in mixtures rich in one of the anions when the other component starts to perform. It seems that at equimolar fractions, the interactions between the ions decrease to almost zero. Therefore, PFP results confirm the ability of each IL (anion) to fit into the other IL, with changes upon mixing leading mainly from steric effects.

3.2 Nanoscopic characterization via Molecular Dynamics simulations

The nanostructural analysis of the considered mixed ionic liquids was conducted using MD simulations across the entire composition range. The molecular arrangements were initially characterized via the connection matrix (*cmat*), which was considered to identify relevant interacting (relevant) atomic pairs. The *cmat* analysis considers relevant site-site Radial Distribution Functions (RDFs), considers the first peak of each RDF (short-range strong interactions, e.g. hydrogen bonding) and characterize it by its distance (peak maximum) and intensity, then the information is color-coded to visually represent significant intermolecular interactions within the mixtures (Figure 7). Hydrogen bonding in [EMIM]-based ILs occurs through two C-H sites in the imidazolium ring: H1 and H4/H5 (Figure 1). In the case of neat [EMIM][$MeSO_3$] (x = 0) and neat [EMIM][BF_4] the anion oxygen and fluorine atoms are hydrogen bonded to both imidazolium C-H sites, although interactions through C-H1 site are preferentially produced. For the studied composition range, the mechanisms of cation-anion hydrogen bonding are maintained as the *cmat* spots show, thus both types of anions are simultaneously hydrogen bonded to the [EMIM] cation. The absence of additional significant spots in the *cmats* suggests that hydrogen bonding is the primary force driving ion pairing in the studied mixtures, with competing effects between the two types of anions. RDFs (Figure 8) were analyzed in detail for

the hydrogen bonding interactions. Results in Figure 8a confirm the formation of anion(s) – cation hydrogen bonds. Nevertheless, these RDFs are very different for interactions through cation H1 and H4/H5 sites. In the case of interactions through [EMIM](H1), a first intense RDF peak appears at 2.3 – 2.4 Å, less intense for [$MeSO_3$] than for [BF_4], this first peak is followed by several additional peaks at larger distances, with similar patterns for both types of anions, which confirms interactions beyond anion-cation dimmers, i.e. ion clustering. In the case of interactions through the [EMIM](H4-5), a first peak at slightly larger distances than for [EMIM](H1) is inferred, but although this peak confirms anions being hydrogen bonded also to these cation sites, the peak intensities are lower and thus preferential interaction with [EMIM](H1) is inferred, for both anions and in the whole composition range. Additionally, further RDF peaks are inferred for interactions through [EMIM](H4/5), showing again ions clustering. The integration of RDFs leads to the number of ions around a central one, i.e. solvation numbers (*N*), which are larger for then interaction around the [EMIM](H1) than around [EMIM](H4-5), both for [BF_4] and [$MeSO_3$], i.e. confirming preferential solvation around the [EMIM](H1), but not discarding hydrogen bonding around [EMIM](H4-5), Figure 8a. The solvation numbers for the first solvation shell, $N_{1st\ shell}$, where the first shell is defined according to the first minima in RDFs (Figure 8a), correspond to those ions interacting via hydrogen bonding (short-range contacts), Figure 8c. The $N_{1st\ shell}$ confirm interactions [EMIM](H1) > [EMIM](H4/5) and linear evolution in the whole composition range, which would be on the root of the small deviations of ideality (experimentally) reported in Figures 2b and 2d. Therefore, the liquid nanostructuring being characterized from the view point of cation-anion interactions by the replacement of [$MeSO_3$] by [BF_4] anions in the cation hydrogen bonding sites in parallel with the mixture composition, i.e. anion content. Regarding the number of hydrogen bonds for the two types of acceptor sites in [EMIM], results in Figure 8d shows that interaction through [EMIM](H1) is roughly 2.7 times larger (slightly larger for [$MeSO_3$] than for [BF_4]) than through [EMIM](H4/H5). Additionally, the total number of cation-anion hydrogen bonds developed by each type of anion is computed and the ratio between those developed by [BF_4] to those by [$MeSO_3$] is reported in Figure 8d. Although results in Figure 8c showed linear evolution of all the considered types of hydrogen bonds, those results for the ratio for both types of anions reported in Figure 8d (black points) indicated a clearly no linear

evolution, i.e. a larger number of cation – [BF_4] hydrogen bonds beyond the expected from increasing [BF_4] content. This effect would be the root of the deviations from the ideality of the considered IL mixtures leading e.g. to the negative excess volume reported in Figure 2b. Nevertheless, although this effect shows an clearly non-linear evolution of intermolecular forces (hydrogen bonding) with composition, as the size and shape of both anions is similar and their large trend to interact with both types of hydrogen bond acceptor sites in [EMIM] cation, the effect results in a minor contractive effect upon mixing, i.e. small deviations from ideal mixing behavior.

Further details on the ionic arrangements around the hydrogen bonding sites are inferred from the Spatial Distribution Functions (SDFs) around the [EMIM] cation, Figure 9, which provide further details on solvation mechanisms. The distribution of [BF_4] and [$MeSO_3$] anions around [EMIM] cation exhibit very similar properties: a solvation shell extending from the [EMIM](H1) towards the [EMIM](H4-5) hydrogen bond acceptor sites, with the case of [BF4] showing spots more localized around these sites whereas for [$MeSO_3$] a closed shell around the cation is inferred. Likewise, for both anions two consecutive solvation shells are well defined, i.e. cation-anion aggregation beyond neat dimers is inferred.

Geometrical properties of the developed hydrogen bonds were studied using Combined Distributed Functions (CDFs), in particular for the cation – anion interaction via the [EMIM](H1) sites, Figure 10. Hydrogen bonding is confirmed for both anions via donor-acceptor separation and orientation. Nevertheless, the complex patterns for interactions and solvation as reported in Figures 8 and 9 results in the CDFs with extended interaction spots, considering wide interaction regions at a range of interaction angles. This mechanism of interaction around the cation hydrogen bonding sites is maintained in the whole composition range and supports the orientation flexibility and ability of hydrogen bonding reforming around the cation acceptor sites.

Results in Figures 8 and 9 confirmed ionic interaction beyond the formation of simple dimmers, thus the large range aggregation mechanisms were analyzed via domain analysis considering all the involved ions (cations and both types of anions, Figure 11). For neat ILs, i.e. x = 0 or 1, a single domain is inferred (Figure 11), with these domains having large volumes, Figure 11b, being non-spherical for [$MeSO_3$] and having larger sphericity for [BF_4], Figure 11d. on the

contrary once mixed ILs are formed a disruptive effect is clearly inferred as reported in Figure 11a where the number of domains increases then decreasing again with increasing [BF_4] content. This effect may result from the large number of developed hydrogen bonds via interactions with [BF4], Figure 8d, which would lead to a disruption of IL structuring for [$MeSO_3$] – rich mixtures, which decreases the disruption once [BF_4] – rich mixtures are formed. This trend would lead to division of domains in smaller ones, but not to a large number (the larger number of domains is 6, obtained for x = 0.2), but these domains are more spherical, Figure 11b, which would decrease the available free volume, i.e. leading to more efficient packings, slightly negative excess volume, Figure 2b. Further analysis is carried out considering the sizes of cation - anion clusters evolving with mixing composition (Figure 12). These results the presence of small populations of monomers, 18 % on average in the whole mixture composition range with differences of 1% in the mixture range and no trend with composition, i.e. non-associated (hydrogen bonded) ions represent a minor population independently of the considered anion. Likewise, the population of small clusters (2 to 5 ions) of 17 % and medium sized clusters (6 to 10 ions) of 6.4 % is clearly lower than the very large aggregates (>10 ions) being 58.6 % on average and almost constant in the studied composition range. These cluster size results agree with the domain distribution in Figure 11 and shows the large trend of both ions to develop large hydrogen bonded networks in the whole mixed fluid, which is maintained in the whole composition range.

The dynamic behavior of the mixed ILs is firstly analyzed through the dynamic properties of the developed hydrogen bonds as they are the intermolecular force governing the dynamic properties of the whole mixed fluids. For this purpose, Reactive Flux Analysis (RFA) reveals hydrogen bond lifetimes ($\tau_{forward}$) and hydrogen bonding reforming times ($\tau_{backward}$), i.e. the time an hydrogen bond remains upon forming and the time an ion requires to form a new hydrogen bond once the previous one is broken, respectively. The hydrogen bonds developed through [EMIM](H1) position are compared for both types of anions in Figure 13, although both ones are labile interactions those developed through [MeSO3] have longer lifetimes with the exception of [BF_4] – rich mixtures. Likewise, the reforming times are also small for both anions, larger for [$MeSO_3$], thus confirming a dynamic pattern of intermolecular forces (hydrogen bonding) with living times lower than 50 ps and reforming times lower than 175 ps. Therefore, although results

in previous sections confirmed large hydrogen bonded networks in the whole mixture composition range, these networks are largely dynamic, especially for [BF4] – rich mixtures, which would be on the roots of the behavior of viscosity as reported in Figure 2c, highlighting the intimate connection between structure and ionic dynamics.

The ionic dynamic is firstly characterized through the center-of-mass Velocity Distribution Functions as reported for all the involved ions in Figure 14. The reported VDFs show two main results: *i*) the VDF peaks show a single maxima between 30 to 32 m s^{-1} which is the same for [EMIM] and for the two types on anions, i.e. ions move paired as a result of the strong hydrogen bonding and the clustering reported, and *ii*) these mobility patterns remains constant in the whole composition range as a results of the almost negligible changes in the clustering distribution, Figure 12. Additionally, the center-of-mass mean square displacements (*msd*) were calculated and the corresponding self-diffusion coefficients, *D*, were obtained from the Einstein's equation, Figure 15. The reported results also showed two main trends: *i*) for a fixed composition *D* values are almost the same for all the involved ions, i.e. ions diffuse paired (in agreement with results in Figure 14), and *ii*) *D* values evolve in a non – linear way with mixture composition. The non-linear evolution of *D* with mixture composition would justify the reported experimental evolution of dynamic viscosity, Figures 2e and 2f, as both properties are related through the Einstein-Stokes equation, i.e. *D* values are lower than a reference linear evolution with composition, i.e. ions diffuse faster which would result in lower viscosity, and thus in negative mixing viscosity, Figure 2f. This dynamic behavior is also paired with the change in the number of domains, Figure 11a, which would allow faster ionic diffusion. Therefore, although from the viewpoint of hydrogen bonding evolution with composition, the replacement of [$MeSO_3$] per [BF_4] does not have a large effect in the volumetric properties (Figure 2b), the changes in dynamic properties (Figure 2f) are remarkably larger as a result of the changes in the domain distribution of developed ionic clusters. Therefore, the considered IL mixtures show a complex nanoscopic pattern beyond the simplified picture of anionic replacement as a non-ideal liquid mixture.

4. CONCLUSIONS

The comprehensive study of the binary mixtures of ionic liquids (ILs) [EMIM][BF_4] and [EMIM][$MeSO_3$] has provided significant insights into their macroscopic, thermodynamic, and nanoscopic behaviors. Experimental measurements of density and viscosity across a temperature range of 283.15 to 313.15 K, combined with calculations of excess properties, reveal a nuanced interplay between molecular interactions and structural organization. The density measurements suggest near-ideal mixing behavior, with almost linear progression across compositions and temperatures. However, deviations are observed in the density correlation with the nature of anions, indicating the influence of molecular interactions and packing considerations. The complex volumetric behavior is evident from the excess molar volume patterns, which show minima at equimolar compositions and maxima at compositions rich in either [EMIM][BF_4] or [EMIM][$MeSO_3$]. These patterns reflect subtle mixed fluid behavior, largely influenced by steric effects and the rearrangement of intermolecular forces. The thermal expansion coefficient and its excess property exhibit non-linear behavior, with negative values indicating less compressible mixtures, particularly at equimolar compositions. Viscosity measurements reveal significant non-linear behavior, especially at lower temperatures, with [EMIM][$MeSO_3$] exhibiting much higher viscosities than [EMIM][BF_4]. The VFT model parameters, including fragility, confirm the complex dynamic behavior of the mixtures, with viscosity deviations pointing to efficient packing and reduced frictional forces.

Thermodynamic analysis through COSMO calculations reveals exothermic mixing behavior, with excess enthalpy showing significant negative values, indicative of non-ideal mixing. The positive excess entropy suggests an entropy-driven mixing process, which, together with the negative Gibbs energy of mixing, underscores the enthalpic dominance in these systems without phase separation. The symmetric activity coefficients and their values at infinite dilution suggest minor changes in intermolecular forces upon mixing, with both ILs showing similar affinities for each other.

Molecular dynamics simulations provide a detailed nanoscopic characterization, highlighting the primary role of hydrogen bonding in cation-anion interactions. The simulations

confirm that hydrogen bonding occurs preferentially through the H1 site of the imidazolium ring, with both anions competing for these interactions. The spatial distribution functions and combined distributed functions support these findings, showing extensive hydrogen bonding and ion clustering beyond simple dimers. Domain analysis reveals that mixing disrupts the large ionic domains observed in neat ILs, leading to smaller, more spherical domains with efficient packing. This disruption is more pronounced in [$MeSO_3$]-rich mixtures, where [BF_4] anions introduce significant changes in the structuring. The dynamic properties, analyzed through reactive flux analysis and velocity distribution functions, show that hydrogen bonds are highly dynamic, with lifetimes and reforming times indicating rapid reorganization of the ionic network. The self-diffusion coefficients derived from mean square displacements also exhibit non-linear behavior with composition, correlating with the experimental viscosity data.

Overall, the study demonstrates that the binary mixtures of [EMIM][BF_4] and [EMIM][$MeSO_3$] exhibit complex behavior driven by intricate molecular interactions and structural dynamics. The detailed macroscopic and nanoscopic analyses provide a comprehensive understanding of the factors influencing the thermodynamic and dynamic properties of these IL mixtures, highlighting the significant role of hydrogen bonding, steric effects, and efficient packing in determining their behavior.

ACKNOWLEDGEMENTS

We acknowledge SCAYLE (Supercomputación Castilla y León, Spain) for providing supercomputing facilities. The statements made herein are solely the responsibility of the authors.

SUPPLEMENTARY MATERIAL

Table S1 (ILs considered in this work); Table S2 (properties of neat ILs and comparison with literature); Table S3 (properties of mixed ILs); Table S4 (VFT fitting parameters for viscosity); Table S5 (Redlich-Kister parameters for excess and mixing properties); Table S6 (parameters for PFP fitting to excess volume); Table S7 (force field parameters for MD simulations); Table S8 (systems for MD simulations); equations for the calculation of thermodynamic properties.

Figure captions

Figure 1. Ions forming ILs considered in this work as well as labelling for relevant atoms.

Figure 2. Experimental thermophysical properties for *x* [EMIM][BF_4] + (1-*x*) [EMIM][$MeSO_3$], where *x* stands for mole fraction, as a function of temperature. (a) Density (ρ), (b) excess molar volume (V^E), (c) isobaric thermal expansion coefficient (α_p), (d) excess isobaric thermal expansion coefficient (α_P^E), (e) dynamic viscosity (η), and (f) mixing viscosity ($\Delta\eta$). Black arrows indicate increasing temperature for guiding purposes. Dashed arrows in panels b,d,f indicate the composition for relevant minimum/maximum.

Figure 3. Results from COSMO calculations for *x* [EMIM][BF_4] + (1-*x*) [EMIM][$MeSO_3$], at (a-c) 303.15 K and (d) as function of temperature. (a) (H^E) Excess enthalpy, (G^E) excess Gibbs free energy, (S^E) excess entropy; (b) activity coefficients (γ), showing values at infinite dilution (γ_i^∞).

Figure 4. Fitting parameters of VFT equation for experimental dynamic viscosity , and Angell's fragility parameter, D_f, for *x* [EMIM][BF_4] + (1-*x*) [EMIM][$MeSO_3$]where stands for mole fraction, in the 283.15 to 313.15 K temperature range.

Figure 5. (a,b) Excess partial molar volume of component *i*, $\bar{V}_i^E$, and (c) values at infinite dilution, $\bar{V}_i^{E,\infty}$, for *x* [EMIM][BF_4] + (1-*x*) [EMIM][$MeSO_3$], where stands for mole fraction, as a function of temperature. Black arrows indicate increasing temperature for guiding purposes. Panels a and b show results for [EMIM][$EtSO_4$] and [EMIM][$MeSO_3$], respectively. (d) Relationship between $\bar{V}_i^{E,\infty}$ and activity coefficients at infinite dilution, γ_i^∞, as obtained from COSMO calculations.

Figure 6. (a) Comparison of experimental, symbols, and PFP (lines) excess molar volume, V^E, for *x* [EMIM][BF_4] + (1-*x*) [EMIM][$MeSO_3$]where stands for mole fraction, in the 283.15 to 313.15 K temperature range. Panel b shows PFP interactional contribution to total excess molar volume. Panel c shows χ_{12} PFP interaction parameter as a function of composition. Panel d shows χ_{12} PFP interaction parameter at equimolar composition as a function of temperature. Parameters required for PFP calculations reported in Table S6 (Supplementary Information).

Figure 7. Connection matrix, *cmat*, analysis of the reported atoms for *x* [EMIM][BF_4] + (1-*x*) [EMIM][$MeSO_3$] at 298.15 K from MD simulations. The color in each square represents both the intensity and distance of the first maximum for the corresponding RDF. Atom labelling as in Figure 1.

Figure 8. (a) Site – site Radial Distribution Functions, *g*(*r*), (b) corresponding integrals, *N*, for the reported atomic pairs, (c) *N* for the first solvation shell, $N_{1st\ shell}$ (defined as the first minima in panel a, with *r* = 3.90 and 3.10 Å for interactions with H1 and H4-5 in [EMIM], respectively), and (d) relevant ratios for $N_{1st\ shell}$. All results for *x* [EMIM][BF_4] + (1-*x*) [EMIM][$MeSO_3$] at 298.15 K from MD simulations. Atom labelling as in Figure 1.

Figure 9. Spatial Distribution Functions around central [EMIM] cation for the reported molecules in *x* [EMIM][BF_4] + (1-*x*) [EMIM][$MeSO_3$] at 298.15 K from MD simulations. Atom labelling as in Figure 1.

Figure 10. Combined Distribution Functions for the distance and angles between relevant sites in *x* [EMIM][BF_4] + (1-*x*) [EMIM][$MeSO_3$] at 298.15 K from MD simulations. Atom labelling as in Figure 1.

Figure 11. Domain analysis in *x* [EMIM][BF_4] + (1-*x*) [EMIM][$MeSO_3$] at 298.15 K from MD simulations. Number of domains, *D*, average domain volume, *V*, and isoperimetric index, *Q*, are reported. Domains were calculated for those involving [EMIM] + [BF_4] + [$MeSO_3$].

Figure 12. Cluster analysis for cation - anion aggregation *x* [EMIM][BF_4] + (1-*x*) [EMIM][$MeSO_3$] at 298.15 K from MD simulations. Results show percentage distribution of cluster composed of *n* molecules (*n-mers*). Atoms selected for

clusters analysis are those corresponding to hydrogen bonding interactions: [EMIM]: H1,H4,H5; [MeSO3]: O1-3; [BF4]: F1-4. Atom labels as in Figure 1.

Figure 13. Dynamics of hydrogen bonds for the reported interacting pairs in *x* [EMIM][BF_4] + (1-*x*) [EMIM][$MeSO_3$] at 298.15 K from MD simulations. Forward process stands for the living time of an hydrogen bond once formed, backward stands for the time required for developing a new hydrogen bond after breaking.

Figure 14. Center-of-mass Velocity Distribution Functions for the reported molecules in *x* [EMIM][BF_4] + (1-*x*) [EMIM][$MeSO_3$] at 298.15 K from MD simulations.

Figure 15. Center-of-mass Self-Diffussion Coefficients for the reported molecules in *x* [EMIM][BF_4] + (1-*x*) [EMIM][$MeSO_3$] at 298.15 K from MD simulations.

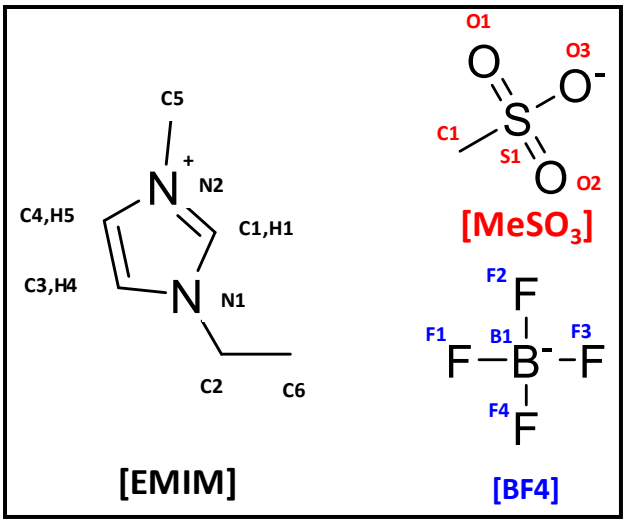

Figure 1

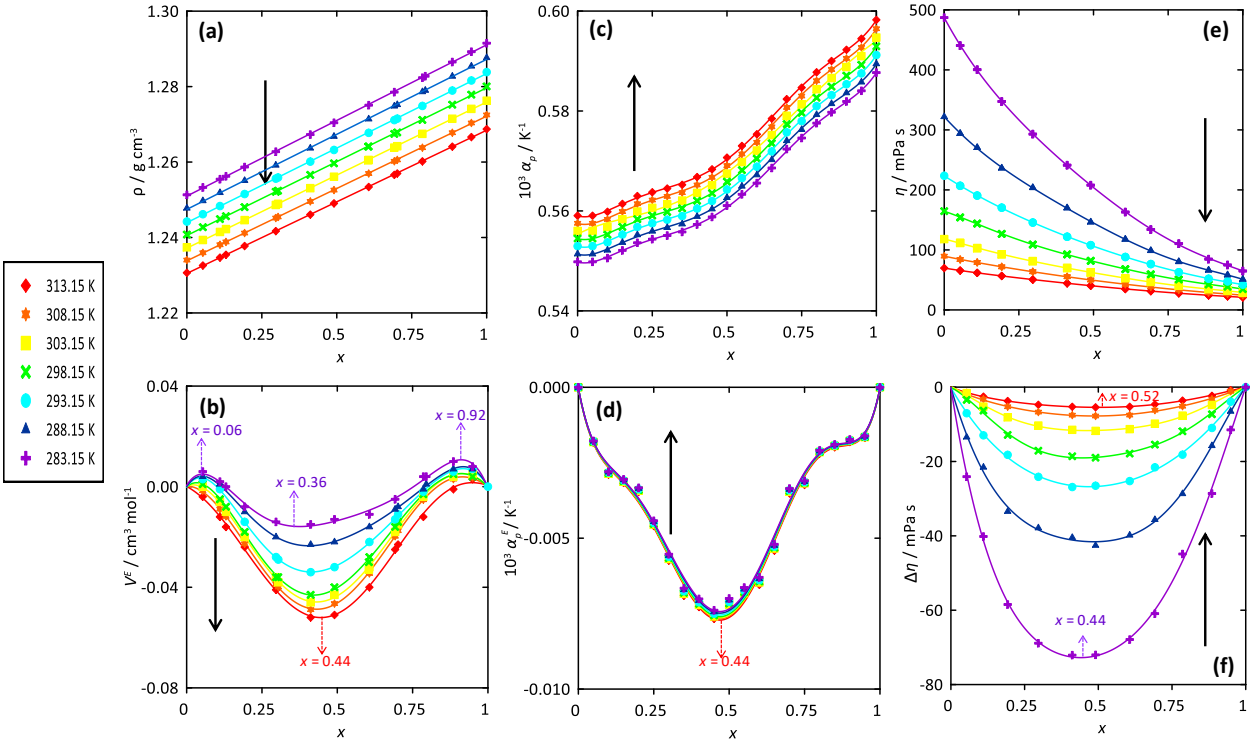

Figure 2

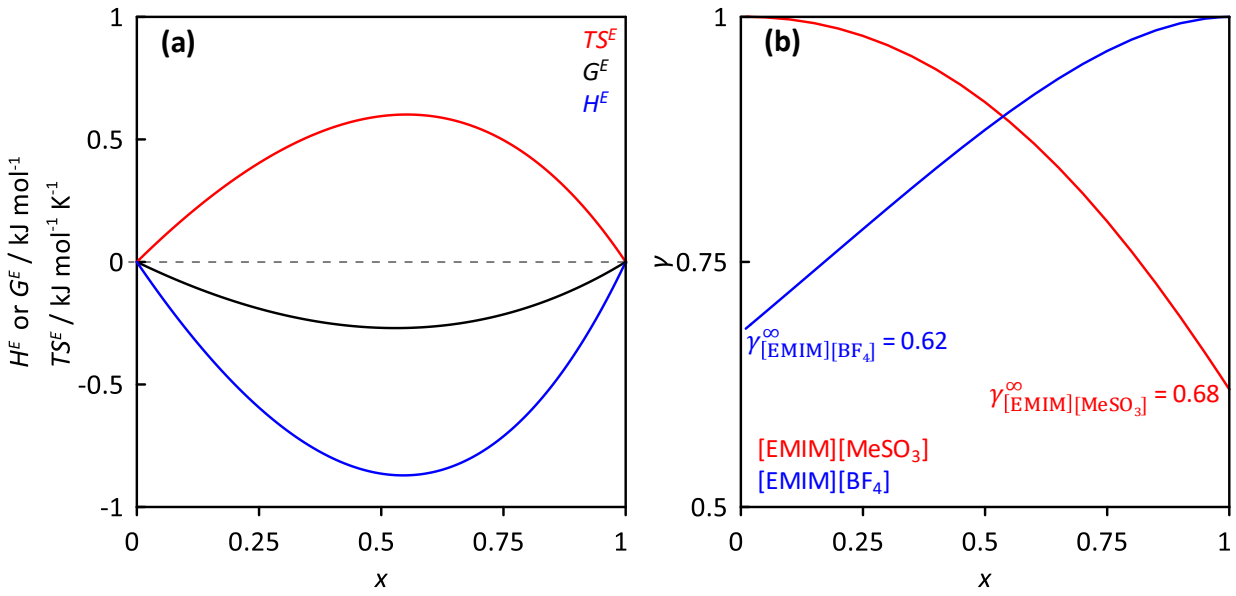
(a)
TS^E
G^E
H^E
H^E or G^E / kJ mol^{-1}
TS^E / kJ mol^{-1} K^{-1}
1
0.5
0
-0.5
-1
0
0.25
0.5
0.75
1
x
(b)
γ
1
0.75
0.5
$\gamma^{\infty}_{[EMIM][BF_4]}$ = 0.62
$\gamma^{\infty}_{[EMIM][MeSO_3]}$ = 0.68
[EMIM][MeSO$_3$]
[EMIM][BF$_4$]

Figure 3

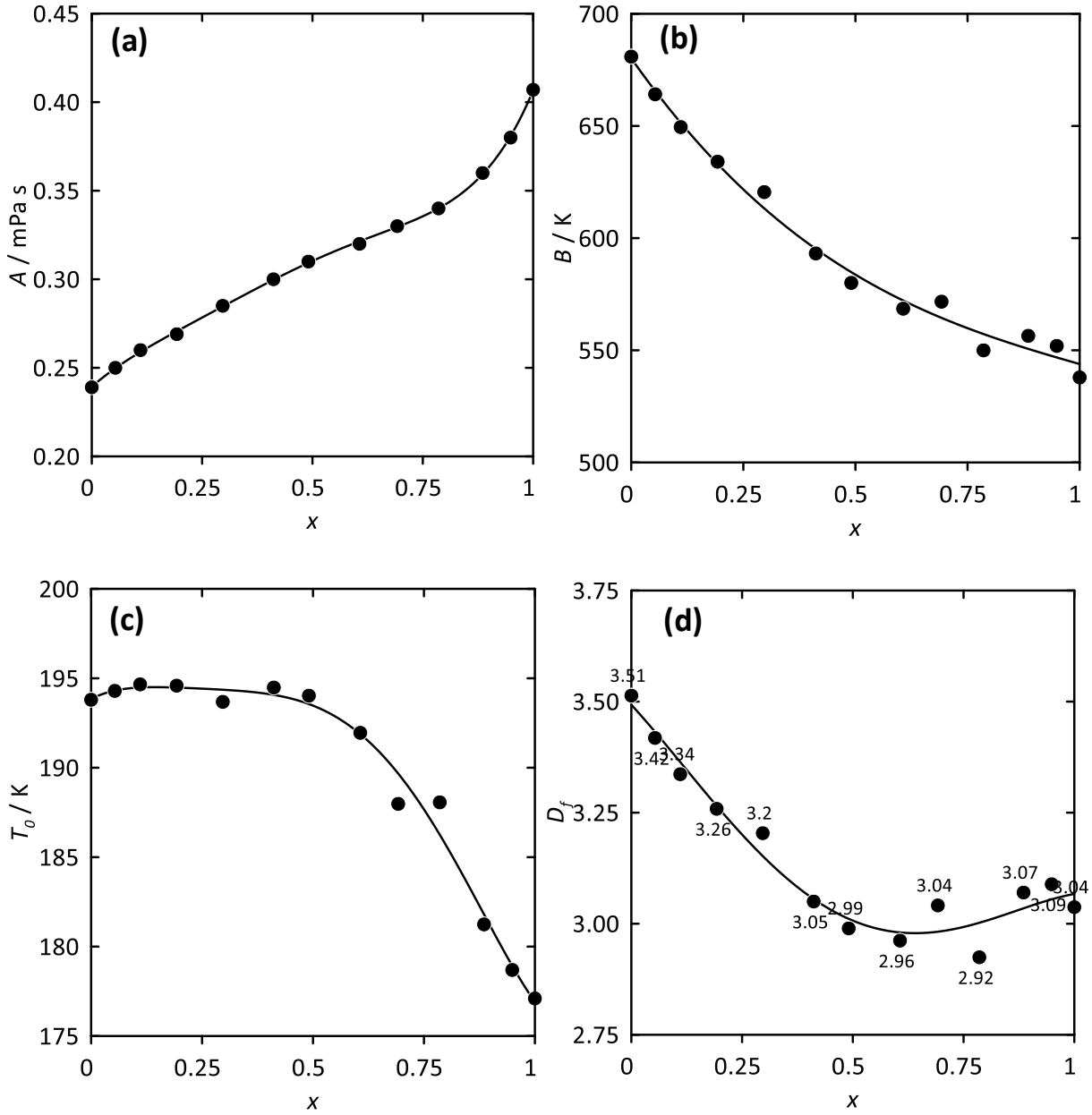
(a)
A / mPa s
x
(b)
B / K
x
(c)
T_0 / K
x
(d)
D_f
x
3.51
3.42
3.34
3.26
3.2
3.05
2.99
2.96
3.04
2.92
3.07
3.09
3.04

Figure 4

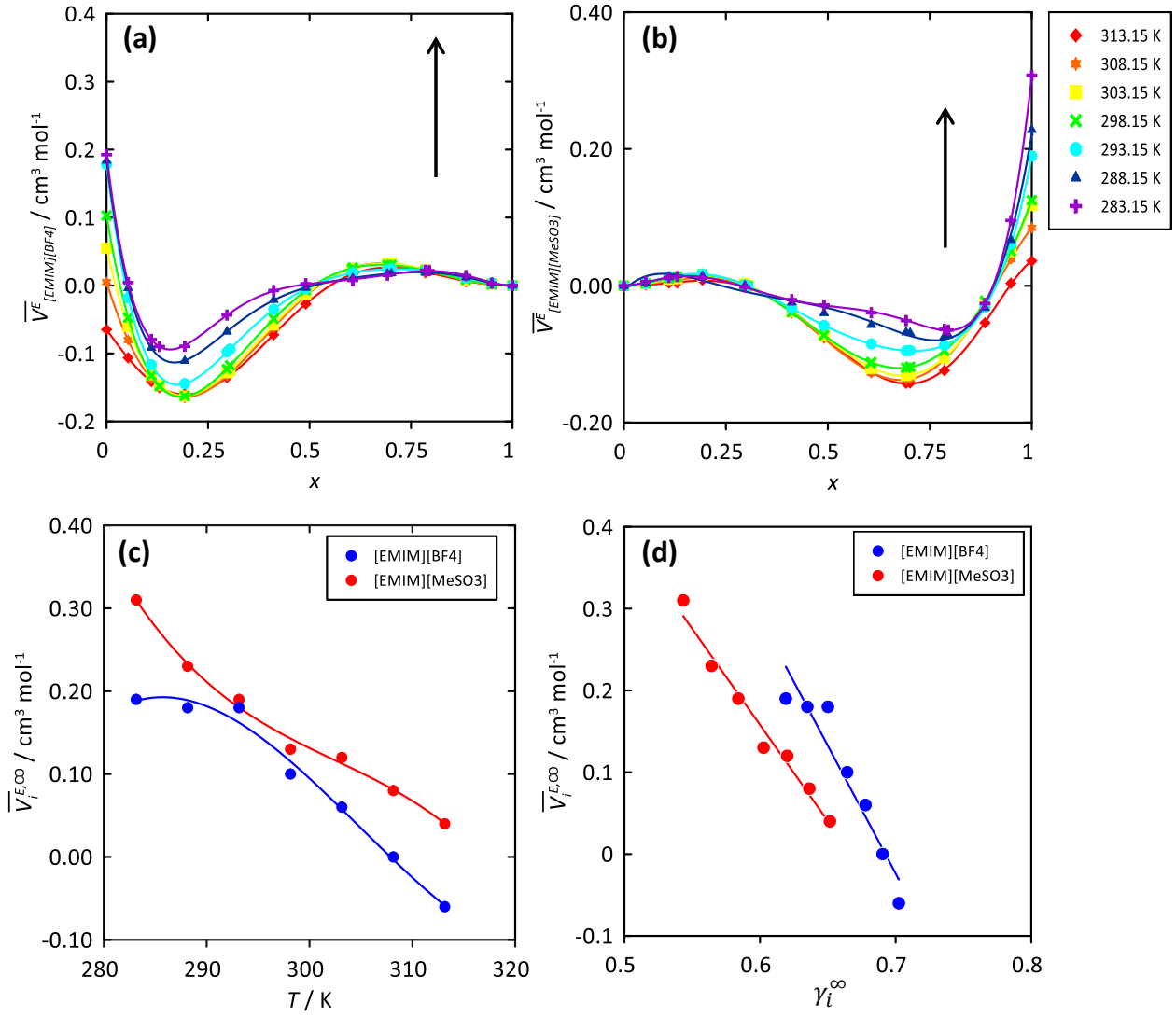
(a)
(b)
(c)
(d)
313.15 K
308.15 K
303.15 K
298.15 K
293.15 K
288.15 K
283.15 K
[EMIM][BF4]
[EMIM][MeSO3]
x
T / K
γ_i^∞

Figure 5

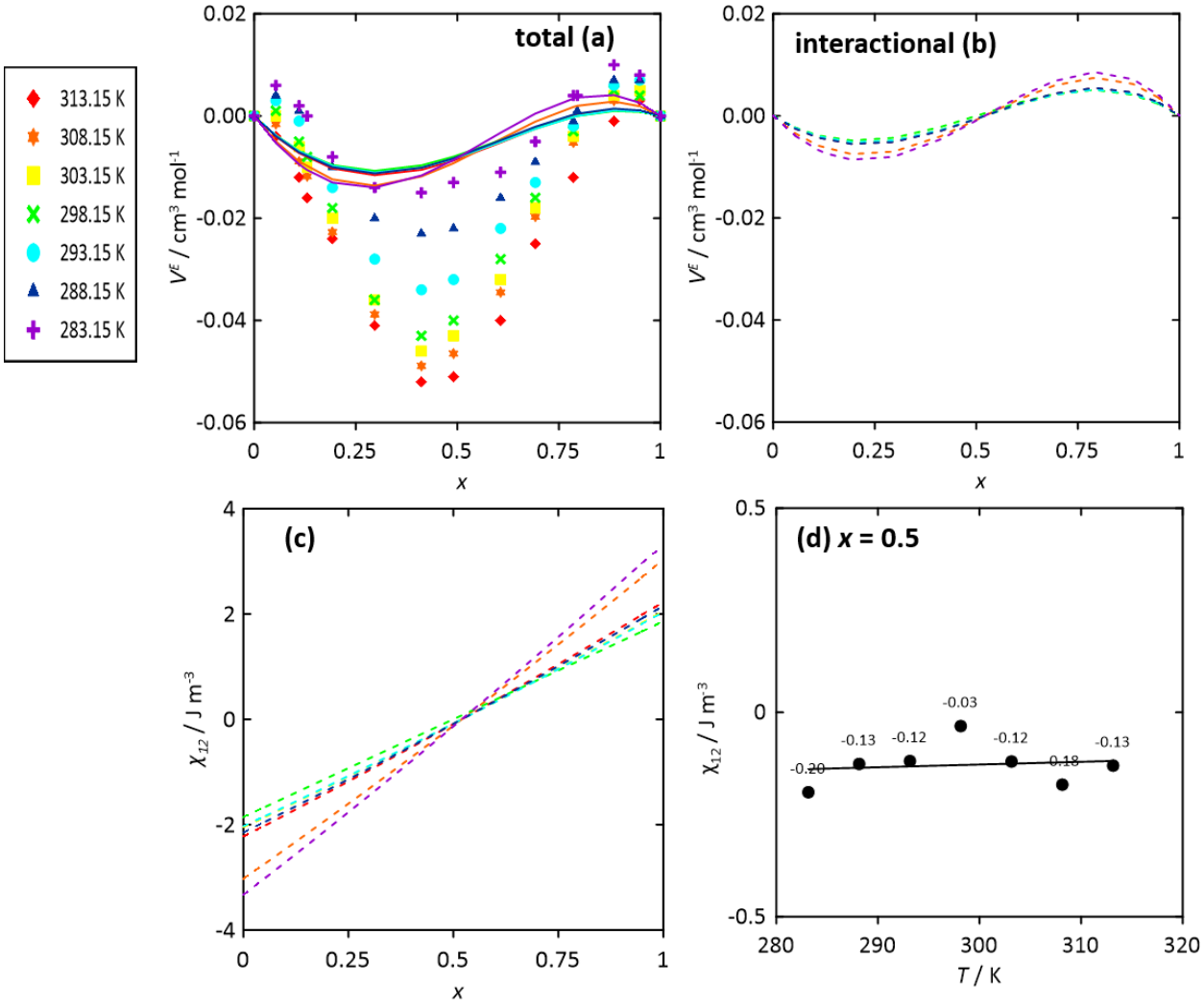
313.15 K
308.15 K
303.15 K
298.15 K
293.15 K
288.15 K
283.15 K
total (a)
interactional (b)
(c)
(d) x = 0.5
V^E / cm^3 mol^{-1}
χ_{12} / J m^{-3}
x
T / K
-0.03
-0.13
-0.12
-0.12
-0.13
-0.20
-0.18

Figure 6

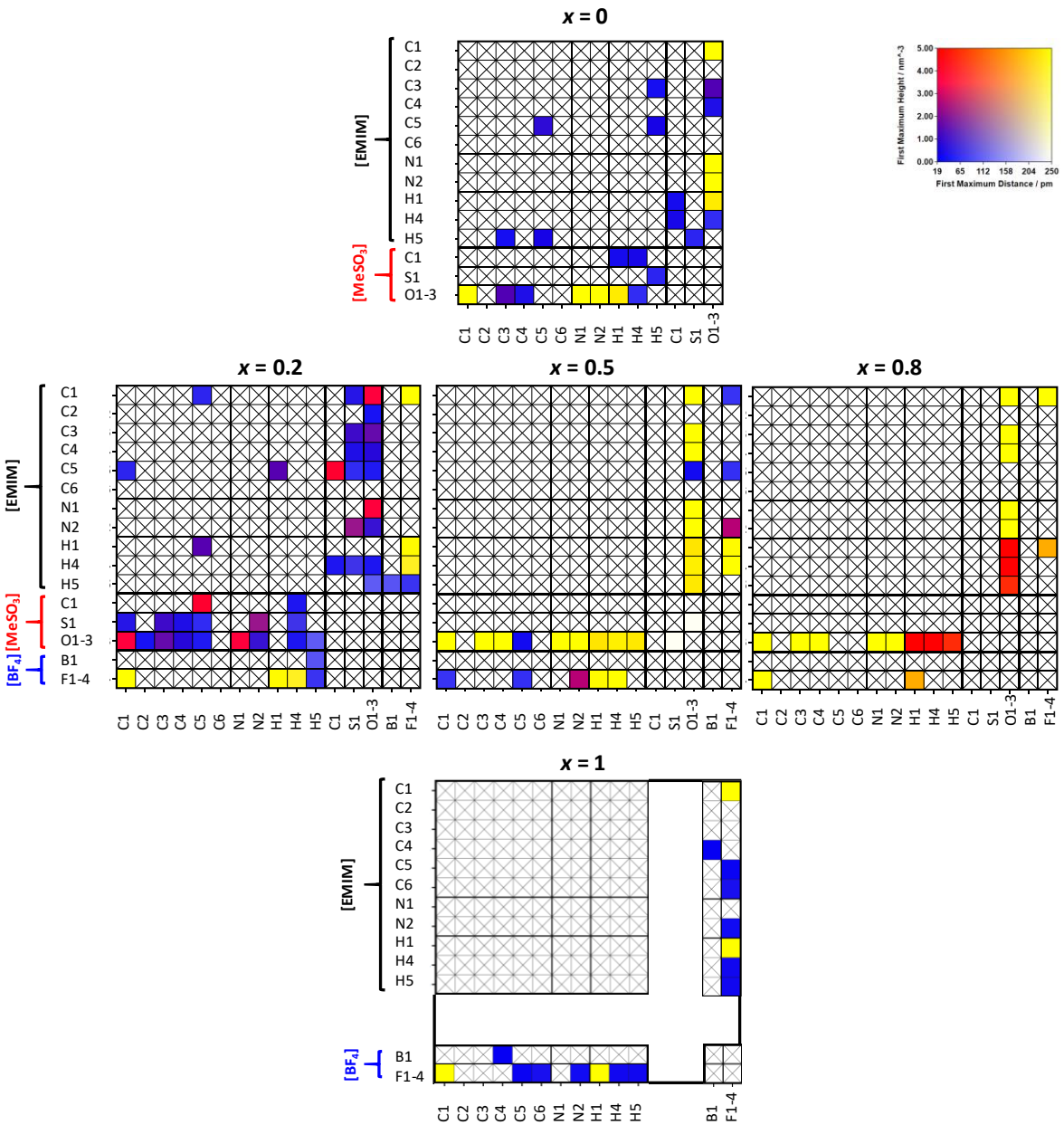
x = 0
x = 0.2
x = 0.5
x = 0.8
x = 1
[EMIM]
[MeSO3]
[BF4]
C1
C2
C3
C4
C5
C6
N1
N2
H1
H4
H5
S1
O1-3
B1
F1-4
First Maximum Height / nm^-3
First Maximum Distance / pm

Figure 7

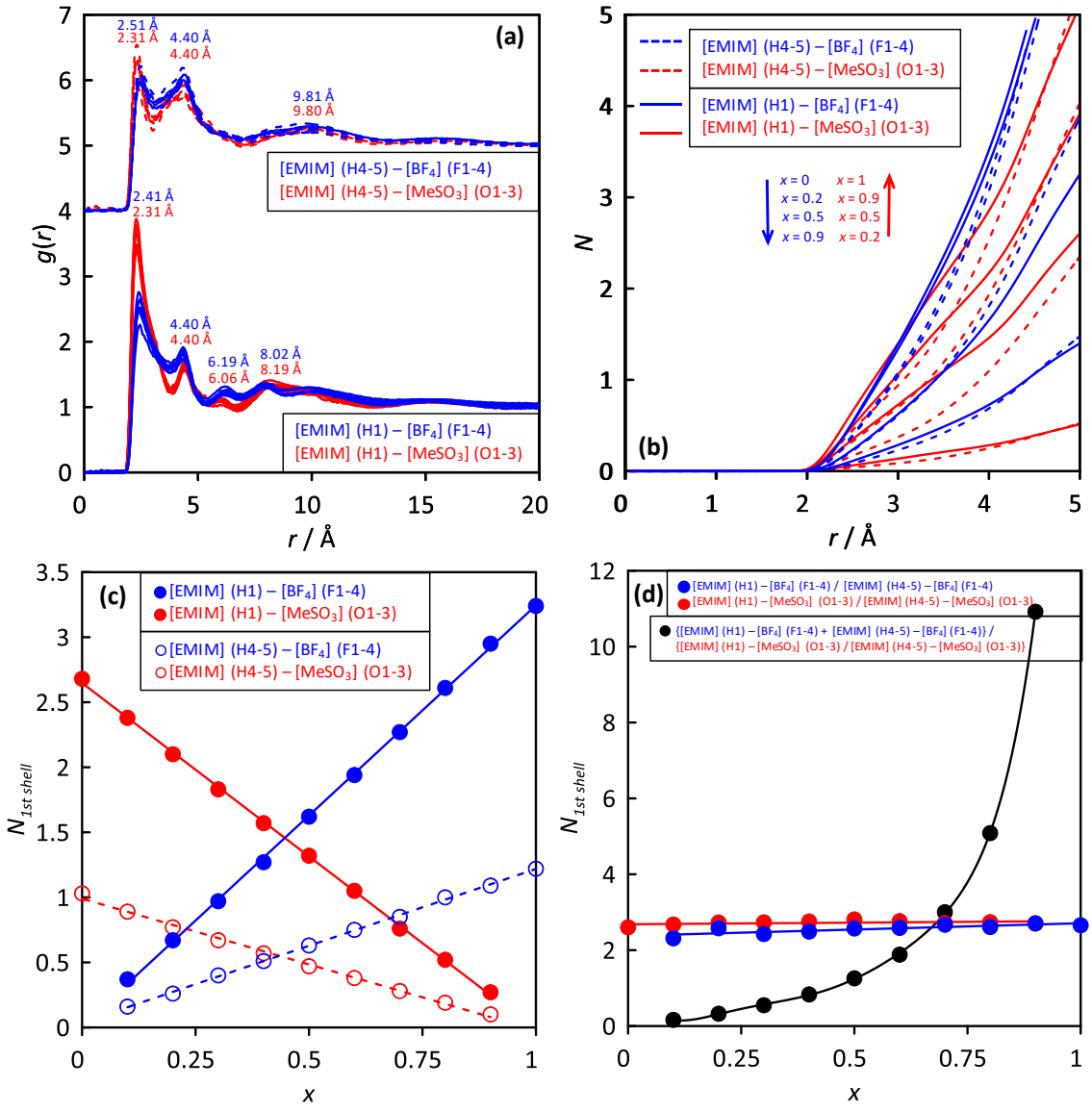
(a)
g(r)
r / Å
2.51 Å
2.31 Å
4.40 Å
4.40 Å
9.81 Å
9.80 Å
2.41 Å
2.31 Å
4.40 Å
4.40 Å
6.19 Å
6.06 Å
8.02 Å
8.19 Å
[EMIM] (H4-5) – [BF4] (F1-4)
[EMIM] (H4-5) – [MeSO3] (O1-3)
[EMIM] (H1) – [BF4] (F1-4)
[EMIM] (H1) – [MeSO3] (O1-3)
(b)
N
r / Å
x = 0 x = 1
x = 0.2 x = 0.9
x = 0.5 x = 0.5
x = 0.9 x = 0.2
(c)
N1st shell
x
(d)
N1st shell
x
{[EMIM] (H1) – [BF4] (F1-4) + [EMIM] (H4-5) – [BF4] (F1-4)} /
{[EMIM] (H1) – [MeSO3] (O1-3) / [EMIM] (H4-5) – [MeSO3] (O1-3)}

Figure 8

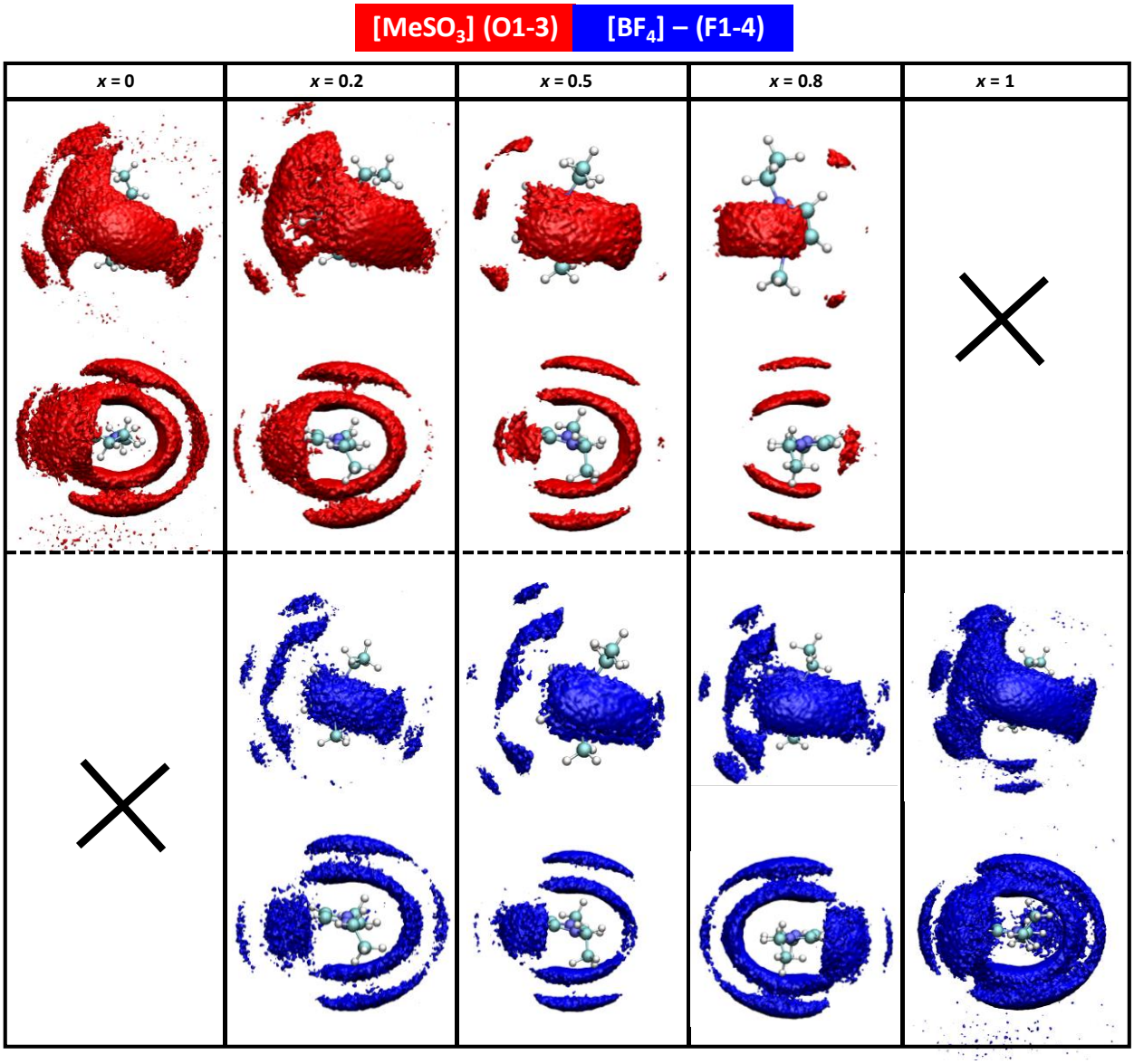

Figure 9

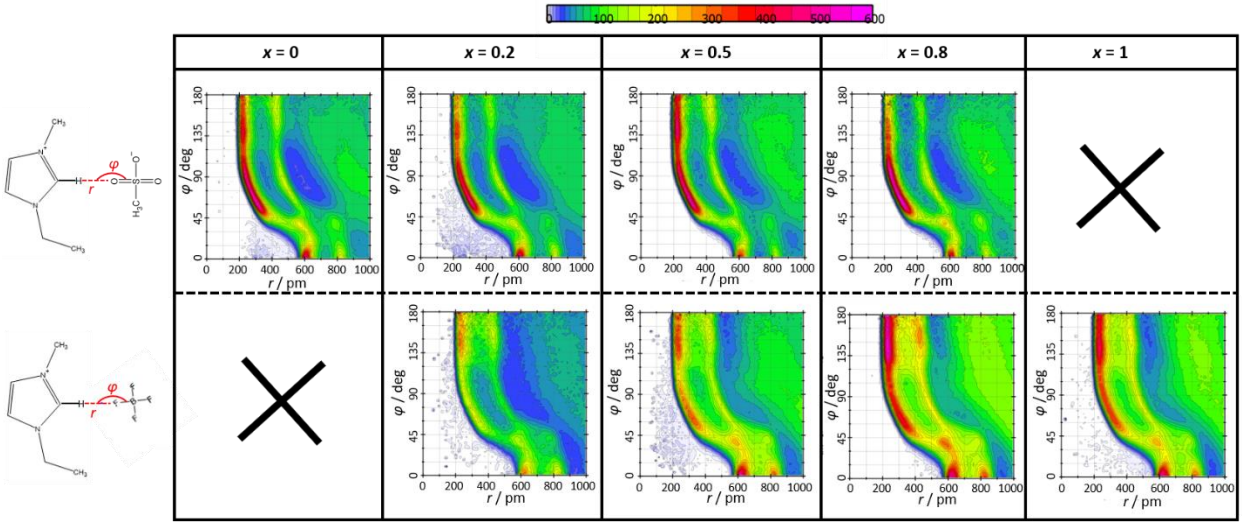
0
100
200
300
400
500
600
x = 0
x = 0.2
x = 0.5
x = 0.8
x = 1
φ / deg
r / pm
0
45
90
135
180
0
200
400
600
800
1000

Figure 10

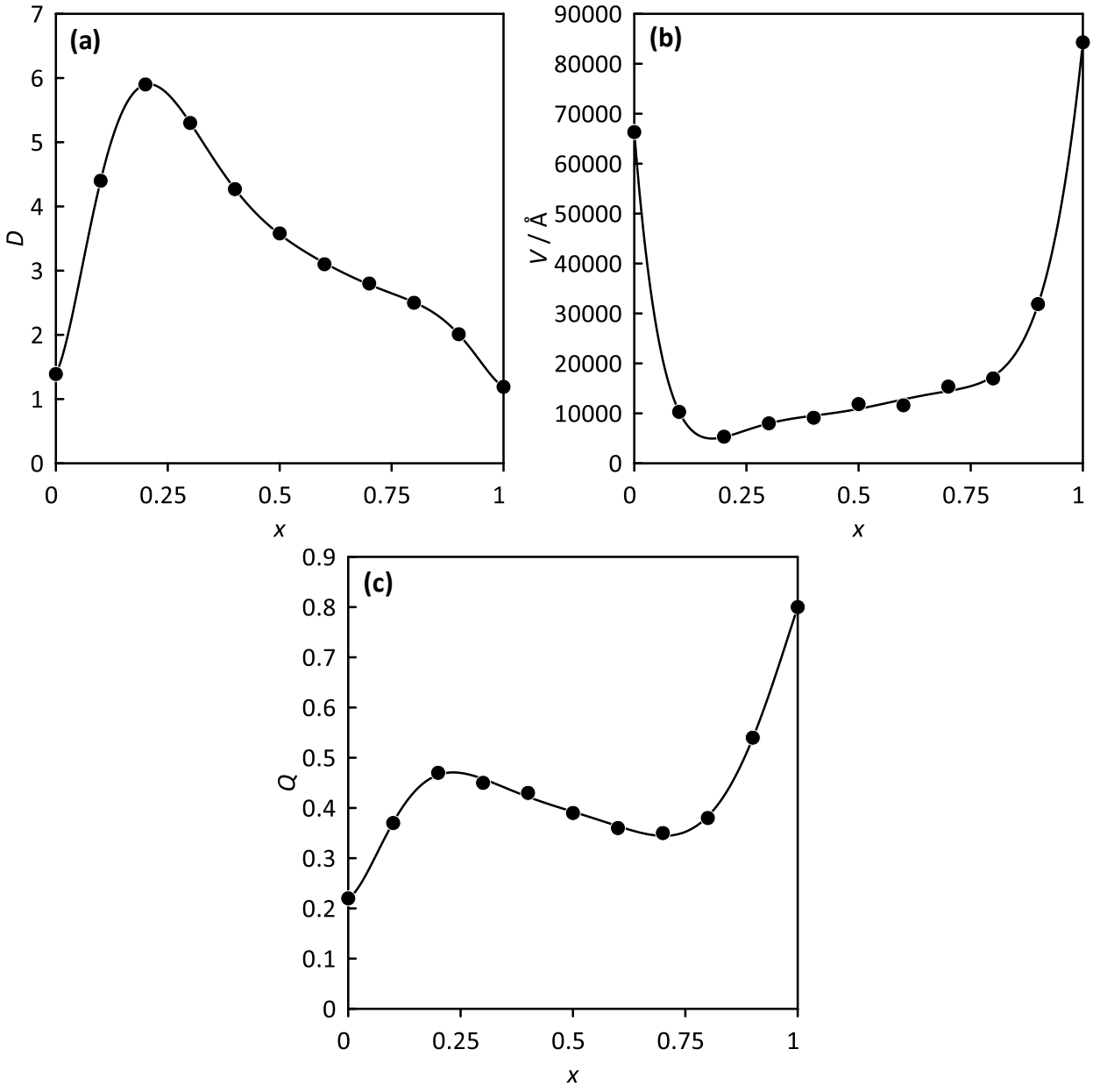

Figure 11

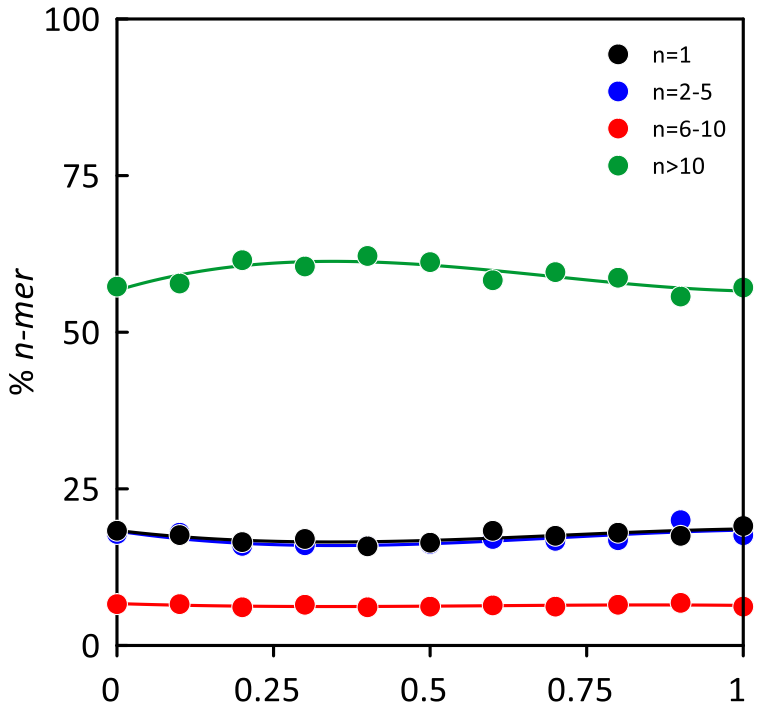

Figure 12

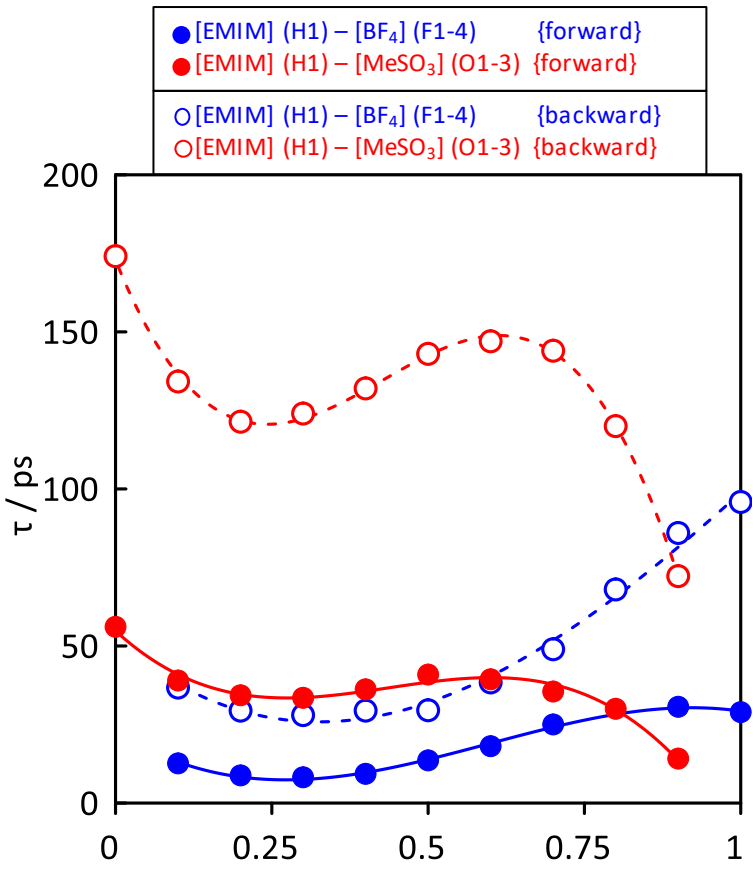
[EMIM] (H1) – [BF4] (F1-4) {forward}
[EMIM] (H1) – [MeSO3] (O1-3) {forward}
[EMIM] (H1) – [BF4] (F1-4) {backward}
[EMIM] (H1) – [MeSO3] (O1-3) {backward}
τ / ps
200
150
100
50
0
0
0.25
0.5
0.75
1

Figure 13

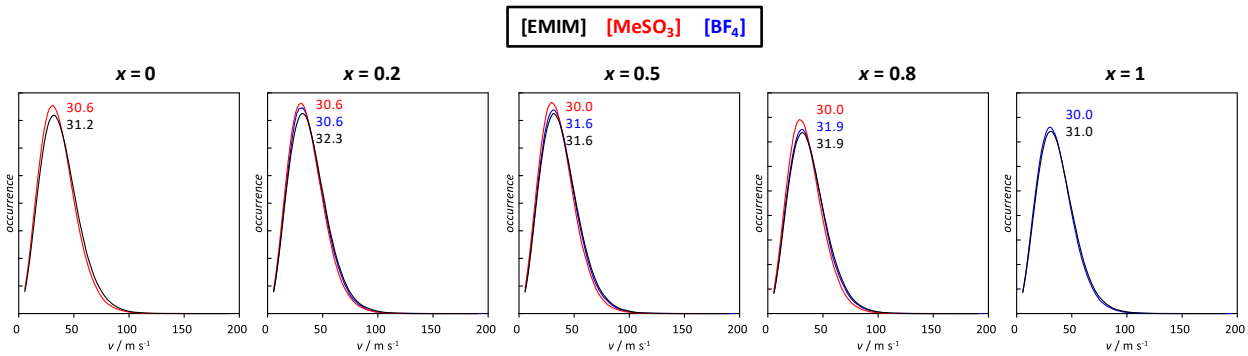
[EMIM] [MeSO3] [BF4]
x = 0
30.6
31.2
x = 0.2
30.6
30.6
32.3
x = 0.5
30.0
31.6
31.6
x = 0.8
30.0
31.9
31.9
x = 1
30.0
31.0
occurrence
v / m s-1
0
50
100
150
200

Figure 14

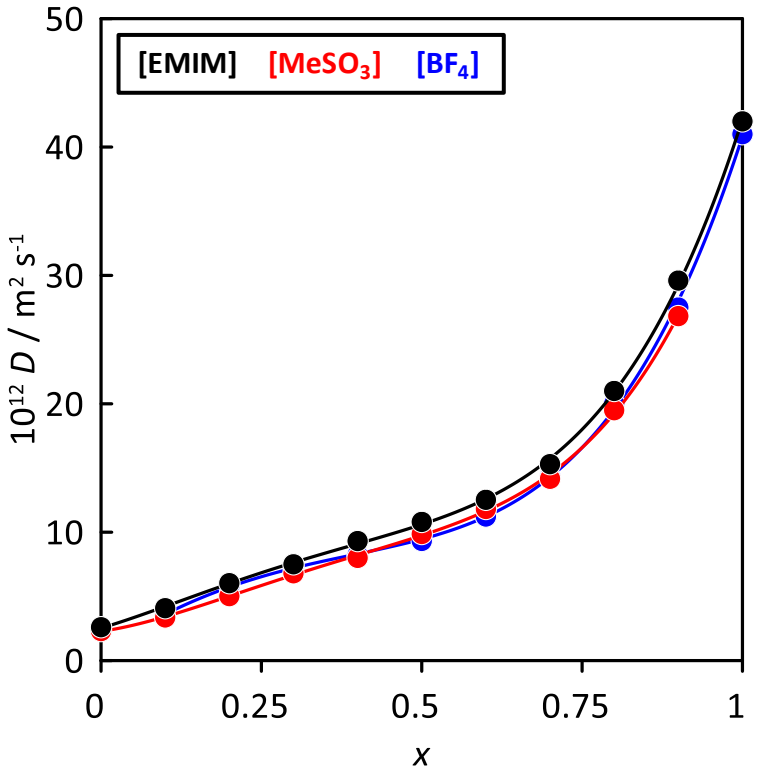

Figure 15

References

[1] S. Brahma, R.L. Gardas, History and Development of Ionic Liquids, History and development of ionic liquids. In: Handbook of Ionic Liquids: Fundamentals, Applications, and Sustainability, Editors: P. Singh, S. Rajkhoowa, A. Sen, J. Sarma, Ed. Wiley – VCH, 2023.

[2] S.K. Singh, A.W. Savoy, Ionic liquids synthesis and applications: An overview, J. Mol. Liq. 297 (2020) 112038.

[3] P. Walden, Über die Molekulargrösse und elektrische Leitfähigkeit einiger geschmolzener Salze. Bull Acad Imper Sci (St Petersburg) 8: 405–422, Benrath und Wainoff, 1914.

[4] J.S. Wilkes, M.J. Zaworotko, Air and Water Stable 1-Ethyl-3-methylimidazolium Based Ionic Liquids, J. Chem. Soc. Chem. Comm. (1992) 965-967.

[5] H. Ohno, M. Yoshizawa-Fujita, Y. Kohno, Functional design of ionic liquids: Unprecedented liquids that contribute to energy technology, bioscience, and materials sciences, Bull Chem Soc Jpn 92 (2019) 852–868.

[6] R. Huang, H. Liu, Z. Wei, Y. Jiang, K. Pan, X. Wang, J. Kong, Insights into the quantitative structure–activity relationship for ionic liquids: a bibliometric mapping analysis, Environ. Sci. Poll. Res. 30 (2023) 95054-95076.

[7] W. Silva, M. Zanatta, A.S. Ferreira, M.C. Corvo, E.J. Cabrita, Revisiting ionic liquid structure-property relationship: A critical analysis, Int J Mol Sci 21 (2020) 1–37.

[8] F. Philippi, T. Welton, Targeted modifications in ionic liquids – from understanding to design, Phys. Chem. Chem. Phys. 23 (2021) 6993-7021.

[9] R. Shi, Y. Wang, Dual Ionic and Organic Nature of Ionic Liquids, Scientific Rep. 6 (2016) 19644.

[10] B. Wang, L. Qin, T. Mu, Z. Xue, G. Gao, Are Ionic Liquids Chemically Stable? Chem Rev 117 (2017) 7113–7131.

[11] K. Ghandi, A Review of Ionic Liquids, Their Limits and Applications, Green Sus. Chem. 4 (2014) 44–53.

[12] Y. Cao, T. Mu, Comprehensive Investigation on the Thermal Stability of 66 Ionic Liquids by Thermogravimetric Analysis, Ind. Eng. Chem. Res. 53 (2014) 8651-8664.

[13] E.I. Izgorodina, Towards large-scale, fully ab initio calculations of ionic liquids, Phys. Chem. Chem. Phys. 13 (2011) 4189–4207.

[14] F. Philippi, T. Welton, Targeted modifications in ionic liquids - From understanding to design, Phys. Chem. Chem. Phys. 23 (2021) 6993–7021.

[15] G. Chatel, J.F.B. Pereira, V. Debbeti, H. Wang, R.D. Rogers, Mixing ionic liquids-"simple mixtures" or “double salts”? Green Chem. 16 (2014) 2051–2083.

[16] P. Sappidi, J.E. Bara, C.H. Turner, Molecular-level behavior of imidazolium-based ionic liquid mixtures, Chem. Eng. Sci. 229 (2021) 116073.

[17] R.P. Matthews, I.J. Villar-Garcia, C.C. Weber, J. Griffith, F. Cameron, J.P. Hallett, P.A. Hunt, T. Welton, A structural investigation of ionic liquid mixtures, Phys. Chem. Chem. Phys. 18 (2016) 8608–8624.

[18] H. Niedermeyer, J.P. Hallett, I.J. Villar-Garcia, P.A. Hunt, T. Welton, Mixtures of ionic liquids, Chem. Soc. Rev. 41 (2012) 7780–7802.

[19] K. R. Seddon J. Chem. Technol. Biotechnol. 68 (1997) 68 351.

[20] A.C. Stenson, K.N. West, W.M. Reichert, P. Klomkaew, C.G. Cssity, B.M. Dobyns, B. Siu, J.H. Dvis, Multi-ion ionic liquids and a direct, reproducible, diversity-oriented way to make them, Chem COMMUN. 51 (2015) 15914-15916.

[21] M. Atilhan, B. Anaya, R. Ullah, L.T. Costa, S. Aparicio, Double Salt Ionic Liquids Based on Ammonium Cations and Their Application for CO_2 Capture, J. Phys. Chem. C 120 (2016) 17829-17844.

[22] M. Niemczak, T. Rzemieniecki, A. biedziak, K. Marcinkowska, J. Pernak, Synthesis and Structure–Property Relationships in Herbicidal Ionic Liquids and their Double Salts, ChemPlusChem 83 (2018) 529-541.

[23] H. Zhang, X. Cui, P. Li, T. Feng, H. Feng, Measurement and correlation for the electrical conductivity of double salt ionic liquids with triple ions, Measurement and correlation for the electrical conductivity of double salt ionic liquids with triple ions, J. Mol. Liq. 365 (2022) 120193.

[24] Z. Song, X. Hu, Y. Zhou, T. Zhou, Z. Qi, K. Sundmacher, Rational design of double salt ionic liquids as extraction solvents: Separation of thiophene/n-octane as example, AIChE J. 65 (2019) e16625.

[25] N.S. Elstone, K. Shimizu, E.V. Shaw, P.D. Lane, L. D’Andrea, B. Deme, N. Mahmoudi, S.E. Rogers, S. Youngs, M.L. Costen, K.G. McKendrick, J.N. Canongia-Lopes, D.W. Bruce, J.M. Slattery, Understanding the Liquid Structure in Mixtures of Ionic Liquids with Semiperfluoroalkyl or Alkyl Chains, J. Phys. Chem. B 127 (2023) 7394-7407.

[26] N.S. Elstone, K. Shimizu,E.V. Shaw, P.D. Lane, L. D'Andrea, B. Demé, N. Mahmoudi, S.E. Rogers, S. Youngs, M.L. Costen, K.G. McKendrick, J.N. Canongia-Lopes, D.W. Bruce, J.M. Slattery, Understanding the Liquid Structure in Mixtures of Ionic Liquids with Semiperfluoroalkyl or Alkyl Chains, J. Phys. Chem. B 127 (2023) 7394-7407.
[27] T. Cosby, U. Kapoor, J. Sangoro, Mesoscale Organization and Dynamics in Binary Ionic Liquid Mixtures, J. Phys. Chem. Lett. 10 (2019) 6274-6280.
[28] J.L. Trenzado, Y. Rodríguez, A. Gutiérrez, A. Cincotti, S. Aparicio, Experimental and molecular modeling study on the binary mixtures of [EMIM][BF4] and [EMIM][TFSI] ionic liquids, J. Mol. Liq. 334 (2021) 116049.
[29] P. Sharma, S. Sharma, H. Kumar, Introduction to ionic liquids, applications and micellization behaviour in presence of different additives, J. Mol. Liq. 393 (2024) 123447.
[30] O.O. Okatura, T.J. van der Noot, Temperature dependence of viscosity for room temperature ionic liquids, J. Electoanal. Chem. 568 (2004) 167-181.
[31] D. Santos, H.S. Bamufleh, H. Uslu, Prigogine-Flory-Patterson evaluation of systems with ionic liquids + water or methanol: A study of specific interactions, J. Mol. Liq. 253 (2018) 23-27.
[32] S. Grimme, J. Antony, H. Krieg, A consistent and accurate ab initio parametrization of density functional dispersion correction (DFT-D) for the 94 elements H-Pu, J. Chem. Phys. 132 (2010) 154104.
[33] S. G. Balasubramani, G.P. Chen, S. Coriani, M. Diedenhofen, M.S. Frank, Y.J. Franzke, F. Furche, R. Grotjahn, M.E. Harding, C.Hättig, A.H.B. Helmich-Paris, et al., J. Chem. Phys. 152 (2020) 184107.
[34] BIOVIA COSMOtherm, Release 2021; Dassault Systèmes. http://www.3ds.com
[35] A. P. Lyubartsev, A. Laaksonen, MdynaMix – A Scalable Portable Parallel MD Simulation Package for Arbitrary Molecular Mixtures, Comput. Phys. Commun. 128 (2000) 565-589.
[36] V. Zoete, M. A. Cuendet, A. Grosdidier, O. Michielin, SwissParam. A fast force field generation tool for small organic molecules. J. Comput. Chem. 32 (2011) 2359-2368.
[37] L. Martínez, R., Andrade, E. G. Birgin, J. M. Martínez, Packmol: a package for building initial configurations for molecular dynamics simulations, J. Comput. Chem. 30, (2009) 2157-2164..
[38] W. G. Hoover, Canonical dynamics: Equilibrium phase-space distributions, Phys. Rev. A 31 (1985) 1695.
[39] U. L. Essmann, M. L. Perera, T. Berkowitz, H. Darden, H. Lee, L. G. Pedersen, A smooth particle mesh ewald method, J. Chem. Phys. 103 (1995) 8577-8593.
[40] T.A. Halgren, Merck Molecular Force Field. V. Extension of MMFF94 Using Experimental Data, Additonal Computational Data, and Empirical Rules, J. Comput. Chem. 17 (1996) 616-641.
[41] W. Humphrey, A. Dalke, K. Schulten, VMD - Visual Molecular Dynamics, J. Molec. Graphics 14 (1996) 33-38.
[42] M. Brehm, B. KirchneR. TRAVIS - A free analyzer and visualizer for Monte Carlo and Molecular Dynamics trajectories. J. Chem. Inf. Model. 51 (2011) 2007-2023.
[43] P. Navia, J. Troncoso, L. Romani, Excess Magnitudes for Ionic Liquid Binary Mixtures with a Common Ion, J. Chem. Eng. Data 52 (2007) 1369 – 1374.
[44] A.S.L. Gouveia, L.G. Tomé, I.M. Marrucho, Density, Viscosity, and Refractive Index of Ionic Liquid Mixtures Containing Cyano and Amino Acid-Based Anions, J. Chem. Eng. Data 61 (2016) 83-93.
[45] Q. Liu, L. Ma, S. Wang, Z. Ni, X. Fu, J. Wang, Q. Zheng, Study on the properties of density, viscosity, excess molar volume, and viscosity deviation of [C2mim][NTf2], [C2mmim][NTf2], [C4mim][NTf2], and [C4mmim][NTf2] with PC binary mixtures, J. Mol. Liq. 325 (2021) 114573.
[46] J.N. Canongia Lopes, T.C. Cordeiro, J.M.S.S. Esperança, H.J.R. Guedes, S. Huq, L.P.N. Rebelo, K.R. Seddon, Deviations from ideality in mixtures of two ionic liquids containing a common ion, J. Phys. Chem. B 109 (2005) 3519–3525.
[47] E.M. Živković, N. V. Živković, D.M. Majstorović, A.M. Stanimirović, M.L. Kijevčanin, Volumetric and transport properties of binary liquid mixtures with 1-ethyl-3-methylimidazolium ethyl sulfate as candidate solvents for regenerative flue gas desulfurization processes, J. Chem. Thermodyn. 119 (2018) 135–154.
[48] B. Golub, D. Ondo, R. Ludwig, D. Paschek, Why Do Liquids Mix? The Mixing of Protic Ionic Liquids Sharing the Same Cation Is Apparently Driven by Enthalpy, Not Entropy, J. Chem. Phys. Lett. 13 (2022) 3556-3561.
[49] M. Chakraborty, S. Barik, A. Mahapatra, M. Sakar, Binary mixtures of ionic liquids: Ideal, non-ideal, or quasi-ideal? J. Chem. Phys. 154 (2021) 224507.
[50] S. Jiang, Y. Hu, Z. Liu, C. Ren, Viscosity of Ionic Liquids. In: Zhang, S. (eds) Encyclopedia of Ionic Liquids. Springer, Singapore, 2022.

[51] C. Schreiner, S. Zugmann, R. Hartl, H.J. Gores, Temperature Dependence of Viscosity and Specific Conductivity of Fluoroborate-Based Ionic Liquids in Light of the Fractional Walden Rule and Angell's Fragility Concept, J. Chem. Eng. Data 55 (2010) 4372 – 4377.
[52] A. Stoppa, R. Buchner, G. Hefter, How ideal are binary mixtures of room-temperature ionic liquids? J. Mol. Liq. 153 (2010) 46-51.
[53] A.M. Pinto, H. Rodríguez, Y.J. Colón, A. Arce Jr, A. Arce, A. Soto, Absorption of Carbon Dioxide in Two Binary Mixtures of Ionic Liquids, Ind. Eng. Chem. Res. 52 (2013) 5975 – 5984.
[54] H. Wang, S.P. Kelley, J.W. Brentley, G.M Chatel, J. Shamshina, J.F.B. Pereira, V. Debbeti, A.S. Myerson, R.D. Rogers, Ionic Fluids Containing Both Strongly and Weakly Interacting Ions of the Same Charge Have Unique Ionic and Chemical Environments as a Function of Ion Concentration, ChemPhysChem 16 (2015) 993-1002.

5.1.4.1. Información experimental III

Tabla 20. Comparación de los datos experimentales con la literatura citada, tanto de las densidades, ρ (g cm-3), como de las viscosidades dinámicas, η (mPa s), de los compuestos puros a las temperaturas de trabajo.

	ρ / g cm^{-3}		η / mPa s		ρ / g cm^{-3}		η / mPa s	
T / K	exp.	Lit.	exp.	Lit.	exp.	Lit.	exp.	Lit.
	[EMIM][BF_4]				[EMIM][$MeSO_3$]			
283.15	1.29151	1.29704[a]	64.86	67.8[a]	1.25132	1.25140[k]	487.18	450[u]
		1.29200[b]		-		1.25200[b]		439.7[v]
		1.29089®		-		1.25204[l]		-
288.15	1.28766	1.28803[d]	50.91	54.1[p]	1.24777	1.24810[k]	321.98	337.6[w]
		1.28820[b]		55.5[q]		1.24840[b]		-
		1.28674®		-		1.24849[l]		-
293.15	1.28384	1.28390[f]	42.04	43.4[a]	1.24422	1.24440[n]	223.54	233.1[w]
		1.28390[g]		44.19[p]		1.24440[m]		210.91[x]
		1.28389[h]		-		1.24400[o]		-
298.15	1.28005	1.27990[f]	34.69	36.17[p]	1.24078	1.24090[m]	164.56	166.8[w]
		1.28000[g]		36.93[g]		1.24110[n]		155[u]
		1.28007[d]		-		1.24140[k]		-
303.15	1.27626	1.27626[g]	29.02	30.13[p]	1.23740	1.23740[m]	118.04	117[u]
		1.27630[f]		30.54®		1.23780[n]		113.17[x]
		1.27626[h]		-		1.23700[o]		120[y]
308.15	1.27249	1.27240[g]	24.58	25.557[s]	1.23402	1.23390[m]	89.63	87[y]
		1.27248[d]		26.0[q]		1.23440[n]		93.58[w]
		1.27260[i]		-		1.23280[p]		84.98[v]
313.15	1.26873	1.26803®	21.01	21.537[s]	1.23065	1.23100[n]	69.76	69[l]
		1.26860[g]		22.61[g]		1.23000[o]		67.31[x]
		1.26857[j]		-		1.23050[m]		72.8[w]

(a) Sanmamed et al., 2010
(b) Seki et al., 2012
® Gutiérrez et al., 2018
(d) Zech et al., 2010
® Ayranci & Sahin, 2018
(f) Gupta et al., 2020
(g) Song and Chen, 2014
(h) Sharma et al., 2014
(i) Darolia et al., 2022
(j) Srinivasa Rao et al., 2017
(k) Mohan et al., 2022
(l) Hasse et al., 2009
(n) Bioucas et al., 2022
(m) Rabari et al., 2014
(o) Krannich et al., 2016
(p) Marium et al., 2017
(q) Schreiner et al., 2010
® Rilo et al., 2010
(s) Narsimlu et al., 2019
(t) Zhang et al., 2004
(u) Tenney et al., 2014
(v) Vallejo et al., 2020
(w) Vatascin et al., 2021
(x) Bioucas et al., 2018
(y) Singh et al., 2014

Ayranci, E., & Sahin, E. M. (2018). Journal of Solution Chemistry, 47(2), 246–261.

Bioucas, F. E. B., Queirós, C. S. G. P., Lozano-Martín, D., Ferreira, M. S., Paredes, X., Santos, Â. F., Santos, F. J. V., Lopes, M. L. M., Lampreia, I. M. S., Lourenço, M. J. V., de Castro, C. A. N., & Massonne, K. (2022). Industrial and Engineering Chemistry Research, 61(5), 2280–2305.

Bioucas, F. E. B., Vieira, S. I. C., Lourenço, M. J. V., Santos, F. J. V., Nieto De Castro, C. A., & Massonne, K. (2018). Industrial and Engineering Chemistry Research, 57(25), 8541–8551.

Darolia, P. J., Malik, S., Garg, S., & Sharma, V. K. (2022). Chemical Data Collections, 41.

Gupta, H., Malik, S., Sharma, D., & Sharma, V. K. (2020). Chemical Data Collections, 28.

Gutiérrez, A., Atilhan, M., Alcalde, R., Trenzado, J. L., & Aparicio, S. (2018). Journal of Molecular Liquids, 255, 199–207.

Hasse, B., Lehmann, J., Assenbaum, D., Wasserscheid, P., Leipertz, A., & Fröba, A. P. (2009). Journal of Chemical and Engineering Data, 54(9), 2576–2583.

Krannich, M., Heym, F., & Jess, A. (2016). Journal of Chemical and Engineering Data, 61(3), 1162–1176.

Marium, M., Auni, A., Rahman, M. M., Mollah, M. Y. A., & Susan, M. A. B. H. (2017). Journal of Molecular Liquids, 225, 621–630.

Mohan, M., Kumar, N., Goud, V. V., Simmons, B. A., Sale, K. L., Gladden, J. M., Singh, S., & Banerjee, T. (2022). Fluid Phase Equilibria, 562.

Narsimlu, V., Reddy, K. C. S., Krishna, T. V., Mohan, T. M., & Rao, V. S. (2019). Journal of Chemical Thermodynamics, 139.

Rabari, D., Patel, N., Joshipura, M., & Banerjee, T. (2014). Journal of Chemical and Engineering Data, 59(3), 571–578.

Rilo, E., Vila, J., Pico, J., García-Garabal, S., Segade, L., Varela, L. M., & Cabeza, O. (2010). Journal of Chemical and Engineering Data, 55(2), 639–644.

Sanmamed, Y. A., González-Salgado, D., Troncoso, J., Romani, L., Baylaucq, A., & Boned, C. (2010). Journal of Chemical Thermodynamics, 42(4), 553–563.

Schreiner, C., Zugmann, S., Hartl, R., & Gores, H. J. (2010). Journal of Chemical and Engineering Data, 55(5), 1784–1788.

Seki, S., Tsuzuki, S., Hayamizu, K., Umebayashi, Y., Serizawa, N., Takei, K., & Miyashiro, H. (2012). Journal of Chemical and Engineering Data, 57(8), 2211–2216.

Sharma, V. K., Solanki, S., & Bhagour, S. (2014). Journal of Chemical and Engineering Data, 59(4), 1140–1157.

Singh, M. P., Mandal, S. K., Verma, Y. L., Gupta, A. K., Singh, R. K., & Chandra, S. (2014). Journal of Chemical and Engineering Data, 59(8), 2349–2359.

Song, D., & Chen, J. (2014). Journal of Chemical and Engineering Data, 59(2), 257–262.

Srinivasa Rao, V., Vijaya Krishna, T., Madhu Mohan, T., & Madhusudana Rao, P. (2017). Journal of Chemical Thermodynamics, 104, 150–161.

Tenney, C. M., Massel, M., Mayes, J. M., Sen, M., Brennecke, J. F., & Maginn, E. J. (2014). Journal of Chemical and Engineering Data, 59(2), 391–399.

Vallejo, J. P., Liñeira del Río, J. M., Fernández, J., & Lugo, L. (2020). Journal of Molecular Liquids, 319.

Vataščin, E., Havlová, M., & Dohnal, V. (2021). Fluid Phase Equilibria, 548.

Zech, O., Stoppa, A., Buchner, R., & Kunz, W. (2010). Journal of Chemical and Engineering Data, 55(5), 1774–1778.

Zhang, S., Li, X., Chen, H., Wang, J., Zhang, J., & Zhang, M. (2004). Journal of Chemical and Engineering Data, 49(4), 760–764.

Tabla 21. Densidades (ρ), viscosidades cinemáticas (ν), viscosidades dinámicas (η), volúmenes molares de exceso (VE) y desviaciones en la viscosidad ($\Delta\eta$) del sistema {(x) [EMIM][B_4] + (1-x) [EMIM][$MeSO_3$]} a diferentes temperaturas.

X	ρ / g cm^{-3}	ν / mm^2 s^{-1}	η / mPa s	V^E / cm^3 mol^{-1}	$\Delta\eta$ / mPa s
		283.15 K			
0.05337	1.25328	351.53	440.57	0.006	-24.080
0.11040	1.25546	318.92	400.40	0.002	-40.166
0.13040	1.25624	-	-	0.000	-
0.19260	1.25868	275.99	347.38	-0.008	-58.463
0.29665	1.26275	232.05	293.03	-0.014	-68.877
0.41168	1.26728	190.37	241.25	-0.015	-72.076
0.49072	1.27042	163.67	207.93	-0.013	-72.009
0.60652	1.27508	127.95	163.15	-0.011	-67.883
0.69196	1.27854	104.83	134.03	-0.005	-60.919
0.78563	1.28236	86.185	110.52	0.004	-44.875
0.79522	1.28276	-	-	0.004	-
0.88541	1.28652	65.794	84.645	0.010	-28.608
0.94897	1.28925	58.109	74.917	0.008	-11.492
		288.15 K			
0.05337	1.24973	235.30	294.06	0.004	-13.451
0.11040	1.25189	216.07	270.50	0.001	-21.553
0.19260	1.25509	188.29	236.33	-0.010	-33.444
0.29665	1.25916	161.77	203.69	-0.020	-37.871
0.41168	1.26368	134.47	169.93	-0.023	-40.451
0.49072	1.26680	115.55	146.38	-0.022	-42.574
0.60652	1.27140	92.604	117.74	-0.016	-39.830
0.69196	1.27482	77.476	98.768	-0.009	-35.638
0.70177	1.27521	-	-	-0.008	-
0.78563	1.27862	62.832	80.338	-0.001	-28.679
0.79522	1.27900	-	-	0.001	-
0.88541	1.28273	51.617	66.211	0.007	-15.757
0.94897	1.28542	45.297	58.226	0.007	-6.5119
		293.15 K			
0.05337	1.24617	165.98	206.83	0.003	-7.0240
0.11040	1.24833	152.63	190.54	-0.001	-12.971
0.19260	1.25152	136.13	170.37	-0.014	-18.215
0.29665	1.25560	115.94	145.57	-0.028	-24.132
0.30418	1.25590	-	-	-0.029	-
0.41168	1.26011	96.775	121.95	-0.034	-26.876
0.49072	1.26320	85.461	107.95	-0.032	-26.523
0.60652	1.26774	69.562	88.187	-0.022	-25.271
0.69196	1.27112	60.091	76.383	-0.013	-21.567
0.70177	1.27150	-	-	-0.011	-
0.78563	1.27487	49.244	62.780	-0.002	-18.170
0.88541	1.27895	40.543	51.852	0.006	-10.987
0.94897	1.28162	36.969	47.380	0.007	-3.9225

Tabla 21. Continuación.

X	ρ / g cm^{-3}	ν / mm^2 s^{-1}	η / mPa s	V^E / cm^3 mol^{-1}	$\Delta\eta$ / mPa s
		298.15 K			
0.05337	1.24273	124.09	154.21	0.001	-3.426
0.11040	1.24488	115.60	143.91	-0.005	-6.313
0.13040	1.24565	-	-	-0.008	-
0.19260	1.24805	101.51	126.70	-0.018	-12.855
0.29665	1.25212	87.005	108.94	-0.036	-17.096
0.30418	1.25241	-	-	-0.036	-
0.41168	1.25660	73.612	92.501	-0.043	-18.596
0.49072	1.25966	64.984	81.858	-0.040	-18.974
0.60488	1.26409	-	-	-0.030	-
0.60652	1.26414	53.730	67.922	-0.028	-17.870
0.69196	1.26747	46.739	59.240	-0.016	-15.455
0.70177	1.26785	-	-	-0.014	-
0.78563	1.27117	39.850	50.656	-0.003	-11.875
0.88541	1.27521	33.148	42.271	0.005	-7.3004
0.94897	1.27787	30.329	38.757	0.004	-2.5591
		303.15 K			
0.05337	1.23934	90.129	111.70	0.000	-1.5921
0.11040	1.24147	82.954	102.99	-0.006	-5.2299
0.13040	1.24223	-	-	-0.010	-
0.19260	1.24461	74.549	92.784	-0.020	-8.1132
0.29665	1.24863	65.117	81.307	-0.036	-10.327
0.30418	1.24893	-	-	-0.038	-
0.41168	1.25308	55.792	69.912	-0.046	-11.482
0.49072	1.25611	49.832	62.594	-0.043	-11.763
0.60488	1.26049	-	-	-0.033	-
0.60652	1.26055	41.851	52.755	-0.032	-11.293
0.69196	1.26383	36.890	46.623	-0.018	-9.8187
0.70177	1.26420	-	-	-0.015	-
0.78563	1.26748	31.912	40.448	-0.004	-7.6555
0.88541	1.27148	27.080	34.432	0.004	-4.7883
0.94897	1.27410	25.059	31.928	0.005	-1.6336
		308.15 K			
0.05337	1.23595	68.002	84.047	-0.0016	-2.1067
0.11040	1.23807	63.970	79.199	-0.0089	-3.2449
0.13040	1.23882	-	-	-0.0118	-
0.19260	1.24118	57.866	71.822	-0.0227	-5.2751
0.29665	1.24516	51.090	63.615	-0.0388	-6.7140
0.30418	1.24545	-	-	-0.0399	-
0.41168	1.24957	44.266	55.313	-0.0489	-7.5335
0.49072	1.25257	39.868	49.937	-0.0465	-7.7682
0.60652	1.25696	33.934	42.654	-0.0345	-7.5186
0.69196	1.26020	30.483	38.415	-0.0197	-6.1999
0.70177	1.26057	-	-	-0.0175	-
0.78563	1.26381	26.422	33.392	-0.0052	-5.1304
0.88541	1.26777	22.700	28.778	0.0030	-3.2538
0.94897	1.27036	21.092	26.794	0.0036	-1.1031

Tabla 21. Continuación.

X	ρ / g cm^{-3}	ν / mm^2 s^{-1}	η / mPa s	V^E / cm^3 mol^{-1}	$\Delta\eta$ / mPa s
		313.15 K			
0.05337	1.23258	53.265	65.653	-0.004	-1.5046
0.11040	1.23468	50.078	61.830	-0.012	-2.5474
0.13040	1.23543	-	-	-0.016	-
0.19260	1.23775	45.770	56.652	-0.024	-3.7185
0.29665	1.24170	40.722	50.565	-0.041	-4.7333
0.41168	1.24607	35.646	44.417	-0.052	-5.2739
0.49072	1.24905	32.360	40.419	-0.051	-5.4189
0.60652	1.25340	27.866	34.927	-0.040	-5.2659
0.69196	1.25661	24.991	31.404	-0.025	-4.6239
0.70177	1.25698	-	-	-0.023	-
0.78563	1.26019	22.101	27.851	-0.012	-3.6111
0.88541	1.26409	19.207	24.279	-0.001	-2.3189
0.94897	1.26663	17.920	22.698	0.003	-0.8014

Tabla 22. Parámetros (Ak) obtenidos para un ajuste polinómico en el caso de las propiedades ρ, ν, y con la ecuación de Redlich y Kister (6) para VE, Δη, así como las desviaciones estándar (s) para el sistema binario (x)[EMIM][BF_4]+(1-x)[EMIM][$MeSO_3$].

Propiedad	A_0	A_1	A_2	A_3	A_4	A_5	A_6	s
				283,15 K				
ρ (g/cm^3)	1.251	0.038	0.002	-	-	-	-	4.74E-05
ν (mm^2·s^{-1})	389.31	-759.19	1218.3	-1951.8	1727.9	-	-	0.9566
η (mPa·s)	487.15	-936.33	1508.1	-2442.5	2169.6	-720.98	-	1.2211
V^E (cm^3·mol^{-1})	-0.054	0.035	0.023	0.186	0.267	-0.257	-	4.09E-04
Δη (mPa·s)	-288.42	43.361	-101.25	91.921	17.884	-	-	1.3108
				288,15 K				
ρ (g/cm^3)	1.248	0.038	0.002	-	-	-	-	5.14E-05
ν (mm^2·s^{-1})	258.14	-459.98	754.30	-1361.9	1313.5	-464.31	-	0.7664
η (mPa·s)	322.11	-565.21	934.71	-1710.7	1656.1	-585.81	-	0.9669
V^E (cm^3·mol^{-1})	-0.088	0.075	0.115	-0.038	0.103	-0.016	0.082	6.92E-04
Δη (mPa·s)	-166.27	5.275	-70.304	73.840	42.145	-	-	0.9732
				293,15 K				
ρ (g/cm^3)	1.244	0.039	-0.001	0.002	-	-	-	5.09E-05
ν (mm^2·s^{-1})	179.05	-246.19	120.97	-21.150	-	-	-	0.5906
η (mPa·s)	223.34	-316.63	226.21	-157.69	67.282	-	-	0.6181
V^E (cm^3·mol^{-1})	-0.126	0.119	0.171	-0.111	0.134	-	-	4.65E-04
Δη (mPa·s)	-107.37	23.465	4.669	-83.409	-100.02	115.81	106.29	0.5428
				298,15 K				
ρ (g/cm^3)	1.241	0.039	-0.001	0.002	-	-	-	5.59E-05
ν (mm^2·s^{-1})	133.18	-178.46	87.417	-14.798	-	-	-	0.5102
η (mPa·s)	164.77	-196.32	-40.534	347.36	-383.79	143.57	-	0.6251
V^E (cm^3·mol^{-1})	-0.161	0.143	0.258	-0.123	0.018	-0.007	-	5.94E-04
Δη (mPa·s)	-75.363	13.338	-20.451	-17.469	50.667	-	-	0.5018

Tabla 22. Continuación.

Propiedad	A_0	A_1	A_2	A_3	A_4	A_5	A_6	s
				303,15 K				
ρ (g/cm^3)	1.237	0.038	-0.001	0.002	-	-	-	5.67E-05
ν (mm^2·s^{-1})	95.621	-117.84	53.473	-8.440	-	-	-	0.3173
η (mPa·s)	118.32	-142.26	62.108	-9.049	-	-	-	0.3959
V^E (cm^3·mol^{-1})	-0.174	0.139	0.294	-0.109	-0.034	-	-	5.41E-04
Δη (mPa·s)	-47.668	-0.441	18.215	31.895	-121.52	-41.542	148.36	0.2369
				308,15 K				
ρ (g/cm^3)	1.234	0.038	-0.002	0.002	-	-	-	5.61E-05
ν (mm^2·s^{-1})	72.474	-81.338	32.128	-3.915	-	-	-	0.1754
η (mPa·s)	89.512	-100.12	48.849	-23.206	9.662	-	-	0.2228
V^E (cm^3·mol^{-1})	-0.185	0.143	0.305	-0.104	-0.073	-	-	4.59E-04
Δη (mPa·s)	-31.229	3.562	6.554	-11.929	-35.035	19.638	32.206	0.2833
				313,15 K				
ρ (g/cm^3)	1.231	0.038	-0.001	0.002	-	-	-	5.21E-05
ν (mm^2·s^{-1})	56.510	-59.624	21.968	-2.279	-	-	-	0.1229
η (mPa·s)	69.654	-74.712	41.886	-29.279	13.591	-	-	0.1291
V^E (cm^3·mol^{-1})	-0.202	0.128	0.289	-0.158	-0.090	0.117	-	6.91E-04
Δη (mPa·s)	-21.836	0.801	0.735	-1.837	-15.836	9.799	14.827	0.1260

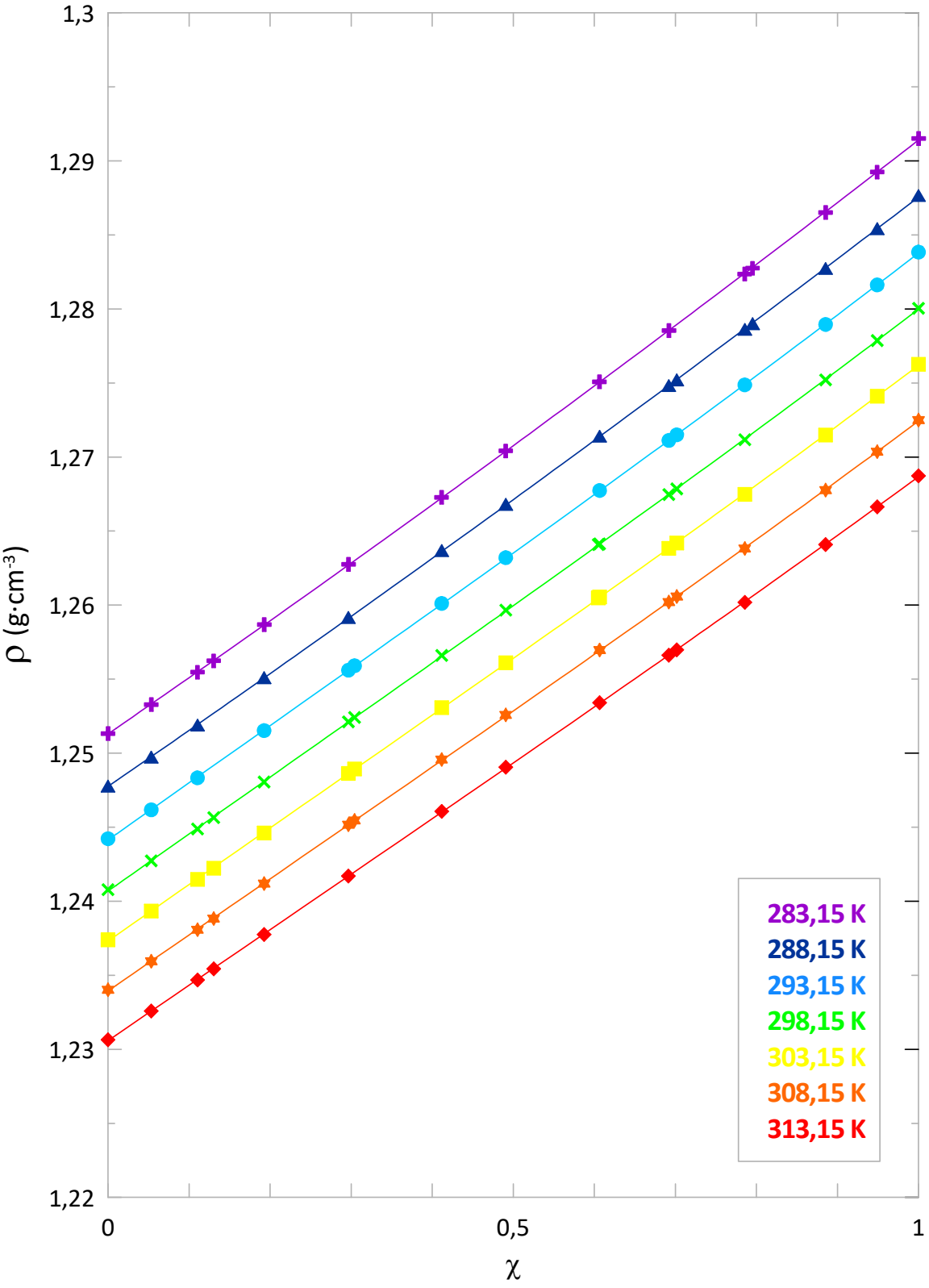

Figura 65. Variación de la densidad del sistema (x)[EMIM][BF_4]+(1-x)[EMIM][$MeSO_3$] en función de la temperatura: (+)283,15K, (▲)288,15K, (●)293,15K, (x)298,15K, (■)303,15K, (*)308,15K, (♦)313,15K.

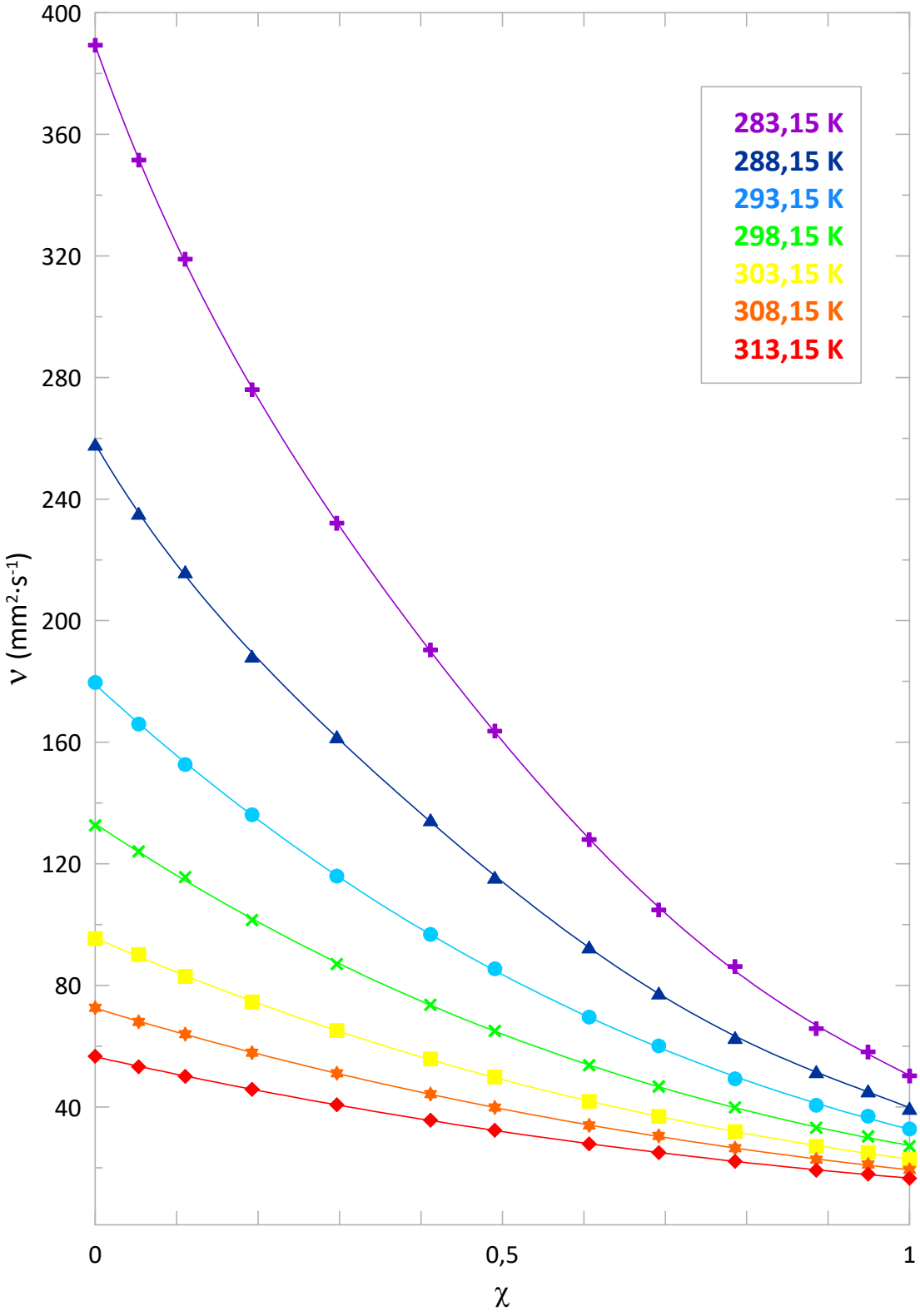

Figura 66. Variación de la viscosidad cinemática del sistema (x)[EMIM][BF_4]+(1-x)[EMIM][$MeSO_3$] en función de la temperatura: (+)283,15K, (▲)288,15K, (●)293,15K, (x)298,15K, (■)303,15K, (*)308,15K, (♦)313,15K.

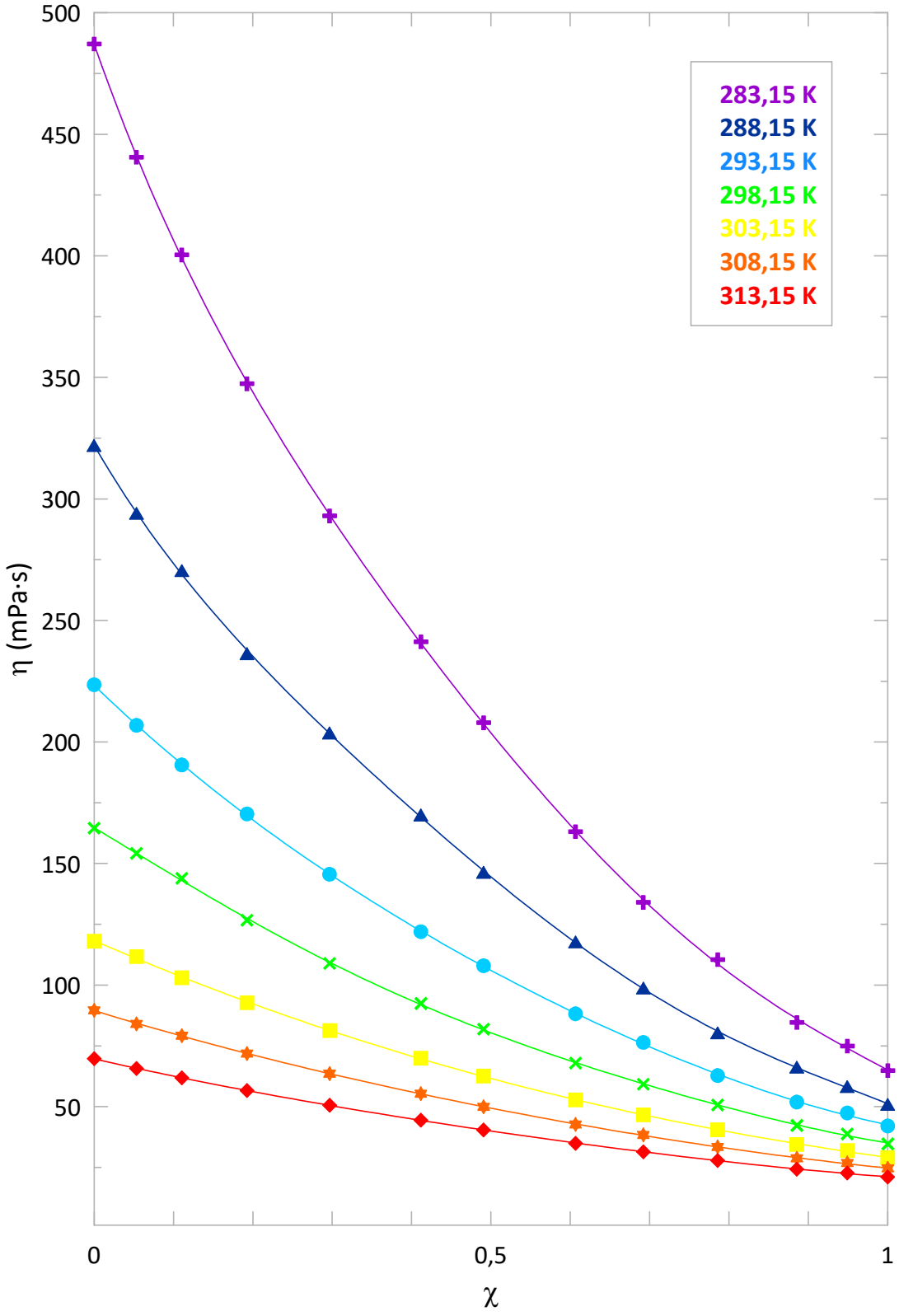

Figura 67. Variación de la viscosidad dinámica del sistema (x)[EMIM][BF_4]+(1-x)[EMIM][$MeSO_3$] en función de la temperatura: (+)283,15K, (▲)288,15K, (●)293,15K, (x)298,15K, (■)303,15K, (*)308,15K, (♦)313,15K.

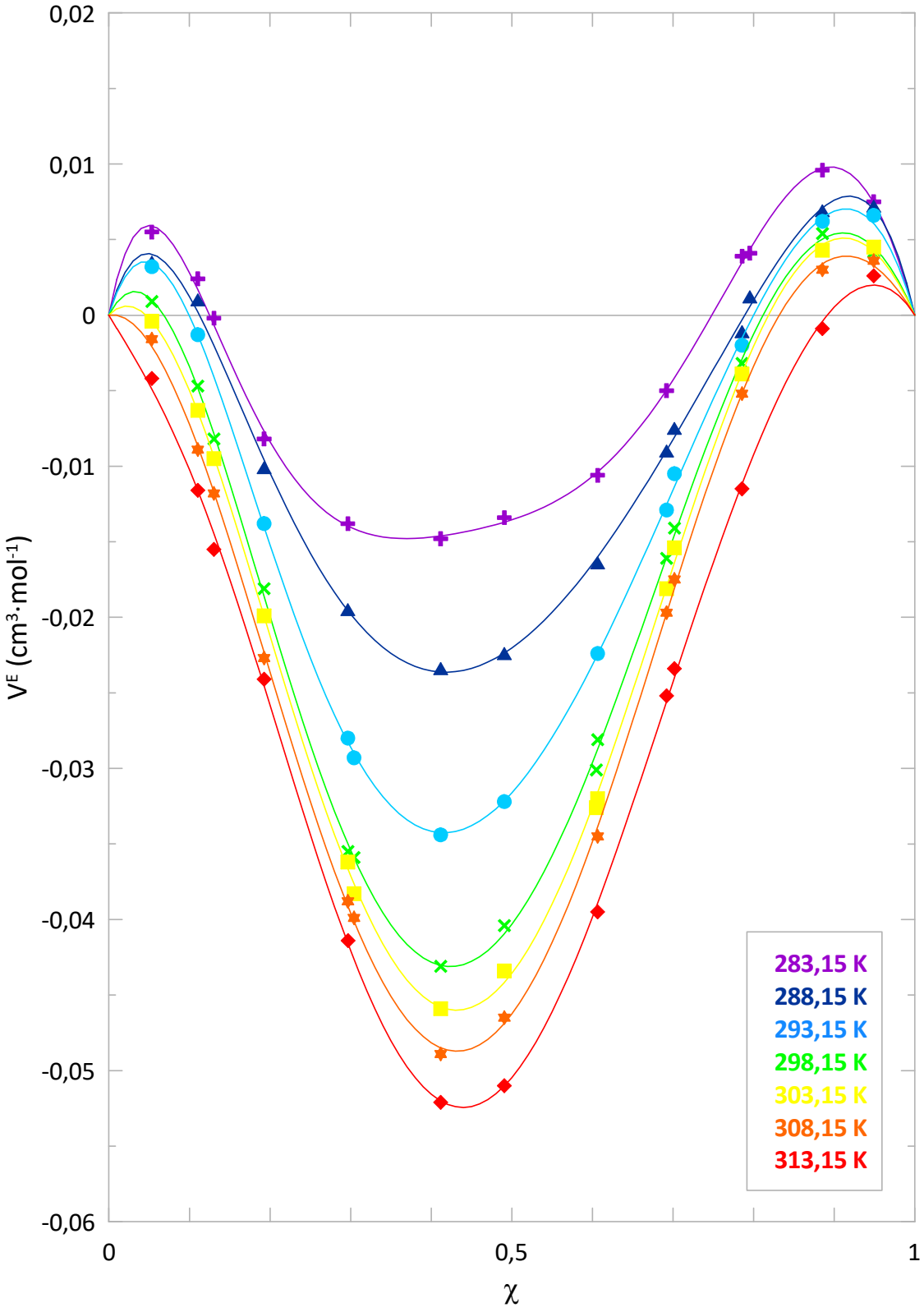

Figura 68. Volumen molar de exceso del sistema (x)[EMIM][BF_4]+(1-x)[EMIM][$MeSO_3$] en función de la temperatura: (+)283,15K, (▲)288,15K, (●)293,15K, (x)298,15K, (■)303,15K, (*)308,15K, (♦)313,15K.

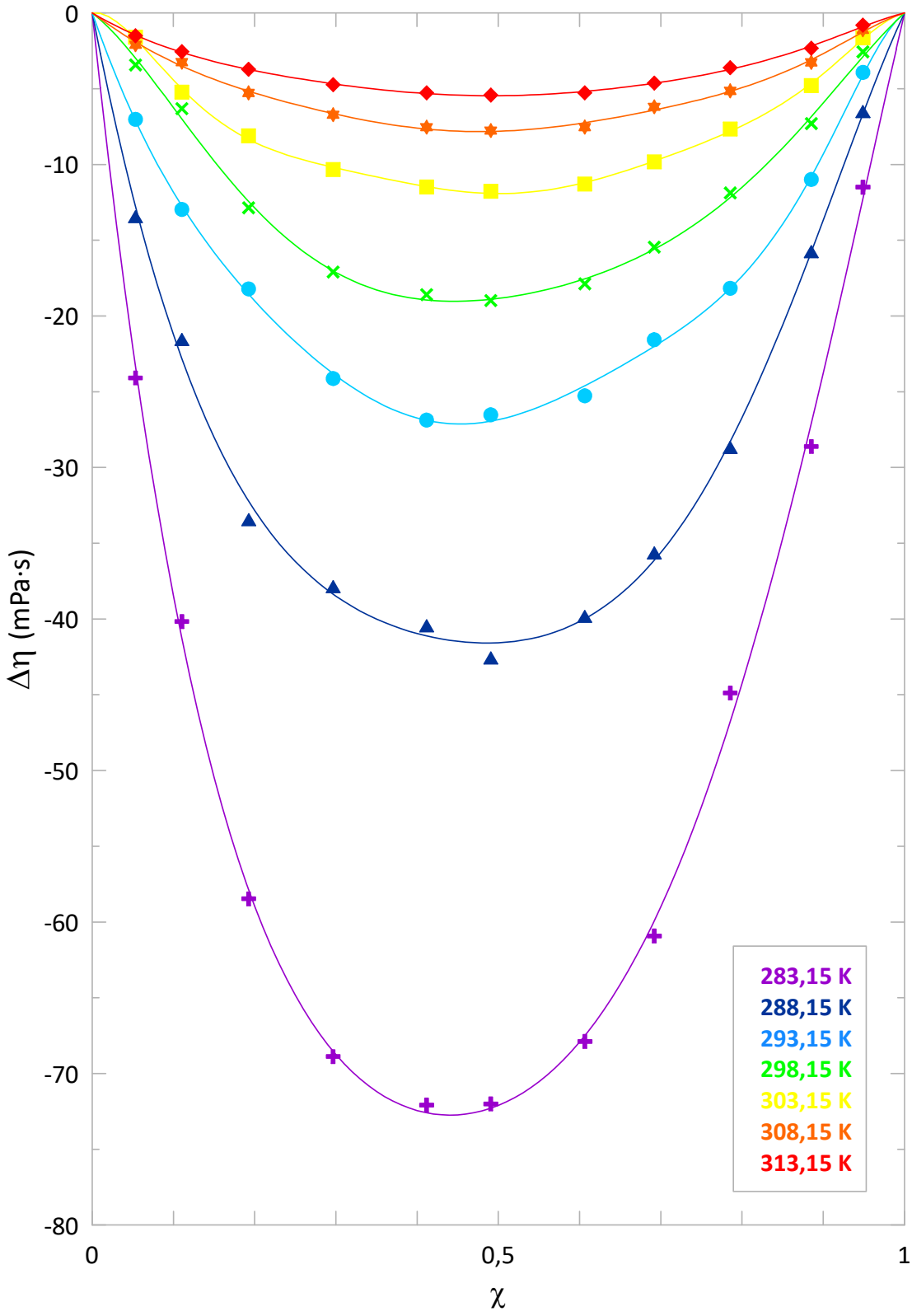

Figura 69. Desviaciones de la viscosidad del sistema (x)[EMIM][BFO₄]+(1-x)[EMIM][MeSO₃] en función de la temperatura: (+)283,15K, (▲)288,15K, (●)293,15K, (x)298,15K, (■)303,15K, (*)308,15K, (♦)313,15K

.

5.2. Publicaciones DES

5.2.1. Publicación IV

Título:	**Unveiling the High-Pressure Behavior of Thymol+Carvone NADES: A Combined Experimental-Computational Approach**				
Autores:	Ylenia Rodríguez [a], Cristina Benito[b], Santiago Aparicio [b], José L. Trenzado [a]				
Afiliación:	[a]) Departamento de Física, Universidad de Las Palmas de Gran Canaria, 35017 Las Palmas G.C., Spain [b]) Department of Chemistry, University of Burgos, 09001 Burgos, Spain				
Revista:	The Journal of Supercritical Fluids				
Factor impacto (IF):	3.4	**Cuartil (JRC):**	Q2	**Citas:**	2
Editor:	Elsevier	**Fecha de publicación:**	02/10/2024		

The Journal of Supercritical Fluids 215 (2025) 106408

Contents lists available at ScienceDirect

The Journal of Supercritical Fluids

journal homepage: www.elsevier.com/locate/supflu

Unveiling the high-pressure behavior of thymol+carvone NADES: A combined experimental-computational approach

Ylenia F. Rodríguez [a], Cristina Benito [b], Santiago Aparicio [b,*], Jose L. Trenzado [a,*]

[a] Department of Physics, University of Las Palmas de Gran Canaria, Las Palmas G.C. 35017, Spain
[b] Department of Chemistry, University of Burgos, Burgos 09001, Spain

HIGHLIGHTS

- Highlighting type V DESs and their potential advantages.
- Emphasizing the understudied nature of HP behavior in NADES.
- Introducing PC-SAFT EoS for phase equilibria modeling.
- Highlighting the focus on intermolecular hydrogen bonding in MD simulations.
- Framing the research in the context of HP application optimization.

GRAPHICAL ABSTRACT

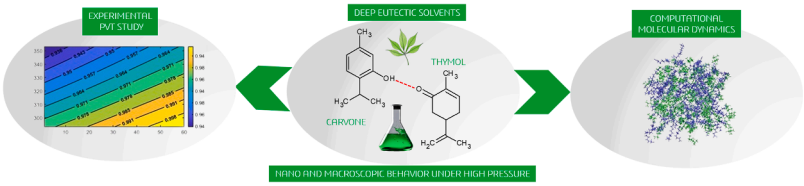

ARTICLE INFO

Keywords:
Natural deep eutectic solvents
High-pressure
PC-SAFT equation of state
Modeling
Molecular dynamics
Thymol + Carvone

ABSTRACT

this study considers the high-pressure behavior of thymol + carvone Natural Deep Eutectic Solvent using a combined experimental and computational approach. Experimentally, PVT (pressure – volume/density - temperature) measurements were conducted to characterize the fluid volumetric behavior as well as compressibility and internal pressure, which are directly related with hydrogen bonding and nanoscopic structuring. Likewise, these measurements provide crucial insights into the thermodynamic properties of the considered fluid under high pressure, which is pivotal for scaling up and process design for high pressure operations. Computationally, the PC-SAFT equation of state was employed to predict phase equilibria and PVT behavior, Machine Learning for density predictions, while Density Functional Theory and Classical Molecular Dynamics simulations were considered for the structural and dynamic characterization. These simulations provides insights into the electronic structure, intermolecular interactions (hydrogen bonding), liquid structuring and they unveil the pressure's impact on microscopic interactions, structural organization, and transport properties. This comprehensive investigation aims to shed light on the behavior under high pressure, facilitating their optimization for applications in chemical processing, energy storage, and materials science.

1. Introduction

Deep eutectic solvents (DESs) have emerged as a new class of solvents [1], offering a sustainable alternative to conventional volatile organic compounds (VOCs) [2]. Their diverse physicochemical properties [3], and their remarkable tunability, including biodegradability (although persistent DES have been also prepared) [4], low vapor pressure [5], and tailored viscosity [6], among others, have spurred research across various scientific disciplines and industrial domains [7]. Although the most relevant application of DESs stands on their use as

* Corresponding authors.
E-mail addresses: sapar@ubu.es (S. Aparicio), jose.trenzado@ulpgc.es (J.L. Trenzado).

https://doi.org/10.1016/j.supflu.2024.106408
Received 29 July 2024; Received in revised form 13 September 2024; Accepted 15 September 2024
Available online 2 October 2024
0896-8446/© 2024 Published by Elsevier B.V.

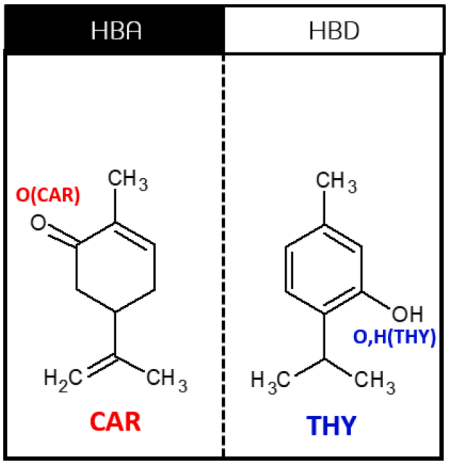

Fig. 1. Molecular structures of compounds used in this work for NADES preparation.

green and sustainable solvents [8], DESs also offer unique advantages as reaction media for various catalytic processes [9]. Their ability to dissolve both polar and non-polar compounds, coupled with their tunability, allows for tailored interactions between catalysts and substrates. This can lead to improved reaction efficiency, selectivity, and catalyst reusability. In electrochemistry [10], the ionic conductivity of some types of DESs, tunable viscosity, and compatibility with various electrode materials make DESs promising candidates for electrolytes in electrochemical devices. They can be tailored to optimize ionic transport while remaining compatible with sensitive electrode materials, potentially leading to advancements in batteries, fuel cells, and supercapacitors. Regarding extraction and separation, DESs exhibit high selectivity towards specific compounds, making them valuable tools for extracting valuable components from complex mixtures. This has significant implications for the extraction of natural products [11], pharmaceuticals, valuable components from biomass [12] as well as for operations such as CO_2 capture [13] or gas pollutants removal [14]. Their biodegradability and (mostly) low toxicity [15] further enhances their appeal for sustainable processes [16]. In biotechnology, the biocompatibility and tunability of many DESs make them attractive for diverse biotechnological applications [17]. They can be used for cell immobilization, which involves encapsulating cells within a DES matrix to facilitate specific biocatalytic processes. Additionally, DESs can modulate enzyme activity and aid in the development of novel biomaterials with tailored properties. In the case of pharmaceutical Applications (Therapeutic DESs) [18], these fluids are being explored as potential drug delivery systems due to their ability to solubilize poorly water-soluble drugs. They can also be used to design drug formulations with controlled release properties, potentially improving drug efficacy and patient compliance.

Regarding types of DESs, i.e. DESs classifications, it offers a framework for understanding their diverse properties [19]. The most common classification system categorizes DESs based on the nature of their components leading to five different main types: *i*) *type I:* DESs involving the combination of a quaternary ammonium salt (QAS) as the hydrogen bond acceptor (HBA) and a metal halide as the hydrogen bond donor (HBD). This type is known for its high ionic character and good thermal stability; *ii*) *type II:* the HBA remains a QAS, but the HBD is a metal halide hydrate. This type often exhibits lower melting points compared to type I DESs; *iii*) *type III:* this widely studied category combines a QAS (HBA) with a neutral HBD such as an organic acid, sugar, or alcohol. Type III DESs offer a broader range of functionalities and tunability; *iv*) *type IV:* DESs incorporating transition metal complexes as HBAs or HBDs. They are less common but offer unique properties like enhanced catalytic activity; *v*) *type V:* this emerging category [20] breaks away from the traditional ionic framework. Here, both HBA and HBD are devoid of ionic components, potentially leading to advantages like lower viscosity and higher thermal stability. However, type V DESs are still under active initial investigation. Moreover, within these types, DESs can be further categorized as ionic or non-ionic based on the presence or absence of net ionic character. Type I, II, and most type IV DESs are typically ionic, while type III and V can be ionic or non-ionic depending on the specific components used. Likewise, types III and V DESs, particularly those utilizing readily available and renewable bio-based components (Natural DESs, NADES [21]), are currently the most studied and widely used category due to their diverse properties, tunability, and potential for sustainability. (NA)DESs can also be categorized based on their affinity for water. Hydrophobic DESs [22] exhibit a low affinity for water, making them suitable for dissolving poorly water-soluble compounds. This is particularly valuable for pharmaceutical and environmental applications. Conversely, hydrophilic DESs readily mix with water, offering advantages for applications requiring water solubility while maintaining the unique properties of DESs. This classification system allows researchers to choose DESs with tailored water interactions for specific needs.

Despite the flourishing research on DESs, understanding their behavior under high pressure (HP) remains a relatively unexplored territory [23]. PVT (Pressure-Volume-Temperature) studies offer a crucial window into this domain, providing data on density, volume,

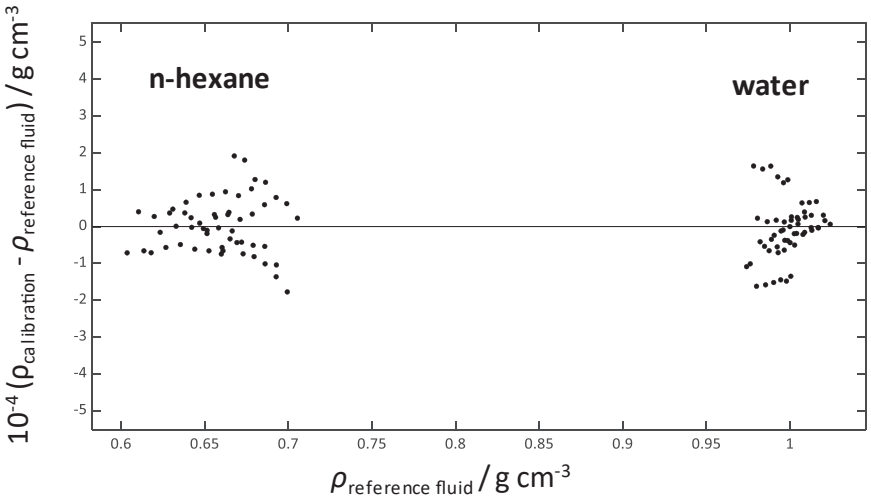

Fig. 2. Deviations of the calibration equation [47] for n-hexane and water as reference fluids [45,46].

Table 1
Results for the THY: CAR (1: 1) NADES reporting experimental properties as a function of pressure and temperature. Density, ρ, thermal expansion coefficient, α_P, isothermal compressibility, κ_T, and internal pressure, P_i.

T / K	P / MPa	ρ / g cm^{-3}	$10^3\,\alpha_P$ / K^{-1}	κ_T/ TPa^{-1}	P_i / MPa
293.15	1.0	0.9757	0.795	525.6	442.4
303.15	1.0	0.9680	0.805	548.6	444.0
313.15	1.0	0.9601	0.813	573.8	442.5
323.15	1.0	0.9524	0.816	600.9	437.9
333.15	1.0	0.9448	0.816	630.0	430.5
343.15	1.0	0.9373	0.812	661.2	420.4
353.15	1.0	0.9297	0.804	694.7	407.9
293.15	5.0	0.9778	0.786	528.1	431.4
303.15	5.0	0.9701	0.796	550.5	433.4
313.15	5.0	0.9621	0.802	575.0	432.1
323.15	5.0	0.9544	0.805	601.4	427.7
333.15	5.0	0.9468	0.804	629.9	420.5
343.15	5.0	0.9392	0.800	660.4	410.5
353.15	5.0	0.9316	0.791	693.2	398.1
293.15	10.0	0.9805	0.776	529.4	419.5
303.15	10.0	0.9729	0.784	550.9	421.7
313.15	10.0	0.9653	0.790	574.3	420.6
323.15	10.0	0.9576	0.792	599.8	416.4
333.15	10.0	0.9501	0.790	627.3	409.4
343.15	10.0	0.9425	0.784	656.9	399.5
353.15	10.0	0.9351	0.774	688.5	387.2
293.15	20.0	0.9856	0.756	526.4	401.1
303.15	20.0	0.9782	0.763	546.0	403.6
313.15	20.0	0.9707	0.766	567.7	402.7
323.15	20.0	0.9633	0.766	591.2	398.7
333.15	20.0	0.9559	0.762	616.7	391.7
343.15	20.0	0.9487	0.754	644.2	381.8
353.15	20.0	0.9417	0.743	673.7	369.3
293.15	30.0	0.9907	0.738	515.7	389.7
303.15	30.0	0.9835	0.743	533.5	392.3
313.15	30.0	0.9762	0.745	553.2	391.5
323.15	30.0	0.9689	0.743	574.9	387.4
333.15	30.0	0.9618	0.737	598.4	380.1
343.15	30.0	0.9548	0.727	623.8	369.9
353.15	30.0	0.9480	0.713	651.2	356.8
293.15	40.0	0.9956	0.722	497.6	385.6
303.15	40.0	0.9885	0.725	513.6	388.2
313.15	40.0	0.9813	0.725	531.5	387.2
323.15	40.0	0.9741	0.721	551.2	382.8
333.15	40.0	0.9673	0.713	572.7	375.0
343.15	40.0	0.9606	0.702	596.0	364.0
353.15	40.0	0.9539	0.686	621.3	350.0
293.15	50.0	1.0006	0.708	472.0	389.7
303.15	50.0	0.9937	0.709	486.1	392.3
313.15	50.0	0.9866	0.707	502.1	391.0
323.15	50.0	0.9797	0.701	519.8	385.9
333.15	50.0	0.9729	0.692	539.3	377.2
343.15	50.0	0.9663	0.678	560.7	365.1
353.15	50.0	0.9596	0.661	584.0	349.8
293.15	60.0	1.0052	0.696	439.3	404.2
303.15	60.0	0.9983	0.695	451.6	406.7
313.15	60.0	0.9913	0.691	465.7	404.9
323.15	60.0	0.9845	0.684	481.5	398.9
333.15	60.0	0.9778	0.672	499.0	388.9
343.15	60.0	0.9713	0.657	518.3	375.1
353.15	60.0	0.9651	0.638	539.3	357.7

Uncertainties: 0.0001 g cm^{-3} (ρ); 0.001 K^{-1} ($10^3\,\alpha_P$); 0.1 TPa^{-1} (κ_T); 0.1 MPa (P_i).

Table 2
Fitting coefficients of experimental density (g cm^{-3}) for the THY: CAR (1: 1) NADES as a function of pressure (MPa) and temperature (K), (Table 1) according to equation (1).

parameter	
a00	1.032
a10	0.0006716
a01	0.0008905
a20	$2.798\bullet10^{-6}$
a11	$-2.852\bullet10^{-6}$
a02	$-5.392\bullet10^{-6}$
a30	$-1.267\bullet10^{-8}$
a21	$-7.648\bullet10^{-9}$
a12	$7.867\bullet10^{-9}$
a03	$5.793\bullet10^{-9}$
goodness of fit	
SSE	$1.003\bullet10^{-6}$
R^2	0.9999
RMSE	0.0002

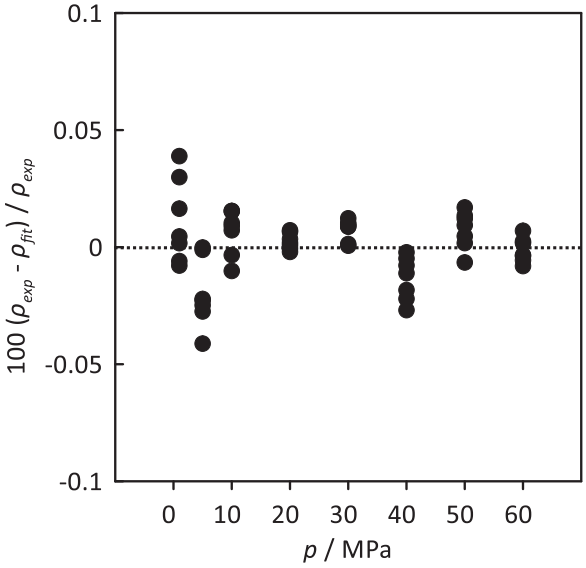

Fig. 3. Results for THY: CAR (1: 1) NADES reporting the deviation between experimental density, ρ_{exp}, and density from fitting experimental $P\rho T$ data to equation (1), ρ_{fit}, with coefficients in Table 2.

Table 3
Pure component PC-SAFT parameters for the THY: CAR (1: 1) NADES components considered in this work.

Compound	m_i^{seg}	σ_i /Å	ε_i / k_B(K)	N_{site}	ε^{AiBi}/k_B(K)	κ^{AiBi} / Å^3
THY	2.90	4.20	250.5	2B	3504.5	0.05
CAR	3.06	4.21	293.1	-	-	-

and compressibility of DESs under varying pressure and temperature conditions [24]. The HP studies on (NA)DES allows to analyze how the fluids compacting under compression, and the corresponding liquid structure changes, modifies solvating ability and transport properties [25]. The relevance of HP-PVT studies on DESs is multifaceted. Firstly, it allows for the prediction of DES behavior in HP applications, such as biomass processing or supercritical fluid extraction. Secondly, it helps elucidate the interplay between pressure, intermolecular forces, and liquid structure, paving the way for rational DES design for specific HP applications. Finally, it contributes to the development of accurate thermodynamic models for DESs, crucial for process simulation and optimization. The scarcity of systematic HP-PVT research on DESs highlights a critical gap in knowledge. A more comprehensive understanding is necessary to unlock the full potential of DESs in HP applications. Research should encompass a broader range of DES types, pressures, and temperatures, coupled with advanced computational modeling to provide a deeper theoretical foundation. This systematic approach will propel DESs towards becoming robust and predictable materials for the next generation of HP technologies.

Therefore, with the objective of advancing in the micro-macroscale knowledge of NADES under HP conditions, the archetypical NADES

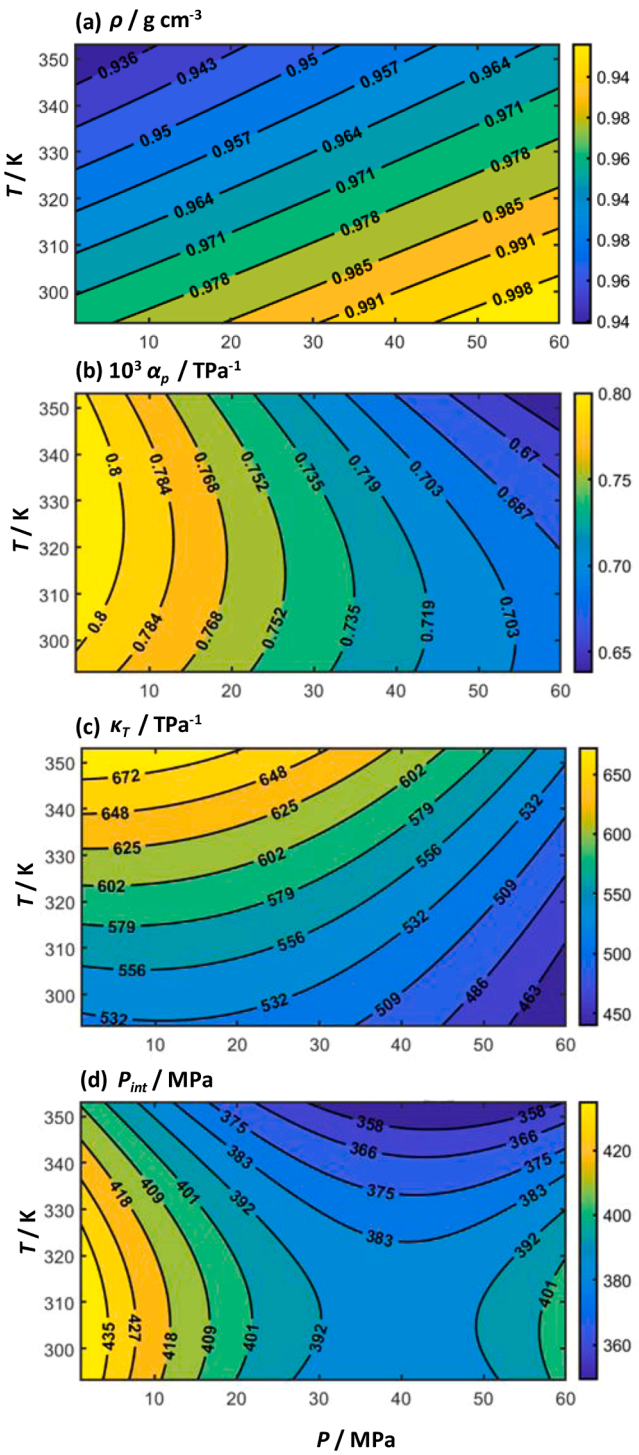

Fig. 4. Results for THY: CAR (1: 1) NADES reporting experimental properties as a function of pressure and temperature plotting fit to equation (1) with coefficients in Table 2 for density and the corresponding calculated properties. Density, ρ, thermal expansion coefficient, α_P, isothermal compressibility, κ_T, and internal pressure, P_i.

formed by thymol (THY) + carvone (CAR) was considered in this work. NADES based on THY have been proposed for several applications like extraction of natural compounds for the food industry [26] or from vegetal sources [27], removal of pollutants from aqueous phases [28], CO_2 absorption [29], analytical chemistry [30] or drug delivery [31], among many others. In the case of CAR, it has also been used for gas treatment operations [32], extraction of natural compounds for vegetal sources [33] or water treatment operations for pollutants removal [34]. Likewise, the combination of THY and CAR leads to hydrophobic NADES to be used for a plethora of possible technological applications. Moreover, the production of both components from natural sources [35,36], at low cost and minimal environmental impact [37], leading to sustainable and safe solvents. The THY: CAR NADES was considered in this work for 1: 1 mol ratio (THY mole fraction, $x_{THY} = 0.5$), in spite of the results reported in this work indicate that the eutectic composition appears at $x_{THY} = 0.39$. The reason for the selection of the equimolar composition to be studied in this work stands on the development of a NADES with contains the (relevant) properties of both compounds in equal proportion to produce the most suitable combination.

Experimentally, PVT measurements will be employed to characterize the NADES' PVT behavior under varying pressure and temperature conditions. Computationally, the PC-SAFT equation of state (EoS) will be implemented to model phase equilibria, alongside Density Functional Theory (DFT in the Tight Binding approach, DFT-TB) and Classical Molecular Dynamics (MD) simulations were considered to unveil the pressure's influence on microscopic interactions, structural organization, and transport properties. Likewise, Machine Learning (ML) – based methods were used for predicting PVT behavior. This combined approach seeks to establish a comprehensive understanding of the interplay between HP, intermolecular forces, and the evolution of NADES' liquid nanostructure. This knowledge will be instrumental in optimizing NADES performance for HP applications, paving the way for advancements in fields like chemical processing and materials science.

2. Materials and methods

2.1. Experimental PVT studies

THY (CAS: 89–83–8, purity 99.5 %) and CAR (CAS: 99–49–0, purity 99.5 %), were purchased from MERCK and used without further purification, Fig. 1. The THY:CAR (1: 1) NADES was prepared by accurately weighing (Mettler AT261 balance, $\pm 1 \times 10^{-5}$ g) the corresponding components and mixing them in closed glass flasks. The mixtures were stirred for 12 hours at 313 K. Transparent, colorless liquids were formed without any turbidity. Drying was performed under vacuum (Heidolph rotary evaporator) at 313 K for 24 hours. Water content was measured using a Karl-Fischer coulometric titrator (Metrohm 831 KF) and found to be 0.10 wt%. This low water content is considered negligible for NADES properties [38]. The prepared NADES was stored in sealed flasks and remained liquid at 293 K for at least three months without turbidity.

PVT Measurements were carried out using a high-pressure apparatus utilizing a vibrating tube densimeter [39]. This setup has proven reliable for DESs characterization and aligns with previous studies on ionic liquids (ILs) [40] and NADESs [23]. The scarcity of PVT data on (NA)DES further supports this approach, as several studies utilize vibrating tube devices [41–44]. The automated apparatus consists of an Anton Paar DMA512P high-pressure unit with a U-shaped vibrating tube cell connected to an Anton Paar DMA58 digital densimeter. The oscillation period of the vibrating tube is measured with a ±0.01 μs uncertainty. An external Julabo LH50 bath controls the cell temperature, monitored by Pt100 thermometers with an uncertainty of ± 0.01 K. Pressure is controlled using a Teledyne ICO 100DM syringe pump and measured with a pressure transducer, with ±0.01 MPa uncertainty. Calibration was performed with Milli-Q water (resistivity 18.2 MΩ cm) and n-hexane (Merck, 99.9 % purity) as reference fluids, using established literature data for their densities [45,46]. The working equation relating vibrating period to density is the 14-parameter equation established by Ihmels et al. [47]. Fig. 2 shows the deviations of the calibration equation indicating the suitable performance of the calibration procedure. Through error analysis, the density expanded uncertainty (calculated considering the uncertainties of temperature, pressure and oscillation period measurements, as well as those for density data of reference fluids used in calibration) was determined to be ±0.001 g cm^{-3} [48].

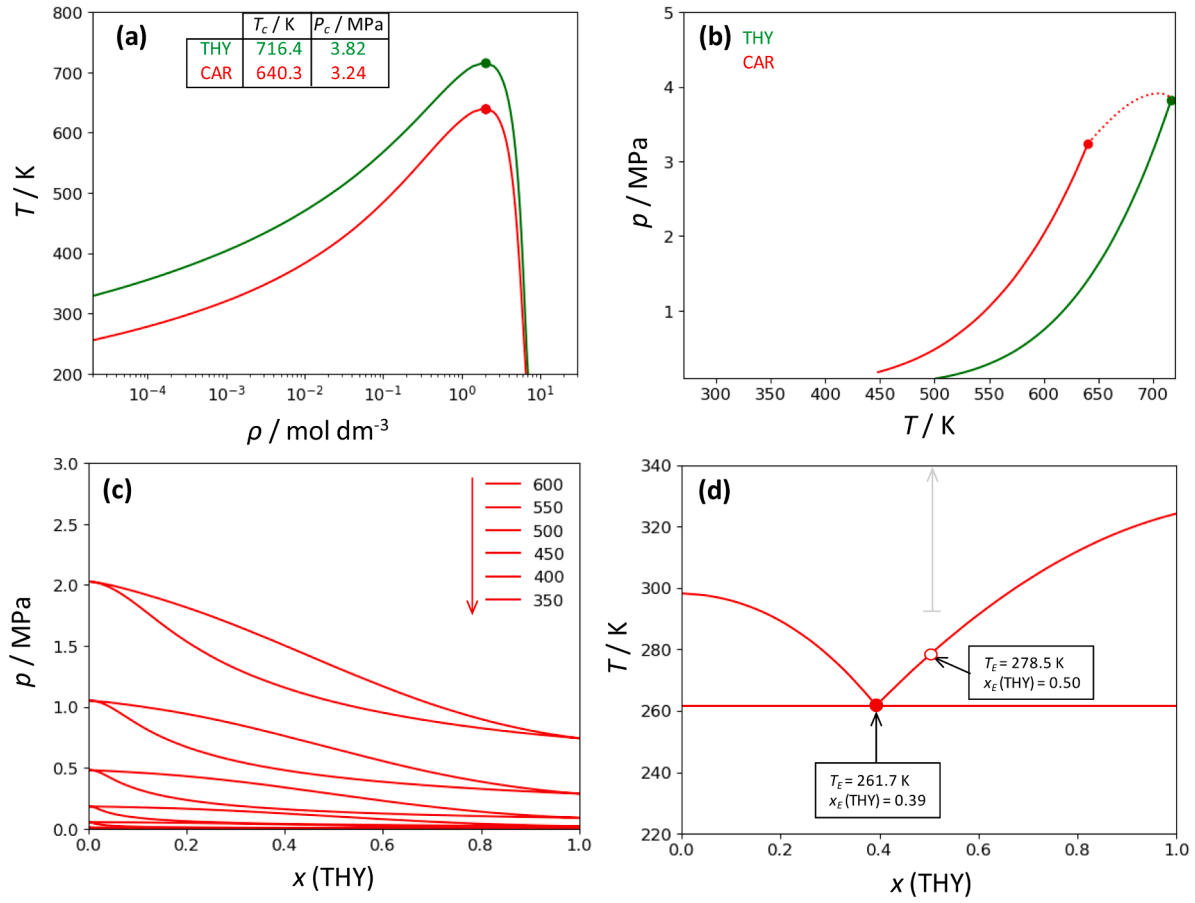

Fig. 5. PC-SAFT predictions, pure compound parameters in Table 3, for (a) vapor – liquid saturation curves and (b) global phase diagrams (type I according to the van Konynenburg classification) with circles indicating predicted critical points, for THY: CAR (1: 1) NADES, with dashed line indicating critical locus, (c) isothermal vapor – liquid equilibria at the reported temperatures (in K), (d) solid-liquid equilibria with (filled circles) eutectic point, (empty circles) equimolar composition considered in this work for experimental and computational studies, (gray arrows) temperature range considered in this work. All the results for THY: CAR (1: 1) NADES obtained with binary interaction parameter $k_{12} = -0.10$.

The obtained PVT data (Table 1) was fitted to Eq. 1 (fitting coefficients in Table 2, deviations in Fig. 3), from this fitting equation and parameters, relevant derived thermophysical properties were calculated: *i*) Thermal expansion coefficient (α_p, Eq. 2), ii) isothermal compressibility (κ_T, Eq. 3), and *iii*) internal pressure (P_i, Eq. 4) (Fig. 3):

$$\rho = a_{00} + a_{10}\quad T + a_{01}\quad p + a_{20}\quad T^2 + a_{11}\quad Tp + a_{02}\quad p^2 + a_{30}\quad T^3 + a_{21}\quad T^2p + a_{12}\quad Tp^2 + a_{03}\quad p^3 \tag{1}$$

$$\alpha_p = -\frac{1}{\rho}\left(\frac{\partial \rho}{\partial T}\right)_p \tag{2}$$

$$\kappa_T = \frac{1}{\rho}\left(\frac{\partial \rho}{\partial p}\right)_T \tag{3}$$

$$P_i = T\frac{\alpha_p}{\kappa_T} - p \tag{4}$$

Additionally, as P_i is related with internal energy (U, Eq. 5), this property offers valuable insights into NADESs molecular level structuring due to its correlation with intermolecular forces within the liquid [49]. Analyzing changes in P_i can help us understand and quantify the strength of these interactions, liquid cohesive forces, which significantly impact NADESs properties like solvation behavior, viscosity, and thermal stability [50], as larger P_i values indicate stronger intermolecular forces within the NADESs. As P_i essentially represents the pressure that arises from these intermolecular interactions within the liquid, when a NADES undergoes isothermal expansion, work against these cohesive forces is done, which is reflected in the changes in internal energy, which is precisely what P_i captures.

$$P_i = \left(\frac{\partial U}{\partial V}\right)_T \tag{5}$$

2.2. PC-SAFT EoS modelling

PC-SAFT molecular – based EoS was considered for the prediction of PVT and relevant phase equilibria properties [51]. PC-SAFT studies for THY: CAR (1: 1) NADES were carried out using pure component parameters (reported in Table 3), with the considered NADES treated as binary mixtures of the corresponding components. THY was modelled as a 2B associative compound (i.e. hydrogen bond donor - acceptor) because of the presence of the hydroxyl group, whereas CAR was considered as non-associative (i.e. only hydrogen bond acceptor), considering the keto functional group. Mixtures (NADES) were treated considering a temperature independent binary interaction parameter $k_{12} = -0.10$.

2.3. PVT predictions via machine learning

ML methods were applied for the prediction of density as a function of pressure and temperature (PVT behavior). For model development, the PVT data obtained in this work was combined with data for type V NADES obtained from the literature to develop training and validation datasets (Supplementary Information, ML_DATABASE.xlsx) [23,52,53].

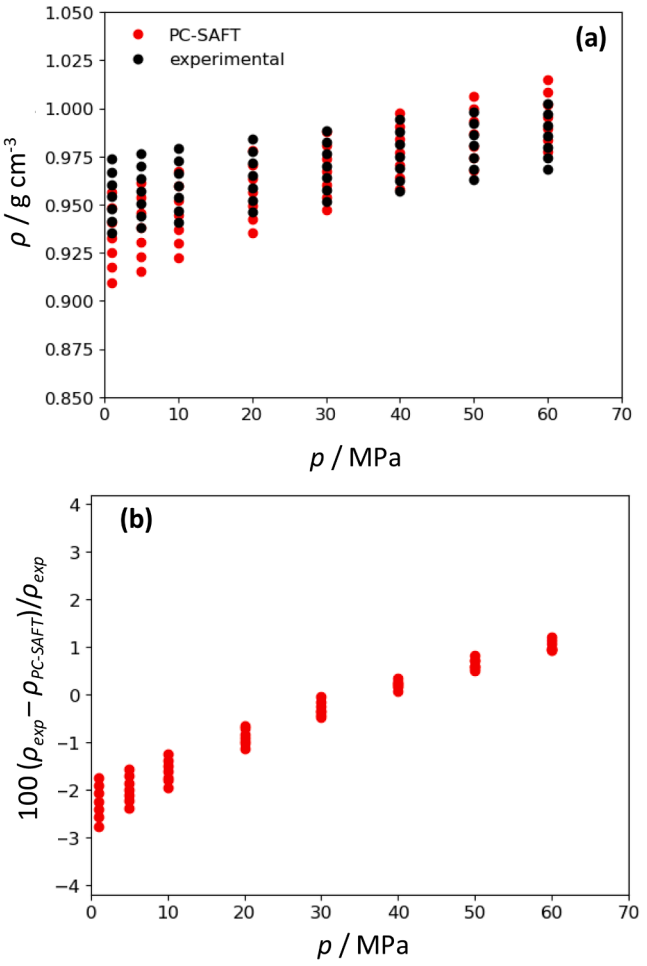

Fig. 6. (a) PC-SAFT predictions for density (ρ) and (b) percentage deviations between experimental (exp) and predicted (PC-SAFT) density with pure compound parameters as reported in Table 3 and $k_{12} = -0.10$ for THY: CAR (1:1) NADES.

The available literature PVT data for type III NADES were not considered as the molecular nature of type V NADES in comparison with the ionic character for type III DES hinders the development of a single predictive model. The considered data are in the 293.15–413.15 K temperature range, 0.1–60 MPa pressure range and 0.8–1.0 g cm^{-3} density range. Seven different NADES were considering totaling 642 experimental points, 25 % used for training and 75 % for validation purposes. For the development of predictive models, 3D molecular descriptors by as in KrakenX [54] were considered, which were calculated from optimized structures of isolated molecules, with the Online Chemical Database (OCHEM) Descriptors Calculator [55]. Therefore 252 molecular descriptors were considered for each HBA/HBD (Supplementary Information, ML_DATABASE.xlsx). All the ML calculations were carried out using MATLAB. Different ML methods were considered, including (*i*) linear regressions, (ii) regression trees, (*iii*) Support Vector Machines (SVM), (*iv*) Gaussian Process Regression (GPR), (*v*) ensembles of trees, and (*vi*) Neural Networks with the model leading to the lower Root Mean Square Error (RMSE) being selected for predicting PVT properties of type V NADES.

2.4. Density functional theory – tight binding

Software and Model: DFT-TB simulations were carried out with DFTB+ program [56]. Slater–Koster (SK) files corresponding to the Third-Order Parameterization for Organic and Biological Systems (3OB) were applied [57,58]. The self-consistent calculations were carried out with 10^{-6} tolerance. The k-points meshes corresponded to a 4 × 4 × 4 distribution with the self-consistent calculations carried out with 10^{-6} tolerance. **Systems preparation and equilibration:** initial cubic simulation boxes containing 10 THY and 10 CAR molecules (500 total atoms) were built using the Amorphous Cell program in Biovia Materials Studio [59] corresponding to the experimental densities. Simulation boxes for systems at 323 K and 0.1, 1, 10, 20, 30, 40, 50 and 60 MPa were prepared. These initial simulation boxes were pre-equilibrated using geometry (classical MD approach) optimization into the Forcite module within Biovia Materials Studio software [60] considering the using the COMPASS III force field [61]. **Production runs:** the previously equilibrated structures were considered for geometrical optimization of the considered systems considering Periodic Boundary Conditions in the three space directions (with 0.1 kJ mol^{-1} as a convergence criterion).

2.5. Molecular dynamics simulations

Software, Molecular Model and Force Field: MD simulations were conducted using the Forcite module within Biovia Materials Studio software [48]. Both THY and CAR molecules were described using the COMPASS III force field [49]. **Simulation Setup:** cubic simulation boxes with 1000 total molecules (500 THY and 500 CAR) were prepared using the Amorphous Cell program in Biovia Materials Studio [47] to achieve an initial density of 1 g cm^{-3}. Periodic boundary conditions were applied in all directions for all simulated systems. **Systems preparation and equilibration**: initial simulation boxes were subjected to consecutive heating (up to 500 K) and cooling cycles (to the target temperature) in the NVT (constant number of molecules – constant volume – constant temperature) ensemble, then followed by NVT simulations at the target temperature for 20 ns, with equilibration assured by the constancy of total potential energy and density. **Production runs:** after equilibrations, NPT ensemble simulations were performed at 323 K and pressures ranging from 0.1 to 60 MPa, with each simulation lasting for 100 total ns, with a timestep of 1 fs, with the first 20 ns considered for pressure equilibration and the last 80 ns for analysis. **Thermostat and Barostat:** the Nose-Hoover thermostat [62] was employed for temperature control and the Parrinello-Rahman barostat [63] for the desired pressures. **Non-bonded Interactions:** long-range electrostatic interactions were handled using the Ewald summation method [64] with van der Waals potential with Waldman-Hagler mixing rules [65], and a cutoff distance of 15 Å. **Data Analysis:** visualization, analysis, and post-processing of the MD trajectories were performed using VMD [66] and TRAVIS [67].

3. Results and discussion

3.1. Experimental PVT study

Experimental PVT properties (density-pressure-temperature) for the considered NADES in the 293.15 – 353.15 K and 1–60 MPa are reported in Table 1. These experimental data were fitted according to Eq. (1), fitting coefficients in Table 2. The proposed 10-parameters fitting equation and coefficients led to excellent fit, as inferred from results in Fig. 3. Therefore, the equation and fitting parameters allowed the accurate calculation of derived properties (α_p, κ_T, and P_i) from experimental PVT data, Table 2. All these properties are plotted as a function of pressure and temperature in Fig. 4. The considered NADES has hydrophobic nature and thus it is less dense than water, with density in the 0.93–1.00 g cm^{-3} range for the considered pressures – temperatures. The hydrophobic nature of the considered NADES opens many opportunities for its use in applications such as pollutants removal from drinking or waste waters [68], valuable molecules extraction [69] or solubilization of poorly soluble drugs [70], among others.

Density evolves in a linear way with increasing temperature and pressure, Fig. 4a. The α_p are in the 0.64–0.82 10^{-3} K^{-1}, which are in the

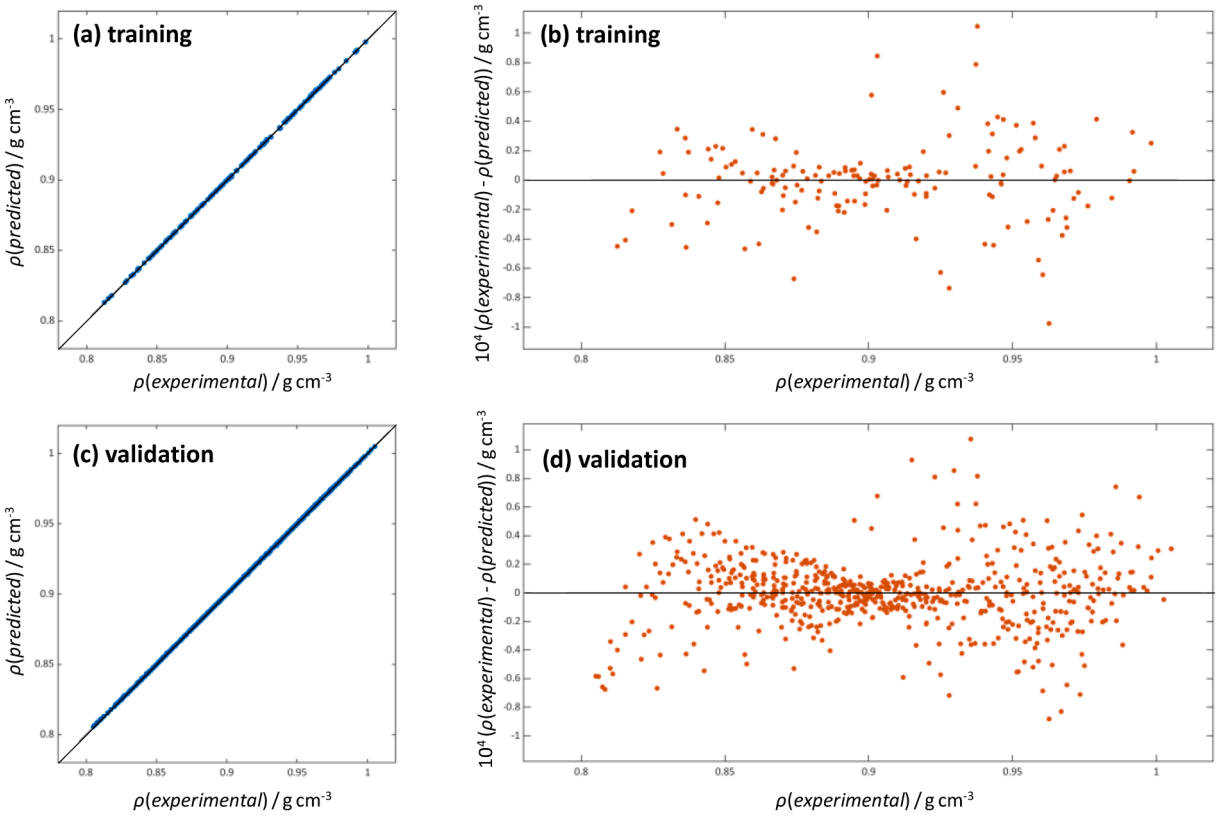

Fig. 7. Results of NADES density predictions in comparison with experimental density data. Predictions obtained using *rational quadratic GAUSSIAN PROCESS REGRESSION* with Principal Components Analysis (10 features) considering KrakenX molecular descriptors (125) for NADES components as well as pressure and temperature. $N = 642$ (25 % for training + 75 % for validation), P range = 0.1–60 MPa, T range = 293.15–413.15 K. NADES: menthol + thymol (1: 1) [23], thymol + carvone (1: 1) [this work], thymol + 1,8-cineole (1: 1) [41], thymol + camphor (1: 1) [41], menthol + octanoic acid (1: 1) [40], menthol + decanoic acid (1: 1) [40], menthol + dodecanoic acid (2: 1) [40].

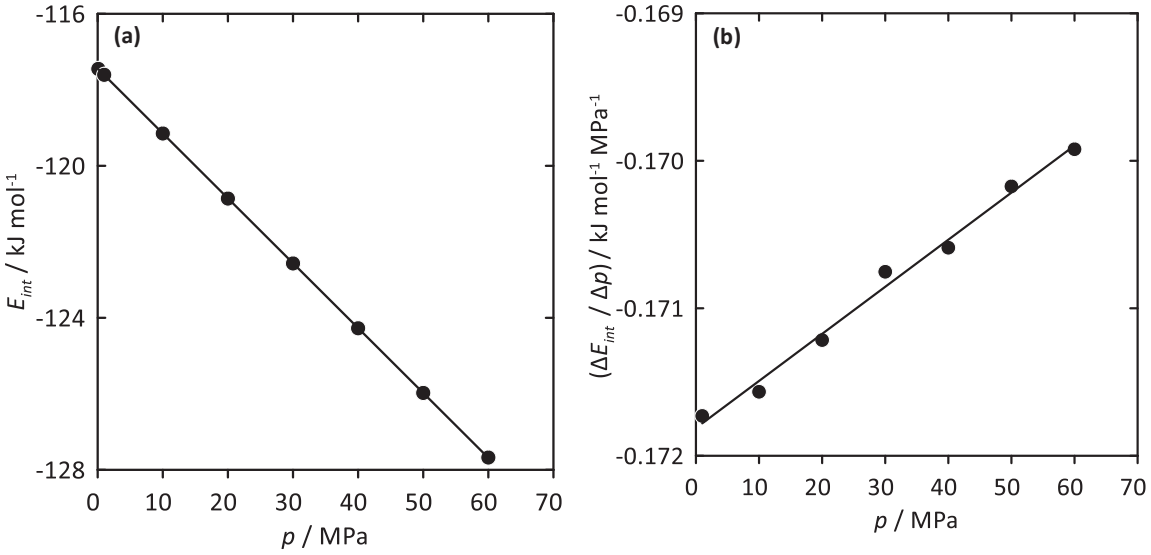

Fig. 8. DFT-TB results for THY: CAR (1: 1) at 303 K and the reported pressures. Panel a, shows intermolecular interaction energy, E_{int}, per THY – CAR pair, and panel b, shows the changes of this property with pressure.

range of other type V hydrophobic NADES such as menthol: thymol [71] or menthol: fatty acids [32], and they are remarkably higher than those for type III DES, which are frequently lower than 0.5 10^{-3} K^{-1} [29,30]. The larger α_p for hydrophobic type V NADES would stand in the absence of ionic species, i.e. lower coulombic contributions to intermolecular interactions, which leads to more compressible fluids in comparison with type III (ionic) NADES. Nevertheless, the temperature and pressure evolution of α_p is remarkably non-linear (Fig. 4b). For isobaric conditions, at moderated pressures, α_p increases upon heating and then decreases, with the temperature corresponding to the inflection point

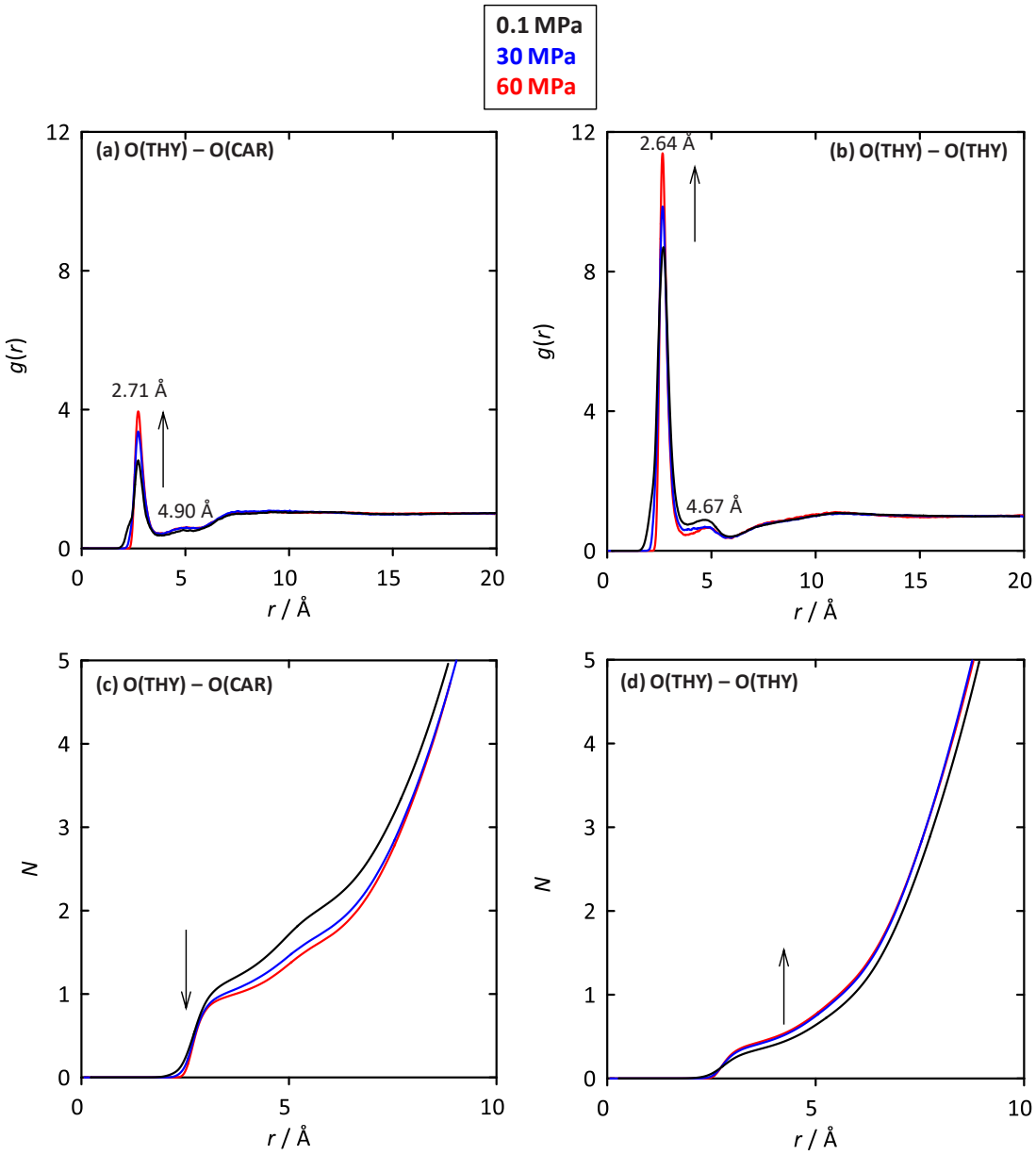

Fig. 9. (a,b) Radial Distribution Functions, $g(r)$, for the reported atoms and (c,d) integration of $g(r)$ (solvation numbers, N) for THY: CAR (1: 1) from Molecular Dynamics simulations at 303 K and the reported pressures.

being 323.15 K for 1 MPa, decreasing as the pressure increasing in such a way that at high pressure (60 MPa), α_p decreases upon heating in the considered temperature range. This anomalous behavior of α_p has not been reported for other hydrophobic type V NADES, e.g. menthol + fatty acids [40] showed α_p showed increasing α_p with temperature under isothermal conditions as well as archetypical type III DES formed by choline chloride and urea [72]. Nevertheless, decreasing α_p upon heating has also been reported for type III DES [30], as well as for ILs [40, 73]. This behavior of α_p is a thermodynamic anomaly and according to the requirements of α_p for the critical point of any fluid [74], it must lead to minima in α_p vs temperature curves. These minima have not been found in the considered THY: CAR NADES as the experimental measurements were carried out far from the critical point (T_c 658 = K, P_c = 3.7 MPa, as predicted from PC-SAFT calculations). Nevertheless, the decrease in α_p for the highest considered pressure (60 MPa) is only a 8.3 % on going from 293.15 to 353.15 K (60 K range), i.e. 9.7 10^{-7} K^{-2} slope, which is slightly larger than the values obtained for ILs but not so large, which would lead to negative slopes for α_p vs temperature at high pressures. For example, in the case of [C_4mim][Ntf_2] α_p decreases (at 60 MPa) a 4.6 % (i.e. 5.0 10^{-7} K^{-2} slope), which is roughly the half of the change obtained in this work for THY: CAR, but agrees with the lower α_p for the IL (less compressible fluid).

The behavior of κ_T (Fig. 4c) is also largely non-linear, although for this property increasing values are obtained upon heating and decreasing with increasing pressure, thus no anomalies were found. Likewise, κ_T are larger for THY: CAR than for type III DES [52–54], which agrees with other type V NADES [40], showing how these non-ionic fluids are less compressible than ionic type III ones. For the obtained P_i, a remarkably complex behavior is inferred, Fig. 4d. As this property is a quantification of intermolecular forces, a first inspection of Fig. 4d shows complex evolution of these interactions upon heating and compression, following a clearly non-linear trend. P_i vs temperature evolves through maxima at roughly 303 K whereas P_i vs pressure evolves through minima at roughly 40 MPa, analogous through previous results for menthol – thymol type V NADES [23] as well as for other type III and

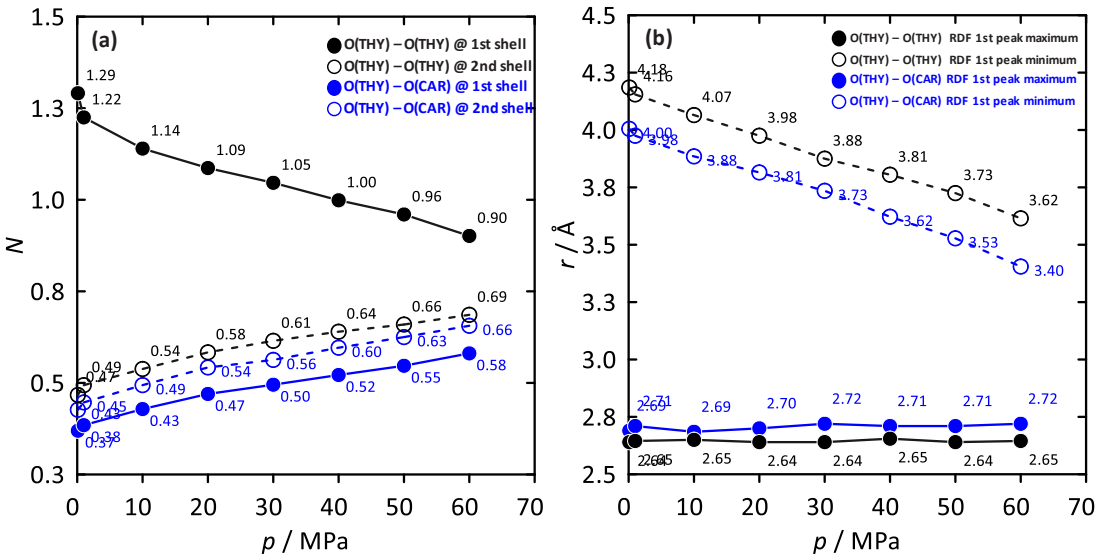

Fig. 10. Properties of Radial Distribution Functions (RDFs) for the reported atom pairs in THY: CAR (1: 1) from Molecular Dynamics simulations at 303 K and the reported pressures. (a) Integration (*N*) of RDFs 1st peak (1st solvation shell) and 2nd peak (2nd solvation shell), (b) position (*r*) of the first RDF peak indicating maxima and minima.

V DES [38] and ILs [75]. Regarding the behavior of $\left(\frac{\partial P_i}{\partial T}\right)_p$, the development of maxima shows a change in fluid structural organization, i.e. changes in intermolecular forces, from temperatures lower than 303 K, $\left(\frac{\partial P_i}{\partial T}\right)_p > 0$, and higher than this value, $\left(\frac{\partial P_i}{\partial T}\right)_p < 0$. This behavior is typical of largely hydrogen bonded fluids [76], and shows the weakening of these forces (hydrogen bonds) from a temperature (303 K for THY: CAR) upon heating under isobaric conditions. In the case of $\left(\frac{\partial P_i}{\partial p}\right)_T < 0$ for pressures lower than 40 MPa and of $\left(\frac{\partial P_i}{\partial p}\right)_T > 0$ for larger pressures, the main factor should be the increase of repulsive forces upon compression leading to a decrease in P_i, with the slope inversion for high pressure resulting from the rearrangement of fluid structuring allowing a certain improvement of intermolecular interactions even under steric repulsion. Likewise, Cohesive Energy Density (*ced*) was calculated from vaporization enthalpy (inferred from PC-SAFT, 67.1 +/- 2.1 kJ mol^{-1} in the studied temperature range) and experimental density. The inferred *ced* are similar to those of P_i, e.g. at 298.15 K and 1 MPa, *ced* = 439.1 MPa is inferred in comparison with P_i = 442.4 MPa, i.e. leading to $n = P_i / ced$ close to unity, in contrast with other DES [38]. Therefore, intermolecular forces in the considered NADES show a complex landscape, evolving for a largely hydrogen bonded at close to ambient temperatures and pressures, with a subsequent modification upon heating and compressing.

3.2. PC-SAFT modelling and machine learning predictions

The properties of the considered type V NADES where studied according to the PC-SAFT EoS, which was previously probed to be suitable for DES thermodynamic properties [38]. In a first stage, relevant properties of NADES and their components were predicted, Fig. 5. The experimental determination of the properties reported in Figs. 5a to 5c is extremely difficult and thus not available in the literature. Therefore, although it is not possible to carry out comparison among PC-SAFT predictions and experimental data for properties reported in Figs. 5a to 5c, PC—SAFT predictions may be considering a reliable initial estimation to be used for industrial application purposes, e.g. for properties such as critical points, global phase diagrams, or Vapor – Liquid equilibria. Regarding the Solid – Liquid equilibria (SLE, including eutectic composition), Fig. 5d, Li et al. [77] measured the SLE for THY: CAR NADES. Although these authors did not report the eutectic composition and temperature, as glass transitions were reported, the general features of the SLE diagram agree with those from PC-SAFT in Fig. 5d.

Regarding the predictions of critical properties from PC-SAFT, their uncertainties can not be established as it has been probed [78] that this EoS leads to inherent divergences near the critical point for uncertainties, regardless of the model parameters uncertainties.

The saturation curve in terms of density is reported in Fig. 5a, CAR is slightly less dense than THY, because of the presence of hydrogen bonding in neat THY, but critical temperatures are very large for both components and so for the THY: CAR 1: 1 NADES. Therefore, the vapor pressures and global phase diagram for THY + CAR mixtures reported in Fig. 5b, shows almost negligible evaporation at close to ambient condition, which is important for avoiding atmospheric contamination (i.e. the considered NADES is not a Volatile Organic Solvent), and this mixture is a Type I system, in terms of phase equilibria, according to the van Konynenburg classification [79]. The predicted isothermal Vapor - Liquid equilibria, Fig. 5c, show non-azeotropic behavior and small volatilities. Additionally, the SLE was predicted using PC-SAFT, Fig. 5d. The eutectic points is formed at CAR rich mixtures (roughly at THY: CAR 1: 2 mol ratio), nevertheless the studied mixture considered in this work (THY: CAR 1: 1) shows a remarkably low melting temperature (278.5 K), thus being suitable for industrial applications, and although not being the true eutectic composition, it may be considered as a Low Melting Mixture (LMM [80]) close to the eutectic point being liquid at required temperature – pressure conditions.

Moreover, PVT data was predicted using a single temperature independent binary interaction parameter (BIP), $k_{12} = -0.10$. The negative sign of this parameter indicates THY – CAR heteroassociations via hydrogen bonding. Results reported in Fig. 6 indicate the performance of the PC-SAFT EoS. Hernandez – Serrano et al. [38] applied PC-SAFT for PVT predictions of type III and type V DES, including menthol + camphor and menthol + thymol NADES, reporting differences in the −0.5–2 % range for a similar pressure – temperature range as considered in this work. Results in Fig. 6a show how PC-SAFT slightly underpredicts density at low pressures, fulfill the experimental values at intermediate pressures, and overpredicts at very high pressures, leading to deviations in the −3 to +1 % range, Fig. 6b. It has been probed that the use of temperature dependent BIPs led to better predictions of DES volumetric properties [81]. Likewise, the decrease of performance for PC-SAFT

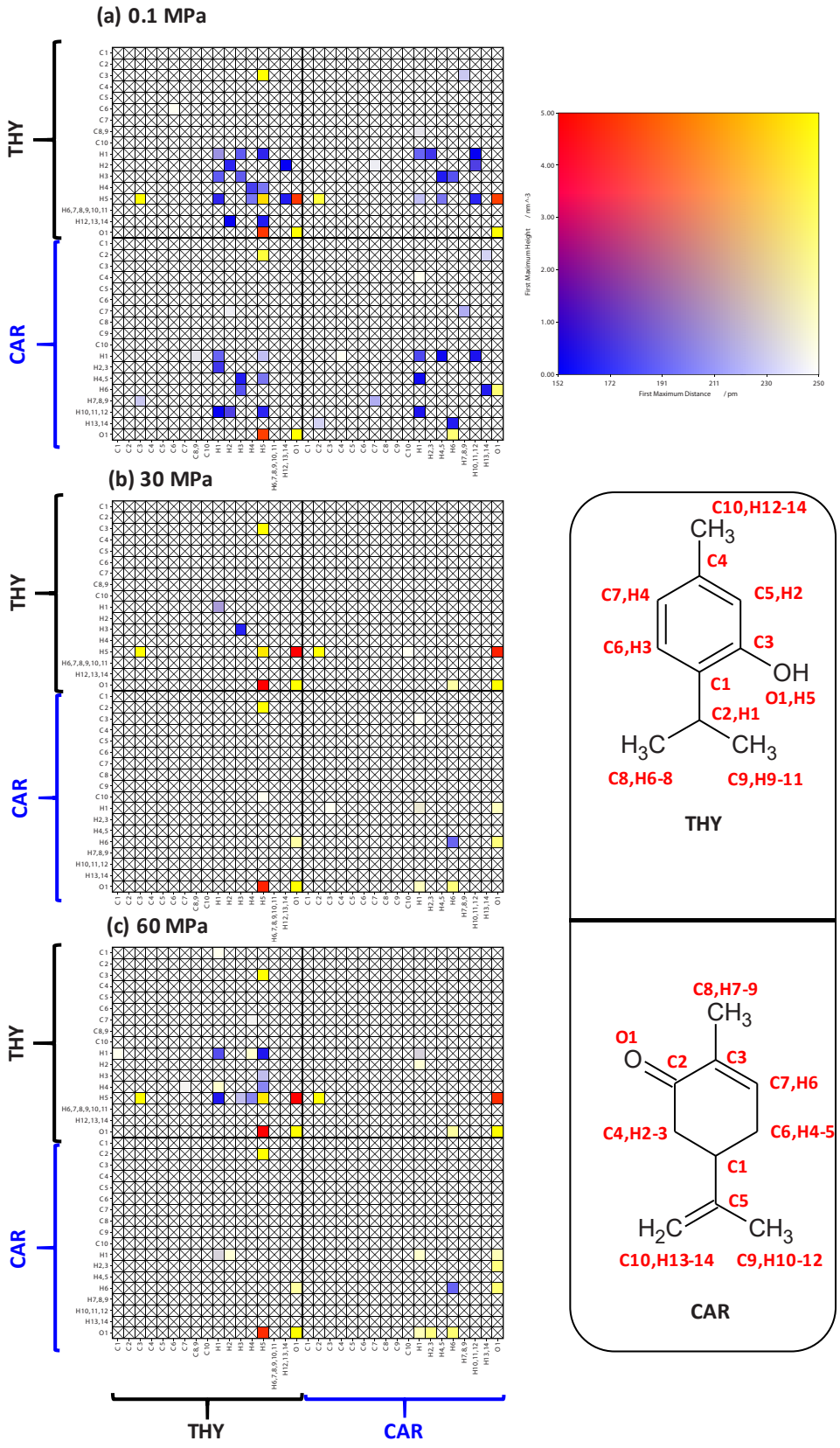

Fig. 11. Connection matrix analysis for possible hydrogen bonds for pairs in THY: CAR (1: 1) from Molecular Dynamics simulations at 303 K and the reported pressures. Rows and columns represent all possible atoms. The color of each square corresponds to the intensity and distance of the first maximum in the corresponding radial distribution functions with the color scale indicated in the panel on the top right corner.

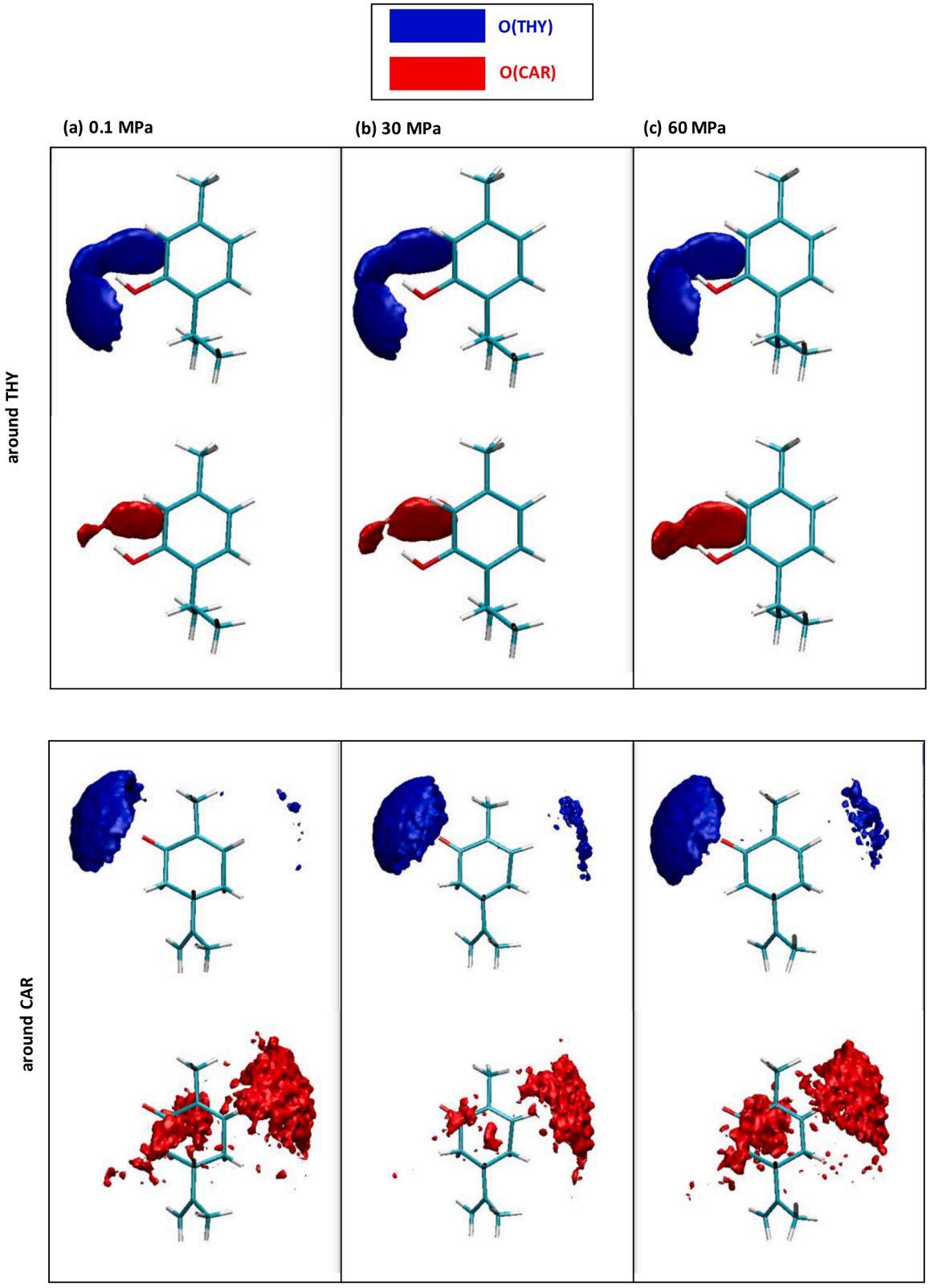

Fig. 12. Spatial Distribution Functions, SDFs, of NADES components around a central THY or CAR molecule in THY: CAR (1: 1) from Molecular Dynamics simulations at 303 K and the reported pressures.

predictions for high pressure have been also reported even including polar terms in the EoS (PCP-SAFT) [82]. Therefore, although PC-SAFT for the considered NADES may be considered as suitable, further research on the temperature and pressure dependence of BIPs is required to improve predictions, specially for high pressure – high temperature conditions.

A second approach was considered for PVT predictions based on Quantitative Structure Property Relationships (QSPR, where property

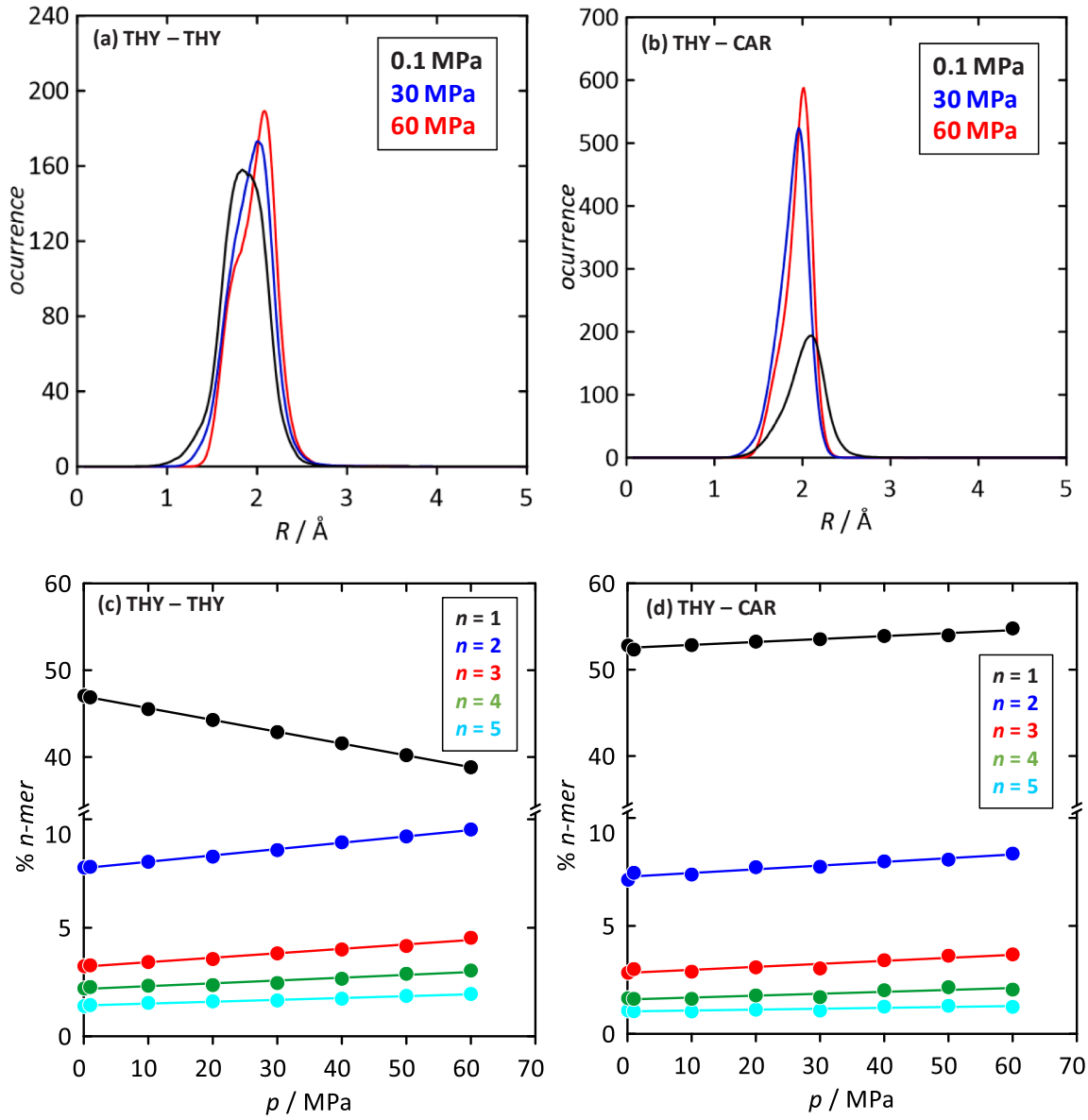

Fig. 13. Cluster analysis showing (a,b) size distribution, *R* standing for cluster radium, and (c,d) oligomer percentage distribution where *n* stands for the number of HBA – HBD pairs. All results from in THY: CAR (1: 1) from Molecular Dynamics simulations at 303 K and the reported pressures.

stands for density as a function of pressure and temperature) considering relevant molecular descriptors and ML methods. To build a suitable database of PVT data for type V DES, results obtained in this work for THY: CAR were combined with those available in the literature for menthol + thymol (1: 1) [23], thymol + 1,8-cineole (1: 1) [41], thymol + camphor (1: 1) [41], menthol + octanoic acid (1: 1) [40], menthol + decanoic acid (1: 1) [40], menthol + dodecanoic acid (2: 1) [40], leading to a collection of $N = 642$ data in the $P = 0.1$–60 MPa and $T = 293.15$–413.15 K ranges. This database was randomly divided into (25 % for training + 75 % for validation). Molecular descriptors were calculated for independent NADES components considering KrakenX method [42], Supplementary Information. The matrix of (252) molecular descriptors was filtrated via Principal Components Analysis and reduced to 10 relevant features. Different methods (Section 2.3) were considered, where GPR led to the best results, which are reported in Fig. 7. Results show excellent correlative ability of the developed model (Figs. 7a and 7b), even considering the chemical diversity of DES components and the wide density range (roughly 0.8–1.0 g cm^{-3}), with deviations in the +/- 1 10^{-4} g cm^{-3} range. Likewise, the developed model shows high predictive ability (validation set, Figs. 7c and 7d), and thus, the developed model can be used for PVT predictions using a set of 10-simple molecular descriptors, which can be inferred from structures of isolated molecular components of type V NADES.

3.3. Molecular modelling

To gain deeper insights into the nanoscopic structuring of the considered THY: CAR (1: 1) NADES, theoretical studies were considered using two different approaches. Firstly, DFT-TB studies were carried out on THY: CAR clusters containing 10 THY: CAR pairs, i.e. to mimic local ordering in the liquid phase, which were simulated considering Periodic Boundary Conditions, under different pressure and isothermal conditions, therefore inferring structural changes under compression via a DFT approach. Results in Fig. 8a show the pressure evolution of the intermolecular interaction energy, evolving through a linear relationship. These results indicate strong THY – CAR intermolecular forces (hydrogen bonding), the compression leads to a reinforcement of these interactions. The changes of intermolecular interaction with pressure, Fig. 8b, increase regularly at a rate of 0.17 kJ mol^{-1} MPa^{-1}. Experimental studies in previous section showed that upon compression steric

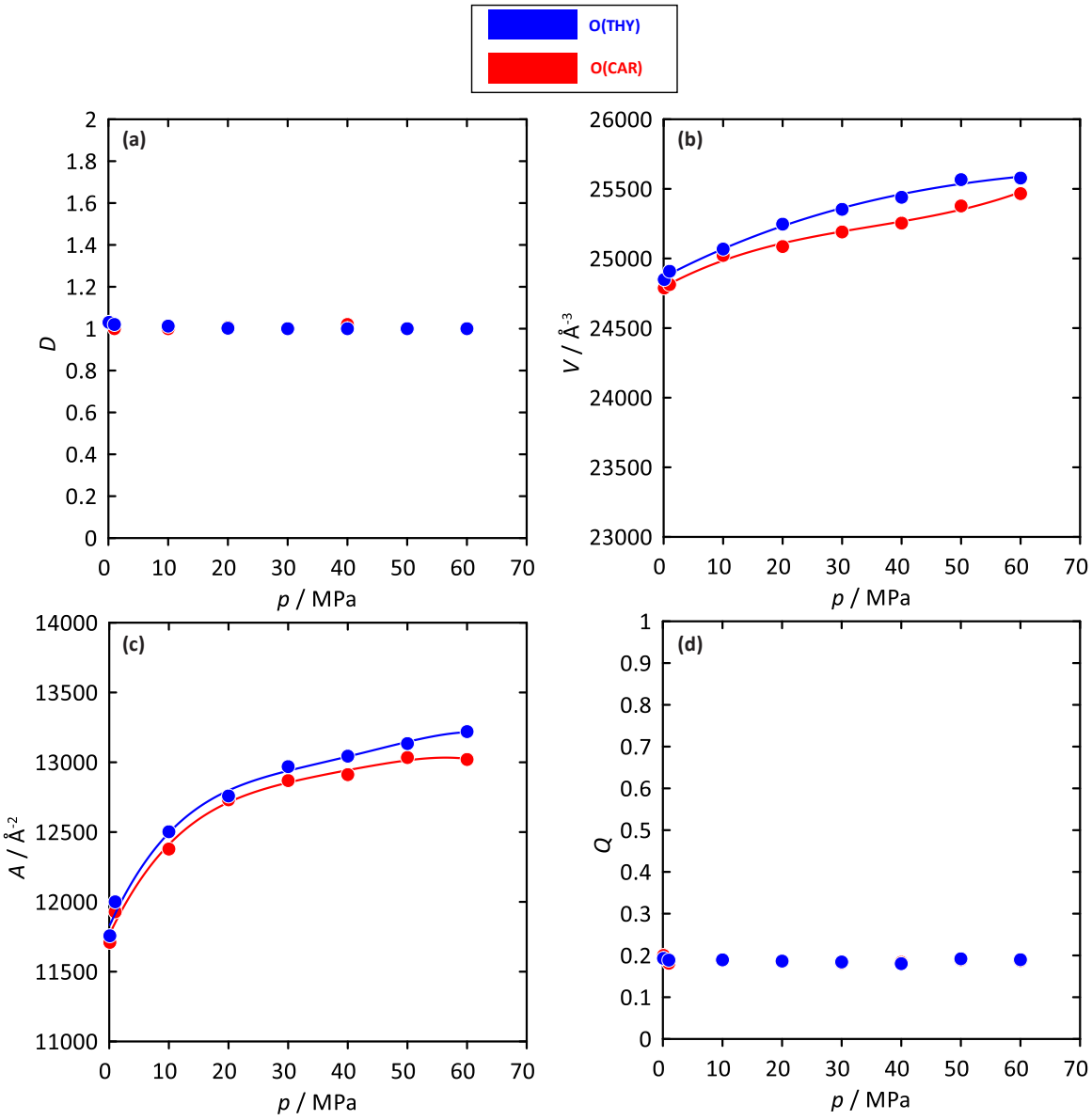

Fig. 14. Domain analysis in in THY: CAR (1: 1) from Molecular Dynamics simulations at 303 K and the reported pressures. Average values for Domain count, *D*, isoperimetric quotient, *Q*, domain volume, *V*, and domain area, *A*, are reported for each compound.

forces started to develop relevant role, this could be on the root of the moderate increase of intermolecular interaction energy reported in Fig. 8, as the fluid is compressed intermolecular distances decrease so intermolecular forces should increase but the development of steric hindrance, specially at high pressures, led to a counterbalance effect, and thus intermolecular interaction energy only increased a 9 % on going from 0.1 to 60 MPa.

Studies on NADES fluid using MD simulations allowed to infer detailed nanoscopic information on structuring, intermolecular forces (hydrogen bonding) and dynamics. Fig. 9 shows Radial Distribution Functions (RDFs) for relevant atomic sites. In THY – CAR NADES two main intermolecular features may be considered: *i*) THY – CAR hetero-associations (OH from THY as donor CO from CAR as acceptor) and *ii*) THY – THY homoassociations (with OH in THY acting both as donor and acceptor sites). RDF results in Figs. 9a and 9b confirm the development of both types of hydrogen bonds as proved by the narrow and intense RDF peaks with maxima at 2.6 – 2.7 Å. Nevertheless, the characteristics for the RDFs corresponding to both interactions are different. Whereas in both cases the first intense RDF peak corresponding to HBA – HBD hydrogen bonding is inferred, which indicates interactions beyond the formation of simple dimers, the intensity of both the first peak and the shoulder are larger for THY – THY than for THY – CAR pairs. The pressure effect on THY: CAR NADES properties does not show changes on the position of RDF peaks, i.e. both types of interactions remain upon compression, but the integration of these RDFs, solvation numbers, shows a decrease for THY – CAR and an increase for THY – THY, but in both cases a minor disruption considering the large pressure range studied. Therefore, both types of hydrogen bonds show different sensitivities to compression: i) THY – CAR increase and ii) THY – THY decrease of extension. This effect is clarified in results reported in Fig. 9 where the solvation numbers are plotted as a function of pressure for the different interactions and solvation shells, i.e. direct hydrogen bonding (1st shell around each donor / acceptor site) and further organization hydrogen bonding induced (2nd shell). 1st solvation shell decreases close to linearly for THY – THY with increasing pressure whereas the opposite effect is inferred for THY – CAR. In the case of 2nd shell an increase is inferred for both types of interactions. Likewise, the nature of the hydrogen bond does not change upon compression as the position of

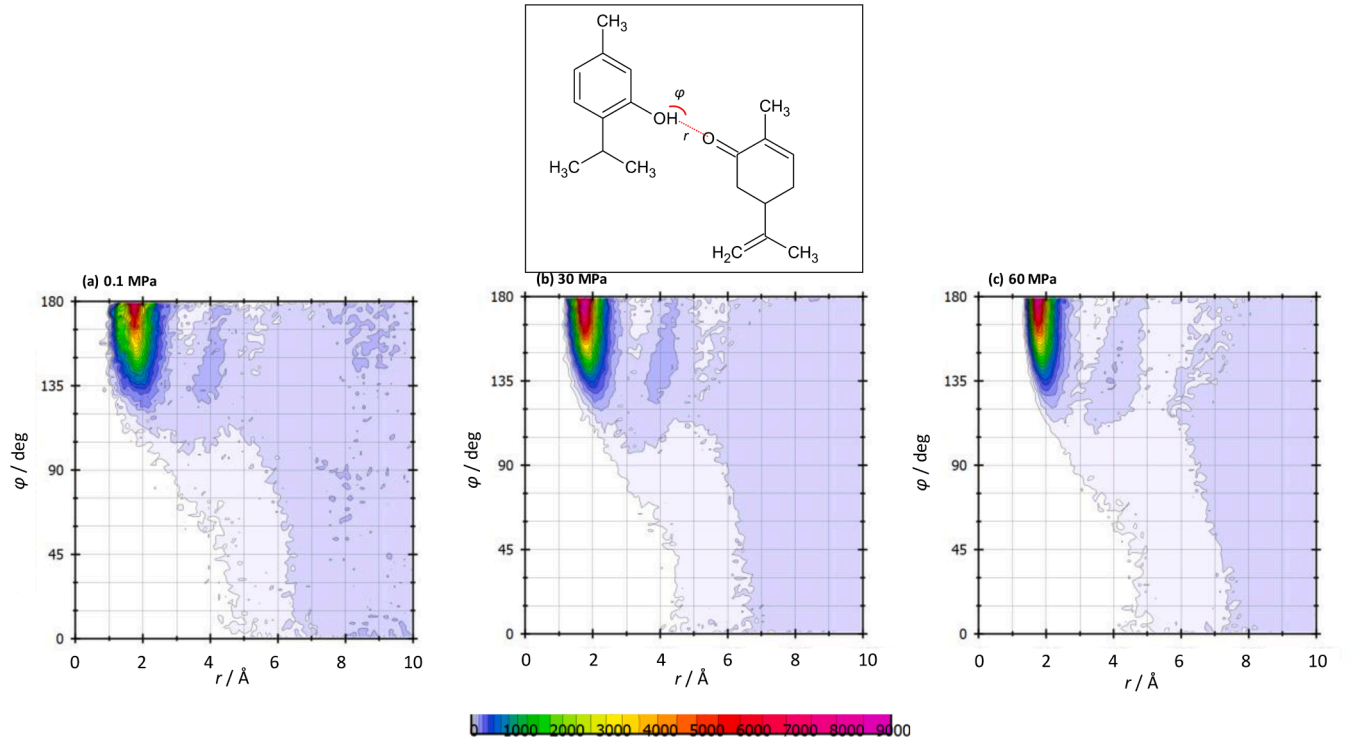

Fig. 15. Combined Distribution Functions for the reported interatomic separation and angle (corresponding to THY – CAR Hydrogen Bonding) in THY: CAR (1:1) from Molecular Dynamics simulations at 303 K and the reported pressures.

the maxima for the peak of the 1st shell (Fig. 10b) remains constant, whereas for the second shell it decreases upon compression. Therefore, the compression effect appears in the shells beyond those in direct contact through hydrogen bonding, which may lead to steric effects which would be on the root of the changes in internal pressure slopes fort high pressure inferred from experimental study.

The fingerprints of all the intermolecular interactions are obtained from Connection Matrix (*cmat*) analysis, which summarized all the RDFs in terms of peak position and intensity for all the relevant possible interacting pairs, Fig. 11. Regarding hydrogen bonding, the main interactions correspond to THY – THY and THY – CAR interactions via the OH group in THY (red spots), which remain in the whole pressure range. The main changes upon compression beyond those in hydrogen bonding stans on the van der Waals (polar) interactions. Blue spots in Fig. 11a corresponding to interaction between CH sites (both THY – THY and THY - CAR) vanishes upon compression, thus indicating weakening of polar intermolecular forces, in parallel with those from hydrogen bonding decreasing in extension. This results from the molecular reorientations upon compression as a result of the rearrangement of solvation shells (Fig. 10b for the 2nd shell), which points to smaller shells (decrease of radii, Fig. 10b) but with increasing number of molecules (Fig. 10a), i.e. denser solvation shells increasing steric hindrance and hindering van der Waals like contacts. Nevertheless, these changes are produced beyond the direct contacts leading to hydrogen bonding, as results in Fig. 12 for Spatial Distribution Functions (SDFs) indicate very minor changes in 1st solvation shell properties. Regarding the distribution around THY molecules, THY and CAR molecules occupy the same spatial region around the OH site in THY, with the main change corresponding to a CAR densification, in agreement with results in Fig. 10a. In the case of spatial distribution around CAR, a densification of THY molecules around CAR is inferred, not only around the CO site but also on the opposite site corresponding to the densification in the 2nd shell.

Hydrogen bonding and additional intermolecular interactions should lead to the formation of clusters involving both THY and CAR molecules, which properties in terms of size and a aggregation are reported in Fig. 13. For THY – THY clustering, Fig. 13a, compression shifts the cluster sizes to larger radius, i.e. decreasing THY – THY interactions, whereas for THY – CAR the opposite trend is inferred, Fig. 13b. Regarding the number of molecules present in the dimmers, Figs. 13c and 13d, the population of dimmers decreases upon compression for THY – THY ($n = 1$), whereas for THY – CAR increases, but for larger aggregates all the populations increases. These results confirm the decrease of extension for THY – THY direct hydrogen bonding (dimmers) on the contrary to THY – CAR, and for all the cases the densification resulting from compression leading to the development of larger aggregates and so for steric hindrance effects. Beyond the clusters sizes and composition, Domain analysis (Fig. 14) allows to infer the extension of aggregation along the whole fluid as well as the connection between the different clusters. Results in Fig. 14a indicate a single domain both for THY and CAR, i.e. the hydrogen bonded aggregates are fully connected leading to a supramolecular hydrogen bonded network. The densification upon compression leads to an increase of the size of the domains both in terms of volume (Fig. 14b) and surface area (Fig. 14c), with all those domains having no spherical shapes as indicated by the low isoperimetric index (Fig. 14d).

For the analysis of the properties of the developed hydrogen bonds, Combined Distribution Functions (CDFs) were calculated considering donor – acceptor distance and angle distributions, for THY – CAR interactions, Fig. 15. The results confirm (red spots) that hydrogen bonding is maintained in the whole pressure range, with the main relevant effect upon compression consisting in the narrowing of interacting sites as a result of densification. Further analysis on the orientation around the hydrogen bonding sites is reported in Fig. 16. Around THY molecules, the dipole vectors of OH groups are totally oriented around the THY acceptor site and concentrated around the H-atom, with this effect slightly weakened upon compression (red spots). CAR around THY are also totally centered and oriented around the OH-THY site. Additionally, around central CAR, the orientation and concentration of OH-THY around CO-CAR is reinforced upon compression, in agreement with results reported in Fig. 10, whereas the distribution of CAR

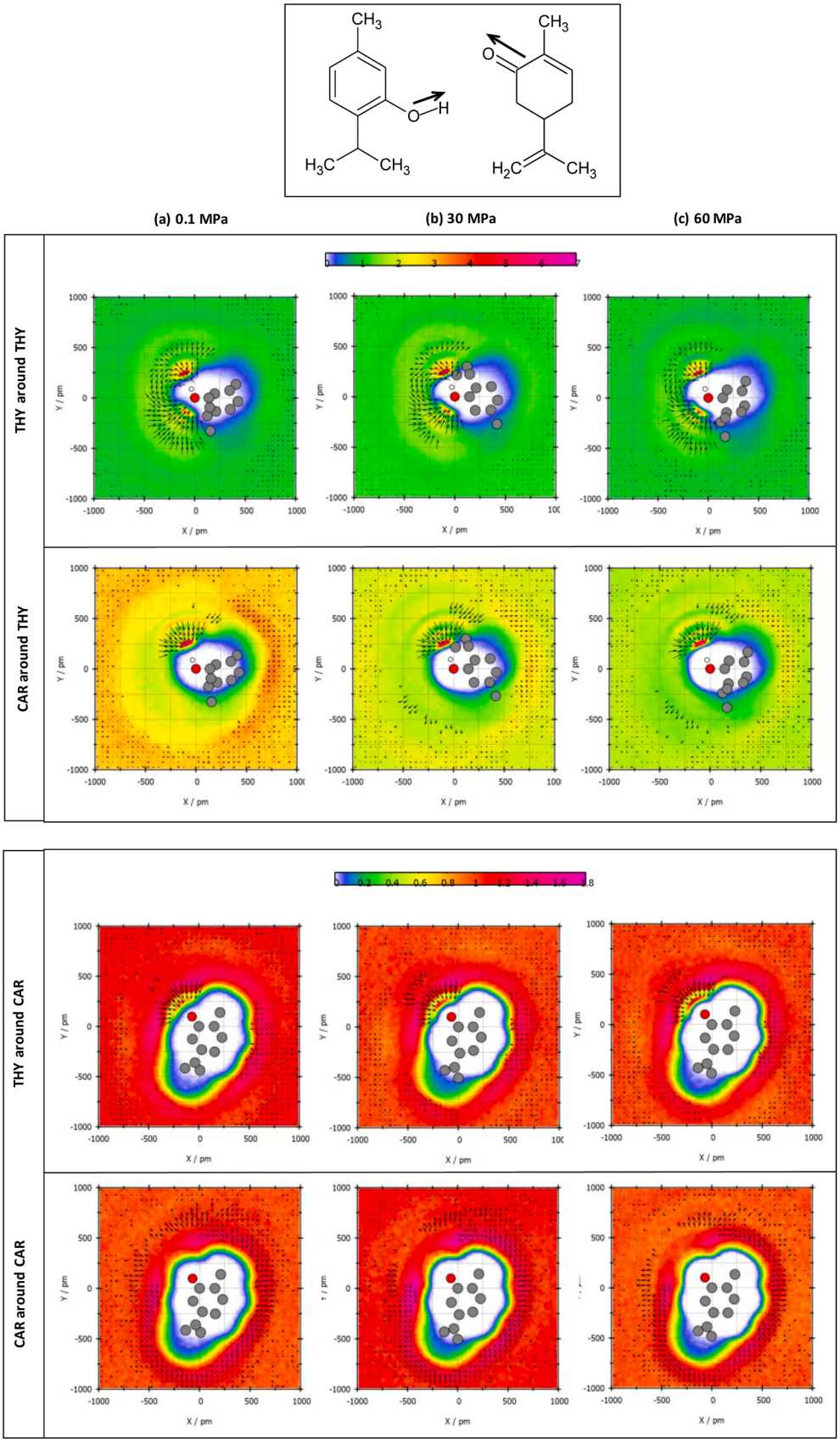

Fig. 16. Distribution of molecules around a central one in THY: CAR (1:1) from Molecular Dynamics simulations at 303 K and the reported pressures. Arrows indicate the distribution of vectors relevant for intermolecular hydrogen bonding.

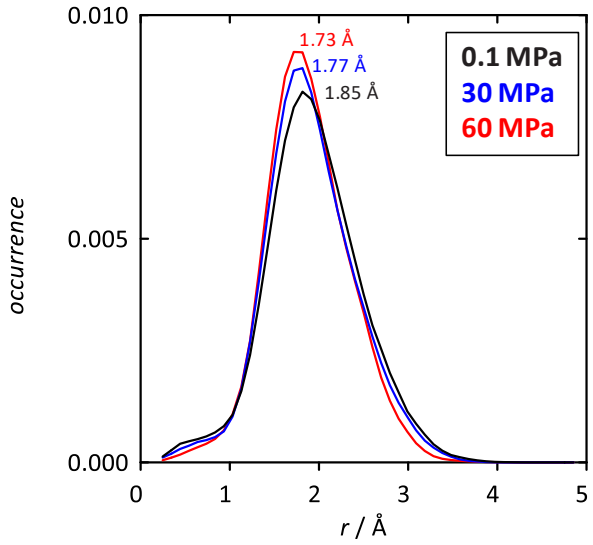

Fig. 17. Hole distribution in THY: CAR (1: 1) from Molecular Dynamics simulations at 303 K and the reported pressures.

molecules is randomly placed around central CAR excluding the CO-CAR site. Therefore, THY – THY decreasing upon compression in contrast with THY – CAR ones.

The compression of THY – CAR leads to densification, therefore to a redistribution of developed empty space inside, i.e. hole sizes. Results in Fig. 17, show the hole distribution upon compression. The results indicate that holes, having small size for any pressure, decrease in size with increasing pressure. This would result from the decrease in solvation shells reported in Fig. 10b, and also would be on the root of the increase in steric hindrance, because of the consideration that hydrogen bonds are maintained in high pressure conditions.

The dynamic properties of the fluid were analyze considering different relevant features. First, although the results have confirmed hydrogen bonding in the studied pressure range, the dynamic of hydrogen bonding was studied considering living times and also time for reforming hydrogen bonds after breaking (Fig. 18). The first relevant result stand on the more dynamic character of THY – CAR hydrogen bonds than those for THY – THY (3–4 times larger times for THY – THY ones), both for living times as well as for reforming times. The labile nature of the THY – CAR hydrogen bond is also manifested in the fast reforming process whereas for THY – THY large reforming times are required. In both cases, the living time and the reforming increases upon compression, although this effect is more remarkable for THY – THY interactions. The different dynamic of THY – THY bonds may be justified considering that molecular reorientation is required for developing new interactions, thus leading to slow reforming process but also increasing living times, which agrees with the dipolar distribution reported in Fig. 16. Beyond the dynamics of the hydrogen bonds, the molecular mobility is analyzed through the (center-of-mass) self-diffusion coefficients, *D*, obtained from the mean square displacements and the Einstein's equation, Fig. 19. The *D* results indicate slower diffusion for THY molecules than for CAR ones, in agreement with the larger degree of THY hydrogen bonding, Fig. 10, and the slower dynamics of the THY – THY interactions, Fig. 18. Both for THY and CAR, *D* decrease upon compression following a close to linear trend. Results in Fig. 13 indicated changes in the degree of (clustering) association upon compression, thus, the changes in the extension of hydrogen bonding (Fig. 10), dynamic properties of interactions (Fig. 18) and clustering changes leading to different hydrodynamic radii upon compression, would lead to the *D* reported in Fig. 19. The molecular mobility is also analyzed considering the Velocity Distribution Functions (VDFs) reported in Fig. 20 where slower rates are inferred for THY than for CAR, and slower rates upon compression confirms the mobility decrease in the studied temperature range. Therefore, the dynamics of the considered NADES is characterized by larger diffusing clusters with stronger hydrogen bonding diffusing slower upon compression, with larger effect, slower rates, for THY than for CAR molecules as a result of the nature of the differences between THY - THY and THY – CAR intermolecular hydrogen bonding.

4. Conclusions

This study provides a comprehensive investigation into the properties of a type V natural deep eutectic solvent composed of thymol and carvone in a 1:1 molar ratio. The system was studied considering a multifaceted approach combined experimental measurements, theoretical modeling, and molecular simulations to elucidate the behavior of this NADES under various pressure and temperature conditions. The main findings may be summarized as:

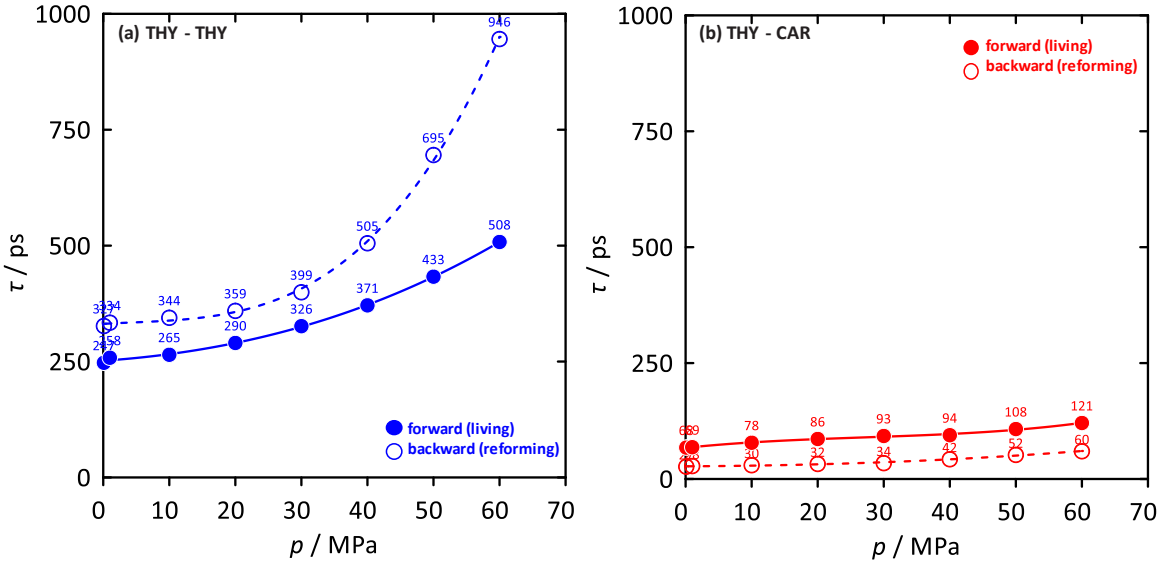

Fig. 18. Dynamics of hydrogen bonding for the reported donor – acceptor pairs showing living and reforming times, τ, in THY: CAR (1: 1) from Molecular Dynamics simulations at 303 K and the reported pressures.

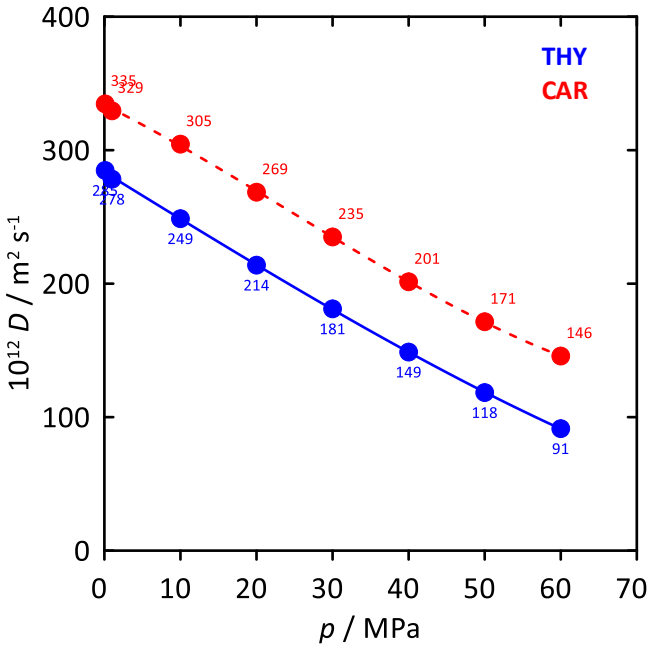

Fig. 19. Center-of-mass Self-Diffusion coefficient, *D*, for THY and CAR in THY: CAR (1: 1) from Molecular Dynamics simulations at 303 K and the reported pressures.

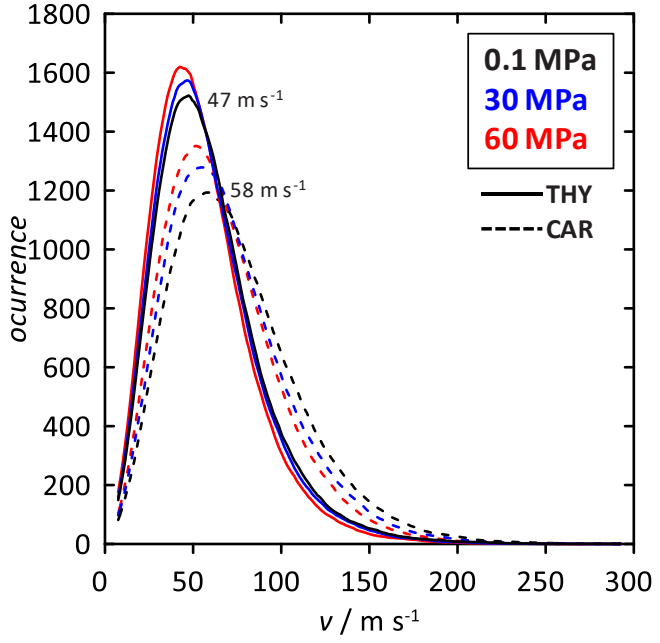

Fig. 20. Center-of-mass Velocity Distribution Function, *v*, for THY and CAR in THY: CAR (1: 1) from Molecular Dynamics simulations at 303 K and the reported pressures.

- PVT Properties**:** experimentally derived pressure-volume-temperature (PVT) data for a wide range of pressures (1–60 MPa) and temperatures (293.15–353.15 K) were measured. This data allowed us to determine crucial thermodynamic properties such as density, thermal expansion coefficient, isothermal compressibility, and cohesive energy density, which are pivotal for process design purposes involving the considered solvent.
- Hydrophobic Character**:** The NADES exhibited a hydrophobic nature, with density increasing as both pressure and temperature rose.
- Thermal Expansion**:** The thermal expansion coefficient displayed non-linear unusual behavior with pressure, decreasing at higher pressures.
- Intermolecular Forces**:** Internal pressure measurements revealed complex intermolecular forces that evolved with temperature and pressure changes.
- PC-SAFT modeling with a single temperature-independent binary interaction parameter provided satisfactory PVT predictions.
- A machine learning model based on molecular descriptors achieved excellent agreement with experimental PVT data for both the studied NADES and other type V NADES from literature.
- Molecular Insights**:** Simulations revealed the presence of both THY-THY and THY-CAR hydrogen bonding interactions. Compression led to a reinforcement of THY-CAR interactions and a weakening of THY-THY interactions.
- Dynamic Behavior**:** The NADES was characterized by larger diffusing clusters with stronger hydrogen bonding, exhibiting decreased mobility upon compression.

4.1. *Implications and future directions*

This work significantly advances our understanding of the PVT properties, intermolecular interactions, and nanoscale structure of the THY:CAR NADES. The developed machine learning model offers a promising tool for rapid and accurate PVT prediction for this class of solvents, potentially accelerating future research and development.

Our findings contribute to the broader development of NADES for various applications, particularly those requiring knowledge of their behavior under pressure and temperature variations. This could be especially valuable in industries such as pharmaceuticals, cosmetics, and green chemistry, where understanding solvent behavior under different conditions is crucial.

This study provides a solid foundation for further exploration and utilization of type V NADES, paving the way for their optimized use in various scientific and industrial applications.

CRediT authorship contribution statement

Cristina Benito: Visualization, Validation, Investigation, Formal analysis, Data curation. **Santiago Aparicio:** Writing – review & editing, Writing – original draft, Visualization, Validation, Supervision, Software, Resources, Project administration, Methodology, Investigation, Funding acquisition, Formal analysis, Data curation, Conceptualization. **Jose Trenzado:** Writing – review & editing, Writing – original draft, Visualization, Validation, Supervision, Methodology, Investigation, Formal analysis, Data curation, Conceptualization. **Ylenia Rodríguez:** Writing – review & editing, Writing – original draft, Visualization, Validation, Methodology, Investigation, Formal analysis, Data curation.

Declaration of Competing Interest

The authors declare that they have no known competing financial interests or personal relationships that could have appeared to influence the work reported in this paper

Data availability

Data will be made available on request.

Acknowledgements

This work was funded by Agencia Estatal de Investigación (Spain, Project NADES for PFAS, Ref.: PID2022-142405OB-I00) and Junta de Castilla y León (Spain, Project NADES for Nature, Ref.: BU047P23). We also acknowledge SCAYLE (Supercomputación Castilla y León, Spain)

for providing supercomputing facilities. The statements made herein are solely the responsibility of the authors.

Appendix A. Supporting information

Supplementary data associated with this article can be found in the online version at doi:10.1016/j.supflu.2024.106408.

References

[1] B.B. Hansen, S. Spittle, B. Chen, D. Poe, Y. Zhang, J.M. Klein, A. Horton, L. Asdhikari, T. Zelovich, B.W. Doherty, B. Gurkan, E.J. Maginn, A. Ragauskas, m, T.A. Dadmun, Zawodzinski, G.A. Baker, M.E. Tuckerman, R.F. Savinell, J. R. Sangoro, Deep eutectic solvents: a review of fundamentals and applications, Chem. Rev. 121 (2021) 1232–1285.

[2] F.M. Perna, P. Vitale, V. Capriati, Deep eutectic solvents and their applications as green solvents, Curr. Opin. Green Sustain. Chem. 21 (2020) 27–33.

[3] K.A. Omar, Physicochemical properties of deep eutectic solvents: a review, J. Mol. Liq. 360 (2022) 119524.

[4] A. Azzouz, M. Hayyan, Are deep eutectic solvents biodegradable? Process Saf. Environ. Prot. 176 (2023) 1021–1025.

[5] D.O. Abranches, J.A.P. Coutinho, Everything you wanted to know about deep eutectic solvents but were afraid to be told, Ann. Rev. Chem. Biomol. Eng. 14 (2023) 141–163.

[6] T. El-Achkar, H. Greige-Gerges, S. Fourmentin, Basics and properties of deep eutectic solvents: a review, Environ. Chem. Lett. 19 (2021) 3397–3408.

[7] S.S. Ijardar, V. Singh, R.L. Gardas, Revisiting the PHysicochemical Properties and Applications of Deep Eutectic Solvents, Molecules 27 (2022) 1368.

[8] A. Prabhune, R. Dey, Revisiting the physicochemical properties and applications of deep eutectic solvents, J. Mol. Liq. 379 (2023) 121676.

[9] M. Shaibuna, L.V. Theresa, K. Sreekumar, Neoteric deep eutectic solvents: history, recent developments, and catalytic applications, Soft Matter 18 (2022) 2695–2721.

[10] A.A. Abbott, Deep eutectic solvents and their application in electrochemistry, Curr. Opin. Green Sustain. Chem. 36 (2022) 100649.

[11] J. Zuo, S. Geng, Y. Kong, P. Ma, Z. Fan, Y. Zhang, A. Dong, Current progress in natural deep eutectic solvents for the extraction of active components from plants, Crit. Rev. Anal. Chem. 53 (2023) 177–198.

[12] W. Wang, D.J. Lee, Lignocellulosic biomass pretreatment by deep eutectic solvents on lignin extraction and saccharification enhancement: a review, Bioresour. Technol. 339 (2021) 125587.

[13] Y. Liu, Z. Dai, Z. Zhang, S. Zeng, F. Li, Z. Zhang, Y. Nie, L. Zhang, S. Zhang, X. Ji, Ionic liquids/deep eutectic solvents for CO_2 capture: reviewing and evaluating, Green Energy Environ. 6 (2021) 314–328.

[14] P. Makos-Chelstowska, VOCs absorption from gas streams using deep eutectic solvents – a review, J. Hazard. Mater. 448 (2023) 130957.

[15] J. Torregrosa-Crespo, X. Marset, G. Guillena, D.J. Ramon, R.M. Martinez-Espinosa, New guidelines for testing "Deep eutectic solvents" toxicity and their effects on the environment and living beings, Sci. Total Environ. 704 (2020) 135382.

[16] J. Liu, X. Li, K.H. Row, Development of deep eutectic solvents for sustainable chemistry, J. Mol. Liq. 362 (2022) 119654.

[17] J.A. Kist, H. Zhao, K.R. Mitchell-Koch, G.A. Baker, The study and application of biomolecules in deep eutectic solvents, J. Mater. Chem. B 9 (2021) 536–566.

[18] S. Kalantri, A. Vora, Eutectic solutions for healing: a comprehensive review on therapeutic deep eutectic solvents (TheDES), Drg. Devel. Ind. Pharm. (2024), https://doi.org/10.1080/03639045.2024.2345131.

[19] K.A. Omar, R. Sadeghi, Database of deep eutectic solvents and their physical properties: a review, J. Mol. Liq. 384 (2023) 121899.

[20] D.O. Abranches, J.A.P. Coutinho, Type V deep eutectic solvents: design and applications, Curr. Opin. Green Sustain. Chem. 35 (2022) 100612.

[21] Y. Liu, J.B. Friesen, J.B. McAlpine, D.C. Lankin, S.N. Chen, G.F. Pauli, Natural deep eutectic solvents: properties, applications, and perspectives, J. Nat. Prod. 81 (2018) 679–690.

[22] D.J.G.P. van Osch, C.H.J.T. Dietz, S.E.E. Warrag, M.C. Kroon, The curious case of hydrophobic deep eutectic solvents: a story on the discovery, design, and applications, ACS Sustain. Chem. Eng. 8 (2020) 10591–10612.

[23] C. Benito, R. Alcalde, M. Atilhan, S. Aparicio, High-pressure properties of type V natural deep eutectic solvents: the case of menthol: thymol, J. Mol. Liq. 376 (2023) 121398.

[24] V. Hernandez-Serrano, J. Muñoz-Embid, F. Bergua, C. Lafuente, M. Artal, pVT behaviour of hydrophilic and hydrophobic eutectic solvents, J. Mol. Liq. 382 (2023) 122019.

[25] D. Peng, M. Minceva, Predicting the density and viscosity of deep eutectic solvents at atmospheric and elevated pressures, Fluid Phase Equilib. 582 (2024) 114086.

[26] P. Demmelmayer, L. Steiner, H. Weber, M. Kienberger, Thymol-menthol-based deep eutectic solvent as a modifier in reactive liquid–liquid extraction of carboxylic acids from pretreated sweet sorghum silage press juice, Sep. Purif. Sci. Technol. 310 (2023) 123060.

[27] N.H.C.S. Silva, E.S. Morais, C.S.R. Freire, M.G. Freire, A.J.D. Silvestre, Extraction of high value triterpenic acids from Eucalyptus globulus biomass using hydrophobic deep eutectic solvents, Molecules 25 (2020) 210.

[28] O.G. Sas, L. Villar, A. Dominguez, B. Gonzalez, E.A. Macedo, Environ. Technol. Innov. 25 (2022) 102170.

[29] A.R. Harifi-Mood, M. Sarafrazi, CO2 solubility in terpenoid-based hydrophobic deep eutectic solvents: an experimental and theoretical study, J. Environ. Chem. Eng. 11 (2023) 109177.

[30] A. Mostafa, H. Shaaban, A.M. Alqarni, M. Alghamadi, S. Alsultan, J.S. Al-Saeed, S. Alsaba, A. AlMaslem, Y. Alshehry, R. Ahmad, Vortex-assisted dispersive liquid–liquid microextraction using thymol based natural deep eutectic solvent for trace analysis of sulfonamides in water samples: assessment of the greenness profile using AGREE metric, GAPI and analytical eco-scale, Microchem. J. 183 (2022) 107976.

[31] V. Vanoli, J. Pietrowska, G. de, Araujo-Lima, M.E. di Pietro, F.B. Vangosa, A. Mele, F. Castiglione, Supramolecular hydrophobic eutectogels based on menthol-thymol as thermo- and pH-responsive drug delivery systems, ACS Appl. Eng. Mater. 2 (2024) 388–396.

[32] P.M. Chelstowska, E. Slupek, A. Kramarz, J. Gebicki, New carvone-based deep eutectic solvents for siloxanes capture from biogas, Int. J. Mol. Sci. 22 (2021) 9551.

[33] Z. Li, Y. Ma, F. Hollman, Y. Wang, Study on green extraction of limonene from orange peel and cascade catalysis to produce carvol and carvone in deep eutectic solvents, Flavour Frag. J. 37 (2022) 254–261.

[34] A. Maletta, A. Gutierrez, P.J. Tan, J. Springstead, S. Aparicio, M. Atilhan, Separation of phenolic compounds from water by using monoterpenoid and fatty acid based hydrophobic deep eutectic solvents, J. Mol. Liq. 381 (2023) 121806.

[35] A. Escobar, M. Perez, G. Romanelli, G. Blustein, Thymol bioactivity: a review focusing on practical applications, Arab. J. Chem. 13 (2020) 9243–9269.

[36] C.C.R. de Carvalho, M.M.R. da Fonseca, Carvone: why and how should one bother to produce this terpene, Food Chem. 95 (2006) 413–422.

[37] J.A. Becerra, J.M. González, A.L. Villa, Comparison by life-cycle assessment of alternative processes for carvone and verbenone production, Molecules 27 (2022) 5479.

[38] S. Rozas, C. Benito, R. Alcalde, M. Atilhan, S. Aparicio, Insights on the water effect on deep eutectic solvents properties and structuring: The archetypical case of choline chloride + ethylene glycol, J. Mol. Liq. 344 (2021) 117717.

[39] S. Aparicio, B. García, R. Alcalde, M.J. Dávila, J.M. Leal, PVTx measuremnts of the N-methylpyrrolidone / methanol mixed solvent: cubic and SAFT EOS analyses, J. Phys. Chem. B 110 (2006) 6933–6942.

[40] S. Aparicio, R. Alcalde, B. García, J.M. Leal, High-Pressure study of the methylsulfate and tosylate imidazolium Ionic Liquids, J. Phys. Chem. B 113 (2009) 5593–5606.

[41] R.B. Leron, D.S. Hill-Wong, M.H. Li, Densities of a deep eutectic solvent based on choline chloride and glycerol and its aqueous mixtures at elevated pressures, Fluid Phase Equilib. 335 (2012) 32–38.

[42] R.B. Leron, M.H. Li, High-pressure volumetric properties of choline chloride–ethylene glycol based deep eutectic solvent and its mixtures with water, Thermochim. Acta 546 (2012) 54–60.

[43] E.A. Crespo, J.M.L. Costa, A.M. Palma, B. Soares, M.C. Martin, J.J. Segovia, P. J. Carvalho, J.A.P. Coutinho, Thermodynamic characterization of deep eutectic solvents at high pressures, Fluid Phase Equilib. 500 (2019) 112249.

[44] O.G. Sas, G.R. Ivanis, M.L. Kijevcanin, B. Gonzalez, A. Dominguez, I.R. Radovic, High pressure densities and derived thermodynamic properties of deep eutectic solvents with menthol and saturated fatty acids, J. Chem. Thermodyn. 162 (2021) 106578.

[45] W. Wagner, A. Pruss, The IAPWS formulation 1995 for the thermodynamic properties of ordinary water substance for general and scientific use, J. Chem. Phys. Ref. Data 31 (2002) 387–535.

[46] R. Span, W. Wagner, Equations of state for technical applications. I. Simultaneously optimized functional forms for nonpolar and polar fluids, Int. J. Thermophys. 24 (2003) 41–109.

[47] E.C. Ihmels, Jr Gmehling, Densities of toluene, carbon dioxide, carbonyl sulfide, and hydrogen sulfide over a wide temperature and pressure range in the sub- and supercritical state, Ind. Eng. Chem. Res. 40 (2001) 4470–4477.

[48] M.J. Davila, R. Alcalde, M. Atilhan, S. Aparicio, $P\rho T$ measurements and derived properties of liquid 1-alkanols, J. Chem. Thermodyn. 47 (2012) 241–259.

[49] V.N. Kartsev, S.N. Shtykov, K.E. Pakin, D.V. Batov, Intermolecular forces and the internal pressure of liquids, J. Struct. Chem. 53 (2012) 1087–1093.

[50] V. Hernandez-Serrano, J. Muñoz-Embid, F. Bergua, C. Lafuente, M. Artal, pVT behaviour of hydrophilic and hydrophobic eutectic solvents, J. Sol. Chem. 382 (2023) 122019.

[51] F. Tumakaka, J. Gross, G. Sdowski, Thermodynamic modeling of complex systems using PC-SAFT, Fluid Phase Equilib. 228-229 (2005) 89–98.

[52] O.G. Sas, G.R. Ivanis, M.L. Kijevcanin, B. Gonzalez, A. Dominguez, I.R. Radovic, High pressure densities and derived thermodynamic properties of deep eutectic solvents with menthol and saturated fatty acids, J. Chem. Thermodyn. 162 (2021) 106578.

[53] Unpublished Results.

[54] V. Venkatraman, B.K.B.K. Alsberg, KRAKENX: software for the generation of alignment-independent 3D descriptors, J. Mol. Model. 22 (2016) 1–8.

[55] I. Sushko, S. Novotarskyi, R. Körner, A.K. Pandey, M. Rupp, W. Teetz, S. Brandmaier, A. Abdelaziz, V.V. Prokopenko, V.Y. Tanchuk, R. Todeschini, A. Varnek, G. Marcou, P. Ertl, V. Potemkin, M. Grishina, J. Gasteiger, S.C. Baskin, V.A. Palyulin, E.V. Radchenko, W.J. Welsh, V. Kholodovych, D. Chekmarev, A. Cherkasov, J. Aires-de-Sousa, Q.Y. Zhang, A. Bender, F. Nigsch, L. Patiny, A. Williams, V. Tkachenko, I.V. Tetko, Online chemical modeling environment (OCHEM): web platform for data storage, model development and publishing of chemical information, J. Comput. -Aided Mol. Des. 25 (2011) 533–554.

[56] B. Hourahine, B. Aradi, V. Blum,F. Bonafé, A. Buccheri, C. Camacho, C. Cevallos, M.Y. Deshaye, T. Dumitrică, A. Dominguez, S. Ehlert, M. Elstner, T. van der Heide, J. Hermann, S. Irle, J.J. Kranz, C. Köhler, T. Kowalczyk, T. Kubař, I.S. Lee,

V. Lutsker, R.J. Maurer, S.K. Min, I. Mitchell, C. Negre, T.A. Niehaus, A.M. N. Niklasson, A.J. Page, A. Pecchia, G. Penazzi, M.P. Persson, J. Řezáč, C. G. Sánchez, M. Sternberg, M. Stöhr, F. Stuckenberg, A. Tkatchenko, V. W.-z. Yu, T. Frauenheim, , DFTB+, a software package for efficient approximate density functional theory based atomistic simulations, J. Chem. Phys. 152 (2020) 124101.
[57] M. Gaus, A. Goez, M. Elstner, Parametrization and benchmark of DFTB3 for organic molecules, J. Chem. Theory Comput. 9 (2013) 338–354.
[58] M. Kubillus, T. Kubař, M. Gaus, J. Řezáč, M. Elstner, Parameterization of the DFTB3 method for Br, Ca, Cl, F, I, K, and Na in organic and biological systems, J. Chem. Theory Comput. 11 (2015) 332–342.
[59] BIOVIA, Dassault Systèmes, BIOVIA Amorphous Cell, Release 2022 (22.1.0.3462), Dassault Systèmes, San Diego, 2022.
[60] BIOVIA, Dassault Systèmes, BIOVIA Forcite, Release 2022 (22.1.0.3462), Dassault Systèmes, San Diego, 2022.
[61] R.L.C. Akkermans, N.A. Spenley, S.H. Robertson, COMPASS III: automated fitting workflows and extension to ionic liquids, Mol. Simul. 47 (2021) 540–551.
[62] W.G. Hoover, Canonical dynamics: equilibrium phase-space distributions, Phys. Rev. A 31 (1985) 1695.
[63] M. Parrinello, A. Rahman, Polymorphic transitions in single crystals: a new molecular dynamics method, J. Appl. Phys. 52 (1981) 7182–7190.
[64] U.L. Essmann, M.L. Perera, T. Berkowitz, H. Darden, H. Lee, L.G. Pedersen, A smooth particle mesh Ewald method, J. Chem. Phys. 103 (1995) 8577–8593.
[65] M. Waldman, A.T. Hagler, New combining rules for rare-gas Van der-Waals parameters, J. Comput. Chem. 14 (1993) 1077–1084.
[66] W. Humphrey, A. Dalke, K. Schulten, VMD - visual molecular dynamics, J. Mol. Graph. 14 (1996) 33–38.
[67] M. Brehm, B. KirchneR, TRAVIS - A free analyzer and visualizer for Monte Carlo and molecular dynamics trajectories, J. Chem. Inf. Model. 51 (2011) 2007–2023.
[68] M. Marchel, M.P. Rayaroth, C. Wang, L. Kong, J.A. Khan, G. Boczkaj, Hydrophobic (deep) eutectic solvents (HDESs) as extractants for removal of pollutants from water and wastewater – A review, Chem. Eng. J. 475 (2023) 144971.
[69] A.K. Dwamena, Recent advances in hydrophobic deep eutectic solvents for extraction, Separations 6 (2019) 9.
[70] S. Panbachi, J. Baranek, M. Kuentz, Hydrophobic deep eutectic solvent (HDES) as oil phase in lipid-based drug formulations, Int. J. Pharm. 661 (2024) 124418.
[71] C. Benito, R. Alcalde, M. Atilhan, S. Aparicio, High - Pressure properties of type V natural deep eutectic solvents: the case of menthol: thymol, J. Mol. Liq. 376 (2023) 121398.
[72] R.B. Leron, M.H. Li, High-pressure density measurements for choline chloride: urea deep eutectic solvent and its aqueous mixtures at T = (298.15 to 323.15) K and up to 50 MPa, J. Chem. Thermodyn. 54 (2012) 293–301.
[73] M. Tariq, A.P. Serro, J.L. Mata, B. Saramago, J.M.S.S. Esperança, J.N.C. Lopes, High-temperature surface tension and density measurements of 1-alkyl-3-methylimidazolium bistriflamide ionic liquids, Fluid Phase Equilib. 294 (2010) 131–138.
[74] J.M.S.S. Esperanca, M. Tariq, A.B. Pereiro, J.M.M. Araujo, K.R. Seddon, L.P. N. Rebelo, Anomalous and not-so-common behavior in common ionic liquids and ionic liquid-containing Systems, Front. Chem. 7 (2019), https://doi.org/10.3389/fchem.2019.00450.
[75] J. Klomfar, M. Souckova, J. Patek, Low Temperature Densities from (218 to 364) K and up to 50 MPa in Pressure and Surface Tension for Trihexyl(tetradecyl) phosphonium Bis(trifluoromethylsulfonyl)imide and Dicyanamide and 1-Hexyl-3-methylimidazolium Hexafluorophosphate, J. Chem. Eng. Data 59 (2014) 2263–2274.
[76] Y. Marcus, Internal pressure of liquids and solutions, Chem. Rev. 113 (2013) 6536–6551.
[77] K. Li, J.H. Nam, S. Kang, J. Lee, Carvone and its eutectic mixtures as novel, biodegradable, and tunable solvents to extract hydrophobic compounds in substitution for volatile toxic solvents, Food Chem. 374 (2022) 131630.
[78] P.J. Walker, S. Mueller, I. Smimova, , Confidence-interval and uncertainty-propagation analysis of SAFT-type equations of state, J. Chem. Eng. Data 69 (2023) 495–508.
[79] J.S. Rowlinson, F.L. Swinton, Liquids and Liquid Mixtures, Butterworth-Heinemann, 1982.
[80] Y. Chen, Z. Yu, Low-melting mixture solvents: extension of deep eutectic solvents and ionic liquids for broadening green solvents and green chemistry, Green Chem. Eng. (2023), https://doi.org/10.1016/j.gce.2023.11.001.
[81] E. Cea-Klapp, I. Polishuk, R.I. Canales, H. Quinteros-Lama, J.M. Garrido, Estimation of thermodynamic properties and phase equilibria in systems of deep eutectic solvents by PC-SAFT EoS, Ind. Eng. Chem. Res. 59 (2020) 22292–22300.
[82] D. Peng, M. Minceva, Predicting the density and viscosity of deep eutectic solvents at atmospheric and elevated pressures, Fluid Phase Equilib. 582 (2024) 114086.

5.2.2. Publicación V

Título:	**Harnessing nature's building blocks: Deep Eutectic Solvents derived from monoterpenoids and fatty acids**				
Autores:	José L. Trenzado [a], Ylenia Rodríguez [a], Alberto Gutiérrez [b], Alberto Cincotti [c], Santiago Aparicio [b]				
Afiliación:	[a]) Departamento de Física, Universidad de Las Palmas de Gran Canaria, 35017 Las Palmas G.C., Spain [b]) Department of Chemistry, University of Burgos, 09001 Burgos, Spain				
Revista:	Journal of Chemical Physics				
Factor impacto (IF):	6.633	**Cuartil (JRC):**	Q1	**Citas:**	-
Editor:	Elsevier	**Fecha de publicación:**	*En revisión*		

Harnessing Nature's Building Blocks: Deep Eutectic Solvents Derived from Monoterpenoids and Fatty Acids

Ylenia F. Rodríguez,[a] Santiago Aparicio[b*] Jose L. Trenzado[a*]

[a] Department of Physics, University of Las Palmas de Gran Canaria, 35017 Las Palmas G.C., Spain

[b] Department of Chemistry, University of Burgos, 09001 Burgos, Spain

[*]Corresponding authors: jose.trenzado@ulpgc.es (J.L.T) and sapar@ubu.es (S. A.)

Abstract: This study investigates hydrophobic Natural Deep Eutectic Solvents based on monoterpenoids and saturated fatty acids through a comprehensive experimental and molecular modeling approach. Novel eutectic mixtures were formulated using hydrogen bond acceptors including menthol, thymol, 1,8-cineole, carvone, and geraniol, combined with hydrogen bond donors comprising decanoic acid, tetradecanoic acid, and octadecanoic acid. Experimentally, crucial thermophysical properties such as density and viscosity were quantified across various molar ratios and temperatures. Complementary theoretical investigations employed COSMOtherm, Density Functional Theory – Tight Binding and classical Molecular Dynamics simulations to elucidate nanoscopic properties and structural organization within the solvents. Molecular modeling techniques facilitated a detailed nanoscopic characterization of the fluid systems, with particular emphasis on intermolecular interactions, specifically hydrogen bonding networks. The integration of experimental data and computational results enabled the establishment of robust structure-property relationships, contributing to the development of an effective solvent design strategy within the framework of sustainable chemistry. This multifaceted approach provides valuable insights into the fundamental characteristics and behavior of monoterpenoid-based hydrophobic solvents, potentially advancing their application in various fields of green chemistry and sustainable technologies.

Keywords: Natural Deep Eutectic Solvents; fatty acids; monoterpenoids; thermophysics; molecular simulation.

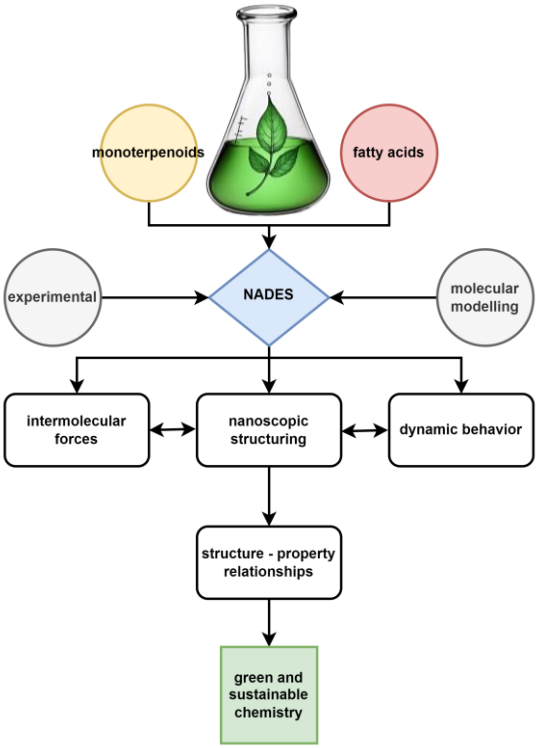

Graphical Abstract

1. Introduction

Over the past three decades, ionic liquids (ILs) have gained considerable attention from the scientific community. Ionic liquids, molten salts which remain liquid at room temperature, offer an enormous potential due to their customizable properties, which can be tuned accordingly their application. They can be used in very diverse areas and perform very different purposes, replacing traditional organic solvents that present inherent toxicity and high volatility. One of the fundamental goals of green chemistry is to identify alternative solvents that can replace environmentally harmful solvents, while still maintaining their properties and efficiency. Nevertheless, the environmental and safety implications of ILs remain a topic of intense debate, mainly due to their poor biodegradability, biocompatibility, and sustainability [1]. To overcome the drawbacks of ILs regarding greenness and sustainability, Deep Eutectic Solvents (DESs) have emerged as a promising new generation of alternative solvents.

Abbott introduced the term "Deep Eutectic Solvents" for the first time in 2003 [2], to refer to a new generation of sustainable solvents. DESs are formed as mixtures of compounds, typically defined by their hydrogen bonding interactions, exhibiting significantly lower melting points than their individual components, a phenomenon known as eutectic depression. Although eutectic mixtures are produced for specific molar ratios, the term DES is largely used in the literature even for mixtures not being strictly the eutectic composition but with remarkably lower melting temperature than those of the components. Chen et al. [3] recently proposed to use the term Low – Melting Mixture Solvents (LMMS) to define all these mixture, leading to a wider definition of DES concept.

From the thermodynamic viewpoint, DESs are commonly defined as binary or ternary mixtures of compounds that can associate mainly via hydrogen bonds [4], leading to melting point depression. However, it is important to note that not all eutectic mixtures can be considered a priori as DESs, with this term specifically reserved for those mixtures with a eutectic point temperature far below that of an ideal liquid mixture [5]. This melting temperature depression is attributed to the formation of a hydrogen bonding between a Hydrogen Bond Donor (HBD) and a Hydrogen Bond Acceptor (HBA) at a well-defined stoichiometric proportion, which would be the molecular basis for the DES formation and the deviations from the thermodynamic ideality in the liquid mixtures.

DESs have been considered in a wide range of applications, one of the initial areas of interest as a class of solvents was for metallurgic processes, such as extraction/recycling of metals in solution, refining, and electroplating/electrodeposition [6]. Owing to their eco-friendly properties, studies have shifted towards demonstrating their effectiveness in removing various pollutants from wastewater [7], removing nitrogen compounds from fuels, or exploring their potential in the biomass processing area, particularly in the pre-treatment of lignocellulose and conversion of sugars [8, 9]. Moreover, DESs has been proposed to be used in different fields such extraction operations [10], biocatalysis processes [11] or pharmaceutical industry [12].

DESs have several advantages over traditional Volatile Organic Solvents, being the first ones regarding their easy preparation, nonreactive character and versatility, as a result of the large number of HBA – HBD combinations leading to DES formation [13]. Considering the types of HBA / HBD used for DES preparation, they are usually classified into five categories, labelled from type I to type V [14], with those belonging to type III (formed the combination of salts and organic compounds) and type V (mixtures of molecular compounds) leading to the larger attention [15].

An additional classification on DESs is based on the origin (renewable / non-renewable) or the HBA / HBD compounds leading to DES formation. In this case, DESs based on compounds with totally natural origin (such as terpenes, organic acids, sugars or amino acids) have been proposed, leading to the so called Natural DESs (NADES) [16,17], which are the most suitable option considering safety, environmental impact and sustainability. Additionally, considering the large effect that water content has on DES / NADES properties and nanoscopic structuring [18,19], as well as the need of developing DES / NADES under dry conditions for certain applications [20], hydrophobic DES / NADES have been developed [21]. Therefore, Type V Hydrophobic NADES (HNADES) combines most of the relevant features, which have considered for different applications [22,23, 24, 25], including largely relevant ones such as water treatment [26] of for drug delivery purposes and therapeutic applications [27, 28]. In particular, HNADES combining monoterpenoid and long-chain fatty acids has attracted the interest for several applications [15, 29].

Therefore, the growing demand for sustainable and environmentally benign solvents has spurred significant interest in NADES as alternatives to Volatile Organic Compounds (VOCs).

However, despite considerable progress in NADES research, a knowledge gap remains in the systematic exploration of hydrophobic NADES, particularly those derived from combinations of monoterpenoids and saturated fatty acids, the synergistic potential of combining these two classes of natural compounds as hydrogen bond donor and acceptor systems in hydrophobic NADES needs deeper understanding of their nanoscopic properties and their relationship with macroscopic behavior, which is of great relevance given the abundance and diverse functionalities of both monoterpenoids and fatty acids in nature. Monoterpenoids, readily available from essential oils, offer a range of cyclic structures and functional groups, while fatty acids provide varying aliphatic chain lengths, influencing the overall hydrophobicity and other key properties of the resulting NADES. This knowledge gap hinders the rational design of hydrophobic NADES tailored for specific applications. A deeper understanding of the structure-property relationships in these novel solvent systems is crucial for unlocking their potential in areas like extraction, catalysis, and materials processing. Specifically, how the choice of monoterpenoid and fatty acid, their molar ratios, and temperature influence the thermophysical properties (e.g., viscosity, density) and microscopic interactions within these NADES remains poorly understood. Furthermore, a comprehensive investigation integrating both experimental characterization and advanced computational modeling is lacking. Such an integrated approach is essential to elucidate the underlying molecular mechanisms governing the behavior of these complex mixtures and to guide the development of optimized hydrophobic NADES for sustainable applications.

Therefore, in this work, HNADES based on the suitable combination of monoterpenoids and (saturated) fatty acids were developed. Five monoterpenoids, acting as HBA, and three saturated fatty acids, acting as HBD, were considered, exploring the possible HNADES for all HBA – HBD combinations in several molar ratios. The monoterpenoids were selected considering different molecular functionalities (Figure 1): menthol (MEN), thymol (THY), 1,8-cineole (CIN), carvone (CAR) and geraniol (GER). Saturated fatty acids were studied as a function of alkyl chain length: decanoic acid (C10AC), tetradecanoic acid (C14AC) and octaecanoic acid (C18AC). In this way, the effect of the different chemical functionalities of the monoterpenoid on the HBA – HBD hydrogen bonding as well as the hydrophobic nature of the formed HNADES as a function of the fatty acid

chain length was explored and their effects on the physicochemical properties and nanoscopic arrangements were studied.

The HNADES explored in this study, composed of monoterpenoids and saturated fatty acids, may hold significant potential across diverse applications. Their tailored hydrophobicity and biocompatibility make them attractive candidates for extraction processes**,** particularly for isolating lipophilic compounds from natural sources like plant material or biological matrices. They could also serve as sustainable solvents in biocatalysis, facilitating enzymatic reactions involving hydrophobic substrates while minimizing environmental impact. Furthermore, their tunable properties open doors for applications in pharmaceutical formulations, where they might enhance the solubility and bioavailability of hydrophobic drugs. In materials science, these NADES could be utilized as green solvents in the synthesis or processing of polymers and other materials. Finally, their unique solvation properties could be exploited in analytical chemistry, potentially improving the extraction and separation of hydrophobic analytes. The bio-based nature and biodegradability of these NADES align with the principles of green chemistry, offering a sustainable alternative to conventional organic solvents in various industrial sectors.

The study was carried out combining a experimental approach on the main physicochemical properties of the developed HNADES with a multiscale molecular modelling analysis, thus allowing to infer structure–property relationships, to realize detailed macroscopic physicochemical characterization and extensively characterize their properties at the microscale, Figure 1b. The experimental study was centred in the determination of density and dynamic viscosity, which are highly relevant for both process design and understanding the nanoscopic properties of the solvents. First, from a process design perspective, density and viscosity are fundamental thermophysical properties that influence the flow behavior, mixing, and transport properties of solvents, all of which are crucial parameters for scale-up and optimization in industrial applications. Specifically, viscosity dictates the ease of solvent handling and pumping in various processes, relevant in heat and mass transfer operations, while density impacts phase behavior and solvent dispersion characteristics in mixtures. These properties are therefore essential for designing efficient, cost-effective processes in green chemistry and sustainable technologies. Second, density and viscosity are directly linked to the nanoscopic structure and

intermolecular interactions within the solvent system. The molecular arrangement and the extent of hydrogen bonding between the hydrogen bond acceptors and donors influence both the packing of molecules (which affects density) and the resistance to flow (which affects viscosity). By examining these macroscopic properties, insights can be gained into the underlying molecular organization and the strength and nature of intermolecular forces, particularly hydrogen bonding networks. Thus, density and viscosity serve as important experimental probes to infer the molecular-level behavior of the solvents, helping to establish a clearer connection between their thermophysical characteristics and the nanoscopic structure of the solvent systems.

Theoretical analysis was performed by employing: *i*) COSMOtherm approach (focusing on thermodynamic properties), *ii*) COSMOperm approach (focusing on biological properties via the interaction of the developed HNADES with model plasma cell membranes), *iii*) Density Functional Theory (in the Tight Binding approach, DFT-TB; focusing on short-range interactions, mainly hydrogen bonding), and *iv*) Classical Molecular Dynamics (MD) simulation methods (to analyze the properties in the liquid phase at the nanoscopic level and its relationship with macroscopic behavior). The reported results allows a multiscale characterization of the developed HNADES, with particular attention to the pivotal role of hydrogen bonding in liquid structuring and properties.

This study introduces a class of hydrophobic Natural Deep Eutectic Solvents (NADES) by exploring the hitherto under-investigated combination of monoterpenoids and saturated fatty acids as hydrogen bond donor-acceptor systems. This innovative approach yields unique eutectic mixtures composed of naturally occurring monoterpenoids (menthol, thymol, 1,8-cineole, carvone, and geraniol) and fatty acids with varying chain lengths (decanoic, tetradecanoic, and octadecanoic acid). It is provided a comprehensive experimental and computational investigation of these novel NADES. Experimentally, key thermophysical properties—density and viscosity—across a range of molar ratios and temperatures were measured. Computationally, a multi-scale modeling approach was applied, integrating COSMOtherm, DFT-Tight Binding, and classical Molecular Dynamics simulations. This allowed to probe the nanoscale properties and structural organization of the solvents, with a particular emphasis on hydrogen bonding networks and

intermolecular interactions. Critically, the integration of experimental and computational findings establishes a clear structure-property relationship, providing a powerful tool for the rational design of sustainable solvents. This work significantly advances the understanding and application of monoterpene-based hydrophobic solvents in green chemistry and sustainable technologies, opening new avenues for the development of bio-based, environmentally benign alternatives to traditional organic solvents.

2. Materials and methods

2.1 Experimental studies

The sources, their CAS number, molar mass and purity of compounds used for the HNADES preparation are reported in Table S1 (Supplementary Information). Saturated fatty acid used as HBD (C10AC, C14AC and C18AC) and two of monoterpenoid used as HBA (MEN and THY) were solid at room temperature; but due to their melting point CIN, CAR and GER, also used as HBD, were at liquid state at room temperature. Independent of their phase at room temperature, all of them were used without further purification and stored in a dry, dark place in delivery bottles. The combinations between three HBDs and five HBAs produce a total of 15 possible different HNADES, with the specific studied mole ratios listed in Table S2 (Supplementary information). HNADES were prepared weighing the appropriate masses of each component using Mettler Toledo balance (Model AE240, with a stated accuracy to $\pm 4 \cdot 10^{-4}$ g cm^{-3}), and mixing them in closed glass flasks. The mixtures were stirred for at least 8 hours between room temperature and 313.15 K. The prepared HNADES (mixtures) were stored at 293 K in sealed flasks in a dry and dark place.

Density, ρ, and kinematic viscosity, v, measurements were carried out as a function of temperature in the 283.15 to 313.15 K range, in 5 K steps at atmospheric pressure (Table S2, Supplementary Information). Density measurements were performed with a vibrating tube densimeter model DMA5000 (Anton Paar, uncertainty $\pm 1 \cdot 10^{-4}$ g cm-3), with Peltier control for the cell temperature (uncertainty ±0.01 K). To fill the tube, a syringe was used to carefully introduce approximately 1 mL of the sample, ensuring the prevention of bubble formation. Kinematic viscosity was measured at atmospheric pressure using a Ubbelohde microviscometer.

The microviscometer was immersed in a circulating water bath with a cell temperature (CT-52, Schott Instruments, ± 0.01 K uncertainty) and an automatic control unit (AVS350, Schott, ViscoSystem®, ± 0.01 s uncertainty). Experiments were repeated three times at each temperature for all molar ratios studied and the results were averaged.

From experimental ρ data, the thermal expansion coefficient, α_p, for each NADES were calculated from linear fits of ρ vs temperature ($R^2 > 0.9999$) according to eq. (1):

$$\alpha_p = -\frac{1}{\rho}\left(\frac{\partial \rho}{\partial T}\right)_p \quad (1)$$

The temperature dependence of viscosity was analyzed in terms of the Arrhenius and Vogel–Fulcher–Tammann (VFT) equations:

$$\eta = Ae^{\frac{E_a}{RT}} \quad (2)$$

$$\eta = A_{VFT}e^{\frac{B}{T-T_0}} \quad (3)$$

VFT fits allowed the calculation of the so-called Angell's fragility parameter, D_f:

$$D_f = \frac{B}{T_0} \quad (4)$$

2.2 COSMOtherm thermodynamics and COSMOperm

The structures of monomers for monoterpenoids (HBA) and fatty acids (HBD) structures were optimized at BP86/def-TZVP theoretical level using TURBOMOLE in TmoleX (v21.0.1) software [30], from which COSMO files were calculated and considered for COSMOtherm calculations using COSMOthermX software [31]. These simulations led to σ-profiles, solid – liquid equilibria (including eutectic point), boiling point (T_{boil}), vapor pressure (p_{vap}), octanol-water partition coefficients (K_{OW}) and solubility in water (s). Additionally, HBA : HBD hydrogen bonded 1 : 1 dimmers were built, optimized, and COSMO files were obtained for the optimized dimmer structures. A POPC lipid bilayer with (water to lipid 49.1 ratio) [32] was considered and the interaction of HBA : HBD dimers (COSMO files) with this bilayer was analyzed considering COSMOperm calculations at 303 K, which allowed to predict the permeability of the considered HBA : HBD pairs, as free energy profiles for the permeation in the bilayer, and geometrical properties into the model cell membrane [33].

2.4 Density Funtional Theory – Tight Binding

DFT-TB simulations for C10AC : HBA NADES were carried out with DFTB+ program [34]. The Slater–Koster (SK) files corresponding to the Third-Order Parameterization for Organic and Biological Systems (3OB) were applied [35,36]. The self-consistent calculations were carried out with 10^{-6} tolerance. The k-points meshes corresponded to a 4 × 4 × 4 distribution with the self-consistent calculations carried out with 10^{-6} tolerance. Initially, monoterpene + fatty acid dimers were built and optimized to analyze the nature of hydrogen bonding. Likewise, the structure and properties of larger clusters were studied. For this purpose, initial cubic simulation boxes were built with the Amorphous Cell program in Biovia Materials Studio [37] corresponding to the experimental densities and considering: *i*) C10AC : HBA (1 : 1) NADES: boxes containing 10 C10AC + 10 HBA molecules; *ii*) C10AC + MEN with 1 : 2 (5 C10AC + 10 MEN molecules) and 2 : 1 (10 C10AC + 5 MEN molecules), and *iii*) C14AC + MEN 1 : 4 (5 C10AC + 20 MEN molecules) and C18AC + MEN 1 : 8 (5 C10AC + 40 MEN molecules). These initial simulation boxes were equilibrated using geometry (classical MD approach) optimization into the Forcite module within Biovia Materials Studio software [38] considering the using the COMPASS III force field [39]. The previously equilibrated structures were considered for DFT-TB developing geometrical optimization of the considered systems considering Periodic Boundary Conditions in the three space directions, with 0.1 kJ mol^{-1} as a convergence criterion.

2.5 Molecular Dynamics simulations

Classical MD simulations were carried out with the Forcite module within Biovia Materials Studio software [38] with the COMPASS III force field [39]. The following systems were studied by MD simulations: *i*) monoterpenoid (MEN, THY, CIN, CAR, GER) + C10AC (1 : 1), to study (HBA) monoterpenoid effect (MD_study_01), *ii*) MEN + C10AC (2 : 1) and MEN + C10AC (1 : 2), to study mole ratio effect (MD_study_02), *iii*) MEN + C14AC (4 : 1) and MEN + C18AC (8 : 1), to study fatty acid chain length effect (MD_study_01).

Cubic simulation boxes were prepared using the Amorphous Cell as in the previous section for DFT-TB studies. Systems for MD_study_01 contained 100 (HBA) + 100 (HBD) molecules; systems for MD_study_02 contain MEN + C10AC (100 : 50) and MEN + C10AC (50 : 100) molecules; systems for MD_study_03 contain MEN + C14AC (200 : 50) and MEN + C18AC (400 : 50). All the simulations were carried out Biovia Materials Studio [37]. The initial simulation

boxes were subjected to consecutive heating (up to 500 K) and cooling cycles (to the target temperature) in the NVT ensemble, then followed by NVT simulations at the target temperature for 20 ns, with equilibration assured by the constancy of total potential energy and density. After equilibration steps, production runs in the NPT ensemble simulations were performed at 298 K and 1 bar, with a timestep of 1 fs, to 100 ns, with the last 80 ns used for analysis. The Nose-Hoover thermostat [40] was employed for temperature control and the Parrinello-Rahman barostat [41] for pressure. Long-range electrostatic interactions were handled using the Ewald summation method [42] with van der Waals potential with Waldman-Hagler mixing rules [43], and a cutoff distance of 15 Å. Visualization, analysis, and post-processing of the MD trajectories were performed using VMD [44] and TRAVIS [45].

3. Results and discussion

3.1 Experimental and COSMOtherm study

The HNADES considered in this work initially considered three fatty acids (C10AC, C14AC and C18AC) combined with five different monoterpenoids (MEN, THY, GER, CIN, CAR), Figure 1. For these combinations, three molar ration were considered (2:1, 1:1 and 1:2) and prepared to analyze the possible HNADES formation (i.e. liquid at close to ambient temperature, 293 K; Table S2, Supplementary Information). Therefore, experimental properties could not be determined for all mixtures, as not all the molar ratios tested led to liquid phases at (close to) room temperature. As the chain length of the saturated fatty acids increases, the HNADES melting temperature increases (C10AC, 303 K; C14AC, 326K; C18AC, 343K), all of them over room temperature, and thus leading to increasing temperatures for the developed mixtures. Therefore, for C14AC and C18AC possible HNADES only monoterpenoid mixtures were considered studying 1:1, 1:2, 1:4,1:6,1:8, and 1:10 (acid : monoterpenoid). For C14AC systems, THY did not lead to liquid phases at any of the considered mole fractions (T < 313.15 K), and for the remaining monoterpenoids only for rich monoterpenoid mixtures. In the case of systems with C18AC, HNADES with melting temperatures were obtained only for systems with MEN at 1:8 and 1:10 mole fractions (Table S2, Supplementary Information).

The characteristics of the molecules involved in HNADES development are initially analyzed by using COSMOtherm method, which involves the analysis of the COSMO σ-profiles and charge distribution for the monoterpenoids and fatty acids, Figure 2. The σ-profiles allow to identify non-polar, hydrogen bonding and acceptor regions in the molecules [46]. Regarding monoterpenoids, whereas CIN and CAR may act only as HBAs, MEN, THY and GER (having hydroxyl groups) may act both as HBAs and HBDs. The corresponding σ-profiles, Figure 2a, show large peaks in the nonpolar region for the non-polar region, with this non-polar region divided in two peaks, thus corresponding to two well different surface areas prone to develop interactions via van der Waals interactions both among monoterpenoids as well as with the large non-polar regions of the fatty acids, Figure 2b. THY and CAR show a larger non-polar peak with the formation of an HBA smaller peak, MEN and GER show similar behavior but with smaller peaks; and CIN displays the lowest two parallel peaks in the non-polar region. The profiles of the fatty acids exhibit similar σ-profiles (Fig. 2b), showing a large peak with a slight shoulder in the non-polar region. THY molecule exhibits de largest electron density region around the ring, Figure 2c, corroborated by the highest peak in σ-profiles. MEN displays a high electron density focussed around the hydroxyl group, as well as CAR concentrates the high electron density around the oxygen atom. The CIN molecule is characterized by high electron density region around the ether group surrounded by a large non-polar bulky region, which is showed in the σ-profiles (Figure 2c). For the three fatty acids it is confirmed that they present HBA and HBD character, due to the high electron density region around both oxygen atoms and the low electron density in the hydroxyl hydrogen atom (Figure 2d), as well as the large hydrophobic character as showed by the large non-polar peak in σ-profile.

COSMOtherm method was used for predictions of the Solid-Liquid equilibria (SLE) and the corresponding eutectic points, Figure 3. The effect of fatty acid alkyl chain length for MEN containing HNADES (the only monoterpenoid among those studied experimentally leading to HNADES formation with fatty acids up to C18AC; Table S2, Supplementary Information), Figures 3a to 3c. Eutectic formation is confirmed for all the considered acids and it is predicted that the temperature of eutectic point increases as the HBD chain length increases, which agrees with the melting temperatures of pure HBDs, while the eutectic mole fraction shifts toward MEN – rich

mixtures. These SLE diagrams confirm, in agreement with experimental results, that it is possible to develop HNADES with fatty acids (up to C18AC) and MEN being liquid for temperatures close to the ambient one but for MEN - rich mixtures. The monoterpenoid effect on SLE is studied in Figures 3a, 3d – 3g for C10AC, and although eutectic point is confirmed for all the systems, the characteristics of them is remarkably dependent on the considered monoterpenoid. The eutectic composition correspond to roughly 2:1 monOterpenoid : fatty acid ratio for (MEN, CIN, CAR), whereas it is 1 : 1 for THY and 7:1 for GER. Likewise, it is remarkable the low eutectic temperature for CIN HNADES and the larger one for THY HNADES. It can be seen that, except C10AC:MEN, the temperature of eutectic point of the HNADES is related to the magnitude of the main non-polar peak in σ-profile: the weaker peak, the lower eutectic temperature.

The behavior of C18AC containing mixtures, i.e. largely hydrophobic systems is experimentally studied for fatty acid : monoterpenoid 1 : 2 molar ratio in Figure 4a. Initially formed systems upon HBA – HBD mixing at 293.15 K evolve to a gel-like material, which upon heating to 321.15 K evolve to transparent liquid phases (all above the highest temperature for the considered range of experimental physicochemical properties studies, 313.15 K; Table S2, Supplementary Information). The effect is reversed upon cooling with the recuperation of jellified phases. The predicted solid(gel) to liquid temperatures with COSMOtherm are compared with experimental data, Figure 4b, showing excellent agreement (largest difference of 6 K obtained). Regarding the kinetic study of liquid – solid (gel) transitions (Fig. 4c) show that C18AC:MEN and C18AC:GER present respectively the shortest and largest time for the formation of solid (gel) phases in the cooling process.

HNADES usually exhibits high thermal stability and negligible vapor pressure, as well as per definition for hydrophobic DES, low water affinity. These are some of the most desirable properties for separation or extraction applications as alternatives to conventional solvents considering the sustainability of the developed processes. COSMOtherm was applied for the prediction of the normal boiling temperature and vapor pressure (at 303.15 K) of the considered HNADES, Figures 5a and 5b, respectively. It could be observed that all HNADES exhibit a high boiling point, above 478.3 K, providing them with a considerably broad operational temperature range (wide liquid range). Vapor pressure values are negligible and decrease with the HBD chain

length, which assure no vapor emissions under operational conditions, thus being safe and sustainable solvents. This negligible volatility is related with the strong interactions via hydrogen bonding between the HBA and the HBD [**¡Error! Marcador no definido.**]. Figures 5c and 5d shows the hydrophobic character of the considered HNADES, via the octanol-water coefficient (log(K_{OW})) and solubility in water. The log(K_{OW}) values, in the range of 7.4–11.3, shows the largely hydrophobic (lipophilic) character of all the HNADES; although the HBDs in the considered NADESs contain OH groups, and also polar groups are present in the HBA molecules (Figures 1 and 2), the formation of HNADESs via hydrogen bonding results in the generation of large hydrophobic regions that remain exposed and impart the hydrophobic character. Therefore, almost water insoluble HNADES are produced (Figure 5c), which discards water contamination when these solvents are used, thus decreasing their environmental impact and increasing their sustainability.

To infer deeper insights into the safety of the considered HNADES, their interaction with model plasma membranes is studied vis COSMOperm simulations. It is proposed that the interaction of target molecules with plasma membranes is a relevant Molecular Initiating Event (MiE) in Adverse Outcome Pathways (AoPs) [47] to analyze the possible toxicity and thus the safety of the molecules. The behavior of the HNADES molecules at a model POPC (1-palmitoyl-2-oleoyl-sn-glycero-3-phosphocholine) lipid bilayer was firstly analyzed considering molecular permeabilities across the bilayer, i.e. how feasible is the molecules penetrating into the cell wall? Results in Figure 6a reveals relatively high permeability results, which are consistent with the log(K_{OW}) coefficient i.e. large hydrophobic character for the considered HNADESs allows to cross the lipid bilayer easily, leading to molecules places close to the lipid bilayer center, i.e. in the apolar region of the lipidic chains, Figures 6b and 6c. Likewise, the penetration of molecules across the bilayer is characterized by the free energy profiles reported in Figure 6d, which discards the development of penetration barriers and shows the large molecular stabilization in when molecules are placed in the (apolar) center of the bilayer, especially for long chain fatty acids. The entropy variations for the crossing mechanism, Figure 6e, indicates two maxima around and beyond the polar head region of the bilayers, which is produced by the changes in the molecular arrangements on crossing this polar region evolving toward a parallel arrangement

of apolar domains with alkyl chains of fatty acids in the central lipid bilayer region. This molecular rearrangement when crossing the polar region leads to a small resistance to crossing, which is vanished once the central apolar region is reached, Figure 6f. Therefore, it should be remarked that the considered HNADES components are able to cross the plasma membranes, although their fitting into the bilayer structure via accommodation of apolar domains would lead to minor perturbations of membranes properties.

Experimental relevant thermophysical properties (density and dynamic viscosity are also reported in this work. Density data are reported in Figure 7a. All fluids are less dense than water, as a consequence of their hydrophobic character, with the lower densities inferred for GER – containing HNADES, and the temperature effect being linear for all of them. However, their behavior in function of molar ratio in the HNADES varies significantly according to the HBA. At equal molar ratio, the density decreases in the order of THY > CAR > CIN > MEN > GER. For THY, CAR and CIN density values increase with the increase of HBA in the HNADES composition. This may be related to the decrease in the quantity of lengthy saturated fatty acid chains, and the presence of HBA molecules allow better packing. But two of the studied NADES shows a very different results: C10AC:MEN densities are independent from the composition and C10AC:GER shows an inverse behavior, density increases with the presence of HBD. The α_p values, being in the (0.8 to 0,9)·10^{-4} K^{-1} range (Figure 7b), increase linearly with temperature, which indicate that these are compressible fluids. The observed low density and thermal expansion coefficients for the studied NADES system indicate that they exhibited a large free volume, mainly as a consequence of the presence of the long alkyl chains in fatty acids. The viscosity decreases in a non-Arrhenius way with an increase in the temperature (Figure 7c). The largest viscosity values were obtained for C10AC:MEN, and the lowest values were obtained for the C10AC:CAR. HNADES with CAR, CIN and THY show very low viscosity values with slight variations at temperatures above 298.15K. The low viscosity of the considered HNADES at close to ambient temperatures discard possible heat or mass transfer problems when these HNADES are scaled up. The calculated VFT parameters allowed to infer Angell's strength (fragility measurement) parameter, Df. The fit of experimental viscosity data with temperature was initially carried out via Arrhenius equation but the poor results led to the need of fitting to VFT equation, which led to suitable

fitting results, Table S3 (Supplementary Information) and Figure 8, thus discarding the Arrhenius behaviour of the considered fluids. These non-Arrhenius viscosity behaviour rises from the formation of polar and apolar domains into the fluid via the aggregation of alkyl (hydrophobic) domains paired with hydrogen bonded regions. The calculated D_f values follows the order CAR > CIN > GER > THY > MEN, being in the 6 to 19 range, indicating moderately fragile fluids, with C10AC:CAR HNADES being the stronger (from the dynamics viewpoint) fluid. The calculated T_0 VFT-parameter is related to the glass transition temperature, with the reported values (Figure 9) being remarkably low, thus showing the large liquid stability of the considered HNADES.

3.2 DFT-TB modelling

The following step considered the analysis of the properties of intermolecular forces in the developed HNADES, which are on the roots of the particular properties reported in the previous section. In a first step, HBA : HBD (1 : 1) hydrogen bonded dimmers were considered as models of minimal clusters containing the information on the basic structure of HNADES. The most stable dimmers were obtained and the strength of hydrogen bonding quantified via the interaction energy, Δ*E*, defined as the difference among the total energy for the cluster and the sum of those for the isolated components (monomers), Figure 10a. The reported Δ*E* values indicate strong interactions in all the cases, increasing with fatty acid alkyl chain and following the ordering [THY] < [CAR] < [CIN] < [MEN] < [CAR]. Values reported in Figure 10a are a measure of a single HBA : HBD hydrogen bonding, thus, to consider longer range effect, i.e. interaction among neighbor interacting dimmers, larger cluster were considered. In the case of C10AC – containing HNADES, clusters with 10 pairs were considered and the energy per pair was reported in Figure 10b. The comparison of Δ*E* values from Figures 10a and 10b indicate that in HNADES there are also relevant intermolecular forces beyond hydrogen bonding as values for 10-oligomers are more than twice those of dimmers. The presence of large apolar domains in the considered molecules, Figure 2, leads to van der Waals interactions among these apolar domains which considering the large number of van der Waals contacts leads to a large increase in Δ*E* values, which results both from hydrogen bonding and apolar interactions. In the case of HNADES containing C14AC and C18AC, as the molar ratios leading to liquid phases at ambient temperature correspond to 4 : 1 and 4 : 1 (monoterpenoid : acid), respectively, Table S2 (Supplementary

Information), the fatty acid content is lower than in those with C10AC; nevertheless, the values in oligomers are larger than in dimmers, thus confirming the relevant role of apolar domains aggregation of the considered HNADES structuring.

3.3 MD simulations

The analysis of liquid phase properties at the nanoscopic level is analyzed via MD simulations. Radial Distribution Functions (RDFs) are considered for the hydrogen bonding donor – acceptor sites studying monoterpenoid and fatty acid effect, Figure 11. From the considered monoterpenoids, MEN, THY and GER (containing OH group), may act both as hydrogen bond donor or acceptor, whereas CIN and CAR may act only also as hydrogen bond acceptors, through their ether of carbonyl groups, respectively. Likewise, fatty acids may act both as donor and acceptors. Therefore, in the considered HNADES, a complex landscape of hydrogen bonds may be inferred: *i*) monoterpenoid self-association, *ii*) fatty acid self-association, through a) OH – OH or b) OH - CO, *iii*) monoterpenoid – fatty acid heteroassociation with a) monoterpenoid acting as donor or b) fatty acid acting as acceptor; therefore, leading to five possible types of hydrogen bonds, for which the corresponding RDFs are considered, Figure 11. From these five possible hydrogen bonds all of them were confirmed via RDFs with the exception of fatty acid self – aggregation via OH – OH interaction, which is discarded (Figures 11d and 11i) as RDFs indicate wide bands at distances not corresponding to hydrogen bonds. It is confirmed the presence of monoterpenoid self-aggregation (MEN, THY, GER), Figure 11a, with negligible effects of alkyl chain in fatty acid (Figure 11f). Regarding fatty acid self-aggregation, it is dependent on the monoterpenoid (Figure 11e), more intense for CIN and CAR than for the remaining ones as they are not self-associated thus competing with donor sites in the acid, and decreasing with fatty acid chain length, Figure 11j. For monoterpenoid – fatty acid interaction, the fatty acid acting as donor (OH), Figure 11b, leads to more extensive hydrogen bonding than those with the monoterpenoid (MEN, THY, GER) acting as donor (Figure 11c), with minor effect by the fatty acid chain length. The fatty acid – monoterpenoid interaction with the acid acting as donor is largely dependent on the type of monoterpenoid, leading to the less intense values for CIN and CAR, having non-OH groups.

The spatial orientation of molecules around hydrogen bonding sites is analyzed via Spatial Distribution Functions (SDFs), Figure 12. The reported results around monoterpenoid molecules show similar distributions for those compounds having hydroxyl groups (MEN, THY, GER) with hydroxyl groups from neighbor mononoterpenoid molecules as well as those from fatty acids competing and placed around the central monoterpenoid hydroxyl group, Figure 12a. The effect of increasing fatty acid alkyl chain is the increasing concentration of neighbor monoterpenoid molecules around the central one as the amount of fatty acid decreases and their trend to self-associate also increases. In the case of CIN and CAR as they may act only as hydrogen bond acceptors, with fatty acid hydroxyl groups place around the oxygen acceptor site and the neighbor monoterpenoid molecules at outer regions. For the distribution around a central fatty acid molecule, results confirm hydrogen bonding with monoterpenoid via hydroxyl – hydroxyl interaction and acid – acid via carbonyl – hydroxyl interaction, with largely ordered shells around the fatty acid COOH group. Regarding fatty acid self-association with increasing alkyl chain length, Figure 12b, as the acid chain length increases the acid – acid self-association decreases replaced by acid – monoterpenoid interactions.

Domain analysis was carried out to analyze long range analysis of aggregation beyond directly hydrogen bonded short - range interactions, Figure 13. The first relevant result stand on the development of isolated domains both for fatty acids. For a fixed HNADES, the number of domains for the corresponding monoterpenoid and the fatty acid are the same, i.e. the structure is characterized by domains of both typed of compounds interpenetrated via hydrogen bonding. The number of domains for HNADES with monoterpenoids not containing hydroxyl groups (CIN and CAR) is larger than those for systems containing hydroxyl groups, specially for GER, with shows almost a continuous domain for both HNADES components. As the alkyl chain of the fatty acid increases, the number of domains also increases, specially for the monoterpenoid, which points to the disruptive effect of long chain lengths in the fatty acid isolates those monoterpenoid domains.

The dynamic properties of the HNADES are initially analyzed via the center-of-mass Velocity Distribution Functions (VDFs). The monoterpenoid – fatty acid hydrogen bonding as well as the similar extension of domains leads to similar mobilities for both components of the

HNADES, Figure 14. The type of monoterpenoid has very minor effects on mobilities, the maxima of VDF curves is almost independent of the monoterpenoid type, the only remarkable difference is the widening of VDF curves, specially for CIN and CAR containing HNADES, which indicate more particles moving at faster rates, i.e. in agreement with lower viscosities for CIN and CAR containing HNADES. The effect of fatty acid chain length on VDFs is also almost negligible, Figures 14c and 14d. Further analysis of HNADES dynamic properties is carried out via the self-diffusion coefficients, *D*, as obtained from mean square displacement and Einstein's equation, Figure 15a. As for VDFs, the calculated *D* values are only slightly lower for the fatty acid than for the monoterpenoid for a fixed HNADES, but it indicated dynamic pairing of both components. The order of *D* coefficients follow the same order of experimental viscosity, Figure 7. The results in Figure 15b indicate a linear relationship among *D* and inverse of viscosity, which indicate the same hydrodynamic radius for the diffusing species for a fixed fatty acid independently of the type of monoterpenoid. On the contrary, increasing fatty acid chain changes the *D* vs inverse viscosity ratio, as the longer chain length leads to larger diffusing species.

Another relevant dynamic property of the considered HNADES stands on the dynamics of the formed hydrogen bond, for which the living time and the reforming time of each type of hydrogen bond is calculated, Figure 16. The first main result stand of longer living times than reforming times for all the interactions, i.e. once an hydrogen bond is broken is it is readily formed as a consequence of the strength of the developed interactions, Figure 10. Those systems containing CAR or CIN monoterpenoids lead to more labile interactions, specially for monoterpenoid - fatty acid ones, both in the living time and the readiness of reforming. Increasing fatty acid chain length also leads to hydrogen bonds with slightly lower living times but also with faster reforming. Therefore, the developed hydrogen bonds are strong, with medium living times (in the hundreds ps range) but quickly reformed. This combination of strong and dynamic hydrogen bonds will be on the roots of the nanostructure of the fluids.

4. Conclusions

Based on the comprehensive experimental, computational, and simulation studies presented, a series of novel hydrophobic natural deep eutectic solvents composed of fatty acids

and monoterpenoids have been successfully developed and characterized. These HNADES exhibit promising properties for potential applications in separation and extraction processes. The formation of eutectic mixtures was confirmed for all systems, with the eutectic point characteristics heavily dependent on the specific monoterpenoid and fatty acid combination. Notably, these HNADES demonstrate high thermal stability, negligible vapor pressure, and low water affinity, making them environmentally friendly alternatives to conventional solvents. Their hydrophobic nature, as evidenced by high octanol-water partition coefficients and low water solubility, suggests minimal environmental impact and increased sustainability in industrial applications. While the HNADES components can permeate model plasma membranes, their interaction with lipid bilayers appears to cause only minor perturbations, indicating potentially low toxicity. The thermophysical properties, including density and viscosity, were found to be favorable for practical applications, with low viscosities at ambient temperatures reducing potential heat or mass transfer issues during scale-up. Simulations revealed a complex hydrogen bonding network within the HNADES, with both self-association and heteroassociation between monoterpenoids and fatty acids. The formation of interpenetrating domains of monoterpenoids and fatty acids contributes to the unique structural properties of these solvents. The dynamic nature of the hydrogen bonds, characterized by medium living times and quick reforming, underlies the nanostructure of the fluids. Overall, this study provides valuable insights into the structure-property relationships of HNADES, paving the way for their rational design and application in sustainable industrial processes.

Acknowledgements

This work was funded by Agencia Estatal de Investigación (Spain, Project NADES for PFAS, Ref.: PID2022-142405OB-I00), Junta de Castilla y León (Spain, Project NADESforNature, Ref.: BU047P23) and European Union (Horizon 2020 program, project WORLD: H2020-MSCA-RISE-2019-WORLD-GA-873005). We also acknowledge SCAYLE (Supercomputación Castilla y León, Spain) for providing supercomputing facilities. The statements made herein are solely the responsibility of the authors.

Supplementary Information

Chemicals used in this work (Table S1), experimental properties (Table S2), results of fitting experimental viscosity data to Arrhenius and VFT models (Table S3).

Figure Captions

Figure 1. (a) Molecular structures of compounds used in this work for NADES preparation and (b) methodology considered in this work.

Figure 2. (a,b) σ-profiles and (c,d) charge distributions, calculated from COSMO for the monomers involved in NADES considered in this work.

Figure 3. COSMOtherm predictions for the Solid-Liquid equilibria of the reported systems. In each panel, (O) shows the corresponding eutectic point (T_e and x_e); (x) shows relevant compositions for NADES formation (1:2, 1:1 and 2:1 mole ratios in panels a, d-g; 1:, 1:6 and 1:4 in panels b and c; for organic acid : monoterpenoid i : j ratios); shadowed areas show 283.15 to 313.15 K temperature range, close to ambient conditions for which experimental and computational studies were carried out.

Figure 4. (a) Experimental results for the melting of C18AC : HBA (1 : 2) systems from gel to liquid transitions, (b) experimental and COSMOtherm solid(gel) – to liquid temperatures, $T_{S\text{-}L,}$ (c) kinetic study of liquid – solid (gel) transitions showing the time for the formation of solid (gel) phases. In panel b: (filled) experimental data, (dashed) COSMOtherm (Figure 2).

Figure 5. Relevant environmental properties and hydrophobic character of the considered monomers and NADES studied in this work from COSMOtherm calculations. (a) Normal boiling temperature, T_{boil}, (b) normal vapor pressure at 303.15 K, P_v, (c) octanol-water partition coefficient, log(K_{OW}), at 303.15 K, (d) solubility in water, s, at 303.15 K.

Figure 6. COSMOperm results for the interaction between the reported HBA : HBD (1 : 1) NADES clusters and a POPC bilayer + water system at 303.15 K. (a) Permeability, P, (b) mean position from the bilayer center, d_{mean}, (c) distribution probability, (d) free energy, ΔG, (e) entropy, ΔS, and (f) resistance, R. All results as a function of bilayer depth, d, where d = 0 stands for the bilayer geometrical center.

Figure 7. Experimental density, ρ, thermal expansion coefficient, α_p, and dynamic viscosity, η, for C10AC : HBA (i : j) NADES as a function of temperature. Panel (d) shows Angel's fragility parameter, D_f, obtained from the fit of experimental viscosity to the VFT equation.

Figure 8. AARD % for the fit of experimental viscosity data to Arrhenius (eq. 2) and VFT (eq. 3) models for C10AC : HBA (i : j) NADES.

Figure 9. T_0 parameter from the fit of experimental viscosity to VFT model (eq. 3) for C10AC : HBA (i : j) NADES.

Figure 10. (a) Interaction energy, ΔE, for monoterpenoid + C10AC dimmers, and (b) interaction energy per number of fatty acid molecules in monoterpenoid + fatty acid simulation boxes (as defined in section 2.4).

Figure 11. Site – site Radial Distribution Functions, $g(r)$, for the reported atoms (labelling as in Figure 1), for (a toe) monoterpenoid C10AC : HBA (1 : 1) and (f to j) {C10AC or C14AC or C18AC} : MEN, {1 : 1, 1 : 4, 1 :8}, respectively, from MD simulations at 298 K and 1 bar, except for systems with C14AC and C18AC which were carried out at 313 K.

Figure 12. Spatial Distribution Functions for the reported atoms (labelling as in Figure 1), for (a) monoterpenoid C10AC : HBA (1 : 1) and (b) {C10AC or C14AC or C18AC} : MEN, {1 : 1, 1 : 4, 1 :8}, from MD simulations at 298 K and 1 bar, except for systems with C14AC and C18AC which were carried out at 313 K.

Figure 13. Domain analysis for (a) monoterpenoid C10AC : HBA (1 : 1) and (b) {C10AC or C14AC or C18AC} : MEN, {1 : 1, 1 : 4, 1 :8}, from MD simulations at 298 K and 1 bar, except for systems with C14AC and C18AC which were carried out at 313 K. (solid bars) Monoterpenoids; (dashed bars) fatty acid.

Figure 14. Center-of-mass Velocity Distribution Function for the reported molecules, in (a,b) monoterpenoid C10AC : HBA (1 : 1) and (c,d) {C10AC or C14AC or C18AC} : MEN, {1 : 1, 1 : 4, 1 :8}, from MD simulations at 298 K and 1 bar, except for systems with C14AC and C18AC which were carried out at 313 K.

Figure 15. Center-of-mass self-diffusion coefficient, D, and its relationship with viscosity, η, in monoterpenoid C10AC : HBA (1 : 1) and {C10AC or C14AC or C18AC} : MEN, {1 : 1, 1 : 4, 1 :8}, from MD simulations at 298 K and 1 bar, except for systems with C14AC and C18AC which were carried out at 313 K.

Figure 16. Dynamics of hydrogen bonding showing living time (filled) and reforming time (dashed) for the reported pairs in monoterpenoid C10AC : HBA (1 : 1) and {C10AC or C14AC or C18AC} : MEN, {1 : 1, 1 : 4, 1 :8}, from MD simulations at 298 K and 1 bar, except for systems with C14AC and C18AC which were carried out at 313 K.

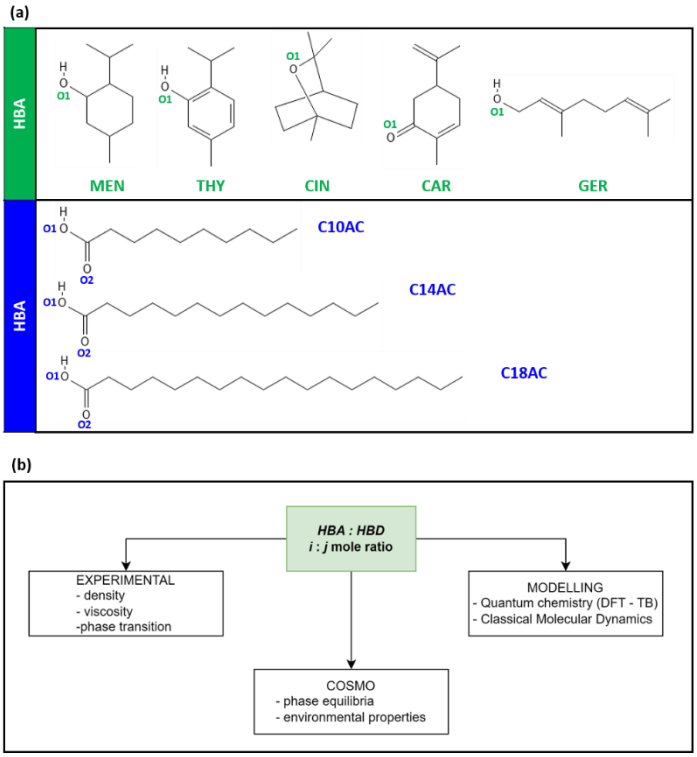
(a)
HBA
MEN
THY
CIN
CAR
GER
HBA
C10AC
C14AC
C18AC
(b)
HBA : HBD
i : j mole ratio
EXPERIMENTAL
- density
- viscosity
-phase transition
MODELLING
- Quantum chemistry (DFT - TB)
- Classical Molecular Dynamics
COSMO
- phase equilibria
- environmental properties

Figure 1

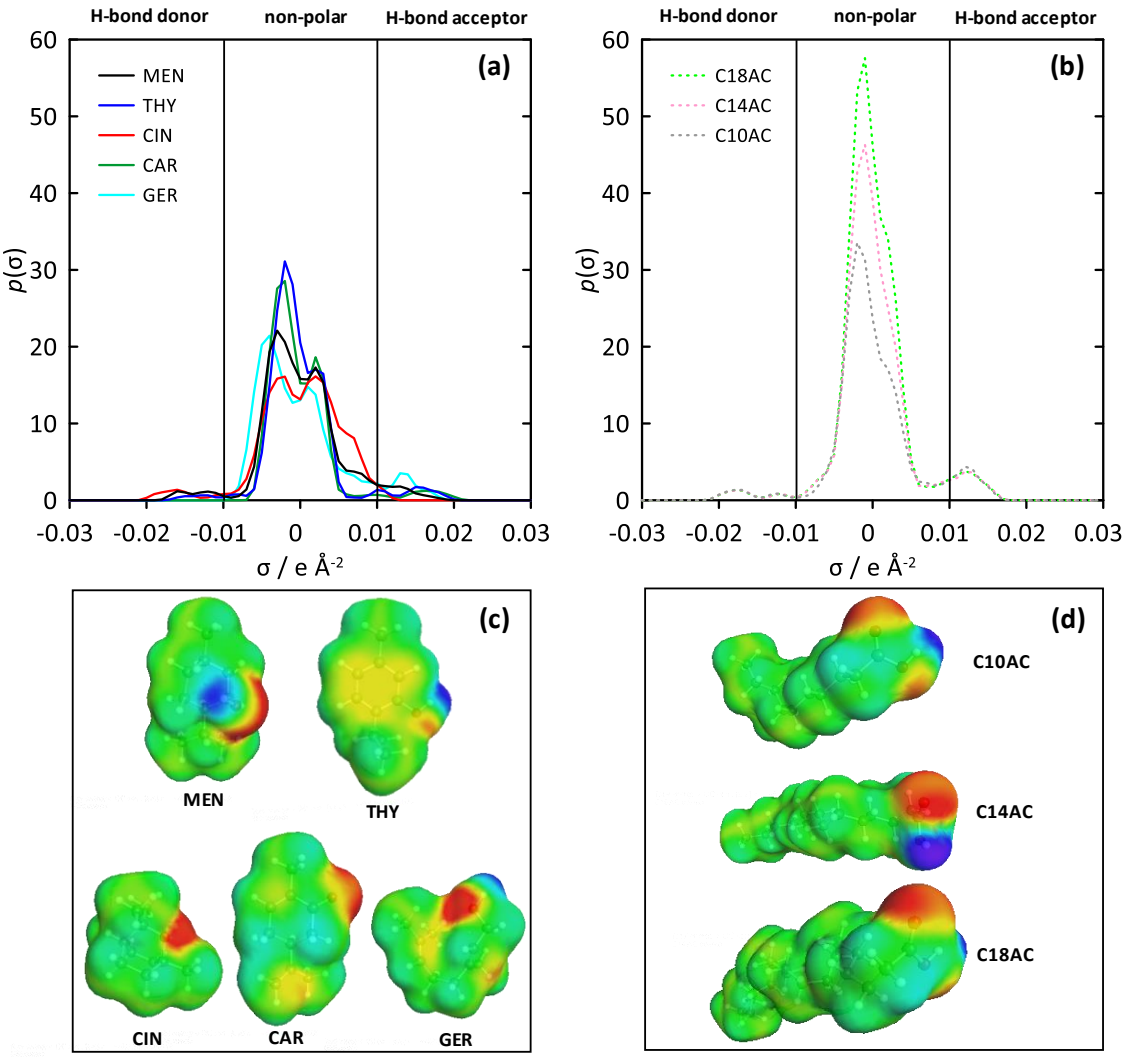
H-bond donor
non-polar
H-bond acceptor
(a)
MEN
THY
CIN
CAR
GER
p(σ)
σ / e Å-2
(b)
C18AC
C14AC
C10AC
(c)
MEN
THY
CIN
CAR
GER
(d)
C10AC
C14AC
C18AC

Figure 2

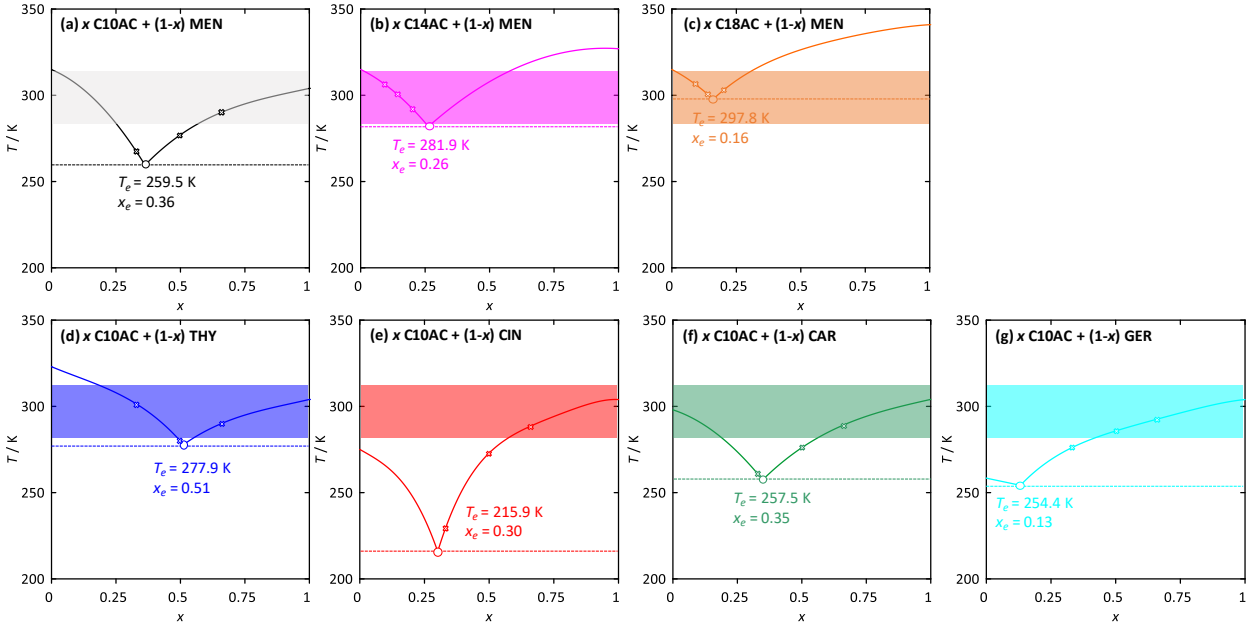
(a) x C10AC + (1-x) MEN
T_e = 259.5 K
x_e = 0.36
(b) x C14AC + (1-x) MEN
T_e = 281.9 K
x_e = 0.26
(c) x C18AC + (1-x) MEN
T_e = 297.8 K
x_e = 0.16
(d) x C10AC + (1-x) THY
T_e = 277.9 K
x_e = 0.51
(e) x C10AC + (1-x) CIN
T_e = 215.9 K
x_e = 0.30
(f) x C10AC + (1-x) CAR
T_e = 257.5 K
x_e = 0.35
(g) x C10AC + (1-x) GER
T_e = 254.4 K
x_e = 0.13
T / K
x

Figure 3

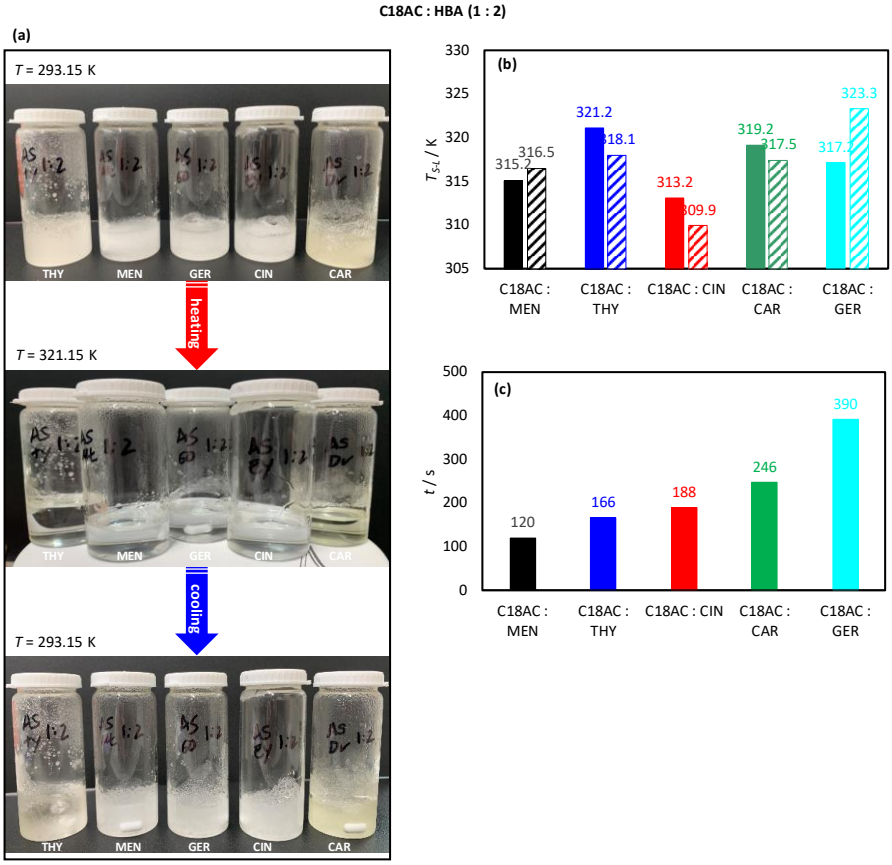
C18AC : HBA (1 : 2)
(a)
T = 293.15 K
THY
MEN
GER
CIN
CAR
heating
T = 321.15 K
cooling
T = 293.15 K
(b)
T_{sl} / K
315.2
316.5
321.2
318.1
313.2
309.9
319.2
317.5
317.2
323.3
C18AC : MEN
C18AC : THY
C18AC : CIN
C18AC : CAR
C18AC : GER
(c)
t / s
120
166
188
246
390

Figure 4

HBD : HBA (1 : 1)

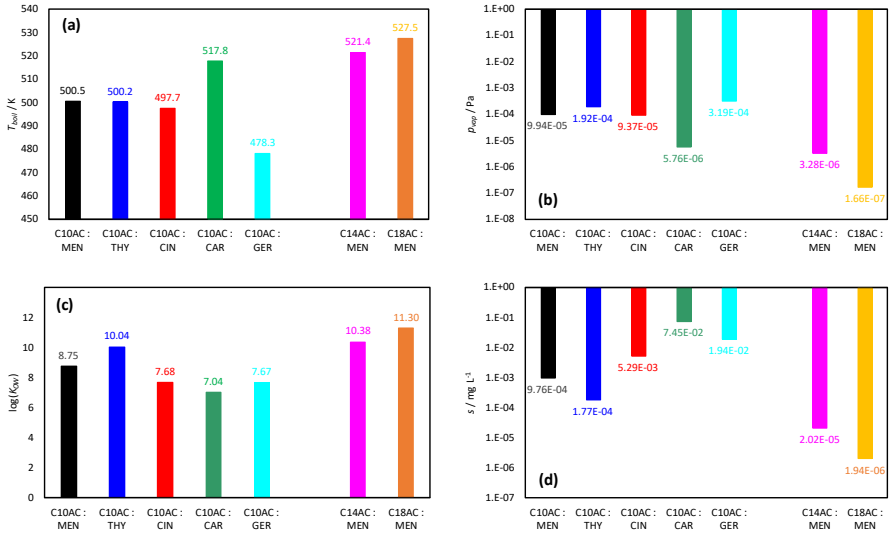

Figure 5

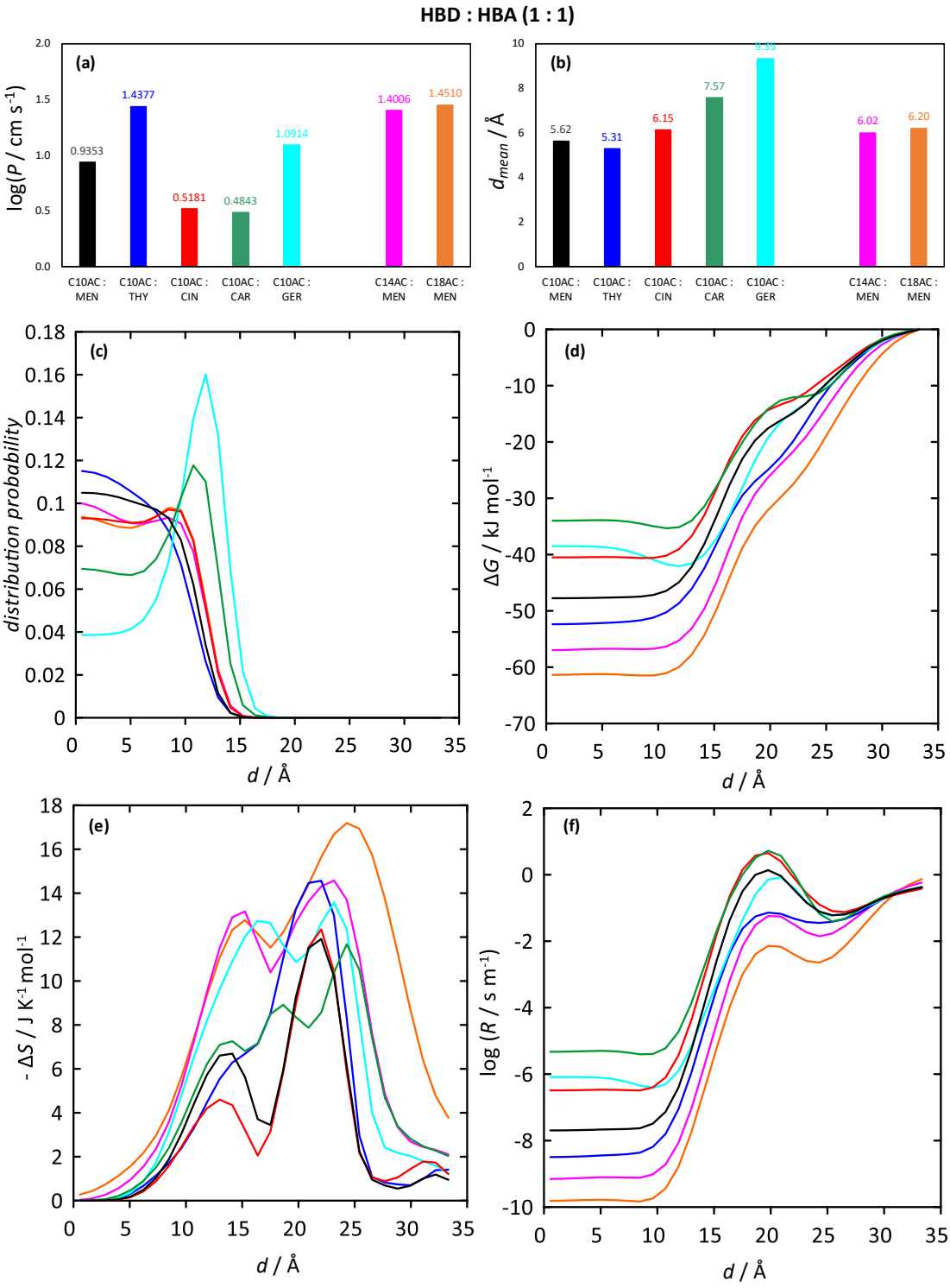
HBD : HBA (1 : 1)
(a)
log(P / cm s-1)
0.9353
1.4377
0.5181
0.4843
1.0914
1.4006
1.4510
C10AC : MEN
C10AC : THY
C10AC : CIN
C10AC : CAR
C10AC : GER
C14AC : MEN
C18AC : MEN
(b)
dmean / Å
5.62
5.31
6.15
7.57
9.35
6.02
6.20
(c)
distribution probability
d / Å
(d)
ΔG / kJ mol-1
d / Å
(e)
- ΔS / J K-1 mol-1
d / Å
(f)
log (R / s m-1)
d / Å

Figure 6

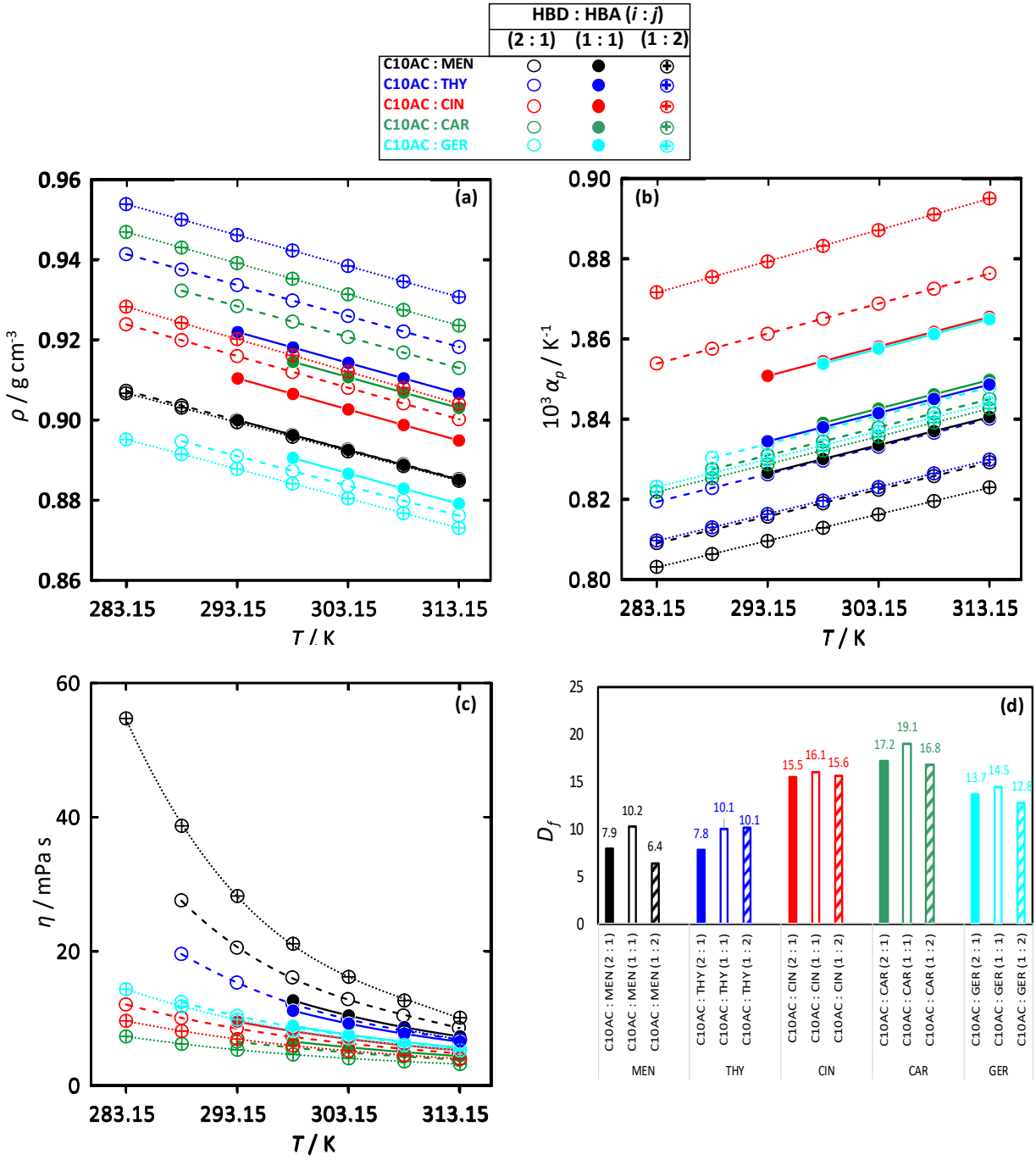
HBD : HBA (i : j)
(2 : 1)
(1 : 1)
(1 : 2)
C10AC : MEN
C10AC : THY
C10AC : CIN
C10AC : CAR
C10AC : GER
(a)
ρ / g cm-3
T / K
(b)
10³ αp / K-1
T / K
(c)
η / mPa s
T / K
(d)
Df
7.9
10.2
6.4
7.8
10.1
10.1
15.5
16.1
15.6
17.2
19.1
16.8
13.7
14.5
12.8
C10AC : MEN (2 : 1)
C10AC : MEN (1 : 1)
C10AC : MEN (1 : 2)
C10AC : THY (2 : 1)
C10AC : THY (1 : 1)
C10AC : THY (1 : 2)
C10AC : CIN (2 : 1)
C10AC : CIN (1 : 1)
C10AC : CIN (1 : 2)
C10AC : CAR (2 : 1)
C10AC : CAR (1 : 1)
C10AC : CAR (1 : 2)
C10AC : GER (2 : 1)
C10AC : GER (1 : 1)
C10AC : GER (1 : 2)
MEN
THY
CIN
CAR
GER

Figure 7

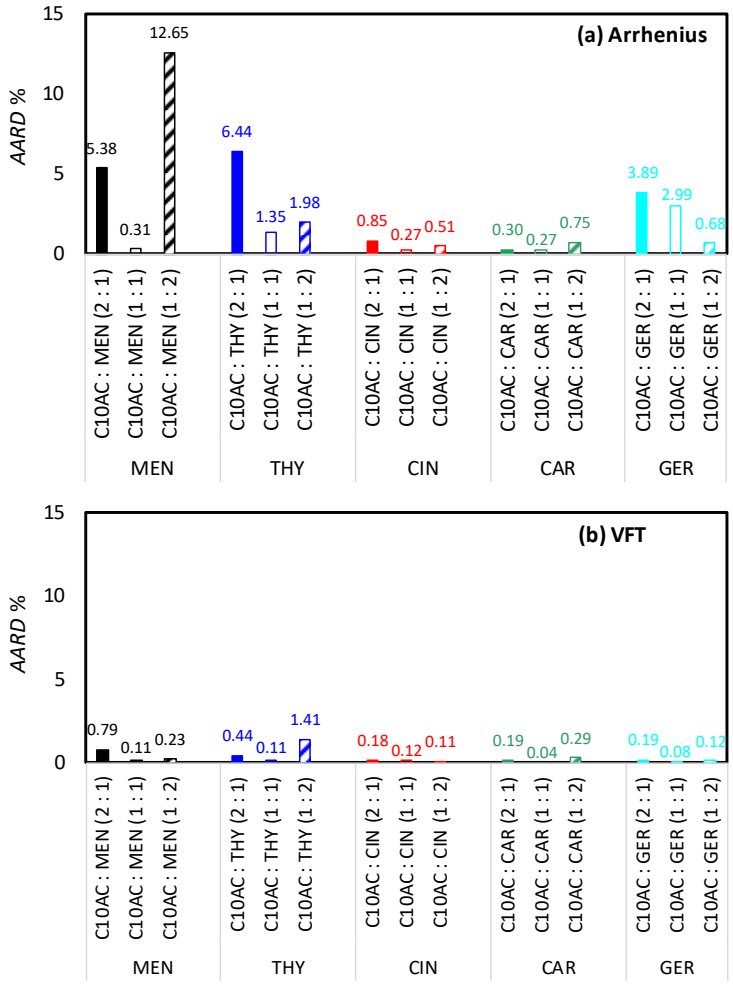
(a) Arrhenius
AARD %
15
10
5
0
5.38
0.31
12.65
6.44
1.35
1.98
0.85
0.27
0.51
0.30
0.27
0.75
3.89
2.99
0.68
C10AC : MEN (2 : 1)
C10AC : MEN (1 : 1)
C10AC : MEN (1 : 2)
C10AC : THY (2 : 1)
C10AC : THY (1 : 1)
C10AC : THY (1 : 2)
C10AC : CIN (2 : 1)
C10AC : CIN (1 : 1)
C10AC : CIN (1 : 2)
C10AC : CAR (2 : 1)
C10AC : CAR (1 : 1)
C10AC : CAR (1 : 2)
C10AC : GER (2 : 1)
C10AC : GER (1 : 1)
C10AC : GER (1 : 2)
MEN
THY
CIN
CAR
GER
(b) VFT
AARD %
15
10
5
0
0.79
0.11
0.23
0.44
0.11
1.41
0.18
0.12
0.11
0.19
0.04
0.29
0.19
0.08
0.12
C10AC : MEN (2 : 1)
C10AC : MEN (1 : 1)
C10AC : MEN (1 : 2)
C10AC : THY (2 : 1)
C10AC : THY (1 : 1)
C10AC : THY (1 : 2)
C10AC : CIN (2 : 1)
C10AC : CIN (1 : 1)
C10AC : CIN (1 : 2)
C10AC : CAR (2 : 1)
C10AC : CAR (1 : 1)
C10AC : CAR (1 : 2)
C10AC : GER (2 : 1)
C10AC : GER (1 : 1)
C10AC : GER (1 : 2)
MEN
THY
CIN
CAR
GER

Figure 8

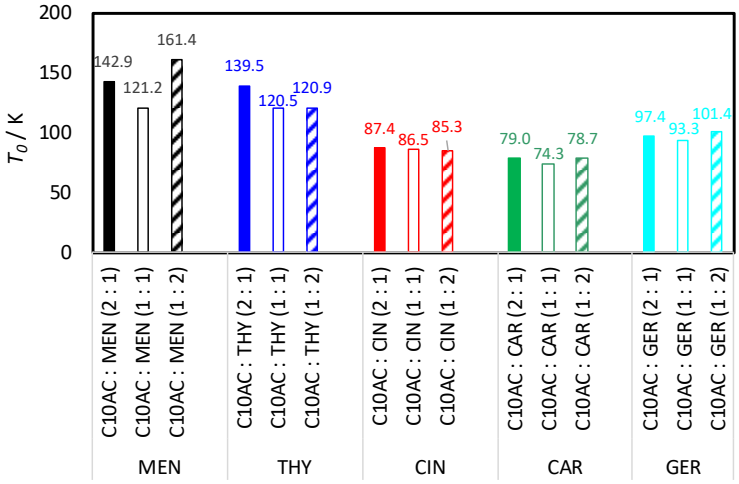
200
150
100
50
0
T_0 / K
142.9
121.2
161.4
139.5
120.5
120.9
87.4
86.5
85.3
79.0
74.3
78.7
97.4
93.3
101.4
C10AC : MEN (2 : 1)
C10AC : MEN (1 : 1)
C10AC : MEN (1 : 2)
C10AC : THY (2 : 1)
C10AC : THY (1 : 1)
C10AC : THY (1 : 2)
C10AC : CIN (2 : 1)
C10AC : CIN (1 : 1)
C10AC : CIN (1 : 2)
C10AC : CAR (2 : 1)
C10AC : CAR (1 : 1)
C10AC : CAR (1 : 2)
C10AC : GER (2 : 1)
C10AC : GER (1 : 1)
C10AC : GER (1 : 2)
MEN
THY
CIN
CAR
GER

Figure 9

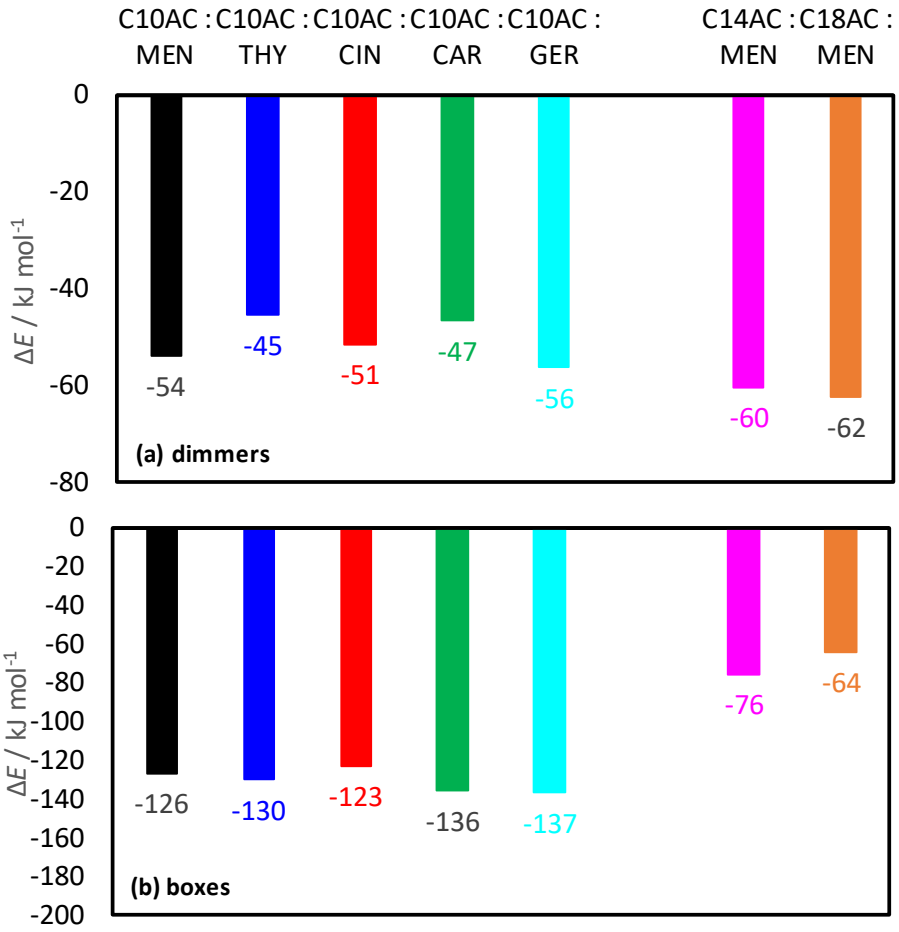
C10AC : MEN
C10AC : THY
C10AC : CIN
C10AC : CAR
C10AC : GER
C14AC : MEN
C18AC : MEN
ΔE / kJ mol-1
0
-20
-40
-60
-80
-54
-45
-51
-47
-56
-60
-62
(a) dimmers
ΔE / kJ mol-1
0
-20
-40
-60
-80
-100
-120
-140
-160
-180
-200
-126
-130
-123
-136
-137
-76
-64
(b) boxes

Figure 10

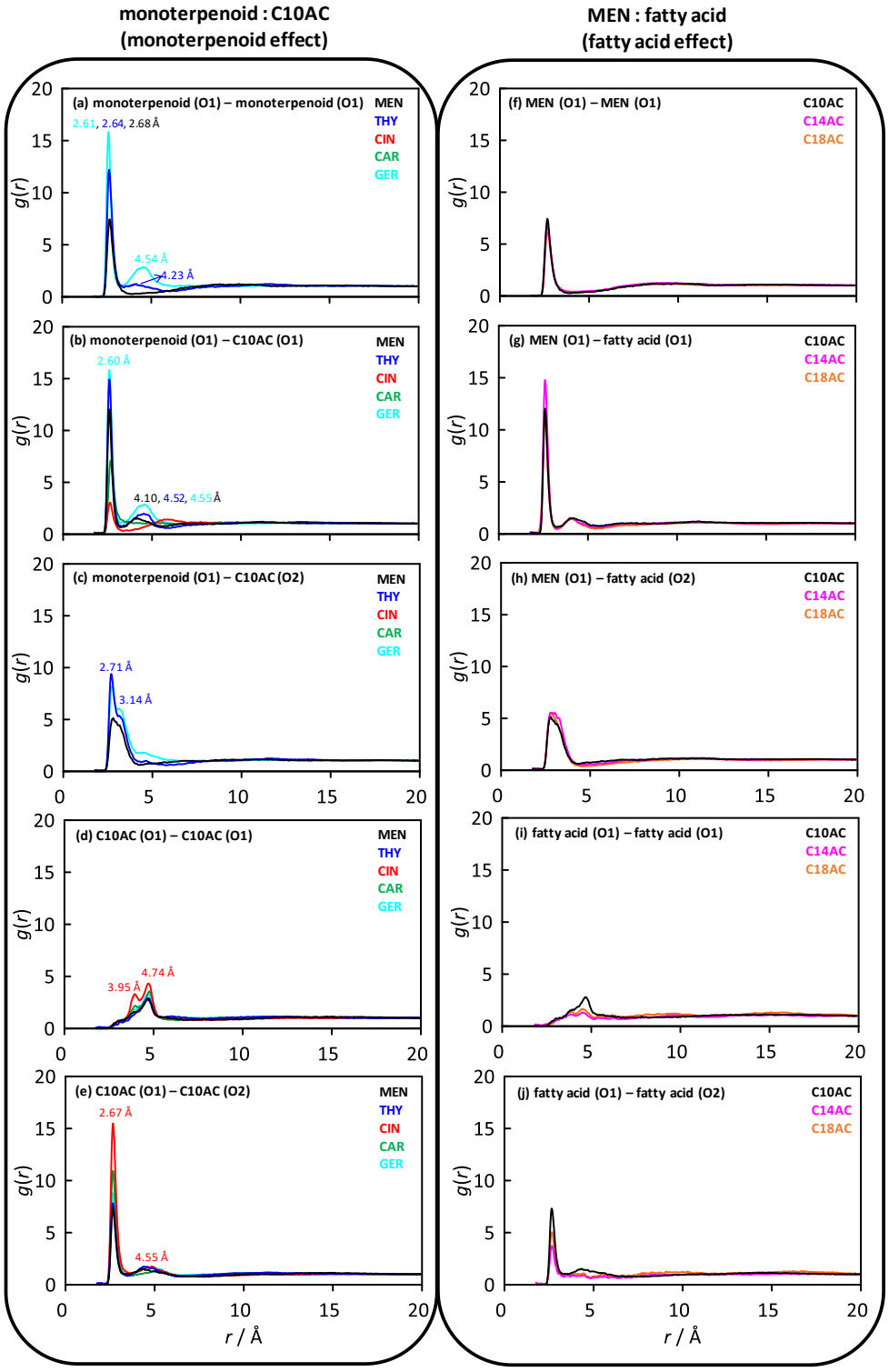
monoterpenoid : C10AC
(monoterpenoid effect)
MEN : fatty acid
(fatty acid effect)
(a) monoterpenoid (O1) – monoterpenoid (O1)
2.61, 2.64, 2.68 Å
4.54 Å
4.23 Å
(b) monoterpenoid (O1) – C10AC (O1)
2.60 Å
4.10, 4.52, 4.55 Å
(c) monoterpenoid (O1) – C10AC (O2)
2.71 Å
3.14 Å
(d) C10AC (O1) – C10AC (O1)
3.95 Å
4.74 Å
(e) C10AC (O1) – C10AC (O2)
2.67 Å
4.55 Å
(f) MEN (O1) – MEN (O1)
(g) MEN (O1) – fatty acid (O1)
(h) MEN (O1) – fatty acid (O2)
(i) fatty acid (O1) – fatty acid (O1)
(j) fatty acid (O1) – fatty acid (O2)
MEN
THY
CIN
CAR
GER
C10AC
C14AC
C18AC
g(r)
r / Å

Figure 11

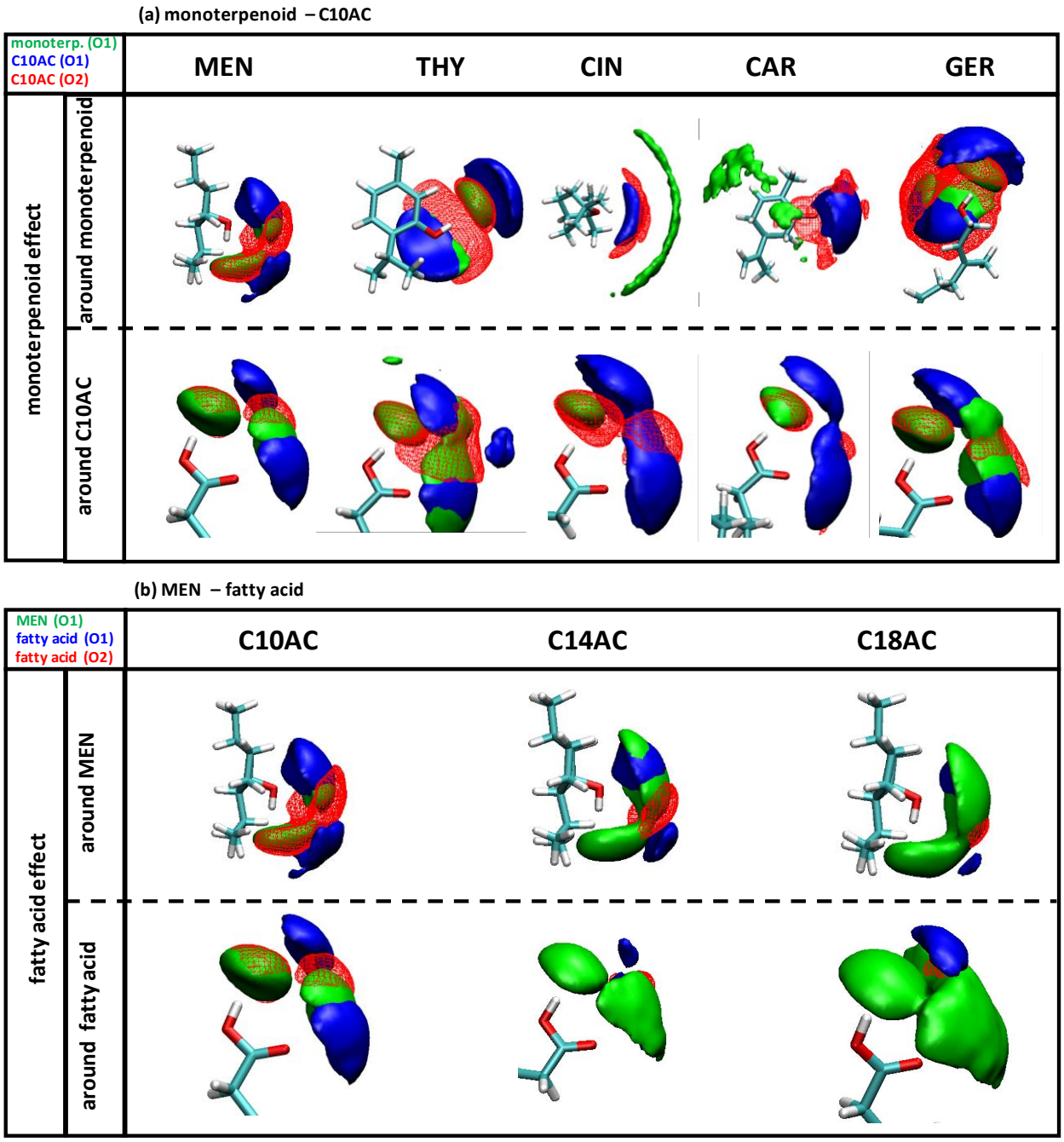
(a) monoterpenoid – C10AC
monoterp. (O1)
C10AC (O1)
C10AC (O2)
MEN
THY
CIN
CAR
GER
monoterpenoid effect
around monoterpenoid
around C10AC
(b) MEN – fatty acid
MEN (O1)
fatty acid (O1)
fatty acid (O2)
C10AC
C14AC
C18AC
fatty acid effect
around MEN
around fatty acid

Figure 12

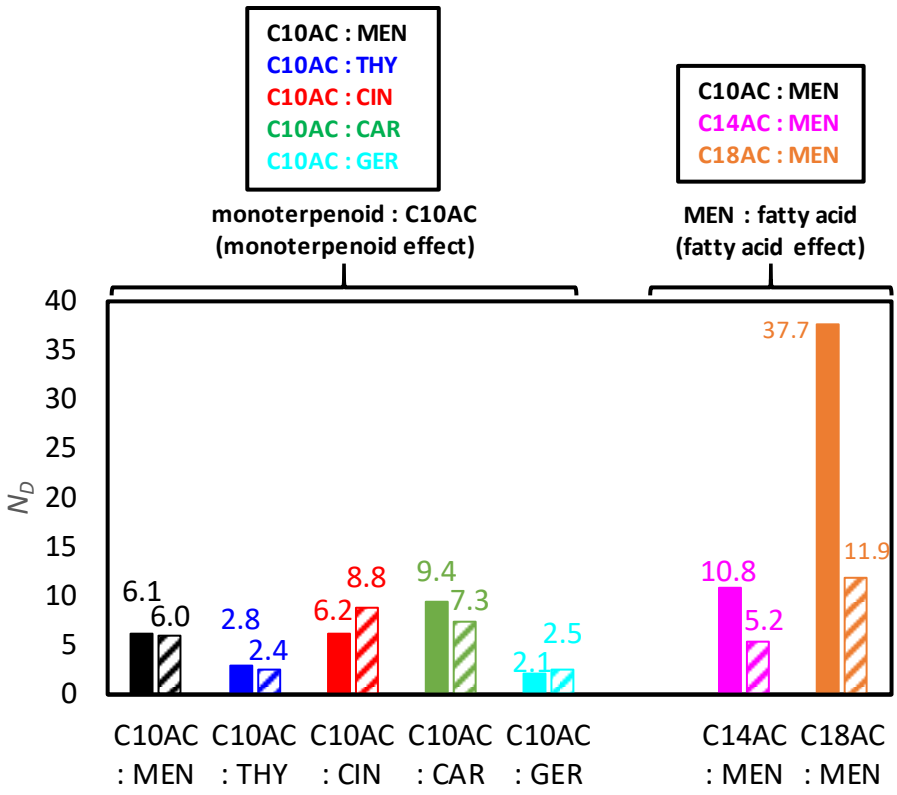
C10AC : MEN
C10AC : THY
C10AC : CIN
C10AC : CAR
C10AC : GER
C10AC : MEN
C14AC : MEN
C18AC : MEN
monoterpenoid : C10AC
(monoterpenoid effect)
MEN : fatty acid
(fatty acid effect)
N_D
40
35
30
25
20
15
10
5
0
6.1
6.0
2.8
2.4
6.2
8.8
9.4
7.3
2.1
2.5
10.8
5.2
37.7
11.9
C10AC : MEN
C10AC : THY
C10AC : CIN
C10AC : CAR
C10AC : GER
C14AC : MEN
C18AC : MEN

Figure 13

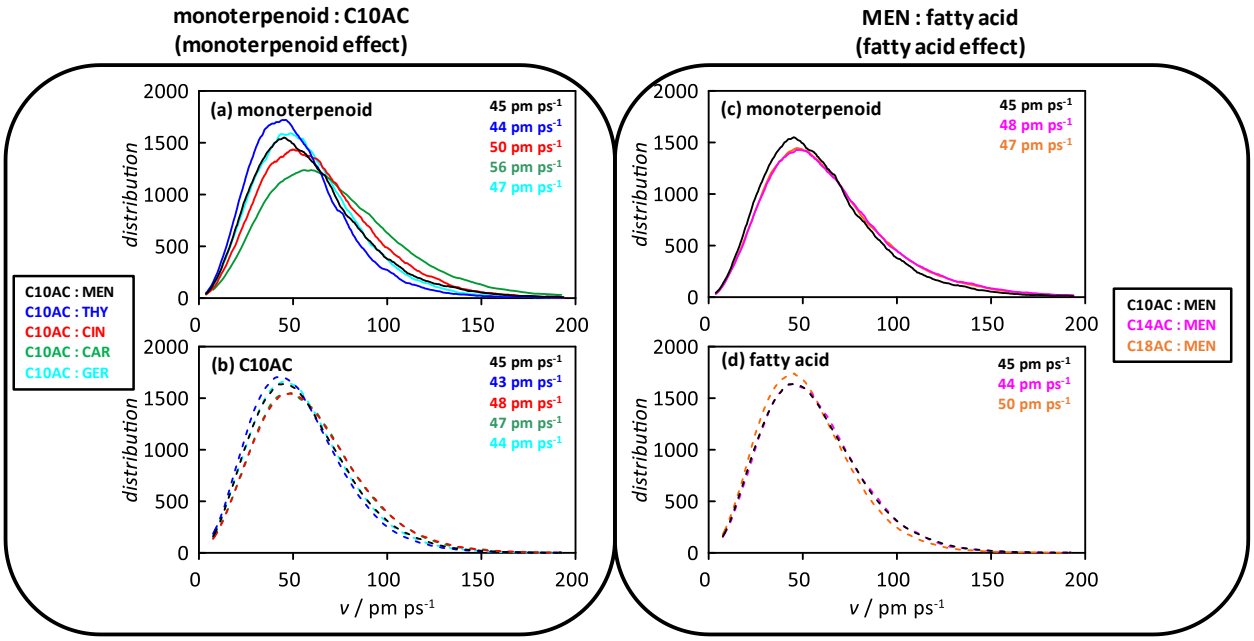
monoterpenoid : C10AC
(monoterpenoid effect)
MEN : fatty acid
(fatty acid effect)
(a) monoterpenoid
45 pm ps-1
44 pm ps-1
50 pm ps-1
56 pm ps-1
47 pm ps-1
(b) C10AC
45 pm ps-1
43 pm ps-1
48 pm ps-1
47 pm ps-1
44 pm ps-1
(c) monoterpenoid
45 pm ps-1
48 pm ps-1
47 pm ps-1
(d) fatty acid
45 pm ps-1
44 pm ps-1
50 pm ps-1
C10AC : MEN
C10AC : THY
C10AC : CIN
C10AC : CAR
C10AC : GER
C10AC : MEN
C14AC : MEN
C18AC : MEN
distribution
v / pm ps-1
0
500
1000
1500
2000
0
50
100
150
200

Figure 14

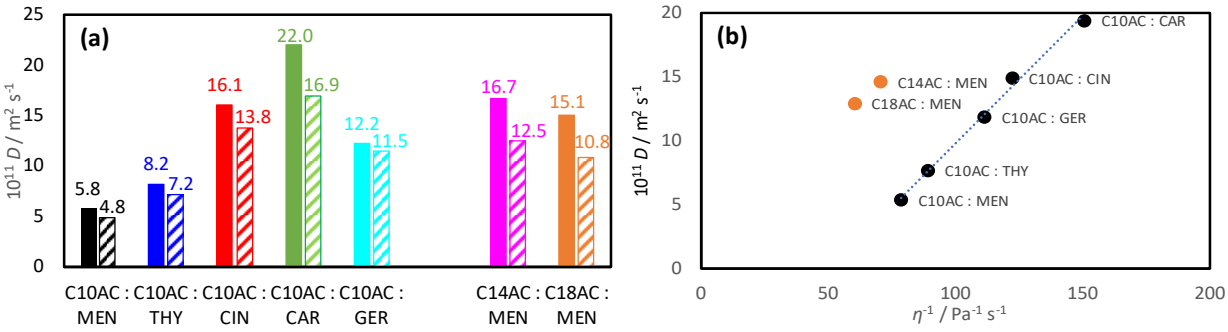
(a)
$10^{11}\,D$ / m^2 s^{-1}
25
20
15
10
5
0
5.8
4.8
8.2
7.2
16.1
13.8
22.0
16.9
12.2
11.5
16.7
12.5
15.1
10.8
C10AC : MEN
C10AC : THY
C10AC : CIN
C10AC : CAR
C10AC : GER
C14AC : MEN
C18AC : MEN
(b)
$10^{11}\,D$ / m^2 s^{-1}
20
15
10
5
0
C10AC : CAR
C14AC : MEN
C10AC : CIN
C18AC : MEN
C10AC : GER
C10AC : THY
C10AC : MEN
0
50
100
150
200
η^{-1} / Pa^{-1} s^{-1}

Figure 15

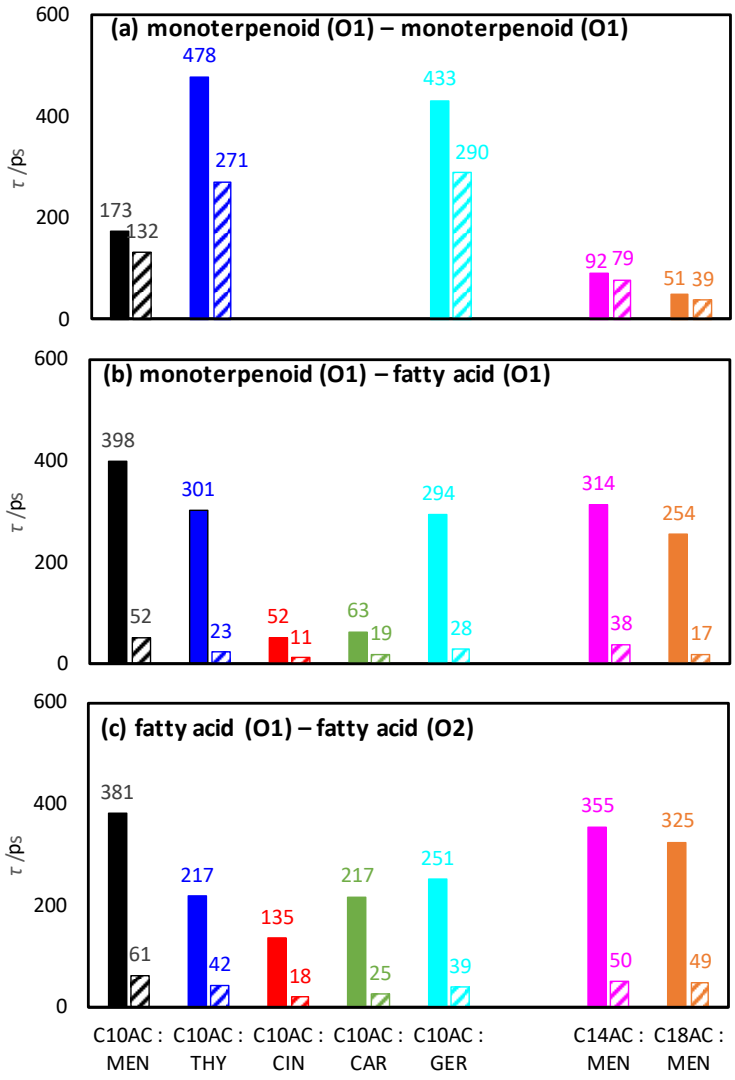
(a) monoterpenoid (O1) – monoterpenoid (O1)
(b) monoterpenoid (O1) – fatty acid (O1)
(c) fatty acid (O1) – fatty acid (O2)
τ /ps
600
400
200
0
173
132
478
271
433
290
92
79
51
39
398
52
301
23
52
11
63
19
294
28
314
38
254
17
381
61
217
42
135
18
217
25
251
39
355
50
325
49
C10AC : MEN
C10AC : THY
C10AC : CIN
C10AC : CAR
C10AC : GER
C14AC : MEN
C18AC : MEN

Figure 16

References

[1] Paiva, A., Craveiro, R., Aroso, I., Martins, M., Reis, R. L., & Duarte, A. R. C., Natural deep eutectic solvents - Solvents for the 21st century. In ACS Sustainable Chemistry and Engineering, American Chemical Society, 2014, Vol. 2, Issue 5, pp. 1063–1071.

[2] Abbott, A. P., Capper, G., Davies, D. L., Rasheed, R. K., & Tambyrajah, V., Novel solvent properties of choline chloride/urea mixtures. Chemical Communications, 2003, 1, 70–71.

[3] Y. Chen, Z. Yu, Low-melting mixture solvents: extension of deep eutectic solvents and ionic liquids for broadening green solvents and green chemistry, Green Chem. Eng. 5 (2024) 409-417.

[4] El Achar, T., Greige-Gerges, H., & Fourmentin, S., Basics and properties of deep eutectic solvents: a review. In Environmental Chemistry Letters Springer Science and Business Media Deutschland GmbH, 2021, Vol. 19, Issue 4, pp. 3397–3408.

[5] Perna, F. M., Vitale, P., & Capriati, V., Deep eutectic solvents and their applications as green solvents. In Current Opinion in Green and Sustainable Chemistry, Elsevier B.V., 2020, Vol. 21, pp. 27–33.

[6] Hansen, B. B., Spittle, S., Chen, B., Poe, D., Zhang, Y., Klein, J. M., Horton, A., Adhikari, L., Zelovich, T., Doherty, B. W., Gurkan, B., Maginn, E. J., Ragauskas, A., Dadmun, M., Zawodzinski, T. A., Baker, G. A., Tuckerman, M. E., Savinell, R. F., & Sangoro, J. R., Deep Eutectic Solvents: A Review of Fundamentals and Applications. In Chemical Reviews, . American Chemical Society, 2021, Vol. 121, Issue 3, pp. 1232–1285.

[7] K. Yuan, F. Li, L. Peng, X. Zhao, H. Song, Separation of 1,8-Cineole and terpenes by Liquid-liquid extraction with green alkanediols, J. Mol. Liq., 2022, 350.

[8] Gunny, A. A. N.; Arbain, D.; Nashef, E. M.; Jamal, P. Applicability Evaluation of Deep Eutectic Solvents-cellulase System for Lignocellulose Hydrolysis. Bioresour. Technol. 2015, 181, 297− 302.

[9] Maletta, A., Gutiérrez, A., Jian Tan, P., Springstead, J., Aparicio, S., & Atilhan, M. Separation of phenolic compounds from water by using monoterpenoid and fatty acid based hydrophobic deep eutectic solvents. Journal of Molecular Liquids, 2023, 381.

[10] Dai, Y. T.; Witkamp, G. J.; Verpoorte, R.; Choi, Y. H. Natural deep eutectic solvents as a new extraction media for phenolic metabolites in Carthamus tinctorius L. Anal. Chem. 2013, 85, 6272− 6278.

[11] Gotor-Fernández V, Paul CE: Deep eutectic solvents for redox biocatalysis. J. Biotechnol. 2019, 293:24–35.

[12] Alvarez, M.S., Zhang, Y. Sketching neoteric solvents for boosting drugs bioavailability. J. Contr. Release. 2019, 311–312, 225–232.

[13] Martins, M. A. R., Pinho, S. P., & Coutinho, J. A. P., Insights into the Nature of Eutectic and Deep Eutectic Mixtures. Journal of Solution Chemistry, 2019, 48(7), 962–982.

[14] D.O. Abranches, J.A.P. Coutinho, Everything You Wanted to Know about Deep Eutectic Solvents but Were Afraid to Be Told, Ann. Rev. Chem. Biochem. Eng. 14 (2023) 141-163.

[15] Van Osch, D. J. G. P., Dietz, C. H. J. T., Van Spronsen, J., Kroon, M. C., Gallucci, F., Van Sint Annaland, M., & Tuinier, R., A Search for Natural Hydrophobic Deep Eutectic Solvents Based on Natural Components. ACS Sustainable Chemistry and Engineering, 2019, 7(3), 2933–2942.

[16] Y. Liu, J.B. Friesen, J.B. McAlpine, D.C. Lankin, S.N. Chen, G.F. Pauli, Natural Deep Eutectic Solvents: Properties, Applications, and Perspectives, J. Nat. Prod. 81 (2018) 679-690.

[17] P Satija, A. Chambyal, G. Singh, G. Singh, S. Devi, J. Singh, Natural Deep Eutectic Solvents (NADES): Manufacture, Characteristics, and Their Significance as Designer Solvents, Chem. Sel. 9 (2024) DOI: 10.1002/slct.202401212

[18] R. Ninayan, A.S. Levshakova, E.M. Khairulina, O.S. Veza, I.I. Tumkin, A. Ostendorf, L.S. Lagunov, A.A. Manshina, A.Y. Shishov, Water-induced changes in choline chloride-carboxylic acid deep eutectic solvents properties Coll. Surf. A 679 (2023) 135243.

[19] M.N. Nolasco, S.N. Pedro, C. Vilela, P.D. Vaz, P. Ribeiro-Claro, S. Rudic, S.F. Parker, C.S.R. Freire, M.G. Freire, A.J.D Silvestre, Front. Phys. 10 (2022) DOI: 10.3389/fphy.2022.834571

[20] M. Marchel, M.P. Rayaroth, C. Wang, L. Kong, J.A. Khan, G. Baczkaj, Hydrophobic (deep) eutectic solvents (HDESs) as extractants for removal of pollutants from water and wastewater – A review, Chem. Eng. J. 475 (2023) 144971.

[21] D.J.G.P. van Osch, C.H.J.T. Dietz, S.E.E. Warrag, M.C. Kroon, The Curious Case of Hydrophobic Deep Eutectic Solvents: A Story on the Discovery, Design, and Applications, ACS Sustainable Chem. 8 (2020) 10591-10612.

[22] Ribeiro, B. D.; Florindo, C.; Iff, L. C.; Coelho, M. A.; Marrucho, I. M. Menthol-Based Eutectic Mixtures: Hydrophobic Low Viscosity Solvents. ACS Sustain. Chem. Eng. 2015, 3, 2469−2477.
[23] Rozas, S., Zamora, L., Benito, C., Atilhan, M., & Aparicio, S., A study on monoterpenoid-based natural deep eutectic solvents. Green Chemical Engineering, 2023, 4(1), 99–114.
[24] Deepika, Juneja, S., & Pandey, S. Water Miscibility, Surface Tension, Density, and Dynamic Viscosity of Hydrophobic Deep Eutectic Solvents Composed of Capric Acid, Menthol, and Thymol. Journal of Chemical and Engineering Data, 2022, 67(11), 3400–3413.
[25] Al-Bodour, A., Alomari, N., Gutiérrez, A., Aparicio, S., & Atilhan, M., Exploring the thermophysical properties of natural deep eutectic solvents for gas capture applications: A comprehensive review. In Green Chemical Engineering. KeAi Communications Co., 2021.
[26] L. Fortunato, L. Al-Fuhaid, S. Murgolo, C. De Ceglie, G. Mascalo, L. Flivene, J.S. Vrouwenvelder, G.J. Witkamp, A. Farinha, Removal of polyfluoroalkyl substances (PFAS) from water using hydrophobic natural deep eutectic solvents (NADES): A proof of concept study, J. Water Proc. Eng. 56 (2023) 104401.
[27] Florindo, C., Lima, F., Ribeiro, B. D., & Marrucho, I. M. Deep eutectic solvents: overcoming 21st century challenges. In Current Opinion in Green and Sustainable Chemistry. Elsevier B.V.2019, Vol. 18, pp. 31–36.
[28] K. Kongpol, P. Chaiao, P. Shuapan, P. Kongduk, W. Chunglok, G. Yusakul, Therapeutic hydrophobic deep eutectic solvents of menthol and fatty acid for enhancing anti-inflammation effects of curcuminoids and curcumin on RAW264.7 murine macrophage cells, RSC Adv. 12 (2022) 17443–17453.
[29] Ribeiro, B. D.; Florindo, C.; Iff, L. C.; Coelho, M. A.; Marrucho, I. M. Menthol-Based Eutectic Mixtures: Hydrophobic Low Viscosity Solvents. ACS Sustain. Chem. Eng. 2015, 3, 2469−2477.
[30] C. Steffen, K. Thomas, U. Huniar, A. Hellweg, O. Rubner, A. Schroer, TmoleX – A graphical user interface for TURBOMOLE, J. Comput. Chem. 31 (2010) 2967-2970.
[31] BIOVIA COSMOtherm, Release 2021; Dassault Systèmes. http://www.3ds.com
[32] S. Jakobtorwihen, T. ingram, I. Smirnova, Combination of COSMOmic and molecular dynamics simulations for the calculation of membrane–water partition coefficients, J. Comput. Chem. 34 (2013) 1332-1340.
[33] J.A.H. Schwöbel, A. Ebert, K. Bittermann, K.U. Goss, A. Klamt, COSMOperm: Mechanistic Prediction of Passive Membrane Permeability for Neutral Compounds and Ions and Its pH Dependence, J. Phys. Chem. B. 2020, 124, 3343-3354.
[34] B. Hourahine, B. Aradi, V. Blum,F. Bonafé, A. Buccheri, C. Camacho, C. Cevallos, M. Y. Deshaye, T. Dumitrică, A. Dominguez, S. Ehlert, M. Elstner, T. van der Heide, J. Hermann, S. Irle, J. J. Kranz, C. Köhler, T. Kowalczyk, T. Kubař, I. S. Lee, V. Lutsker, R. J. Maurer, S. K. Min, I. Mitchell, C. Negre, T. A. Niehaus, A. M. N. Niklasson, A. J. Page, A. Pecchia, G. Penazzi, M. P. Persson, J. Řezáč, C. G. Sánchez, M. Sternberg; M. Stöhr, F. Stuckenberg, A. Tkatchenko, V. W.-z. Yu, T. Frauenheim, DFTB+, a software package for efficient approximate density functional theory based atomistic simulations, J. Chem. Phys. 152 (2020) 124101.
[35] M. Gaus, A. Goez, and M. Elstner, Parametrization and benchmark of DFTB3 for organic molecules, J. Chem. Theory Comput. 9 (2013) 338–354.
[36] M. Kubillus, T. Kubař, M. Gaus, J. Řezáč, and M. Elstner, Parameterization of the DFTB3 method for Br, Ca, Cl, F, I, K, and Na in organic and biological systems, J. Chem. Theory Comput. 11 (2015) 332–342.
[37] BIOVIA, Dassault Systèmes, BIOVIA Amorphous Cell, Release 2022 (22.1.0.3462), San Diego: Dassault Systèmes, 2022.
[38] BIOVIA, Dassault Systèmes, BIOVIA Forcite, Release 2022 (22.1.0.3462), San Diego: Dassault Systèmes, 2022.
[39] R.L.C. Akkermans, N.A. Spenley, S.H. Robertson, COMPASS III: automated fitting workflows and extension to ionic liquids, Mol. Sim. 47 (2021) 540-551.
[40] W. G. Hoover, Canonical dynamics: Equilibrium phase-space distributions, Phys. Rev. A 31 (1985) 1695.
[41] M. Parrinello, A. Rahman, Polymorphic Transitions in Single Crystals: A New Molecular Dynamics Method, J. Appl. Phys. 52 (1981) 7182-7190.
[42] U.L. Essmann, M.L. Perera, T. Berkowitz, H. Darden, H. Lee, L.G. Pedersen, A smooth particle mesh Ewald method, J. Chem. Phys. 103 (1995) 8577-8593.
[43] M. Waldman, A. T. Hagler, New combining rules for rare-gas Van der-Waals parameters, J. Comput. Chem. 14 (1993) 1077-1084.
[44] W. Humphrey, A. Dalke, K. Schulten, VMD - Visual Molecular Dynamics, J. Molec. Graphics 14 (1996) 33-38.
[45] M. Brehm, B. KirchneR. TRAVIS - A free analyzer and visualizer for Monte Carlo and Molecular Dynamics trajectories. J. Chem. Inf. Model. 51 (2011) 2007-2023.

[46] J.L. Trenzado, C. Benito, M. Atilhan, S. Aparicio, Hydrophobic Deep eutectic Solvents based on cineole and organic acids, Journal of Molecular Liquids 377 (2023) 121322.
[47] Collaborative Adverse Outcome Pathway Wiki (AOP-Wiki) . Version 2.7. OECD. https://aopwiki.org/events Accesed September 30, 2024.

5.2.2.1. Información experimental V

Tabla 23. Densidad experimental, ρ (g cm-3), y viscosidad dinámica, η (mPa s), para los NADES (HBA + HBD) descritos en las relaciones molares consideradas (i : j) en función de la temperatura, T. Los sistemas indicados con (-) se prepararon pero no formaron NADES líquidos a las temperaturas indicadas.

		T / K						
		283.15	288.15	293.15	298.15	303.15	308.15	313.15
		ρ / g cm^{-3}						
C10AC : THY	2:1	0.941292	0.937438	0.93358	0.929728	0.925871	0.92201	0.91814
	1:1	-	-	0.92184	0.918002	0.914156	0.91030	0.90646
	1:2	0.954059	0.950208	0.94634	0.942485	0.938621	0.93475	0.93087
C10AC : MEN	2:1	0.907204	0.903557	0.89989	0.896228	0.892557	0.88887	0.88517
	1:1	-	-	0.89987	0.896165	0.89245	0.88873	0.88500
	1:2	0.906839	0.903232	0.89960	0.895969	0.892322	0.88866	0.88498
C10AC : GER	2:1	-	0.894664	0.89094	0.887234	0.883521	0.87980	0.87608
	1:1	-	-	-	0.890486	0.886535	0.88280	0.87906
	1:2	0.895310	0.891638	0.88795	0.884275	0.880589	0.87689	0.87319
C10AC : CIN	2:1	0.923793	0.919844	0.91587	0.911886	0.907951	0.90407	0.90012
	1:1	-	-	0.91028	0.906426	0.902551	0.89867	0.89480
	1:2	0.928462	0.924413	0.92036	0.916315	0.91227	0.90822	0.90417
C10AC : CAR	2:1	-	0.932191	0.92832	0.924460	0.920608	0.91675	0.91290
	1:1	-	-	-	0.914437	0.910597	0.90676	0.90293
	1:2	0.947118	0.94322	0.93931	0.935428	0.931537	0.92764	0.92376
		η / mPa s						
C10AC : THY	2:1	-	19.566	15.303	12.145	9.830	8.134	6.777
	1:1	-	-	-	11.235	9.309	7.798	6.615
	1:2	-	-	-	-	-	8.265	6.786
C10AC : MEN	2:1	-	27.568	20.505	16.062	12.825	10.390	8.550
	1:1	-	-	-	12.755	10.506	8.763	7.396
	1:2	54.708	38.680	28.207	21.085	16.146	12.614	10.047
C10AC : GER	2:1	-	12.407	10.329	8.699	7.406	6.361	5.511
	1:1	-	-	-	8.988	7.667	6.598	5.726
	1:2	14.301	11.737	9.766	8.215	6.981	5.983	5.177
C10AC : CIN	2:1	12.032	10.017	8.442	7.218	6.210	5.388	4.725
	1:1	-	-	9.591	8.186	7.027	6.083	5.323
	1:2	9.582	8.057	6.857	5.900	5.104	4.452	3.918
C10AC : CAR	2:1	-	-	6.482	5.590	4.865	4.270	3.778
	1:1	-	-	-	6.647	5.782	5.068	4.466
	1:2	7.257	6.147	5.260	4.558	3.985	3.517	3.127

Tabla 24. Continuación.

		T / K						
		283.15	288.15	293.15	298.15	303.15	308.15	313.15
		ρ / g cm^{-3}						
C14AC : THY	1:1	-	-	-	-	-	-	-
	1:2	-	-	-	-	-	-	-
	1:4	-	-	-	-	-	-	-
	1:6	-	-	-	-	-	-	-
	1:8	-	-	-	-	-	-	-
	1:10	-	-	-	-	-	-	-
C14AC : MEN	1:1	-	-	-	-	-	-	-
	1:2	-	-	-	-	-	-	-
	1:4	-	-	-	-	0.888475	0.88488	0.88127
	1:6	-	-	0.89637	0.891596	0.888852	0.88542	0.88187
	1:8	0.903698	0.900198	0.89665	0.893091	0.889509	0.88590	0.88227
	1:10	0.903823	0.900329	0.89679	0.893233	0.889650	0.88604	0.88240
C14AC : GER	1:1	-	-	-	-	-	-	-
	1:2	-	-	-	-	-	-	-
	1:4	-	-	-	-	0.875049	0.87142	0.86779
	1:6	-	0.896120	0.88715	0.879502	0.874945	0.87130	0.86766
	1:8	0.893795	0.890043	0.88281	0.878161	0.874472	0.87084	0.86720
	1:10	0.889204	0.885603	0.88199	0.878375	0.874751	0.87111	0.86745
C14AC : CIN	1:1	-	-	-	-	-	-	-
	1:2	-	-	-	-	-	-	-
	1:4	-	-	-	0.913470	0.909466	0.90546	0.90145
	1:6	0.928128	0.924056	0.91998	0.915909	0.911839	0.90776	0.90368
	1:8	0.929759	0.925693	0.92159	0.917497	0.913389	0.90927	0.90514
	1:10	0.930283	0.926146	0.92200	0.917858	0.913713	0.90956	0.90541
C14AC : CAR	1:1	-	-	-	-	-	-	-
	1:2	-	-	-	-	-	-	-
	1:4	-	-	-	-	-	-	-
	1:6	-	-	-	-	-	-	-
	1:8	0.973919	0.966654	0.95777	0.947982	0.942542	0.93865	0.93475
	1:10	-	0.965870	0.95693	0.948809	0.944885	0.94097	0.93706
		η / mPa s						
C14AC : THY	1:1	-	-	-	-	-	-	-
	1:2	-	-	-	-	-	-	-
	1:4	-	-	-	-	-	-	-
	1:6	-	-	-	-	-	-	-
	1:8	-	-	-	-	-	-	-
	1:10	-	-	-	-	-	-	-
C14AC : MEN	1:1	-	-	-	-	-	-	-
	1:2	-	-	-	-	-	-	-
	1:4	-	-	-	-	24.880	18.591	14.239
	1:6	-	-	53.358	36.686	26.191	19.198	14.459
	1:8	-	40.448	65.194	44.557	31.114	22.603	16.904
	1:10	-	-	62.054	41.400	28.727	20.617	15.217

Tabla 25. Continuación.

		T / K						
		283.15	288.15	293.15	298.15	303.15	308.15	313.15
		ρ / g cm^{-3}						
C14AC : GER	1:1	-	-	-	-	-	-	-
	1:2	-	-	-	-	-	-	-
	1:4	-	-	-	-	7.969	6.806	5.859
	1:6	-	-	7.171	8.629	7.291	6.226	5.358
	1:8	-	-	11.204	9.379	7.978	6.847	5.925
	1:10	-	-	9.662	8.087	6.845	5.850	5.041
C14AC : CIN	1:1	-	-	-	-	-	-	-
	1:2	-	-	-	-	-	-	-
	1:4	-	-	-	6.120	5.314	4.646	4.097
	1:6	-	6.648	6.116	5.355	4.384	4.116	3.649
	1:8	7.380	6.359	5.529	4.843	4.273	3.798	3.397
	1:10	6.201	5.333	4.632	4.058	3.577	3.174	2.834
C14AC : CAR	1:1	-	-	-	-	-	-	-
	1:2	-	-	-	-	-	-	-
	1:4	-	-	-	-	-	-	-
	1:6	-	-	-	-	-	-	-
	1:8	-	-	-	4.047	3.473	3.101	2.785
	1:10	-	-	-	3.627	3.191	2.831	2.535
		ρ / g cm^{-3}						
C18AC : THY	1:1	-	-	-	-	-	-	-
	1:2	-	-	-	-	-	-	-
	1:4	-	-	-	-	-	-	-
	1:6	-	-	-	-	-	-	-
	1:8	-	-	-	-	-	-	-
	1:10	-	-	-	-	-	-	-
C18AC : MEN	1:1	-	-	-	-	-	-	-
	1:2	-	-	-	-	-	-	-
	1:4	-	-	-	-	-	-	-
	1:6	-	-	-	-	-	-	-
	1:8	-	-	-	-	0.897362	0.88619	0.88045
	1:10	-	-	-	0.899183	0.893260	0.88473	0.88094
C18AC : GER	1:1	-	-	-	-	-	-	-
	1:2	-	-	-	-	-	-	-
	1:4	-	-	-	-	-	-	-
	1:6	-	-	-	-	-	-	-
	1:8	-	-	-	-	-	-	-
	1:10	-	-	-	-	-	-	-
9C18AC : CIN	1:1	-	-	-	-	-	-	-
	1:2	-	-	-	-	-	-	-
	1:4	-	-	-	-	-	-	-
	1:6	-	-	-	-	-	-	-
	1:8	-	-	-	-	0.914161	0.90567	0.90161
	1:10	-	-	-	0.921974	0.911830	0.90665	0.90259

Tabla 26. Continuación.

		T / K						
		283.15	288.15	293.15	298.15	303.15	308.15	313.15
		ρ / g cm^{-3}						
C18AC : CAR	1:1	-	-	-	-	-	-	-
	1:2	-	-	-	-	-	-	-
	1:4	-	-	-	-	-	-	-
	1:6	-	-	-	-	-	-	-
	1:8	-	-	-	-	-	-	-
	1:10	-	-	-	-	-	-	-
		η / mPa s						
C14AC : THY	1:1	-	-	-	-	-	-	-
	1:2	-	-	-	-	-	-	-
	1:4	-	-	-	-	-	-	-
	1:6	-	-	-	-	-	-	-
	1:8	-	-	-	-	-	-	-
	1:10	-	-	-	-	-	-	-
C14AC : MEN	1:1	-	-	-	-	-	-	-
	1:2	-	-	-	-	-	-	-
	1:4	-	-	-	-	-	-	-
	1:6	-	-	-	-	-	-	-
	1:8	-	-	-	-	-	-	16.686
	1:10	-	-	-	-	-	22.496	16.624
C14AC : GER	1:1	-	-	-	-	-	-	-
	1:2	-	-	-	-	-	-	-
	1:4	-	-	-	-	-	-	-
	1:6	-	-	-	-	-	-	-
	1:8	-	-	-	-	-	-	-
	1:10	-	-	-	-	-	-	-
C14AC : CIN	1:1	-	-	-	-	-	-	-
	1:2	-	-	-	-	-	-	-
	1:4	-	-	-	-	-	-	-
	1:6	-	-	-	-	-	-	-
	1:8	-	-	-	-	-	4.136	3.667
	1:10	-	-	-	-	-	4.970	3.340
C14AC : CAR	1:1	-	-	-	-	-	-	-
	1:2	-	-	-	-	-	-	-
	1:4	-	-	-	-	-	-	-
	1:6	-	-	-	-	-	-	-
	1:8	-	-	-	-	-	-	-
	1:10	-	-	-	-	-	-	-

Capítulo 6
Conclusiones y líneas futuras

6.1. Conclusiones

Se han analizado las propiedades macroscópicas y nanoscópicas de diversos DSILs y NADES, empleando métodos experimentales y computacionales con el fin de inferir la relación entre su comportamiento observable, su estructura y las fuerzas intermoleculares existentes. El desarrollo de esta investigación ha demostrado la relevancia de profundizar en la comprensión de las interacciones moleculares, con el objetivo de mejorar la modelización de estos disolventes para abordar de manera óptima la resolución de problemas de índole industrial, energético, médico o medioambiental.

Las principales conclusiones derivadas del trabajo llevado a cabo en esta Tesis Doctoral se pueden resumir en los siguientes puntos:

- Se han determinado las densidades (ρ) de los DSIL [EMIM][BF_4]+[EMIM][$EtSO_4$], [EMIM][BF_4]+[EMIM][$MeSO_3$] y [EMIM][$EtSO_4$]+[EMIM][$MeSO_3$] haciendo uso de un densímetro digital basado en el principio de oscilación mecánica de tubo vibrante, para todo el intervalo de composiciones a las temperaturas 283.15, 288.15, 293.15, 298.15, 303.15, 308.15 y 313.15 K a presión atmosférica. A partir de los valores de densidad obtenidos, en conjunto con la fracción molar de cada mezcla y las propiedades de los componentes puros, se calcularon también los volúmenes molares de exceso (V^E), los volúmenes parciales molares de exceso ($\bar{V}_i^E$) y a dilución infinita ($V_\infty^{\bar{E}}$).

- Para los mismos DSIL en las mismas condiciones anteriormente citadas, se han medido experimentalmente las viscosidades cinemáticas (υ) mediante la utilización de un microviscosímetro capilar Ubbelohde con detección optoelectrónica. Los resultados experimentales obtenidos, combinados con los valores de densidad para las mismas fracciones molares, se han utilizado para obtener los valores de viscosidad dinámica (η) y de desviación de la viscosidad $(\Delta\eta)$.

- Se han aplicado diversas correlaciones y modelos para establecer relaciones entre algunos de los parámetros obtenidos. Se han correlacionado los datos de fracción molar tanto con el volumen molar de exceso, como con la desviación de la viscosidad, haciendo uso de la ecuación de Redlich y Kister. Se ha empleado la ecuación de Vogel – Fulcher – Tamman (VFT) para realizar el ajuste de la viscosidad, dado que en ningún caso se ajustaba al modelo de Arrhenius. Asimismo, se ha utilizado la teoría de Prigogine – Flory – Patterson (PFP) para el análisis y la predicción del volumen molar de exceso.

- El análisis de las propiedades termofísicas de las mezclas binarias utilizadas en este estudio pone de manifiesto:

    - Se observan diversos patrones de comportamiento en función de la combinación de aniones, aunque en general la relación entre la densidad y la composición no se

comporta de manera ideal ni lineal. Esto indica que no se produce una simple sustitución de aniones, sino que la presencia de diferentes aniones genera efectos complejos debido a la variación de las fuerzas intermoleculares. Los sistemas que contienen [EMIM][$MeSO_3$] presentan un comportamiento volumétrico más complejo, con valores negativos de volúmenes molares de exceso para ciertas fracciones molares. Este comportamiento indica mayor grado de empaquetamiento, probablemente relacionado con la contribución de las fuerzas intermoleculares de este anión. Los coeficientes de expansión térmica isobáricos obtenidos para estos DSIL coinciden que se trata de mezclas con menor grado de compresibilidad.

- Los DSIL analizados en este estudio exhiben un comportamiento no ideal similar de la evolución de la viscosidad en función de la composición. Todos ellos muestran valores negativos de la desviación de la viscosidad en todo el intervalo de composiciones, alcanzando mínimos en zonas próximas a la fracción equimolar y disminuyendo su valor absoluto a medida que aumenta la temperatura. Este comportamiento indica una posible reducción de la superficie disponible para fricción o debilitamiento de las fuerzas intermoleculares. En ILs que contienen el catión $[EMIM]^+$ es habitual encontrar valores negativos de la desviación de la viscosidad. Por otra parte, es posible observar que el orden de magnitud es considerablemente mayor para las mezclas que contienen [EMIM][$MeSO_3$], lo que sugiere mayores efectos disruptivos en comparación con otros aniones estudiados en este trabajo.

- En los DSIL mencionados, se llevó a cabo un estudio exhaustivo de las interacciones moleculares a nivel atómico mediante cálculos DFT y métodos de simulación MD. Los cálculos DFT permitieron el análisis de la naturaleza y la magnitud de las fuerzas intermoleculares, en especial de los enlaces de hidrógeno, considerando diferentes modelos de agrupaciones moleculares. Por otro lado, las simulaciones MD ofrecieron una comprensión más profunda de los efectos considerando sistemas mayores tales como las interacciones de largo alcance, la distribución y el empaquetamiento molecular, así como la evolución dinámica de las trayectorias.

  - Los resultados obtenidos a partir de los cálculos DFT evidencian que sin importar el tamaño del sistema (dímeros, trímeros o tetrámeros) o la naturaleza de los aniones estudiados, el enlace de hidrógeno se produce preferentemente a través del sitio CH1 del $[EMIM]^+$ (situado entre los átomos de N del catión) con ambos aniones compitiendo por estas interacciones. La energía de interacción muestra variaciones en función del tamaño del sistema, generalmente alcanzando valores más altos en los tetrámeros, lo que sugiere la presencia de efectos cooperativos en clústeres de

mayor tamaño, donde podrían formarse enlaces de hidrógeno adicionales o intensificarse interacciones débiles, como las fuerzas de Van der Waals.

- Las simulaciones MD evidenciaron interacciones significativas catión-anión en los sitios CH1 y CH4-5 del $[EMIM]^+$, destacando el mecanismo de sustitución anión-catión como el prevalente. Las SDF confirmaron la preferencia de los aniones a concentrarse en áreas próximas a CH1. El anión $[MeSO_3]^-$ exhibe una distribución más extendida alrededor del catión, lo que se traduce en un mayor número de enlaces de hidrógeno. Por otro lado, los aniones $[BF_4]^-$ y $[EtSO_4]^-$ presentan una distribución más restringida en presencia del $[MeSO_3]^-$, y en mayor medida en los CH4-5. Estos puntos de enlace también suponen una contribución importante en las interacciones totales del sistema y con las agrupaciones vecinas. Las CDF confirmaron la geometría uniforme de los enlaces de hidrógeno entre aniones y composiciones, mostrando en todos los casos un amplio enlace de hidrógeno.

- El estudio de los dominios mostró ciertas diferencias en los dominios de los aniones, evidenciando cambios durante las mezclas, lo que en términos generales resultó en dominios más pequeños y esféricos. No obstante, a pesar de estas diferencias individuales, la distribución porcentual de clústeres es muy similar en los tres DSIL estudiados. Los tres presentan distribuciones análogas, con altos porcentajes de grandes agrupaciones a lo largo de la composición, lo que permite inferir que el reemplazo de aniones no genera modificaciones en el tamaño del clúster. Asimismo, las propiedades dinámicas, evaluadas mediante análisis de flujo reactivo y funciones de distribución de velocidad, muestran que los enlaces de hidrógeno son altamente dinámicos, con tiempos de vida y de reformación que sugieren una rápida reorganización de la red iónica.

- Se ha realizado un estudio de las propiedades termofísicas de los NADES hidrófobos compuestos por los monoterpenoides mentol (MEN), timol (THY), Eucaliptol (CIN), D-Carvone (CAR) y geraniol (GER), actuando como HBA; así como sus combinaciones con los ácidos grasos saturados ácido decanoico (C10AC), ácido mirístico (C14AC) y ácido esteárico (C18AC), actuando estos como HBD. En aquellos ratios molares que permitieron que la mezcla se mantuviera en estado líquido a temperatura ambiente, se han determinado experimentalmente las densidades (ρ), haciendo uso de un densímetro digital, y las viscosidades cinemáticas (υ), mediante la utilización de un microviscosímetro capilar Ubbelohde, mediante procedimientos equivalentes a las medidas realizadas en las mezclas de líquidos iónicos. Estas propiedades se han medido a las temperaturas 283.15, 288.15, 293.15, 298.15, 303.15, 308.15 y 313.15 K a presión atmosférica.

- Todos los NADES exhiben temperaturas de fusión superiores a la temperatura ambiente, aumentando esta a medida que aumenta la longitud de la cadena de los ácidos grasos. Debido a su naturaleza hidrófoba, todos los NADES presentan una densidad menor que la del agua, mostrando una evolución lineal en función de la temperatura. Para los NADES C10AC:THY, C10AC:CIN y C10AC:CAR, los valores de densidad aumentan cuando aumenta la proporción de HBA en la composición. Este fenómeno puede atribuirse a la disminución de la presencia de cadenas largas de los ácidos grasos saturados, lo que permite un mejor empaquetamiento. Sin embargo, la evolución de la densidad de C10AC:MEN es independiente de la composición, mientras que C10AC:GER, presenta un comportamiento inverso que los anteriores.

- Los valores de viscosidad obtenidos no se ajustan a la ecuación de Arrhenius para ninguno de los NADES estudiados. En todos los casos, la viscosidad disminuye a medida que aumenta la temperatura, siendo C10AC:THY, C10AC:CIN y C10AC:CAR, los que presentan los valores de viscosidad más bajos. El comportamiento de la viscosidad en función de la temperatura puede sugerir la formación de dominios polares y apolares en el fluido, provocado por la formación de dominios hidórfobos (cadenas alquílicas) que se emparejan a través de enlaces de hidrógeno. En términos generales, las propiedades termofísicas evaluadas resultaron favorables de cara a aplicaciones prácticas, reduciendo los posibles problemas de transferencia de calor o masa.

- Para analizar las propiedades estructurales y sus interacciones a nivel nanoscópico se utilizaron diversas herramientas de simulación incluyendo COSMOtherm, simulaciones DFT y de dinámica molecular.

  - Mediante el método COSMOtherm se examinó la distribución de cargas en las moléculas y se predijeron los perfiles de equilibro sólido-líquidos de los NADES. En lo que respecta a la distribución de cargas, se observa que los monoterpenoides CIN y CAR solo pueden actuar como HBA, mientras que el resto de moléculas analizadas pueden actuar como HBA o como HBD. La distribución de la densidad electrónica en los monoterpenoides varía según su estructura, mientras que en los tres ácidos grasos la densidad electrónica se concentra alrededor del oxígeno del grupo carboxilo, siendo más baja alrededor del átomo de hidrógeno hidroxilo. En lo que respecta a la predicción de los puntos eutécticos, se confirma la existencia del punto eutéctico para todas los NADES estudiados, observándose que la temperatura del punto eutéctico aumenta a medida que aumenta la longitud de la cadena del HBD.

  - Se han llevado a cabo análisis de las diversas interacciones entre monoterpenoides y ácidos grasos a través de herramientas como funciones de distribución radial,

espacial o de velocidad. Mientras que las interacciones entre los ácidos grasos y los monoterpenoides dependen ampliamente del tipo de monterpenoide, se confirma que para agregaciones entre monoterpenoides, el efecto de las cadenas de ácidos grasos es mínimo. También se observa que los ácidos grasos tienden a situarse en torno al grupo hidroxilo de los HBA MEN, THY y GER. En el caso de las moléculas de ácidos grasos, los resultados indican que a medida que la longitud de la cadena disminuye, aumenta la asociación con monoterpenoides. Además se evidencia la formación de enlaces de hidrógeno con monoterpenoides a través de la interacción hidroxilo-hidroxilo e hidroxilo-carbonil, con amplias superficies alrededor del grupo -COOH del ácido. El análisis de las propiedades dinámicas concluye que existen movilidades similares para ambos componentes de los NADES, aunque el aumento de las cadenas de los ácidos grasos aumenta la capacidad de difusión.

- Se analizó el comportamiento a alta presión del NADES THY:CAR (1:1), fundamental para la aplicación de estos solventes en procesos a gran escala. Se realizaron mediciones de presión, volumen y temperatura entre 1 y 60 MPa en un rango de temperaturas desde 293.15 K a 353.15 K. Los resultados indicaron que, al aumentar la presión y la temperatura, el carácter hidrófobo de los NADES aumenta, así como la complejidad en las fuerzas intermoleculares. El aumento de la presión refuerza las interacciones THY:THY, mientras que debilita las THY:CAR.

- La combinación entre datos experimentales y resultados computacionales ha permitido esclarecer la relación entre la estructura y las propiedades de estos NADES, lo que contribuye al desarrollo de una estrategia más eficaz para el diseño de disolventes sostenibles. La estabilidad térmica, la hidrofobicidad y la capacidad para atravesar membranas que presentan estos NADES los convierte en una alternativa ecológica y con toxicidad baja, a los disolventes tradicionales.

6.2. Líneas de investigación futuras

Como sucede generalmente con los proyectos que se desarrollan dentro del ámbito académico de las tesis doctorales, a lo largo del proceso de investigación surgen nuevas líneas que merecen ser exploradas. En este caso, las posibles líneas de investigación futura identificadas han sido:

1- Se han llevado a cabo estudios sobre mezclas binarias de líquidos iónicos con el catión común imidazol, examinando el efecto de la naturaleza y estructura del anión en las propiedades y la interacción de estas mezclas. En este contexto resultaría interesante ampliar la línea de investigación incorporando al estudio la combinación con aniones de otra naturaleza o diferentes longitudes de cadena alquílica, con el propósito de ampliar y profundizar las conclusiones obtenidas en relación al impacto del anión en las propiedades termofísicas de los líquidos iónicos. Adicionalmente, con el objetivo de

complementar el análisis, podría ser relevante considerar la influencia del catión, mediante la opción de la variación del catión, con cationes de diferente naturaleza o variando la longitud de sus cadenas alquílicas.

2- Varias mezclas binarias de líquidos iónicos propuestas exhibieron comportamientos inesperados. En la fase inicial de homogeneización, estos DSIL formaron un gel a temperatura ambiente. Este fenómeno ha sido observado por otros grupos de investigación, aunque no se han encontrado referencias en la literatura actual. La formación de esta fase gel a temperatura ambiente impidió la medida de la densidad y viscosidad, no obstante, se llevó a cabo un análisis exhaustivo de su comportamiento en una rampa de temperatura más amplia que la habitual, con el fin de evaluar y delimitar su comportamiento en función de la temperatura. Los resultados obtenidos se presentan en el Anexo I. El estudio de otras propiedades de estos DSIL proporcionaría información adicional a la investigación realizada, así como permitiría profundizar en la comprensión de su comportamiento.

3- A pesar de que se han estudiado múltiples ratios molares de los diferentes NADES, no se ha logrado determinar de manera experimental el ratio molar que corresponde a su punto eutéctico para alguna de estas mezclas. Como consecuencia, no ha sido posible la determinación experimental de sus propiedades termofísicas. En este sentido, la investigación podría continuar ampliando el rango de ratios molares analizados para dichas mezclas.

4- Se han definido unas condiciones de presión y temperatura comunes para el análisis tanto de los DSIL como de los NADES. Como propuesta de línea de investigación futura, resulta de interés la ampliación de los márgenes de temperatura en los que se han realizado los estudios experimentales. Esto permitiría evaluar de manera más amplia el comportamiento termodinámico y estructural de los sistemas estudiados.

5- Por otra parte, de la literatura científica es posible extraer que la presencia de agua en las mezclas tiene un impacto significativo en sus propiedades finales. Continuaría aportando valor al trabajo realizado, llevar a cabo un análisis del comportamiento y las propiedades de estas mezclas al modificar el porcentaje de agua que contienen

Capítulo 7
Referencias

Abbott, A. P. Application of Hole Theory to the Viscosity of Ionic and Molecular Liquids. *ChemPhysChem*, (2004), *5*(8), 1242–1246.

Abbott, A. P.; Al-Barzinjy, A. A.; Abbott, P. D.; Frisch, G.; Harris, R. C.; Hartley, J.; Ryder, K. S. Speciation, physical and electrolytic properties of eutectic mixtures based on CrCl3·6H2O and urea. *Physical Chemistry Chemical Physics*, (2014), *16*(19), 9047.

Abbott, A. P.; Boothby, D.; Capper, G.; Davies, D. L.; Rasheed, R. K. Deep Eutectic Solvents Formed between Choline Chloride and Carboxylic Acids: Versatile Alternatives to Ionic Liquids. *J Am Chem Soc*, (2004), *126*(29), 9142–9147.

Abbott, A. P.; Capper, G.; Davies, D. L.; Rasheed, R. K.; Tambyrajah, V. Novel solvent properties of choline chloride/urea mixtures. *Chemical Communications*, (2003), *1*, 70–71.

Abbott, A. P.; Capper, G.; Gray, S. Design of improved deep eutectic solvents using hole theory. *ChemPhysChem*, (2006), *7*(4), 803–806.

Abbott, A. P.; Cullis, P. M.; Gibson, M. J.; Harris, R. C.; Raven, E. Extraction of glycerol from biodiesel into a eutectic based ionic liquid. *Green Chemistry*, (2007), *9*(8), 868.

Abo-Hamad, A.; Hayyan, M.; AlSaadi, M. A.; Hashim, M. A. Potential applications of deep eutectic solvents in nanotechnology. *Chemical Engineering Journal*, (2015), *273*, 551–567.

Aghaie, M.; Rezaei, N.; Zendehboudi, S. A systematic review on CO2 capture with ionic liquids: Current status and future prospects. In *Renewable and Sustainable Energy Reviews* (Vol. 96, pp. 502–525). Elsevier Ltd.

Ahmadi, R.; Kazemi, G.; Ramezani, A. M.; Safavi, A. Shaker-assisted liquid-liquid microextraction of methylene blue using deep eutectic solvent followed by back-extraction and spectrophotometric determination. *Microchemical Journal*, (2019), *145*, 501–507.

Aki, S. N. V. K.; Mellein, B. R.; Saurer, E. M.; Brennecke, J. F. *High-Pressure Phase Behavior of Carbon Dioxide with Imidazolium-Based Ionic Liquids*. (2004).

Alberto, J.; Arriaga, J.; Fortín, S. *La Teoría Cuántica de Átomos en Moléculas y su rol en la reducción de la química a la física*.

Al-Bodour, A.; Alomari, N.; Gutiérrez, A.; Aparicio, S.; Atilhan, M. Exploring the thermophysical properties of natural deep eutectic solvents for gas capture applications: A comprehensive review. In *Green Chemical Engineering*. KeAi Communications Co.

Almeida, H. F. D.; Neves, M. C.; Trindade, T.; Marrucho, I. M.; Freire, M. G. Supported ionic liquids as efficient materials to remove non-steroidal anti-inflammatory drugs from aqueous media. *Chemical Engineering Journal*, (2020), *381*, 122616.

Alsanea, S.; Liu, D. BITC and S-Carvone Restrain High-Fat Diet-Induced Obesity and Ameliorate Hepatic Steatosis and Insulin Resistance. *Pharm Res*, (2017), *34*(11), 2241–2249.

Altamash, T.; Amhamed, A.; Aparicio, S.; Atilhan, M. Effect of hydrogen bond donors and acceptors on Co2 absorption by deep eutectic solvents. *Processes*, (2020), *8*(12), 1–15.

Altamash, T.; Nasser, M. S.; Elhamarnah, Y.; Magzoub, M.; Ullah, R.; Qiblawey, H.; Aparicio, S.; Atilhan, M. Gas solubility and rheological behavior study of betaine and alanine based natural deep eutectic solvents (NADES). *J Mol Liq*, (2018), *256*, 286–295.

An, J.-H.; Jin, F.; Kim, H. S.; Ryu, H. C.; Kim, J. S.; Kim, H. M.; Kiyonga, A. N.; Min, D. S.; Youn, W.; Kim, K. H.; Jung, K. Application of ionic liquid to polymorphic transformation of anti-viral/HIV drug adefovir dipivoxil. *Arch Pharm Res*, (2016), *39*(5), 646–659.

An, J.-H.; Kim, W.-S. Antisolvent Crystallization Using Ionic Liquids As Solvent and Antisolvent for Polymorphic Design of Active Pharmaceutical Ingredient. *Cryst Growth Des*, (2013), *13*(1), 31–39.

Anastas, P.; Eghbali, N. Green Chemistry: Principles and Practice. *Chem Soc Rev*, (2010), *39*(1), 301–312.

Anthony, J. L.; Maginn, E. J.; Brennecke, J. F. *Gas Solubilities in 1-* n *-Butyl-3-methylimidazolium Hexafluorophosphate* (pp. 260–269).

Arce, A.; Rodríguez, H.; Soto, A. Use of a green and cheap ionic liquid to purify gasoline octane boosters. *Green Chem.*, (2007), *9*(3), 247–253.

Austen, C.; Ansari, Y.; Zhao, Z. Ionic Liquids: Past, present and future. In *Faraday Discussions* (Vol. 154, pp. 9–27).

Austen, C.; Byrne, N.; Belieres, J.-P. Parallel Developments in Aprotic and Protic Ionic Liquids: Physical Chemistry and Applications. *Acc Chem Res*, (2007), *40*(11), 1228–1236.

Azzouz, A.; Hayyan, M. Potential applications of deep eutectic solvents in nanotechnology: Part II. *Chemical Engineering Journal*, (2023), *468*, 143563.

Benito, C.; Alcalde, R.; Atilhan, M.; Aparicio, S. High-pressure properties of type V Natural Deep Eutectic Solvents: The case of menthol: thymol. *J Mol Liq*, (2023), *376*.

Bera, A.; Agarwal, J.; Shah, M.; Shah, S.; Vij, R. K. Recent advances in ionic liquids as alternative to surfactants/chemicals for application in upstream oil industry. *Journal of Industrial and Engineering Chemistry*, (2020), *82*, 17–30.

Berkert, U.; Allinger, N. Molecular Mechanics. *American Chemical Society* , (1982), *177*.

Bioucas, F. E. B.; Vieira, S. I. C.; Lourenço, M. J. V.; Santos, F. J. V.; Nieto De Castro, C. A.; Massonne, K. [CH3SO3] - A Suitable New Heat Transfer Fluid? Part 1. Thermophysical and Toxicological Properties. *Ind Eng Chem Res*, (2018), *57*(25), 8541–8551.

Bonhôte, P.; Dias, A.-P.; Papageorgiou, N.; Kalyanasundaram, K.; Grätzel, M. Hydrophobic, Highly Conductive Ambient-Temperature Molten Salts. *Inorg Chem*, (1996), *35*(5), 1168–1178.

Borja, C. *Redalyc.Líquidos Iónicos: Métodos de Síntesis y Aplicaciones*. (2015).

Boto, R. A.; Contreras-García, J.; Tierny, J.; Piquemal, J.-P. Interpretation of the reduced density gradient. *Mol Phys*, (2016), *114*(7–8), 1406–1414.

Branco, L. C.; Carrera, G. V.; Aires-de-Sousa, J. Physico-chemical properties of task-specific ionic liquids. . In *Ionic liquids: theory, properties, new approaches* (pp. 61–94).

Brandt, A.; Gräsvik, J.; Hallett, J. P.; Welton, T. Deconstruction of lignocellulosic biomass with ionic liquids. *Green Chemistry*, (2013), *15*(3), 550.

Bueren-Calabuig, J. A. *Dinámica molecular*.

Burke, K.; Wagner, L. *ABC of ground-state DFT*.

Cadena, C.; Anthony, J. L.; Shah, J. K.; Morrow, T. I.; Brennecke, J. F.; Maginn, E. J. Why is CO2 so Soluble in Imidazolium-Based Ionic Liquids? *J Am Chem Soc*, (2004), *126*(16), 5300–5308.

Cannon, M. R.; Manning, R. E.; Bell, J. D. Viscosity Measurement. Kinetic Energy Correction and New Viscometer. *Anal Chem*, (1960), *32*(3), 355–358.

Cao, J.; Su, E. Hydrophobic deep eutectic solvents: the new generation of green solvents for diversified and colorful applications in green chemistry. In *Journal of Cleaner Production* (Vol. 314). Elsevier Ltd.

Carneiro, A. P.; Rodríguez, O.; Macedo, E. A. Solubility of xylitol and sorbitol in ionic liquids – Experimental data and modeling. *J Chem Thermodyn*, (2012), *55*, 184–192.

Caro, M. N. *Análisis experimental y teórico de diversas propiedades termofísicas de sistemas ternarios compuestos de glimes alcoholes y DI-N-Butiléter, y de sus componentes binarios*.

Chatel, G.; Pereira, J. F. B.; Debbeti, V.; Wang, H.; Rogers, R. D. Mixing ionic liquids-"simple mixtures" or “double salts”? In *Green Chemistry* (Vol. 16, Issue 4, pp. 2051–2083). Royal Society of Chemistry.

Chen, J.; Fan, X.; Zhou, L.; Gao, X. Treatment with geraniol ameliorates methionine-choline-deficient diet-induced non-alcoholic steatohepatitis in rats. *J Gastroenterol Hepatol*, (2016), *31*(7), 1357–1365.

Chen, X.-C.; Sun, P.-R.; Liu, H.-L. Hierarchically Crosslinked Gels Containing Hydrophobic Ionic Liquids towards Reliable Sensing Applications. *Chinese Journal of Polymer Science*, (2020), *38*(4), 332–341.

Chen, Y.; Han, X.; Liu, Z.; Yu, D.; Guo, W.; Mu, T. Capture of Toxic Gases by Deep Eutectic Solvents. *ACS Sustain Chem Eng*, (2020), *8*(14), 5410–5430.

Chen, Y.; Mu, T. Revisiting greenness of ionic liquids and deep eutectic solvents. In *Green Chemical Engineering* (Vol. 2, Issue 2, pp. 174–186). KeAi Communications Co.

Choi, Y. H.; van Spronsen, J.; Dai, Y.; Verberne, M.; Hollmann, F.; Arends, I. W. C. E.; Witkamp, G.-J.; Verpoorte, R. Are Natural Deep Eutectic Solvents the Missing Link in Understanding Cellular Metabolism and Physiology? *Plant Physiol*, (2011), *156*(4), 1701–1705.

Chowdhury, Md. R.; Moshikur, R. M.; Wakabayashi, R.; Tahara, Y.; Kamiya, N.; Moniruzzaman, M.; Goto, M. Ionic-Liquid-Based Paclitaxel Preparation: A New Potential Formulation for Cancer Treatment. *Mol Pharm*, (2018), *15*(6), 2484–2488.

Dai, Y.; van Spronsen, J.; Witkamp, G. J.; Verpoorte, R.; Choi, Y. H. Natural deep eutectic solvents as new potential media for green technology. *Anal Chim Acta*, (2013), *766*, 61–68.

Dai, Y.; Verpoorte, R.; Choi, Y. H. Natural deep eutectic solvents providing enhanced stability of natural colorants from safflower (Carthamus tinctorius). *Food Chem*, (2014), *159*, 116–121.

Das, S.; Rahman, M.; Kundu, D.; Majee, A.; Hajra, A. Task-specific ionic-liquid-catalyzed efficient synthesis of indole derivatives under solvent-free conditions. *Can J Chem*, (2010), *88*(2), 150–154.

de Castro, C. N.; C. Ribeiro, A. P.; I.C., S.; P. Franca, J. M.; J.V., M.; V., F.; M.S, S.; Goodrich, P.; Hardacre, C. Synthesis, Properties and Physical Applications of IoNanofluids. In *Ionic Liquids - New Aspects for the Future*. InTech.

Deepika; Juneja, S.; Pandey, S. Water Miscibility, Surface Tension, Density, and Dynamic Viscosity of Hydrophobic Deep Eutectic Solvents Composed of Capric Acid, Menthol, and Thymol. *J Chem Eng Data*, (2022), *67*(11), 3400–3413.

Díaz, J.; Rey, R.; Barrero, R. Líquidos iónicos: propiedades fisicoquímicas y aplicación potencial en el mejoramiento de crudos pesados Ionic liquids: physicochemical properties and potential application in upgrading of heavy crude oils. *Rev.Ion*, (2012), *25*(1), 61–87.

Długosz, O.; Ochnik, M.; Sochocka, M.; Franz, D.; Orzechowska, B.; Anna, C.-K.; Agata, D.; Banach, M. Antimicrobial and antiviral activity of selenium sulphide nanoparticles synthesised in extracts from spices in natural deep eutectic solvents (NDES). *Sustainable Materials and Technologies*, (2022), *32*, e00433.

Dong, K.; Liu, X.; Dong, H.; Zhang, X.; Zhang, S. Multiscale Studies on Ionic Liquids. In *Chemical Reviews* (Vol. 117, Issue 10, pp. 6636–6695). American Chemical Society.

Earle, M. J.; Seddon, K. R. Ionic liquids. Green solvents for the future*. In *Chemical and Engineering News* (Vol. 72, Issue 7).

El Achkar, T.; Greige-Gerges, H.; Fourmentin, S. Basics and properties of deep eutectic solvents: a review. In *Environmental Chemistry Letters* (Vol. 19, Issue 4, pp. 3397–3408). Springer Science and Business Media Deutschland GmbH.

Espino, M.; de los Ángeles Fernández, M.; Gomez, F. J. V.; Silva, M. F. Natural designer solvents for greening analytical chemistry. In *TrAC - Trends in Analytical Chemistry* (Vol. 76, pp. 126–136). Elsevier B.V.

Faraji, M. Determination of some red dyes in food samples using a hydrophobic deep eutectic solvent-based vortex assisted dispersive liquid-liquid microextraction coupled with high performance liquid chromatography. *J Chromatogr A*, (2019), *1591*, 15–23.

Farajzadeh, M. A.; Abbaspour, M.; Kazemian, R. Synthesis of a green high density deep eutectic solvent and its application in microextraction of seven widely used pesticides from honey. *J Chromatogr A*, (2019), *1603*, 51–60.

Farajzadeh, M. A.; Afshar Mogaddam, M. R.; Aghanassab, M. Deep eutectic solvent-based dispersive liquid–liquid microextraction. *Analytical Methods*, (2016), *8*(12), 2576–2583.

Fernández, M. de los Á.; Boiteux, J.; Espino, M.; Gomez, F. J. V.; Silva, M. F. Natural deep eutectic solvents-mediated extractions: The way forward for sustainable analytical developments. In *Analytica Chimica Acta* (Vol. 1038, pp. 1–10). Elsevier B.V.

Finotello, A.; Bara, J. E.; Narayan, S.; Camper, D.; Noble, R. D. Ideal gas solubilities and solubility selectivities in a binary mixture of room-temperature ionic liquids. *Journal of Physical Chemistry B*, (2008), *112*(8), 2335–2339.

Florindo, C.; Branco, L. C.; Marrucho, I. M. Development of hydrophobic deep eutectic solvents for extraction of pesticides from aqueous environments. *Fluid Phase Equilib*, (2017), *448*, 135–142.

Florindo, C.; Lima, F.; Ribeiro, B. D.; Marrucho, I. M. Deep eutectic solvents: overcoming 21st century challenges. In *Current Opinion in Green and Sustainable Chemistry* (Vol. 18, pp. 31–36). Elsevier B.V.

Florindo, C.; McIntosh, A. J. S.; Welton, T.; Branco, L. C.; Marrucho, I. M. A closer look into deep eutectic solvents: exploring intermolecular interactions using solvatochromic probes. *Physical Chemistry Chemical Physics*, (2018), *20*(1), 206–213.

Florindo, C.; Romero, L.; Rintoul, I.; Branco, L. C.; Marrucho, I. M. From Phase Change Materials to Green Solvents: Hydrophobic Low Viscous Fatty Acid-Based Deep Eutectic Solvents. *ACS Sustain Chem Eng*, (2018), *6*(3), 3888–3895.

Fortin, T. J.; Laesecke, A.; Freund, M.; Outcalt, S. Advanced calibration, adjustment, and operation of a density and sound speed analyzer. *Journal of Chemical Thermodynamics*, (2013), *57*, 276–285.

Freemantle, Michael. Ionic liquids may boost clean technology development. *Chem. Eng. News* , (1998), *76*(13), 32–37.

Fumino, K.; Ludwig, R. Analyzing the interaction energies between cation and anion in ionic liquids: The subtle balance between Coulomb forces and hydrogen bonding. In *Journal of Molecular Liquids* (Vol. 192, pp. 94–102). Elsevier.

Fuster, F.; Silvi, B. Does the topological approach characterize the hydrogen bond? *Theoretical Chemistry Accounts: Theory, Computation, and Modeling (Theoretica Chimica Acta)*, (2000), *104*(1), 13–21.

Gaiser, H. F.; Popescu, R.; Gerthsen, D.; Feldmann, C. Ionic-liquid-based synthesis of GaN nanoparticles. *Chemical Communications*, (2020), *56*(15), 2312–2315.

Gao, X.; Mariani, A.; Jeong, S.; Liu, X.; Dou, X.; Ding, M.; Moretti, A.; Passerini, S. Prototype rechargeable magnesium batteries using ionic liquid electrolytes. *J Power Sources*, (2019), *423*, 52–59.

García, G.; Aparicio, S.; Ullah, R.; Atilhan, M. Deep eutectic solvents: Physicochemical properties and gas separation applications. *Energy and Fuels*, (2015), *29*(4), 2616–2644.

García, G.; Atilhan, M.; Aparicio, S. Interfacial Properties of Deep Eutectic Solvents Regarding to CO2 Capture. *Journal of Physical Chemistry C*, (2015), *119*(37), 21413–21425.

García-Miaja, G.; Troncoso, J.; Romaní, L. Excess molar properties for binary systems of alkylimidazolium-based ionic liquids+nitromethane. Experimental results and ERAS-model calculations. *J Chem Thermodyn*, (2009), *41*(3), 334–341.

Ghandi, K. A Review of Ionic Liquids, Their Limits and Applications. *Green and Sustainable Chemistry*, (2014), *04*(01), 44–53.

Gómez, J. *Teoría Cuántica de Átomos en Moléculas*.

González, E. J.; Palomar, J.; Navarro, P.; Larriba, M.; García, J.; Rodríguez, F. On the volatility of aromatic hydrocarbons in ionic liquids: Vapor-liquid equilibrium measurements and theoretical analysis. *J Mol Liq*, (2018), *250*, 9–18.

Gotor-Fernández, V.; Paul, C. E. Deep eutectic solvents for redox biocatalysis. In *Journal of Biotechnology* (Vol. 293, pp. 24–35). Elsevier B.V.

Gracia, O. *Herramientas de cribado virtual aplicadas a inhibidores de tirosina quinasas. Contribución al desarrollo del programa PRALINS para el diseño de quimiotecas combinatorias.* [Universidad Ramon Llull].

Gray, G. E.; Kohl, P. A.; Winnick, J. Stability of Sodium Electrodeposited from a Room Temperature Chloroaluminate Molten Salt. *J Electrochem Soc*, (1995), *142*(11), 3636–3642.

Greaves, T. L.; Drummond, C. J. Protic ionic liquids: Properties and applications. In *Chemical Reviews* (Vol. 108, Issue 1, pp. 206–237).

Gunny, A. A. N.; Arbain, D.; Nashef, E. M.; Jamal, P. Applicability evaluation of Deep Eutectic Solvents-Cellulase system for lignocellulose hydrolysis. *Bioresour Technol*, (2015), *181*, 297–302.

Gupta, H.; Kataria, J.; Sharma, D.; Sharma, V. K. Topological investigations of molecular interactions in binary ionic liquid mixtures with a common ion: Excess molar volumes, excess isentropic compressibilities, excess molar enthalpies and excess molar heat capacities. *J Chem Thermodyn*, (2016), *103*, 189–205.

Gupta, H.; Malik, S.; Chandrasekhar, M.; Sharma, V. K. Thermodynamic investigations of excess heat capacities of ternary liquid mixtures containing [Bmmim][BF4] + [Bmim][BF4] or [Emim][BF4] + cyclopentanone or cyclohexanone. *J Therm Anal Calorim*, (2018), *131*(2), 1653–1669.

Gutiérrez, A. *Modelización teórica de sistemas basados en líquidos iónicos, disolventes eutécticos de bajo punto de fusión, sales fundidas y otros disolventes empleando técnicas de simulación molecular para diversas aplicaciones industriales*. Universidad de Burgos.

Gutiérrez, A.; Atilhan, M.; Alcalde, R.; Trenzado, J. L.; Aparicio, S. Insights on the mixtures of imidazolium based ionic liquids with molecular solvents. *J Mol Liq*, (2018), *255*, 199–207.

Hagiwara, R.; Hirashige, T.; Tsuda, T.; Ito, Y. A Highly Conductive Room Temperature Molten Fluoride: EMIF·2.3HF. *J Electrochem Soc*, (2002), *149*(1), D1.

Haider, M. B.; Jha, D.; Kumar, R.; Marriyappan Sivagnanam, B. Ternary hydrophobic deep eutectic solvents for carbon dioxide absorption. *International Journal of Greenhouse Gas Control*, (2020), *92*, 102839.

Hansen, B. B.; Spittle, S.; Chen, B.; Poe, D.; Zhang, Y.; Klein, J. M.; Horton, A.; Adhikari, L.; Zelovich, T.; Doherty, B. W.; Gurkan, B.; Maginn, E. J.; Ragauskas, A.; Dadmun, M.; Zawodzinski, T. A.; Baker, G. A.; Tuckerman, M. E.; Savinell, R. F.; Sangoro, J. R. Deep Eutectic Solvents: A Review of Fundamentals and Applications. In *Chemical Reviews* (Vol. 121, Issue 3, pp. 1232–1285). American Chemical Society.

Hauk, D. B.; Torres, R. B.; Dangelo, J. V. H. Measurement and correlation of high-pressure volumetric properties of binary mixtures of 1-Ethyl-3-methylimidazolium bis(trifluoromethylsulfonyl)imide ([EMIM][NTf2]) with alcohols. *J Chem Thermodyn*, (2023), *185*, 107122.

Hayes, R.; Warr, G. G.; Atkin, R. Structure and Nanostructure in Ionic Liquids. In *Chemical Reviews* (Vol. 115, Issue 13, pp. 6357–6426). American Chemical Society.

Hayyan, A.; Hashim, M. A.; Hayyan, M.; Mjalli, F. S.; AlNashef, I. M. A new processing route for cleaner production of biodiesel fuel using a choline chloride based deep eutectic solvent. *J Clean Prod*, (2014), *65*, 246–251.

Hayyan, A.; Mjalli, F. S.; AlNashef, I. M.; Al-Wahaibi, T.; Al-Wahaibi, Y. M.; Hashim, M. A. Fruit sugar-based deep eutectic solvents and their physical properties. *Thermochim Acta*, (2012), *541*, 70–75.

Hayyan, M.; Abo-Hamad, A.; AlSaadi, M. A.; Hashim, M. A. Functionalization of graphene using deep eutectic solvents. *Nanoscale Res Lett*, (2015), *10*(1), 324.

Herce-Sesa, B.; Pirkwieser, P.; López-López, J. A.; Jirsa, F.; Moreno, C. Selective liquid phase micro-extraction of metal chloro-complexes from saline waters using ionic liquids. *J Clean Prod*, (2020), *262*, 121415.

Hohenberg, P.; Kohn, W. Inhomogeneous Electron Gas. *Physical Review*, (1964), *136*(3B).

HUMPHREY, W. VMD-Visual Molecular Dynamics. *J Mol Graph*, (1996), *14*, 33–38.

Iida, M.; Er, H. Physicochemical Properties of Ionic Liquids Containing N-alkylamine-Silver(I) Complex Cations or Protic N-alkylaminium Cations. In *Ionic Liquids: Theory, Properties, New Approaches*.

Ikeda, M.; Aniya, M. Understanding the Vogel–Fulcher–Tammann law in terms of the bond strength–coordination number fluctuation model. *J Non Cryst Solids*, (2013), *371*, 53–57.

Isosaari, P.; Srivastava, V.; Sillanpää, M. Ionic liquid-based water treatment technologies for organic pollutants: Current status and future prospects of ionic liquid mediated technologies. *Science of The Total Environment*, (2019), *690*, 604–619.

Izgorodina, E. I. Towards large-scale, fully ab initio calculations of ionic liquids. *Physical Chemistry Chemical Physics*, (2011), *13*(10), 4189–4207.

Jayachandran, M.; Chandrasekaran, B.; Namasivayam, N. Effect of geraniol, a plant derived monoterpene on lipids and lipid metabolizing enzymes in experimental hyperlipidemic hamsters. *Mol Cell Biochem*, (2015), *398*(1–2), 39–53.

Jenkins, H. D. B. Ionic liquids-an overview. *Sci Prog*, (2011), *94*(3), 265–297.

Jouyban, A.; Farajzadeh, M. A.; Nemati, M.; Alizadeh Nabil, A. A.; Afshar Mogaddam, M. R. Preparation of ferrofluid from toner powder and deep eutectic solvent used in air-assisted liquid-liquid microextraction: Application in analysis of sixteen polycyclic aromatic hydrocarbons in urine and saliva samples of tobacco smokers. *Microchemical Journal*, (2020), *154*, 104631.

JUERGENS, U. R.; DETHLEFSEN, U.; STEINKAMP, G.; GILLISSEN, A.; REPGES, R.; VETTER, H. Anti-inflammatory activity of 1.8-cineol (eucalyptol) in bronchial asthma: a double-blind placebo-controlled trial. *Respir Med*, (2003), *97*(3), 250–256.

Júlio, A.; Costa Lima, S. A.; Reis, S.; Santos de Almeida, T.; Fonte, P. Development of ionic liquid-polymer nanoparticle hybrid systems for delivery of poorly soluble drugs. *J Drug Deliv Sci Technol*, (2020), *56*, 100915.

Kaiser, B.; Laesecke, A.; Schmeck, M. Experimental study and correlation of the viscosity of 2,2,2-trifluoroethanol (TFE)-water mixtures. *Int J Thermophys*, (1989), *10*(3), 713–726.

Kamatou, G. P. P.; Vermaak, I.; Viljoen, A. M.; Lawrence, B. M. Menthol: A simple monoterpene with remarkable biological properties. *Phytochemistry*, (2013), *96*, 15–25.

Kar, M.; Plechkova, N. V.; Seddon, K. R.; Pringle, J. M.; MacFarlane, D. R. Ionic Liquids-Further Progress on the Fundamental Issues. In *Australian Journal of Chemistry* (Vol. 72, Issue 2, pp. 3–10). CSIRO.

Kaur, G.; Kumar, H.; Singla, M. Diverse applications of ionic liquids: A comprehensive review. In *Journal of Molecular Liquids* (Vol. 351). Elsevier B.V.

Kaur, P.; Rajani, N.; Kumawat, P.; Singh, N.; Kushwaha, J. P. Performance and mechanism of dye extraction from aqueous solution using synthesized deep eutectic solvents. *Colloids Surf A Physicochem Eng Asp*, (2018), *539*, 85–91.

Kim, J.; Shi, Y.; Kwon, C. J.; Gao, Y.; Mitragotri, S. A Deep Eutectic Solvent-Based Approach to Intravenous Formulation. *Adv Healthc Mater*, (2021), *10*(18).

Kleiner, B.; Fleischer, P.; Schörken, U. Biocatalytic synthesis of biodiesel utilizing deep eutectic solvents: A two-step-one-pot approach with free lipases suitable for acidic and used oil processing. *Process Biochemistry*, (2016), *51*(11), 1808–1816.

Kohn, W.; Sham, L. J. Self-Consistent Equations Including Exchange and Correlation Effects. *Phys. Rev. A.* , (1965), *140*.

Kong, M. J. *Los líquidos iónicos a temperatura ambiente (RTILs): Propiedades, aplicaciones y perspectivas futuras. Room temperature ionic liquids (RTILs): Properties, applieations and future prospeets*.

Kumełan, J.; Tuma, D.; Maurer, G. Simultaneous solubility of carbon dioxide and hydrogen in the ionic liquid [hmim][Tf2N]: Experimental results and correlation. *Fluid Phase Equilib*, (2011), *311*(1), 9–16.

Lei, Z.; Chen, B.; Koo, Y. M.; Macfarlane, D. R. Introduction: Ionic Liquids. In *Chemical Reviews* (Vol. 117, Issue 10, pp. 6633–6635). American Chemical Society.

Lei, Z.; Han, J.; Zhang, B.; Li, Q.; Zhu, J.; Chen, B. Solubility of CO 2 in binary mixtures of room-temperature ionic liquids at high pressures. *J Chem Eng Data*, (2012), *57*(8), 2153–2159.

Li, T.; Song, Y.; Li, J.; Zhang, M.; Shi, Y.; Fan, J. New low viscous hydrophobic deep eutectic solvents in vortex-assisted liquid-liquid microextraction for the determination of phthalate esters from food-contacted plastics. *Food Chem*, (2020), *309*, 125752.

Li, X.; Hou, M.; Han, B.; Wang, X.; Zou, L. Solubility of CO 2 in a Choline Chloride + Urea Eutectic Mixture. *J Chem Eng Data*, (2008), *53*(2), 548–550.

Li, Z.; Wei, Q.; Yuan, R.; Zhou, X.; Liu, H.; Shan, H.; Song, Q. A new room temperature ionic liquid 1-butyl-3-trimethylsilylimidazolium hexafluorophosphate as a solvent for extraction and preconcentration of mercury with determination by cold vapor atomic absorption spectrometry. *Talanta*, (2007), *71*(1), 68–72.

Liao, H.; Jiang, Y.; Zhou, Z.; Chen, S.; Sun, S. Shape-Controlled Synthesis of Gold Nanoparticles in Deep Eutectic Solvents for Studies of Structure–Functionality Relationships in Electrocatalysis. *Angewandte Chemie International Edition*, (2008), *47*(47), 9100–9103.

Liu, W.; Zong, B.; Wang, X.; Cai, J.; Yu, J. A highly efficient vortex-assisted liquid–liquid microextraction based on natural deep eutectic solvent for the determination of Sudan I in food samples. *RSC Adv*, (2019), *9*(30), 17432–17439.

Liu, X.; Bian, Y.; Zhao, J.; Wang, Y.; Zhao, L. Menthol-based deep eutectic solvent in dispersive liquid-liquid microextraction followed by solidification of floating organic droplet for the determination of three bisphenols with UPLC-MS/MS. *Microchemical Journal*, (2020), *159*.

Liu, Y.; Friesen, J. B.; McAlpine, J. B.; Lankin, D. C.; Chen, S. N.; Pauli, G. F. Natural Deep Eutectic Solvents: Properties, Applications, and Perspectives. In *Journal of Natural Products* (Vol. 81, Issue 3, pp. 679–690). American Chemical Society.

Liu, Y.; Zhao, E.; Zhu, W.; Gao, H.; Zhou, Z. Determination of four heterocyclic insecticides by ionic liquid dispersive liquid–liquid microextraction in water samples. *J Chromatogr A*, (2009), *1216*(6), 885–891.

Lu, T.; Chen, F. Multiwfn: A multifunctional wavefunction analyzer. *J Comput Chem*, (2012), *33*(5), 580–592.

Macfarlane, D. R.; Tachikawa, N.; Forsyth, M.; Pringle, J. M.; Howlett, P. C.; Elliott, G. D.; Davis, J. H.; Watanabe, M.; Simon, P.; Angell, C. A. Energy applications of ionic liquids. In *Energy and Environmental Science* (Vol. 7, Issue 1, pp. 232–250). Royal Society of Chemistry.

Magalí, S. *Estudio teórico de las propiedades estructurales, electrónicas, y de la reactividad química de nanoestructuras de molibdeno.* Universidad Nacional de La Plata.

Maletta, A.; Gutiérrez, A.; Jian Tan, P.; Springstead, J.; Aparicio, S.; Atilhan, M. Separation of phenolic compounds from water by using monoterpenoid and fatty acid based hydrophobic deep eutectic solvents. *J Mol Liq*, (2023), *381*.

Marcus, Y. *Ionic Liquid Properties From Molten Salts to RTILs*.

Martins, M. A. R.; Crespo, E. A.; Pontes, P. V. A.; Silva, L. P.; Bülow, M.; Maximo, G. J.; Batista, E. A. C.; Held, C.; Pinho, S. P.; Coutinho, J. A. P. Tunable Hydrophobic Eutectic Solvents Based on Terpenes and Monocarboxylic Acids. *ACS Sustain Chem Eng*, (2018), *6*(7), 8836–8846.

Martins, M. A. R.; Pinho, S. P.; Coutinho, J. A. P. Insights into the Nature of Eutectic and Deep Eutectic Mixtures. *J Solution Chem*, (2019), *48*(7), 962–982.

Matta, C. F.; Boyd, R. J. *The quantum theory of atoms in molecules : from solid state to DNA and drug design*. Wiley-VCH.

Matthews, R. P.; Villar-Garcia, I. J.; Weber, C. C.; Griffith, J.; Cameron, F.; Hallett, J. P.; Hunt, P. A.; Welton, T. A structural investigation of ionic liquid mixtures. *Physical Chemistry Chemical Physics*, (2016), *18*(12), 8608–8624.

Miran, M. S.; Kinoshita, H.; Yasuda, T.; Susan, M. A. B. H.; Watanabe, M. Hydrogen bonds in protic ionic liquids and their correlation with physicochemical properties. *Chemical Communications*, (2011), *47*(47), 12676–12678.

Mišan, A.; Nađpal, J.; Stupar, A.; Pojić, M.; Mandić, A.; Verpoorte, R.; Choi, Y. H. The perspectives of natural deep eutectic solvents in agri-food sector. *Crit Rev Food Sci Nutr*, (2020), *60*(15), 2564–2592.

Moreno Martínez, P.; Ortiz-Martínez, V. M.; Sánchez Segado, S.; Salar-García, M. J.; los Ríos, A. P. de; Hernández Fernández, F. J.; Lozano-Blanco, L. J.; Godínez, C. Deep eutectic solvents for the extraction of fatty acids from microalgae biomass: Recovery of omega-3 eicosapentaenoic acid. *Sep Purif Technol*, (2022), *300*, 121842.

Nandwani, S. K.; Malek, N. I.; Chakraborty, M.; Gupta, S. Insight into the Application of Surface-Active Ionic Liquids in Surfactant Based Enhanced Oil Recovery Processes–A Guide Leading to Research Advances. *Energy & Fuels*, (2020), *34*(6), 6544–6557.

Narsimlu, V.; Reddy, K. C. S.; Krishna, T. V.; Mohan, T. M.; Rao, V. S. Thermodynamic and theoretical investigations on [Emim][Bf4]/[Bmim][Bf4] and aniline binary mixtures. *Journal of Chemical Thermodynamics*, (2019), *139*.

Niedermeyer, H.; Hallett, J. P.; Villar-Garcia, I. J.; Hunt, P. A.; Welton, T. Mixtures of ionic liquids. *Chem Soc Rev*, (2012), *41*(23), 7780–7802.

Ohno, H.; Yoshizawa-Fujita, M.; Kohno, Y. Functional design of ionic liquids: Unprecedented liquids that contribute to energy technology, bioscience, and materials sciences. In *Bulletin of the Chemical Society of Japan* (Vol. 92, Issue 4, pp. 852–868). Chemical Society of Japan.

Oliveira, F. S.; Dohrn, R.; Pereiro, A. B.; Araújo, J. M. M.; Rebelo, L. P. N.; Marrucho, I. M. Designing high ionicity ionic liquids based on 1-ethyl-3-methylimidazolium ethyl sulphate for effective azeotrope breaking. *Fluid Phase Equilib*, (2016), *419*, 57–66.

Omar, K. A.; Sadeghi, R. Physicochemical properties of deep eutectic solvents: A review. In *Journal of Molecular Liquids* (Vol. 360). Elsevier B.V.

Orrling, K. M.; Wu, X.; Russo, F.; Larhed, M. Fast, Acid-Free, and Selective Lactamization of Lactones in Ionic Liquids. *J Org Chem*, (2008), *73*(21), 8627–8630.

Paiva, A.; Craveiro, R.; Aroso, I.; Martins, M.; Reis, R. L.; Duarte, A. R. C. Natural deep eutectic solvents - Solvents for the 21st century. In *ACS Sustainable Chemistry and Engineering* (Vol. 2, Issue 5, pp. 1063–1071). American Chemical Society.

Paiva, A.; Matias, A. A.; Rita, A.; Duarte, C. *How do we drive deep eutectic systems towards an industrial reality?*

Patel, T.; Ishiuji, Y.; Yosipovitch, G. Menthol: A refreshing look at this ancient compound. *J Am Acad Dermatol*, (2007), *57*(5), 873–878.

Patil, V.; Mahajan, S.; Kulkarni, M.; Patil, K.; Rode, C.; Coronas, A.; Yi, G.-R. Synthesis of silver nanoparticles colloids in imidazolium halide ionic liquids and their antibacterial activities for gram-positive and gram-negative bacteria. *Chemosphere*, (2020), *243*, 125302.

Pedro, S. N.; Freire, C. S. R.; Silvestre, A. J. D.; Freire, M. G. The role of ionic liquids in the pharmaceutical field: An overview of relevant applications. In *International Journal of Molecular Sciences* (Vol. 21, Issue 21, pp. 1–50). MDPI AG.

Perdew, J. P.; Burke, K.; Ernzerhof, M. Generalized Gradient Approximation Made Simple. *Phys Rev Lett*, (1996), *77*(18), 3865–3868.

Pérez-Recalde, M.; Ruiz Arias, I. E.; Hermida, É. B. Could essential oils enhance biopolymers performance for wound healing? A systematic review. *Phytomedicine*, (2018), *38*, 57–65.

Perna, F. M.; Vitale, P.; Capriati, V. Deep eutectic solvents and their applications as green solvents. In *Current Opinion in Green and Sustainable Chemistry* (Vol. 21, pp. 27–33). Elsevier B.V.

Petrowsky, M.; Fleshman, A. M.; Frech, R. Application of the Compensated Arrhenius Formalism to Fluidity Data of Polar Organic Liquids. *J Phys Chem B*, (2013), *117*(10), 2971–2978.

Philippi, F.; Welton, T. Targeted modifications in ionic liquids - From understanding to design. *Physical Chemistry Chemical Physics*, (2021), *23*(12), 6993–7021.

Pinto, A. M.; Rodríguez, H.; Arce, A.; Soto, A. Combined physical and chemical absorption of carbon dioxide in a mixture of ionic liquids. *Journal of Chemical Thermodynamics*, (2014), *77*, 197–205.

Pitacco, W.; Samorì, C.; Pezzolesi, L.; Gori, V.; Grillo, A.; Tiecco, M.; Vagnoni, M.; Galletti, P. Extraction of astaxanthin from Haematococcus pluvialis with hydrophobic deep eutectic solvents based on oleic acid. *Food Chem*, (2022), *379*, 132156.

Prabhune, A.; Dey, R. Green and sustainable solvents of the future: Deep eutectic solvents. *J Mol Liq*, (2023), *379*, 121676.

Rahali, S.; Zarrougui, R.; Marzouki, M.; Ghodbane, O. Electrodeposition of silver from the ionic liquid Butylpyridinium dicyanamide. *Journal of Electroanalytical Chemistry*, (2020), *871*, 114289.

Rahman, M. S.; Roy, R.; Jadhav, B.; Hossain, M. N.; Halim, M. A.; Raynie, D. E. Formulation, structure, and applications of therapeutic and amino acid-based deep eutectic solvents: An overview. *J Mol Liq*, (2021), *321*, 114745.

Randall, M. The significance of the activity coefficient. *Transactions of the Faraday Society*, (1927), *23*, 498.

Redlich, O.; Kister, A. T. Algebraic Representation of Thermodynamic Properties and the Classification of Solutions. *Ind Eng Chem*, (1948), *40*(2), 345–348.

Ribeiro, B. D.; Florindo, C.; Iff, L. C.; Coelho, M. A. Z.; Marrucho, I. M. Menthol-based eutectic mixtures: Hydrophobic low viscosity solvents. *ACS Sustain Chem Eng*, (2015), *3*(10), 2469–2477.

Rozas, S. *In-silico desing of deep eutectic solvents for gas separation and energy-related operations*.

Rozas, S.; Alomari, N.; Aparicio, S.; Atilhan, M. Nanoscopic study on carvone-terpene based natural deep eutectic solvents. *J Chem Phys*, (2021), *155*(22).

Rozas, S.; Zamora, L.; Benito, C.; Atilhan, M.; Aparicio, S. A study on monoterpenoid-based natural deep eutectic solvents. *Green Chemical Engineering*, (2023), *4*(1), 99–114.

Sakaebe, H.; Matsumoto, H. N-Methyl-N-propylpiperidinium bis(trifluoromethanesulfonyl)imide (PP13–TFSI) – novel electrolyte base for Li battery. *Electrochem Commun*, (2003), *5*(7), 594–598.

Salvador, A. Romero. Líquidos iónicos a temperatura ambiente: un nuevo medio para las reacciones químicas. *Rev. Real Acad. Cienc. Exact. Fís. Nat.(Esp)* , (2008), *102*(1), 79–90.

Santana-Mayor, Á.; Rodríguez-Ramos, R.; Herrera-Herrera, A. V.; Socas-Rodríguez, B.; Rodríguez-Delgado, M. Á. Deep eutectic solvents. The new generation of green solvents in analytical chemistry. In *TrAC - Trends in Analytical Chemistry* (Vol. 134). Elsevier B.V.

Sappidi, P.; Bara, J. E.; Turner, C. H. Molecular-level behavior of imidazolium-based ionic liquid mixtures. *Chem Eng Sci*, (2021), *229*.

Sas, O. G.; Sánchez, P. B.; González, B.; Domínguez, Á. Removal of phenolic pollutants from wastewater streams using ionic liquids. *Sep Purif Technol*, (2020), *236*, 116310.

Sato, T.; Morinaga, T.; Ishizuk, T. Preparation, Physicochemical Properties and Battery Applications of a Novel Poly(Ionic Liquid). In *Ionic Liquids - New Aspects for the Future*. InTech.

Schrödinger, E. An Undulatory Theory of the Mechanics of Atoms and Molecules. *Physical Review*, (1926), *28*(6), 1049–1070.

Sen, N.; Singh, K. K.; Mukhopadhyay, S.; Shenoy, K. T. Flow synthesis of 1-ethyl-3-methylimidazolium ethyl sulfate in a PTFE micro-capillary: an experimental and numerical study. *Microfluid Nanofluidics*, (2023), *27*(12), 82.

Shahbaz, K.; Mjalli, Farouq. S.; Hashim, M. A.; ALNashef, Inas. M. Using Deep Eutectic Solvents for the Removal of Glycerol from Palm Oil-Based Biodiesel. *Journal of Applied Sciences*, (2010), *10*(24), 3349–3354.

Shi, Y.; Li, X.; Shang, Y.; Li, T.; Zhang, K.; Fan, J. Effective extraction of fluorescent brightener 52 from foods by in situ formation of hydrophobic deep eutectic solvent. *Food Chem*, (2020), *311*, 125870.

Shiflett, M. B.; Yokozeki, A. Separation of carbon dioxide and sulfur dioxide using room-temperature ionic liquid [bmim][MeSO4]. *Energy and Fuels*, (2010), *24*(2), 1001–1008.

Silva, J. M.; Pereira, C. V.; Mano, F.; Silva, E.; Castro, V. I. B.; Sá-Nogueira, I.; Reis, R. L.; Paiva, A.; Matias, A. A.; Duarte, A. R. C. Therapeutic Role of Deep Eutectic Solvents Based on Menthol and Saturated Fatty Acids on Wound Healing. *ACS Appl Bio Mater*, (2019), *2*(10), 4346–4355.

Silva, J. M.; Silva, E.; Reis, R. L.; Duarte, A. R. C. A closer look in the antimicrobial properties of deep eutectic solvents based on fatty acids. *Sustain Chem Pharm*, (2019), *14*, 100192.

Silva, W.; Zanatta, M.; Ferreira, A. S.; Corvo, M. C.; Cabrita, E. J. Revisiting ionic liquid structure-property relationship: A critical analysis. In *International Journal of Molecular Sciences* (Vol. 21, Issue 20, pp. 1–37). MDPI AG.

Singh, S. K.; Savoy, A. W. Ionic liquids synthesis and applications: An overview. In *Journal of Molecular Liquids* (Vol. 297). Elsevier B.V.

Sitze, M. S.; Schreiter, E. R.; Patterson, E. V.; Freeman, R. G. Ionic Liquids Based on FeCl 3 and FeCl 2 . Raman Scattering and ab Initio Calculations. *Inorg Chem*, (2001), *40*(10), 2298–2304.

Smith, E. L.; Abbott, A. P.; Ryder, K. S. Deep Eutectic Solvents (DESs) and Their Applications. In *Chemical Reviews* (Vol. 114, Issue 21, pp. 11060–11082). American Chemical Society.

Sorouraddin, S. M.; Farajzadeh, M. A.; Dastoori, H.; Okhravi, T. Development of an air-assisted liquid-liquid microextraction method based on a ternary solidified deep eutectic solvent in extraction and preconcentration of Cd(II) and Zn(II) ions. *Int J Environ Anal Chem*, (2021), *101*(11), 1567–1580.

Stott, P. Transdermal delivery from eutectic systems: enhanced permeation of a model drug, ibuprofen. *Journal of Controlled Release*, (1998), *50*(1–3), 297–308.

Tan, J.; Lee, S. Y.; Chew, K. W.; Lam, M. K.; Lim, J. W.; Ho, S.-H.; Show, P. L. A review on microalgae cultivation and harvesting, and their biomass extraction processing using ionic liquids. *Bioengineered*, (2020), *11*(1), 116–129.

Tan, Z.; Welz-Biermann, U.; Yan, P.-F.; Liu, Q.-S.; Fang, D.-W. Thermodynamic Properties of Ionic Liquids - Measurements and Predictions -. In *Ionic Liquids: Theory, Properties, New Approaches*. InTech.

Tian, Y.; Feng, X.; Zhang, Y.; Yu, Q.; Wang, X.; Tian, M. Determination of Volatile Water Pollutants Using Cross-Linked Polymeric Ionic Liquid as Solid Phase Micro-Extraction Coatings. *Polymers (Basel)*, (2020), *12*(2), 292.

Torres, G.; Nájera, F.; Vida, Y. *Introducción a la Química Computacional*.

Trenzado, J. L. *Análisis experimental y teórico de diversas propiedades termofísicas de los sistemas ternarios [C5H10O2 + C7H16 + (C8H18, C8H17Cl, C8H18O)] y sus constituyentes binarios en el intervalo de temperaturas (283.15-313.15) K*.

Trenzado, J. L.; Rodríguez, Y.; Gutiérrez, A.; Cincotti, A.; Aparicio, S. Experimental and molecular modeling study on the binary mixtures of [EMIM][BF4] and [EMIM][TFSI] ionic liquids. *J Mol Liq*, (2021), *334*.

Troter, D. Z.; Todorović, Z. B.; Đokić-Stojanović, D. R.; Stamenković, O. S.; Veljković, V. B. Application of ionic liquids and deep eutectic solvents in biodiesel production: A review. *Renewable and Sustainable Energy Reviews*, (2016), *61*, 473–500.

Umapathi, R.; Attri, P.; Venkatesu, P. Thermophysical Properties of Aqueous Solution of Ammonium-Based Ionic Liquids. *J Phys Chem B*, (2014), *118*(22), 5971–5982.

Vaidya, A.; Mitragotri, S. Ionic liquid-mediated delivery of insulin to buccal mucosa. *Journal of Controlled Release*, (2020), *327*, 26–34.

Van Osch, D. J. G. P.; Zubeir, L. F.; Van Den Bruinhorst, A.; Rocha, M. A. A.; Kroon, M. C. Hydrophobic deep eutectic solvents as water-immiscible extractants. *Green Chemistry*, (2015), *17*(9), 4518–4521.

Van Wazcr, J. R.; Lyons, J. W. Viscosity and Flow Measurement. *Interscience Pubi*, (1963).

Vataščin, E.; Havlová, M.; Dohnal, V. Phase equilibria and volumetric and viscosity behavior of the aqueous double salt ionic liquid [EMIM][SCN]x[MeSO3](1-x). *Fluid Phase Equilib*, (2021), *548*.

Ventura, S. P. M.; E Silva, F. A.; Quental, M. V.; Mondal, D.; Freire, M. G.; Coutinho, J. A. P. Ionic-Liquid-Mediated Extraction and Separation Processes for Bioactive Compounds: Past, Present, and Future Trends. In *Chemical Reviews* (Vol. 117, Issue 10, pp. 6984–7052). American Chemical Society.

Walczak, M.; Michalska-Sionkowska, M.; Kaczmarek, B.; Sionkowska, A. Surface and antibacterial properties of thin films based on collagen and thymol. *Mater Today Commun*, (2020), *22*, 100949.

Walden, P. Über die Molekulargrösse und elektrische Leitfähigkeit einiger geschmolzener Salze. Bull Acad Imper Sci (St Petersburg) 8: 405–422. In *Zeitschr. f. Elektrochemie* (Vol. 59, Issue 5). Benrath und Wainoff.

Wang, B.; Qin, L.; Mu, T.; Xue, Z.; Gao, G. Are Ionic Liquids Chemically Stable? In *Chemical Reviews* (Vol. 117, Issue 10, pp. 7113–7131). American Chemical Society.

Wang, H.; Li, J.; Zeng, X.; Tang, X.; Sun, Y.; Lei, T.; Lin, L. Extraction of cellulose nanocrystals using a recyclable deep eutectic solvent. *Cellulose*, (2020), *27*(3), 1301–1314.

Wang, M.; Zhang, L.; Gao, L.; Pi, K.; Zhang, J.; Zheng, C. Improvement of the CO2 absorption performance using ionic liquid [NH2emim][BF4] and [emim][BF4]/[bmim][BF 4] mixtures. *Energy and Fuels*, (2013), *27*(1), 461–466.

Wang, Z.-W.; Wang, L.-S. Friedel–Crafts phosphylation of benzene catalyzed by [trEHAm]Cl-XAlCl3 ionic liquids. *Appl Catal A Gen*, (2004), *262*(1), 101–104.

Weingärtner, H. Understanding ionic liquids at the molecular level: Facts, problems, and controversies. In *Angewandte Chemie - International Edition* (Vol. 47, Issue 4, pp. 654–670).

Weldemhret, T. G.; Bañares, A. B.; Ramos, K. R. M.; Lee, W.-K.; Nisola, G. M.; Valdehuesa, K. N. G.; Chung, W.-J. Current advances in ionic liquid-based pre-treatment and depolymerization of macroalgal biomass. *Renew Energy*, (2020), *152*, 283–299.

Welton, T. Ionic liquids: a brief history. In *Biophysical Reviews* (Vol. 10, Issue 3, pp. 691–706). Springer Verlag.

Wilkes, J. S.; Zaworotko, M. J.; Etmeim+, F. *Air and Water Stable 1-Ethyl-3-methylimidazolium Based Ionic Liquids*.

Wöhler, F.; Liebig, J. Untersuchungen über die Natur der Harnsäure. *Annalen Der Pharmacie*, (1838), *26*(3), 241–336.

Xiao, H. Ionic Liquid Lubricants: Basics and Applications. *Tribology Transactions*, (2017), *60*(1), 20–30.

Xu, K.; Zhang, S.; Angell, C. A. Room Temperature Inorganic “Quasi-Molten Salts” as Alkali-Metal Electrolytes. *J Electrochem Soc*, (1996), *143*(11), 3548–3554.

Xu, Q. B.; Wang, X. Y.; Wang, P.; Cheng, L. Z.; Wan, Y. P.; Wang, Z. Q. Sustainable and superhydrophobic coating from epoxidized soybean oil and stearic acid on cotton fabric etched by deep eutectic solvent. *Mater Today Chem*, (2022), *26*, 101211.

Yadav, A.; Guha, A.; Pandey, A.; Pal, M.; Trivedi, S.; Pandey, S. Densities and dynamic viscosities of ionic liquids having 1-butyl-3-methylimidazolium cation with different anions and bis(trifluoromethylsulfonyl)imide anion with different cations in the temperature range (283.15 to 363.15) K. *Journal of Chemical Thermodynamics*, (2018), *116*, 67–75.

Yang, D.; Wang, Y.; Li, H.; Yang, Y. Acid-base-governed deep eutectic solvent-based microextraction combined with magnetic solid-phase extraction for determination of phenolic compounds. *Microchimica Acta*, (2020), *187*(2), 124.

Yang, S.; Lu, X.; Zhang, Y.; Xu, J.; Xin, J.; Zhang, S. Separation and characterization of cellulose I material from corn straw by low-cost polyhydric protic ionic liquids. *Cellulose*, (2018), *25*(6), 3241–3254.

Yang, Y.; Zhao, J.; Li, Y. Theoretical Study of the ESIPT Process for a New Natural Product Quercetin. *Sci Rep*, (2016), *6*(1), 32152.

Yang, Z.; Huang, Z.-L. Enzymatic synthesis of sugar fatty acid esters in ionic liquids. *Catal Sci Technol*, (2012), *2*(9), 1767.

Yoshizawa, M.; Xu, W.; Angell, C. A. Ionic Liquids by Proton Transfer: Vapor Pressure, Conductivity, and the Relevance of Δp *K* a from Aqueous Solutions. *J Am Chem Soc*, (2003), *125*(50), 15411–15419.

Yuan, Z.; Liu, H.; Yong, W. F.; She, Q.; Esteban, J. Status and advances of deep eutectic solvents for metal separation and recovery. In *Green Chemistry* (Vol. 24, Issue 5, pp. 1895–1929). Royal Society of Chemistry.

Zafarani-Moattar, M. T.; Shekaari, H. Application of Prigogine–Flory–Patterson theory to excess molar volume and speed of sound of 1-n-butyl-3-methylimidazolium hexafluorophosphate or 1-n-butyl-3-methylimidazolium tetrafluoroborate in methanol and acetonitrile. *J Chem Thermodyn*, (2006), *38*(11), 1377–1384.

Zainal-Abidin, M. H.; Hayyan, M.; Wong, W. F. Hydrophobic deep eutectic solvents: Current progress and future directions. In *Journal of Industrial and Engineering Chemistry* (Vol. 97, pp. 142–162). Korean Society of Industrial Engineering Chemistry.

Zandu, S. K.; Chopra, H.; Singh, I. Ionic Liquids for Therapeutic and Drug Delivery Applications. *Curr Drug Res Rev*, (2020), *12*(1), 26–41.

Zarrougui, R.; Dhahbi, M.; Lemordant, D. Transport and Thermodynamic Properties of Ethylammonium Nitrate–Water Binary Mixtures: Effect of Temperature and Composition. *J Solution Chem*, (2015), *44*(3–4), 686–702.

Zhang, D.; Deng, Y. F.; Li, C. B.; Chen, J. Separation of Ethyl Acetate−Ethanol Azeotropic Mixture Using Hydrophilic Ionic Liquids. *Ind Eng Chem Res*, (2008), *47*(6), 1995–2001.

Zhang, H.; Luo, Y.; Chen, D.; Liu, H.; Cui, P.; Yang, J. Ionic liquid-derived core–shell gold@palladium nanoparticles with tiny sizes for highly efficient electrooxidation of ethanol. *Green Energy & Environment*, (2021), *6*(2), 229–235.

Zhang, H.; Wu, Y.; Zhang, J.; Wu, Z.; Zhan, X. Separation cellulose nanocrystals from microcrystalline cellulose using hydrated deep eutectic solvent and high shear force. *Ind Crops Prod*, (2022), *189*, 115781.

Zhang, K.; Li, S.; Liu, C.; Wang, Q.; Wang, Y.; Fan, J. A hydrophobic deep eutectic solvent-based vortex-assisted dispersive liquid–liquid microextraction combined with HPLC for the determination of nitrite in water and biological samples. *J Sep Sci*, (2019), *42*(2), 574–581.

Zhang, Q.; De Oliveira Vigier, K.; Royer, S.; Jérôme, F. Deep eutectic solvents: Syntheses, properties and applications. *Chem Soc Rev*, (2012), *41*(21), 7108–7146.

Zhang, Q.; Zhang, S.; Deng, Y. Recent advances in ionic liquid catalysis. *Green Chemistry*, (2011), *13*(10), 2619–2637.

Zhang, X.; Zhang, X.; Dong, H.; Zhao, Z.; Zhang, S.; Huang, Y. Carbon capture with ionic liquids: Overview and progress. In *Energy and Environmental Science* (Vol. 5, Issue 5, pp. 6668–6681).

Zhao, H. Review: Current studies on some physical properties of ionic liquids. *Phys Chem Liquids*, (2003), *41*(6), 545–557.

Zhao, H. Innovative applications of ionic liquids as “green” engineering liquids. In *Chemical Engineering Communications* (Vol. 193, Issue 12, pp. 1660–1677).

Zheng, C.; Zhou, J.; Pei, Y.; Yang, B. Equilibrium Thermodynamic Properties of Aqueous Solutions of Ionic Liquid 1-Ethyl-3-Methylimidazolium Methanesulfonate [EMIM][MeSO3]. *Sci Rep*, (2020), *10*(1), 3174.

Zheng, Y.; Wang, D.; Kaushik, S.; Zhang, S.; Wada, T.; Hwang, J.; Matsumoto, K.; Hagiwara, R. Ionic Liquid Electrolytes for Next-generation Electrochemical Energy Devices. In *EnergyChem* (Vol. 4, Issue 3). Elsevier B.V.

Zhou, F.; Liang, Y.; Liu, W. Ionic liquid lubricants: Designed chemistry for engineering applications. *Chem Soc Rev*, (2009), *38*(9), 2590–2599.

Zhou, W.; Zhang, M.; Kong, X.; Huang, W.; Zhang, Q. Recent Advance in Ionic-Liquid-Based Electrolytes for Rechargeable Metal-Ion Batteries. In *Advanced Science* (Vol. 8, Issue 13). John Wiley and Sons Inc.

Zhou, Y. *Ionic Liquids as Lubricant Additives-a Review*.

Zubeir, L. F.; van Osch, D. J. G. P.; Rocha, M. A. A.; Banat, F.; Kroon, M. C. Carbon Dioxide Solubilities in Decanoic Acid-Based Hydrophobic Deep Eutectic Solvents. *J Chem Eng Data*, (2018), *63*(4), 913–919.

Anexo I
Geles DSILs

Durante la fase de experimentación, se observaron comportamientos inesperados en la mezcla de ciertos DSIL. Específicamente, de los seis DSIL propuestos, las combinaciones de [EMIM][TSFI] con [EMIM][MeSO3] y [EMIM][TSFI] con [EMIM][EtSO4] mostraron características a temperatura ambiente que las diferenciaban de las demás mezclas binarias estudiadas. Su singularidad radica en que estas mezclas presentan un estado altamente viscoso a temperatura ambiente, podría decirse que cuando se homogeniza la mezcla, adquiere una consistencia similar a la de un *gel* (figura 70). A pesar de que la consistencia a temperatura ambiente obstaculizó la ejecución del diseño experimental tal como se había previsto, se llevó a cabo un análisis térmico exhaustivo de estos DSIL para evaluar y delimitar su comportamiento en función de la temperatura.

Figura 70. Aspecto del DSIL x[EMIM][TSFI]+(1-x)[EMIM][MeSO3], a la fracción molar x=0.9 a temperatura ambiente. Se observa antes de la agitación dos fases totalmente líquidas, mientras que tras agitación se aprecia en la imagen que la mezcla presenta una consistencia similar a la de un gel .

Para ambos DSIL se prepararon según el procedimiento habitual 5 fracciones molares (0.1 / 0.3 / 0.5 / 0.7 / 0.9) y se observó la evolución de su aspecto y comportamiento en el rango de temperaturas comprendido entre los 298,15 K y los 358,15 K en intervalos de 10,0 K. Las muestras fueron colocadas en un baño maría a diversas temperaturas y se mantuvieron en condiciones constantes durante un período de 22 a 24 horas. El seguimiento de su comportamiento comenzó el día de la preparación, denominado *día 0*. Tras alcanzar la temperatura máxima del rango estudiado, las muestras se mantuvieron a temperatura ambiente durante 48 horas (*día +48h*). El propósito de la observación *día +48h* fue evaluar el comportamiento de los DSIL después de un intervalo prolongado de estabilidad térmica, verificando si volvían a su estado gel inicial. A continuación, se presentan de manera detallada los resultados cualitativos obtenidos en cada una de las fracciones molares estudiadas.

I. Estudio [EMIM][TSFI] + [EMIM][$MeSO_3$]

Mezcla 0,1 [EMIM][TSFI] + 0,9 [EMIM][$MeSO_3$]

La mezcla permanece transparente y homogénea a lo largo del rango de temperaturas estudiado.

Día 0	25°C	35°C	45°C

55°C	65°C	75°C	85°C	D+48h

Mezcla 0,3 [EMIM][TSFI] + 0,7 [EMIM][$MeSO_3$]

La mezcla permanece transparente y homogénea a lo largo del rango de temperaturas estudiado.

Día 0	25°C	35°C	45°C

55°C	65°C	75°C	85°C	D+48h

<u>Mezcla 0,5 [EMIM][TSFI] + 0,5 [EMIM][$MeSO_3$]</u>

En esta fracción molar, tras agitación inicial (día 0), aparece en el seno de la mezcla sólidos con aspecto de "hilos" cortos y finos. Tras 24 horas a 25 °C estos "hilos" se depositan en el fondo del tarro, sin embargo, tras agitación se dispersan por todo el líquido. Este comportamiento se mantiene entre los 25 °C y los 55 °C.

A 65 °C, 75 °C y 85 °C desaparece por completo cualquier tipo de partícula sólida, quedando un líquido totalmente transparente y homogéneo, que no sufre variaciones al agitarlo.

Después de haberlo sometido a la rampa de temperatura, tras 48 horas a temperatura ambiente, vuelven a aparecer en el seno de la mezcla estos "hilos" finos y cortos que se dispersan con facilidad en la mezcla.

Día 0		25°C	
Antes agitar	Tras agitación	Antes agitar	Tras agitación
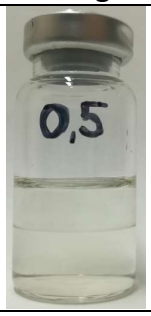			

35°C		45°C	
Antes agitar	Tras agitación	Antes agitar	Tras agitación

55°C		65°C	75°C
Antes agitar	Tras agitación		
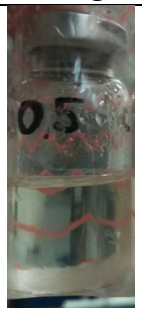			

85°C	48h	
	Antes agitar	Tras agitación
		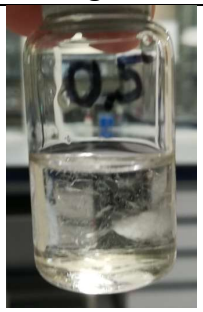

Mezcla 0,7 [EMIM][TSFI] + 0,3 [EMIM][$MeSO_3$]

Inicialmente tras la agitación (día 0), aparecen en la mezcla partículas muy pequeñas a una concentración muy baja. Sin embargo, cuando sometemos la mezcla a 25 °C durante 24 horas aparecen unos copos opacos que ocupan más del 50% del volumen de la mezcla. Tras agitación, la mezcla se vuelve translúcida, pero en apariencia homogénea.

Este comportamiento se mantiene en todo el rango de temperaturas estudiado. A medida que aumenta la temperatura, se observa de manera cualitativa como el volumen total de los copos sólidos disminuye. En apariencia generando una capa más compacta en el fondo del tarro.

Tras 48h a temperatura ambiente, la mezcla no vuelve a su comportamiento inicial. Permanece en el fondo del frasco un volumen total de partículas similar a las temperaturas intermedias.

Día 0		25°C	
Antes agitar	Tras agitación	Antes agitar	Tras agitación

35°C		45°C	
Antes agitar	Tras agitación	Antes agitar	Tras agitación

55°C		65°C	
Antes agitar	Tras agitación	Antes agitar	Tras agitación

75°C		85°C	
Antes agitar	Tras agitación	Antes agitar	Tras agitación

D+48h	
Antes agitar	Tras agitación
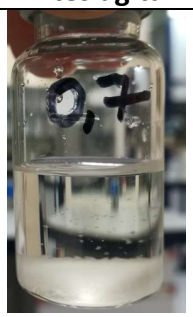	

<u>Mezcla 0,9 [EMIM][TSFI] + 0,1 [EMIM][$MeSO_3$]</u>

Tras una leve agitación inicial, la mezcla se transforma en un gel de forma inmediata. En el fondo del frasco permanece una pequeña fracción líquida sin mezcla, que una vez se forma el gel, no se puede integrar con el resto. La viscosidad del gel es tan alta que no discurre por las paredes interiores del frasco.

El comportamiento observable en todo el rango de temperaturas, **25°C a 85°C,** permanece constante. Tras un período de 22 a 24 horas al baño maría para cada temperatura, la mezcla exhibe dos fases bien diferenciadas: en la parte inferior del frasco se observa una fase aparentemente sólida, su apariencia es de polvo muy fino y compacto. En la fase superior un líquido translúcido, sin presencia aparente de sólidos en su seno. Una vez se realiza la agitación, se forma una mezcla translúcida en apariencia homogénea.

Después de 48h a temperatura ambiente aparecen nuevamente dos fases, pero en esta ocasión el líquido que queda en la fase superior antes de la agitación no presenta una apariencia tan nítida como a temperaturas mayores. Tras la agitación, vuelve a convertirse en una mezcla translúcida de apariencia homogénea, pero sin llegar a convertirse en un gel.

Día 0		**25°C**	
Antes agitar	**Tras agitación**	**Antes agitar**	**Tras agitación**
35°C		**45°C**	
Antes agitar	**Tras agitación**	**Antes agitar**	**Tras agitación**
55°C		**65°C**	
Antes agitar	**Tras agitación**	**Antes agitar**	**Tras agitación**
		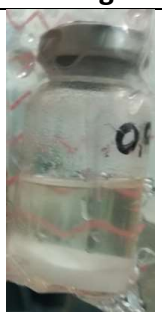	

75°C		85°C	
Antes agitar	**Tras agitación**	**Antes agitar**	**Tras agitación**

D+48h	
Antes agitar	**Tras agitación**
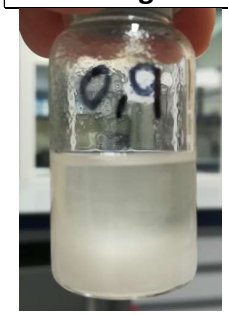	

La tabla que se muestra a continuación presenta un resumen cualitativo de la apariencia de las mezclas antes de realizar la agitación de las mismas, en todas las fracciones molares y temperaturas estudiadas.

Tabla 27. Resumen cualitativo del comportamiento de la mezcla [EMIM][TSFI] + [EMIM][$MeSO_3$].

<table>
<tr><th></th><th>0,1
[EMIM][TSFI]</th><th>0,3
[EMIM][TSFI]</th><th>0,5
[EMIM][TSFI]</th><th>0,7
[EMIM][TSFI]</th><th>0,9
[EMIM][TSFI]</th></tr>
<tr><td>Día 0</td><td rowspan="10">Mezcla transparente y homogénea</td><td rowspan="10">Mezcla transparente y homogénea</td><td rowspan="5">Sólidos
Líquido transparente</td><td rowspan="10">Sólidos
Líquido transparente</td><td>Gel</td></tr>
<tr><td>25 °C</td><td rowspan="9">Sólidos
Líquido transparente</td></tr>
<tr><td>35 °C</td></tr>
<tr><td>45 °C</td></tr>
<tr><td>55 °C</td></tr>
<tr><td>65 °C</td><td rowspan="3">Mezcla transparente y homogénea</td></tr>
<tr><td>75 °C</td></tr>
<tr><td>85 °C</td></tr>
<tr><td>D+48 h</td><td>Sólidos
Líquido transparente</td></tr>
</table>

II. Estudio [EMIM][TSFI] + [EMIM][EtSO$_4$]

Mezcla 0,1 [EMIM][TSFI] + 0,9 [EMIM][EtSO$_4$]

La mezcla permanece transparente y homogénea a lo largo del rango de temperaturas estudiado.

Día 0	25°C	35°C	45°C

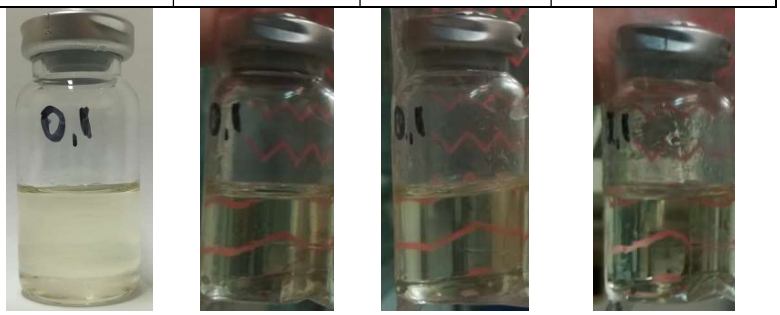

55°C	65°C	75°C	85°C	D+48h

Mezcla 0,3 [EMIM][TSFI] + 0,7 [EMIM][EtSO$_4$]

Tras realizar la agitación inicial (día 0) aparecen ciertos sólidos en el seno en la mezcla.

La mezcla se comporta de la misma manera entre 25°C y 85°C. A partir de 25°C las partículas sólidas desaparecen, quedando una mezcla homogénea y totalmente transparente.

Después de 48h no se vuelven a apreciar sólidos en la mezcla, homogénea y totalmente transparente.

Día 0		25°C	35°C	45°C
Antes agitar	Tras agitación			

55°C	65°C	75°C	85°C	D+48h

<u>Mezcla 0,5 [EMIM][TSFI] + 0,5 [EMIM][$EtSO_4$]</u>

A esta fracción molar, tras la agitación inicial, se forman unos pocos copos muy finos y translúcidos en el fondo del frasco.

La mezcla se comporta de la misma manera entre 25 °C y 85 °C. A partir de 25 °C las partículas sólidas desaparecen, quedando una mezcla homogénea y totalmente transparente.

Después de 48h no se vuelven a apreciar sólidos en la mezcla, homogénea y totalmente transparente.

Día 0		25°C
Antes agitar	Tras agitación	
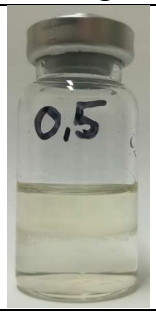		

35°C	45°C	55°C	65°C
			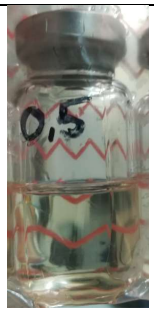

75°C	85°C	48h
		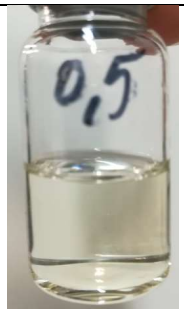

Mezcla 0,7 [EMIM][TSFI] + 0,3 [EMIM][EtSO$_4$]

Tras realizar la mezcla inicial, (día 0) aparecen unas pequeñas partículas en el líquido. A 25 °C y 35 °C se observa en el fondo del frasco una fase de las partículas sólidas. Al agitar, la mezcla se vuelve turbia, pero de apariencia homogénea.

El comportamiento observable entre 45 °C y 85 °C es el mismo: desaparece de manera visible las partículas sólidas observadas anteriormente, quedando una mezcla homogénea y transparente.

Tras 48h a temperatura ambiente la mezcla vuelve a su comportamiento inicial, observándose de nuevo pequeñas partículas en la mezcla.

Día 0		25°C	
Antes agitar	Tras agitación	Antes agitar	Tras agitación
	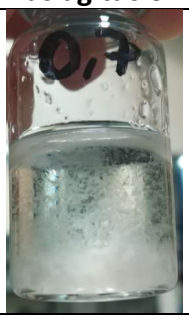		

35°C		45°C	55°C
Antes agitar	Tras agitación		

65°C	75°C	85°C

48h	
Antes agitar	Tras agitación
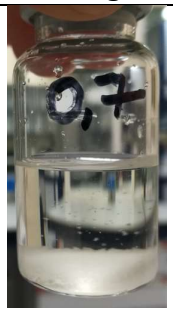	

<u>Mezcla 0,9 [EMIM][TSFI] + 0,1 [EMIM][$EtSO_4$]</u>

Tras una leve agitación inicial, la mezcla se transforma en un gel de forma inmediata. En el fondo del frasco permanece una pequeña fracción líquida sin mezcla, que una vez se forma el gel, no se puede integrar con el resto. La viscosidad del gel es tan alta que no discurre por las paredes interiores del frasco.

Tras 24 horas a 25 °C, se observan hay dos fases bien diferenciadas, en esta ocasión la fase superior es la fase gelificada y la inferior la fase líquida, al contrario que con el DSIL 0,9[EMIM][TSFI]+0,1[EMIM][MeSO3]. Se realiza agitación y no se consigue obtener una mezcla homogénea.

En el rango de temperaturas entre 35 °C y 45 °C, también se observan dos fases bien diferenciadas, pero a estas temperaturas sí es posible mezclar ambas fases completamente, quedando una mezcla en apariencia homogénea. **A 55 °C, 65°C y 85 °C,** no se aprecia separación de fases, permanece una mezcla líquida homogénea pero translúcida. Sin embargo, a 75 °C es posible observar una difusa separación de fases, pero a esta temperatura la aparente fase sólida se encuentra bajo la fase líquida.

Después de 48h la mezcla no vuelve a su comportamiento inicial. Aparecen de nuevo dos fases, y tras una leve agitación, la mezcla vuelve a convertirse en una mezcla translúcida de apariencia homogénea, pero no gelifica.

Día 0		25°C	
Antes agitar	Tras agitación	Antes agitar	Tras agitación
	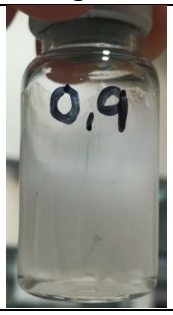		

35°C		45°C	
Antes agitar	Tras agitación	Antes agitar	Tras agitación
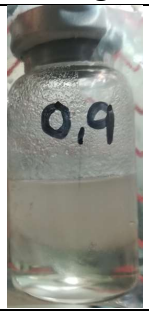	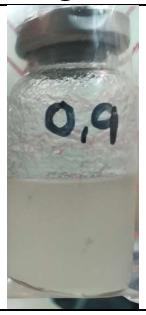		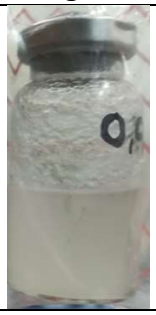

55°C	65°C	75°C	
		Antes agitar	Tras agitación
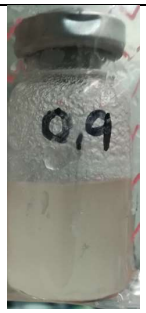	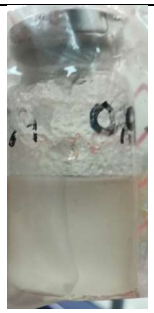	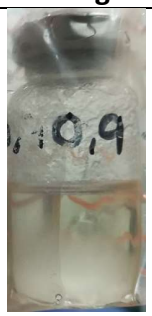	

85°C	48h	
	Antes agitar	Tras agitación
	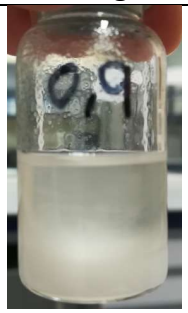	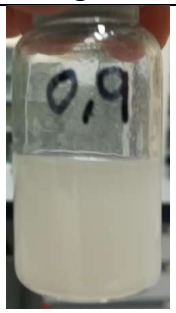

La tabla que se muestra a continuación presenta un resumen cualitativo de la apariencia de las mezclas antes de realizar la agitación de las mismas, en todas las fracciones molares y temperaturas estudiadas.

Tabla 28. Resumen cualitativo del comportamiento de la mezcla [EMIM][TSFI] + [EMIM][EtSO$_4$].

<table>
<tr><th></th><th>0,1
[EMIM][TSFI]</th><th>0,3
[EMIM][TSFI]</th><th>0,5
[EMIM][TSFI]</th><th>0,7
[EMIM][TSFI]</th><th>0,9
[EMIM][TSFI]</th></tr>
<tr><td>Día 0</td><td rowspan="8">Mezcla transparente y homogénea</td><td>Sólidos
Líquido transparente</td><td>Sólidos
Líquido transparente</td><td rowspan="3">Sólidos
Líquido transparente</td><td>Gel</td></tr>
<tr><td>25 °C</td><td rowspan="6">Mezcla transparente y homogénea</td><td rowspan="6">Mezcla transparente y homogénea</td><td rowspan="7">Sólidos
Líquido transparente</td></tr>
<tr><td>35 °C</td></tr>
<tr><td>45 °C</td><td rowspan="5">Mezcla transparente y homogénea</td></tr>
<tr><td>55 °C</td></tr>
<tr><td>65 °C</td></tr>
<tr><td>75 °C</td></tr>
<tr><td>85 °C</td><td rowspan="2">Sólidos
Líquido transparente</td></tr>
<tr><td>D+48 h</td></tr>
</table>